NOAA Technical Memorandum OAR ARL-278

DEPARTMENT OF COMMERCE
UNITED STATES OF AMERICA

Climatography of the Idaho National Laboratory 4th Edition

K.L. Clawson
J.D. Rich
R.M. Eckman
N.F. Hukari
D. Finn
B.R. Reese

NOAA/ Air Resources Laboratory/ Field Research Division
Idaho Falls, Idaho

Air Resources Laboratory (ARL)
College Park, Maryland

June 2018

---

noaa NATIONAL OCEANIC AND
ATMOSPHERIC ADMINISTRATION

Office of Oceanic and
Atmospheric Research

NOAA Technical Memorandum OAR ARL-278

Climatography of the Idaho National Laboratory 4th Edition

K.L. Clawson
J.D. Rich
R.M. Eckman
N.F. Hukari
D. Finn
B.R. Reese

NOAA/ Air Resources Laboratory/ Field Research Division
Idaho Falls, Idaho

Air Resources Laboratory (ARL)
College Park, Maryland

June 2018

UNITED STATES
DEPARTMENT OF COMMERCE

Wilbur Ross
Secretary

NATIONAL OCEANIC AND
ATMOSPHERIC ADMINISTRATION

Benjamin Friedman
Under Secretary for Oceans
and Atmosphere/Acting
Administrator

Office of Oceanic and
Atmospheric Research

Craig McLean
Assistant Administrator
Oceanic & Atmospheric
Research

NOTICE

This report was prepared as an account of work sponsored by an agency of the United States Government. Neither the United States Government nor any agency thereof, or any of their employees, makes any warranty, expressed or implied, or assumes any legal liability or responsibility for any third party's use, or the results of such use, of any information, apparatus, product, or process disclosed in this report, or represents that its use by such third party would not infringe on privately owned rights. Mention of a commercial company or product does not constitute an endorsement by NOAA/OAR. Use of information from this publication concerning proprietary products or tests of such products for publicity or advertising is not authorized.

PREFACE

This climatology is a product of the Field Research Division (FRD) of the Air Resources Laboratory (ARL). The ARL is a component of the National Oceanic and Atmospheric Administration's (NOAA) Office of Oceanic and Atmospheric Research (OAR). NOAA is a federal agency "that enriches life through science. [Its] reach goes from the surface of the sun to the depths of the ocean floor as [it] work[s] to keep citizens informed of the changing environment around them. From daily weather forecasts, severe storm warnings, and climate monitoring to fisheries management, coastal restoration and supporting marine commerce, NOAA's products and services support economic vitality and affect more than one-third of America's gross domestic product. NOAA's dedicated scientists use cutting-edge research and high-tech instrumentation to provide citizens, planners, emergency managers and other decision makers with reliable information they need when they need it (http://www.noaa.gov/about-our-agency, accessed August 22, 2016).

NOAA's Vision of the Future

NOAA's vision of the future is for the nation to have: 1) resilient ecosystems, communities, and economies; and 2) healthy ecosystems, communities and economies that are resilient in the face of change. "Earth's ecosystems support people, communities, and economies. Our own human health, prosperity, and well-being depend upon the health and resilience of natural and social ecosystems. Managing this interdependence requires timely and usable scientific information to make decisions. Human well-being requires preparing for and responding to changes within these natural systems. NOAA's mission of science, service, and stewardship is directed to a vision of the future where societies and their ecosystems are healthy and resilient in the face of sudden or prolonged change.

"A vision of resilience will guide NOAA and its partners in a collective effort to reduce the vulnerability of communities and ecological systems in the short-term, while helping society avoid or adapt to potential long-term environmental, social, and economic changes. To achieve this vision we must understand current Earth system conditions, project future changes, and help people make informed decisions that reduce their vulnerability to environmental hazards and stresses that emerge over time, while at the same time increase their ability to cope with them. Resilient human communities and economies maintain or improve their health and vitality over time by anticipating, absorbing, diffusing, and adapting to change. Resilient communities and institutions derive goods from ecosystems in a way that does not compromise ecosystem integrity, yet is economically feasible and socially just for future generations." (http://www.noaa.gov/our-mission-and-vision, accessed August 24, 2016) ARLFRD shares NOAA's vision with an emphasis on fostering resiliency in the INL community and the surrounding ecosystem through the study of local weather and climate.

NOAA's Mission

NOAA's Mission is to understand and predict changes in climate, weather, oceans, and coasts, to share that knowledge and information with others, and to conserve and manage coastal and marine ecosystems and resources. NOAA specifically seeks to: 1) understand and predict changes in climate, weather, oceans and coasts; 2) share that knowledge and information with others; and 3) conserve and manage coastal and marine ecosystems and resources. These three objectives come under the main thrusts of science, service, and stewardship.

"Science at NOAA is the systematic study of the structure and behavior of the ocean, atmosphere, and related ecosystems; integration of research and analysis; observations and monitoring; and environmental modeling. NOAA science includes discoveries and ever new understanding of the oceans and atmosphere, and the application of this understanding to such issues as the causes and consequences of climate change, the physical dynamics of high-impact weather events, the dynamics of complex ecosystems and biodiversity, and the ability to model and predict the future states of these systems. Science provides the foundation and future promise of the service and stewardship elements of NOAA's mission.

"Service is the communication of NOAA's research, data, information, and knowledge for use by the Nation's businesses, communities, and people's daily lives. NOAA services include climate predictions and projections; weather and water reports, forecasts and warnings; nautical charts and navigational information; and the continuous delivery of a range of Earth observations and scientific data sets for use by public, private, and academic sectors.

"Stewardship is NOAA's direct use of its knowledge to protect people and the environment, as the Agency exercises its direct authority to regulate and sustain marine fisheries and their ecosystems, protect endangered marine and anadromous species, protect and restore habitats and ecosystems, conserve marine sanctuaries and other protected places, respond to environmental emergencies, and aid in disaster recovery. The foundation of NOAA's long-standing record of scientific, technical, and organizational excellence is its people. NOAA's diverse functions require an equally diverse set of skills and constantly evolving abilities in its workforce.

"Also underlying NOAA's continued success is its unique infrastructure. NOAA's core mission functions require satellite systems, ships, buoys, aircraft, research facilities, high-performance computing, and information management and distribution systems. The agency provides research-to-application capabilities that can recognize and apply significant new understanding to questions, develop research products and methods, and apply emerging science and technology to user needs. NOAA invests in and depends heavily on the science, management, and engagement capabilities of its partners. Collectively, NOAA's organizational enterprise-wide capabilities — its people, infrastructure, research, and partnerships — are essential for NOAA to achieve its vision, mission, and long-term goals." (http://www.noaa.gov/our-mission-and-vision, accessed August 23, 2016) ARLFRD is likewise focused on science, service, and stewardship, with emphases on understanding and predicting changes in climate and weather, and sharing that knowledge and information with others.

OAR's Vision and Mission

OAR's vision is to be a trusted world leader in observing, modeling, understanding and predicting the Earth system. OAR's mission is to conduct research to understand and predict the Earth system; develop technology to improve NOAA science, service and stewardship; and transition the results so they are useful to society. "Within NOAA, OAR serves a unique role. NOAA's other line offices specialize in operational services: managing environmental data, providing information on ocean environments, delivering weather forecasts and warnings, and acting as stewards of living marine resources and habitats. OAR, on the other hand, specializes in improving these capabilities, and improving our understanding of the Earth system across these mission areas. OAR conducts R&D that increases our knowledge of climate, weather, oceans and coasts, and it increases the effectiveness of NOAA's service lines, as well as a great range of partners in the public, private, and academic sectors.

"OAR supports the R&D for ocean, Great Lakes, and atmosphere that private, academic, and other government organizations would not otherwise provide. The results of R&D at OAR are essential public goods that are produced nowhere else. They include environmental data sets; peer-reviewed journal articles; predictive models of weather, climate, and ecological systems; training and education on the science and technology we create; new commercial technologies; as well as the next generation of scientists, engineers, and entrepreneurs. The anticipated benefits of these outputs are not always predictable, may not even be measurable, and could take many years to realize. Nevertheless, we know that we cannot benefit from the science and technology of tomorrow without investing in research and development today. Reward requires risk, and this is the role of OAR." (OAR Strategic Plan, April 2014) ARLFRD contributes to OAR's mission by conducting research in weather and climate that results in environmental data sets and peer-reviewed journal articles.

ARL's Vision and Mission

ARL's vision is to maintain a world-renowned research laboratory highly regarded for its scientific accomplishments in atmospheric dispersion, atmospheric chemistry, climate observations and analysis, and boundary layer science. ARL's mission is to provide the highest quality atmospheric and meteorological research and services to our partners, the research community, and society to protect human health and our environment.

"The R&D conducted by ARL over the past 65+ years is directed toward the protection of human health and the environment. This includes improving the understanding and/or prediction of serious societal issues, such as air pollution, airborne release and dispersion of harmful materials from accidents or through malicious intent, deposition of harmful materials onto our terrestrial and aquatic ecosystems, and changes in our climate. When necessary and where appropriate, ARL scientists work across locations to conduct research via atmospheric modeling, assessments, and field studies.

"ARL's R&D is conducted in four research areas with an emphasis on transitioning Research to Applications (R2A) within NOAA and to operations in other agencies. ARL also produces assessments and reports; publishes in the peer reviewed literature; and develops and operates internet-based applications and display systems." (ARL Strategic Plan, 2015-2019) ARL's four R&D themes are: 1) atmospheric transport and dispersion, 2) atmospheric chemistry and deposition, 3) climate observations and analyses, and 4) boundary layer characterization. ARLFRD supports ARL's mission by participation in ARL's R&D themes, with the exception of atmospheric chemistry and deposition.

ARLFRD's Mission

ARLFRD's mission is to "improv[e] our understanding of atmospheric transport, dispersion and air-surface exchange processes. To support this mission, we: 1) conduct experiments to better understand atmospheric transport and dispersion, 2) improve both the theory and models of air-surface exchange processes, 3) develop exciting technology and instrumentation to carry out our mission, and 4) support DOE's Idaho National Laboratory with meteorological forecasts and provide emergency response capabilities.

"FRD's science helps its customers better understand the atmospheric boundary layer, including the dispersion of chemical, biological, and nuclear agents in order to determine appropriate emergency actions or policy responses. FRD's science helps air quality managers become better informed about how and where air pollution is moving and what populations may be affected. Using this science-based information, air quality controls and regulations can be improved.... At the local level, FRD's science specifically helps ensure the safety of INL personnel and neighboring residents." (http://www.noaa.inel.gov, accessed August 23, 2016)

Units of Measure

It is general NOAA policy to express all units of measure using the protocols established in the International System of Units [Système Internationale (SI)]. However, this climatological document is intended not only for the scientifically oriented reader, but also for general public consumption. Therefore, following the prevailing local custom, SI convention is not strictly followed in this publication. Instead, the U.S. customary system, or American system, is used for such measures as distance and temperature. SI units are invoked only when they are commonly used in the United States.

FOREWORD

This edition of the INL Site climatography is the third and final such publication for me as the senior author. It has been very enjoyable for me to come to know the climate of Southeastern Idaho in a very detailed way. Having been born and lived most of my life here, I've been curious about the local weather and climate since I began working on my father's potato farm at a young age. Weather is so "front and center" in a farmer's life and it's very hard to ignore. The study of weather and climate, specifically agricultural meteorology, eventually became the focus of my formal post-secondary and graduate education. I was fortunate to have been able to return to work here after a short hiatus to obtain an advanced education and a brief employment stint with the USDA.

Over fifty years have passed since the first climatography was published by George R. Yanskey, Earl H. Markee, Jr., and Alden P. Richter in 1966. It is fitting that a new edition be publish this year to commemorate that occasion. A host of colleagues have helped to make this publication and its predecessor possible, who I gratefully acknowledge. My current colleagues who prepared data summaries and wrote various sections, are formally acknowledged on the title page as coauthors. However, there are a myriad of current and former colleagues, too numerous to name and some who have been forgotten with the passage of time, upon whose current and previous work this publication builds. There are also numerous engineers and technicians who labored diligently to maintain the equipment and software that is so vital to data collection. Still others provided office and budgetary support. The Field Research Division has been supported by many unsung and unacknowledged contributors. This foreword is a small attempt to provide that much deserved recognition.

At the close of calendar year 2016, I will retire from full-time employment at FRD. I have had the privilege of serving as director of the division for more than 13 years (and also serving as acting director for a couple more years on two separate occasions). My career with FRD spans almost 31 years and my career as a federal civil servant spans more than 33 years. Much has changed over those years. For example, computers have replaced typewriters for the preparation of manuscripts, among many other uses. The Internet has revolutionized access to information, most of which was previously found only in the printed word. As I clean out my office to make room for a new occupant, I can now discard my hoarded files of photocopied research papers and my collection of printed professional journals. It will be interesting to observe what new inventions and technology will be utilized in the continuing study of weather and climate and in the preparation of the next INL Site climatography.

Kirk L. Clawson, Ph.D.
August 23, 2016

This page intentionally left blank.

TABLE OF CONTENTS

Page

LIST OF FIGURES

This page intentionally left blank.

LIST OF TABLES

INTRODUCTION

HISTORICAL CONTEXT

This climatography is the most recent in a series of publications designed to provide meteorological statistics to support design engineering, facility operations, and operational safety at of the U.S. Department of Energy's (DOE's) Idaho National Laboratory (INL) and the Idaho Cleanup Project (ICP). It builds on more than 65 years of continuous meteorological observations by the Air Resources Laboratory Field Research Division (ARLFRD) of the National Oceanic and Atmospheric Administration (NOAA).

The INL Site was originally known as the National Reactor Testing Station (NRTS) and was managed by the U.S. Atomic Energy Commission (AEC). In 1949, the same year the NRTS was created, the U.S. Weather Bureau established a Weather Bureau Research Station as part of the Special Projects Section. By agreement with the Reactor Development Division of the AEC, the station was staffed with a full complement of meteorologists and technicians at the NRTS. This station is now known officially as NOAA ARLFRD, and unofficially to the personnel at the INL simply as NOAA. The initial objective of the station was to describe the meteorology and climatology of the NRTS with the focus on protecting the health and safety of site workers and nearby residents. The office provided a full range of hourly and daily climatological observations including balloon soundings, which were transmitted to the U.S. Weather Bureau [and later the National Weather Service (NWS)] observations network.

After 15 complete years of meteorological data collection, the first complete climatography of the INL Site was published (Yanskey et al. 1966). It was based on an assemblage of four previous reports (DeMarrais 1958a,b; DeMarrais and Islitzer 1960; Johnson and Dickson 1962). All of these early reports were written primarily to: 1) provide engineers, health physicists, scientists, and other researchers with a source of meteorological information pertinent to designing, locating, and operating nuclear reactors and support facilities, and 2) provide insight into the atmospheric aspects of health physics. The first edition was quite advanced for its time. It included the usual summaries of winds, temperature, precipitation, etc., but also included a discussion of transport and diffusion as it was understood at that time. The publication also included results from tetroon studies of wind flow patterns over the INL Site. Once the 1966 climatography was published, regular meteorological observations related solely to synoptic forecasting were reduced to allow for more intensive research on atmospheric transport and diffusion issues. Basic meteorological observations continued in order to satisfy DOE environmental and safety requirements.

In 1989, a second edition of the INL Site climatography (Clawson, et al., 1989) was issued to integrate new information acquired since the publication of the first edition. The data period of record made it possible to calculate full 30-year normalized climatological summaries for all important atmospheric parameters. It also included an updated treatment of atmospheric transport and dispersion from INL Site sources. The 2nd edition reflected most notably on the considerable strides made in the state-of-the-science of atmospheric transport and diffusion that occurred in the 1970's and 1980's. Much of this progress was based on field validation of numerical models of which ARLFRD was a major contributor. Some of the field validation work occurred on-site at the INL, increasing the value of ARLFRD's research. The second edition of the climatography proved to be the single most popular publication of ARLFRD with both on-site users and the general public.

By 1993, a new telemetered weather observation network that reported not only winds and air temperature, but also precipitation, atmospheric moisture, barometric pressure, and solar radiation was fully operational. The system provided continuous five-minute meteorological data across the INL Site as well as a large area around the INL Site covering approximately 10,000 sq. mi. A radar wind profiler and radio acoustic sounding system (RASS) had also been installed in 1992 to provide continuous upper air wind and air temperature data throughout the atmospheric mixing layer. After 13 years of quality-controlled data collection from each of these systems, a third edition of the INL Site climatography was published in 2007 (Clawson et al, 2007). It built on the material found in its predecessors using the 15 years of continuous meteorological data from the 30+ station network. The third edition introduced the use of three microclimate zones for the INL Site (INL North, INL Southwest, and INL Southeast) based primarily on wind flow patterns. It also contained the results of research investigations into the regional wind flows of the Eastern Snake River Plain and new evapotranspiration statistics for the INL Site. Furthermore, it contained a completely revamped section on atmospheric transport and diffusion.

Today, ARLFRD continues its basic mission to furnish INL Site-specific forecasts, severe weather notifications and alerts, atmospheric dispersion expertise, emergency operations support, and climatological and real-time meteorological data to DOE. ARLFRD has taken full advantage of the Internet to disseminate real-time meteorological data and climatological data to the INL and the general public through its NOAA/INL Weather Center (NIWC) web site (http://niwc.noaa.inel.gov). Data are also shared with other partners such as the Idaho Department of Environmental Quality (http://www.idahoop.org), the INL Environmental Surveillance, Education and Research Program (http://www.idahoeser.com), MesoWest (http://mesowest.utah.edu), NOAA's Meteorological Assimilation Data Injest System (MADIS, https://madis.noaa.gov/), and the U.S. Bureau of Reclamation's Agrimet Program (http://www.usbr.gov/pn/agrimet/) and the NOAA National Centers for Environmental Information (see for example http://www.ncdc.noaa.gov/cdo-web/datasets/GHCND/stations/GHCND:USW00094143/detail).

Over 50 years have passed since the first complete edition of the INL Site climatography was issued. An additional 9 years of climatological data have been collected since the most recent (3^{rd}) edition of the INL Site climatography was published. It is fitting that this fourth edition be prepared and published, now that the first five years of the current decade have passed. Perhaps the cycle for updating the INL Site climatography can be every 5 years rather than decades.

CONTENTS

In this edition, the order of topical presentations found in the first three editions is preserved. In addition to climatological parameters updated through 2015, the current INL Site climatography contains new research focused on the outflows of the Birch Creek Valley that strongly affect the wind regime of the Specific Manufacturing Capability (SMC) on the north end of the INL Site. Information that has been deemed to be historical in nature has not been incorporated in this edition. Instead, the reader is referred to earlier editions for this information. It is anticipated that this current edition of the INL Site climatography will, like its predecessors, continue to be useful to planners and operations staff who support the current INL and ICP mission directives of revitalized nuclear reactor research and completion of the legacy cleanup.

Section 2 provides a description of the topographical setting of the INL Site and describes three local INL Site climate zones as a context for the discussion of meteorological variables that follows in a succeeding chapter. Section 3 summarizes the data sources used for the climatography, including the NOAA/INL Mesoscale Meteorological Monitoring Network (mesonet), the historical CFA thermoscreen, the radar wind profiler with radio acoustic sounding system (RASS), the sound detection and ranging instrument (sodar), and the atmospheric eddy correlation surface energy flux station. Section 4 discusses the general Eastern Snake River Plain (ESRP) climatology in the context of its topographical setting and geophysical setting. This is reason for naming this publication a climatography rather than a climatology. Section 5 supplies specific climatological data for winds, air temperatures, precipitation, atmospheric moisture, solar/terrestrial radiation, atmospheric pressure, and special phenomena, including range fires. Section 6 presents information on atmospheric transport and diffusion.

Some information is best presented in the independent format of appendices. Several are included in this publication. Appendix A provides wind roses for all of the NOAA/INL mesonet stations. Appendix B presents a complete set of climatological air temperature means and extremes. Appendix C provides historical precipitation data including snow fall and snow depth information. Appendix D explains the NOAA/INL Weather Center web site, and Appendix E gives the NOAA/INL Mesonet instrument specifications.

Many of the tables found in this publication are also available at the NIWC web site. These tables are continually updated as new information is collected. Even though this printed publication will eventually be rendered obsolete by the passage of time, it is envisioned that the NIWC web site will always contain up-to-date and relevant climatological information.

One note of clarification for the reader of this climatography. The term Idaho National Lab, or INL, has a come to include functions and locations outside of the INL Site proper. For example, the Research and Education Campus in Idaho Falls, ID is now a part of the INL. However, further use of the term INL as a location in this document actually refers to the INL Site proper.

This page is intentionally left blank.

AREA PHYSIOGRAPHIC DESCRIPTION

The climatology of the INL cannot be fully understood without a knowledge of the topography and some of the geological features of the site itself and the surrounding area. The INL occupies an 890 square mile area located along the western edge of the Eastern Snake River Plain (ESRP) in southeastern Idaho. The ESRP is the segment of the Snake River Plain that extends from Twin Falls, Idaho, northeast to the Yellowstone Plateau as shown in Fig. 1. Lying at the foot of the Lost River, Lemhi, and Bitterroot Mountain Ranges, the average elevation of the INL is about 5,000 ft. above mean sea level (msl). The mountains rise to approximately 11,000 ft. above msl (Fig. 2), which is approximately 6,000 ft. above the average elevation of the INL. The tallest peak in Idaho, Borah Peak, at 12,662 ft. msl, is part of the Lost River Range. It is located only 45 mi. from the western border of the INL. Borah Peak was the site of the largest earthquake in Idaho with a magnitude of 6.9. It occurred on October 28, 1983 (USGS, 2009). Thirteen of the 15 highest peaks in Idaho are found in the Lost River Range.

The general orientation of the ESRP is northeast to southwest. Long, deep mountain valleys bordering the INL immediately to the northwest, however, are perpendicularly oriented

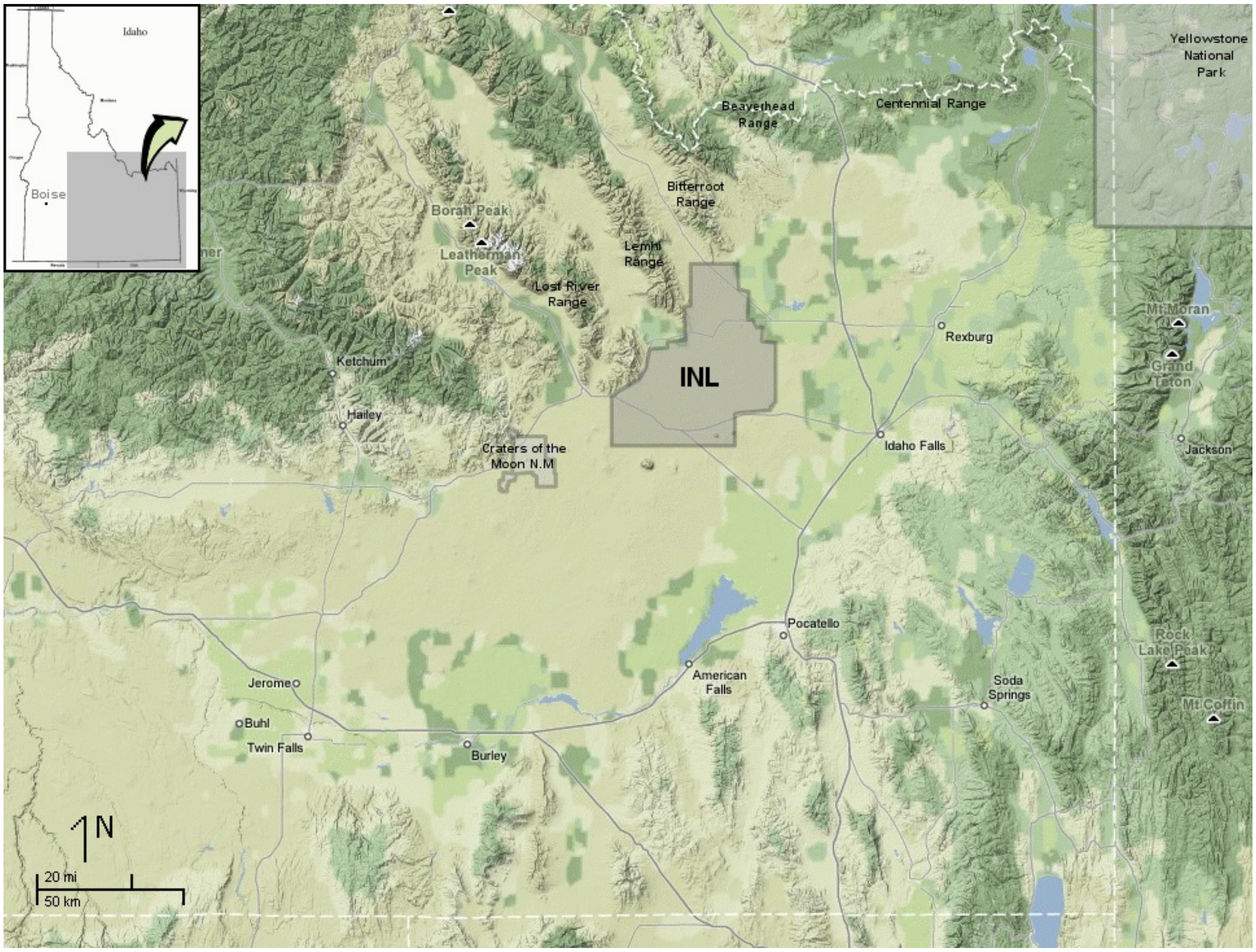

Figure 1. INL location on Eastern Snake River Plain, Idaho.

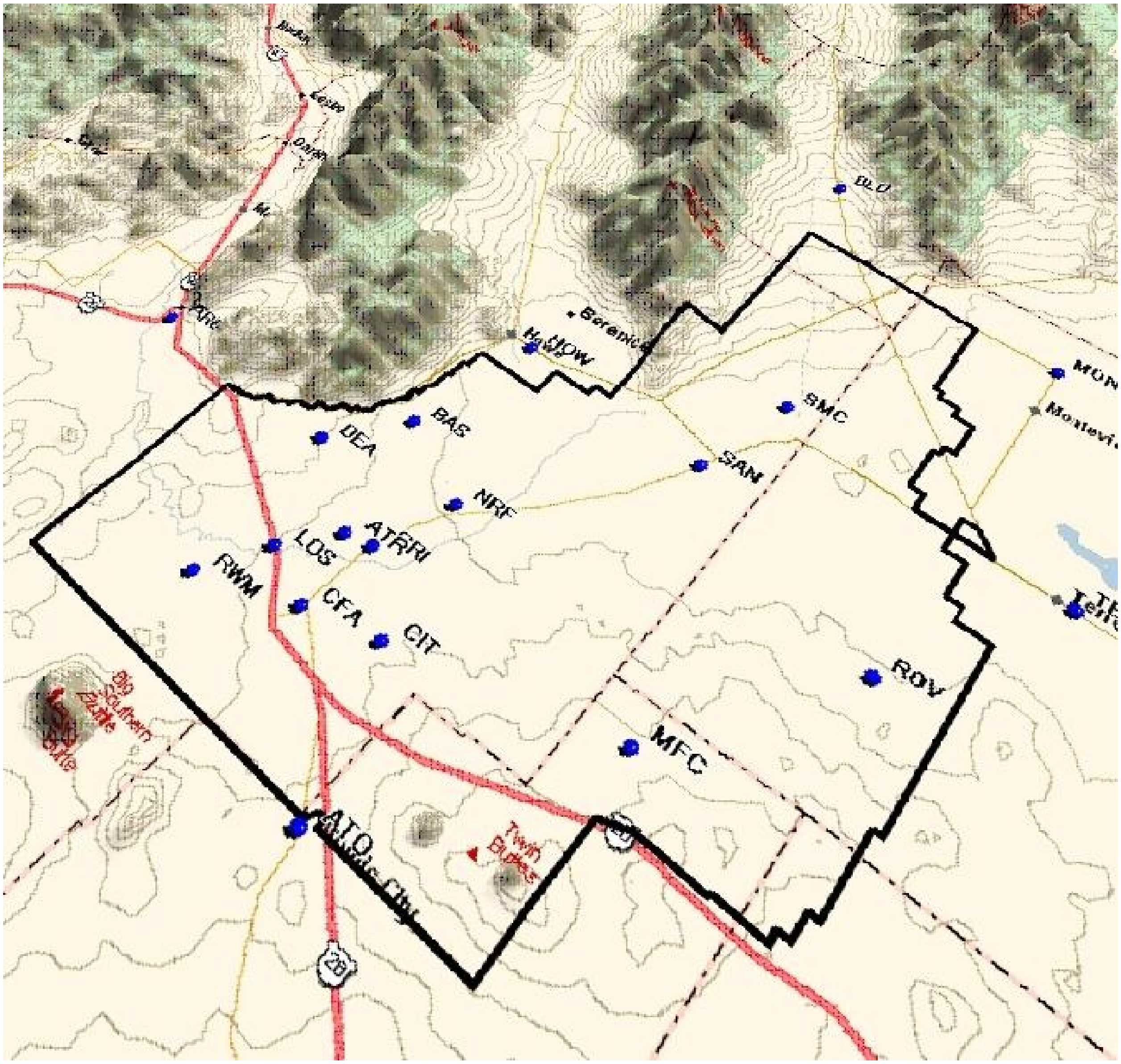

Figure 2. Prominent terrain features on and near the INL. The image has been tilted and rotated approximately 45 degrees clockwise so that the top of the image is northwest, and the height of the mountains has been enhanced to better show the relationship of nearby mountain ranges to the INL. Little Lost River Valley is located top center bordered by the Lost River Mountain Range on the left and the Lemhi Range to the right. To the right of the Lemhi Range is Birch Creek Valley and the Bitterroot Range. Big Southern Butte is located center left and the Twin Buttes are found in the bottom-center of the image.

in a northwest-southeast direction. Each of these mountain valleys empty into the Lost River Basin (LRB) which is a closed drainage basin and an internal geographic feature of the ESRP (Fig. 3). A close examination of the topography shows the LRB is bounded by a low, gradual rise of up to 200 ft. near the south, southeast, and east boundaries of the INL with a low point near the north end. The total relief outside the LRB in the ESRB is up to 600-700 ft. over a gentle gradient from the Snake River to the rim of the LRB. This topography of the LRB plays a significant

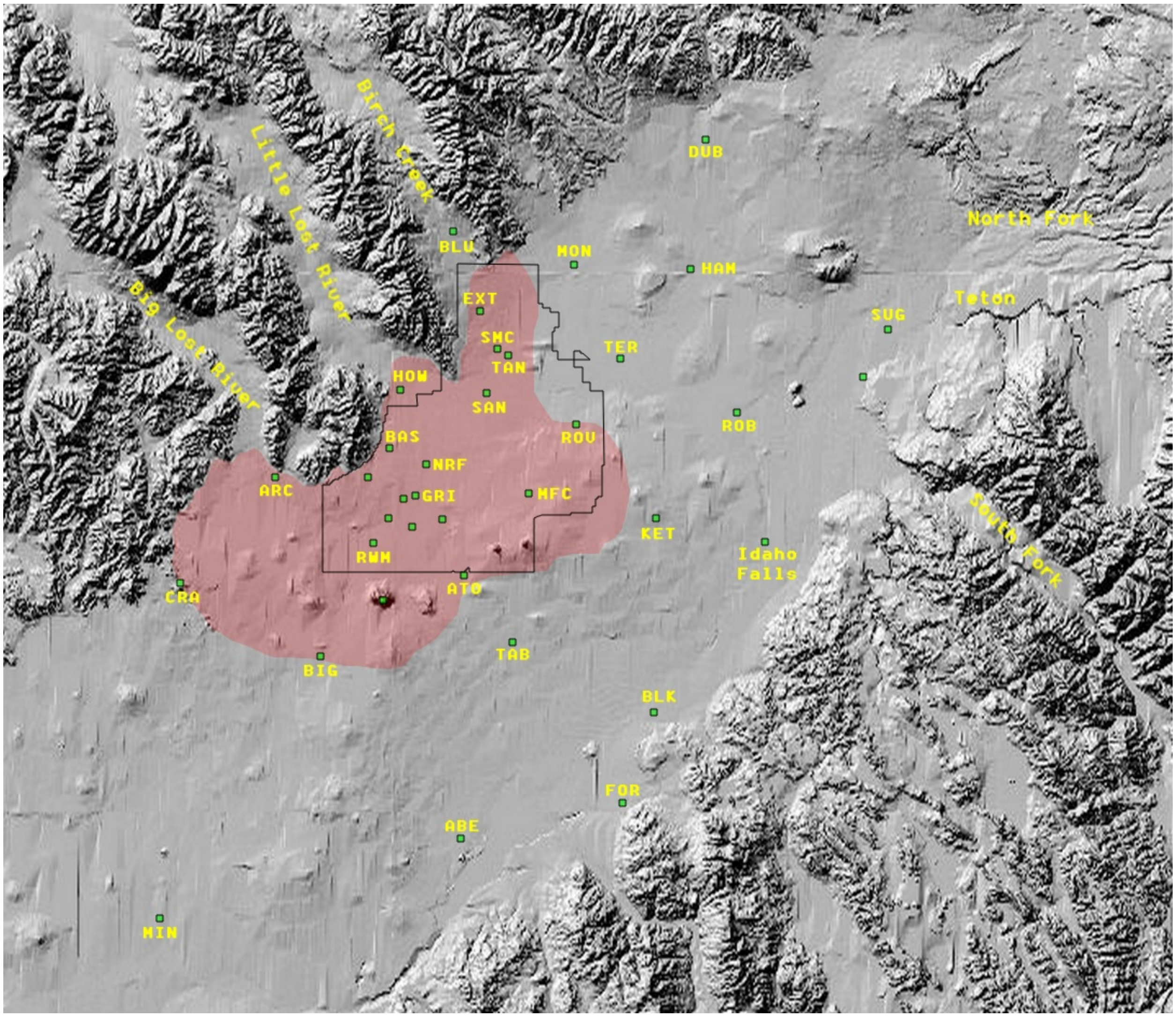

Figure 3. Location map showing the Eastern Snake River Plain, surrounding mountains and valleys, the INL boundary (outline), and the portion of the Lost River basin contained within the Snake River Plain (shaded). The sharp horizontal and vertical lines are due to image rendering and are not actual topographic features.

role in INL weather including temperatures and wind directions, especially in lighter nighttime winds. This will be discussed later.

The general surface of the INL, like that of the entire Snake River Plain, is rolling grass and sagebrush steppe broken by occasional lava outcroppings. On the southwest end of the LRB, a broad, low, volcanic ridge extends from Craters of the Moon National Monument along the southern edge of the INL and northeastward through the eastern INL to south and east of the Mud Lake area. Two buttes, located in the southeast corner of the INL, rise approximately 1,400 and 1,600 ft. above the surface of the valley floor. Just a few miles south of the INL is Big Southern Butte. This butte has an elevation of 7,576 ft. msl and is a major landmark, rising 2,500 ft. above the plain.

Three streams (Big Lost River, Little Lost River, and Birch Creek) enter the ESRP from the northwest and flow through the INL across alluvial fans into playas or sinks. Due to seepage, evaporation, and substantial upstream water diversions for irrigation and power generation, the streams in the INL are usually dry. Only the Big Lost River flows into the playas in the wettest years. Since surface water at the INL flows into closed basins, the only way for surface water to leave the INL is by evaporation or deep drainage into the Snake River Plain aquifer.

The two principal surface materials at the INL, according to the U. S. Geological Survey (Nace et al. 1975), are loess and olivine basalt. Other surface materials include sand, black basalt, playa deposits, alluvial-fan deposits, slope wash and talus, and lakebed sediments with associated beach and bar deposits. A comprehensive survey of INL soils has not been conducted, but Olsen et al. (1995) have gathered information from adjoining county soil surveys and numerous other sources. Most INL soils are Aridisols represented largely by the great group Cambids. Cambids are found extensively in the arid regions of the U.S. (Soil Survey Staff, 1975). Entisols, represented by Torriorthents, and Torrifluvents and Mollisols, represented by Calcixerolls and Haploxerolls, are also common on the INL. The depth of the soil varies from less than an inch on lava flows to approximately 6 ft. in lower lying areas.

The INL lies in a sagebrush steppe ecosystem. The sagebrush steppe is one of the most extensive ecosystems in the Western U.S., comprising an area of 94.2 million acres. This amounts to 12.5% of the total land area of the eleven Western States (USDA Forest Service, 1972). Unlike the soils of the INL, a comprehensive survey of plant communities has been completed by Anderson et al. (1996). The most common native shrub is the Wyoming big sagebrush (*Artemesia tridentata* subspecies *wyomingenesis*), followed by Basin big sagebrush (*Artemesia tridentata* subspecies *tridentata*), green rabbitbrush (*Chrysothamnus viscidiflorus*), gray rabbitbrush (*Chrysothamnus nauseosus*) and winterfat (*Krascheninnikovia lanata*). Common native grasses include thickspiked wheatgrass (*Elymus lanceolatus*), bottlebrush squirreltail (*Elymus elymoides*), Indian ricegrass (*Oryzopsis hymenoides*), and needle-and-thread grass (*Stipa comata*). Many forbes are also found on the INL including tapertip hawksbeard (*Crepis acuminata*), Hood's phlox (*Phlox hoodii*), hoary false yarrow (*Chaenactis douglasii*), paint brushes (e.g. *Castilleja angustifolia*), and globe-mallow (*Sphaeralcea munroana*). Other plant species have either been intentionally introduced or have invaded the INL. Wildfires have burned large amounts of the INL, leaving the soil open immediately afterward to severe wind erosion. Crested wheatgrass (*Agropyron desertorum* or *Agropyron cristatum*) has been planted in some of those areas to control the ensuing dust storms that develop in high wind conditions. Cheat grass (*Bromus tectorum*) has also aggressively encroached some areas of the site.

The physiographic features of the INL cause three distinct local or micro-climatic zones, depicted in Fig. 4. These zones become apparent in a review of INL climatic data, particularly in a review of wind data. The zones should be considered when interpreting data for specific site assessments. The north portion of the INL (SMC southward to approximately NRF) is influenced by down-canyon winds and up-valley flows that originate in the nearby southeast-to-northwest trending mountain valleys and that dominate the terrain northwest of the INL. Northern INL is also influenced by the rain-shadow effects of these mountains. This microclimate zone is called North INL. The southwest portion of the INL (ATR Complex, INTEC, CFA, CITRC, and RWMC) is commonly influenced by shallow nocturnal down-valley winds that are associated with the Big Lost River channel from CFA to INTEC. This area is also influenced by strong pre-frontal southwesterly winds and frequent afternoon winds, also from the southwest, that result from

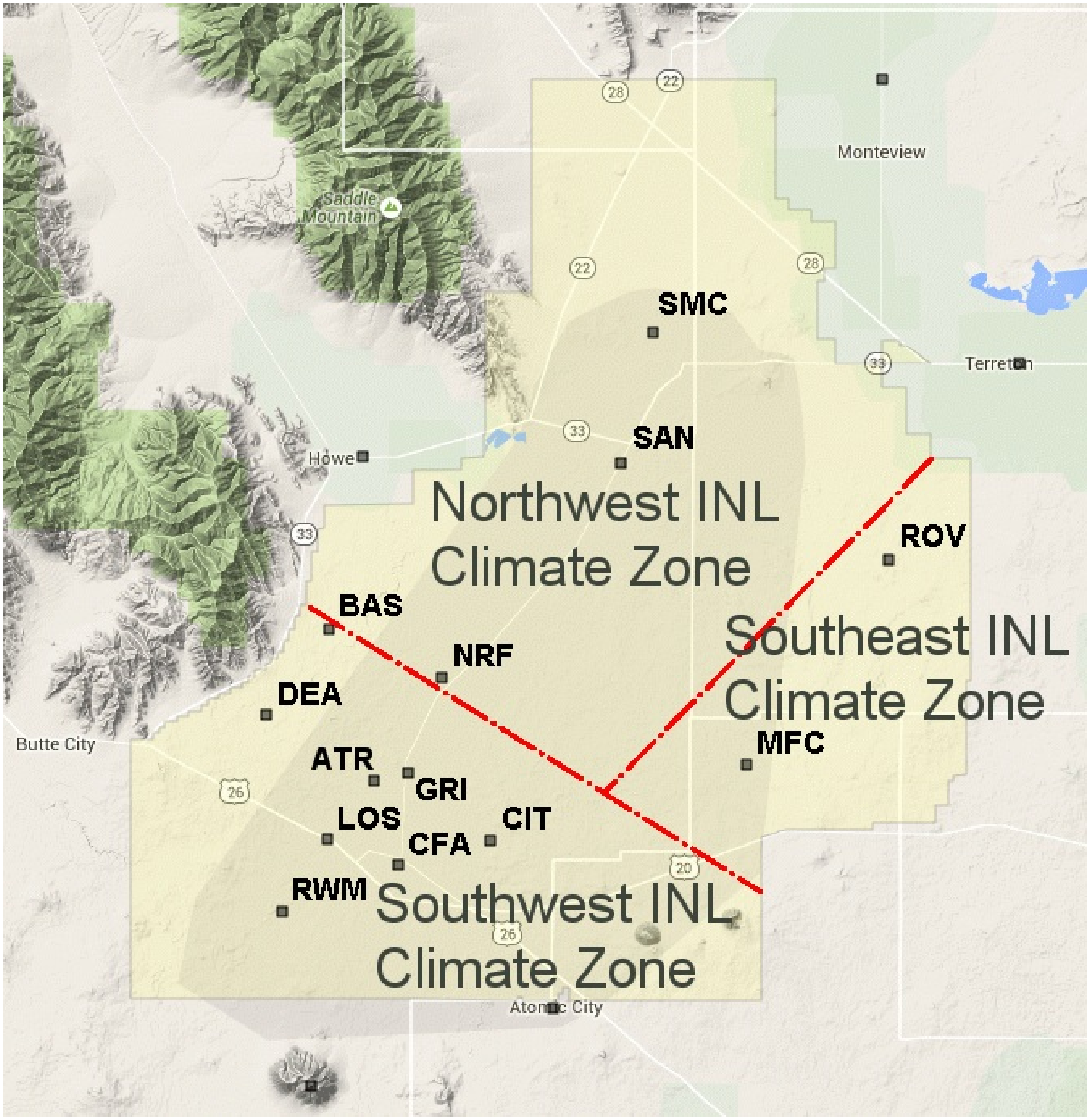

Figure 4. Approximate boundaries of the three distinct microclimate zones of the INL.

the diurnal heating cycle. This zone is called Southwest INL. The southeast portion of the INL (MFC) is isolated from the channeling flows that commonly affect the western portions of the site. In that area, air temperatures, cloud cover, and surface winds are influenced by the subtle features of topography and higher elevation along the southern perimeter of the INL. This zone is called Southeast INL. The meteorological effects of these physiographic features will be clarified in later chapters as they relate to wind fields, transport and diffusion, and other atmospheric parameters.

This page is intentionally left blank.

METEOROLOGICAL DATA SOURCES

NOAA/INL MESONET

What is now called the NOAA/INL Mesonet (MESOscale meteorological monitoring NETwork) began with a single station at the Central Facilities Area (CFA) in 1949. Between 1950 and 1970, six on-site and 16 off-site monitoring stations were added to form an expanded observational network. The number of meteorological monitoring stations continued to expand and change over the years in support of various projects and also in an effort to gain a better understanding of the climatology of the INL and ESRP. The current configuration of the Mesonet meets the needs of INL planners, emergency managers, scientists, engineers, operations personnel, the local National Weather Service (NWS) Weather Forecast Office (WFO) in Pocatello, ID, and the general public.

There were 34 fully automated meteorological observation stations in operation at the INL and surrounding area as of December 31, 2015. Thirteen of these were located within the boundaries of the INL. The remaining stations were sited at key locations throughout the ESRP. Standard meteorological parameters are measured at each Mesonet station. Tables 1 and 2 list the location of each Mesonet station both on and off the INL site, respectively. In the two tables, the station name indicates the general location of the station. Also provided in the tables are the station three-letter ID designator, latitude, longitude, elevation, instrument height, and types of data being collected at each level on the tower. Most of the towers are 50 ft. tall, but there are 5 exceptions. Three tall towers range in height from 150 to 250 ft. and are the "primary" on-site observation stations in each of the three INL microclimate zones. These towers are at Grid 3/INTEC (GRI), MFC, and SMC. Shorter towers are on the summit of Big Southern Butte where aesthetic restrictions limited construction of the tower to only 20 ft., and at Craters of the Moon National Monument where construction of the tower on a lava flow permitted only a 30 ft. tower for safety reasons.

The location of each tower comprising the Mesonet is depicted on maps in Figs. 5 and 6 for on-site and off-site locations, respectively. A typical Mesonet tower, representative of the configuration and instrument layout, is shown in Fig. 7.

Four of the stations are also known as Community Monitoring Stations (CMS). They were sited at places frequented by the public to enhance relations with the local communities. The CMS stations are located at Fort Hall (FOR), Idaho Falls (IDA), Lost River Rest Area (LOS), and Terreton (TER). The CMS stations were developed in partnership with DOE-ID, the State of Idaho INL Oversight Program, the Shoshone-Bannock Tribes, the City of Idaho Falls, and the State of Idaho Transportation Department (ITD) (Crescenti, et al. 2000). The CMS stations include a walk-up kiosk (Fig.7) that displays current meteorological parameters and describes each of the measured variables.

All meteorological instruments were carefully selected to meet required and generally accepted guidelines, as well as voluntary consensus standards, including DOE/EH-0173T, Environmental Regulatory Guide for Radiological Effluent Monitoring and Environmental Surveillance (2004), DOE Guide 151.1-1C, Comprehensive Emergency Management System (2005); and ANSI/ANS 3.11-2015, Determining Meteorological Information at Nuclear Facilities. One suggestion in ANSI/ANS 3.11-2015 that is not followed is the recommendation to use sonic anemometers for measuring wind. However, testing of a sonic anemometer in the Mesonet

Table 1. NOAA/INL Mesonet stations located inside the INL as of December 2015.

				Elevation	Instrument Levels							
Station Name	Station ID	Latitude (deg N)	Longitude (deg W)	MSL (ft)	6 (ft)	20 (ft)	30 (ft)	33 (ft)	50 (ft)	150 (ft)	200 (ft)	250 (ft)
Advanced Test Reactor Complex	ATR	43.584633	112.968667	4,937	t,r,p,s,b				w,T			
Base of Howe Peak	BAS	43.677533	113.006033	4,900	t,r,s,b				w,T			
Central Facilities Area Building 690	CFA	43.532617	112.947733	4,950	t,r,p,s,b,d				w,T			
Critical Infrastructure Test Range Complex	CIT	43.547483	112.869683	4,910	t,r,p,s,b				w,T			
Dead Man Canyon	DEA	43.625067	113.059783	5,108	t,r,s,b				w,T			
Grid 3/INTEC	GRI	43.589700	112.939933	4,897	w,t,r,p,s,b,l			w,T	w,T	w,T	w,T	
Lost River Rest Area	LOS	43.548683	113.009900	4,983	t,r,p,s,b				w,T			
Materials and Fuels Complex	MFC	43.594133	112.651733	5,143	w,t,r,p,s,b,l,d			w,T	w,T	w,T		w,T
Naval Reactor Facility	NRF	43.647867	112.911233	4,847	t,r,p,s,b				w,T			
Radioactive Waste Management Complex	RWM	43.503433	113.046033	5,025	t,r,p,s,b				w,T			
Rover	ROV	43.720600	112.529567	5,008	t,r,s,b				w,T			
Sand Dunes	SAN	43.779667	112.758183	4,820	t,r,p,s,b,d				w,T			
Specific Manufacturing Capability	SMC	43.859767	112.730267	4,790	w,t,r,p,s,b,l			w,T	w,T	w,T		

w: Wind (mean speed, peak 3-second wind gust, mean direction, direction standard deviation)
t: Air temperature (mean, maximum, and minimum)
T: Air temperature (mean)
r: Relative humidity (mean)
p: Precipitation (total)
s: Solar radiation (mean)
b: Barometric pressure (mean)
l: Soil temperature and moisture (mean)
d: Snow depth

Table 2. NOAA/INL Mesonet stations located outside the INL as of December 2015.

				Elevation	Instrument Levels								
Station Name	Station ID	Latitude (deg N)	Longitude (deg W)	MSL (ft)	6 (ft)	20 (ft)	30 (ft)	33 (ft)	50 (ft)	150 (ft)	150 (ft)	200 (ft)	250 (ft)
Aberdeen	ABE	42.954933	112.824533	4,392	w,t,r,p,s,b,l				w,T				
Arco	ARC	43.624550	113.297100	5,290	t,r,p,s				w,T				
Atomic City	ATO	43.443733	112.815650	5,058	t,r,p,s,b				w,T				
Blackfoot	BLK	43.189850	112.333200	4,520	t,r,p,s,b				w,T				
Blue Dome	BLU	44.075000	112.842033	5,680	t,r,p,s				w,T				
Cox's Well	COX	43.294167	113.181283	5,200	t,r,s				w,T				
Craters of the Moon	CRA	43.429183	113.538300	5,996	t,r,s,b		w,T						
Dubois	DUB	44.242383	112.201833	5,465	t,r,p,s,b				w,T				
Fort Hall	FOR	43.022000	112.411983	4,452	t,r,p,s,b				w,T				
Hamer	HAM	44.007417	112.238833	4,843	t,r,p,s				w,T				
Howe	HOW	43.784117	112.977317	4,815	t,r,p,s				w,T				
Idaho Falls	IDA	43.504133	112.050133	4,709	t,r,p,s,b				w,T				
Kettle Butte	KET	43.547567	112.326250	5,190	w,t,r,p,s,b				w,T				
Minidoka	MIN	42.804417	113.589650	4,285	t,r,p,s,b				w,T				
Monteview	MON	44.015367	112.535917	4,797	w,t,r,p,s,b				w,T				
Richfield	RIC	43.060600	114.134583	4,315	t,r,p,s,b				w,T				
Roberts	ROB	43.743517	112.121117	4,760	t,r,p,s				w,T				
Sugar City	SUG	43.896583	111.737617	4,895	t,r,p,s,b				w,T				
Big Southern Butte Summit	SUM	43.396333	113.021850	7,576	t,r,s,b	w							
Taber	TAB	43.318683	112.691800	4,730	t,r,p,s				w,T				
Terreton	TER	43.841683	112.418250	4,792	t,r,p,s,b				w,T				

w: Wind (mean speed, peak 3-second wind gust, mean direction, direction standard deviation)
t: Air temperature (mean, maximum, and minimum)
T: Air temperature (mean)
r: Relative humidity (mean)
p: Precipitation (total)
s: Solar radiation (mean)
b: Barometric pressure (mean)
l: Soil temperature and moisture (mean)
d: Snow depth

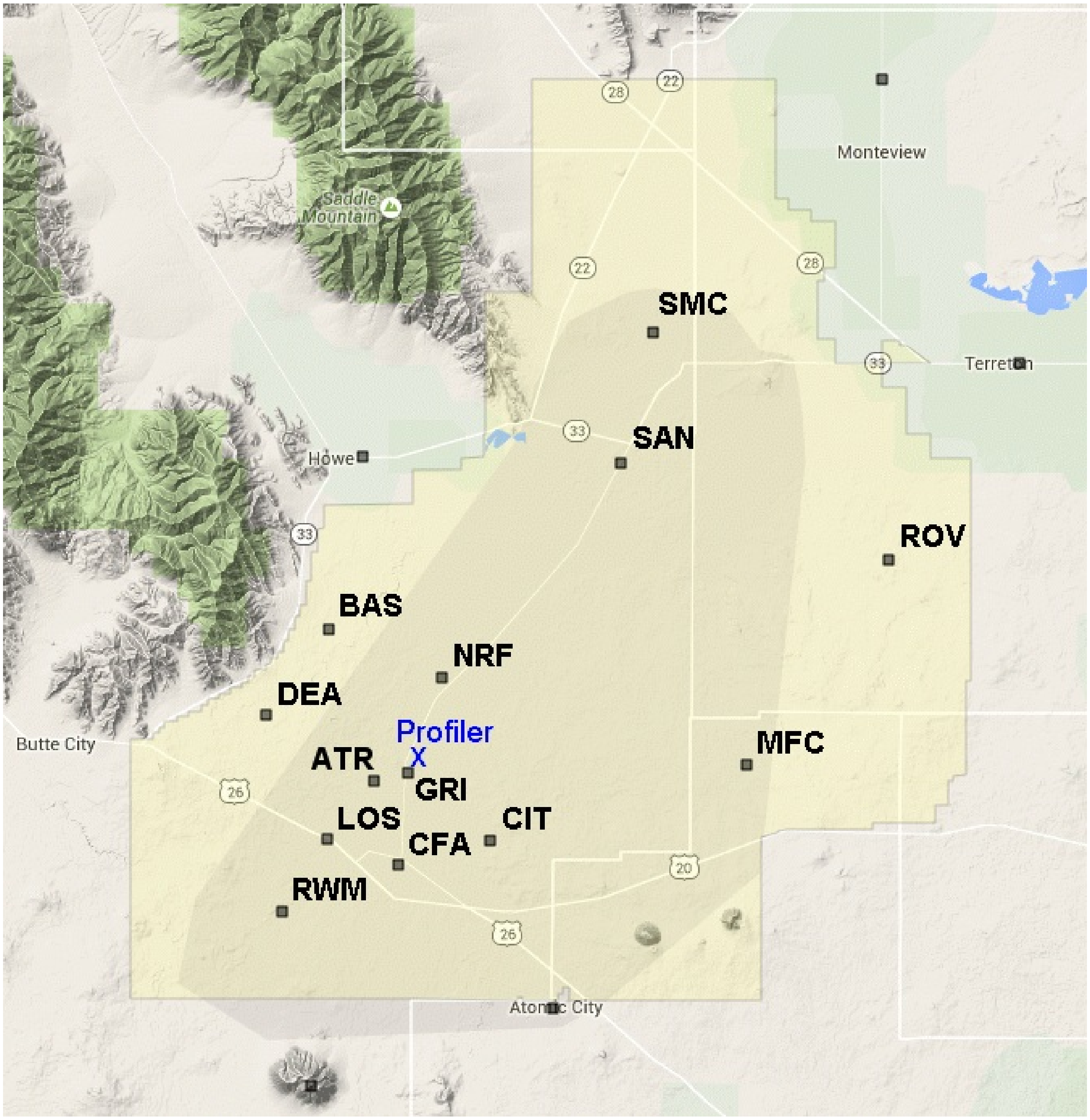

Figure 5. On-site NOAA/INL Mesonet stations as of December 2015.

has demonstrated that cup anemometers and wind vanes perform much better year-round than do sonic anemometers.

Air temperature and relative humidity are measured at all Mesonet stations at the conventional 6 ft. level. Wind measurements (speed and direction, 3-second gusts, and standard deviation of the wind direction) are made at the top of all Mesonet towers. For the three tall towers, wind and air temperature measurements are also recorded at the 6, 33, 50, and 150 ft levels. Additional reported parameters measured at most stations include precipitation, atmospheric pressure, and solar radiation. Soil moisture and soil temperature

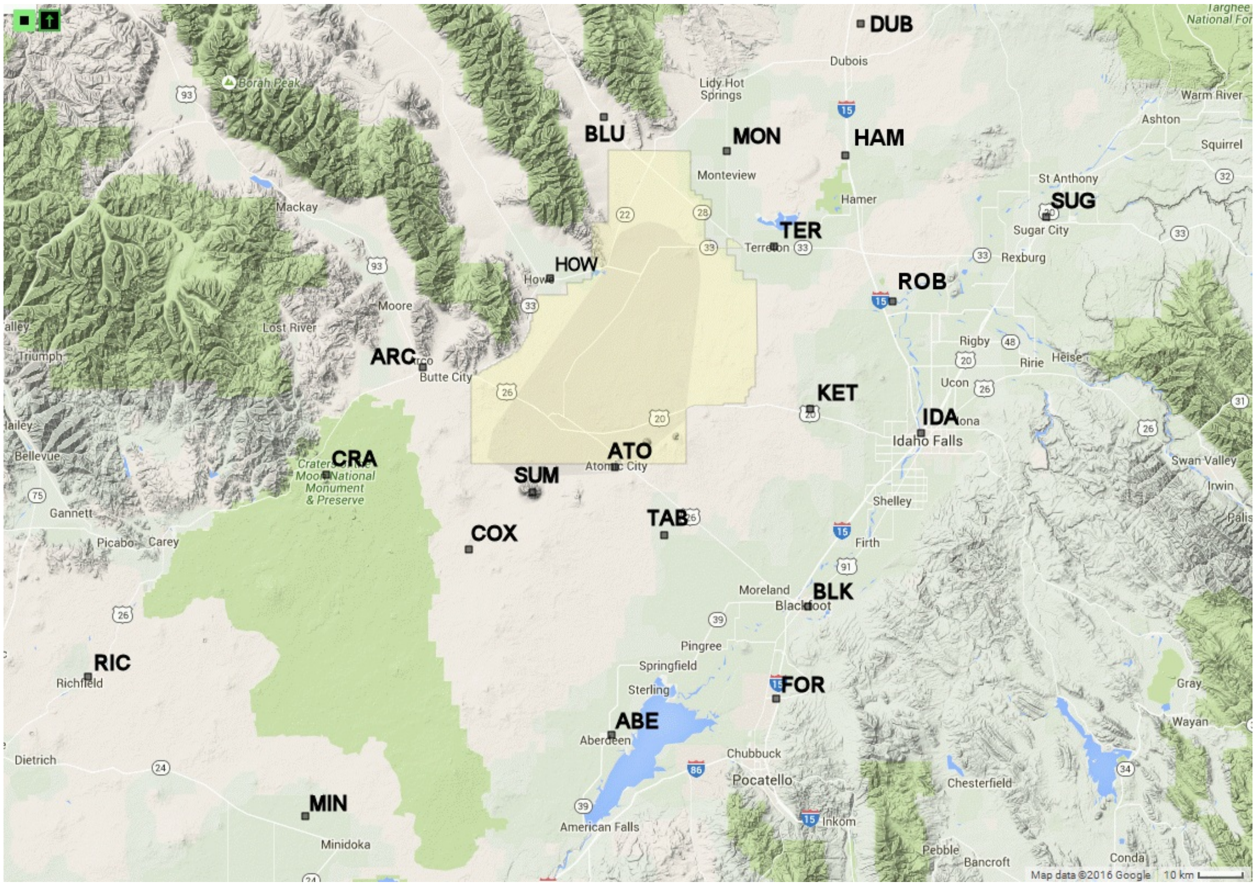

Figure 6. Off-site NOAA/INL Mesonet stations as of December 2015.

measurements are made at GRI, SMC, and MFC at 2, 4, 8, 20, and 40 in. (5, 10, 20, 50, and 100 cm) depths. Snow depth sensors are located at CFA, SAN and MFC. Still more wind measurements are made at the 6 ft. level at the Aberdeen (ABE), Kettle Butte (KET), and Monteview (MON)stations in support of the U.S. Bureau of Reclamation's Agrimet Program. Through a partnership with Agrimet, ARLFRD provides these additional meteorological measurements for regional crop water use modeling. Details of all instrumentation currently in use are provided in Appendix E.

Mesonet data are recorded as averages, totals, or extremes over a 5-minute period. Wind speed, wind direction, air temperature, relative humidity, solar radiation, soil temperature, and soil moisture are measured every 1-second and averaged over the 5-minute period. Precipitation is totaled for the same 5-minute interval. Maximum and minimum air temperatures for the 5-minute period are selected from the maximum and minimum 1-minute average during the 5-minute period. Before July 2013, maximum and minimum air temperatures were selected from one of the 300 one-second scans used to assemble the 5-minute average. That change was made to better match the World Meteorological Organization (WMO) and NWS way of calculating maximum and minimum temperatures. Wind gust is calculated as the maximum of a 3-second running average of the wind speed. Before June, 2006, wind gust was a 1-second average. The wind gust criteria was changed in 2006 to match the WMO guidelines. Data is collected at each station by a data logger and transmitted every 5-minutes over a VHF radio network back to the ARLFRD office.

Figure 7. Example NOAA/INL Mesonet station layout, with the addition of the Community Monitoring Station kiosk (foreground) on the Idaho Falls Greenbelt at the John's Hole Bridge and Forebay.

Data are also stored in data logger memory at each individual station and can be retrieved manually if the radio link breaks for an extended period of time. All of the data are continuously added to the INL climatological database and are immediately made available through the NOAA/INL Weather Center web page (http://niwc.noaa.inel.gov). Each data logger is supplied with power by a deep cycle marine battery for extended operation and data storage in the absence of line power. Only six stations (Base of Howe (BAS), Cox's Well (COX), Craters of the Moon National Presevere (CRA), Deadman (DEA), Rover (ROV), and Big Southern (SUM)) are solar powered; the remainder have AC line power to keep the deep-cycle battery charged.

DATA QUALITY ASSURANCE (QA)

A detailed and comprehensive data quality assurance (QA) program for the NOAA/INL Mesonet was instituted in 1993 (Dickson, 1993; Dickson and George, 1993). It has been periodically reaffirmed by succeeding ARLFRD quality assurance managers. The QA program is based on ASME NQA-1-(2004, 2015), *Quality Assurance Requirements for Nuclear Facility Applications*. As part of the QA program, ARLFRD has adopted the standards listed in ANSI/ANS 3.11-2015, *Determining Meteorological Information at Nuclear Facilities,* and ANSI/ANS 3.2-(1994, 2012), *Managerial, Administrative, and Quality Assurance Controls for the Operational Phase of Nuclear Power Plants* for data quality control guidance. Accordingly, the data quality control program uses a comprehensive set of software tools that consist of both manual and automated processes (George and Hukari, 1995; George, 1996). These tools are continually updated and improved to enhance the data quality evaluations and to make them more efficient, which results in better overall data quality.

Incoming meteorological data are automatically screened by software tools for out of bound values that are too high or too low to be physically possible. The data are then routinely screened by the routine plotting of meteorological data. Every 5-minute data period for every station is plotted and checked for missing or spiked data. Data are also screened in this manner for electronic noise, non-working aspirators that affect air temperature and relative humidity values, for orientation errors in the wind direction, stalled wind sensors, rime icing in the winter that degrades wind speeds and wind directions, erroneous values caused by maintenance, sprinklers, bird droppings, and a host of other potential problems. Plotting of the data allows the meteorologist to identify and flag any of the problems in the database and, if needed, notify a technician to quickly fix the problem. The result is a complete quality controlled dataset with data quality flags for every meteorological variable. Raw data values are fully preserved in this manner and are never substituted even when they are flagged as suspect or bad.

In additional to daily quality control procedures, the entire instrument suite is subjected to twice-yearly inspections and maintenance. During this semiannual visit of each Mesonet station, the performance of every above-ground instrument is challenged either by a collocated NIST-traceable transfer standard instrument or by another industry-accepted calibration technique. Instruments found to be out of tolerance are either repaired and/or calibrated, or replaced. Batteries, bearings, potentiometers, and aspirator fans are replaced at scheduled intervals to prevent instrument failure. Other maintenance activities are also conducted during the visits such as sensor cleaning and realignment. The entire process follows established procedures published as a part of the QA plan and are updated at least annually.

The quality of the data are further enhanced through ARLFRD's membership in the DOE Meteorological Coordinating Council (DMCC). The DMCC is an official working group of the DOE-sponsored Emergency Management Issues Special Interest Group (EMI SIG, see https://sp.eota.energy.gov/EM/). The DMCC, among other functions, provides meteorological program assessments and assist visits of council members programs. The visit participants are highly qualified meteorologists and engineers who use DOE orders and voluntary consensus standards as a basis to review a meteorological program, determine noteworthy practices, and provide a series of observations and recommendations for improvement. The DMCC provided assist visits of the NOAA/INL meteorological program in 2004 and again in 2010 (DMCC, 2004; 2010). ARLFRD followed the recommendations to improve its overall program including its data quality assurance program, which was already at a high level (ARLFRD 2010; 2012). Two of the three noteworthy practices in the 2004 report gave high praise for the data quality assurance program as follows: "The data quality assurance program is detailed and comprehensive and the staff member performing the checks is very experienced and knowledgeable. The quality assurance program uses an excellent software display of trended meteorological data which enhances the data quality evaluations and makes them more efficient. Data recoveries for the numerous meteorological parameters are generally in excess of 99%, which strongly suggests a very reliable system and well executed meteorological data management program."

CFA THERMOSCREEN

The weather station at CFA, installed in 1949, was the first meteorological observation station established at the INL. It is the longest continually operating station on the INL. The dataset collected from this station is known as thermoscreen data because air temperatures were recorded on a thermograph located inside a thermoscreen (also known as a Cotton Region Shelter, Fig. 8). Daily maximum and minimum temperatures were manually extracted from the thermograph record. Eventually a Mesonet

Figure 8. CFA thermoscreen is the longest and most complete air temperature and precipitation dataset at the INL.

station was collocated with the thermoscreen. Daily maximum and minimum air temperatures were then interpolated from the thermograph using air temperatures obtained from the Mesonet station as guidance. In 2010, the thermograph was discontinued and automated air temperature measurements from the collocated Mesonet station have since been used directly as the official CFA Thermoscreen temperatures.

Please be advised that the temperature data prior to August 1966 could be susceptible. The cotton region shelter was first installed near CF612 on an irrigated lawn with shade trees in the area. The shelter was later moved (date unknown) to a roadside location at an intersection where two roads came together. The shelter was located along the roadside where there was asphalt on 2 sides and gravel on a 3rd side. The shelter was then moved in 1966 to its current location near building CF690. The current location has more or less natural soil and vegetation surrounding it.

Daily precipitation, snowfall, and snow depth are also included in the thermoscreen dataset. Precipitation is collected in a rain gauge located about 15 ft. away from the thermoscreen and is manually measured weekly. Daily total precipitation is interpolated from the weekly total using the collocated Mesonet station tipping bucket rain guage. Snow depth is also measured manually at the same time as precipitation and interpolated to a daily depth. Total daily snowfall is estimated using the collocated Mesonet snow depth sensor, the amount of precipitation recorded, air temperature at the time of precipitation, and the NOAA/INL weather camera located at GRI and other nearby Idaho Transportation Department roadside cameras. This dataset is what compromises the National Weather Service cooperative observer station known as observer station known as Idaho Falls 46W (or IDF 46W). The data from IDF 46W are also included in NOAA's National Centers for Environmental Information climate database.

RADAR WIND PROFILER AND RASS

A 500 W, 915 MHz radar wind profiler with a Radio Acoustic Sounding System (RASS) has been operational at the Grid 3 facility (located just north of INTEC) since 1992 (Figs. 5 and 9). The wind profiler measures upper-level wind profiles and the RASS measures upper-level virtual air temperature profiles. The system was patterned after and includes components from the 915 MHZ systems developed by the NOAA Earth System Research Laboratory Physical Sciences Division (Strauch et al., 1984). The radar wind profiler has a vertical range of approximately 521 to 9,498 ft. (160 to 2,900 m) AGL with a vertical resolution set at 333 ft. (100 m). Remotely-sensed measurements for each layer include horizontal wind speed and direction, the standard deviation of the horizontal wind direction (σ_θ), and vertical wind speed. In addition, the radar estimates the refractive index structure parameter (C_N^2). Mixed layer height (z_i) is calculated from the radar return signal strength and has been stored in the database since January 2000. The RASS samples vertical virtual air temperature profiles in range gates of 344 ft. (105 m) from 541 to 5,358 ft. AGL (165 to 1,633 m), or a little less than ½ the maximum height of the wind profiler. The actual maximum measurement heights of both the radar wind profiler and the RASS are dependent on atmospheric conditions and rarely reach the potential maximum measurement heights. The system operates continuously with data output every 30 minutes.

Figure 9. Radar wind profiler and RASS located near Grid 3, just north of INTEC.

In the first and second editions of this report, the upper air wind climatology was derived from uninstrumented pilot balloon (pibal) soundings. These soundings were obtained daily between the hours of 0800-1000 local time for the 15 years prior to 1966. The upper air temperature climatology was derived from special short duration temperature-sonde and tethered balloon studies. The radar wind profiler with RASS provides highly-resolved round-the-clock data for mixing layer characteristics above the sounding site that are much superior to the once-per-day or short-term diurnal daily soundings that formed the previous upper air record. Researchers who are interested in INL upper tropospheric data that are above the ceiling capability of the radar wind profiler should refer to the balloon sounding summaries in Section V of the 2nd Edition Climatography (Clawson et al., 1989).

SODAR

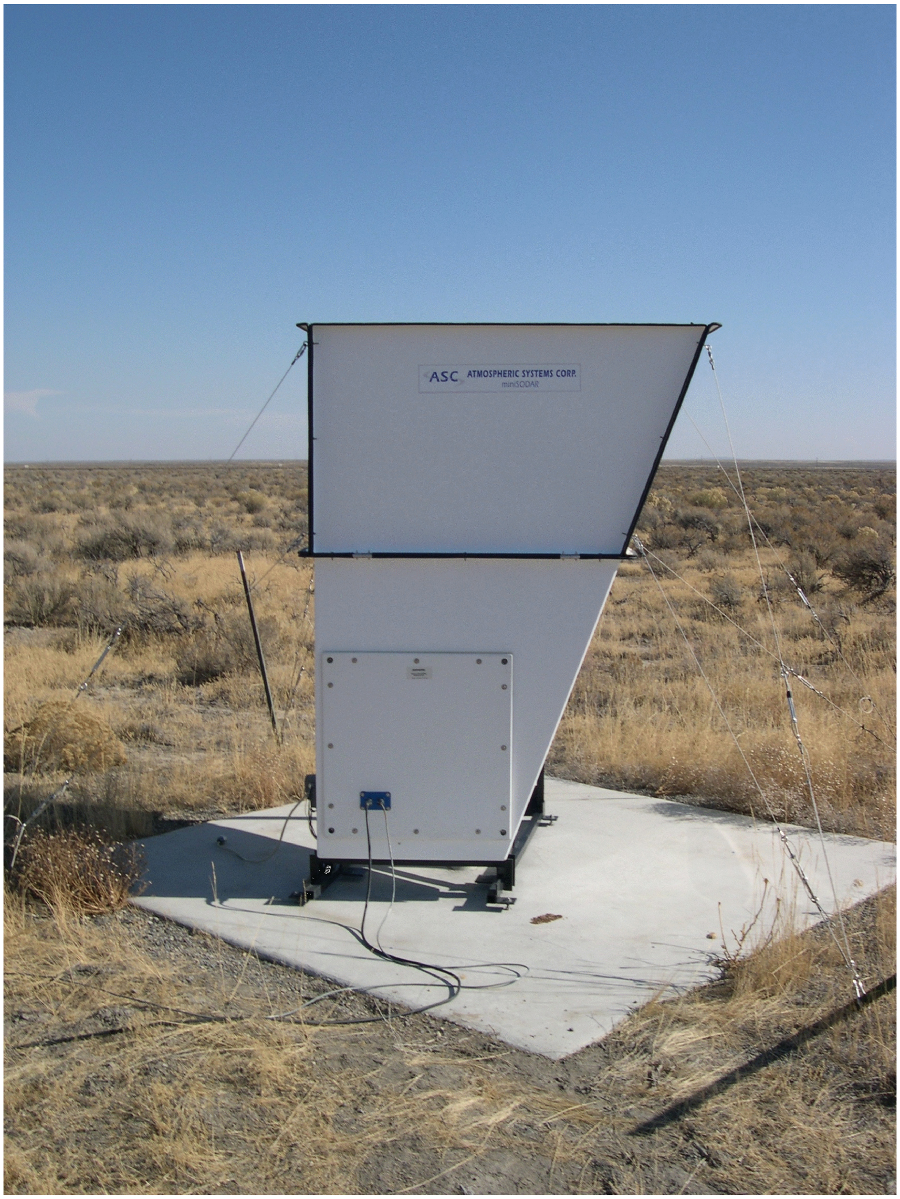

Figure 10. Mini-sodar located near Grid 3 collocated with the radar wind profiler and RASS.

A sodar is a remote sensing device that uses sound to measure vertical profiles of wind speed and direction in the lowest levels of the atmosphere. ARLFRD has an Atmospheric Systems Corporation (ASC) model 4000 Mini-sodar (Fig. 10). This mini-sodar has a vertical range of 66 ft. (20 m) to 722 ft. (220 m) AGL with a resolution of 16 ft. (5 m). The sodar is collocated with the radar wind profiler and RASS at GRI. The sodar and radar provide complementary wind profile measurements. The sodar provides high temporal and vertical resolution profiles near the surface, which is the layer of the atmosphere where the greatest change in wind speed and direction occurs. However, the sodar's vertical range is limited, so the radar profiler provides vertical coverage above that of the sodar. The radar wind profiler does not have the capability to obtain high temporal and vertical resolution profiles, but that high resolution is not needed in the layers of the atmosphere where the radar excels in measurement capability. The top layers measured by the sodar, and the bottom layer of the radar wind profiler overlap, providing a means to observe consistency between the two instruments.

Some of the parameters that are measured by the sodar include layer-average horizontal wind speed and direction, the 3-d wind speed components and their standard deviations, and the signal to noise ratios of the three beams. The sodar operates continuously with data output every 10 minutes. The data are retrieved from the sodar also every 10 minutes and archived as a part of the NOAA/INL Mesonet database. The sodar has produced valid data since April 1, 2009.

ENERGY FLUX STATION

The surface energy flux station located at Grid 3 is a collection of slow and fast response instruments designed to measure energy, mass, and momentum transfers between the surface and atmosphere within the INL's sagebrush steppe ecosystem. Fast response data are also useful for directly determining atmospheric stability, which is a standard input of many dispersion models. This station has been in place since 1999. Fast response instruments (Fig. 11) include a 3-d sonic anemometer and a closed-path infrared gas analyzer for the measurement of water vapor (H_2O) and carbon dioxide (CO_2). An open path infrared gas analyzer was originally installed and various models were used through August 2015. The instruments operate at 10 Hz, which is necessary for invoking eddy covariance process techniques. With eddy covariance processing, fluxes of momentum, mass, and energy are calculated from the data obtained from these instruments every 30 minutes. Both raw and processed data are retrieved every 30 minutes and are stored as part of the NOAA/INL Mesonet dataset.

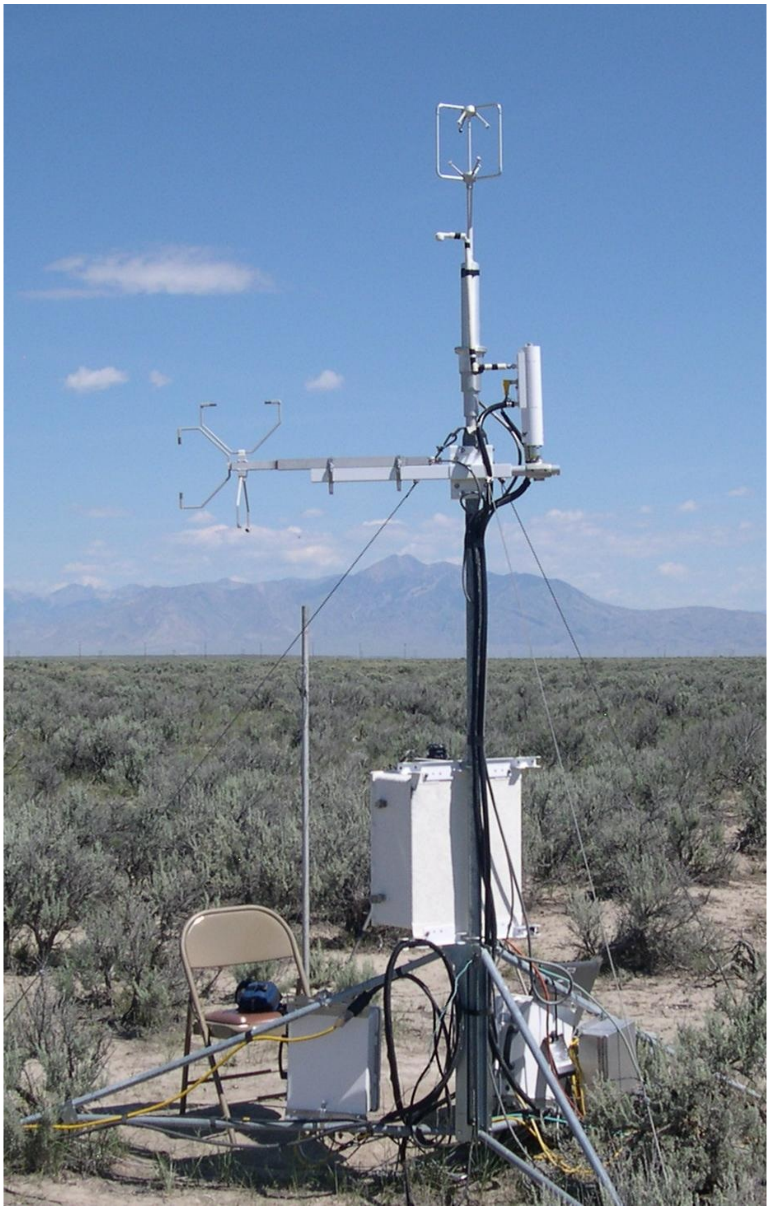

Figure 11. Photograph of the fast response instruments at the energy flux station at Grid 3, including a 3-d sonic anemometer and closed-path infrared gas analyzer. A second 3-d sonic anemometer is also shown, which had been installed for testing purposes.

Slow response measurements that are necessary to calculate the total energy balance are shown in Fig. 12. The instruments include downwelling short wave (solar) radiation, downwelling long wave radiation, upwelling short wave radiation, upwelling long wave radiation, photosynthetically active radiation, naturally aspirated air temperature and relative humidity, barometric pressure, soil temperature, soil moisture, and surface soil heat flux. These instruments are polled every 1.5

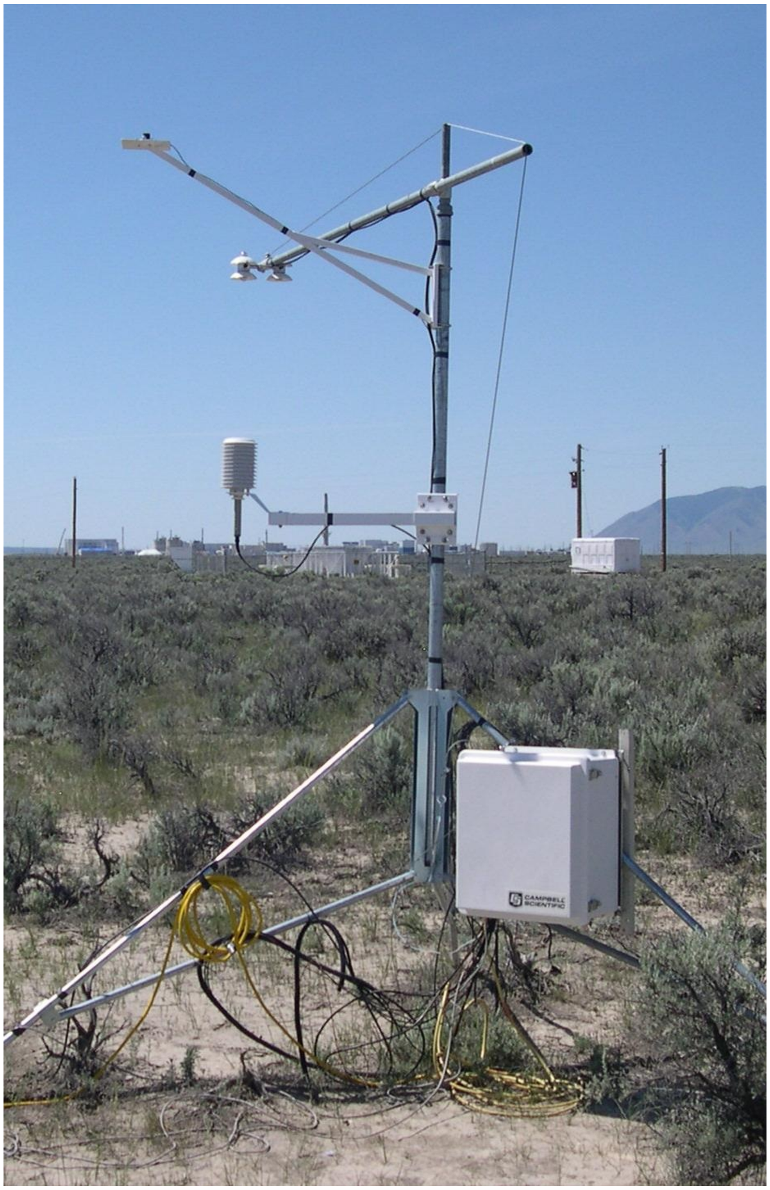

Figure 12. Photograph of the above-ground slow response instruments at the energy flux station at Grid 3, including a 4-component net radiometer, photosynthetically active radiometer, and a naturally aspirated air temperature/relative humidity sensor. (Soil and barometric pressure sensors are not visible.)

seconds and 5 minute averages are subsequently produced. The averaged data are obtained at the end of each averaging period and stored as a part of the NOAA/INL Mesonet database. Data summaries of some of the measurements from the energy flux station are included in this report. However, detailed investigations of CO_2 and H_2O fluxes as well as the surface energy balance have not yet been completed. The production of a climatology of these parameters awaits the completion of those investigations.

INL WEATHER CAMERA

A camera for monitoring weather phenomena during daylight hours was installed at Grid 3 in 1998. The data are transmitted in real-time to the ARLFRD office through a dedicated phone line. The camera can be remotely controlled at the ARLFRD office, and can zoom and pan to areas of interest, such as wildfires or severe storms. The camera has proven to be a very valuable tool for monitoring INL weather from the office in Idaho Falls. Routine archiving of the camera images began in May 2007.

MESONET STATION AND DATA ACQUISITION HISTORY

ARLFRD began collecting meteorological data when the first weather observation station was installed at CFA in 1949. The data were collected manually and by a strip chart recording system. Other stations were installed and discontinued as circumstances dictated. Details of the early stations through 1965 are available in Yanskey et al., 1966. The original system was replaced and automated during the 1969-1970 time period with radio telemetry equipment.

The collection of data from the Mesonet in the 1970's and 1980's was an evolving and complex situation as data collection technology also evolved and improved. The most complete description of the hardware and software used for the collection of Mesonet data during this time period is found in Ackermann and Johnson (1989). Several different computer systems were used to collect and store the data including strip chart recorders, printers, tape recorders, magnetic 9-track tapes, and optical drives over the two decades. In 1986, the installation of a new data acquisition system permitted for the first time limited real-time access to meteorological data for use in plume modeling for emergency support purposes. The second edition of the climatography (Clawson et al, 1989) contains a list of existing Mesonet stations as well as those that had been installed or removed after the publication of the first edition of the climatography.

In 1993, a complete replacement of Mesonet hardware and software provided unimpeded real-time meteorological data collected from across the entire ESRP for use in emergency response atmospheric dispersion models. Instruments, dataloggers, radios, and data collection software were all new and state of the science. Many towers were also replaced. Besides reporting winds and air temperature, which was essentially the only information provided by the old system, the new system also included measurements of atmospheric moisture (relative humidity), barometric pressure, solar radiation, and precipitation. The Mesonet was also expanded to include new stations in areas devoid of critical meteorological data. Some of the new stations included Base of Howe Peak (BAS) and Dead Man Canyon (DEA) on the site and Big Southern Butte Base (BIG), Craters of the Moon National Monument (CRA), and Sugar City (SUG) off-site. The 1993 system forms the backbone of today's NOAA/INL Mesonet.

Another major upgrade to the Mesonet was completed in 2004 with the replacement of the radio telemetry and data recording hardware and software. The meteorological instrumentation remained the same. This upgrade was essentially invisible to the data user. Data recoveries, already in excess of 99% since 1993, were improved. Over 20 years of continuous quality-controlled meteorological data are now available online from Mesonet stations across the INL and the ESRP.

Users of NOAA/INL Mesonet climate data should exercise care when working with older datasets. An understanding of the limitations of the data is important for proper analyses. Some important considerations are given below. Prior to June, 2006, wind gust was calculated as a 1-second average instead of the current 3-second average. Some stations have been known by more than one name while other stations have been relocated, discontinued, or combined. Relocation of stations, even over short distances, can have implications regarding the continuity of the historical data. Some of the early original digital data recorded prior to 1993 were collected every six minutes but the values were only about a 20-second average of the last portion of the six-minute period. Still older data collected with strip charts were later digitized by hand by visually interpreting the strip charts. Caution is therefore advised when working with older Mesonet data.

This climatological report is mainly based on Mesonet data acquired from January 1994 through December 2015 together with CFA thermograph data acquired from January 1950 through December 2015. The dates selected for this report were based on the first and last full years of complete data for these two observation systems. Although more data are available, the use of partial-year data would have skewed the yearly averages. In a few cases and where appropriate, some climatological data and descriptions in this climatography are carried over from previous publications since measurements for those parameters are not part of the current monitoring program and an adequate period of record already exists for those parameters.

Table 3 lists all of the location and name changes that have occurred to Mesonet stations since the start of the current system in 1993. Most of the name changes occurred when the current INL M&O contractor, Battelle Energy Alliance, LLC, changed a number of facility names in 2006. Four new locations were added since 1993 including Fort Hall (FOR), Atomic City (ATO), Lost River (LOS), and Rexburg (RXB). Eight stations have been relocated due to various reasons including the sale of private property, changing landscapes that blocked the airflow to the station, or for the creation of a CMS to improve public relations, as discussed previously. Two stations have been discontinued since 1993: Blackfoot (BLA) and Rexburg (RXB). A new Blackfoot station (BLK) was brought online to become a CMS at the Blackfoot Mountain View Middle School in August 2001. BLA and BLK operated concurrently for about 2 years to compare data between the two locations before BLA was discontinued in May 2003. A comparative analysis of the data from BLA and BLK were included in an appendix of the 3rd edition of the climatography (Clawson et al, 2007). RXB was discontinued in July 2013 because of safety issues with the tower, lack of funding, and radio communication issues between the tower and the ARLFRD office. Surplus instruments from RXB were relocated back to the nearby Sugar City station (SUG) from where they came when it was installed in 2001. The third station listed under the discontinued section in Table 3 is a 250 foot tall tower at CFA that was part of the Mesonet network prior to 1993. The CFA tall tower was not included in the 1993 equipment replacement effort and was subsequently discontinued because of safety concerns with the tower. The current CFA tower known as 690 has been collecting data at CFA since the 1993 upgrade.

Table 3. Changes to NOAA/INL Mesonet stations since in 1993.

Station Name Changes

New ID	New Station Name	Old ID	Old Station Name	Date of Change
On-Site				
ATR	Advanced Test Reactor Complex	RTC	Reactor Technology Complex	Sep-08
		TRA	Test Reactor Area	Mar-06
CIT	Critical Infrstructure Test Range Complex	PBF	Power Burst Facility	Mar-06
MFC	Materials and Fuels Complex	EBR	Experimental Breeder Reactor II	Mar-06
SMC	Special Manufacturing Capability	LOFT[a]	Loss of Fluid Test	Mar-06
Off-Site				
COX	Cox's Well	BIG	Big South Butte (Base)	Mar-06

New Stations

Station	Month/Year Data Collection Started
FOR	Mar-97
LOS	Nov-97
ATO	Sep-99
RXB	Aug-01

Relocated Stations

Station	Old Lat.	Old Long.	Date moved	Reason for Relocation
ABE	42.95497	112.82460	Jun-96	Property was sold.
IDA	43.51130	112.05970	Jun-97	Moved to Idaho Falls Greenbelt to become a CMS[b].
TER	43.81162	112.41410	Aug-97	Moved to become a CMS[b].
RWM	43.50173	113.04020	Jun-98	New building construction blocked wind flow.
HAM	43.96278	112.16670	Nov-99	Moved at landlord's request.
LOS	43.54854	113.00846	Jun-07	Moved across parking lot for expanded rest area.
ROB	43.74221	112.12575	Jul-08	Property was sold.
RIC	43.05841	114.13467	Jan-12	New building construction blocked wind flow.

Discontinued Stations

Station	Old Lat.	Old Lon.	Date Discontinued	Reason for Discontinuation
CFA	43.529000	112.9440	May-97	Tower safety issues.
BLA	43.256010	112.3971	May-03	Equipment removed to BLK to become a CMS[b].
RXB	43.809483	111.8004	Jul-13	Tower safety issues and funding ceased.

a. Station also known as TAN - Test Area North.

b. Community Monitoring Station (CMS).

GENERAL CLIMATOLOGY OF THE ESRP

The location of the ESRP, including its altitude above sea level, its latitude, and its intermountain setting, all greatly affect the climate of the area. The ESRP lies in the middle latitudes known for "westerlies" where a southwest wind is the prevailing wind direction. The westerlies generally move weather systems from west to east. The moderating influence of the Pacific Ocean to the west produces a climate which is usually warmer in the winter and cooler in the summer than is found at locations of similar latitudes in the more continental regions of the United States to the east of the Continental Divide. Cities such as Sioux Falls, SD and even Chicago, IL are at similar latitudes but exhibit much wider annual temperature ranges. Moist air masses from the Pacific Ocean travel across 600 miles of intervening mountain ranges before reaching the ESRP. Much of the moisture is squeezed out of the air during this process.

The ESRP is affected not only by maritime weather systems but also by continental weather systems. Summertime "monsoon" moisture occasionally affects the ESRP climate. The monsoonal moisture is transported north from the western Pacific Ocean off the coast of Mexico by general circulation patterns resulting from the summertime continental high pressure system over North America. Overall, annual precipitation in the ESRP is light and the ESRP is classified as an arid to semi-arid climate primarily because of low annual precipitation.

The type of precipitation at the INL is dependant upon the season. In the summer, precipitation most often falls as rain showers or thunderstorms. In the spring and autumn, rain showers or periods of rain or snow may occur. Most precipitation during the winter comes as snow. Precipitation occurs in every month, but the heaviest accumulations are generally in the spring or early summer. The most intense rainfall is associated with thundershowers particularly in May and June.

The Centennial and Beaverhead Mountain Ranges on the northwest end of the ESRP also affect the local climate. The mountain ranges act as an effective barrier to the movement of most of the intensely cold polar air masses that routinely pass south out of Canada toward the ESRP in the winter. Occasionally, however, pressure gradients become strong enough that cold air spills over the mountains and becomes trapped in the ESRP. The ESRP then experiences below normal temperatures and extreme surface air temperature inversions even during the day for periods lasting usually a week to 10 days. In the summertime and early autumn, the general North American high pressure system usually results in relatively dry air and infrequent clouds. These conditions, along with plentiful dry soil permit intense solar heating of the surface during the day and rapid radiational cooling at night. These factors combine to give a large diurnal range of air temperature near the ground.

The orientation of the ESRP, with mountains bordering on the west and east, tends to channel surface winds along a southwest-northeast axis. This channeling is caused by several factors, most notably the steering of synoptic winds by the topography and diurnal thermally driven circulations within the ESRP. Locations on the west side of the INL often are affected by more local winds generated by the tributary valleys to the west of the INL.

A summary of climatological data from 15 National Weather Service cooperative-observer stations located across the ESRP is given in Table 4. Many of these stations existed long before observations began at the INL Site. The data include extreme daily annual statistics for air temperature and precipitation from the beginning of the period of record for each station through 2012, which is the latest date for which climate summaries are available. The table also includes normal annual air temperatures, cooling and heating degree days, and precipitation levels. Normal values are a 30-year statistical summary of data for the period of 1981-2010. The average annual ESRP air temperature is 43.9 °F, based on 30-year normals from these stations. Air temperatures as high as 108 and as low as -48 °F have been recorded. Average annual ESRP precipitation is 11.42 in., again based on 30-year normals. The highest total daily precipitation was 4.31 in. Annual average snowfall, based on 30-year normals, ranges from 14.5 to 95.7 in.

Table 4. Compilation of temperature and precipitation records for 15 cooperative-observer stations on and surrounding the INL. Normals are from the National Climate Data Center (NCDC) for the 30 year period of 1981-2010. Absolute numbers are from the Western Regional Climate Center (WRCC) for the year the data collection began through October 2012.

National Climatic Data Center ID	Year Data Collection Began	Elevation (ft. msl)	Absolute Maximum Air Temp. (°F)	Absolute Minimum Air Temp. (°F)	Annual Normal Air Temp. (°F)	Annual Normal Cooling Degree Days (DGD/yr)	Annual Normal Heating Degree Days (DGD/yr)	Absolute Maximum Daily Precip. (in.)	Annual Normal Snowfall (in.)	Annual Normal Precip. (in.)
Aberdeen Exp. Station	1914	4,405	104	-42	44.8	297	7,678	2.41	24.5	9.14
Arco 3 SW	1914	5,325	102	-46	43.9	313	8,009	2.44	30.8	10.42
Blackfoot 2 SSW	1895	4,536	108	-40	46.6	445	7,145	2.07	22.8	11.29
Craters of the Moon	1958	5,897	101	-37	43.1	326	8,308	2.98	95.7	15.61
Dubois Exp. Station	1925	5,450	103	-31	43.0	284	8,307	2.60	47.7	12.90
Hamer 4 NW	1948	4,791	105	-48	43.5	273	8,129	2.11	25.5	9.62
Howe	1914	4,820	103	-38	43.9	311	7,996	2.50	14.5	7.78
Idaho Falls 2 ESE	1952	4,765	104	-34	46.0	415	7,335	1.73	27.1	14.25
Idaho Falls FAA AP	1948	4,730	102	-38	44.2	264	7,884	1.73	36.9	10.39
Idaho Falls 46 W	1952	4,938	105	-47	42.3	283	8,557	1.64	25.0	8.66
Minidoka Dam	1947	4,164	108	-41	47.3	463	6,916	1.52	23.4	9.53
Pocatello WSO AP	1939	4,449	104	-33	46.4	390	7,178	4.31	43.4	12.13
Rexburg BYU-Idaho	1977	4,920	102	-36	43.9	251	7,942	1.77	54.9	13.36
Richfield	1910	4,306	105	-40	44.8	378	7,735	2.00	32.2	11.06
St. Anthony 1 WNW	1895	4,950	100	-40	41.6	134	8,666	2.00	42.9	14.54
ESRP Average		N/A	N/A	N/A	43.9	N/A	N/A	N/A	N/A	11.42

This page is intentionally left blank.

SPECIFIC CLIMATOLOGY

This section presents climatological relationships for specific meteorological parameters, including winds, air temperature, precipitation, atmospheric moisture content, and atmospheric pressure. Winds provide the most important transport mechanism affecting site operations and provide the highest potential for off-site impacts; therefore, the wind regime on and around the INL has been monitored in detail for many years. Wind data comprise the largest portion of the INL climatological database. Air temperature is indicative of the thermal energy that drives many atmospheric processes. It is related to buoyant production or suppression of turbulence and thereby to atmospheric stability. Air temperature has also been monitored in detail for many years and comprises the second largest portion of the database. Both of these parameters are currently monitored at many locations both on and offsite (Tables 1 and 2, Figs. 5 and 6).

Precipitation, atmospheric moisture, atmospheric pressure, and solar radiation also comprise a portion of the climatological database. These parameters are currently being measured by the NOAA/INL Mesonet. Other special atmospheric phenomena have been observed and are also found in the climatological database. Descriptions and summaries of each of these types of data are found in the following sections. A few meteorological observations described in former editions of the Climatography of the INL have been discontinued and are not included herein, such as state of the ground. The reader is referred to earlier climatological publications for those descriptions and discussions.

WIND

Wind speed and direction (always recorded as the direction *from* which the wind is blowing) have been continuously monitored at a large number of stations on and surrounding the INL since 1950. The network of wind stations supporting operational requirements at the INL has expanded considerably since the installation of the original six stations. The original stations were improved in a series of upgrades over the years, and new sites were established to form an expanded observational network using 50 ft. towers. There were 34 meteorological observation stations in operation at the INL and surrounding area as of December, 2015. Thirteen of these were located within the boundaries of the INL (Table 1 and Fig. 5) while the remainder were sited at key locations throughout the ESRP (Tables 2 and Fig. 6). Knowledge of the general wind flow patterns on the INL is based on these data records.

The wind pattern over the INL can, at times, be quite complex. As noted previously, the orientation of the bordering mountain ranges, as well as the general orientation of the INL in the ESRP, play important roles in determining the wind regime. The INL is within the latitudes of prevailing westerly winds but these are normally channeled by topography. This channeling usually produces a west-southwest or southwest wind. When the prevailing westerlies at the mountain-top levels (approximately 5,000 ft. above the surface) are strong, the winds channeled across the INL between the mountains become very strong. Some of the highest wind speeds at the INL are observed under these meteorological conditions. The greatest frequency of this wind is in the spring.

Local mountain and valley features exhibit a strong influence on the wind flow under other meteorological conditions, as well. When the winds above the mountain-tops are strong and from a northwesterly direction, channeling in the

ESRP usually continues to produce southwesterly winds over most of the INL. However, at the mouth of Birch Creek, the northwest to southeast orientation of this valley channels strong north and northwest winds into the SMC area. This "Birch Creek" wind may equal or exceed the strongest southwesterly winds recorded at other locations on the INL.

Drainage winds also contribute to the overall wind flow over the INL. On clear or partly cloudy nights with only high thin clouds, the ESRP in general and the INL in particular experience rapid surface radiational cooling. This results in a cooling of the air near the surface that causes the air to become stable and less turbulent. When this occurs, almost all of the ESRP experiences a down-slope wind that follows the terrain from the higher elevations to the north and northeast downward in elevation across the ESRP to the lower elevations to the south and southwest. Simultaneously, air along the slopes of the mountains to the west of the INL cools at a faster rate than the air at the same elevation located aloft over the INL. Consequently, this air becomes more dense and flows or sinks toward the INL floor, forming a down-slope or katabatic wind. When this air reaches the INL, it continues to flow toward lower elevations and becomes part of the overall down-valley wind across the ESRP. This nocturnal down-valley flow is primarily out of the north-northeast.

A reverse flow, opposite in direction to that of the drainage wind, occurs during the daytime when the air along slopes is heated more rapidly than air at the same elevation over the valley. The air rises up the slopes as it becomes less dense. This results in both up-slope and up-valley winds. Up-valley winds are seldom detectable as a separate component of the wind until the synoptic pressure gradient becomes quite weak. Although the mountain and valley winds are predominantly "fair weather" phenomena, they can also occur under other sky cover conditions.

In addition to the local drainage winds, a somewhat stronger wind has been observed during the winter months. It occurs when an outbreak of cold air develops east of the Continental Divide. If the cold air becomes deep enough, it spills over the Continental Divide and flows down across the INL and behaves in the same manner as the general ESRP down-slope wind. The result of this phenomenon is winds from the northeast.

Pressure gradient forces related to passing synoptic weather systems, as well as local storms, all affect the winds of the INL. These storms alter the local flow regime such that winds from any direction can be observed. The frequency of occurrence of these types of wind flow patterns is very small, however.

On-site Surface Wind Characteristics

As introduced in the 3rd edition of the Climatography, the INL is being divided into three mircoclimate zones. The zones are largely a function of the different types of wind regimes observed over the years and not so much a function of air temperature or any other meteorological parameter. The three zones are: 1) Southwest INL, including CFA, ATR, NRF, Grid 3/INTEC, CITRC, and RWMC; 2) Southeast INL which includes MFC; and 3) North INL which includes SMC (Fig. 4). The boundaries between the zones are fluid and certain meteorological conditions may result in the temporary inclusion of one or more stations from one zone into that of another zone. For example, the wind pattern at NRF, ATR, and Grid 3/INTEC may at times more closely follow the wind pattern at SMC than the pattern at CFA and RWMC. However, generally speaking, the three wind regimes are distinct enough from each other to warrant the creation of three microclimate zones. Tall towers are located within each of these areas (GRI, SMC, and MFC, respectively) to document climatic characteristics that are specific to each area.

The characteristics of surface winds have traditionally been described at the INL using a graphical display called a wind rose and that tradition is continued here. A new method of describing wind fields will also be given in a later section that uses cluster analysis. Wind roses are graphs that display the frequency (in percentages) of the occurrence of winds from various direction sectors for selected speed classes. This is an effective method of showing joint wind speed and direction frequency distributions at a glance. The differences between stations, seasons, sensor levels, stability classes, etc., are easily observed in wind roses.

The presentation of wind roses will begin with GRI, which represents the Southwest INL microclimate zone and encompasses the majority of INL facilities. GRI will be followed by SMC, which represents the North INL microclimate zone and is the strongest contrast to the Southwest INL microclimate zone. Finally, data from MFC will be presented, which is a combination of patterns observed at GRI and SMC and represents the Southeast INL microclimate zone.

Southwest INL

Wind roses for GRI are illustrated in Figs. 13 and 14. The GRI tower is located approximately one mile north of INTEC on the east side Lincoln Boulevard, and is representative of wind flow patterns over the Southwest INL microclimate zone. GRI has a cumulative data history that spans decades. GRI has the advantage of being sited close to the Big Lost River channel, where it is easily influenced by both general ESRP down-valley (northeast) breezes that develop during the night and by a shallow surface flow that moves down the Big Lost River Channel (from the southwest). The figures present wind roses from all stability classes as a function of sensor height and time of day (day, night, and all hours). Even though atmospheric stability is not explicitly plotted in the wind roses, the division of night vs. day can generally be thought of as representing stable or unstable conditions, respectively. Data are from the 33 ft. and 200 ft. levels. An examination of the 22-year period of record from January 1994 through December 2015 lead to the following conclusions:

1. A distinct channeling effect of the wind is apparent. The directions with the highest percentages of occurrence are the west-southwest to southwest and north-northeast to northeast quadrants, depending on the time of day.
2. A very small percentage of the wind direction originates from the southeast and northwest quadrants.
3. Much higher wind speeds are observed during lapse conditions (usually daytime) than during inversion (usually nighttime) conditions.
4. Higher wind speeds and therefore, a smaller frequency of calms (period of very low wind speeds), are observed at the 200 ft. level.
5. A higher frequency of calm periods occurs during the winter months while the lowest frequency of calm periods occurs during the spring months (data not shown).
6. Nighttime wind directions are often different between the 33 ft. and 200 ft. levels due to the limited vertical mixing within the atmosphere during inversion (usually nighttime) conditions.
7. Under extremely stable conditions, a shallow surface layer develops that flows locally down-slope toward the north end of the INL, in opposition to the major down-slope flow of the general ESRP toward the southwest, which is observed above the shallow surface layer.

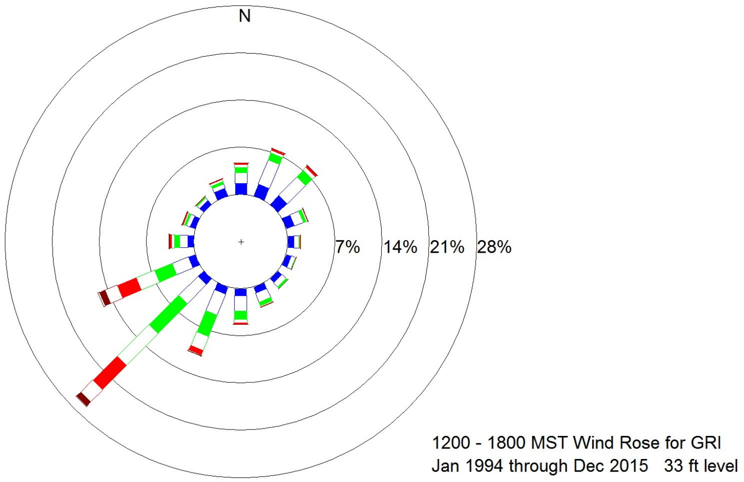

1200 - 1800 MST Wind Rose for GRI
Jan 1994 through Dec 2015 33 ft level

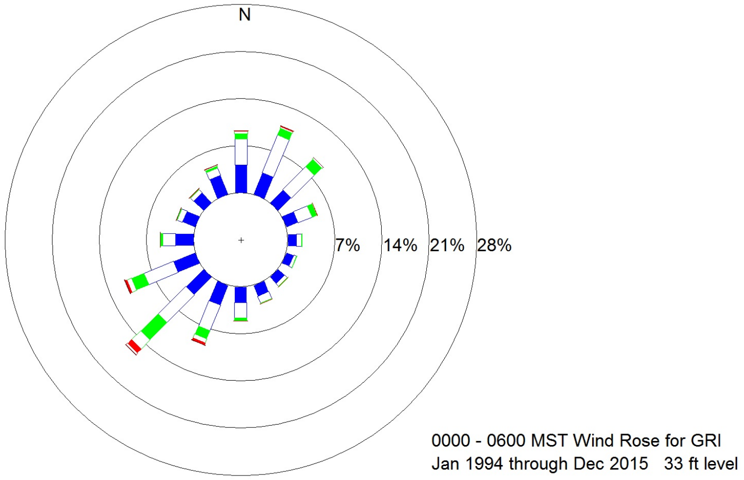

0000 - 0600 MST Wind Rose for GRI
Jan 1994 through Dec 2015 33 ft level

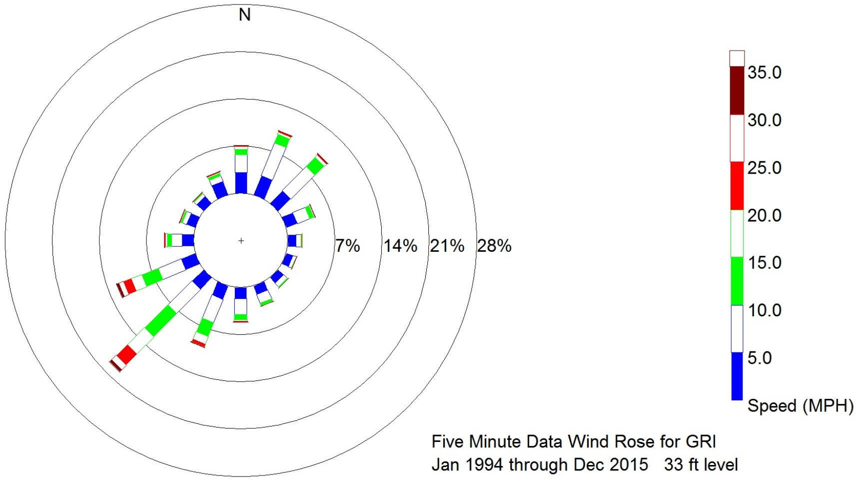

Five Minute Data Wind Rose for GRI
Jan 1994 through Dec 2015 33 ft level

Figure 13. Day (top), night (middle), and all hours (bottom) wind roses for the 33 ft. level at Grid 3, which represents the Southwest INL microclimate zone.

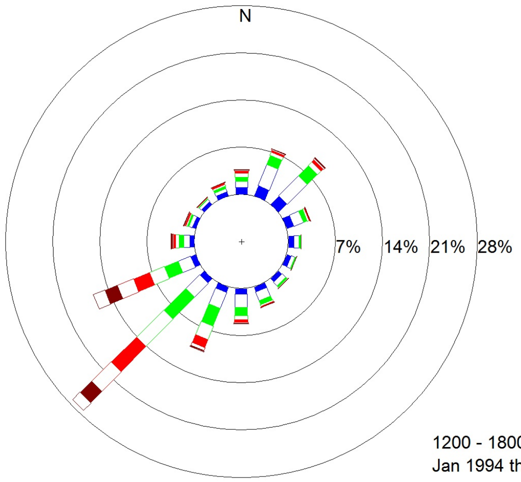

1200 - 1800 MST Wind Rose for GRI
Jan 1994 through Dec 2015 200 ft level

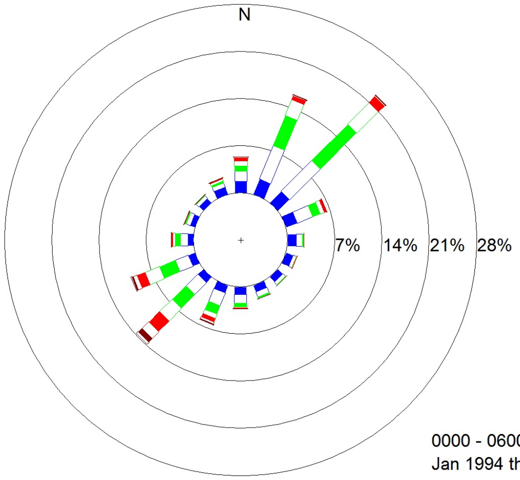

0000 - 0600 MST Wind Rose for GRI
Jan 1994 through Dec 2015 200 ft level

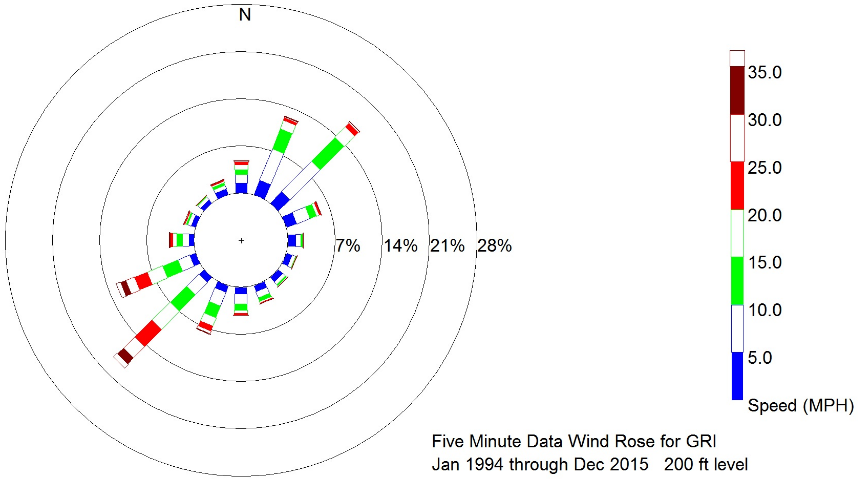

Five Minute Data Wind Rose for GRI
Jan 1994 through Dec 2015 200 ft level

Figure 14. Day (top), night (middle), and all hours (bottom) wind roses for the 200 ft. level at Grid 3, which represents the Southwest INL microclimate zone.

North INL

Wind roses for SMC are illustrated in Figs. 15 and 16. This tower is located immediately northeast of the historic Aircraft Nuclear Propulsion (ANP) hangar, and is representative of wind flow patterns over the North INL microclimate zone. Incidentally, it is the identical source of tall tower data for TAN used in the 2nd Edition Climatography (Clawson et al., 1989). The SMC tower is near the mouth of Birch Creek Valley, and is strongly influenced by flows from that valley. The figures present annual wind roses from all stability classes as a function of sensor height and time of day (day, night, and all hours). Data are from the 33 ft. and 150 ft. levels covering the same time period as the GRI data.

An examination of the data from SMC leads to the following conclusions:

1. A distinct channeling effect of the wind is apparent. The directions with the highest percentages of occurrence are the southwest and northwest to northeast quadrants. The large northwest component at night indicates the strong influence of the Birch Creek drainage at SMC.
2. A very small percentage of the wind direction originates from the west and southeast quadrants.
3. Higher wind speeds are observed during lapse (generally day time) conditions than during inversion (generally night time) conditions.
4. Nocturnal winds are almost exclusively out of the northern quadrant.
5. Higher wind speeds and hence, a smaller frequency of calms, are observed at the 150 ft. level, and large differences in the directional distribution between the surface and elevated sensor levels are noted.
6. A greater diversity of wind direction is observed at SMC when compared to GRI.
7. A much higher frequency of calm periods occurs during the winter months, approximately 2.5 times as often as for any other season. The lowest frequency of calm periods occurs during the summer season (data not shown).

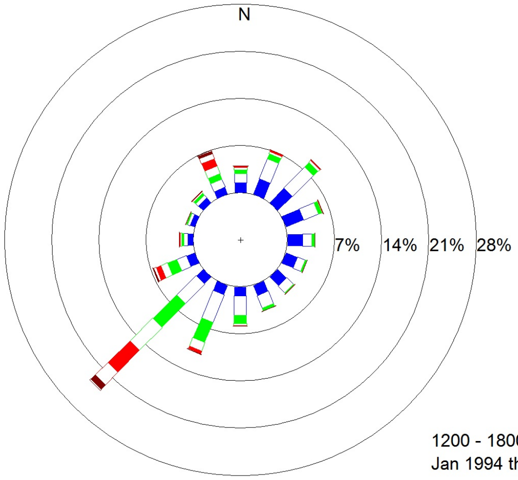

1200 - 1800 MST Wind Rose for SMC
Jan 1994 through Dec 2015   33 ft level

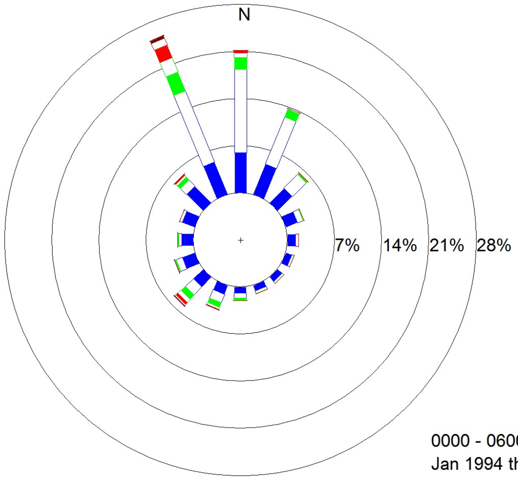

0000 - 0600 MST Wind Rose for SMC
Jan 1994 through Dec 2015   33 ft level

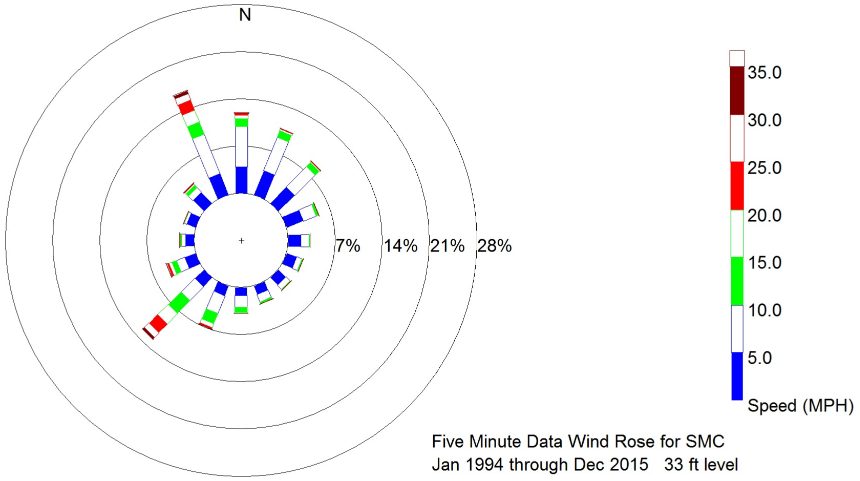

Five Minute Data Wind Rose for SMC
Jan 1994 through Dec 2015   33 ft level

Figure 15. Day (top), night (middle), and all hours (bottom) wind roses for the 33 ft. level at SMC, which represents the North INL microclimate zone.

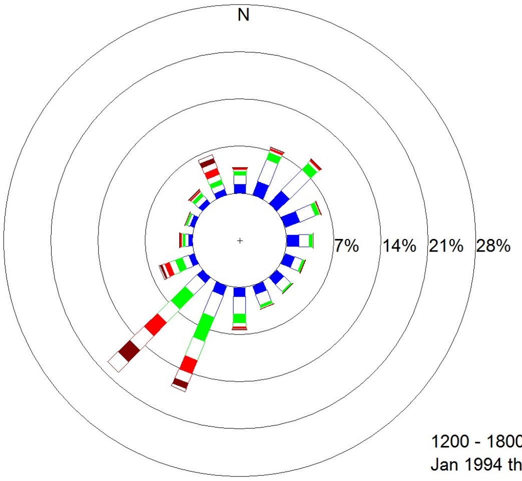

1200 - 1800 MST Wind Rose for SMC
Jan 1994 through Dec 2015 150 ft level

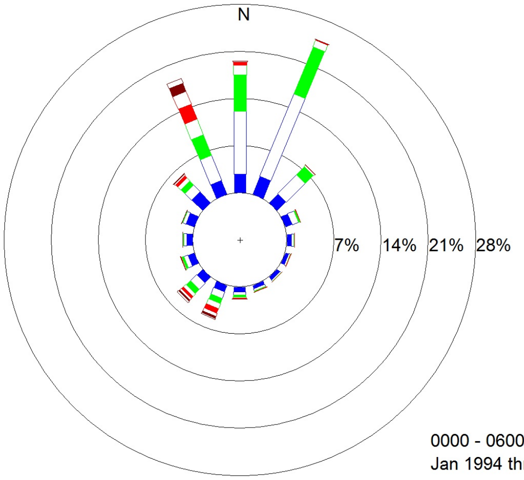

0000 - 0600 MST Wind Rose for SMC
Jan 1994 through Dec 2015 150 ft level

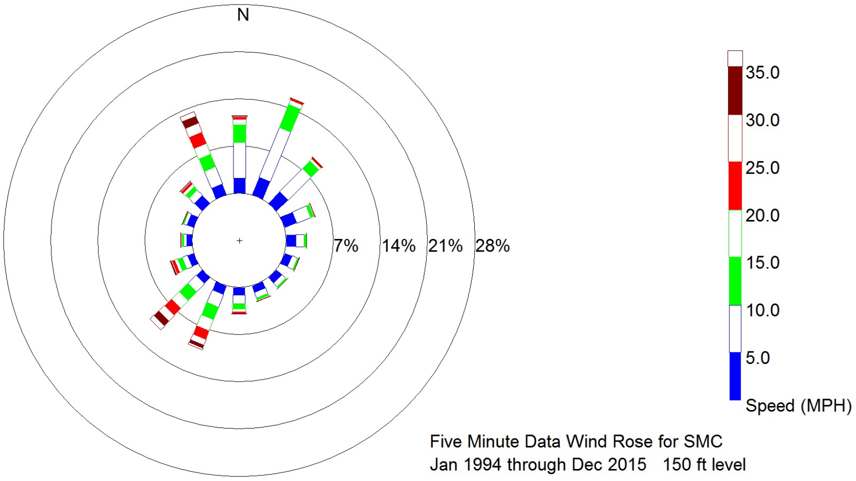

Five Minute Data Wind Rose for SMC
Jan 1994 through Dec 2015 150 ft level

Figure 16. Day (top), night (middle), and all hours (bottom) wind roses for the 150 ft. level at SMC, which represents the North INL microclimate zone.

Southeast INL

Wind roses for the MFC area are illustrated in Figs. 17 and 18. This tower is located on the southeast perimeter of the MFC complex, and is representative of wind flow patterns over the Southeast INL microclimate zone. The figures present wind roses in all stability classes as a function of sensor height and time of day (day, night, and all hours). Data are from the 33 ft. and 250 ft. levels covering the same time period as the GRI and SMC data.

An analysis of the data from MFC leads to the following conclusions:

1. In many respects, daytime winds at MFC are similar to GRI.
2. At night, the 33 ft. MFC winds are more variable in direction than at GRI, and there is a higher frequency of easterly and southerly winds. These differences are likely associated with the higher terrain that runs along the southeast corner of INL (Fig. 2).
3. At MFC, a very small percentage of the wind directions originate from the northwest and southeast quadrants.
4. At night, MFC experiences upper level northwesterly winds to a greater extent than at GRI. This is a result of terrain shielding of NW winds at GRI.
5. At night, MFC experiences upper level southwesterly winds over a greater range in azimuths than at GRI and in contrast to SMC where southwesterly winds are largely absent.
6. Higher wind speeds and a smaller frequency of calms are observed at the 250 ft. level.

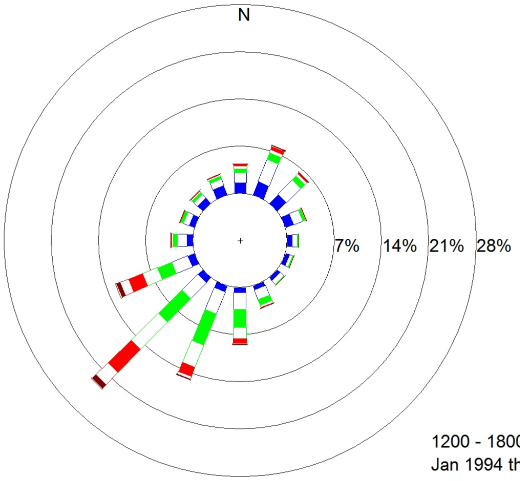

1200 - 1800 MST Wind Rose for MFC
Jan 1994 through Dec 2015   33 ft level

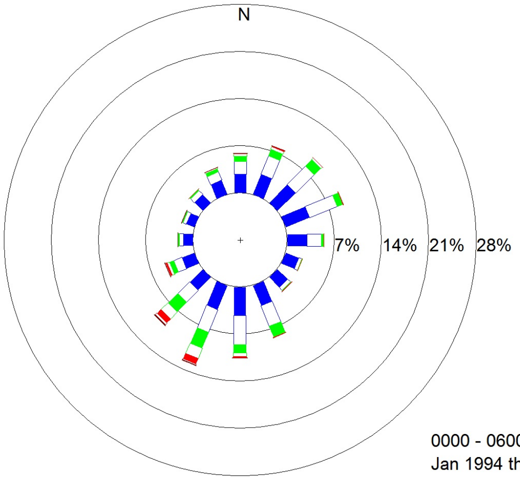

0000 - 0600 MST Wind Rose for MFC
Jan 1994 through Dec 2015   33 ft level

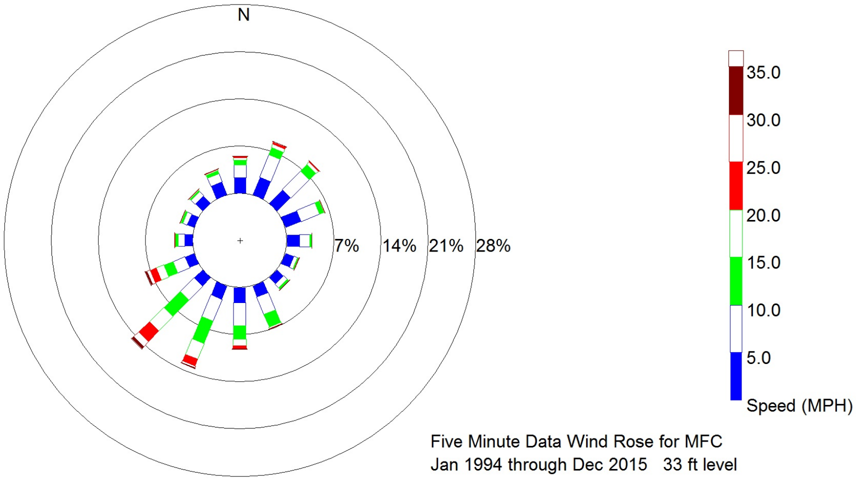

Five Minute Data Wind Rose for MFC
Jan 1994 through Dec 2015   33 ft level

Figure 17. Day (top), night (middle), and all hours (bottom) wind roses for the 33 ft. level at MFC, which represents the Southeast INL microclimate zone.

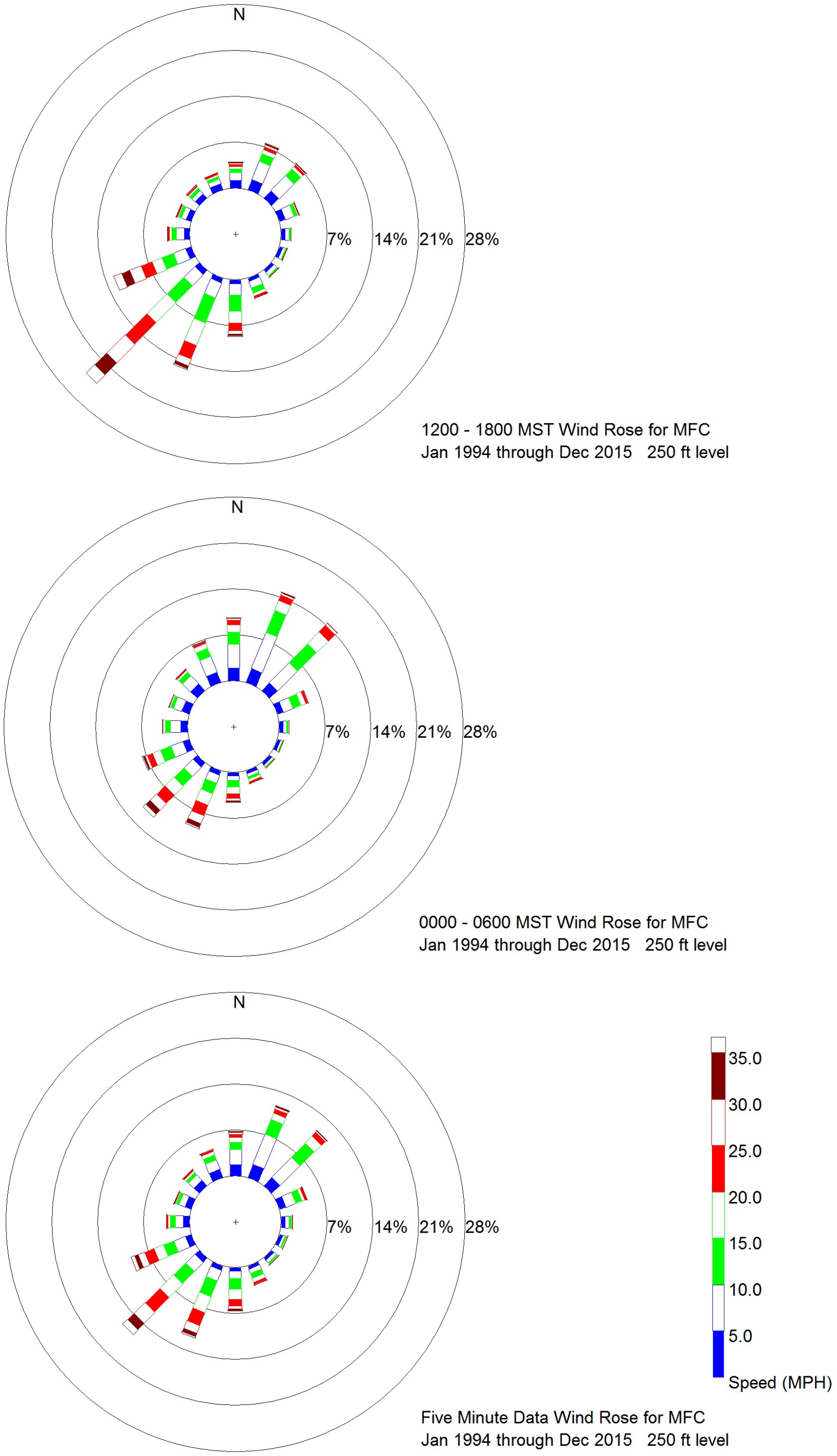

Figure 18. Day (top), night (middle), and all hours (bottom) wind roses for the 250 ft. level at MFC, which represents the Southeast INL microclimate zone.

When considering all wind roses simultaneously, a distinct diurnal trend is evident in the data from all three locations. There is a tendency for an increase in the frequency of winds from the northeast quadrant during the nighttime hours at GRI. The increase is not large, however, and is due to the lag of the diurnal shift of the wind direction after the temperature stability class has changed from lapse to inversion near sunset, and back sometime after sunrise. Thus, southwest winds can continue to blow for some hours after sunset at GRI. Conversely, the northeast winds associated with down-valley drainage conditions can continue to blow in the morning after the inversion has dissipated near the ground. There is also a tendency for shallow (less than 100 ft deep) southwest drainage winds to occur at GRI due to the local sloping of the terrain from southwest to northeast.

The shift of wind direction with a change from lapse to inversion is much more pronounced at SMC than at GRI. This is evidenced by an increase in the percentage of northerly winds at night at SMC. The distribution indicates that, for a certain fraction of time, there exists an opposing wind direction between GRI and SMC. Winds from the southwest at GRI and from the northeast at SMC can be observed simultaneously. The predominant wind direction in the winter season at SMC is from the northeast, while at GRI it is from the southwest.

At GRI, multiple wind layers are frequently observed under nocturnal conditions. A shallow southwesterly surface flow follows the local Lost River Channel slope toward the northeast. This flow often lies below a layer of northeasterly winds at the height of the tower top which follows the northeast-to-southwest slope of the general ESRP at GRI. This middle-layer flow is often capped by yet another layer of upper level winds from the west or southwest that reflects synoptic-scale gradient winds above the atmospheric mixing layer.

On-site Wind Averages and Maximums

Monthly average wind speeds observed at GRI, SMC, and MFC for the period January 1994 through December 2015 are given in Table 5. These stations represent the microclimate zones of Southwest INL, North INL, and Southeast INL, respectively. The months with the highest average wind speeds at all three locations and at all tower levels are April, May, and June. The 33 ft. monthly mean speed values range from 10.2 to 11.0 mph in these months. The month with the lowest average wind speeds at all three locations and at all tower levels is January. The 33 ft. monthly mean speed values range from 5.7 to 7.2 mph in January. Tower top winds at the three stations are of different heights and are, therefore, not directly comparable across sites. MFC shows the highest average wind speeds which would be expected on this, the tallest tower. Likewise, the opposite is true for the SMC tower where the lowest average wind speeds were observed on the shortest tall tower.

Peak wind gusts between January 1994 and December 2015, classified by month and observed at GRI, SMC, and MFC, are given in Table 6. The measurement levels at both 33 ft. and at the tower top are noted. The maximum 1-second gust recorded at GRI at the tower top 200 ft. was 93.1 mph. The maximum gust at the SMC tower top 150 ft. was 80.2 mph, and at MFC 250 ft. it was 84.7 mph. Higher gusts almost always occur at greater heights on each of the towers, where the influence of surface friction is less and eddy sizes are larger. Each site, however, has instances where the maximum annual gust at the 33 ft. level did not occur in the same month as the maximum annual gust at the tower top. High wind gusts at the INL may result from either pressure gradients associated

Table 5. Monthly mean wind speed (mph) values for GRI, SMC, and MFC representing the Southwest, North, and Southeast INL climate zones, respectively.

	Southwest INL (GRI)		North INL (SMC)		Southeast INL (MFC)	
Month	33 ft. (mph)	200 ft. (mph)	33 ft. (mph)	150 ft. (mph)	33 ft. (mph)	250 ft. (mph)
January	6.6	9.4	5.7	7.4	7.2	10.9
February	7.7	10.9	7.1	9.1	8.2	12.1
March	9.9	13.7	9.2	12.2	10.3	14.7
April	10.6	14.4	10.5	13.7	11.0	15.4
May	10.9	14.6	10.4	13.6	11.0	15.3
June	10.8	14.5	10.2	13.3	10.9	15.2
July	10.0	13.7	9.5	12.5	10.1	14.2
August	9.5	13.2	8.8	11.8	9.6	13.7
September	8.8	12.5	8.2	11.2	9.0	13.2
October	8.7	12.4	8.4	11.2	9.1	13.4
November	8.1	11.7	7.2	9.7	8.6	12.8
December	7.1	10.3	6.6	8.8	8.0	12.1
ANNUAL	9.1	12.6	8.5	11.2	9.4	13.6

Note: Data period of records span January 1994 through December 2015.

Table 6. Monthly peak[a] wind speed (mph) values for GRI, SMC, and MFC representing the Southwest, North, and Southeast INL climate zones, respectively.

	Southwest INL (GRI[b])		North INL (SMC[b])		Southeast INL (MFC[b])	
Month	33 ft. (mph)	200 ft. (mph)	33 ft. (mph)	150 ft. (mph)	33 ft. (mph)	250 ft. (mph)
January	63.2	73.3	61.1	68.7	65.3	77.8
February	70.4	81.1	59.8	65.8	73.5	75.3
March	66.0	73.7	74.9	73.1	62.0	69.2
April	76.5	93.1	66.1	78.4	71.3	84.7
May	71.4	68.8	65.8	77.6	73.8	75.2
June	77.2	86.2	71.6	80.2	67.4	82.5
July	81.6	89.6	69.1	72.6	65.5	74.4
August	66.6	75.1	69.6	78.8	70.4	75.7
September	65.4	76.8	65.9	72.8	61.1	68.6
October	65.2	70.3	64.3	74.9	62.4	69.4
November	58.4	66.9	68.5	77.5	62.4	73.1
December	57.3	68.0	59.9	68.9	63.5	72.5
ANNUAL	81.6	93.1	74.9	80.2	73.8	84.7

a. Mesonet peak winds were defined by a 1-second gust duration through May 2006, and by a 3-second gust from June 2006.

b. Data period of record spans January 1994 through December 2015.

with large-scale systems or from local thunderstorms. Most gusts from synoptic systems are channeled from the southwest. Gust directions from thunderstorms are recorded from a variety of directions since they may form in varying locations and move in any direction. Gusts at the 33 ft. level that exceed speeds measured at the tower top are an artifact of separate gust events. Both the monthly average and the maximum gust wind speeds at each of the stations are comparable when sensor height differences are considered.

The relationship between the monthly mean speed, the greatest hourly mean speed, and the greatest peak gust at the GRI 33 ft. level is listed in Table 7. Data from the other two stations are not included here because the data from GRI are representative of most of the features described here. The wind directions for all of the highest hourly speeds listed for GRI are from the west-southwest and southwest. This is not always true at SMC where strong winds are often channeled towards SMC from Birch Creek valley which is located to the northwest.

Table 7. Wind speed means and extremes for 33 ft. tower level at GRI[a].

Month	Monthly Mean Speed (mph)	Greatest Hourly Mean Speed (mph)	Greatest Hourly Mean Direction (deg.)	Greatest Hourly Mean Direction (16^{th})	Greatest Peak Gust[b] Speed (mph)	Greatest Peak Gust[b] Direction (deg)	Greatest Peak Gust[b] Direction (16^{th})
January	6.6	46.2	240	WSW	63.2	240	WSW
February	7.7	38.5	244	WSW	70.4	255	WSW
March	9.9	43.5	243	WSW	66.0	240	WSW
April	10.6	42.5	235	SW	76.5	247	WSW
May	10.9	41.3	242	WSW	71.4	270	W
June	10.8	40.6	250	WSW	77.2	223	SW
July	10.0	40.4	243	WSW	81.6	232	SW
August	9.5	37.9	230	SW	66.6	256	WSW
September	8.8	37.4	236	SW	65.4	240	WSW
October	8.7	42.5	230	SW	65.2	224	SW
November	8.1	39.2	243	WSW	58.4	226	SW
December	7.1	39.5	236	SW	57.3	238	WSW
ANNUAL	9.1	46.2	240	WSW	81.6	232	SW

a. Data period of record spans from January 1994 through December 2015.

b. Mesonet peak winds were defined by a 1-second gust duration through May 2006, and by a 3-second gust from June 2006.

Regional Near-Surface Wind Flow Patterns

Annual, all-stability wind roses for three time periods (day, night, and all hours) have been plotted for all of the NOAA/INL Mesonet stations for analysis of near-surface regional wind flow patterns. The wind roses are presented in Appendix A because they are too numerous to be presented here. When reviewing the individual wind roses, a number of consistent trends become apparent as a result of terrain and atmospheric stability considerations.

Terrain Influences

1. The predominant southwest-northeast wind flow direction of the ESRP is evident in most of the wind roses. This predominance is a result of the orientation of the ESRP when convective heating couples the surface winds with the persistent westerly winds aloft. Prefrontal winds are also invariably southwesterly. Nocturnal drainage winds are from the northeast at most stations. The monitoring stations which strongly exhibit

these occurrences are Idaho Falls (IDA), Kettle Butte (KET), and Sugar City (SUG).

2. Subtle terrain features adjacent to individual stations considerably affect the overall southwest-northeast flow. These features modify the wind direction when a low wind speed prevails, particularly during inversion conditions. The Materials and Fuels Complex (MFC), Rover (ROV), and Terreton (TER) stations have broadened northwest-southeast components due to drainage winds moving northwest from elevated terrain located to the south and east of these stations. CIT has an augmented southerly component that results from slightly higher terrain located to the south. Both Hamer (HAM) and Dubois (DUB) have significant distributions of easterly winds caused by terrain blockage of the airflow at the north end of the ESRP.
3. Channeled canyon cold air drainage dominates the wind distributions at stations located at the boundaries of mountain valleys. Arco (ARC), Blue Dome (BLU), Monteview (MON) and SMC (particularly the lower level) are dominated by this flow pattern. The Sand Dunes (SAN), NRF, and ROV stations have augmented northwesterly winds that result from the influence of these canyon winds as they flow out onto the ESRP. The other monitoring stations that are not specifically enumerated above exhibit some or all of the main flow characteristics given in the preceding discussion.

Atmospheric Stability Influences

In neutral conditions, i.e. stability class D, winds at the upper and lower tower levels show very similar characteristics. No large wind shears are evident. Stability class D is common when the atmospheric thermal gradient is near adiabatic due to high wind speeds with strong mechanical turbulence or during heavy overcast conditions when the net radiation flux is very small. Under high wind conditions, the possibility of a large directional shear with height is minimized.

In stable conditions, i.e. stability classes E and F, the flow near the surface becomes decoupled from the winds aloft. Stability classes E and F indicate the presence of temperature inversions. Large shears in wind direction between the upper and lower levels are manifest under these conditions. Additionally, the surface wind exhibits a large variability in direction (meander) during conditions of low wind speeds.

In unstable conditions, i.e. stability classes A, B, and C, winds at both the upper and lower levels are influenced by buoyant eddies which rise as air is warmed at the surface. Stability classes A through C are common when solar heating is strong and wind speeds are low. The buoyant eddies tend to broaden the directional distribution of low-speed winds which would otherwise exist, because they are somewhat randomly distributed spatially. This disruption is weakest at the upper level where, due to a reduction of frictional effects, the winds are stronger.

Mesonet Wind Field Clusters

Modern computer numerical analyses have made it possible to improve upon the qualitative wind trajectory discussion that first appeared in the 2nd Edition Climatography (Clawson et al., 1989). Cluster analysis techniques provide an improvement over both site-specific wind roses and general trajectories. Carter et al., in an unpublished manuscript written in 2007 (*Identifying Natural Clusters in Eastern Idaho Wind Fields*), described a more rigorous numerical cluster analysis method that identifies and quantifies the occurrence of preferential wind fields. The procedure, called a "k-means" cluster analysis technique, identified a relatively small number of wind fields that accounted for 99.9% of observed INL wind fields. The analysis was based on five-minute averaged data from 32

NOAA/INL Mesonet stations, 13 of which were within the INL boundaries. The period of record examined for the cluster analysis was approximately 5½ years, from November 1993 through February 1999.

Eight wind patterns resulted from the cluster analysis. The patterns, their frequency of occurrence, and general descriptions are given in Table 8. The general descriptions include the various wind patterns described in discussions already provided above, especially terrain-driven and synoptic driven winds. The first three wind patterns occurred nearly 2/3 of the time and explain the bulk of the observed wind fields. The last 4 patterns (5-8) each occurred with a frequency of less than 10% and a combined frequency of less that 25%. However, each of the patterns was uniquely and widely different from any other pattern, thereby requiring separate explanations. Each pattern is described more completely using maps, diagrams, and graphs later in this section.

The most commonly occurring wind field called Drainage Flow (number 1), which was a pattern of generally northeast winds, runs counter to the experience of the common INL site worker. When queried, most would claim that southwest winds (patterns 5 or 7) are the most common at the INL. That perception is correct when one considers that southwest winds mostly occur during the afternoon hours when most site workers are on the job. There are few workers on site at the times of day when Drainage Flow is the common pattern. Also enforcing the site workers notion is the occurrence of the easily remembered wind flow pattern 7, Strong Synoptically-forced SW Flow, which is a pattern of sustained southwest winds that sometimes exceed 40 mph, causing tumbleweeds and other debris to accumulate on fences and other structures. The explanations for these observations are all given below in separate sections for each wind pattern.

The cluster analysis provided a basis for additional ESRP and INL specific wind pattern analyses. Maps of the 8 clusters were created using not only the data from the cluster analysis, but for a much longer period of record extending over 22 years from January 1994 through December 2015. Data for all existing Mesonet stations were included except for RXB and SUM, which had either incomplete or biased data. The maps show representative wind patterns using

Table 8. Cluster-derived ESRP wind patterns, frequency of occurrence, and general descriptions.

Wind Pattern	Frequency of Occurrance (%)	Description
1	26.6	Drainage Flow - light wind speeds from the northeast
2	24.4	Weak Flow - light wind speeds and variable directions
3	12.5	Moderate Up-valley Flow - gentle wind speeds from the south-southwest
4	11.5	Decreasing Up-valley Flow Near Sunset / Moderate Synoptic-affected Flow - gentle to moderate wind speeds from the southwest with light wind speeds and somewhat variable directions in the north
5	8.6	Well-developed Up-valley Flow - moderate wind speeds from the southwest
6	6.6	Down-canyon Flow - gentle to moderate wind speeds from the northwest
7	5.6	Strong Synoptically Forced Southwest Flow - strong wind speeds from the southwest
8	4.1	Strong Synoptically-forced North-northeast Flow - strong wind speeds from the north-northeast

arrows to represent one-hour average speed and direction vectors, with the length of each arrow scaled to the mean wind speed and the orientation of the arrow representing the direction of wind flow at a given Mesonet station. An example is shown in Fig. 19 for wind pattern 1. A representative map is provided for each wind pattern in the separate wind pattern discussions below.

A subsequent analysis was undertaken to describe the frequency of time for which a given wind pattern occurred as a function of time of day for each month of the year. For each pattern, there were 288 calculated data values (12 months by 24 hours). These values were subsequently plotted in color diagrams to provide a visual representation of the relationships. An example for wind pattern 1 is shown in Fig. 20. The most frequent occurrences were colored with red and the least frequent occurrences were colored with blue. Occurrences with intermediate frequencies were indicated using orange, yellow, and green, as indicated in the legend in the lower right corner of the diagram. The number of occurrences were evenly divided into the five color groups, so the red contained 20% of all occurrences, orange contained 20% of all occurrence, and so forth for each of the other colors. Figure 20 shows, for example, that between midnight and 0100 MST in January, wind pattern 1 occurred 34% of the time. In February during the same time of day, wind pattern 1 occurred 35% of the time, while in August between the hours of 1300 to 1400 MST, wind pattern 1 occurred only 2% of the time. The legend in Fig. 20 indicates that the frequencies ranged from 2 (blue) to 64% (red) of the time. The red color represents 20% of highest frequencies of occurrence, ranging from 38 to 64%. Likewise, blue represents 20% of the lowest frequencies of occurrence, and those ranged from 2 to 11%. Green, yellow, and orange represent 12 to 24%, 25 to 33%, and 34 to 37%, respectively. These color-coded diagrams are also included in the discussions below for each wind pattern.

Yet another analysis was undertaken to discover the likelihood of a given wind pattern persisting once it became established and also the relative likelihood of its evolution into a different wind pattern with the passage of time. Numerical values were calculated for each possibility. Color-coded bar graphs were generated from the numerical values to visually describe the persistence likelihoods for each wind pattern. In each graph, a black-outlined bar represents the percent of the time that the winds persisted in the original wind pattern for the duration of hours shown, with the first hour representing the initial formation of the wind pattern. The remaining portion of the graph is a stacked bar graph that shows what wind pattern the initial wind pattern eventually evolved into. A wind pattern could even return to its original pattern within a 24-hour period and this is also shown in the graphs. A legend in the lower right portion of each graph shows the color-coding for each wind pattern type. Using wind pattern 1 as an example to explain these graphs, Fig. 21 shows that wind pattern 1 persisted into the second hour 80% of the time (black-outlined bar). It also evolved during the second hour into wind pattern two 15% of the time, into wind pattern six 2% of the time, and into wind pattern eight 3% of the time. In the third hour after which wind pattern 1 was initially established, it persisted continuously 69% of the time. However, if wind pattern 1 evolved into some other pattern during the previous hour, it evolved back into the original wind pattern 1 during the 3rd hour 72% of the time. Also during the 3rd hour, it evolved into wind pattern two 20% of the time, into wind pattern three 1% of the time, into wind pattern six 2% of the time, and into wind pattern eight 4% of the time. These graphs are included in the separate discussions for each wind pattern below.

Wind Pattern 1, Drainage Flow

The most common wind pattern determined by the cluster analysis program was called Wind Pattern 1, Drainage Flow. It describes a general drainage flow or down-valley pattern of northeasterly winds less than 10 mph throughout the ESRP (Fig. 19). This pattern was observed 26.6% of the time. It was most common between 0100 and 0900 MST during summer and early autumn mornings from June through September when regional pressure gradients were small (Fig 20). It was least common during spring, summer, and autumn afternoons and evenings (April through October, from 1100 through 1900 MST), which is generally when strong solar radiational heating of the surface creates up-valley flow and surface winds become linked to upper-level winds.

The persistence of wind pattern 1, Drainage Flow, over a 24-hour period is shown in Fig. 21. This pattern persisted into the second hour 80% of the time (black-outlined bar). It persisted into the third hour 69% of the time, and continuously into the 12th hour approximately 18% of the time. In 24 hours, wind pattern 1 persisted continuously for only about 5% of the time, but this persistence value is much higher than for any other pattern. The most common pattern it evolved into was wind pattern 2, Weak Flow. It also evolved into wind pattern 3, Moderate Up-valley Flow, with the highest frequency of occurrence in the 1200-1600 MST time period after the onset of Drainage Flow. After about 18 hours of declining return frequency to a minimum of about 32%, the frequency of return to wind pattern 1 increased to about 38% after 24 hours. This indicates a cycling between Drainage Flow transitioning to Weak Flow, then to Moderate Up-valley Flow, back to Weak Flow, and finally back again to Drainage Flow in a daily cycling of down-valley and up-valley flows.

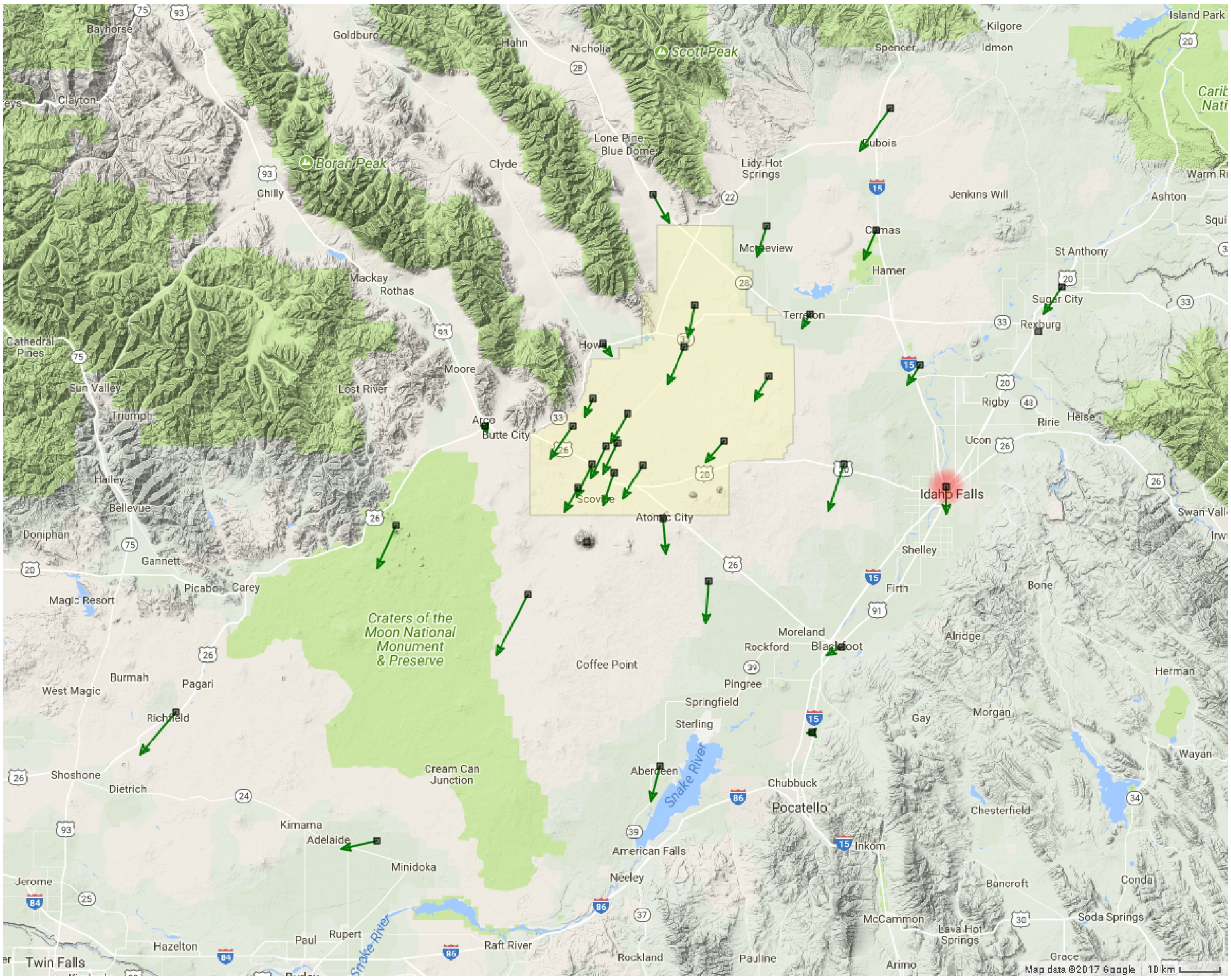

Figure 19. Wind vectors for Wind Pattern 1, Drainage Flow, which describes low wind speed drainage flow from the northeast. Green arrows indicate wind speeds < 11.2 mph.

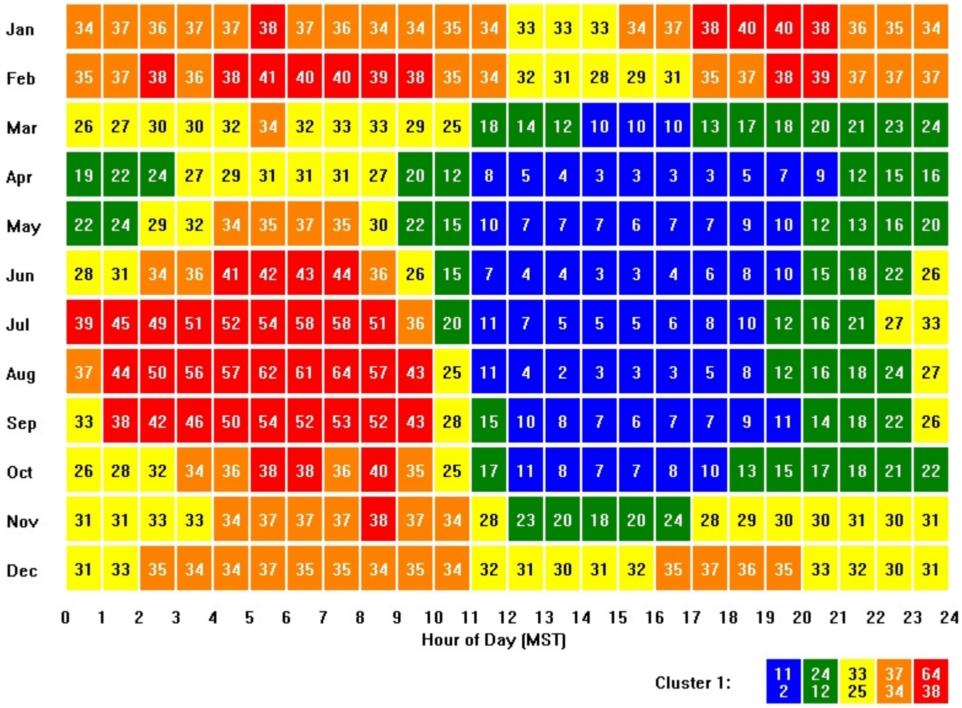

Jan	34	37	36	37	37	38	37	36	34	34	35	34	33	33	33	34	37	38	40	40	38	36	35	34
Feb	35	37	38	36	38	41	40	40	39	38	35	34	32	31	28	29	31	35	37	38	39	37	37	37
Mar	26	27	30	30	32	34	32	33	33	29	25	18	14	12	10	10	10	13	17	18	20	21	23	24
Apr	19	22	24	27	29	31	31	31	27	20	12	8	5	4	3	3	3	3	5	7	9	12	15	16
May	22	24	29	32	34	35	37	35	30	22	15	10	7	7	7	6	7	7	9	10	12	13	16	20
Jun	28	31	34	36	41	42	43	44	36	26	15	7	4	4	3	3	4	6	8	10	15	18	22	26
Jul	39	45	49	51	52	54	58	58	51	36	20	11	7	5	5	5	6	8	10	12	16	21	27	33
Aug	37	44	50	56	57	62	61	64	57	43	25	11	4	2	3	3	3	5	8	12	16	18	24	27
Sep	33	38	42	46	50	54	52	53	52	43	28	15	10	8	7	6	7	7	9	11	14	18	22	26
Oct	26	28	32	34	36	38	38	36	40	35	25	17	11	8	7	7	8	10	13	15	17	18	21	22
Nov	31	31	33	33	34	37	37	37	38	37	34	28	23	20	18	20	24	28	29	30	30	31	30	31
Dec	31	33	35	34	34	37	35	35	34	35	34	32	31	30	31	32	35	37	36	35	33	32	30	31

Figure 20. Temporal frequency of occurrence for Wind Pattern 1, Drainage Flow.

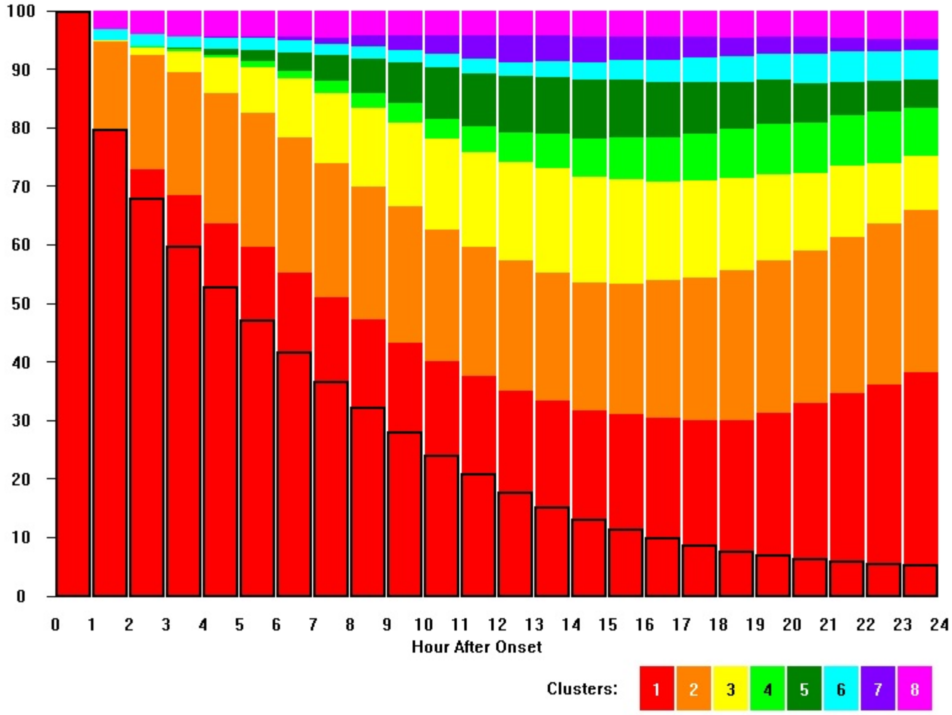

Figure 21. Hourly persistence and transition frequencies of Wind Pattern 1, Drainage Flow.

Wind Pattern 2, Weak Flow

Wind pattern 2, Weak Flow, typically involved light wind speeds (less than 8 mph) with variable wind directions throughout the ESRP as shown in Fig. 22. On an annual basis, it was the second most common wind pattern, occurring 24.4% of the time. It was most common during midsummer, autumn, and early to midwinter nights and early mornings (July to February, 2200 to 0700 MST). This pattern occurred when regional pressure gradients were small and when surface winds were highly decoupled from winds aloft by strong temperature inversions (Fig. 23). It was least common during late spring, summer, and early autumn afternoons when strong solar radiation created up-valley flow (March to October, 1200 to 2000 MST).

Figure 24 depicts the persistence of wind pattern 2, Weak Flow, over a 24-hour time period. Wind pattern 2 was not as persistent as pattern 1, and dropped to less than 50% by hour 3. It persisted continuously for less than 10% of the time after a period of 9 hours and was almost never observed to last continuously over a 24-hour time period. Wind pattern 2 often transitioned into pattern 1, Drainage Flow, or 3 Moderate Up-valley Flow, and then back again, which yet again indicates a 3-phase daily cycling pattern of Drainage Flow, changing to Weak Flow, then to Moderate Up-valley Flow, back to Weak Flow, followed again by Drainage Flow. It is in wind pattern 2 that the microclimate zones of the INL become readily apparent. In wind pattern 2, northerly flow was observed in the North INL zone, southwesterly flow was observed in the Southwest zone, and southerly flow was observed in the Southeast INL zone.

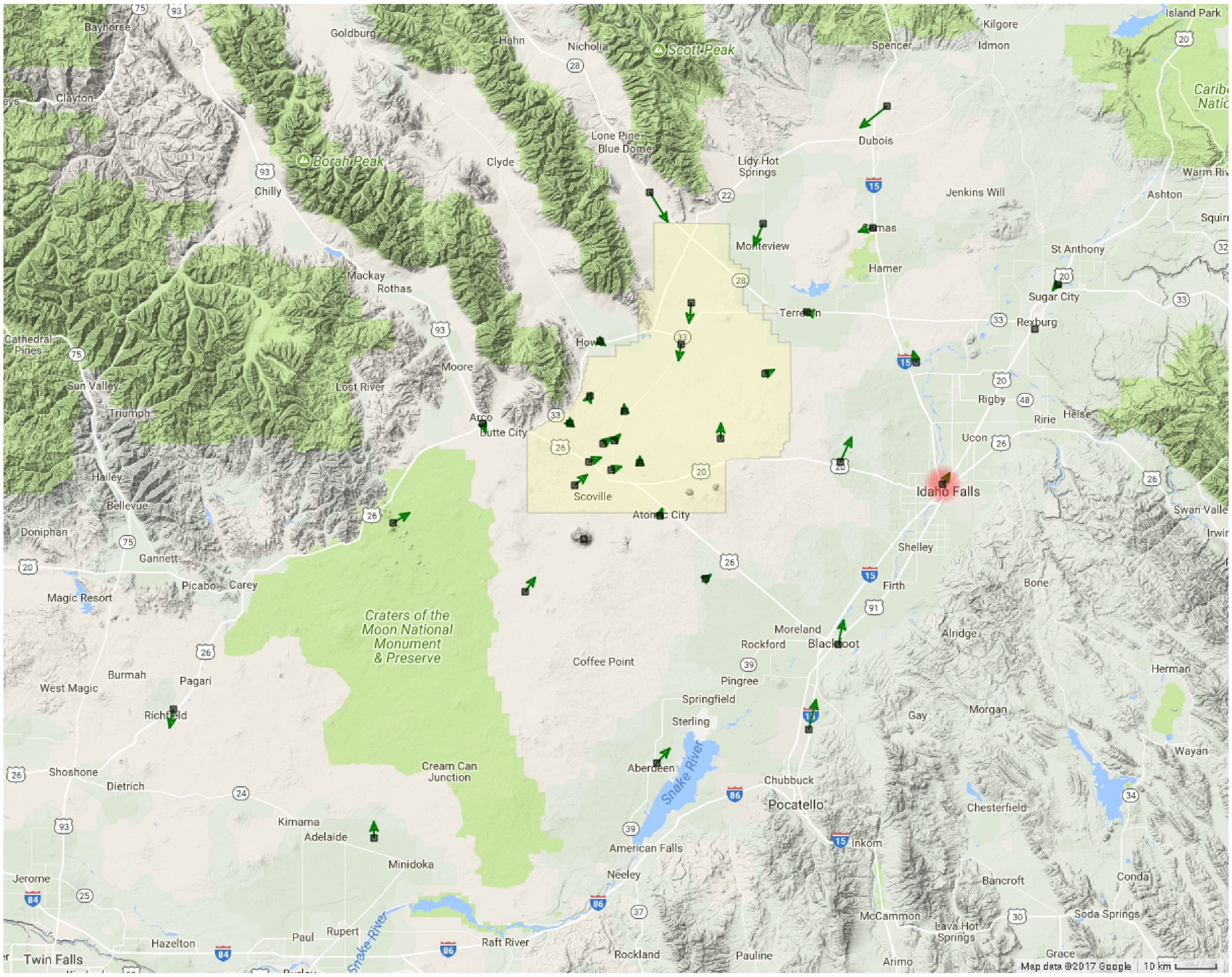

Figure 22. Wind vectors for Wind Pattern 2, Weak Flow, which describes light wind speeds and variable directions. Green arrows indicate wind speeds < 11.2 mph.

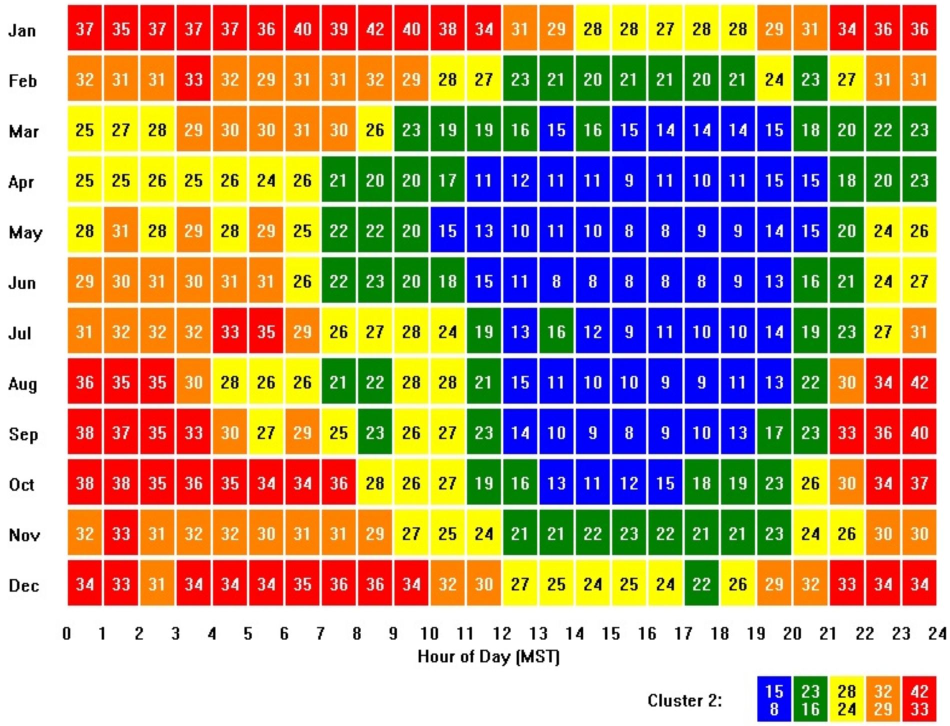

Jan	37	35	37	37	37	36	40	39	42	40	38	34	31	29	28	28	27	28	28	29	31	34	36	36
Feb	32	31	31	33	32	29	31	31	32	29	28	27	23	21	20	21	21	20	21	24	23	27	31	31
Mar	25	27	28	29	30	30	31	30	26	23	19	19	16	15	16	15	14	14	14	15	18	20	22	23
Apr	25	25	26	25	26	24	26	21	20	20	17	11	12	11	11	9	11	10	11	15	15	18	20	23
May	28	31	28	29	28	29	25	22	22	20	15	13	10	11	10	8	8	9	9	14	15	20	24	26
Jun	29	30	31	30	31	31	26	22	23	20	18	15	11	8	8	8	8	8	9	13	16	21	24	27
Jul	31	32	32	32	33	35	29	26	27	28	24	19	13	16	12	9	11	10	10	14	19	23	27	31
Aug	36	35	35	30	28	26	26	21	22	28	28	21	15	11	10	10	9	9	11	13	22	30	34	42
Sep	38	37	35	33	30	27	29	25	23	26	27	23	14	10	9	8	9	10	13	17	23	33	36	40
Oct	38	38	35	36	35	34	34	36	28	26	27	19	16	13	11	12	15	18	19	23	26	30	34	37
Nov	32	33	31	32	32	30	31	31	29	27	25	24	21	21	22	23	22	21	21	23	24	26	30	30
Dec	34	33	31	34	34	34	35	36	36	34	32	30	27	25	24	25	24	22	26	29	32	33	34	34

Figure 23. Temporal frequency of occurrence for Wind Pattern 2, Weak Flow.

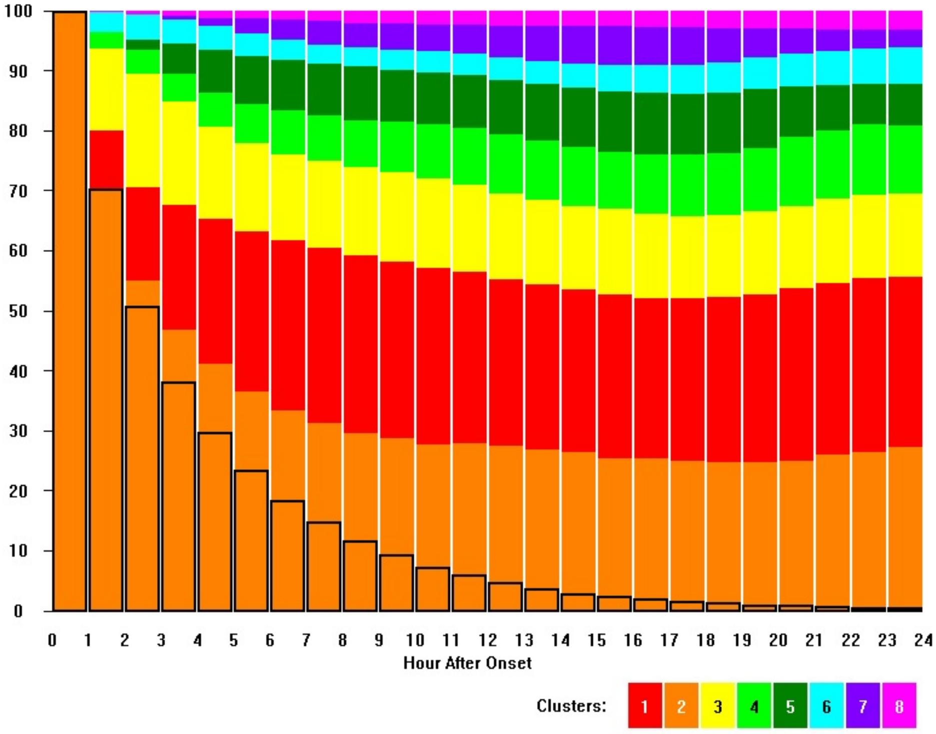

Figure 24. Hourly persistence and transition frequencies of Wind Pattern 2, Weak Flow.

Wind Pattern 3, Moderate Up-valley Flow

Wind pattern 3, Moderate Up-valley Flow, typically consisted of south-southwest winds at 7 to 11 mph throughout the ESRP, as shown in Fig. 25. On an annual basis it was the third most common wind pattern, occurring 12.5% of the time. However, it occurred less than half as frequently as either wind patterns 1 or 2. It was most common during summer afternoons in July through September, from 1000 to 2100 MST, when strong solar surface heating was present (Fig. 26). This surface heating linked surface winds with winds aloft, resulting in south to southwest winds. This pattern was least common during nighttime conditions (0100 to 0800 MST) during all months of year since, at that time, no solar surface heating is available to create an up-valley flow.

Wind pattern 3 continuously persisted only 50% of the time through the 3rd hour and by hour 12 a continuous persistence was almost never observed. Although wind pattern 3 was well defined on a seasonal and daily basis, the likelihood of it persisting once it became established was much less than for wind patterns 1 or 2 (Fig. 27). This pattern, early in its life span, usually either strengthened into wind pattern 5 (Well-developed Up-valley Flow, or weakened into wind patterns 4 and 2 (Decreasing Up-valley and Weak Flows, respectively). If wind pattern 3 persisted for 4 to 5 hours it could transition into wind pattern 1, Drainage Flow, which began to occur near sunset.

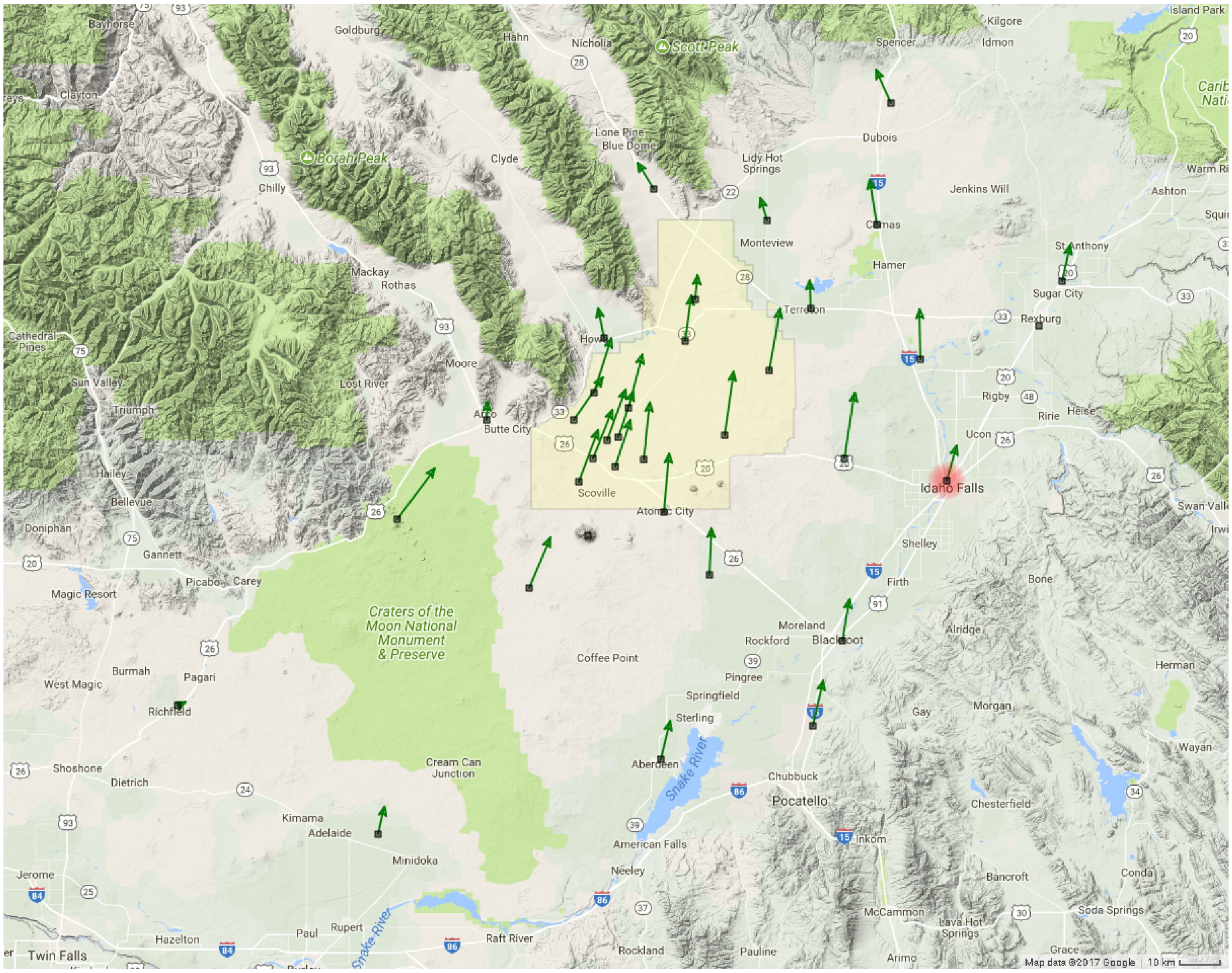

Figure 25. Wind vectors for Wind Pattern 3, Moderate Up-valley Flow, which illustrates moderate solar-driven surface heating resulting in a general south-southwest flow. Green arrows indicate wind speeds < 11.2 mph.

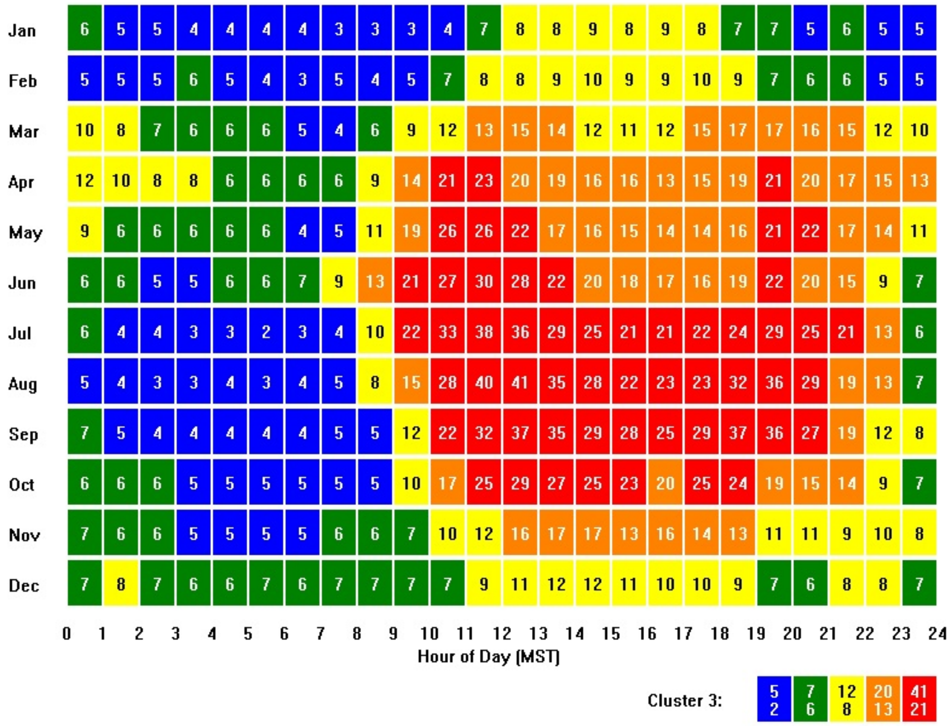

Jan	6	5	5	4	4	4	4	3	3	3	4	7	8	8	9	8	9	8	7	7	5	6	5	5
Feb	5	5	5	6	5	4	3	5	4	5	7	8	8	9	10	9	9	10	9	7	6	6	5	5
Mar	10	8	7	6	6	6	5	4	6	9	12	13	15	14	12	11	12	15	17	17	16	15	12	10
Apr	12	10	8	8	6	6	6	6	9	14	21	23	20	19	16	16	13	15	19	21	20	17	15	13
May	9	6	6	6	6	6	4	5	11	19	26	26	22	17	16	15	14	14	16	21	22	17	14	11
Jun	6	6	5	5	6	6	7	9	13	21	27	30	28	22	20	18	17	16	19	22	20	15	9	7
Jul	6	4	4	3	3	2	3	4	10	22	33	38	36	29	25	21	21	22	24	29	25	21	13	6
Aug	5	4	3	3	4	3	4	5	8	15	28	40	41	35	28	22	23	23	32	36	29	19	13	7
Sep	7	5	4	4	4	4	4	5	5	12	22	32	37	35	29	28	25	29	37	36	27	19	12	8
Oct	6	6	6	5	5	5	5	5	5	10	17	25	29	27	25	23	20	25	24	19	15	14	9	7
Nov	7	6	6	5	5	5	5	6	6	7	10	12	16	17	17	13	16	14	13	11	11	9	10	8
Dec	7	8	7	6	6	7	6	7	7	7	7	9	11	12	12	11	10	10	9	7	6	8	8	7

Figure 26. Temporal frequency of occurrence for Wind Pattern 3, Moderate Up-valley Flow.

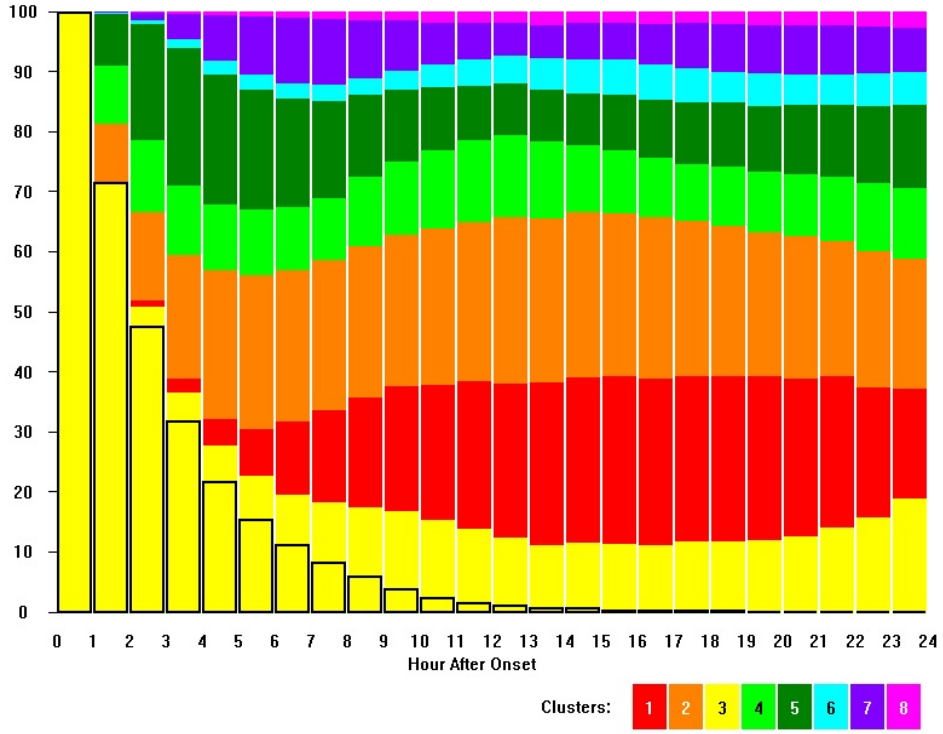

Figure 27. Hourly persistence and transition frequencies of Wind Pattern 3, Moderate Up-valley Flow.

Wind Pattern 4, Decreasing Up-valley Flow Near Sunset, or Moderate Synoptic Affected Flow

Wind pattern 4 occurred most often when either a synoptic weather pattern exerted a moderate influence on the surface winds or when up-valley flows began to decrease near sunset. In this wind pattern, the winds in the North INL microclimate zone and further to north in the rest of the ESRP became somewhat variable in direction with speeds between 6 to 11 mph. Elsewhere the winds remained southwesterly at 12 to 16 mph, as shown in Fig. 28. This pattern reinforces the three INL microclimate zones concept. On an annual basis, this pattern was the fourth most common wind pattern, occurring 11.5% of the time. It was most common during midwinter afternoons and early evenings (January to March, between 1200 and 2100 MST) and also in spring and summer evenings from March through September, between 1900 and 2300 MST (Fig. 29). This flow was typically an inertial flow pattern that simply followed the flow pattern that had developed during the afternoon hours because of surface solar heating (Wind Pattern 3, Moderate Up-valley Flow).

Wind pattern 4 most often transitioned into wind pattern 2, Weak Flow (Fig. 30). However, this pattern also showed significant transition occurrences into wind patterns 3, 5, 6, and 7 (Moderate Up-valley Flow, Well-developed Up-valley Flow, Down-canyon Flow, and Strong Synoptically-forced SW Flow, respectively), and also after hour 7, into wind pattern 1 (Drainage Flow). Wind pattern 4 persisted continuously into hour 3 less than 50% of the time and into hour 12 less than 5% of the time. It rarely persisted continuously longer than 18 hours, indicating that this wind flow pattern is a transitional pattern.

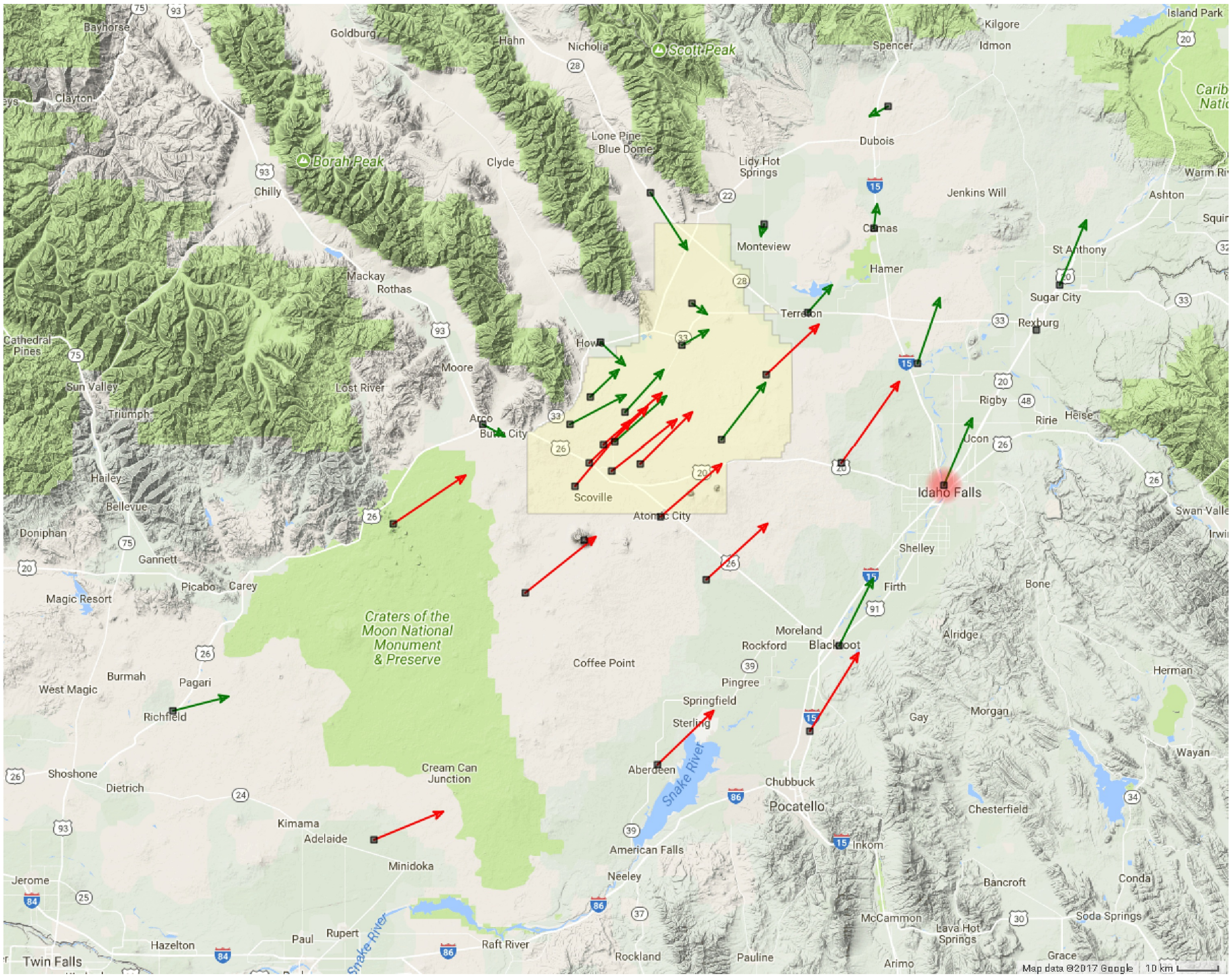

Figure 28. Wind vectors for Wind Pattern 4, decreasing up-slope flow near sunset or moderate synoptically affected flow. Green arrows indicate wind speeds < 11.2 mph. Red arrows indicate wind speeds between 11.2 and 22.4 mph.

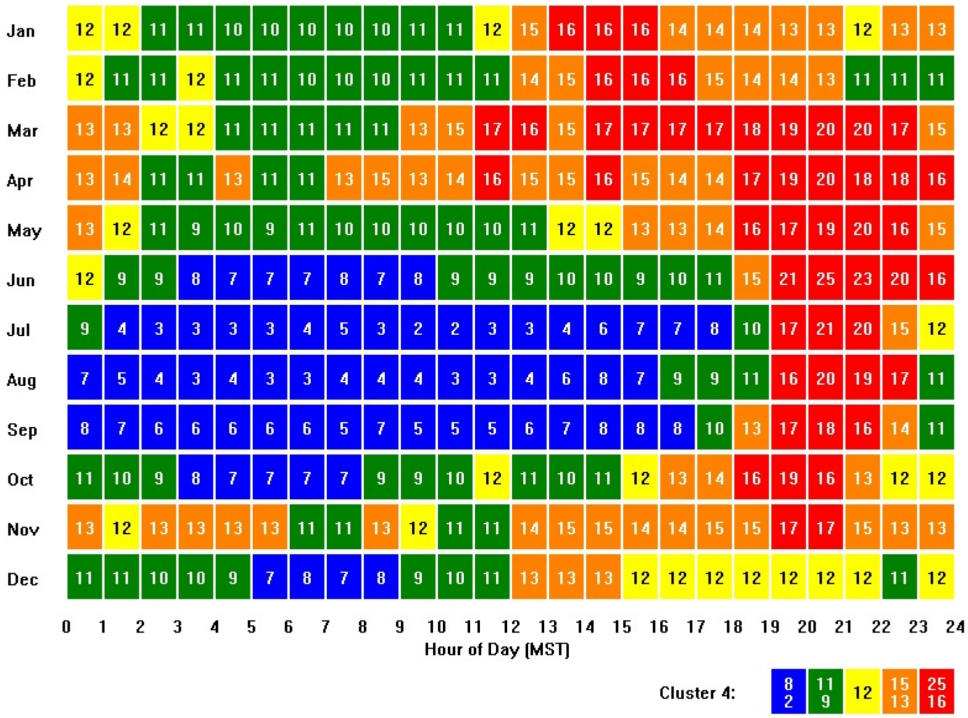

Jan	12	12	11	11	10	10	10	10	10	11	11	12	15	16	16	16	14	14	14	13	13	12	13	13
Feb	12	11	11	12	11	11	10	10	10	11	11	11	14	15	16	16	16	15	14	14	13	11	11	11
Mar	13	13	12	12	11	11	11	11	11	13	15	17	16	15	17	17	17	17	18	19	20	20	17	15
Apr	13	14	11	11	13	11	11	13	15	13	14	16	15	15	16	15	14	14	17	19	20	18	18	16
May	13	12	11	9	10	9	11	10	10	10	10	10	11	12	12	13	13	14	16	17	19	20	16	15
Jun	12	9	9	8	7	7	7	8	7	8	9	9	9	10	10	9	10	11	15	21	25	23	20	16
Jul	9	4	3	3	3	3	4	5	3	2	2	3	3	4	6	7	7	8	10	17	21	20	15	12
Aug	7	5	4	3	4	3	3	4	4	4	3	3	4	6	8	7	9	9	11	16	20	19	17	11
Sep	8	7	6	6	6	6	6	5	7	5	5	5	6	7	8	8	8	10	13	17	18	16	14	11
Oct	11	10	9	8	7	7	7	7	9	9	10	12	11	10	11	12	13	14	16	19	16	13	12	12
Nov	13	12	13	13	13	13	11	11	13	12	11	11	14	15	15	14	14	15	15	17	17	15	13	13
Dec	11	11	10	10	9	7	8	7	8	9	10	11	13	13	13	12	12	12	12	12	12	12	11	12

Figure 29. Temporal frequency of occurrence for Wind Pattern 4, decreasing up-slope flow after sunset or moderate synoptically affected flow.

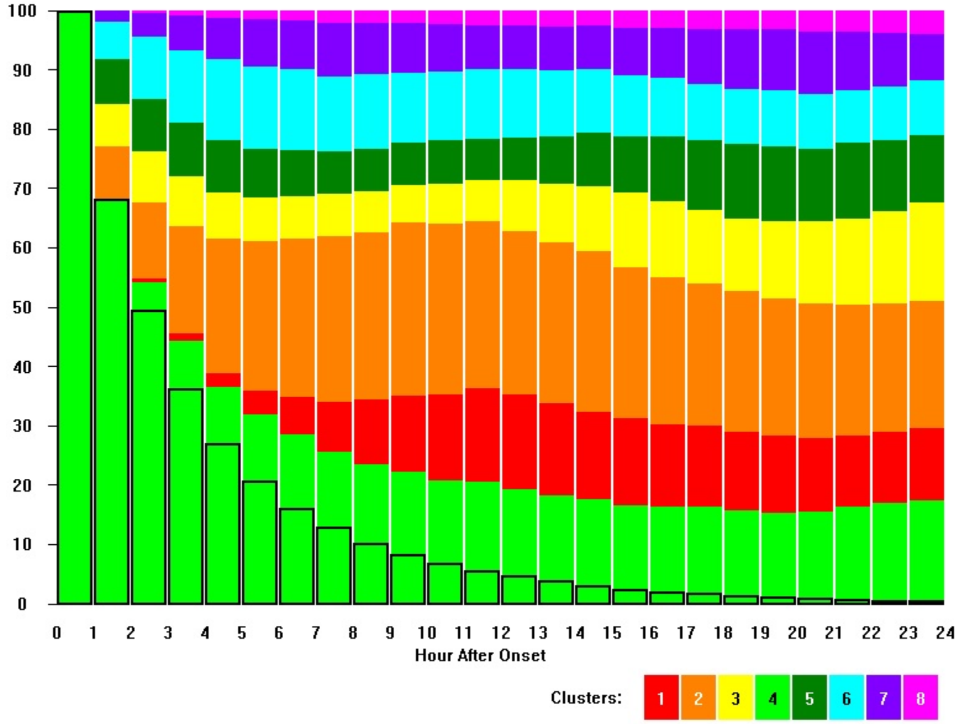

Figure 30. Hourly persistence and transition frequency of Wind Pattern 4, decreasing up-slope flow after sunset or moderate synoptically affected flow.

Wind Pattern 5, Well-developed Up-valley Flow

Wind pattern 5, Well-developed Up-valley Flow, was represented by south-southwest winds at 11 to 18 mph throughout the entire ESRP, as shown in Fig. 31. It differs from wind pattern 3 (Moderate Up-valley Flow) in the strength and unified direction of the wind throughout the entire ESRP. The INL microclimate zones became indistinguishable in wind pattern 5. On an annual basis, this pattern occurred 8.6% of the time. It was most commonly observed during late spring and summer afternoons, from March through September, from 1100 to 1900 MST. Figure 32 shows this relationship quite plainly. This wind pattern developed from very strong solar heating of the earth's surface that subsequently resulted in fully coupled surface winds with winds aloft.

Once wind pattern 5 became established, it continually persisted for about 52% of the time into the third hour, and by the 8th hour, it continuously persisted for less than 10% of the time (Fig. 33). After one to two hours of persistence, this pattern transitioned with nearly equal frequencies into wind patterns 3 (Moderate Up-valley Flow), 4 (Decreasing Up-valley Flow Near Sunset), or 7 (Strong Synoptically-forced SW Flow). Of particular note was the frequency of transition into wind pattern 7 (approximately 25%) and into wind pattern 3 (approximately 15%) early in its lifetime during hours 4, 5, and 6. This indicates that this wind pattern is also a transitional wind pattern. When wind pattern 5 persisted for more than 8 hours, it also transitioned into wind pattern 2 (Weak Flow) approximately 23% of the time. When wind pattern 5 persisted for more than 12 hours, it also transitioned into wind pattern 1 (Drainage flow) approximately 18% of the time. These patterns reinforce the claim that this is a transitional wind pattern.

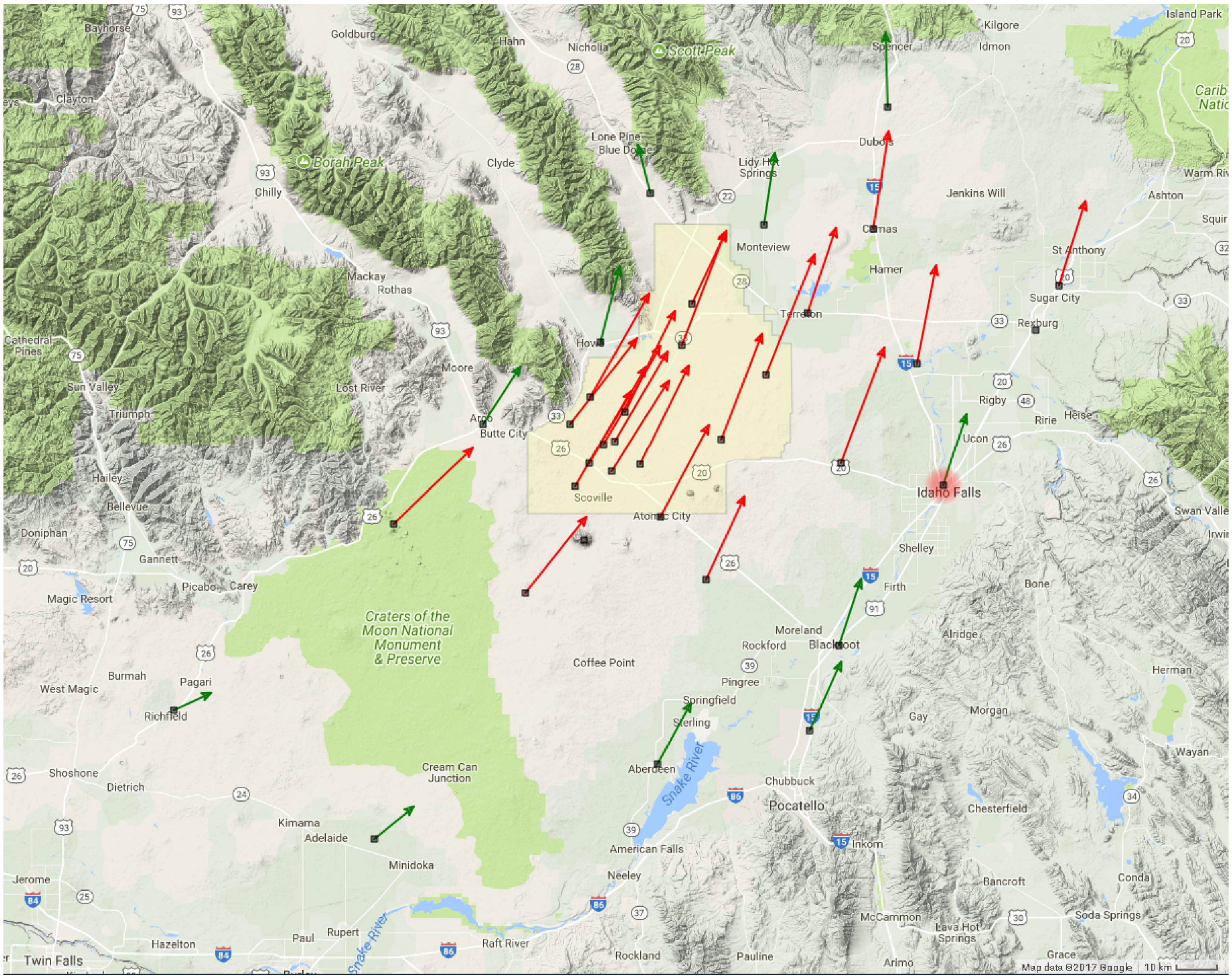

Figure 31. Wind vectors for Wind Pattern 5, Well-developed Up-valley Flow. Green arrows indicate wind speeds < 11.2 mph. Red arrows indicate wind speeds between 11.2 and 22.4 mph.

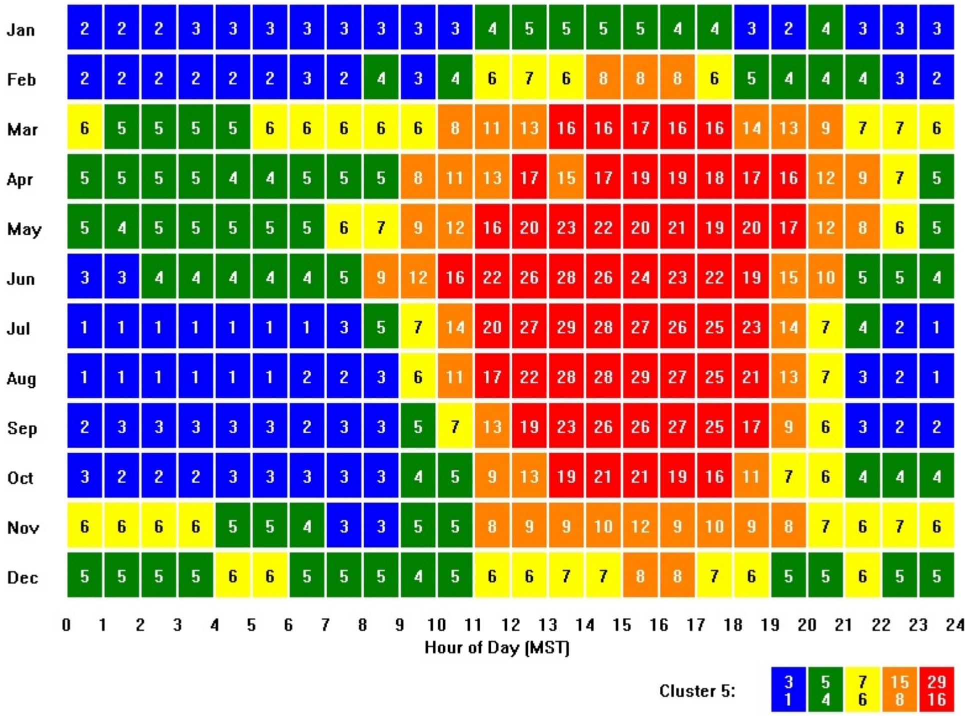

Jan	2	2	2	3	3	3	3	3	3	3	3	4	5	5	5	5	4	4	3	2	4	3	3	3
Feb	2	2	2	2	2	2	3	2	4	3	4	6	7	6	8	8	8	6	5	4	4	4	3	2
Mar	6	5	5	5	5	6	6	6	6	6	8	11	13	16	16	17	16	16	14	13	9	7	7	6
Apr	5	5	5	5	4	4	5	5	5	8	11	13	17	15	17	19	19	18	17	16	12	9	7	5
May	5	4	5	5	5	5	5	6	7	9	12	16	20	23	22	20	21	19	20	17	12	8	6	5
Jun	3	3	4	4	4	4	4	5	9	12	16	22	26	28	26	24	23	22	19	15	10	5	5	4
Jul	1	1	1	1	1	1	1	3	5	7	14	20	27	29	28	27	26	25	23	14	7	4	2	1
Aug	1	1	1	1	1	1	2	2	3	6	11	17	22	28	28	29	27	25	21	13	7	3	2	1
Sep	2	3	3	3	3	3	2	3	3	5	7	13	19	23	26	26	27	25	17	9	6	3	2	2
Oct	3	2	2	2	3	3	3	3	3	4	5	9	13	19	21	21	19	16	11	7	6	4	4	4
Nov	6	6	6	6	5	5	4	3	3	5	5	8	9	9	10	12	9	10	9	8	7	6	7	6
Dec	5	5	5	5	6	6	5	5	5	4	5	6	6	7	7	8	8	7	6	5	5	6	5	5

Figure 32. Temporal frequency of occurrence for Wind Pattern 5, Well-developed Up-valley Flow.

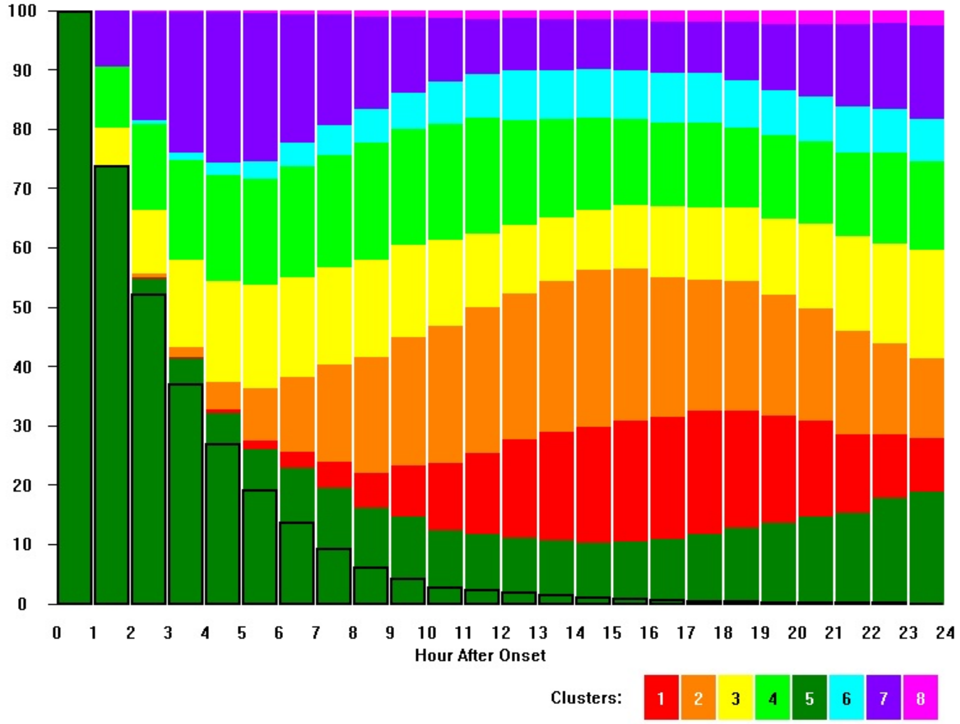

Figure 33. Hourly persistence and transition frequencies of Wind Pattern 5, Well-developed Up-valley Flow.

Wind Pattern 6, Down-canyon Flow

Wind pattern 6, named Down-canyon Flow, exhibited strong flow from the northwest-southeast oriented canyons to the northwest of the INL (Fig 34). These down-canyon winds are more likely caused by gap winds (Finn et al. 2016) or frontal boundaries. The three INL micro climate zones are clearly observed in this wind pattern. North to northwest winds at 10 to 20 mph, with some speeds locally higher, were observed at the mouths of the Big Lost and Little Lost River valleys and at the mouth of Birch Creek valley. The winds out of the Little Lost River valley and Birch Creek valley, in particular, were strong enough that they affected the entire north end of the INL. Indeed, these canyon flows affected winds as far away as MFC and KET, although to a lesser extent with northwest winds at 5 to 15 mph. In the southwest INL climate zone, both light northwest and southwest winds were observed, which reinforces the observation that the INL climate zone boundaries are somewhat fluid, depending on atmospheric conditions. In this case, the boundary between the southwest and north INL climate zones would be drawn with LOS and RWM in the southwest zone, and ATR, GRI, CFA, and CIT in the north zone. Interestingly, westerly and southwesterly winds were also observed in this wind pattern both to the south of the INL and in the far eastern portion of the ESRP. On an annual basis, this pattern occurred 6.6% of the time.

Wind pattern 6 was most commonly observed during April nights from 1600 to 0900 MST and also during other spring and summer evenings (March through July, from 2300 to 0300 MST) when surface winds were well-coupled with northwesterly winds aloft (Fig. 35). Figure 36 shows that wind pattern 6 continuously persisted into hour three less than 40% of the time and continuously persisted for 12 hours less than 10% of the time. However, it did continuously persist for 24 hours approximately 1% of the time. Wind pattern 6 transitioned most often into wind pattern 2 (Weak Flow) approximately 15% of the time in the 2nd hour and as much as 25% of the time in later hours. It also transitioned into wind pattern 1 as much as 20% of the time in later hours.

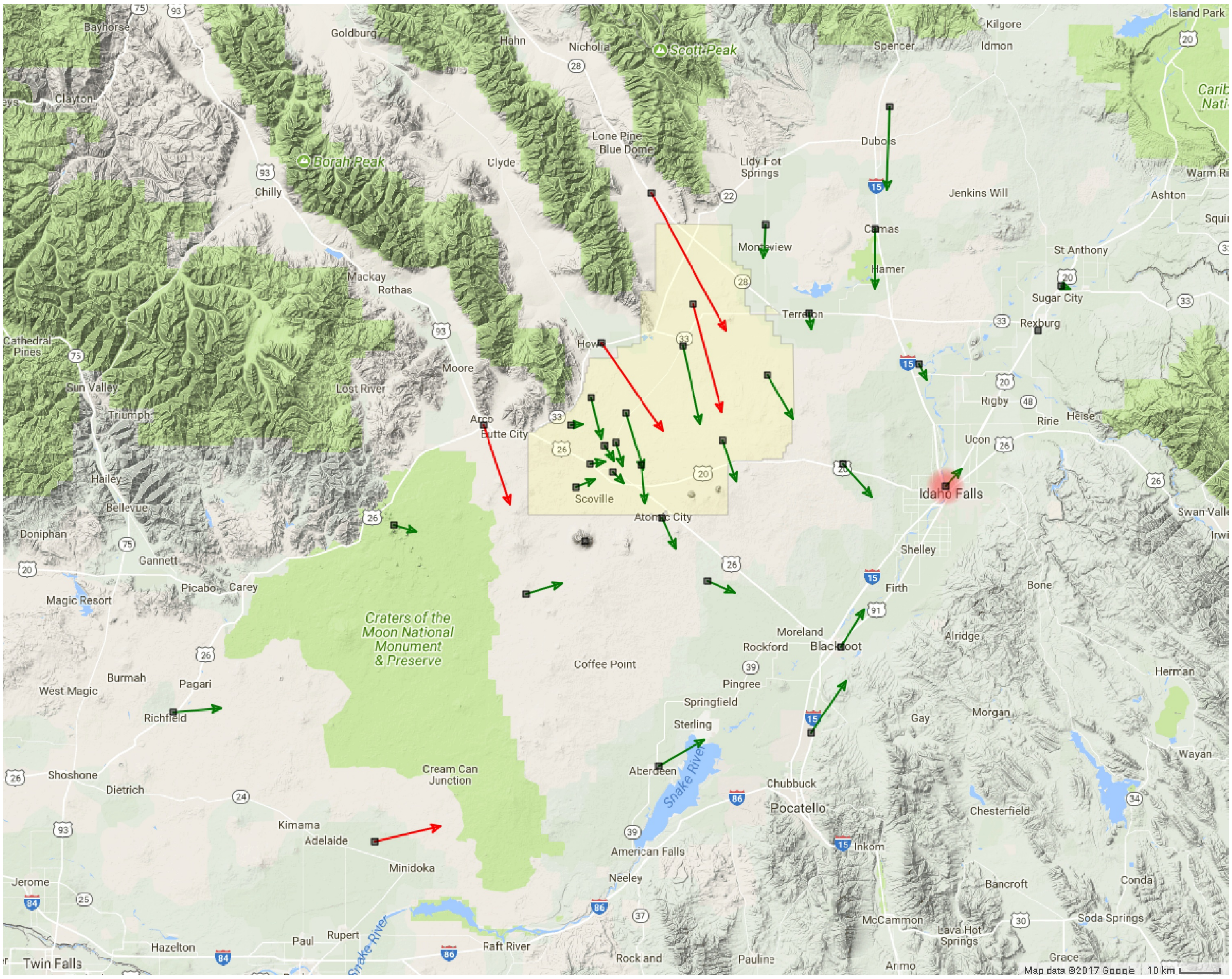

Figure 34. Wind vectors for Wind Pattern 6, Down-canyon Flow aided by synoptic conditions. Green arrows indicate wind speeds < 11.2 mph. Red arrows indicate wind speeds between 11.2 and 22.4 mph.

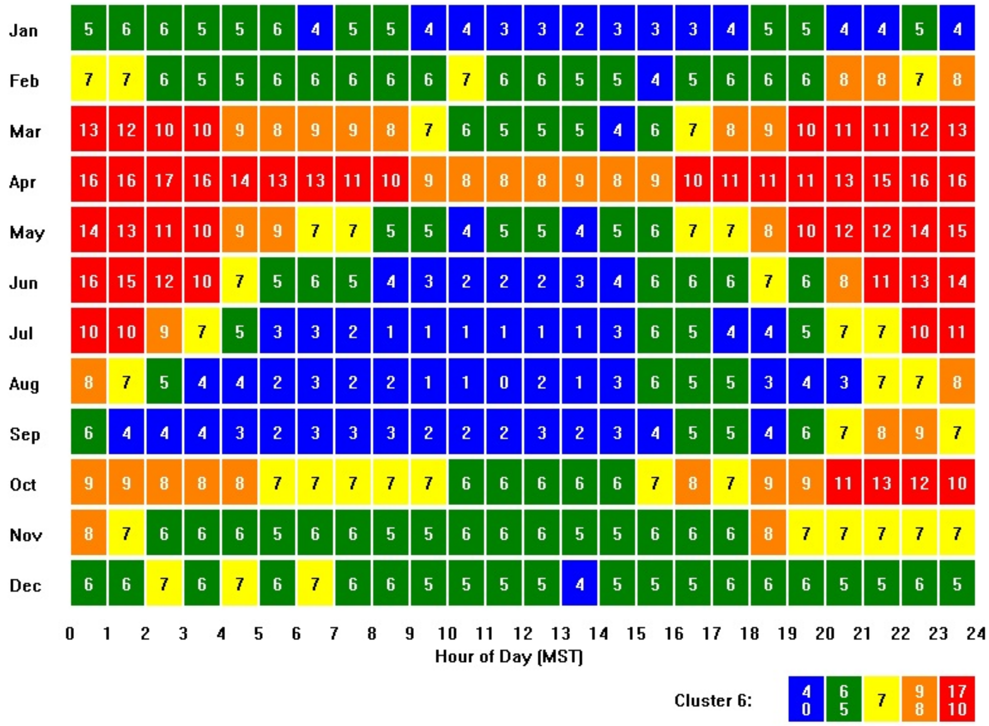

Jan	5	6	6	5	5	6	4	5	5	4	4	3	3	2	3	3	3	4	5	5	4	4	5	4
Feb	7	7	6	5	5	6	6	6	6	6	7	6	6	5	5	4	5	6	6	6	8	8	7	8
Mar	13	12	10	10	9	8	9	9	8	7	6	5	5	5	4	6	7	8	9	10	11	11	12	13
Apr	16	16	17	16	14	13	13	11	10	9	8	8	8	9	8	9	10	11	11	11	13	15	16	16
May	14	13	11	10	9	9	7	7	5	5	4	5	5	4	5	6	7	7	8	10	12	12	14	15
Jun	16	15	12	10	7	5	6	5	4	3	2	2	2	3	4	6	6	6	7	6	8	11	13	14
Jul	10	10	9	7	5	3	3	2	1	1	1	1	1	1	3	6	5	4	4	5	7	7	10	11
Aug	8	7	5	4	4	2	3	2	2	1	1	0	2	1	3	6	5	5	3	4	3	7	7	8
Sep	6	4	4	4	3	2	3	3	3	2	2	2	3	2	3	4	5	5	4	6	7	8	9	7
Oct	9	9	8	8	8	7	7	7	7	7	6	6	6	6	6	7	8	7	9	9	11	13	12	10
Nov	8	7	6	6	6	5	6	6	5	5	6	6	6	5	5	6	6	6	8	7	7	7	7	7
Dec	6	6	7	6	7	6	7	6	6	5	5	5	5	4	5	5	5	6	6	6	5	5	6	5

Figure 35. Temporal frequency of occurrence for Wind Pattern 6, Down-canyon Flow aided by synoptic conditions.

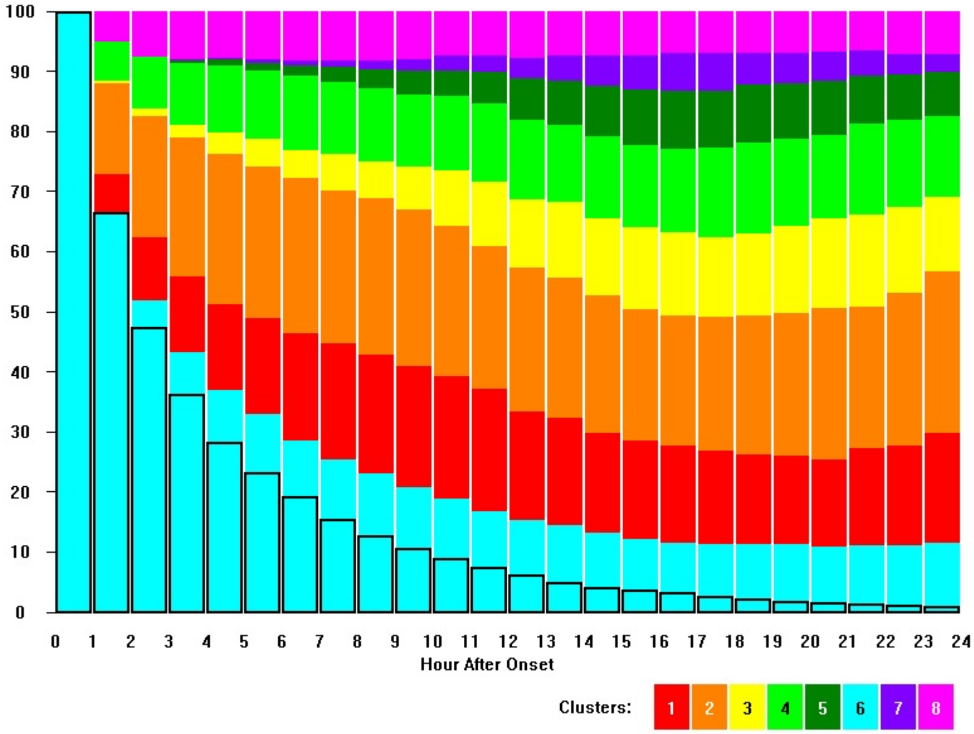

Figure 36. Hourly persistence and transition frequencies of Wind Pattern 6, Down-canyon Flow aided by synoptic conditions.

Wind Pattern 7, Strong Synoptically Forced Southwest Flow

Wind pattern 7 was named Strong Synoptically-forced Southwest Flow, and describes driving southwesterly winds, typically at 15 to 30 mph, throughout the entire ESRP (Fig. 37). Even BLU, which is sheltered by mountains to the southwest indicated southwest winds. On an annual basis, it occurred 5.6% of the time. Figure 38 indicates that wind pattern 7 was most common during spring and summer mid-afternoons (March through September, from 1100 to 1900 MST). The strongest winds in this pattern occurred in the spring simultaneously with a strong frontal passage, and sometimes caused blowing dust. Wind pattern 7 was rarely observed at time periods other than during afternoon hours.

Figure 39 shows that wind pattern 7, once it becomes established, persisted continuously for 5 hours with a frequency of occurrence greater than 40%. However, this frequency dropped rapidly to less than 5% by hour 12. It almost never persisted continuously more than 18 hours. It almost never reestablished itself after evolving into another wind pattern in the first 18 hours, but there was a propensity to return in the time period of 18-24 hours. In the first 12 hours after becoming established, wind pattern 7 was most likely to transition into wind pattern 4 (Moderate Synoptic Affected Flow) about 35% of the time by hour 9. It also evolved into wind pattern 2 (Weak Flow) approximately 25% of the time by hour 15. However, this pattern also evolved into wind pattern 6 (Down-canyon Flow) approximately 15% of the time by hour 12, which is consistent with the movement of a low pressure system initially bringing strong southwesterly flow, followed by strong NE winds out of the canyons to the northwest of the INL.

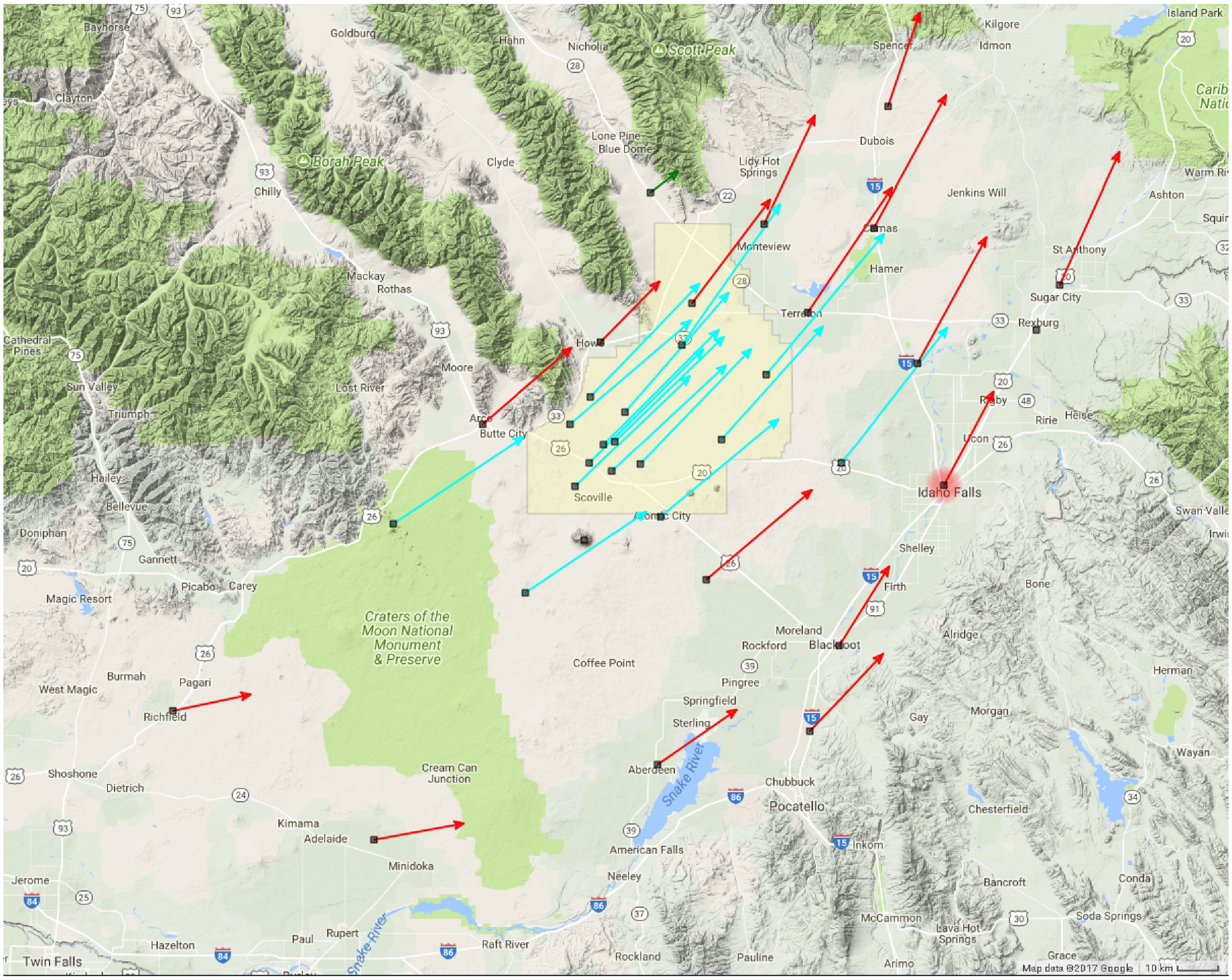

Figure 37. Wind vectors for Wind Pattern 7, Strong Synoptically Forced Southwest Flow. Green arrows indicate wind speeds < 11.2 mph. Red arrows indicate wind speeds between 11.2 and 22.4 mph. Light blue arrows indicate wind speeds > 22.4 mph.

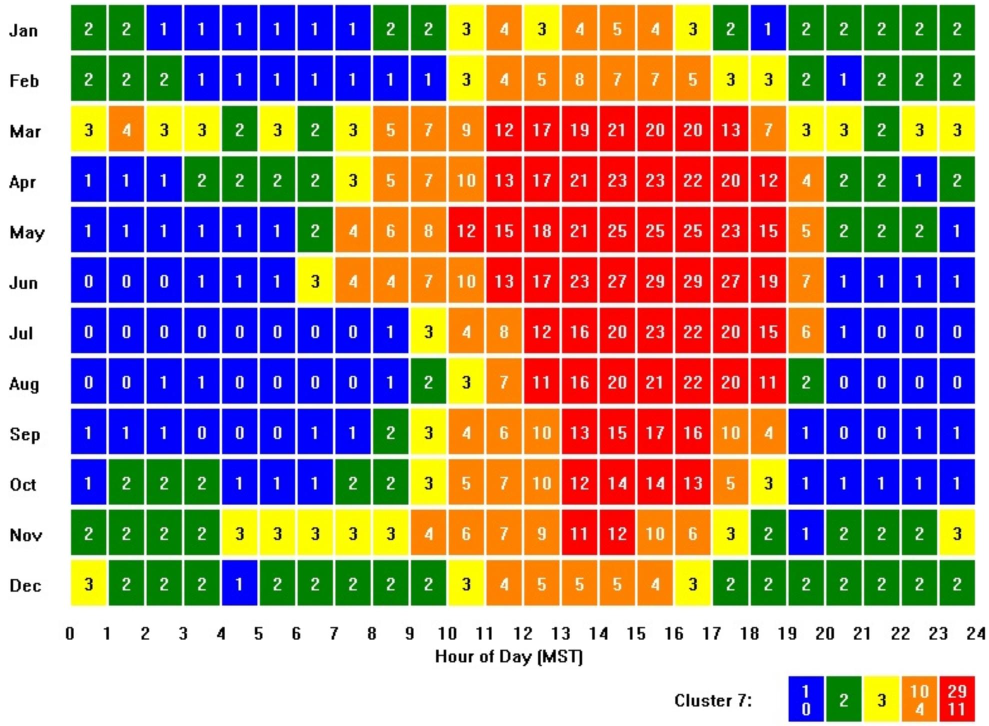

	0	1	2	3	4	5	6	7	8	9	10	11	12	13	14	15	16	17	18	19	20	21	22	23
Jan	2	2	1	1	1	1	1	1	2	2	3	4	3	4	5	4	3	2	1	2	2	2	2	2
Feb	2	2	2	1	1	1	1	1	1	1	3	4	5	8	7	7	5	3	3	2	1	2	2	2
Mar	3	4	3	3	2	3	2	3	5	7	9	12	17	19	21	20	20	13	7	3	3	2	3	3
Apr	1	1	1	2	2	2	2	3	5	7	10	13	17	21	23	23	22	20	12	4	2	2	1	2
May	1	1	1	1	1	1	2	4	6	8	12	15	18	21	25	25	25	23	15	5	2	2	2	1
Jun	0	0	0	1	1	1	3	4	4	7	10	13	17	23	27	29	29	27	19	7	1	1	1	1
Jul	0	0	0	0	0	0	0	0	1	3	4	8	12	16	20	23	22	20	15	6	1	0	0	0
Aug	0	0	1	1	0	0	0	0	1	2	3	7	11	16	20	21	22	20	11	2	0	0	0	0
Sep	1	1	1	0	0	0	1	1	2	3	4	6	10	13	15	17	16	10	4	1	0	0	1	1
Oct	1	2	2	2	1	1	1	2	2	3	5	7	10	12	14	14	13	5	3	1	1	1	1	1
Nov	2	2	2	2	3	3	3	3	3	4	6	7	9	11	12	10	6	3	2	1	2	2	2	3
Dec	3	2	2	2	1	2	2	2	2	2	3	4	5	5	5	4	3	2	2	2	2	2	2	2

Figure 38. Temporal frequency of occurrence for Wind Pattern 7, Strong Synoptically Forced Southwest Flow.

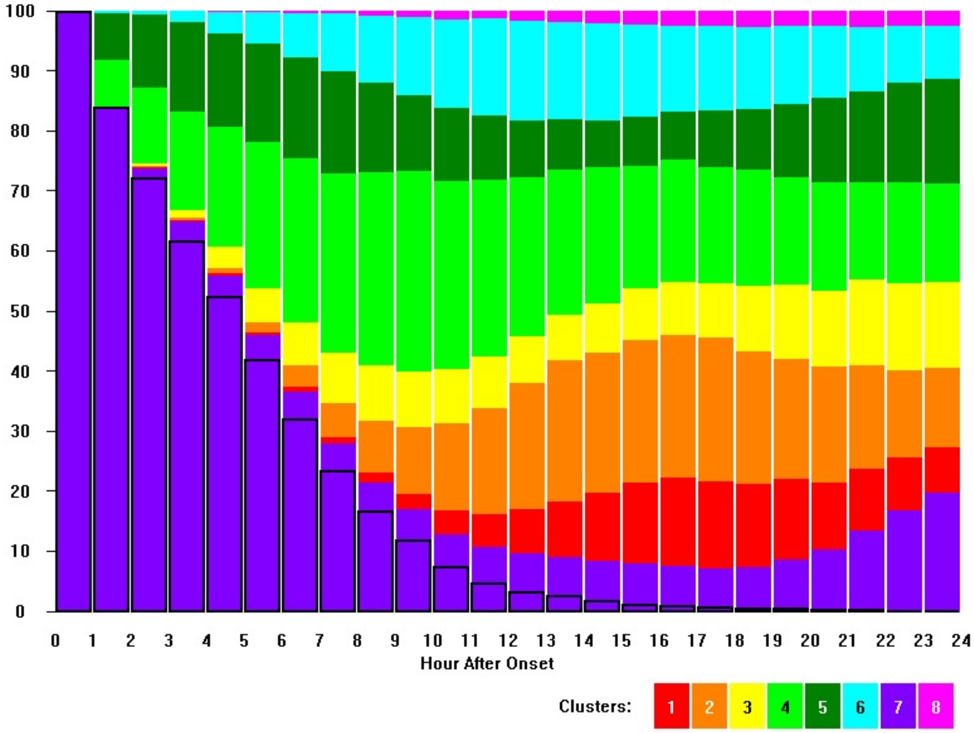

Figure 39. Hourly persistence and transition frequencies of Wind Pattern 7, Strong Synoptically Forced Southwest Flow.

Wind Pattern 8, Strong Synoptically Forced North-northeast Flow

Wind pattern 8 occurred annually only 4.1% of the time. It is called Strong Synoptically Forced North-northeast Flow and is represented by strong synoptic effects that drive north to northeasterly winds at 10 to 20 mph throughout the ESRP. Winds at the mouths of the Little Lost River and Birch Creek valleys exhibited northwesterly flow because of channeling effects (Fig 40). This pattern occurred most often during April and May from 2000 to 1000 MST), as shown in Fig. 41.

Figure 42 shows that wind pattern 8 persisted continuously for three hours approximately 50% of the time and for 12 hours approximately 20% of the time. It persisted continuously for 24 hours approximately 5% of the time. Wind pattern 8 did not return as frequently as other patterns once it transitioned into another pattern. Wind pattern 8 had a relatively large propensity to transition into wind pattern 1 (Drainage Flow) as the influence of synoptic storm energy diminished, even in the second hour after it became established. That frequency ranged as high as 40% six hours after establishment. Wind pattern 8 also transitioned into wind pattern 6 (Down-canyon Flow) up to 10% of the time 2 to 24 hours after becoming established. Transitioning into wind pattern 2 (Weak Flow) was also significant after about the ninth hour after wind pattern 8 became established.

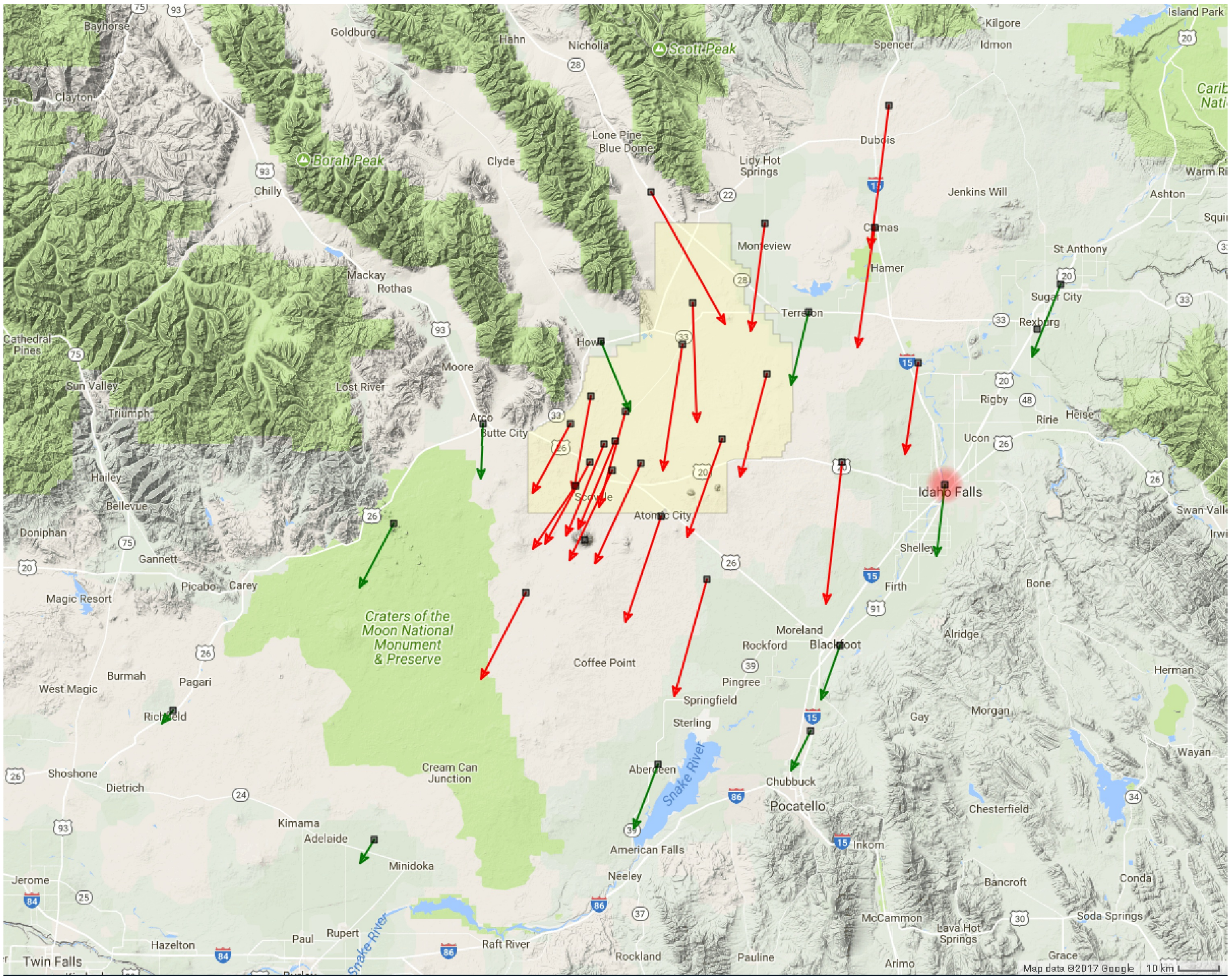

Figure 40. Wind vectors for Wind Pattern 8, Strong Synoptically Forced North-northeast Flow. Green arrows indicate wind speeds < 11.2 mph. Red arrows indicate wind speeds between 11.2 and 22.4 mph.

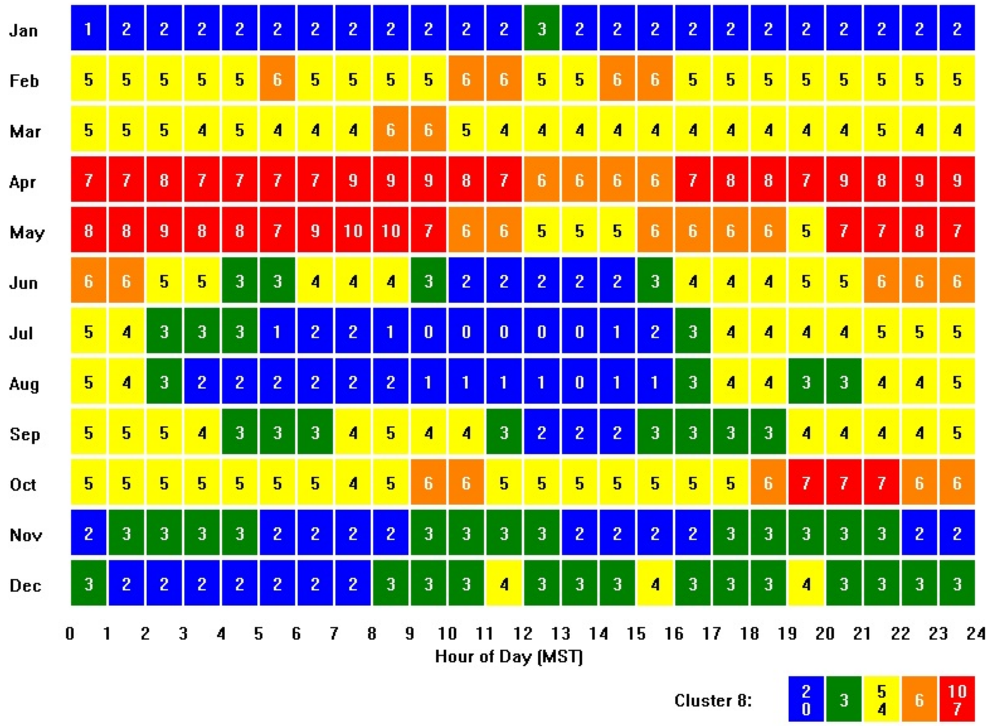

Jan	1	2	2	2	2	2	2	2	2	2	2	2	3	2	2	2	2	2	2	2	2	2	2	2
Feb	5	5	5	5	5	6	5	5	5	5	6	6	5	5	6	6	5	5	5	5	5	5	5	5
Mar	5	5	5	4	5	4	4	4	6	6	5	4	4	4	4	4	4	4	4	4	4	5	4	4
Apr	7	7	8	7	7	7	7	9	9	9	8	7	6	6	6	6	7	8	8	7	9	8	9	9
May	8	8	9	8	8	7	9	10	10	7	6	6	5	5	5	6	6	6	6	5	7	7	8	7
Jun	6	6	5	5	3	3	4	4	4	3	2	2	2	2	2	3	4	4	4	5	5	6	6	6
Jul	5	4	3	3	3	1	2	2	1	0	0	0	0	0	1	2	3	4	4	4	4	5	5	5
Aug	5	4	3	2	2	2	2	2	2	1	1	1	1	0	1	1	3	4	4	3	3	4	4	5
Sep	5	5	5	4	3	3	3	4	5	4	4	3	2	2	2	3	3	3	3	4	4	4	4	5
Oct	5	5	5	5	5	5	5	4	5	6	6	5	5	5	5	5	5	5	6	7	7	7	6	6
Nov	2	3	3	3	3	2	2	2	2	3	3	3	3	2	2	2	2	3	3	3	3	3	2	2
Dec	3	2	2	2	2	2	2	2	3	3	3	4	3	3	3	4	3	3	3	4	3	3	3	3

Figure 41. Temporal frequency of occurrence for Wind Pattern 8, Strong Synoptically Forced North-northeast Flow.

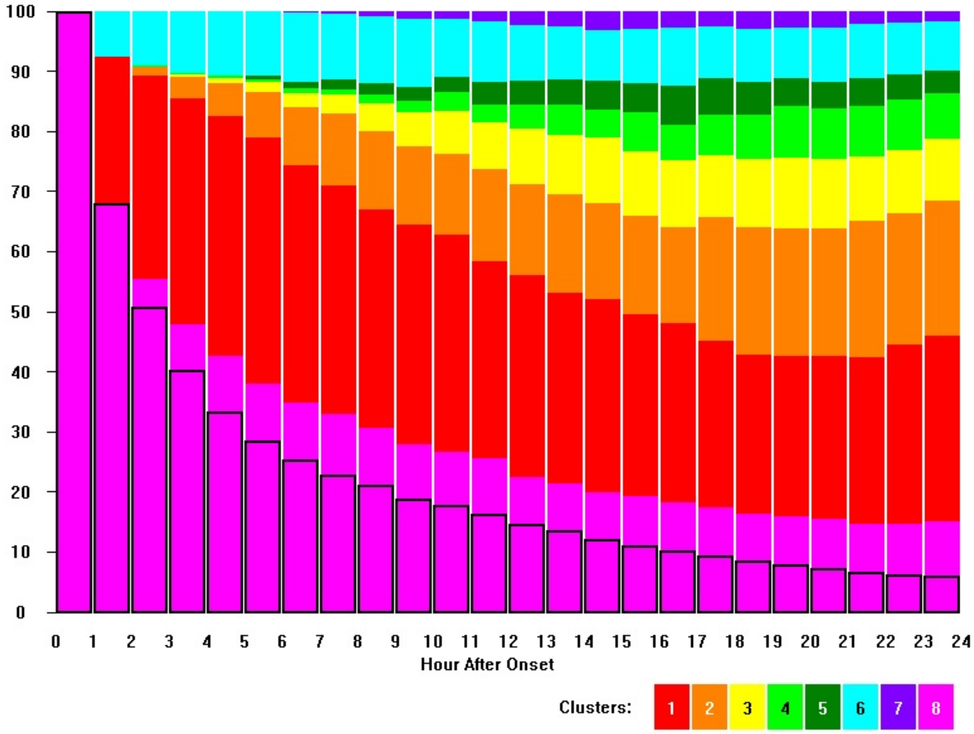

Figure 42. Hourly persistence and transition frequencies of Wind Pattern 8, Strong Synoptically Forced North-northeast Flow.

Seasonal Wind Patterns

The wind patterns derived from the cluster analysis described above also exhibited distinct seasonal dependancies. This subject was previously touched on only lightly, but more detail is given here. Some wind patterns appeared more frequently during some seasons and rarely in others. To illustrate this, the data are presented in stacked bar graphs similar to those already presented. The data period of record is the same as that used previously, i.e., January 1994 through December 2015.

Figure 43 shows the frequency of occurrence of the 8 wind patterns for the month of January. January represents the meteorological winter season. The winter season provides a good foundation on which to base the discussion of the other three seasons. In the winter, wind pattern 1 (Drainage Flow) occurred between 30 to 40% of the time during all hours of the day. There was little diurnal change observed in this pattern. Wind pattern 2 (Weak Flow) appeared about 25 to 35% of the time and exhibited a slight diurnal change between 1100 to 1700 MST, giving way primarily to wind pattern 4 (Decreasing Up-valley Flow Near Sunset). Other wind patterns appeared with a frequency of occurrence of less than 10% each. Some wind patterns were noticeably absent for most hours of the day, such as patterns 7 and 8 (Strong Synoptic-forced SW Flow and Strong Synoptically-forced NNE Flow, respectively). However, there was an increase in wind pattern 7 in January between the hours of 1000 to 1800 up to about 6% and also an increase in the occurrence of wind pattern 8 in February during every hour of the day to about 5%.

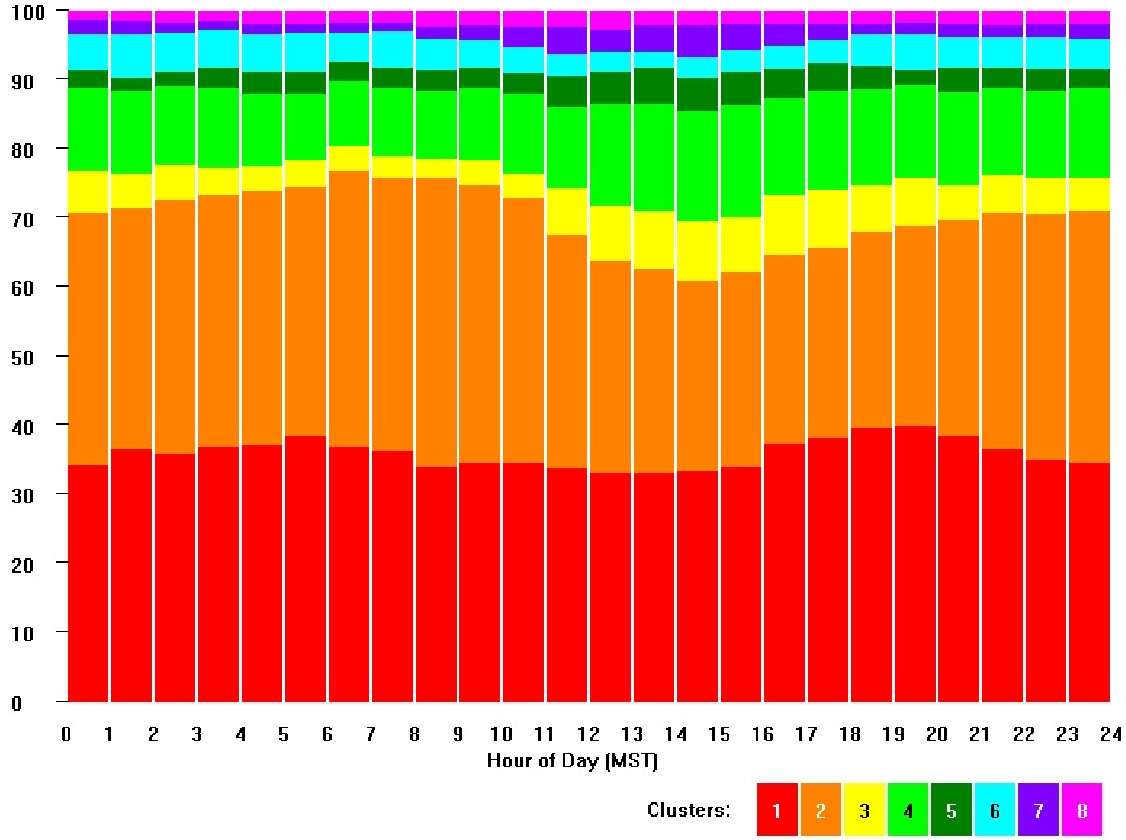

Figure 43. Hourly frequencies of occurrence for all 8 wind patterns for the month of January.

In the spring season, a definite diurnal shape emerged. Wind patterns 1 and 2 (Drainage Flow and Weak Flow) remained the dominate patterns at night, as shown in Fig. 44. This graph is for April, which represent the meteorological spring season. Wind patterns 5 and 7 (Well-developed Up-valley Flow and Strong Synoptically-forced SW Flow) became pronounced between the hours of 1000 and 1900 hours MST, each with a maximum frequency of occurrence of about 20%. The time of the frequency maximum for wind pattern 5 was between 1500 and 1700 hours MST, while the time of the frequency maximum for wind pattern 7 was between 1400 and 1600 MST. Spring is typically the time of year when strong synoptic effects drive southwesterly winds during the afternoon hours. Wind patterns 6 (Down-canyon Flow) and 8 (Strong synoptically-forced NNE Flow) also appeared with a greater frequency. Wind pattern 6 ranged between 10 to 15% and was most common at night. Wind pattern 8 was nearly constant throughout the day at about 8%.

In the summer months, the diurnal pattern observed in the spring months intensified as illustrated in Fig. 45. This graph is for the month of July, which represents the meteorological summer season. Wind patterns 1 and 2 (Drainage Flow and Weak Flow) strongly dominated the nighttime hours with a total frequency of occurrence up to 85%. The most predominant wind pattern at night was wind pattern 1 with a maximum frequency of occurrence of 55% between 0600 and 0800 MST. Strong radiational cooling of the surface caused a decoupling of the surface winds from the wind

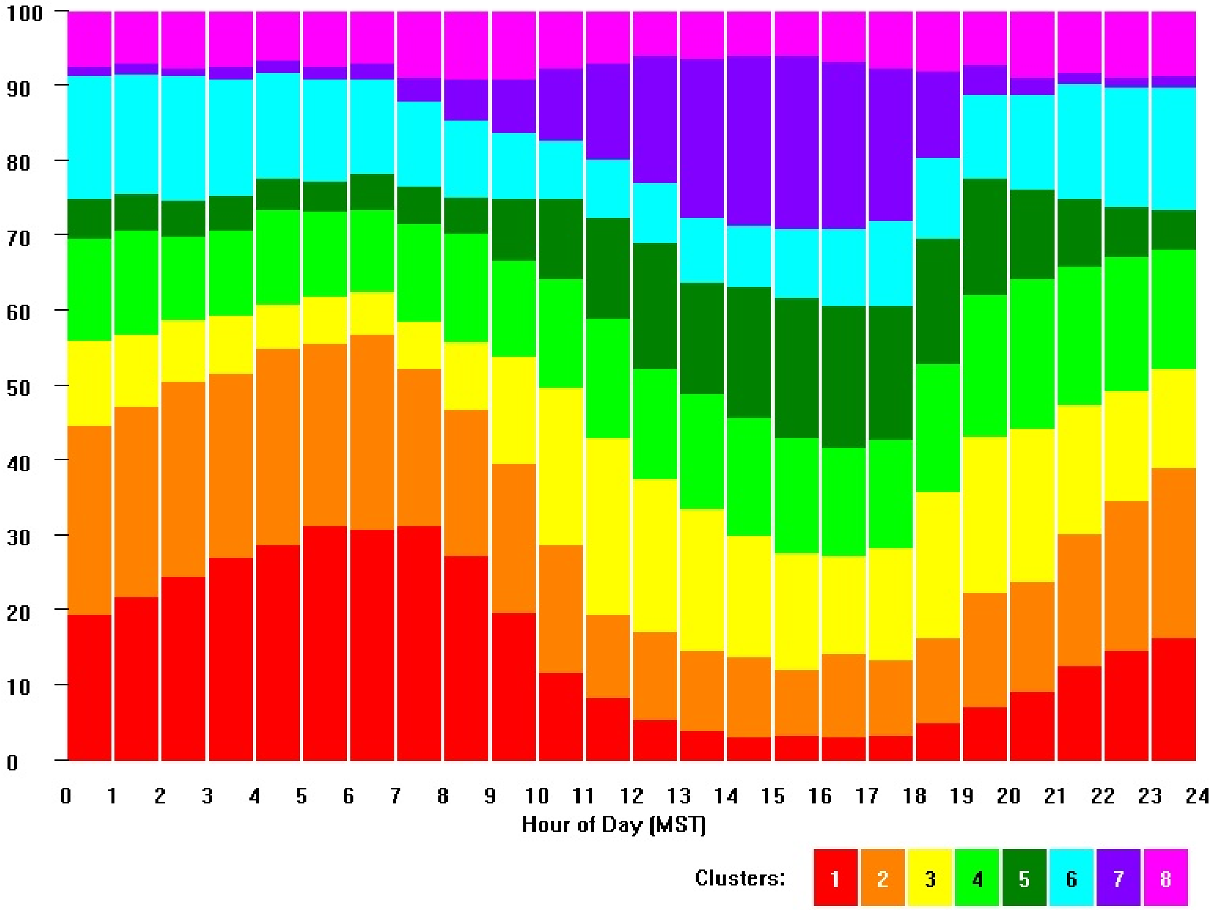

Figure 44. Hourly frequencies of occurrence for all 8 wind patterns for the month of April.

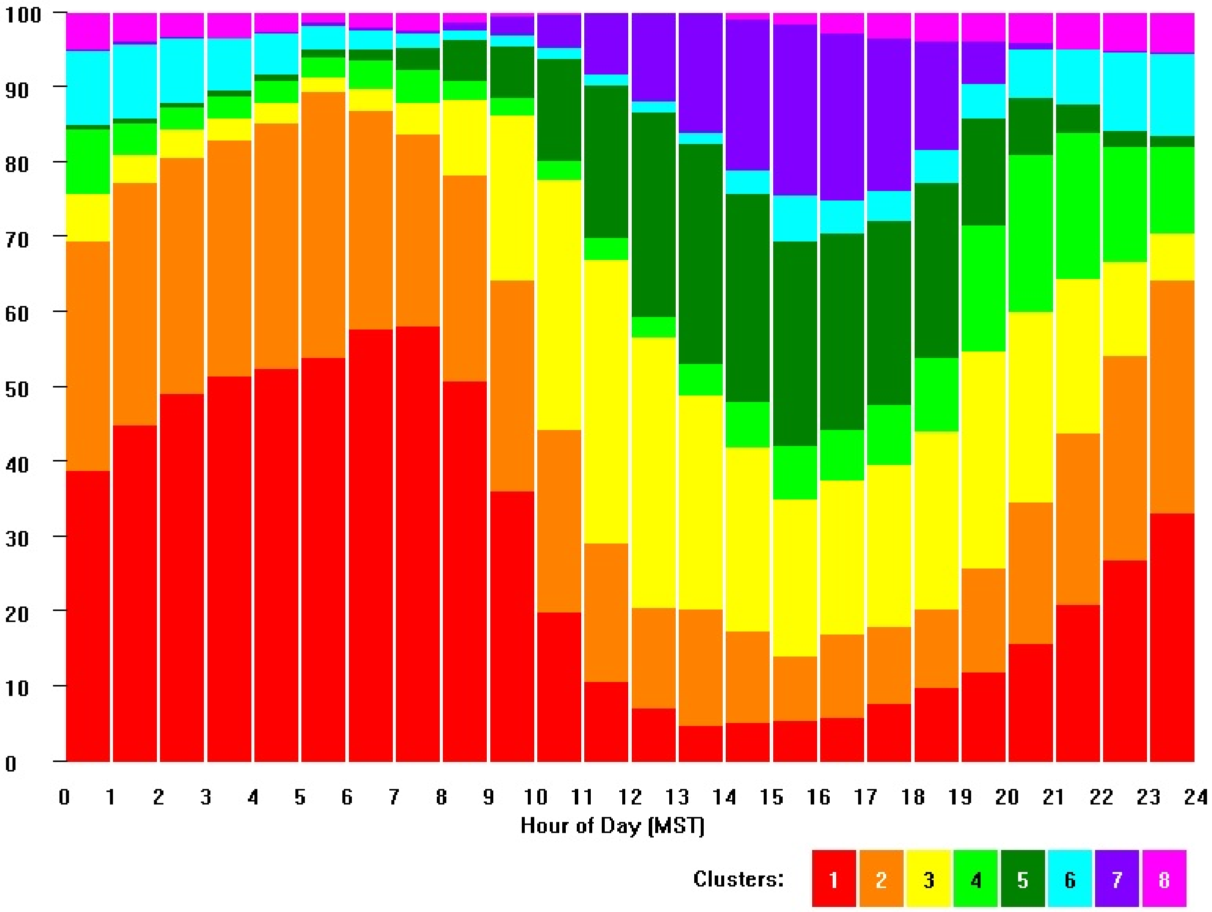

Figure 45. Hourly frequencies of occurrence for all 8 wind patterns for the month of July.

aloft and resulted in general down-valley drainage flow. On the other hand, the daytime hours were strongly dominated by the southwesterly winds of patterns 3, 4, 5, and 7 (Moderate Up-valley Flow, Decreasing Up-valley Flow Near Sunset, Well-developed Up-valley Flow, and Strong Synoptically-forced SW Flow, respectively), with a combined frequency of occurrence also approaching 85%. The most dominant wind pattern during the day was wind pattern 5, with a maximum frequency of occurrence of approximately 30% between 1500 and 1700 MST. The second-most dominant wind pattern during the day was wind pattern 3 and 7, with a maximum frequency of occurrence of approximately 25% also between the hours of 1500 to 1600 MST. Strong solar heating of the surface in the summer coupled the surface winds with winds aloft to drive the up-valley flow during the daytime hours.

Autumnal wind patterns are shown in Fig. 46 for the month of October. The fall pattern maintained much of the summertime characteristics but exhibited a preponderance of lighter winds indicative of so-called "Indian Summers." At night, the combination of wind patterns 1 and 2 (Drainage Flow and Weak Flow) still dominated with a combined total frequency of occurrence just under 70%. Wind pattern 1 was the most predominant pattern with a maximum frequency of occurrence of just under 60% between the hours of 0600 and 0800 MST. Wind pattern 2 was nearly as dominant with a maximum frequency of occurrence of approximately 38% near midnight.

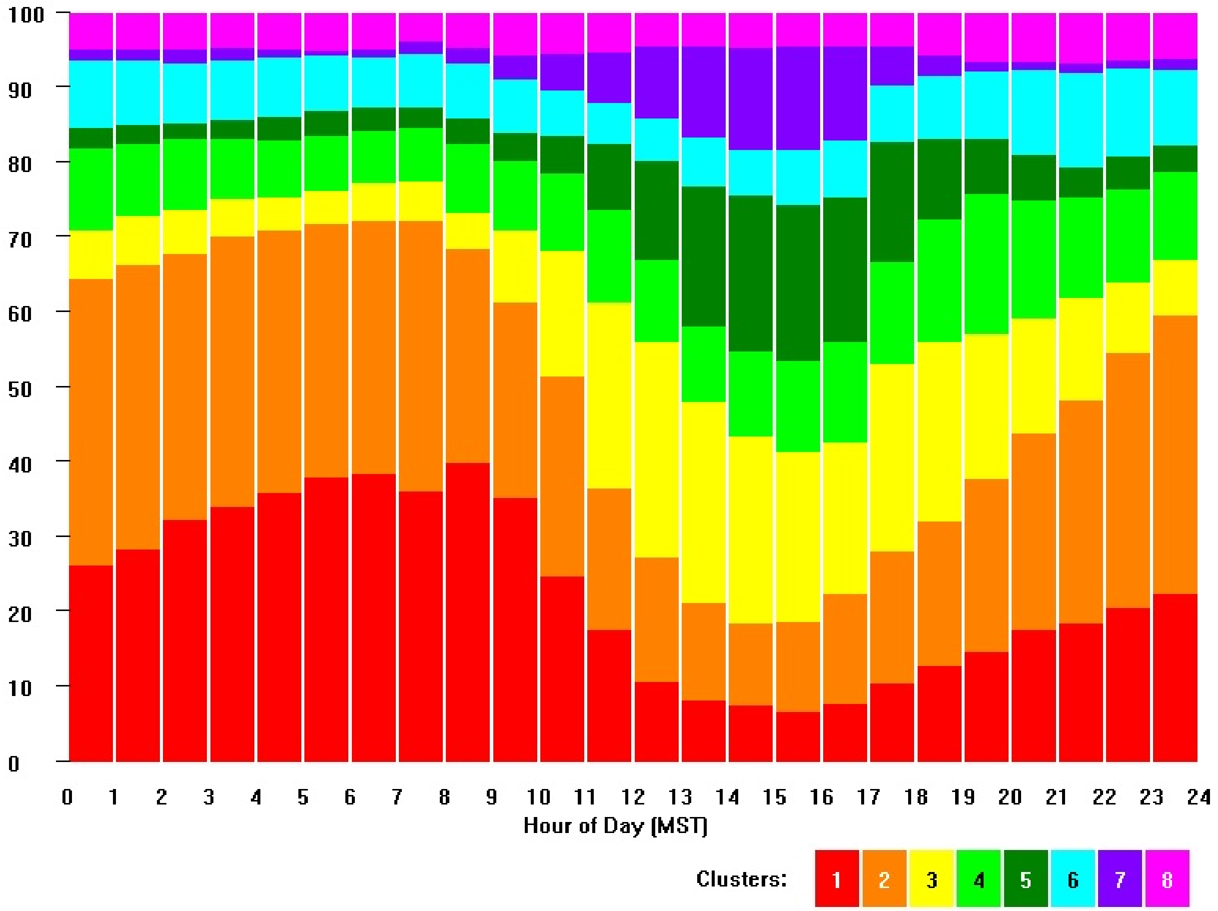

Figure 46. Hourly frequencies of occurrence for all 8 wind patterns for the month of October.

Southwesterly winds predominated in the daytime, but wind pattern 7 (Strong Synoptically-forced SW Flow) yielded to the lighter winds of pattern 3 (Moderate Up-valley Flow). A step-wise discontinuity near sunset was observed in wind patterns 5 (Well-developed Up-valley Flow) and 7 during autumn evenings near sunset indicating a rather abrupt transition from strong southwesterly flow to patterns 2 and 3 in the absence of solar heating of the surface.

Surface Wind Channeling Mechanisms in the Snake River Plain

It is clear from the previous discussions that the winds within the ESRP are generally channeled along the southwest-northeast axis of the topography. Channeling of this type is common in valleys, but the detailed physical mechanisms that cause it have not been studied in detail until recently The more widespread use of mesoscale numerical models (Pielke, 2002) has allowed researchers to simulate the three-dimensional structure of the winds within valleys, which has led to a better understanding of channeling mechanisms.

The type of channeling that has been studied the longest is thermally driven winds (Egger, 1990; Whiteman, 1990). These are winds caused by differential heating and cooling within a valley, resulting in up-valley winds during the day and down-valley winds at night. Thermally forced wind systems are most likely to be observed when synoptic-scale winds are light. Due to the general orientation of the ESRP, thermally driven winds in the ESRP are expected to produce southwest winds during the day and northeast winds at night.

Channeling in valleys can also be produced by interactions of synoptic-scale flows with the topography. Whiteman and Doran (1993) identified two potential mechanisms by which synoptic-scale winds can be channeled along a valley axis. One mechanism, called forced channeling, assumes that the valley sidewalls simply act as obstacles that tend to block the cross-valley component of the synoptic-scale wind while providing little hindrance to the along-valley component. The wind within the valley is channeled in the direction that matches the along-valley component of the synoptic-scale wind.

The second mechanism by which synoptic-scale winds can be channeled is called pressure-driven channeling. It was first suggested to explain the observed winds within the shallow Upper Rhine Valley in Germany (Wippermann, 1984; Gross and Wippermann, 1987). The channeling arises from imbalances in the forces acting on the air within the valley. In flat terrain outside the valley, the wind direction is determined by a balance among the synoptic-scale pressure-gradient force, the Coriolis force, and surface drag. The winds are roughly parallel to the isobars, with some turning towards low pressure due to the surface drag. Within a valley, however, blockage by the sidewalls tends to hinder the accelerations associated with the Coriolis force, resulting in a more dominant pressure-gradient force. As a result, the wind accelerates along the valley axis from high to low pressure.

This second mechanism, pressure-driven channeling, is an important mechanism in broad, shallow valleys such as the Upper Rhine Valley and the Tennessee River Valley in eastern Tennessee (Whiteman and Doran, 1993; Eckman, 1998). Forced channeling, however, appears to be more important in small valleys and canyons, such as the smaller corrugations that run along the floor of the Tennessee River Valley (Eckman, 1998). Both of these mechanisms are expected to be more important in stable conditions when the valley sidewalls are a more effective barrier to cross-valley winds. In daytime convective conditions the valley sidewalls may become less of a barrier to the wind. Additionally, deep, turbulent mixing that can develop on sunny days tends to couple the winds at the surface to the winds aloft. Under such conditions, neither forced nor pressure-driven channeling may be effective, and the valley winds may be closely aligned with the winds aloft. Whiteman and Doran (1993) call this scenario downward momentum transport, because vertical mixing by turbulence is a major factor in masking the channeling effects. Eckman (1998) simply calls this “un-channeled flow”, as it represents a situation in which the topography has little effect on the near-surface winds.

In considering the importance of these various channeling mechanisms for the ESRP, the question arises as to how they can be distinguished. One method is to compare the wind direction within the valley with the wind direction aloft just above the valley. Each mechanism produces a distinct relationship between these winds. For the ESRP, the mechanisms are expected to produce the relationships shown in Fig. 47. Thermally driven winds are decoupled from the winds aloft, therefore the valley wind can be either up-valley or down-valley for any direction of wind aloft. Both forced channeling and pressure - driven channeling produce abrupt shifts in the valley wind direction at certain directions of winds aloft, but the shift points for the two mechanisms differ by 90°. With un-channeled

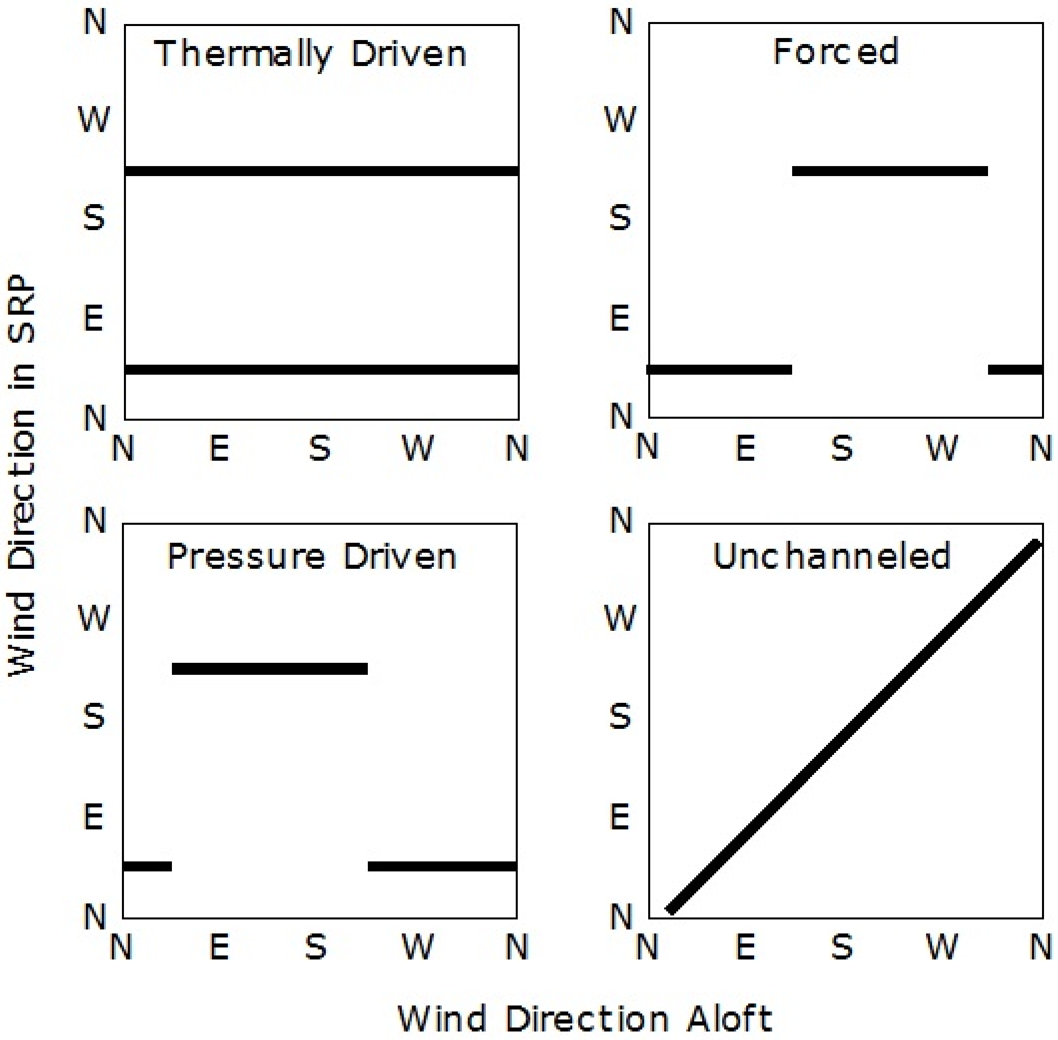

Figure 47. Expected relationship of surface winds within the ESRP to winds aloft for different channeling mechanisms.

flow, the wind direction aloft and wind direction in the valley are the same.

Both the wind data presented earlier in this climatography and the data used by Stewart et al. (2002) suggest that thermally driven flows can be important in the ESRP when the synoptic winds are light. However, they are by no means the dominant feature. Figure 48, for example, shows wind roses for the CFA tower representing both nighttime (0000-0600 MST) and daytime (1200-1800 MST) conditions. If thermally driven flows were dominant, one would expect daytime southwesterly winds and nighttime northeasterly winds. While the figure does show an increased frequency of lighter northeasterly winds at night, southwesterly winds are common during both time periods.

Figure 49 shows day and night wind roses for the BLU tower located within the Birch Creek tributary valley. The Birch Creek Valley is oriented perpendicular to the orientation of the ESRP, i.e. northwest to southeast. This location shows a much more distinct diurnal wind reversal from northwesterly (down-valley) winds at night to southeasterly (up-valley) winds during the day. Hence, thermally driven flows appear to be more

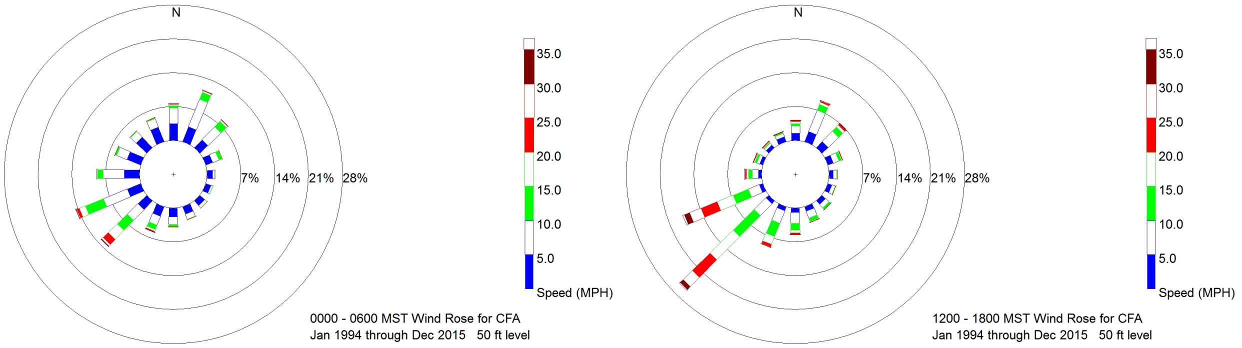

Figure 48. Wind roses at the CFA tower for night (left) and daytime (right) periods.

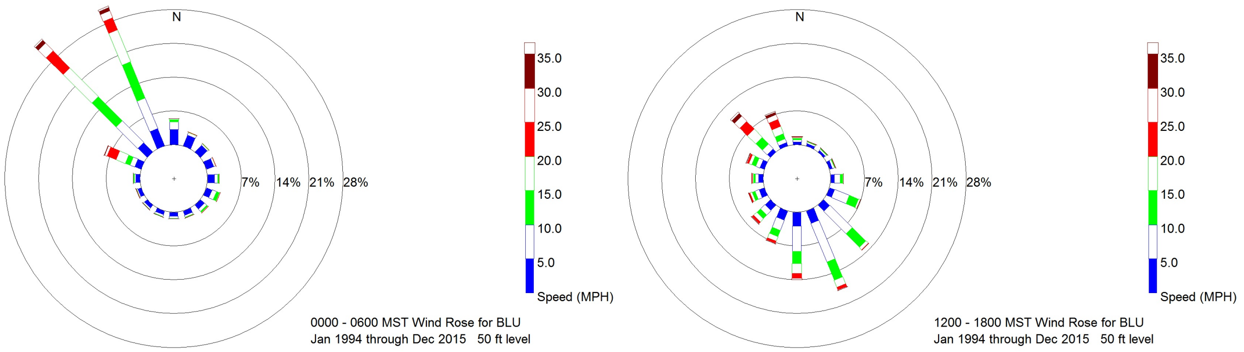

Figure 49. Wind roses at the BLU tower for night (left) and daytime (right) periods.

of a factor in the tributary valleys to the west of the INL than in the ESRP itself. However, northwesterly daytime winds at BLU are not uncommon, suggesting that other channeling mechanisms are still at work in the Birch Creek Valley.

A special case of pressure-driven channeling are called gap flows. Gap flows are winds driven by a pressure gradient through some type of topographic constriction between two air masses. Strong gap flow winds develop in the Birch Creek Valley and push out onto the ESRP and affect the northern end of the INL (Finn et al. 2016). These are generated at nighttime, most commonly when synoptic forcing is weak. Differential cooling regimes between air masses above and below a constriction in the Birch Creek Valley creates a pressure gradient that forces air from a sub-basin in the upper valley into the lower valley with strong acceleration through the gap. As a result, strong winds out of the northwest can be seen at SMC and the northern end of the INL. Occasionally gap winds can reach the southern end of the INL but the strength will be lighter the further south from the Birch Creek Valley. More information regarding the gap flows from the Birch Creek Valley can be found in Finn et al. 2016.

Kossmann et al. (2002) reported some preliminary work in the Snake River Plain regarding the relative importance of forced and pressure-driven channeling, and concluded that pressure driven channeling appears to be more dominant. However, they used winds at the 700 mb level from the Boise, Idaho rawinsonde as a surrogate for the winds aloft in all of the Snake River Plain. Given that Boise is over 150 miles removed from the eastern part of the plain, this could result in considerable error. Therefore a field project was conducted in late December

2012 through late September 2013 with one of the objectives to gain a better understanding of the interaction of flows from the intermontane valleys bounding the ESRP and the thermal flow regime of the ESRP.

Typical Diurnal Cycles in Summertime Wind Patterns for the INL

An analysis of data from a field study was conducted for 3-month period from May through July of 2013. It examined the typical diurnal cycle in wind patterns over the INL for the 3-month period by calculating diurnal averages of wind speed and wind direction by height and time for all of the measurements. Some of the key results from that study will be summarized here from an unpublished document (Finn et al., 2014). In the absence of synoptic forcing, summertime wind flows on and near the INL follow a characteristic diurnal pattern.

Midday

Generally, wind directions over the INL are well-organized and southwesterly by midday, with flows near the surface fully coupled with flows aloft. Wind speeds near the surface commonly range from under 5-10 mph to over 30 mph, depending upon degree of synoptic influence. Wind speeds tend to be greater across the INL than over adjoining areas of the ESRP. It is suspected that is due, at least in part, to the role that topography related to the Lost River Basin plays. It is also suspected that there is a stronger partitioning of energy into sensible heat flux in the Lost River Basin, when compared to surrounding areas. There is likely a greater partitioning of energy into latent heat fluxes in surrounding areas due to the greater presence of irrigated cropland. Higher sensible heat fluxes would promote earlier and stronger coupling of surface flows with the higher momentum flows aloft resulting in higher wind speeds.

Evening

As evening transition approaches, wind speeds across the INL begin to decrease and surface wind directions become much more variable and disorganized. The variability increases for several hours following transition except for those stations near the mountain valleys. Wind directions in the mountain valleys adjoining the INL to the north begin to shift from up-valley (southeasterly) to down-valley (northwesterly) as well-organized northwesterly outflows begin to develop during transition and persist through much of the night. At some stations on the INL a retrograde counterclockwise rotation sometimes occurs. Stations to the north and east of the INL show an early counterclockwise rotation to more southeast, east, and northerly directions.

After about 2100 h MST, the lower levels of the atmosphere begin to rotate clockwise from southwesterly to northwesterly and northeasterly and decouple from the southwesterly flow aloft. The maximum degree of rotation occur at the lowest levels and is successively less upwards through a depth of about 2,600-2,950 ft. Above that, the average wind direction is southwesterly throughout the diurnal cycle.

Nighttime

Changes in wind speed and direction associated with evening transition occur fairly rapidly for the first few hours following sundown, then more slowly after midnight. Nighttime flows on the INL are driven by several competing factors in thermally-driven, non-synoptic conditions:

1. Regional northeasterly drainage flows down the overall gradient of the Snake River Plain up to 1000-1500 ft. deep.

2. Persistence of the southwesterly winds of daytime through transition into nighttime. Nighttime winds on the INL tend to be bimodal with a major northeast mode and a usually lesser southwest mode. When the ESRP is viewed as a whole, the two modes show a spatial pattern. To the northeast of the INL, the northeasterly mode is clearly dominant at nighttime. To the southwest, the southwesterly mode increases in importance as night progresses. On the INL, it is something of a mixed picture with a tendency toward a major northeast mode and a minor southwest mode. The dominance of the northeast mode for the INL stations tends to increase with time and often does not fully develop until well past midnight and then tend to persist for a few hours after sunrise.

3. Drainage effects associated with the local topography of the Lost River Basin. These are shallow flows, only a few meters deep.

4. Possible influence from mountain valley outflows. This influence is felt mostly at stations closer to the mountains (e.g., SMC, SAN, HOW). At these stations the northwesterly valley outflows often wedge beneath the regional northeasterly drainage flow. In this situation, the full development of the northeast flow is often inhibited until northwesterly outflow has subsided. This is often delayed until sometime after sunrise. Mountain valley outflows are probably insignificant most of the time for central and southern areas of the INL, such as at GRI, but they can strongly affect most of the INL during frontal passages.

Morning

There is generally a lag of several hours from sunrise and the beginning of morning transition until the associated changes in wind speed and direction are complete. Depending on measurement height and location, wind speeds decrease to a post-nighttime minimum anywhere from as early as 1-2 hours after sunrise (about 0500-0600 h MST) to as late as almost 1000 h. The wind speed minimum is generally latest at locations closest to the mountains and most affected by valley flows.

Wind directions in the lower levels of the atmosphere over the INL begin a gradual clockwise rotation from north to northeast through the morning transition period. At GRI the depth of this layer is about 650-1000 ft. Above that layer, the rotation at GRI is counterclockwise, beginning from northwest, between about 1000-3300 ft. At about 0900 h very rapid rotations commence with the lower layer rotating clockwise, the layer above that rotating counterclockwise, and the whole air column becoming coupled with the southwesterly flow aloft, all in less than an hour. Wind speeds begin to increase rapidly to their daytime maxima after the coupling is complete. One result of the rapidity of rotation and coupling is that the southwesterly and northeasterly modes dominate at stations over much of the INL. The rotations are top down. That is, the level above begins to rotate slightly earlier than the level below it.

The evolution of flows during and following morning transition near the mountains and to the north and east of the INL is more complicated. Locations at the north end of the INL, show a steady, uniform rate of clockwise rotation from north-northwest, associated with outflows from Birch Creek Valley, through southeast to southwest over a period of several hours beginning about 0600 h. Locations in or near the mountain valleys (BLU, HOW, ARC) indicate that near-surface, southeasterly, up-valley flows start to overcome the northwesterly, down-valley flows by usually no later than about 0830 h. A few miles away and to the south (SMC), wind directions are similar to those near the mountain valleys. However, the clockwise rotation is less uniform, beginning from north-northeast at about 0600 h, slowing from about 0700-0900 h, then rapidly from northeast to southwest in a way somewhat similar to that observed at GRI.

Off the INL site to the north and east, a clockwise turning at the lower levels of the atmosphere is also observed as part of morning transition. The rotation at stations there begin well before clockwise rotation at the stations on the INL. East-southeasterly winds are prominent at the DUB, HAM, and ROB stations by 0800 h. A little later this mode also appears at the TAB station. What is interesting is that a significant east-southeasterly mode tends to persist well into the afternoon at many of these stations, long after the rapid late morning rotation to southwesterly at stations on the INL is complete. It is speculated that this stalling out of the clockwise rotation represents an effect of topography introduced by the Lost River Basin. Daytime east-southeasterly winds at stations along the east side of the ESRP would be upslope toward the eastern and southern crests of the Lost River Basin. Unless the pressure gradient driving the overall southwesterly up-plain flow along the ESRP is strong enough to overcome this local topographic effect, the clockwise rotation of wind directions at these stations could be slowed or delayed.

The morning transition is usually completed by late morning with a return to the midday condition of a deep, well-mixed boundary layer with flows at the surface fully coupled to flows aloft.

Radar Wind Profiler vs. Tower Winds

The radar wind profiler at the INL, described later in this section, has the potential to provide a better data set for investigating ESRP channeling. Figure 50, for example, shows the wind direction from the 33-ft. level on the GRI tower plotted against the radar profiler wind direction at 5,180 ft. AGL. This latter height was chosen because it is near the 700 mb pressure level in order to be consistent with the Kossmann et al. (2002) study. Periods of light synoptic forcing when the 5,180 ft. wind speed was less than 11 mph were excluded from the analysis. The sizes of the rectangles in the plot are scaled according to their relative frequency within 10° bins along the x axis. Shift points in the GRI wind direction were observed when the upper-level wind was between about 170° and 340°. In comparison with Fig. 47, these data appear to be in better agreement with forced channeling than pressure-driven channeling, which contradicts the Kossmann et al. (2002) results and is somewhat surprising given the results obtained in other wide valleys. However, a closer inspection of the Kossmann et al. (2002) study reveals that the data for the ESRP may in fact be more consistent with forced channeling than pressure-driven channeling.

One caveat with Fig. 50 is that the analysis and plotting procedures may be masking the importance of other mechanisms to some degree. It has previously been noted that periods with light upper-level winds (< 11 mph) were excluded. This eliminates many of the periods with thermally-driven winds at the surface. Additionally, the normalization method for the rectangles obscures the fact that westerly winds aloft are far more frequent than easterly winds. Many of the rectangles on the left side of the plot are based on relatively few cases. Un-channeled flow (downward momentum transport) may be more important than indicated in the plot. Many of the high-wind events at the INL are associated with approaching storm systems, when the upper-level winds are out of the southwest. Downward mixing is clearly a major contributor in these events. However, both forced channeling and unchanneled flow lead to the same result when the wind aloft is out of the southwest (Fig. 47). The unchanneled flow may therefore be masked because it occurs

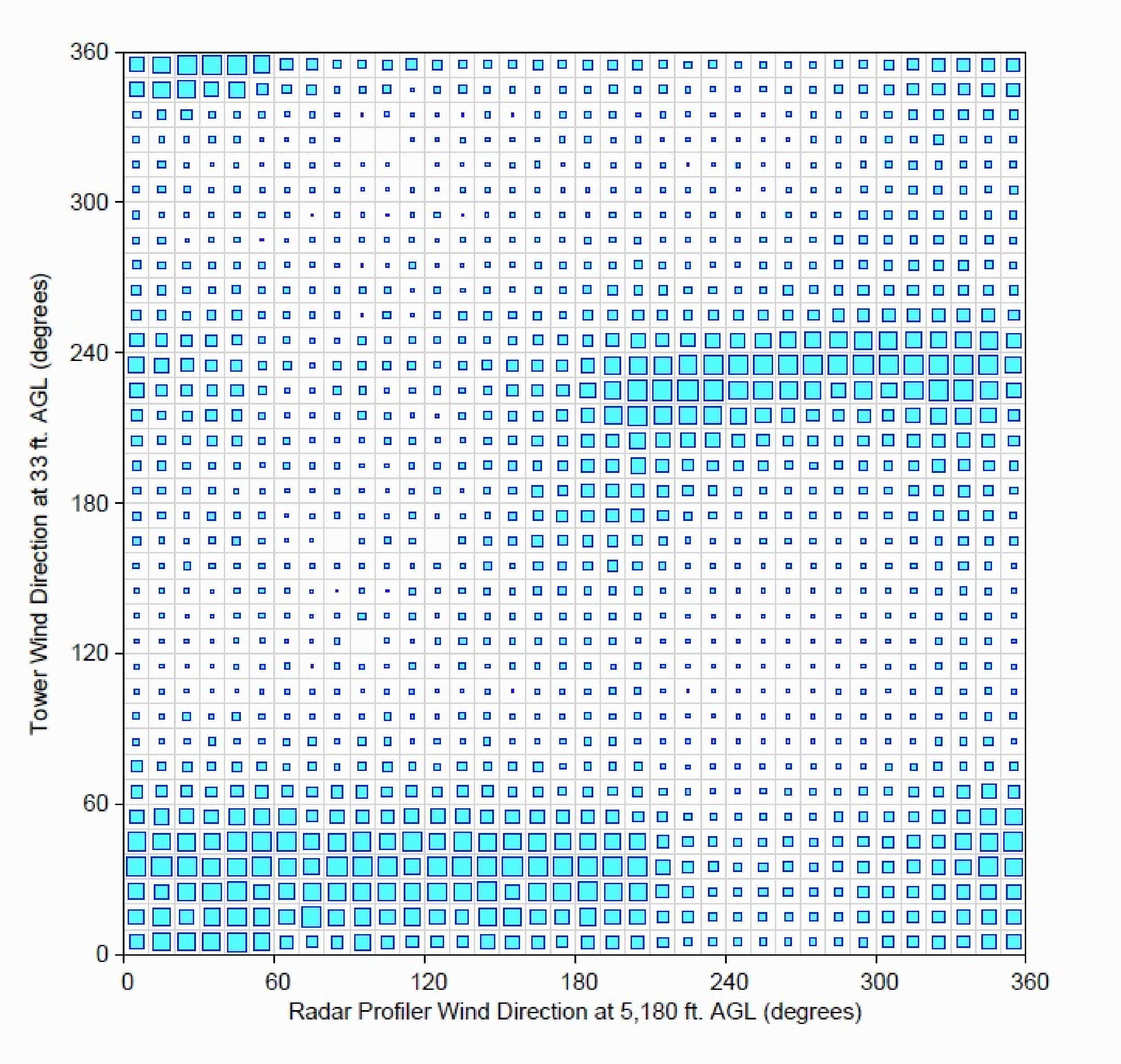

Figure 50. Frequency diagram of Grid 3 Tower (GRI) 33 ft. wind direction versus radar wind profiler wind direction at 5,180 feet AGL. Rectangle sizes are scaled according to relative frequency of the GRI winds in 10° bins. Data period of record spans from January 2000 to December 2015.

preferentially for southwesterly winds aloft. Clearly, there is still considerable work yet to be done in understanding the wind channeling within the ESRP.

Winds Aloft

An extensive record of upper air observations was assembled from routine daily PIBAL observations made at the INL from 1950 to 1965. This record and an accompanying description were published in the first and second editions of the INL climatography (DeMarrais, 1958a and Clawson et al., 1989). Additional short-term measurements supplemented the PIBAL data set and were also published in the 1st and 2nd editions of the INL climatology. After 1965, routine PIBAL observations were discontinued. However, since 1994, upper air data have been acquired by a 915

MHz radar wind profiler with a radio accoustic sounding system (RASS) for measuring wind and virtual air temperature profiles at the INL. The system is located in the Grid 3 atmospheric research area north of INTEC. The radar wind profiler and RASS provide continuous vertical wind and air temperature profiles, whereas only one PIBAL sounding per day comprised most of the early upper air database. The PIBAL record only contained wind speed and direction data that extended to approximately 9,000 ft. above ground level (AGL). The radar wind profiler data are superior to the PIBAL data because the profiler operates continuously throughout the day up to 16,000 ft. AGL, thus providing 24/7 coverage of the continuously changing lower portion of the troposphere.

To date, continuous 30-minute averaged vertical wind profiles have been acquired using 48 range gates from about 490 to 16,140 ft. AGL, with a resolution of about 330 ft. The data period of record spans March 1994 through December 2015. Questionable data acquired by the radar were identified and removed using automatic algorithms developed by Weber and Wuertz (1991) and Weber et al. (1993).

Although the radar wind profiler was in continuous operation except for brief occasional power outages, semiannual maintenance, and minor equipment repairs, various atmospheric conditions caused the data availability in all range gates to be less than complete. This is a well-known characteristic of this type of instrument. An analysis of the data availability showed that the maximum data availability for the radar wind profiler was approximately 80%, as shown in Fig. 51. Maximum data availability (>70%) was observed from the surface to 4,000 ft. AGL between the nighttime hours of 2000 to 1000 MST. During the daytime hours, data availability from the surface to 2,000 ft. dipped to near 60%, particularly around 1400 MST. Fifty percent or better data recovery was generally found up to approximately 6,500 ft. AGL every hour of the day. Twenty-five percent data availability was found up to approximately 10,000 ft., and above 14,000 ft. it was 10% or less. In the region above 14,000 ft. AGL, care must be exercised when describing overall trends because of the low data recovery statistic.

Annual Wind Speed and Direction Characteristics

In the discussion that follows, only annual characteristics of wind speed and wind direction are presented. An analysis of seasonal characteristics is left for another follow-on edition of this work.

A contour plot of daily mean scalar wind speeds together with average direction arrows over the 22-year period of record is provided in Fig. 52. Wind speed generally exhibited the expected increase with height from a minimum average speed of about 10 mph near the surface to a maximum of about 35 mph near 16,000 ft. AGL. Below 5,000 ft. and above 8,000 ft AGL a distinct diurnal wind speed trend was observed. In the region above 8,000 ft., a bulge in the wind speed contours, indicating lower wind speeds, can be seen centered at about 1600-1800 hrs MST. Concurrently, a wind speed maximum in the region below 5,000 ft. can also be seen. This indicates that the wind speed momentum mixes to the surface in the afternoon, a feature previously described in the wind pattern discussion above. Also in the region below 5,000 ft., wind speed reached a minimum between the hours of 0100 to 1000 MST. This overall pattern is consistent with the generally observed diurnal surface wind speed trends. An interesting feature in the contours that is not readily explained is the wind speed minimum of less than 8 mph at about 3,000 ft. AGL between the hours of 0500 to 0600 MST. Additional research is needed to better understand this phenomenon.

Average wind directions (Fig. 52) also show a distinct height and time pattern in the region

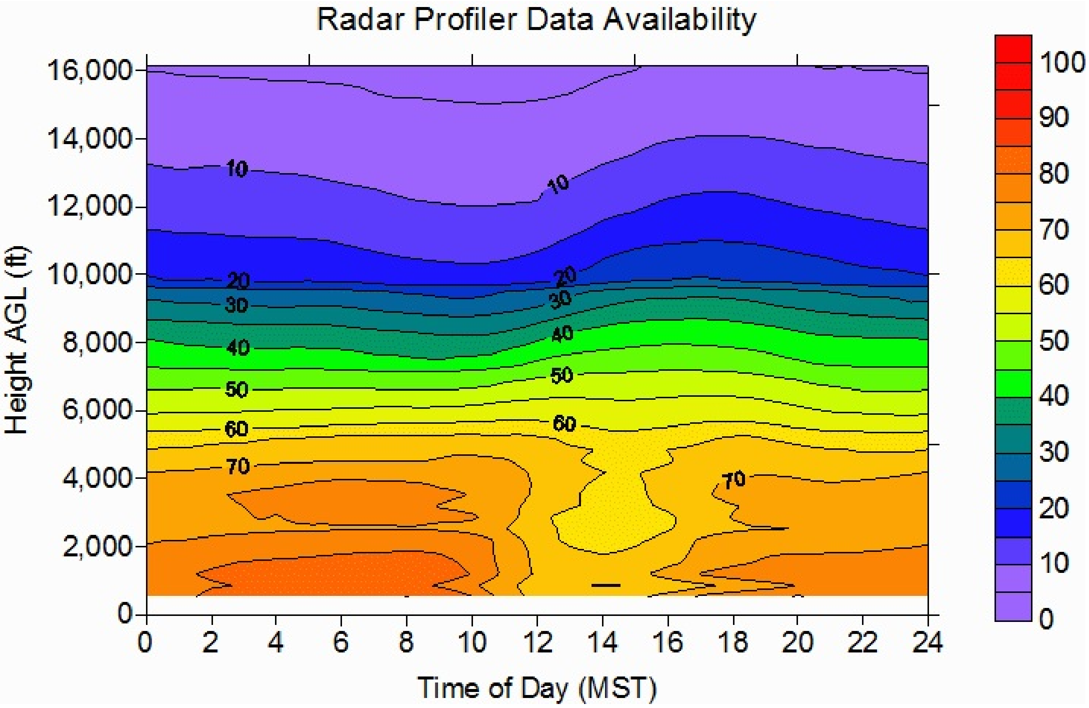

Figure 51. Radar wind profiler data availability (%) as a function of time of day and height AGL.

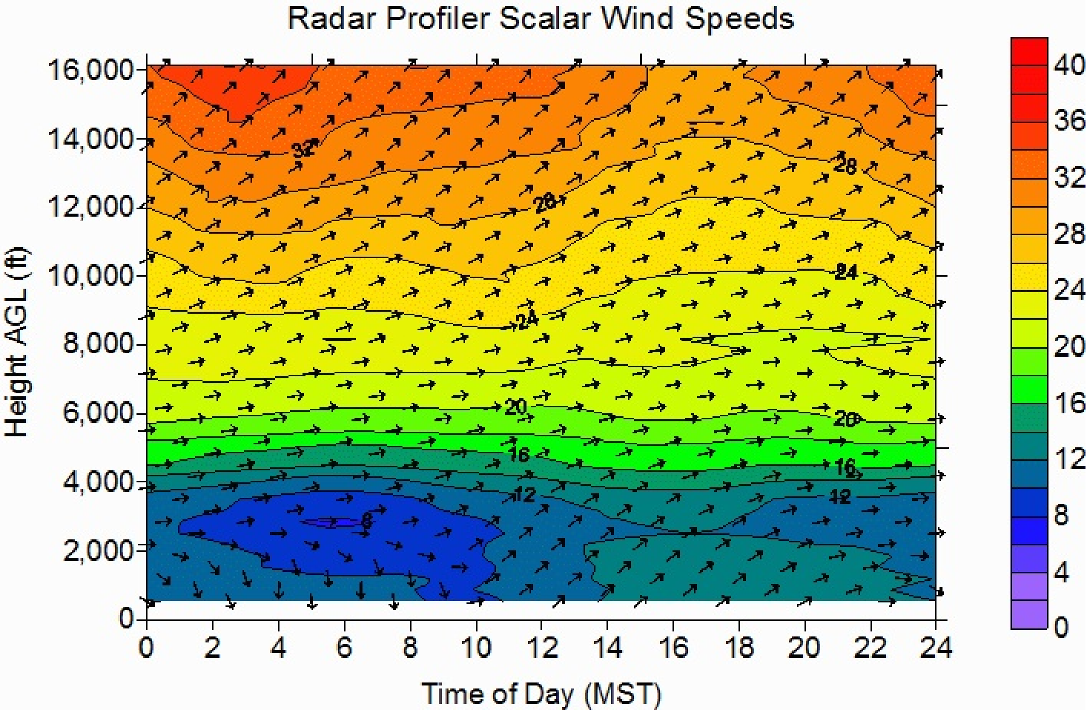

Figure 52. Radar wind profiler derived scalar wind speeds (mph) together with average direction arrows as a function of time of day and height AGL.

below 5,000 ft. AGL. At 5,000 ft., the winds were generally from the west. Near the surface, the winds were from the north between 0200 to 0900 MST. Between 0900 and 1100 MST the winds transitioned to the southwest and remain from that direction until between 2200 to 0100 MST, when the winds transitioned back to the north. Wind directions in the layers between the surface and 5,000 ft. exhibited trends between these two extremes. At heights between 5,000 ft. and 8,000 ft. AGL, the wind direction was generally westerly throughout the entire day. Above 8,000 ft., the wind direction was generally southwesterly the entire day. The radar profiler vector wind speed time/height plot is presented in Fig. 53. It is similar in pattern to the scalar wind speed plot. However, a more distinct diurnal pattern is visible, especially the mixing of the upper winds downward toward the surface in the afternoon hours with a peak around 1600 MST.

Persistence

Figure 54 is a contour plot of the persistence of the wind in the radar wind profiler's measurement volume as a function of time of day. Persistence is the ratio of the vector wind speed to the scalar wind speed. A value near 100% represents a "persistent" wind that varies little in direction over a specified averaging period. A low persistence value represents a highly variable wind direction for the same averaging period. The maximum observed persistence exceeded 75%. However, in general terms, persistence exceeded 65% at altitudes above 8,000 ft. AGL. Persistence declined to 50% between 8,000 and 4,000 ft.

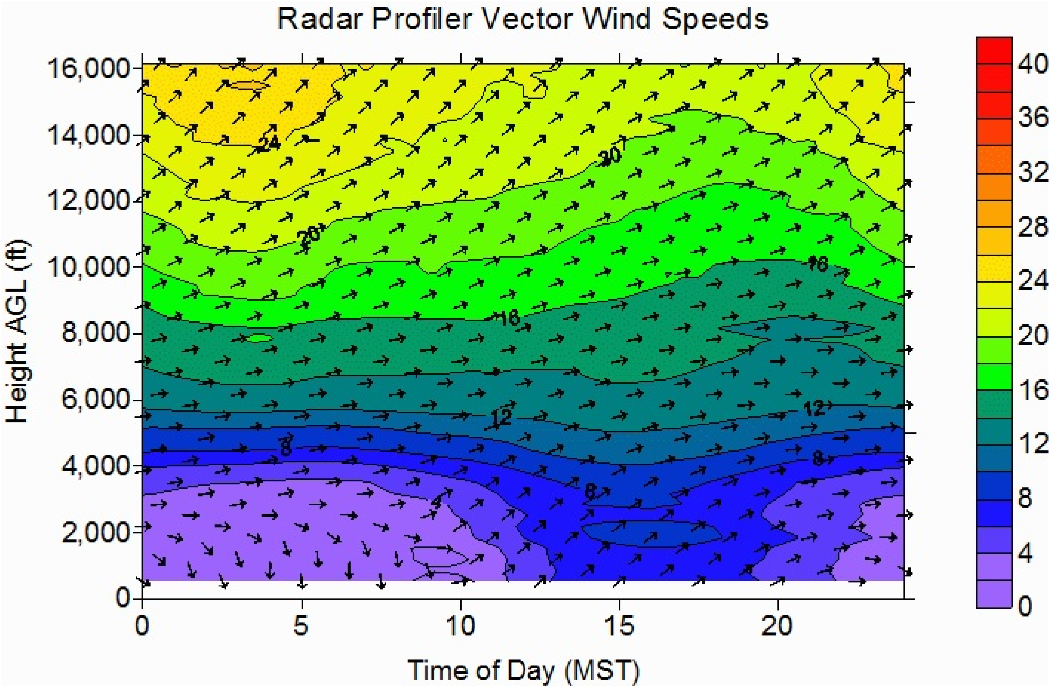

Figure 53. Radar wind profiler derived vector wind speeds (mph) together with average direction arrows as a function of time of day and height AGL.

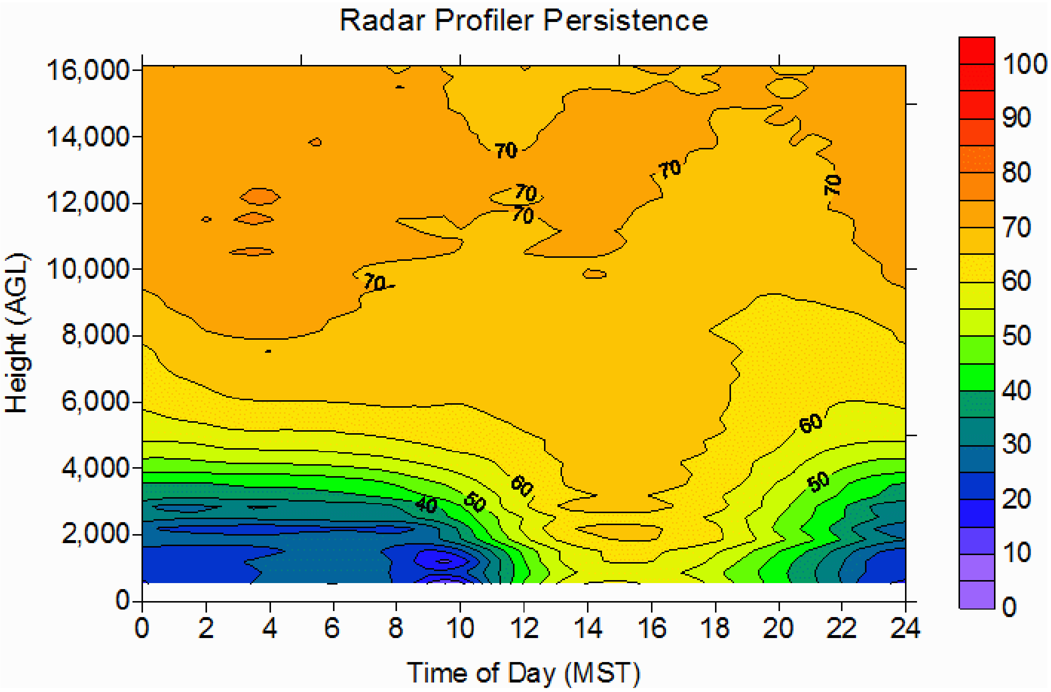

Figure 54. Radar wind profiler derived wind persistence (%) as a function of time of day and height AGL.

AIR TEMPERATURE

Knowledge of air temperatures is necessary for appropriate facility design. Furthermore, knowledge of atmospheric thermal characteristics is important for accurate weather forecasting and is an essential input to airborne effluent dispersion models.

Near-Surface Air Temperatures

Surface air temperatures have been continuously monitored at a large number of stations on and surrounding the INL since its inception. Air temperature instruments have been collocated with wind instruments at almost every measuring station since the creation of the Mesonet. Currently all 34 Mesonet stations include measurements of air temperature from at least two levels: 6 ft. and tower top, which is mostly 50 ft. However, the longest continuous air temperature record is the CFA Thermoscreen record, which was established in 1949.

Surface air temperature patterns can be rather complex at times across the INL, but not as complex as wind patterns. Similar to their effects on wind patterns, topographic features and frontal passages also influence surface air temperatures. Outflow from thunderstorms may also influence air temperatures. Surface air temperatures at the INL have been described in the past with two stations: CFA and TAN, now known as SMC. Although somewhat similar to CFA, a third regime is also known to exist around the MFC area. However, no detailed studies have been undertaken to analyze air temperature patterns similar to what has been done for wind as provided in the previous section. The emphasis on wind patterns is well deserved. Winds at the INL are much more dynamic than air temperatures. Winds also provide the potential for off-site impacts of INL operations through atmospheric transport. Future budgets and relaxed time constraints may permit an air temperature pattern analysis for the INL. At this juncture, however, surface air temperatures will not be described in terms of three distinct microclimate zones. Instead, this edition of the INL climatography will focus on the 66-year CFA Thermoscreen data record. As mentioned earlier in the report please be advised that the Thermoscreen temperature data prior to August 1966 could be susceptible.

Daily Characteristics

The discussion of surface air temperatures begins with a description of average daily conditions at CFA. Table 9 contains daily average temperatures for each day of the year for the 66-year period of record. The daily average air temperature is defined as the average of the minimum and the maximum air temperature in a given day. It is not a time-weighted average.

Using the maximum and minimum averaging method, the data indicate that the average daily air temperature at CFA ranged from a low of 12 °F in early January to a high of 70 °F on several days in mid to late July. Thus, the spread in average daily air temperature for the year is 58 °F.

Average daily air temperature ranges for CFA are also given in Table 9. The daily temperature range is the difference between the maximum and minimum air temperature of a given day. The smallest average daily air temperature range occurred in mid January with a value of about 20 °F. The largest average daily air temperature range occurred on several days in July, August, and early September with a value of about 40 °F. As can be seen, the smallest daily air temperature range occurred in the winter, while the largest daily air temperature range occurred in the summer. This is to be expected because the long summer days provide intense heating of the earth's surface during the day, while dry atmospheric conditions with clear skies permit rapid radiational cooling of the earth's surface at night. These conditions do not prevail in the winter season.

The averages and extremes of daily air temperature ranges at CFA from 1950 through 2015 are summarized in Table 10. The maximum air temperature measured at CFA was 105 °F, recorded on July 13, 2002, while the minimum was -47 °F, recorded on December 23, 1983. Data in the lowest daily minimum column show that every month of the year has had at least one day when the minimum temperature dropped below freezing at CFA. The lowest daily average column indicates severe cold events that have occurred in December, January, and February with daily averages of -20 to -28°F.

Table 9. Average daily air temperature (Ave) and daily air temperature range (Rng) for CFA.

Day	January		February		March		April		May		June		July		August		September		October		November		December	
of Month	Ave (°F)	Rng (°F)	Ave (°F)	Rng (°F)	Ave (°F)	Rng (°F)	Ave (°F)	Rng (°F)	Ave (°F)	Rng (°F)	Ave (°F)	Rng (°F)	Ave (°F)	Rng (°F)	Ave (°F)	Rng (°F)	Ave (°F)	Rng (°F)	Ave (°F)	Rng (°F)	Ave (°F)	Rng (°F)	Ave (°F)	Rng (°F)
1	13	25	17	23	26	23	38	25	46	30	56	32	65	39	69	39	61	39	52	36	35	29	24	23
2	12	24	16	24	26	23	38	25	47	31	56	33	66	38	69	39	62	38	50	35	34	30	24	23
3	13	25	16	25	26	22	37	28	48	31	57	31	66	37	69	36	61	39	49	34	34	30	23	23
4	13	23	17	26	26	25	39	29	48	30	58	32	66	39	69	38	61	40	48	35	35	30	22	24
5	14	23	18	25	27	24	40	29	49	31	58	31	67	38	69	38	61	38	48	36	35	28	20	23
6	14	22	18	28	28	23	40	27	49	29	58	29	67	37	69	38	60	37	48	36	35	28	21	22
7	14	24	21	25	29	23	40	28	49	28	57	30	67	38	69	39	61	39	47	34	35	28	21	23
8	16	23	20	26	30	24	39	29	49	29	57	29	67	40	68	37	60	36	47	34	34	27	18	23
9	17	23	21	25	31	24	40	27	49	30	58	31	68	40	68	39	59	38	48	34	33	28	19	21
10	18	22	21	23	31	24	40	29	49	30	57	30	68	37	69	40	58	36	47	36	32	27	19	23
11	17	23	21	25	30	23	41	30	49	29	58	33	68	37	69	38	58	35	47	32	33	25	18	23
12	17	22	22	23	30	25	42	31	49	30	59	32	68	38	67	39	57	35	46	32	32	24	19	21
13	18	21	22	23	30	25	42	31	51	32	59	32	69	38	68	38	57	37	46	33	32	23	19	23
14	19	20	22	23	31	25	42	30	52	33	59	33	69	38	67	38	56	36	45	34	30	22	18	22
15	19	21	22	21	32	25	42	29	52	31	60	33	69	40	67	37	56	38	44	34	28	24	18	25
16	19	21	23	22	33	24	43	32	52	30	60	32	70	39	67	37	56	36	44	35	28	25	19	22
17	18	22	24	22	33	22	44	30	53	32	60	33	70	37	67	39	56	35	43	36	29	24	18	23
18	18	21	23	23	33	24	43	28	53	31	61	35	69	38	66	38	54	36	43	37	29	23	18	24
19	17	24	24	23	33	25	43	28	54	31	62	35	70	38	66	38	54	36	44	35	28	22	18	24
20	18	23	24	24	33	27	43	29	54	30	62	34	69	38	66	37	52	32	43	36	29	23	18	21
21	17	24	24	23	35	25	44	30	53	30	62	34	69	38	66	36	52	34	42	34	27	24	18	24
22	16	24	24	23	35	25	45	29	53	30	62	35	69	38	64	38	52	37	41	32	27	22	18	22
23	16	25	24	23	35	25	45	28	54	31	63	36	70	38	64	38	52	39	41	32	25	24	16	23
24	16	24	25	24	35	26	44	28	54	30	63	35	70	38	64	38	53	39	41	32	26	24	16	23
25	18	23	25	24	35	27	44	28	54	31	63	35	70	38	64	39	53	38	41	32	26	24	17	23
26	18	23	24	24	36	25	44	27	55	31	63	35	70	39	64	39	53	37	40	31	24	23	16	24
27	18	23	24	24	35	24	44	30	55	31	64	36	70	38	64	38	53	38	38	32	23	24	16	25
28	17	23	25	25	36	25	45	29	55	31	64	38	70	39	64	39	53	37	38	31	24	22	17	22
29	16	23	24	25	36	26	45	29	55	30	64	36	70	36	64	38	52	37	38	30	23	24	16	21
30	16	24			37	27	45	30	55	30	64	38	70	38	63	38	52	37	37	28	24	24	14	22
31	17	23			38	28			55	32			69	38	62	37			36	30			14	25

Note: Data period of record spans January 1950 through December 2015.

Table 10. Daily air temperature extremes summarized by month for CFA.

Month	Highest Daily Maximum (°F)	Lowest Daily Minimum (°F)	Highest Daily Average (°F)	Lowest Daily Average (°F)
January	55	-40	44	-20
February	60	-36	46	-23
March	73	-28	55	-6
April	86	6	63	22
May	96	13	76	30
June	101	22	83	39
July	105	28	83	49
August	102	24	83	46
September	96	12	74	30
October	89	-6	64	10
November	67	-24	57	-9
December	57	-47	47	-28
ANNUAL	105	-47	83	-28

Note: Data period of record spans January 1950 through December 2015.

The annual curve of average daily air temperatures at CFA is shown in Fig 55. The figure shows the average daily maximum and minimum, the highest daily maximum and minimum, and the lowest daily maximum and minimum air temperatures for the 66-year period of record. The purple line represents the average daily temperature. Figure 55 illustrates that average air temperature increased from the first week in January until the third week in January, when the temperature dipped for about two weeks before rising again toward the summer maximum. A winter thaw has been observed on a number of occasions in mid January, followed by more cold weather in late January and early February. In mid-February, average daily temperatures again began to rise toward a summer maximum. After the summer maximum, which occurred in late July, air temperatures declined through the end of December. The decline in air temperature during this time was more rapid than the spring and summer rise in air temperature. The time span from the winter minimum to the summer maximum was approximately seven months. Conversely, the time span from the summer maximum to the winter minimum was approximately five months.

Other features are also evident in Fig. 55. The range between the extreme highest daily maximum and extreme lowest daily minimum air temperatures indicated a seasonal dependence. This is evidenced by the greater distance between the red and blue lines and is particularly noticeable in the December, January, and February time frame. The largest range between the absolute maximum and the absolute minimum air temperature on any given day over the entire period of record was 97 °F, which was observed on December 23. The smallest range between the absolute maximum and the absolute minimum air temperature for a given day was 56 °F on July 26. This again shows that the larger variability in daily air temperatures over the entire period of record was observed in the winter months as compared with the summer months.

The largest differences in air temperature ranges on a given day were mostly a function of the ranges observed in the minimum air

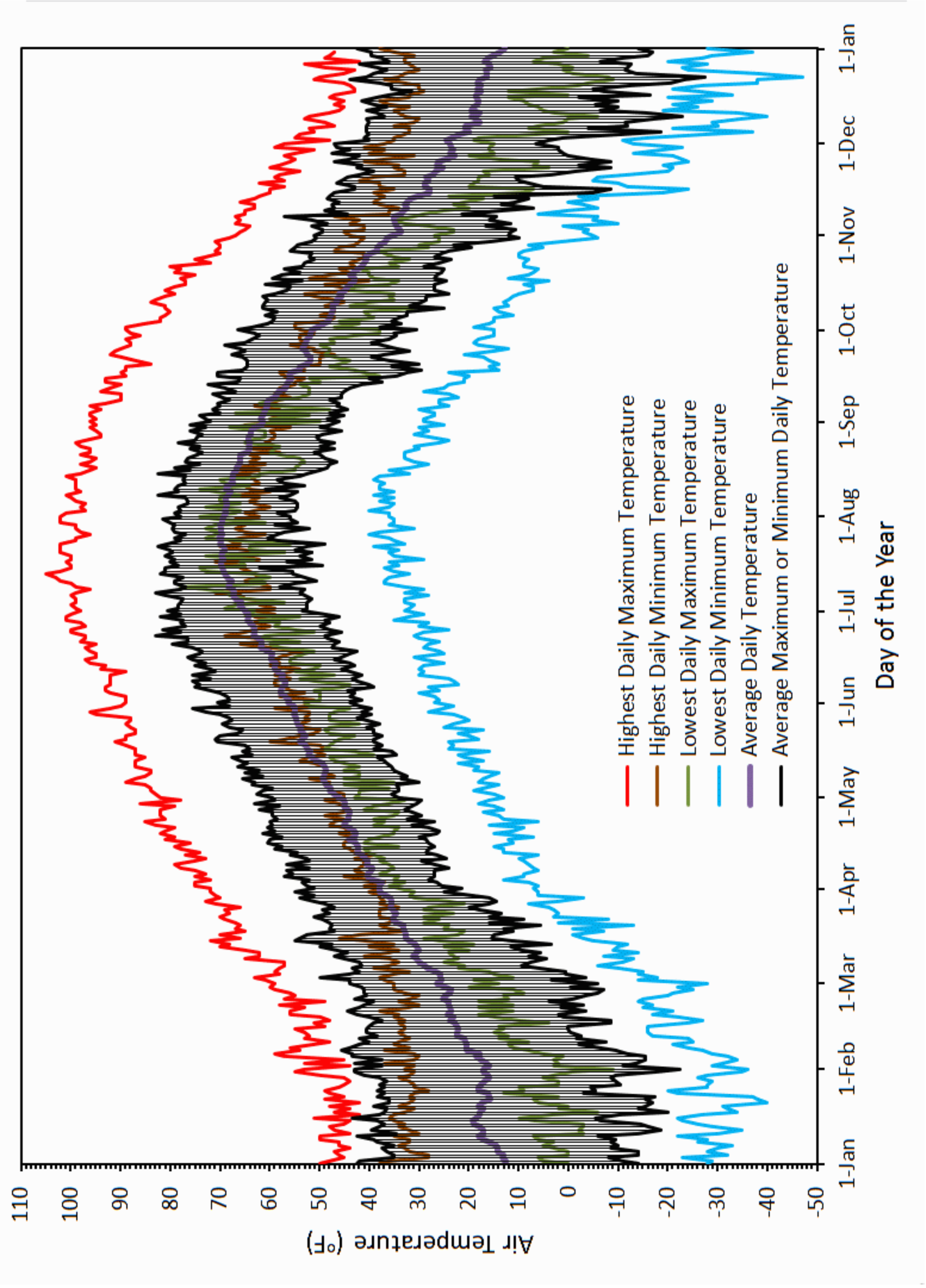

Figure 55. CFA Thermoscreen average daily air temperature (purple), average maximum and minimum daily air temperatures (black), extreme daily maximum air temperatures (red), extreme daily minimum air temperatures (blue), lowest daily maximum air temperatures (green), and highest daily minimum air temperatures (brown). Note: Data period of record spans January 1950 through December 2015.

temperatures. These were also seasonally dependent. The largest range in minimum air temperatures on any given day during the 66-year period of record was 81 °F on December 23, whereas the largest range in maximum temperatures was 62 °F on February 1. The smallest range in minimum air temperature was 21 °F on July 26. Similarly the smallest range in maximum air temperature was 21 °F on July 9.

Two other extreme air temperature characteristics are also illustrated in Fig 55. The highest minimum air temperature ever recorded was 71 °F, which occurred on July 17, 1976 and July 7, 1985. The lowest maximum air temperature recorded was -9 °F, which occurred on February 1, 1989 and December 22, 1990.

In addition to average and extreme values, normal daily maximum and minimum air temperatures are sometimes required for comparing climatological data. These have been calculated for the years 1981 through 2010 by the National Climate Data Center according to established procedures (NCDC, 2011). The procedures smooth and interpolate daily average temperatures based on monthly averages collected for a period of thirty years. This removes the day-to-day "noise" in the traces shown in Fig. 55. However, it also removes the fine-scale features, such as the decline in average air temperature in late January after a slight rise earlier in that same month. Normal maximum and minimum daily air temperatures are listed in Table 11.

The highest 30-year normal daily maximum air temperature for the year was calculated to be 89 °F, while the lowest normal daily minimum air temperature was 4 °F. The highest observed 66-year average daily maximum air temperature for the year was 90 °F and the lowest 66-year average daily minimum air temperature was 1 °F. The calculated highest 30-year normal maximum daily air temperature occurred between July 18 and August 6, whereas the peak in the 66-year averaged daily maximum occurred on July 28. The calculated lowest 30-year normal minimum daily air temperature occurred between December 23 and December 30, whereas the lowest 66-year averaged daily minimum occurred between January 1 and January 4. Thus, there are modest differences between the 66-year average and the 30-year normal daily air temperatures.

Monthly and Annual Characteristics

Monthly and annual average and 30-year normal air temperatures for CFA are given in Table 12. This table also includes the historical highest and lowest of those monthly and annual averages. The large year-to-year variability of average monthly temperatures, especially in the winter season, can readily be seen in this table. For example, the highest monthly average air temperature at CFA has been 34.1 °F in February, while the lowest monthly average air temperature in that same month has been 7.1 °F. The difference in this case, 27 °F, indicates a rather large deviation in monthly air temperatures from year to year during the winter months. Approximately one-third as much year-to-year variability occurred in late summer.

The largest within-month differences were observed for the minimum air temperatures in the winter; particularly in January, where the difference was 31.2 °F. The smallest within-month differences of approximately 10 °F were observed for the minimum temperatures during the spring, summer, and fall months. The variability of the annual air temperature extremes listed in Table 12 is much smaller than the variability of the within-month extremes. Thirty-year normals were very close to the 66-year averages.

Table 11. Thirty-year normal daily maximum and minimum air temperatures for CFA. Normal maximum and minimum air temperatures are thirty-year averages according to procedures established by the National Climate Data Center (NCDC, 2011) and have been calculated for the years 1981 through 2010.

Day	January		February		March		April		May		June		July		August		Sept.		October		Nov.		Dec.	
of Month	Max (°F)	Min (°F)	Max (°F)	Min (°F)	Max (°F)	Min (°F)	Max (°F)	Min (°F)	Max (°F)	Min (°F)	Max (°F)	Min (°F)	Max (°F)	Min (°F)	Max (°F)	Min (°F)	Max (°F)	Min (°F)	Max (°F)	Min (°F)	Max (°F)	Min (°F)	Max (°F)	Min (°F)
1	27	5	29	6	38	15	52	26	62	32	71	41	83	47	89	50	81	44	68	32	51	23	32	10
2	27	5	29	6	39	15	52	26	63	32	71	41	84	48	89	50	81	43	67	31	50	23	32	9
3	27	5	29	6	39	16	53	26	63	33	72	41	84	48	89	50	80	43	67	31	50	22	31	9
4	27	5	29	6	40	16	53	26	63	33	72	41	85	48	89	50	80	43	66	31	49	22	31	8
5	27	5	30	6	40	17	53	26	64	33	72	41	85	48	89	50	80	42	66	30	48	21	31	8
6	28	5	30	7	41	17	54	27	64	34	73	42	85	48	89	50	79	42	65	30	48	21	30	8
7	28	5	30	7	41	18	54	27	64	34	73	42	86	49	88	50	79	41	65	30	47	21	30	7
8	28	5	30	7	42	18	54	27	65	34	73	42	86	49	88	49	78	41	64	29	46	20	30	7
9	28	5	31	7	42	19	55	27	65	35	74	42	86	49	88	49	78	41	64	29	46	20	29	7
10	28	5	31	7	43	19	55	27	65	35	74	42	87	49	88	49	78	40	63	29	45	20	29	6
11	28	5	31	8	43	20	55	27	65	35	75	43	87	49	88	49	77	40	63	28	44	19	29	6
12	28	5	31	8	44	20	56	28	66	36	75	43	87	50	87	49	77	39	62	28	44	19	29	6
13	28	5	32	8	44	20	56	28	66	36	75	43	88	50	87	49	76	39	62	28	43	18	28	6
14	28	5	32	9	45	21	57	28	66	36	76	43	88	50	87	48	76	39	61	28	42	18	28	5
15	28	5	32	9	45	21	57	28	67	36	76	44	88	50	87	48	75	38	61	27	42	17	28	5
16	28	5	33	9	45	22	57	28	67	37	77	44	88	50	86	48	75	38	60	27	41	17	28	5
17	28	5	33	10	46	22	58	29	67	37	77	44	88	50	86	48	74	37	59	27	40	16	28	5
18	28	5	33	10	46	22	58	29	67	37	78	44	89	50	86	48	74	37	59	27	40	16	28	5
19	28	5	34	10	47	23	58	29	68	38	78	44	89	50	86	47	73	37	58	26	39	15	27	5
20	28	5	34	11	47	23	59	29	68	38	78	45	89	50	85	47	73	36	58	26	38	15	27	5
21	28	5	35	11	48	23	59	29	68	38	79	45	89	50	85	47	73	36	57	26	38	14	27	5
22	28	5	35	12	48	23	59	30	68	38	79	45	89	51	85	47	72	35	57	26	37	14	27	5
23	28	5	36	12	48	24	60	30	69	39	80	45	89	51	84	46	72	35	56	25	37	13	27	4
24	28	5	36	13	49	24	60	30	69	39	80	46	89	51	84	46	71	34	56	25	36	13	27	4
25	28	5	36	13	49	24	60	30	69	39	81	46	89	51	84	46	71	34	55	25	35	12	27	4
26	28	5	37	13	50	25	61	31	69	39	81	46	89	51	83	45	70	34	55	25	35	12	27	4
27	28	6	37	14	50	25	61	31	70	39	82	46	89	51	83	45	70	33	54	24	34	11	27	4
28	29	6	38	14	50	25	61	31	70	40	82	47	89	50	83	45	69	33	53	24	34	11	27	4
29	29	6			51	25	62	32	70	40	82	47	89	50	82	45	69	32	53	24	33	11	27	4
30	29	6			51	25	62	32	71	40	83	47	89	50	82	44	68	32	52	23	33	10	27	4
31	29	6			52	26			71	40			89	50	82	44			52	23			27	5

Table 12. Monthly and annual air temperature averages, extreme averages, and normals for CFA.

	Average			Maximum			Minimum			Normal		
Month	Average (°F)	High (°F)	Low (°F)	Average (°F)	High (°F)	Low (°F)	Average (°F)	High (°F)	Low (°F)	Average (°F)	High (°F)	Low (°F)
January	16.4	30.0	7.0	27.9	37.9	19.5	5.0	22.4	-8.8	16.8	28.2	5.3
February	21.7	34.1	7.1	33.7	46.0	21.2	9.7	22.3	-7.1	21.2	32.9	9.5
March	31.9	41.5	18.4	44.2	57.2	31.4	19.6	26.6	4.5	33.3	45.6	21.0
April	42.1	49.3	35.4	56.5	68.6	46.1	27.7	33.1	20.8	42.9	57.3	28.4
May	51.5	58.5	44.9	66.8	77.7	57.8	36.3	40.8	30.2	51.8	67.1	36.5
June	60.1	67.5	54.9	76.7	86.5	69.1	43.5	49.7	39.5	60.4	77.0	43.7
July	68.6	75.7	59.1	87.7	95.5	76.1	49.5	55.9	42.0	68.8	87.9	49.6
August	66.4	70.9	60.3	85.5	90.5	75.4	47.4	53.4	43.0	67.0	86.4	47.6
September	56.2	62.3	48.6	74.7	82.3	64.1	37.8	45.2	31.9	56.5	75.1	37.9
October	43.9	51.0	38.2	60.7	71.7	52.3	27.2	35.2	20.8	43.7	60.1	27.3
November	29.6	36.3	20.3	42.2	51.5	30.8	17.0	24.3	6.4	29.3	41.7	16.9
December	18.4	26.9	7.0	29.9	37.0	20.8	7.0	17.6	-7.3	17.4	28.8	6.0
ANNUAL	42.4	45.5	37.7	57.3	61.3	52.4	27.4	30.2	22.9	42.4	57.3	27.5

Note: Data period of record spans January 1950 through December 2015. Normal period of record spans January 1981 through December 2010.

Monthly and annual averages of diurnal air temperature ranges for CFA are presented in Table 13. The data indicate the average daily air temperature range for the 66-year period of record at CFA ranged from a low of 23 °F in December and January, to a high of 38 °F during July and August. Higher daily air temperature ranges during the period of May to October reflect the relative absence of clouds during these months that would otherwise serve to moderate the radiational cooling of the ground surface at night. Maximum diurnal temperature ranges at CFA exceeded 50 °F during all months, a reflection of the INL's altitude and typically low humidity. Maximum diurnal temperature events occurred almost exclusively during clear-sky conditions, and the largest ranges occurred in the fall, before the ground lost its accumulated summer heat. Normal (30-year) air temperature ranges closely follow the 66-year average.

With climate change a current topic of conversation, the question is sometimes posed if the CFA Thermoscreen air temperature data confirm global warming. An analysis of the daily data was undertaken to answer this question. The analysis was conducted for the entire 66-year period of record from 1950-2015. Daily average, daily maximum, and daily minimum air temperatures were averaged for each year of the record. A linear regression and analysis of variance was conducted on the resulting annual average data set. The results are shown in Fig. 56 and summarized in Table 14. The data showed considerable scatter as indicated by low coefficients of determination (r^2), which were all less than 0.05. In every case, however, the trend was upward. For the average daily air temperature, the slope was 0.018 °F per year, or 0.180 °F per decade. However, the statistical test indicated that the slope was not significantly different from zero. The slope value is about half that of the lowest global warming rate for land surfaces published by the IPCC (2013), which was 0.315 °F per decade for the period 1951 through 2012.

Table 13. Average, maximum, and normal daily air temperature ranges summarized by month for CFA.

Month	Average (°F)	Maximum (°F)	Normal (°F)
January	23	52	23
February	24	50	23
March	25	53	25
April	29	57	29
May	30	55	31
June	33	56	33
July	38	57	38
August	38	59	39
September	37	59	37
October	34	59	33
November	25	52	25
December	23	54	23
ANNUAL	30	59	30

Note: Data period of record spans January 1950 through December 2015. Normal period of record spans January 1981 through December 2010.

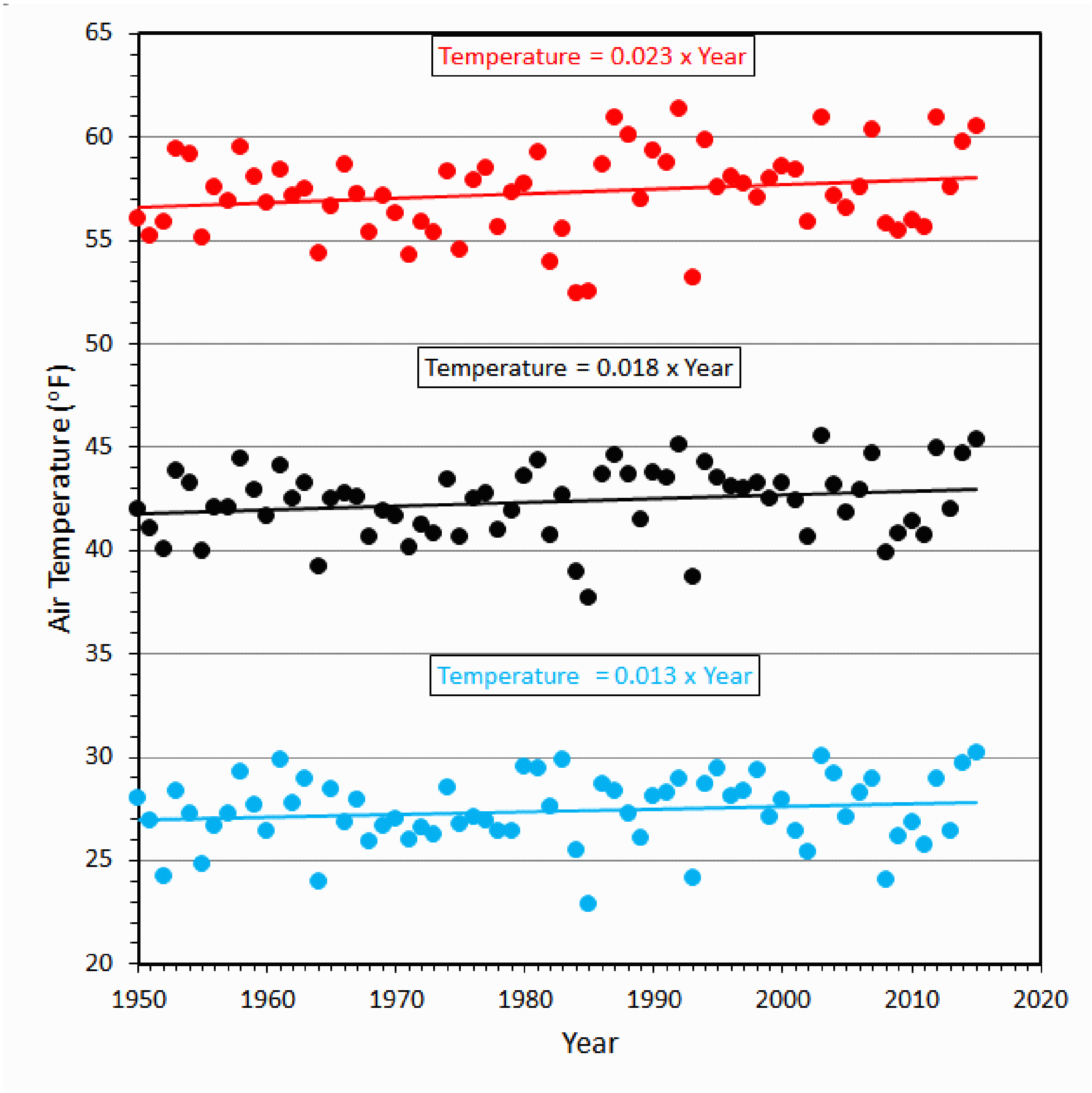

Figure 56. Average annual daily temperature, average annual maximum daily temperature, and average annual minimum daily temperature, with linear regression lines and statistics from 1950 through 2015.

There was evidence of a slightly steeper rise in the annual maximum daily air temperature as compared to minimum daily air temperature. This was significant at the 90% confidence level. The IPCC (2013) concluded that both maximum and minimum daily air temperatures have been rising, but did not publish a rate for each. For the CFA Thermoscreen data, the slope 0.023 °F per year for the average annual maximum temperature was significantly different from zero at the 90% confidence level. Using the calculated slope of the air temperature rise for the CFA Thermoscreen, the total rise in the annual maximum daily air temperature since 1950 is estimated to be 1.49 °F.

A seasonal analysis of the maximum, average, and minimum air temperatures tells a more complete story (Table 14). In the spring and summer months of March through May and June through August, respectively, the rise in air temperature was significant at the 95% level or greater for all values except for the spring average minimum daily air temperature. In the winter, the rise in air temperature was observed for the maximum and average daily air temperature slopes at the 90% confidence level. In the fall months of September through October, the slope was essentially flat, indicating no effect of warming in the autumn season.

Spatial Variability

INL air temperatures may be highly variable from place to place for short periods of time. A cursory review of average monthly temperatures from each of the main Mesonet stations in each of the three microclimate zones (GRI, SMC, and MFC) since 1993 shows at most a 1 °F difference between the stations. Nevertheless, simultaneous spatial differences between the three stations have been observed as large as 32.7 °F. These large differences have been observed mostly during the winter months and are mostly associated with strong temperature inversions. The spatial variation in the summer is not typically as large as in the winter months. Large summertime spatial variations are generally associated with thunderstorms that cool the air locally.

Air temperatures from several locations on and surrounding the INL were compared on days when the extreme highest maximum and extreme lowest minimum air temperatures were observed. On the day the highest maximum air temperature was recorded at CFA (July 13, 2002), the temperatures varied from 96 °F at Rexburg to 106 °F at the Sand Dunes station. On the day the lowest minimum air temperature was recorded (December 23, 1983), the temperatures ranged from -23 °F at Blackfoot to -49 °F at SMC.

Specific Air Temperatures

The occurrences of specific air temperatures are frequently of interest in the analysis of climate. The average, highest, lowest and normal number of days per month or per year (expressed as a percentage) when the maximum air temperature was less than or equal to 32 °F, or greater than or equal to 90 °F, are presented in Table 15 for CFA. These data show that the air temperature on approximately 2/3 of the days in January usually remained below freezing at CFA. That percentage dropped to 43% in February, meaning that on average, 43% of the days had air temperatures that never rose above freezing (32 °F). That percentage dropped to 11% in

Table 14. Slopes of the rise in mean maximum, average, and minimum daily air temperatures obtained by linear regression, together with the confidence interval of the slope and the statistical significance of the slope.

	Spring	Summer	Autumn	Winter	Annual
Maximum	0.053±0.042**	0.045±0.043***	0.004	0.020±0.019*	0.023±0.022*
Average	0.042±0.041***	0.030±0.024**	0.004	0.016±0.016*	0.018
Minimum	0.032±0.026**	0.015	0.005	0.012	0.013

Note: Data period of record spans 1950-2015

* Slope is significantly different from zero at the 90% confidence level.

** Slope is significantly different from zero at the 95% confidence level.

*** Slope is significantly different from zero at the 99% confidence level.

March. Then in April the percentage dropped to zero, meaning that on average, all maximum daily air temperatures in this month usually rose above freezing. This value remained at zero throughout the summer months until the month of October, when the percentage started to rise. January was the month with the highest number of days on average where the air temperature did not rise above freezing, followed by December (57%) and February (43%).

Also shown in Table 15 are the extreme statistics for the percentage of days that remained below freezing. At least one February during the period of record stayed below freezing every single day. January and December exhibited similar behavior at 97% and 94%, respectively. On the other hand, there has been a February when air temperatures rose above freezing every single day of the month. January and December were the only months with some days when air temperature remained below freezing on at least some of the days in the month (19%).

On an annual basis, an average of 16% of all days had air temperatures that never rose above freezing. This occurred as much as approximately 1/3 of all days (35%) or as infrequently as 8% of the days in a year.

On the other extreme, air temperatures usually rose to or above 90 °F only in the summer and early autumn months of June, July, August, and September. On average, the air temperature rose to or above 90 °F on 44% of the days in July and 35% of the days in August and 10% or less of the days in June and September.

Extreme statistics for air temperatures rising to or above 90 °F are also shown in Table 15. The data indicate that air temperatures have risen to or exceeded 90 °F as much as 87% of the days in July and 68% in August. For the months of June and September, the highest frequency of occurrence was 43 and 23%, respectively. May also had 10% of days with 90 °F or greater.

Table 15. Monthly and annual average and normal number of days (%) when the maximum daily air temperature was at or below 32 °F and at or above 90 °F at CFA.

	Number of Days with Maximum Air Temperature ≤32 °F				Number of Days with Maximum Air Temperature ≥90 °F			
Month	Average (%)	Highest (%)	Lowest (%)	Normal (%)	Average (%)	Highest (%)	Lowest (%)	Normal (%)
January	66	97	19	67	0	0	0	0
February	43	100	0	46	0	0	0	0
March	11	61	0	9	0	0	0	0
April	0	0	0	0	0	0	0	0
May	0	0	0	0	0	10	0	0
June	0	0	0	0	10	43	0	7
July	0	0	0	0	44	87	3	45
August	0	0	0	0	35	68	3	38
September	0	0	0	0	4	23	0	5
October	1	10	0	0	0	0	0	0
November	17	73	0	20	0	0	0	0
December	57	94	19	61	0	0	0	0
ANNUAL	16	35	8	17	8	16	1	8

Note: Data period of record spans January 1950 through December 2015. Normal period of record spans January 1981 through December 2010.

There has been at least one year when air temperatures did not rise to or exceed 90 °F in either June or September, and when the percentage of occurrence in July or August was only 3%.

Annually the average percentage of days with air temperatures that rose to or above 90 °F was 8%. It has been as high as 16% and as low as 1%. This means that in the coolest summer at CFA, only 4 days exhibited maximum temperatures that equaled or exceeded 90 °F.

Table 16 is similar in format to Table 15, but highlights the average, highest, and lowest number of days per month or per year (expressed as a percentage) when the minimum air temperature was less than or equal to 32 °F, or less than or equal to 0 °F. These data show that the minimum air temperature at CFA, on average, was at or below freezing over 90% of the days during November, December, January, February, and March. Minimum air temperatures at or below freezing occurred in every month of the year except July, on average.

As expected, the extreme statistics for minimum air temperatures at or below 32 °F show occurrences of 100% of the days in 6 months of the year: November, December, January, February, March, and April. The occurrence was greater than 95% for the month of October, as well. Even July on at least one occasion has exhibited minimum air temperatures at or below freezing on 6% of the days. On the other hand, there have been days during all months of the year when the minimum air temperature did not drop below freezing.

Annually, minimum air temperatures at or below 32 °F occurred on the average 58% of the time. Freezing or colder temperatures have

Table 16. Monthly and annual average and normal number of days (%) when the minimum daily air temperature was at or below 32 °F and at or below 0 °F at CFA.

	Number of Days with Minimum Air Temperature ≤32 °F				Number of Days with Minimum Air Temperature ≤0 °F			
Month	Average (%)	Highest (%)	Lowest (%)	Normal (%)	Average (%)	Highest (%)	Lowest (%)	Normal (%)
January	99	100	94	99	38	77	0	38
February	99	100	89	99	25	86	0	26
March	95	100	81	93	6	42	0	4
April	73	100	37	68	0	0	0	0
May	30	65	3	30	0	0	0	0
June	6	17	0	5	0	0	0	0
July	0	6	0	1	0	0	0	0
August	1	16	0	1	0	0	0	0
September	25	57	0	25	0	0	0	0
October	74	97	39	73	0	3	0	0
November	94	100	73	94	7	23	0	8
December	99	100	84	99	32	68	0	34
ANNUAL	58	64	51	57	9	24	3	9

Note: Data period of record spans January 1950 through December 2015. Normal period of record spans January 1981 through December 2010.

occurred on as few as 51% of the days or as many as 64% of the days in a year.

Reviewing the occurrences of minimum air temperatures at or below 0 °F, this phenomenon occurred in the winter months of December, January, February, in the late autumn month of November, and the early spring month of March. It occurred on average approximately 1/3 of the days in December and January.

The extreme occurrences of minimum air temperatures dropping to or below 0 °F were highest (86%) in the month of February. This has also occurred with a frequency of greater than 2/3 of the time in December and January. Conversely, there have been months when the minimum air temperature did not drop to or below 0 °F. An air temperature ≤0 °F was never observed in the months of April through September.

Annually, minimum air temperatures below 0 °F occurred on the average of 9% of the days. This has been as high as 24% or as low as 3% of the days in a year. Therefore, air temperatures below 0 °F can be expected in every year.

Normalized 30-year statistics listed in Tables 15 and 16 closely followed the 66-year average.

Warm Season Duration

The dates at which the last recorded minimum air temperatures of 32, 28, and 24 °F were observed in the spring and the first occurrence of these temperatures in the fall are often required for agriculture, construction work, and biological studies. Table 17 presents these data for CFA. The number of days between the various dates are also listed. As a reminder, the air temperatures used for this analysis were measured at 5 ft. AGL inside a cotton region shelter. Therefore, the values thus recorded are not entirely representative of vegetative surfaces that are fully exposed to the environment. This means that a radiational frost could occur at ground level and not be indicated by a 32 °F or colder air temperature inside the cotton region shelter.

Using this simple definition, the average frost-free period at CFA was 87 days, with the average dates being 12 June and 07 September for the last and first frosts of the warm season, respectively. The shortest frost-free period at CFA has been 40 days in 1993. The warm season lasted only from 18 July to 27 August. The longest frost-free period was 133 days in 1957. In this case, the last frost occurred on 01 May and returned on 11 September.

The average length of time between a killing frost of 28 °F was 114 days. The average date of the last occurrence of a killing frost in the spring was 25 May and the average date of the first occurrence in the fall was 16 September. The shortest period of time between a hard freeze of 24 °F was 59 days in 1978, while the longest period of time was 173 days in 1963. The corresponding dates were 20 June and 18 August, and 25 April and 15 October, respectively.

The average length of time between a hard freeze, defined as an air temperature at or below 24 °F, was 141 days. The average date of the last occurrence of a hard frost in the spring was 11 May and the first occurrence in the fall was 28 September. The shortest period of time between hard freezes was in 1992, between 12 May and 26 August. The longest period of time between a hard freeze was 183 days, which occurred between 24 April and 24 October, 1963.

Table 17. Dates of the last minimum air temperature of 24, 28, and 32 °F in the spring, the first fall occurrence of these temperatures, and number of days between those dates for CFA.

	Last Spring Occurrence			First Fall Occurrence			Number of Days Between Last Spring & First Fall Occurrence		
Year	Min of 24 °F or below	Min of 28 °F or below	Min of 32 °F or below	Min of 32 °F or below	Min of 28 °F or below	Min of 24 °F or below	24 °F	28 °F	32 °F
1950	20 May	03 Jun	04 Jun	12 Sep	27 Sep	28 Sep	131	116	100
1951	14 May	08 Jun	10 Jun	12 Sep	12 Sep	27 Sep	136	96	94
1952	22 Apr	30 Apr	16 Jun	13 Sep	14 Sep	15 Sep	146	137	89
1953	22 May	23 May	25 Jun	05 Sep	25 Sep	03 Oct	134	125	72
1954	02 May	02 Jun	19 Jun	27 Aug	27 Aug	19 Sep	140	86	69
1955	28 May	28 May	30 Jun	22 Sep	22 Sep	22 Sep	117	117	84
1956	01 May	15 May	22 Jun	31 Aug	06 Sep	22 Sep	144	114	70
1957	27 Apr	28 Apr	01 May	11 Sep	14 Sep	22 Sep	148	139	133
1958	30 Apr	03 May	10 Jun	16 Sep	25 Sep	17 Oct	170	145	98
1959	07 May	21 May	31 May	22 Sep	22 Sep	29 Sep	145	124	114
1960	19 May	19 May	24 May	25 Aug	03 Oct	14 Oct	148	137	93
1961	03 May	08 May	13 May	03 Sep	24 Sep	02 Oct	152	139	113
1962	30 Apr	07 Jun	07 Jun	31 Aug	09 Sep	09 Sep	132	94	85
1963	24 Apr	25 Apr	30 Jun	10 Oct	15 Oct	24 Oct	183	173	102
1964	07 May	09 May	20 Jun	29 Aug	03 Sep	19 Sep	135	117	70
1965	18 May	27 May	27 May	30 Aug	04 Sep	17 Sep	122	100	95
1966	25 Jun	25 Jun	26 Jun	27 Sep	01 Oct	10 Oct	107	98	93
1967	13 May	26 May	31 May	12 Sep	13 Sep	04 Oct	144	110	104
1968	09 May	23 May	30 Jun	04-Sep	23 Sep	08 Oct	152	123	66
1969	30 Apr	30 Apr	29 Jun	31 Aug	04 Sep	03 Oct	156	127	63
1970	14 May	31 May	31 May	09 Sep	10 Sep	10 Sep	119	102	101
1971	18 May	19 May	29 Jun	15 Sep	15 Sep	18 Sep	123	119	78
1972	12 May	13 May	21 May	07 Sep	13 Sep	24 Sep	135	123	109
1973	27 May	18 Jun	02 Jul	15 Sep	17 Sep	03 Oct	129	91	75
1974	16 May	31 May	08 Jun	02 Sep	14 Sep	14 Sep	121	106	86
1975	26 May	26 May	29 May	29 Aug	29 Aug	21 Sep	118	95	92
1976	30 Apr	27 Jun	27 Jun	09-Sep	09 Sep	05 Oct	158	74	74
1977	28 May	30 May	30 May	31 Aug	09 Sep	02 Oct	127	102	93
1978	31 May	20 Jun	26 Jun	15 Aug	18 Aug	19 Sep	111	59	50
1979	08 Jun	09 Jun	15 Jun	11 Sep	12 Sep	04 Oct	118	95	88
1980	17 Apr	19 Apr	07 Jun	01 Sep	04 Sep	17 Oct	183	138	86
1981	17 Apr	14 Jun	08 Jul	03 Sep	20 Sep	26 Sep	162	98	57
1982	05 May	20 May	09 Jun	29 Sep	06 Oct	06 Oct	154	139	112
1983	14 May	16 May	22 May	06 Sep	10 Sep	20 Sep	129	117	107
1984	17 May	02-Jun	12 Jun	07 Sep	22 Sep	24 Sep	130	112	87
1985	13 May	14-May	14 May	20 Sep	20 Sep	23 Sep	133	129	129

Table 17 (Continued).

	Last Spring Occurrence			First Fall Occurrence			Number of Days Between Last Spring First Fall Occurrence		
Year	Min of 24 °F or below	Min of 28 °F or below	Min of 32 °F or below	Min of 32 °F or below	Min of 28 °F or below	Min of 24 °F or below	24 °F	28 °F	32 °F
1986	23 May	06 Jul	06 Jul	19 Sep	21 Sep	21 Sep	121	77	75
1987	20 Apr	02 Jun	02 Jun	17 Aug	17 Sep	18 Sep	151	107	76
1988	03 May	20 May	08 Jun	15 Sep	18 Sep	18 Sep	138	121	99
1989	26 May	21 Jun	21 Jun	10 Sep	13 Sep	16 Oct	143	84	81
1990	01 May	10 May	13 Jun	03 Oct	08 Oct	08 Oct	160	151	112
1991	05 May	28 May	15 Jun	15 Sep	04 Oct	04 Oct	152	129	92
1992	12 May	12 May	12 May	24 Aug	25 Aug	26 Aug	106	105	104
1993	28 Apr	09 May	18 Jul	27 Aug	31 Aug	21 Sep	146	114	40
1994	30 Apr	17 Jun	17 Jun	05 Sep	22 Sep	19 Oct	172	97	80
1995	24 Apr	24 Apr	07 Jun	19 Aug	21 Sep	21 Sep	150	150	73
1996	28 Apr	31 May	19 Jun	06 Sep	06 Sep	06 Sep	131	98	79
1997	09 May	19 May	03 Jul	17 Sep	28 Sep	11 Oct	155	132	76
1998	27 Apr	05 Jun	27 Jun	23 Sep	03 Oct	05 Oct	161	120	88
1999	09 Jun	09 Jun	26 Jun	01 Sep	08 Sep	26 Sep	109	91	67
2000	01 May	12 May	17 Jun	07 Sep	07 Sep	23 Sep	145	118	82
2001	21 May	05 Jun	14 Jun	07 Sep	10 Sep	05 Oct	137	97	85
2002	12 May	17 May	11 Jun	09 Sep	22 Sep	22 Sep	133	128	90
2003	20 May	20 May	20 May	13 Sep	13 Sep	14 Sep	117	116	116
2004	30 Apr	30 Apr	25 May	04 Sep	11 Oct	25 Oct	178	164	102
2005	16 Apr	09 Jun	19 Jun	01 Sep	14 Sep	19 Sep	156	97	74
2006	10 May	13 May	13 May	31 Aug	31 Aug	18 Sep	131	110	110
2007	04 May	24 May	24 May	10 Sep	26 Sep	11 Oct	160	125	109
2008	13 May	08 Jun	13 Jun	02 Sep	24 Sep	24 Sep	134	108	81
2009	21 May	21 May	23 Jun	08 Sep	08 Sep	02 Oct	134	110	77
2010	21 May	18 Jun	18 Jun	03 Sep	07 Sep	12 Oct	144	81	77
2011	02 May	17 Jun	17 Jun	02 Sep	10 Oct	18 Oct	169	115	77
2012	07 Jun	07 Jun	27 Jun	03 Sep	13 Sep	13 Sep	98	98	68
2013	02 May	02 May	15 Jun	19 Sep	19 Sep	01 Oct	152	140	96
2014	13 May	13 May	18 Jun	05 Sep	12 Sep	17 Oct	157	122	79
2015	28 Apr	11 May	11 May	28 Jul	06 Sep	19 Sep	144	118	78
Average	11 May	25 May	12 Jun	07 Sep	16 Sep	28 Sep	141	114	87
Longest	24 Apr	25 Apr	01 May	11 Sep	15 Oct	24 Oct	183	173	133
Shortest	12 May	20 Jun	18 Jul	27 Aug	18 Aug	26 Aug	98	59	40

Freeze/Thaw Cycles

A measure of the amount of weathering that various materials may be exposed to is the frequency at which daily freeze/thaw cycles occur. A freeze/thaw cycle in this instance is defined as a day in which the maximum air temperature exceeded 32 °F and the minimum air temperature fell to or below 32 °F. Again, the temperature values used for this purpose were measured at a height of 5 ft. AGL in a cotton region shelter. As such, the recorded air temperature may be cooler during the day and warmer at night than air temperatures at ground level. Therefore, the actual number of daily freeze/thaw cycles at ground level may potentially be greater than what was determined using this calculation procedure.

The summary of freeze/thaw cycles for CFA is contained in Table 18. The average number of daily freeze/thaw cycles was greatest in the spring and autumn months of March, April, October, and November, where the average daily frequency of occurrence was 73% or greater. That number was lower, as expected, in the late spring and early autumn months, but also in the winter months of December, January, and February. The observed decrease of freeze/thaw cycles in the winter was because maximum daily air temperatures did not climb above freezing as often as in the spring or autumn seasons. The average frequency also declined to zero in July when minimum daily air temperatures remain above freezing. It is noteworthy that on average one daily freeze/thaw cycle occurred in the month of August.

The maximum number of daily freeze/thaw cycles was at or near 100% in the months of February, March and April, and again in October and November. January and December each experienced freeze/thaw cycles a maximum average of 81% of the time. Even July had a maximum 6% occurrence of daily freeze/thaw cycles. On the other hand, December, January, and February, had as few as 6, 3, and 0% daily freeze/thaw cycles, respectively, because maximum air temperatures did not rise above freezing. Other months in which there were no daily freeze/thaw cycles were the summer months of June, July, August, and September.

Each year, on average, the frequency of occurrence of daily freeze/thaw cycles was 41%.

Table 18. Monthly and annual summary of daily freeze/thaw cycles for CFA.

Month	Average Number of Daily Cycles (%)	Maximum Number of Daily Cycles (%)	Minimum Number of Daily Cycles (%)
January	33	81	3
February	55	100	0[a]
March	83	100	39
April	73	100	37
May	30	65	3
June	5	17	0
July	0	6	0
August	1	16	0
September	26	57	0
October	74	97	39
November	77	97	27
December	41	81	6
ANNUAL	41	54	23

Note: Data period of record spans January 1950 through December 2015.

a. Air temperatures remained below freezing the entire month.

Over ½ the days in the most extremely active year had freeze/thaw cycles, but less than ¼ of the days had freeze/thaw cycles in the least active year.

Heating and Cooling Degree Days

Another unit of measure based on air temperature is the degree-day. The degree-day concept can be applied to heating or cooling and is used as a basis for establishing heating and cooling energy requirements and HVAC design considerations. A single heating degree-day (HDD) is accumulated for each degree the average air temperature is less than 65 °F in one day. Conversely, a single cooling degree-day (CDD) is accumulated for each degree the average daily air temperature is greater than 65 °F. The average daily temperature as used here is the average of the daily maximum and the daily minimum air temperature.

The monthly and annual heating degree-day summary for CFA is presented in Table 19. January had the highest average degree-day total of about 1,500 followed by December with about 1,450. July had the lowest average total of 27, followed by August with about 50. Monthly heating degree-day totals as large as approximately 1,800 in January and December have been recorded at CFA. The coldest July and August on record have each accumulated 192 heating degree-days, but the warmest of those two months showed essentially no accumulation of heating degree-days.

Table 19 also shows that the highest single heating degree-day at CFA has been 93 in December. Heating degree-days exceeding 80 have also been observed in both January and February. Heating degree-days greater than 16 have been observed in every month of the year. On the other hand, there have been days in

Table 19. Total monthly and annual average, extreme, and normal heating degree days (HDD) and daily extremes for CFA.

					Daily Extremes	
Month	Average (HDD)	Highest (HDD)	Lowest (HDD)	Normal (HDD)	Highest (HDD)	Lowest (HDD)
January	1,505	1,799	1,086	1,503	85	22
February	1,223	1,623	865	1,235	88	20
March	1,027	1,446	728	989	71	10
April	687	889	471	669	44	2
May	419	623	206	417	35	0
June	179	305	44	176	26	0
July	27	192	0	32	16	0
August	48	192	0	45	20	0
September	271	493	100	267	36	0
October	653	832	433	667	55	0
November	1,062	1,342	860	1,075	74	8
December	1,443	1,799	1,181	1,483	93	18
ANNUAL	8,544	10,268	7,524	8,557	93	0

Note: Data period of record spans January 1950 through December 2015. Normal period of record spans January 1981 through December 2010.

December, January, and February when the HDD total was 22 or less.

The average annual total HDD was approximately 8,550. However, total annual heating degree-days as low as approximately 7,500 and as high as approximately 10,250 have been recorded.

A similar table of total monthly and annual cooling degree-days at CFA is presented in Table 20. Cooling degree-days are usually not accumulated except during the months of June, July, and August. Cooling degree-day accumulations averaged 32, 138, and 93 in those months, respectively. A small accumulation of cooling degree-days has been observed on average in both May and September. The highest accumulation of cooling degree-days was observed in July at 332, with both June and August exceeding 135 while May and September exceeded 25. Conversely, there has been at least one occurrence in which the accumulation of cooling degree-days in May and September has been zero. The CDD in July, the month with the highest average CDD, has been as low as 8.

The daily extremes of cooling degree-days given in Table 20 yield further information on the cooling equipment design capacity requirements. The largest single cooling degree-day observed has been 18. This value has been recorded in the three summer months of June, July, and August. No cooling degree-days have ever been recorded from January through April or from November and December. There have also been days during each of the summer months in which no cooling degree-days were accumulated.

On average, an annual total of 272 cooling degree-days accumulated at CFA. The annual cooling degree-day total was as high as approximately 538 and as low as 35.

Table 20. Total monthly and annual average, extreme, and normal cooling degree days (CDD) and daily extremes for CFA.

					Daily	Extremes
Month	Average (CDD)	Highest (CDD)	Lowest (CDD)	Normal (CDD)	Highest (CDD)	Lowest (CDD)
January	0	0	0	0	0	0
February	0	0	0	0	0	0
March	0	0	0	0	0	0
April	0	0	0	0	0	0
May	2	26	0	2	11	0
June	32	137	3	30	18	0
July	138	332	8	141	18	0
August	93	194	23	100	18	0
September	8	41	0	9	9	0
October	0	0	0	9	2	0
November	0	0	0	0	0	0
December	0	0	0	0	0	0
ANNUAL	272	538	35	283	18	0

Note: Data period of record spans January 1950 through December 2015. Normal period of record spans January 1981 through December 2010.

Thirty-year monthly and annual heating and cooling degree days were similar to the 66-year averages.

Wind Chill and Heat Index

Two environmental indices of human comfort are the wind chill and the heat index. These indices require paired measurements of air temperature together with two additional atmospheric variables. Therefore, the focus of the discussion leaves the CFA Thermoscreen database and turns to the Mesonet database where the needed additional variables of wind speed and humidity were simultaneously recorded.

A unit of measure that describes the amount of cold a human perceives in the air is called wind chill. Wind chill is a measure of how the air temperature feels when wind speed is combined with air temperature (Osczevski and Bluestein, 2005). Wind chill is calculated when the air temperature is at or below about 50 °F and the wind speed is greater than 3 mph. Outside of these specifications, the wind chill is simply equal to air temperature. According to the formula, the higher the wind speed, the lower the resulting wind chill temperature and thus the faster one could suffer the effects of exposure. For example, frostbite of exposed skin occurs in just 30 minutes when wind chill temperatures dip to -20 °F.

There were an average of 13 days per year at CFA in which the wind chill temperature dropped below -20 °F during the 22-year period of record from January 1994 through December 2015. Wind chill temperatures were usually the lowest during December, January, and February. The lowest recorded wind chill temperature at CFA was -50 °F and occurred on February 2, 1996. It is possible for frostbite of exposed skin to occur in as little as 5 to 10 minutes at a wind chill of -50 °F. Therefore, wind chill can be an important personnel safety issue at the INL.

A unit of measure that describes the amount of heat a human perceives in the air is called the heat index. Heat index is a measure of how the air temperature feels when relative humidity is accounted for along with air temperature. The heat index is calculated when relative humidity and air temperature rise above 40% and 80 °F, respectively (Steadman; 1979a, 1979b). Due to the relatively dry climate across the ESRP there were on average less than two days a year in which the relative humidity and air temperature were both at or above the threshold values of 40% and 80 °F.

A heat index value can also be calculated when the relative humidity is below 40% and the air temperature is above 80 °F. The resulting heat index is at or slightly below ambient air temperature, but this value is nevertheless useful in determining the potential for human heat stress. A heat index in the range of 80-89 °F was observed on average about 80 days annually for the 22-year period of record from January 1994 through December 2015. A heat index in the range of 90 to 104 °F was observed on about 30 days annually. These two heat index ranges correspond to rating categories named Caution and Extreme Caution, respectively. Prolonged exposure and/or physical activity in the Caution category can result in fatigue. In the Extreme Caution category, prolonged exposure and/or physical activity can result in sunstroke, heat cramps, and heat exhaustion. Therefore, heat stress can also be an important personnel safety issue at the INL.

Upper Air Temperatures

The vertical variation of air temperature above the ground surface is important for evaluating dispersion characteristics of the atmosphere. Vertical air temperature profiles indicate the thermal stability of the atmosphere and are widely used as indicators of turbulence levels and subsequently the dispersive capability of the lower atmosphere. These data are needed to properly evaluate potential reactor sites as well as for determining the location, height, and design of chimneys and monitoring stations.

Historical studies based on air temperatures recorded by sensors attached to periodically released balloons and air temperatures obtained from sensors attached to tall towers that were recorded on strip charts originally provided valuable atmospheric stability climatological data. Those studies are being greatly enhanced here with data from continuously monitored sensors on tall towers in the NOAA/INL Mesonet and also from remotely-measured virtual air temperature profiles obtained from the RASS at Grid 3.

Profile Characteristics to 250 ft. AGL

The three Mesonet tall towers at the INL provided the basis on which a detailed study of the air temperature structure from the surface up to 250 ft. AGL was undertaken. The tall towers are at GRI, MFC, and SMC. Using the air temperature data from the 6 ft. level and the top of these towers, air temperature stability categories were calculated as a function of season. The following definitions were used to classify air temperature profiles into two main air temperature stability categories as follows:

1. Inversion (or inverted profile), defined as air temperature warming with increasing altitude.
2. Lapse, defined as air temperature cooling with increasing altitude.

The two main categories were further classified into week and strong subdivisions. A weak inversion was defined as an air temperature difference of 0.0 to 4.0 °F. A strong inversion was defined as an air temperature difference greater than 4 °F. A weak lapse was defined as an air temperature difference of 0.0 to -1.0 °F, while a strong lapse was defined as an air temperature difference of less than -1.0 °F. The data for the GRI tower are presented in Table 21. Data from the other two towers were similar.

Strong lapse rates were frequently observed during the spring (March, April, and May) and summer (June, July, and August) months, with a frequency of occurrence of nearly 50% of the time. Weak lapse rates occurred 10% or less of the time in those two seasons. The next most frequently occurring condition during the spring and summer seasons were strong inversions at 23 and 34% of the time, respectively. Strong lapse conditions were less prevalent during the autumn (September, October and November) and winter (December, January, and February) seasons than

Table 21. Seasonal and annual distribution (% of time) of air temperature stability classes for GRI[a].

Season	Strong Lapse[b] <-1.0 °F (%)	Weak Lapse[b] -1.0 to 0.0 °F (%)	Weak Inversion[b] 0.0 to 4.0 °F (%)	Strong Inversion[b] >4.0 °F (%)
Winter	23.8	16.7	26.4	33.1
Spring	47.7	9.8	19.3	23.2
Summer	47.4	4.8	13.8	34.1
Autumn	30.6	12.7	21.1	35.6
ANNUAL	37.5	11.0	20.1	31.5

a. Data period of record spans January 1994 through December 2015.

b. Air temperature measurement heights: 6 and 200 ft. AGL.

during the spring and summer months. Strong inversions occurred more than 1/3 of the time during the summer, autumn and winter months.

Annually, strong lapse was the most prevalent condition (37%) followed by strong inversion (32%) followed by weak inversion (20%), with weak lapse the least frequent condition at 11%. Thus, annual lapse and inversion conditions occurred in nearly equal amounts (48 vs. 52%). However, the strong lapse and strong inversions were the most frequent compared with the weak categories, having occurred 69% to 31% of the time.

A summary of the diurnal shift from a daytime air temperature lapse condition to a nighttime air temperature inversion was first derived from eight years of record at CFA by Johnson and Dickson (1962). An update to that study was conducted using 22 years of data from GRI. The data were compiled as the air temperature difference between 6 and 200 ft. AGL. No attempt was made to eliminate from the data set the cases in which the formation or dissipation of the inversion was obviously controlled by factors other than incoming solar or outgoing terrestrial radiation, which was the procedure used by Johnson and Dickson. The results of the new study are presented in Table 22.

The time of the nocturnal inversion formation depends on the sunset times (as a function of season) and is readily apparent in the data. The onset of the nocturnal inversion began as early as 1651 hours MST in the winter and as late as 1930 hours MST in the summer. There also appeared to be a seasonal dependance on the average beginning time of the nocturnal inversion before sunset for the last half of the year. In May, June, and July, the nocturnal inversion formed approximately 43-48 minutes before sunset. The time declined to a low of 11 minutes before sunset in December. In January, the time started to climb, but did not progress linearly. Further investigation is needed to understand the comparatively large length of time in February and the smaller length of time in April. The longest times before sunset for formation of the nocturnal inversion were 48 minutes in February and June.

The time of the demise of the nocturnal inversion was also seasonally dependant. The inversion dissipated as early as 0612 hours MST in June, and as late as 0939 in January, on average. The length of time after sunrise before the break-up of the inversion occurred was somewhat seasonally dependent, as well. In January and February, the longest times were observed, when the inversion dissipated about 1 hour 35 minutes after sunrise. The shortest time was in April at 47 minutes, while in every other month the length of time was over 1 hour.

The annual average time of the onset of the nocturnal inversion was about 30 minutes before sunset. Also on an annual basis, the nocturnal inversion did not dissipate for about 67 minutes after sunrise.

The average number of hours per day when the nocturnal inversion was present showed a seasonal dependence and ranged from a high of 14.9 hours in January to a low of 10.0 hours in May and June. The annual average number of hours per day for an inversion was 12.4.

The maximum number of hours per day for the occurrence of an inversion was also seasonally dependent. In the months of November, December, January, February, and March, inversions have been observed to last all day. The longest duration of an inversion in the summer months was approximately 15 hours.

The average number of days without an inversion was very small. At a maximum it was 0.1 days per month in February, March, May and December. On an annual basis, the occurrence of days without an inversion were also very small,

Table 22. Average onset and dissipation times of inversion and lapse air temperature profiles together with intensity values for GRI[a].

	Inversion Formation		Inversion Demise		Inversion Characteristics					Lapse Characteristics	
Month	Average Time of Onset (MST)	Average Deviation Before Sunset (Minutes)	Average Time of Dissipation (MST)	Average Deviation After Sunrise (Minutes)	Average Number of Hours Per Day	Maximum Number of Hours Per Day	Average Number of Days Without Inversion	Maximum Intensity[b] (°F)	Longest Period of Duration (Hours)	Maximum Intensity[b] (°F)	Longest Period of Duration (Hours)
January	1707	21	0939	95	14.9	24.0	0.0	32.2	66.1	5.1	36.3
February	1717	48	0909	94	14.3	24.0	0.1	29.4	45.3	6.2	80.4
March	1815	27	0751	63	12.4	24.0	0.1	25.0	34.1	6.9	45.3
April	1904	15	0641	47	10.3	16.4	0.0	25.1	15.2	7.0	41.0
May	1911	43	0616	64	10.0	14.8	0.1	26.2	14.2	7.7	58.8
June	1930	48	0612	77	10.0	14.8	0.0	29.0	13.8	7.8	42.3
July	1927	46	0630	81	10.8	14.8	0.0	27.6	15.3	8.2	21.8
August	1859	39	0657	76	11.7	15.5	0.0	29.6	15.3	7.6	19.8
September	1818	28	0723	68	12.5	18.5	0.0	28.4	15.1	7.0	35.3
October	1734	19	0756	65	13.4	17.1	0.0	26.3	17.1	6.1	42.6
November	1654	19	0829	60	14.0	24.0	0.0	31.1	19.3	5.1	43.8
December	1651	11	0909	68	14.0	24.0	0.1	30.4	104.3	5.5	62.8
ANNUAL	-----	30	-----	67	12.4	24.0	>0.1	32.2	104.3	8.2	80.4

a. Data period of record spans January 1994 through December 2015.

b. Air temperature difference between 6 and 200 ft. AGL.

just slightly greater than 0.1 days per year. Therefore, a nocturnal inversion can be expected to form on almost every day of the year.

As can be seen, inversion intensities can be very large. The maximum inversion intensity ranged from a low of 25.0 °F in March to a high of 32.2 °F in January.

Inversions lasting as long as 104.3 hours have been observed during the period of record. The month of December holds that record. Other inversions of notable length were observed in January, February, and March with durations of 66.1, 45.3, and 34.1 hours, respectively.

The analysis of lapse conditions indicated that maximum intensities were not as strong as for inversions, with maximums ranging from 5.1 °F in January and November, to a high of 8.2 °F in July.

Continuous lapse conditions have lasted for longer than 80 hours in one particular case (February). Every month except for July and August has had periods of lapse conditions which lasted longer than 24 hours. This is probably a feature of strong synoptically driven winds that persisted through the night, which continued the mixing of surface winds and prevented inversion development.

Profile Characteristics Above 250 ft. AGL

Air temperature profiles from the RASS comprise the most recent air temperature data for the region above 250 ft. AGL. Virtual air temperatures aloft have been measured using a RASS that is collocated with the radar wind profiler at Grid 3 (Fig. 9). The RASS signal reaches through approximately one-third the depth of the wind profiler. The RASS also samples vertical range gates of about 300 ft. in size from 525 to 5, 380 ft. AGL. The data are in 30-minute time periods, although the RASS operates for only 5 minutes during each ½-hour cycle. The other 25 minutes of the 30-minute cycle is devoted to the collection of wind data. At least 50% or better data capture has been obtained up to approximately 3,000 ft. AGL (Fig. 57). Above 4,000 ft. AGL, the data availability was generally less than 25%. The RASS also tends to reach higher in the cold season compared to the warm season thus getting more weight in the annual averaging.

It should be noted that virtual air temperature measured by the RASS is not the same as the air temperature measured by a temperature sensor from the NOAA/INL Mesonet. An air temperature measured by the Mesonet is called the dry bulb temperature. However, the difference between virtual air temperature and dry bulb temperature is small and usually less than 1 °F making the difference small enough to be ignored for the purposes of this discussion.

A contour plot of the mean annual virtual air temperature derived from the RASS over the 22-year period of record from March 1994 through December 2015 is provided in Fig. 58. Several diurnal characteristics can be observed in the graph. Isothermal conditions exist from 525 ft. up through about 5,000 ft. AGL, on average, from about 0600 through 0900 MST. This results from the heating of the earth's surface from solar radiation after sunrise. From 0930 through about 1700 MST, the air temperature gradient strengthens as the heating of the earth's surface continues through increased solar radiance. The plot also shows colder air mixing down during this time but this is likely due to a sampling artifact that relates back to the restricted data availability in the summer season. Nonetheless, lapse conditions prevail during this period. With decreased solar radiance in the late afternoon, beginning around 1730 MST, the earth's surface begins to cool and the air temperature gradient relaxes until about

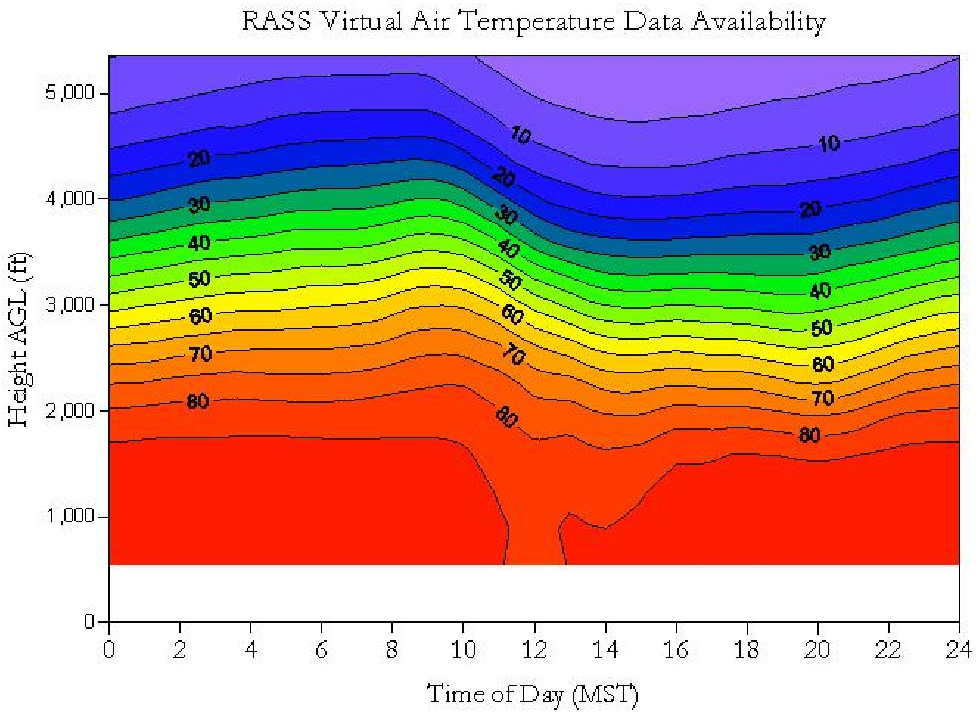

Figure 57. RASS data availability (%) as a function of time and height.

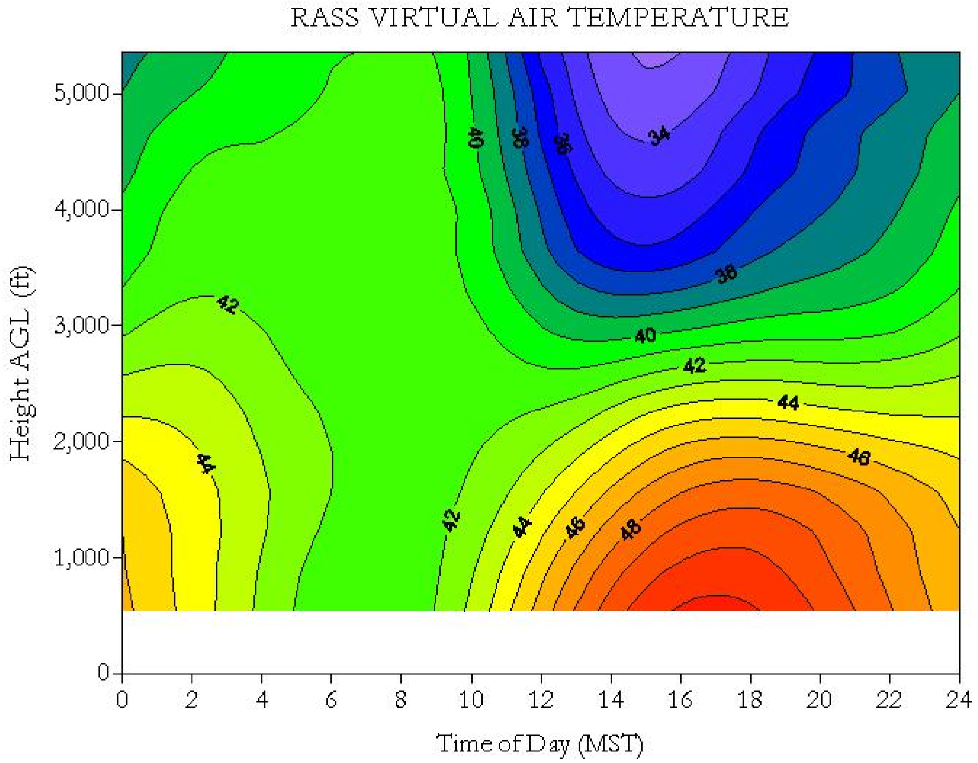

Figure 58. RASS virtual temperature (°F) as a function of time and height.

0300 MST. Between 0300 and 0600 MST an air temperature inversion developed up to a depth of about 2,000 ft. AGL.

The seasonal dependence on average diurnal vertical air temperatures is illustrated in Figs. 59-62 for winter, spring, summer, and autumn, respectively. Average vertical profiles are plotted for every three hours of the day beginning at midnight to represent the diurnal trend. The dry adiabatic lapse rate is also plotted for reference purposes. Air temperatures are plotted only up to 4,000 ft. AGL. Above this region, data availability was less than 25%, which makes data interpretation somewhat unreliable.

At first glance, the winter air temperature profiles appeared to be mostly isothermal, or in other words, constant with height. However on closer inspection, there was evidence of some diurnal heating and cooling that occurred in the lower levels of the sensing volume. Air temperatures at the lowest sensing level of 525 ft. AGL were, on average as cold as 22.8 °F at 0900 MST, and as warm as 27.3 °F at 1600 MST. This air temperature range is obviously small and was less than 5 °F. The shape of the profile also changed diurnally. Inversion conditions were observed between the hours of 0100 and 1130 MST. The inversion was strongest and deepest at 0700 MST when the temperature difference was 1.8 °F between 525 and 3642 ft. AGL. Lapse conditions were marginally observed between the hours of 1330 and 1900 MST. The strongest lapse condition was measured at 1500 MST when the lapse rate was 1.0 °F/1,000 ft. between 525 and 2264 ft. AGL. At other times of the day, between 1130 to 1330 MST and again from 1900 to 0100 MST, the profile was essentially isothermal.

The summer months of June, July, and August, were a stark contrast to the winter season described previously. A strong daily cycle can be seen in the data due to strong surface heating by the sun during the day with a concurrent heating of the lower portion of the atmosphere. Inverted air temperature profiles were observed in the 0200 through 0800 MST profiles, which are represented by the 0300 and 0600 MST profiles in Fig. 61. The inversion strengthened during this time period to a maximum of 1.1 °F between 500 and 1,500 ft. AGL. The time of the maximum inversion was 0700 MST. This was also the time of the coldest temperature (60.8 °F) at the lowest measurement height of 525 ft. The nocturnal inversion completely dissipated by 0830 MST and is represented by the 0900 MST trace. After this time, the air temperature in the lower portions of the measuring volume continued to warm and reached a maximum of 77.2 °F at 525 ft. AGL at approximately 1700 MST. The temperature profiles at 1500, 1800, and 2100 MST showed superadiabatic (very unstable conditions) but, again, this is likely suspect due to poor recovery rates at higher levels reported earlier. This could be warping the profiles. By midnight the profile again exhibited stable conditions and the entire profile exhibited lapse conditions.

The spring (March, April and May) and autumn (September, October, and November) season air temperature profiles were more like the summer season than the winter season. Distinct diurnal trends were readily apparent in both seasons. Both seasons exhibited the daily swing from inverted air temperature profiles at night to lapse conditions during the day. The timing of the nocturnal inversion dissipation was different in the spring compared with autumn. In the spring, the nocturnal inversion dissipated by 0800 MST. In autumn, it dissipated by 1000 MST. The initial formation and depth of the nocturnal inversion was also different for the two seasons. In the spring season, the inversion began at about 0100 MST but only in the lowest 340 ft. of the sensing volume and persisted at that level until about 0530 MST when the

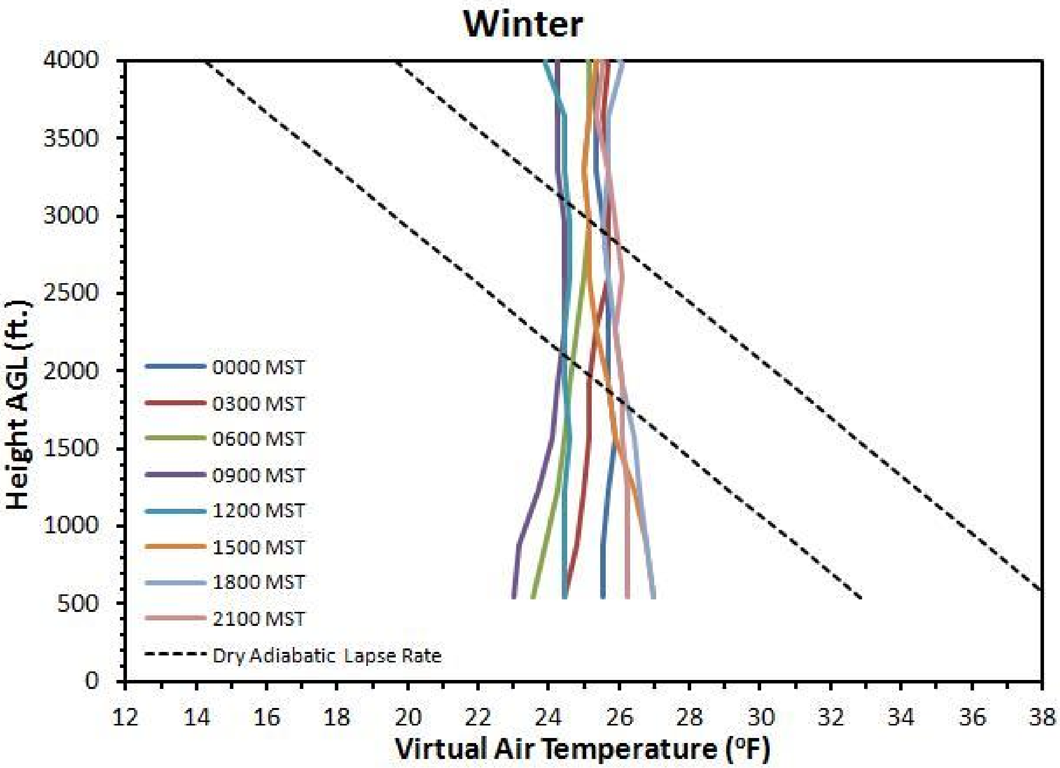

Figure 59. Winter season diurnal RASS virtual air temperature profiles.

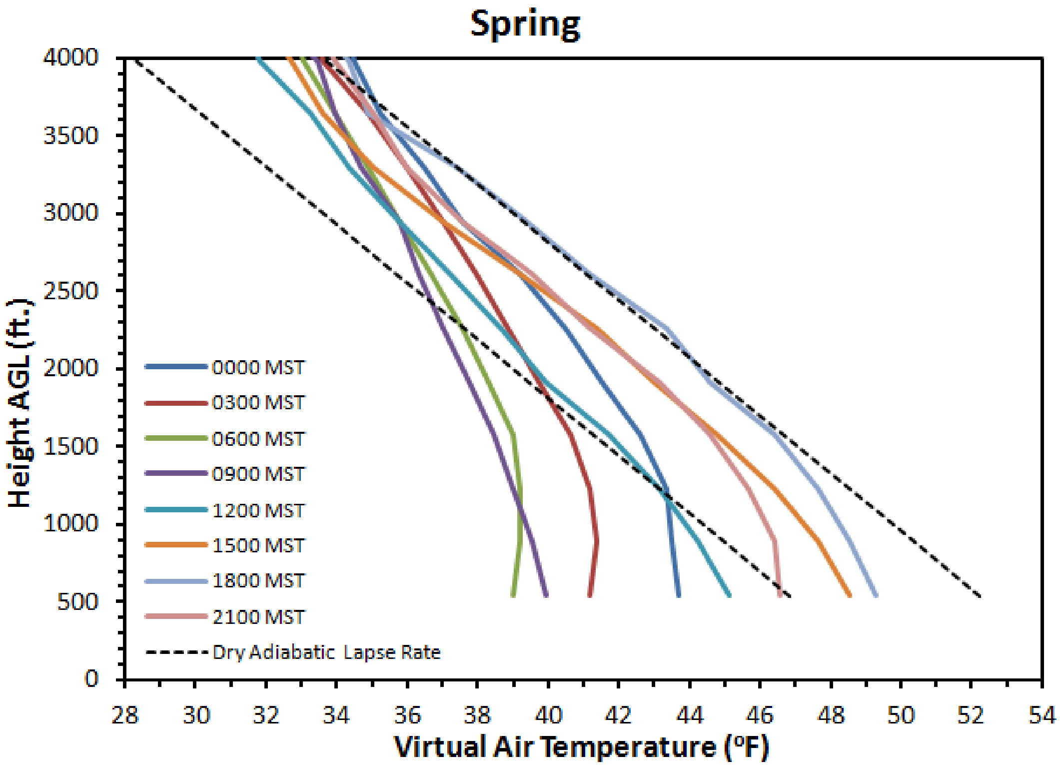

Figure 60. Spring seasonal diurnal RASS virtual air temperature profiles.

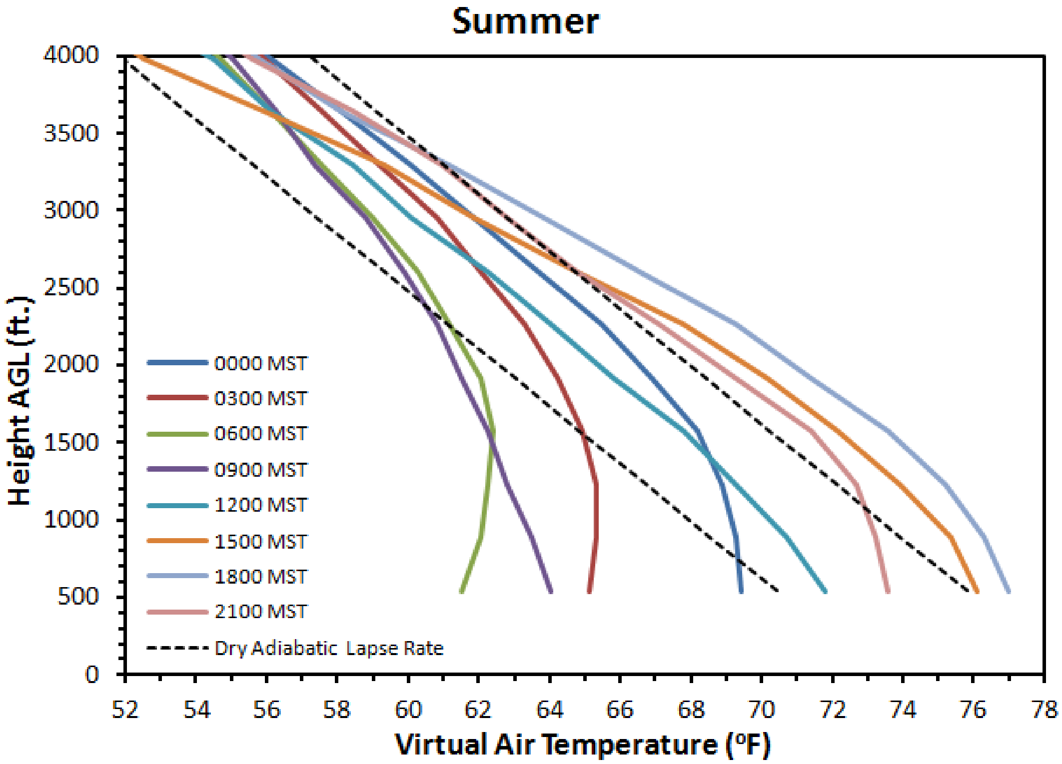

Figure 61. Summer season diurnal RASS virtual air temperature profiles.

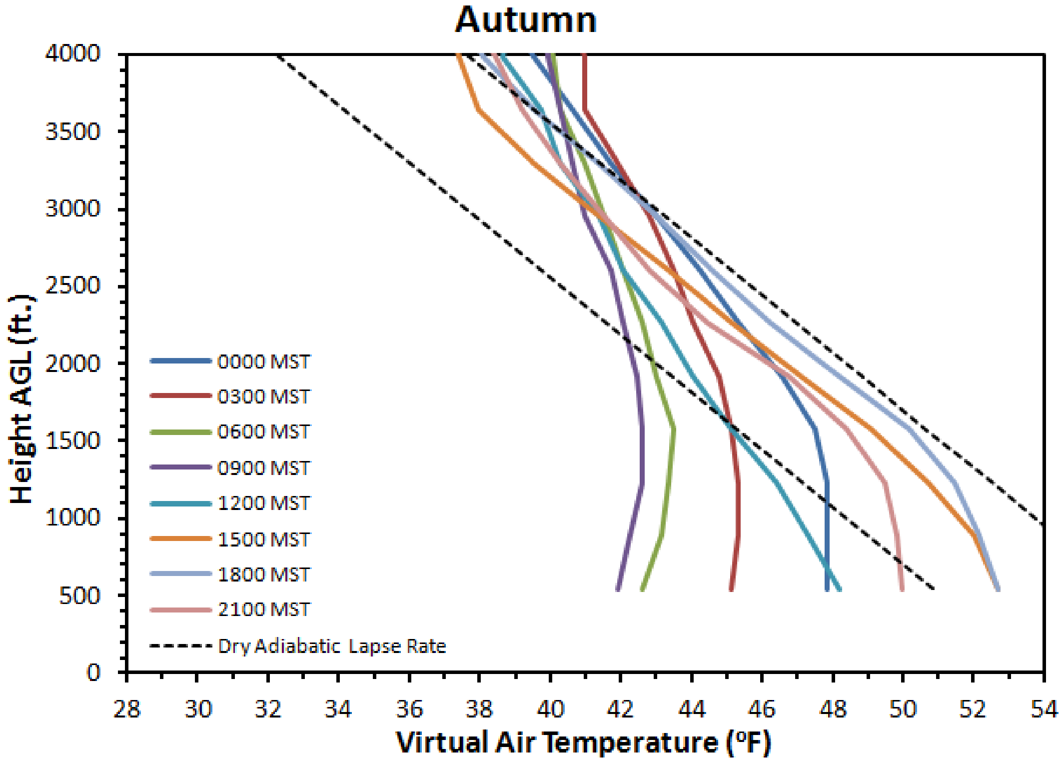

Figure 62. Autumn seasonal diurnal RASS virtual air temperature prfiles.

inversion strengthened into higher levels. In the fall, the nocturnal inversion began to develop as early at 2330 MST and did not remain as shallow. The strongest inversion in the spring occurred at 0700 MST with a maximum difference of 0.2 °F between about 500 and 1,000 ft. AGL. The strongest inversion in the fall occurred at 0800 MST with a maximum air temperature difference of 0.9 °F between about 500 and 1,500 ft. AGL. The range in diurnal air temperature was similar at the 525-ft. level in both the spring and fall seasons at 11.7 and 12.0 °F, respectively. The atmosphere at 4,000 ft. was colder in the springtime and averaged 33.5 °F. In the fall, the air temperature at the same level averaged 39.0 °F. Maximum daytime lapse rates were similar in both the spring and autumn seasons at about 6.0 °F/1,000 ft. and occurred at 1630 MST. However, in the fall the altitude was lower and the altitude range was smaller over which the maximum daytime lapse rates were observed. For the spring season, the maximum lapse rates were observed between 2,000 to 4,000 ft. AGL, whereas for the fall season the range was 1,500 to 3,000 ft. AGL. Thus, daytime lapse conditions in the spring season remained constant over a greater altitude range than was indicated in the autumn profiles.

PRECIPITATION

Daily precipitation has been recorded at the CFA Thermoscreen site since 1950. It has also been recorded at various other locations for various periods of time. For the purposes of this report, the daily CFA Thermoscreen rain guage and associated snow depth and snowfall data will be the primary focus of analyses. However, the Mesonet rain gauge that reports in five-minute intervals and which is also located at CFA, will also be discussed. These two sources of information have different periods of record. For the Thermoscreen data, the period of record is from 1950 to 2015, while the Mesonet data period of record is from 1994 through 2015.

General Characteristics

The type of precipitation that occurs at the INL is dependent on the season of the year. In the summer, precipitation most often falls as rain showers or thunderstorms. In the spring and autumn, rain showers or periods of rain and snow may occur. Most precipitation in the winter comes as snow. Precipitation can occur in any month, but the heaviest accumulations are generally in the spring or early summer. The most intense precipitation periods are associated with thundershowers. Total annual average precipitation is 8.38 in., which gives the INL the designation of an arid climate.

Daily Characteristics

Daily characteristics of precipitation are not as easily determined as air temperature characteristics because of the relatively light and discontinuous nature of precipitation. A graph of average daily precipitation as a function of time shows a large amount of noise in the signal. Therefore, a technique is used to smooth the signal in order to more readily analyze the daily characteristics. First, a graph of average daily accumulated precipitation as a function of time is plotted to render the interpretation much easier. Distinct periods of precipitation are then determined by sight and then linear regression techniques are applied to each of these distinct periods to obtain an average daily precipitation value as a function of time. The slope of the line is the average daily precipitation.

A graph showing accumulated daily precipitation as a function of time for the CFA Thermoscreen rain gauge for the 66-year period of record ending in December 2015 is presented in Fig. 63. Five distinct precipitation periods were determined based on the slope of the curve over time. These time periods are summarized in Table 23 together with a summary of the slope of the line and the correlation coefficient (R) of the linear regression.

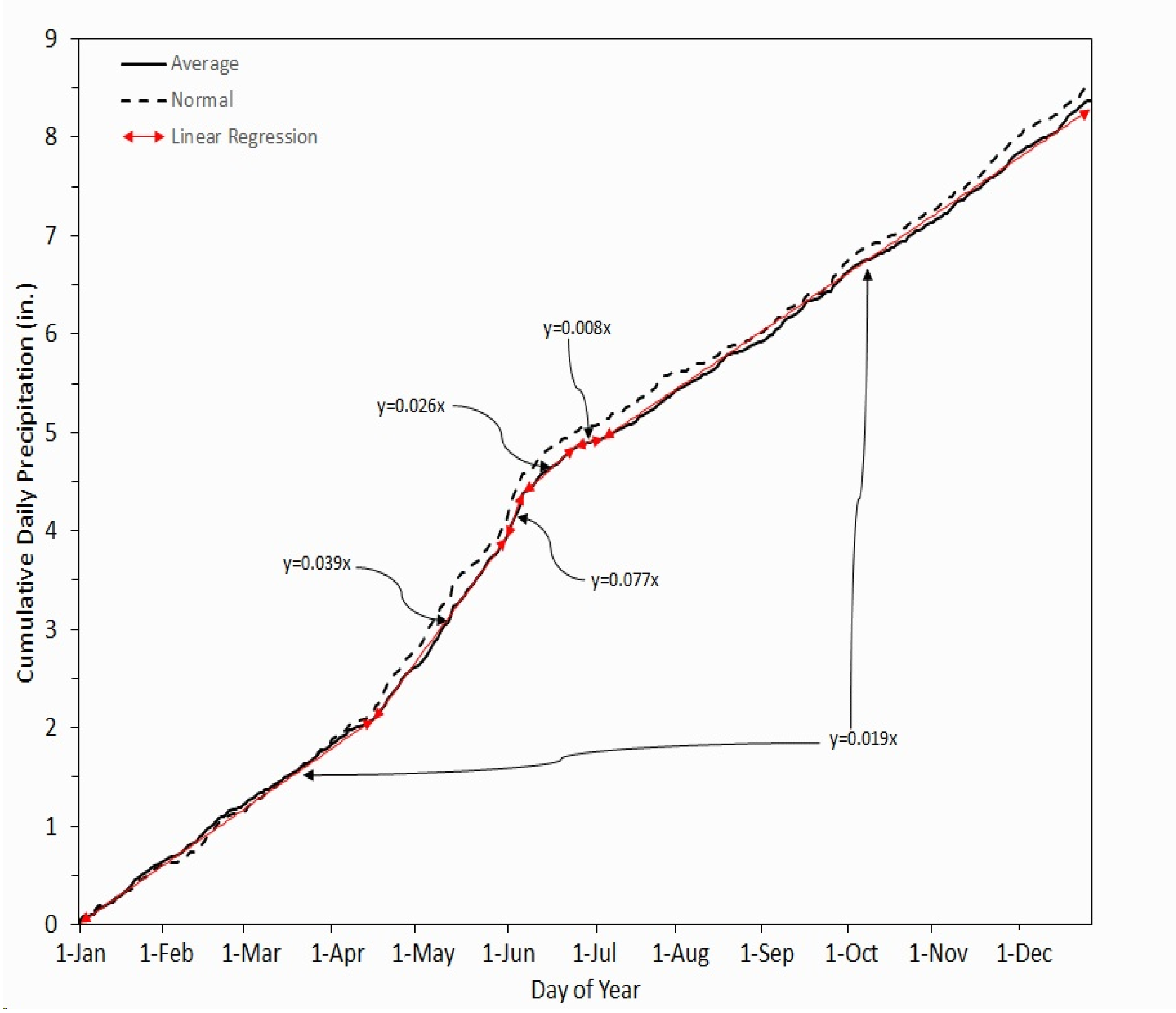

Figure 63. Average and normal daily cumulative precipitation for the CFA Thermoscreen. Linear regression segments are for average daily cumulative precipitation.

Table 23. Segmented linear regression statistics for average daily cumulative precipitation for CFA[a].

Time Period	Slope (in. day^{-1})	Correlation Coefficient (R)
July 10-April 18	0.02	0.999
April 18-June 4	0.04	0.997
June 4-June 10	0.08	0.989
June 10-June 29	0.03	0.993
June 29-July 9	0.01	0.983

a. Data period of record spans March 1950 through December 2015.

The largest period of time with near-constant average daily precipitation extends for a time period of over 9 months, from July 10 through April 18. The slope of the line indicates that the average daily precipitation is approximately 0.02 in. during this time period. The correlation coefficient for the linear regression is very high and exceeds 0.999.

A period of higher daily average precipitation occurs between April 18 and June 29. There are three distinct slope changes within this time period. Between April 18 and June 4, which is a period of about 47 days, the average daily precipitation doubles from that of the 9 month period described above to 0.04 in. The correlation coefficient for the linear regression was approximately 0.997, again indicating excellent agreement. Then, for a period of about 7 days, the slope increases to about 0.08 in. per day, between June 4 and June 10. This is a quadrupling of the average daily precipitation as compared to the previously described 9 month average. The correlation coefficient for the linear regression is 0.989. For a 19-day period after that, the average daily precipitation drops to 0.03 in., between June 10 and June 29. The correlation coefficient is about 0.993.

According to Trewartha (1961) the position of the Pacific anticyclone at 34 degrees North latitude during May and June results in a low pressure at the surface and an upper trough at 500 mb over the interior of the states of Washington and Oregon which results in a flow of maritime southwesterly flow from the Pacific Ocean. The result is the observed short wet season in early summer at the INL.

A curious feature of the curve is the dearth of precipitation for about a 10-day period surrounding Independence Day between June 29 and July 9. During this time period, average daily precipitation drops to 0.01 in. The R value of the regression is approximately 0.983. Trewartha (1961) again explained this phenomenon. In early July, the Pacific high suddenly shifts northward to 40 degrees North latitude with an accompanying shift in the precipitation pattern. For the INL, the result is very little precipitation.

The normal (1981-2010) daily accumulated precipitation curve, obtained from the NCDC (2011) is also shown in Fig. 63. Its pattern is similar to the 66-year average curve, with some minor differences. These differences can be mostly attributed to an oscillation between 0.02 and 0.03 in. of precipitation per day, which causes a snaking effect in the cumulative curve. A notable difference between the average and normal curve is the dip in the steady normal daily precipitation increase as compared to the average daily precipitation increase during the 40-day period between August 23 and October 2. The average curve does not show a concomitant dip and therefore, the dip in the normal curve lacks evidence in the average curve. Hence, an explanation for the difference will not be explored.

A list of greatest daily precipitation totals (midnight to midnight) from CFA are given in Table 24. During the 66-year period of record, there were only 13 days when the daily total precipitation equaled or exceeded 1 in. The greatest daily precipitation value during the period of record was 1.64 in., which occurred on June 10, 1969. In fact, there were three occasions on June 10 when the precipitation exceeded 1 in. In total, there were 4 June days, 3 September days, 2 April and October days, and 1 day each in July, and December when the daily precipitation total exceeded 1 in. Overall, 36 days have exceeded 0.78 in. of precipitation.

On average, daily precipitation totals of 1 in. or greater have occurred once every five years. The longest period of time between days of 1 in. or more of precipitation was between June 1995 and October 2009, which was more than 14 years and 4 months. The next longest time period was 13 years and 5 months from April 1981 to September 1994. The shortest period of time was 9 days, between 09 and 18 September, 1961.

The next shortest period of time was 182 days between October 2009 and April 2010.

Monthly and Annual Characteristics

Monthly and annual average precipitation totals for CFA are presented in Table 25 for the 66-year period of record. A pronounced precipitation peak occurred in May and June, as

Table 24. Greatest daily precipitation totals from the CFA Thermoscreen.

Amount (in.)	Date
1.64	10 Jun 1969
1.55	18 Sep 1961
1.55	05 Jun 1995
1.51	20 Apr 1981
1.36	10 Jun 1954
1.25	23 Jul 1979
1.15	06 Oct 2011
1.14	10 Jun 1963
1.10	04 Apr 2010
1.10	30 Sep 1994
1.09	09 Sep 1961
1.07	22 Dec 1964
1.04	04 Oct 2009
0.96	02 Jan 2006
0.95	16 May 1987
0.93	27 Sep 1989
0.89	04 Mar 1991
0.88	27 Apr 1963
0.85	29 May 1971
0.84	13 Jun 1967
0.84	09 Jun 2006
0.83	21 July 1987
0.82	01 May 1959
0.82	12 Sep 1976
0.82	05 Jun 1993
0.81	09 Jun 1984
0.81	16 Apr 2006
0.80	22 Aug 1960
0.80	16 May 1996
0.79	01 Jul 1987
0.79	18 Feb 1986
0.79	25 Jun 1965
0.79	19 Jan 1969
0.78	06 Jun 1993
0.78	06 Jun 2007
0.78	27 Jul 1984

Note: Data period of record spans March 1950 through December 2015.

was expected from the analysis of daily precipitation discussed earlier. The average for each of these two months was approximately 1.2 in. The greatest monthly precipitation total measured at CFA was 4.64 in. during June 1995. The next highest monthly precipitation total (4.42 in.) occurred in May followed by a total of 4.05 in. during August, which were both greater than 4 in. Months in which precipitation has totaled more than 3 in. include September and December, with 3.52 and 3.43 in., respectively.

There have been instances of no measurable precipitation recorded at CFA (traces excluded) for every month of the year except May. However, the total precipitation in that month was barely measurable at 0.02 in. The average annual precipitation at CFA is 8.38 in. but has been as high as 14.40 in. (1963) and as low as 3.04 in. (2013). Figure 64 shows the average annual total precipitation from the CFA Thermoscreen data for the entire 66-year period of record from 1950-2015. A linear regression was conducted on the annual average dataset. The data showed significant scatter with a slight downward trend and slope of -0.005" per year.

Monthly and annual normal precipitation totals for CFA are also listed in Table 25 for the 30-year period of January 1981 through December 2010 (NCDC 2011). The monthly distribution pattern is similar to that of the average pattern. However, there were appreciable differences noted in several months. The normal precipitation totals that differed by more that 10% from the average precipitation totals were observed for April, July, and August. The differences were 21, 26, and -54%, respectively. The annual normal precipitation total was more than the average precipitation total, but only by about 3%, an insignificant difference.

Table 26 lists the monthly and annual average number of days (from midnight to

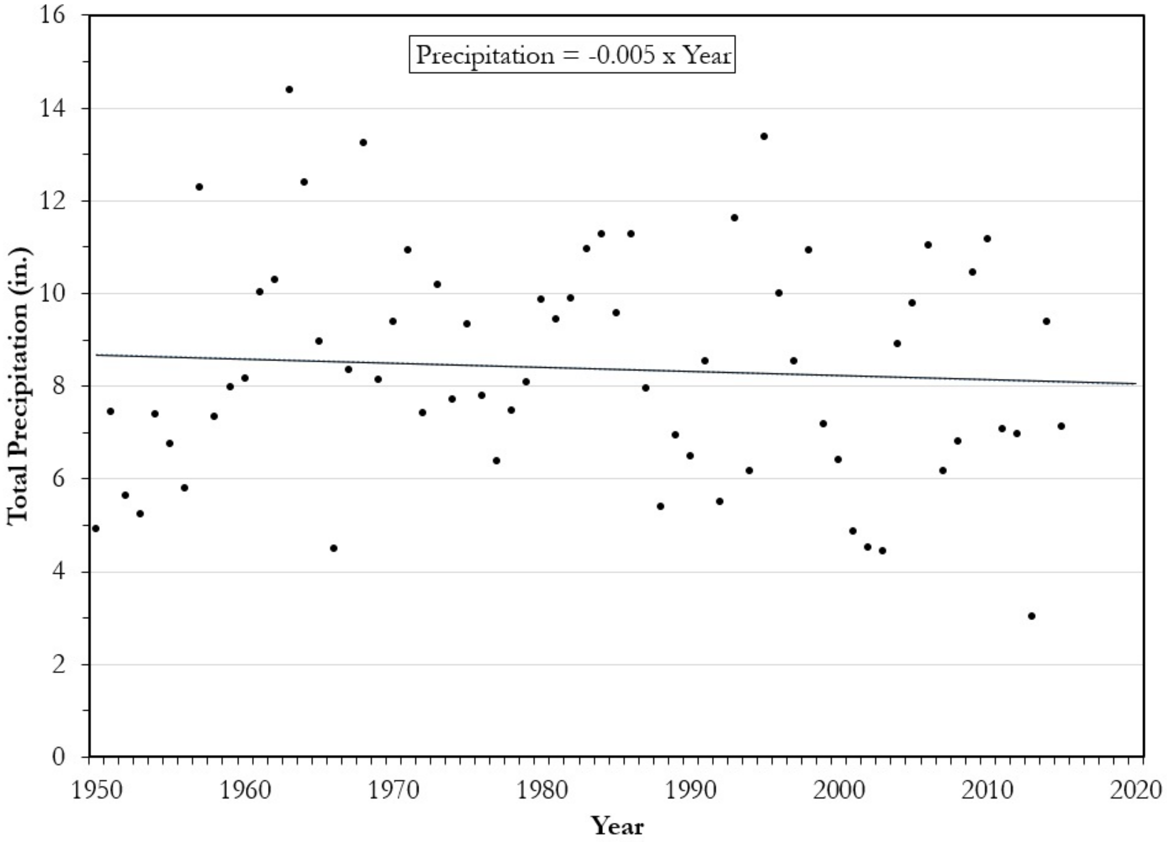

Figure 64. Total annual daily precipitation with linear regression lines and statistics from 1950-2015.

Table 25. Average total monthly and annual precipitation (water equivalent) for CFA[a]

	Average (in.)	Highest (in.)	Lowest (in.)	Normal[b] (in.)
January	0.66	2.56	0.00[c]	0.72
February	0.57	2.40	0.00	0.55
March	0.60	2.03	0.00	0.65
April	0.77	2.50	0.00	0.93
May	1.19	4.42	0.02	1.23
June	1.11	4.64	0.00	1.07
July	0.47	2.29	0.00	0.59
August	0.54	4.05	0.00	0.35
September	0.61	3.52	0.00	0.63
October	0.57	1.88	0.00	0.62
November	0.60	1.74	0.00	0.61
December	0.73	3.43	0.00	0.71
ANNUAL	8.38	14.40	3.04	8.66

a. Data period of record spans March 1950 through December 2015.

b. Data period of record spans January 1981 through December 2010.

Table 26. Monthly and annual average number of days (%) on which precipitation was recorded at CFA.

	Trace or More[a] (%)	0.01 in. or More[b] (%)	0.10 in. or More[b] (%)	0.50 in. or More[b] (%)	1.0 in. or More[b] (%)
January	40	22	7	0.6	0.0
February	35	19	7	0.5	0.0
March	32	19	7	0.3	0.0
April	31	21	8	0.8	0.1
May	35	26	12	1.3	0.0
June	34	22	10	1.7	0.2
July	17	12	4	0.7	0.0
August	21	13	5	0.8	0.0
September	19	13	6	0.8	0.2
October	20	13	6	0.6	0.1
November	27	18	7	0.5	0.0
December	35	22	8	0.5	0.0
ANNUAL	28	18	7	0.7	0.1

a. Data period of record spans March 1950 through September 1983, when record keeping of trace amounts was discontinued.

b. Data period of record spans March 1950 through December 2015.

midnight) as a percentage of occurrence during which specified amounts of precipitation fell at CFA. The data indicate that the frequency of days with a trace of precipitation was higher during the winter, spring, and early summer months. During the period of December through June, approximately 1/3 or more of the days had a trace or more of precipitation. January was the month with the highest frequency of occurrence at 40%. During the late summer and autumn months, a trace or more of precipitation was observed on only about 20% of the days. July was the month with the lowest frequency of occurrence at 17%. On an annual basis, a trace or more of precipitation was observed on 28% of the days.

A higher frequency of days with 0.01 in. or more was likewise observed during the winter, spring, and early summer months. Late summer and autumn months also showed a lower frequency of occurrence. May was the month with the highest frequency of occurrence at 26% while July was the month with the lowest frequency of occurrence at 12%. On an annual basis, 18% of the days have had 0.01 in. or more of precipitation.

For precipitation amounts of 0.10 in. or greater, the pattern is different with the highest frequency of occurrence in late spring and early summer. The month with the highest frequency of occurrence for this amount of precipitation was May at 12%. June also had a significant frequency of occurrence at 10%. July had the lowest frequency of occurrence at 4%. The annual frequency of occurrence was 7% for daily precipitation totals equal to or greater than 0.10 in.

The pattern is also different for precipitation amounts of 0.50 in. or more. Although the late spring and early summer months were when the frequency of occurrence was highest, the month when the frequency of occurrence was lowest was the month of March at 0.3%. June was highest at 1.7% followed by May at 1.3%. Annually, the frequency of occurrence was 0.7%.

Days on which more than 1 in. of precipitation was recorded were rare. Storms of that intensity are usually of the thunderstorm variety and have occurred in April, June, September, and October, as previously discussed. The maximum frequency of occurrence was 0.2% in June and September. The annual frequency of occurrence was 0.1%.

Long periods of time without precipitation are not uncommon at the INL. Table 27 presents a list of time periods lasting just over 1 month or more without measurable precipitation at CFA. Since 1950, there have been 39 periods with at least 35 days or more of no measurable precipitation periods. The longest dry period was 73 days from October 12 through December 23, 1959. Two other dry periods extending for 2 months or more also occurred in the autumn, from October 3 to December 4, 1976 and from September 12 to November 11, 1952. Seventy-four percent of the periods occurred in the summer and autumn seasons with 18 occurrences in the summer and 11 occurrences in the fall season.

Table 27. Longest periods at CFA without measurable (0.01 in. or greater) daily precipitation.

Beginning of Period	Ending of Period	Length of Period (days)
12 Oct 1959	23 Dec 1959	73
03 Oct 1976	04 Dec 1976	63
12 Sep 1952	11 Nov 1952	61
26 Aug 1987	23 Oct 1987	59
25 Jun 2003	20 Aug 2003	57
04 Sep 1999	27 Oct 1999	54
01 Jun 1994	22 Jul 1994	52
01 Oct 1977	21 Nov 1977	52
13 Jun 1953	01 Aug 1953	50
18 Jan 1988	05 Mar 1988	48
13 Jan 1991	28 Feb 1991	47
14 Aug 1967	29 Sep 1967	47
24 Sep 1958	8 Nov 1958	46
24 Aug 1975	06 Oct 1975	44
12 May 2003	23 Jun 2003	43
19 Mar 1977	30 Apr 1977	43
29 Jul 1969	08 Sep 1969	42
18 Sep 2002	29 Oct 2002	42
19 Nov 2011	29 Dec 2011	41
10 Aug 1962	19 Sep 1962	41
08 Jun 1974	17 Jul 1974	40
28 Nov 1991	06 Jan 1992	40
25 Jun 1963	03 Aug 1963	40
29 Aug 1964	06 Oct 1964	39
21 Aug 1994	28 Sep 1994	39
27 Feb 2004	05 Apr 2004	39
22 Aug 1981	29 Sep 1981	39
03 Dec 1962	09 Jan 1963	38
25 Jun 1999	31 Jul 1999	37
24 Jun 1966	30 Jul 1966	37
16 Oct 1993	21 Nov 1993	37
24 Jun 1976	29 Jul 1976	36
03 Oct 1966	07 Nov 1966	36
18 Aug 1953	21 Sep 1953	35
09 Jan 1989	12 Feb 1989	35
04 Mar 1990	07 Apr 1990	35
08 Jan 1992	11 Feb 1992	35
04 Aug 2006	07 Sep 2006	35
04 Jan 2002	07 Feb 2002	35

Note: Data period of record spans March 1950 through December 2015.

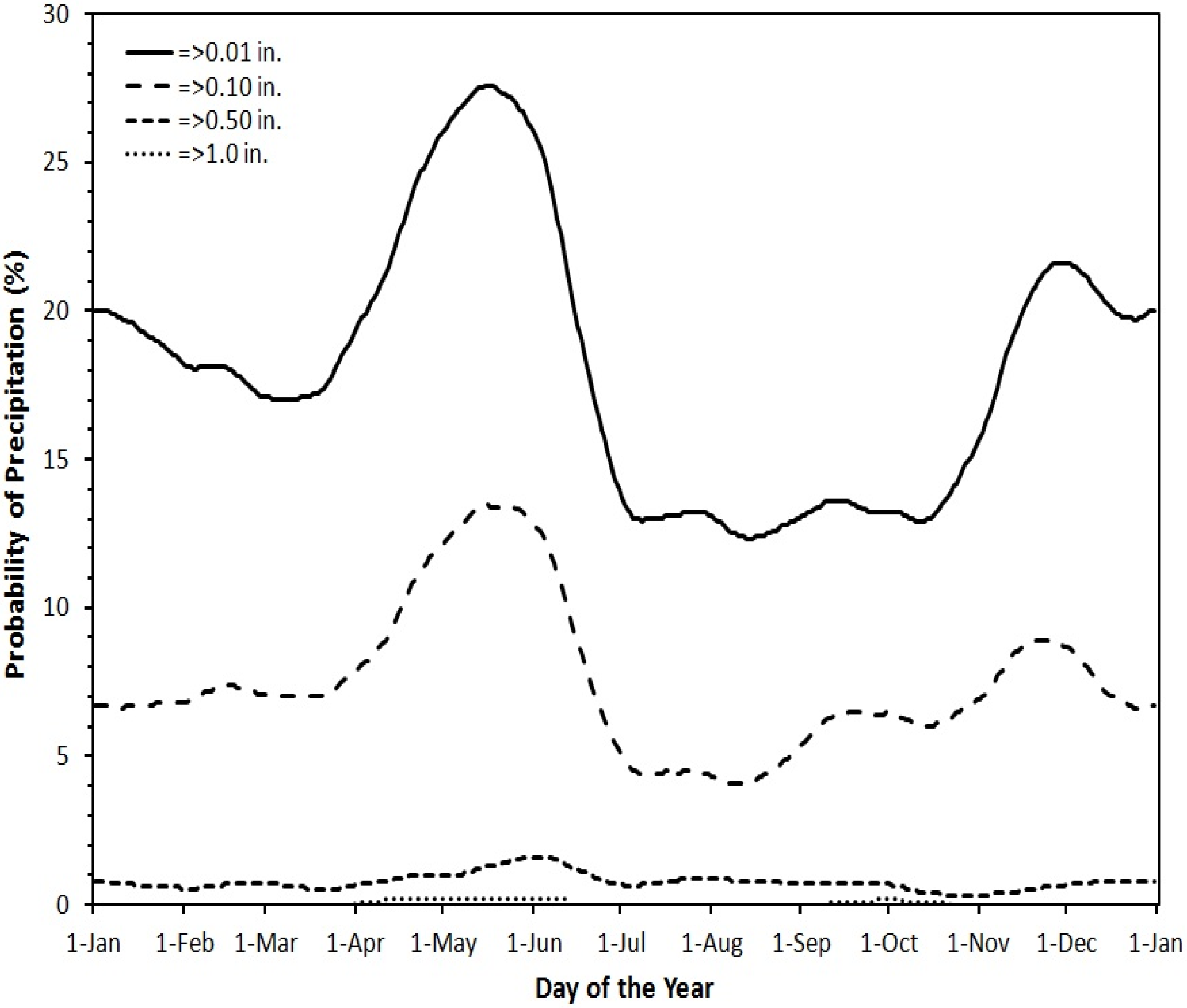

Figure 65. Probability of daily precipitation greater than or equal to 0.01, 0.10, 0.50, and 1.0 in. day^{-1} for the 29-day window centered on a given day of the year.

Precipitation Probabilities

In addition to the analyses of precipitation frequencies previously provided based on the 66-year period of record, the NCDC (2011) also provided 30-year normal probabilities of daily precipitation for specified daily totals. The most recent analysis for the 1981-2010 time period is graphically shown in Fig. 65. The curves are for daily probabilities of precipitation for >0.01, >0.10, >0.50, and >1.0 in. day^{-1} of precipitation for a 29-day period centered on the particular day of interest.

For daily precipitation totals of $\geq$0.01 and $\geq$0.10 in. day^{-1}, the curve is bi-modal with the biggest peaks centered on May 15. For much of the year, the $\geq$0.01 in. day^{-1} curve is about double the value of the $\geq$0.10 in. day^{-1} curve. For the quantities $\geq$0.01 and $\geq$0.10 in. day^{-1}, the maximum probabilities are 27.6% and 13.5, respectively. The tails of this primary maxima extend from about March 5 to about July 4. The type of precipitation associated with these peaks is rain accompanied at times with hail due to thunderstorm activity. The secondary maxima are centered on December 1. For the quantities

$\geq$0.01 and $\geq$0.10 in. day^{-1}, the maximum probabilities of the second maxima are 21.6 and 8.9%, respectively. The tails of the secondary maxima extend from about October 10 to March 5. The type of precipitation associated with the secondary winter maxima is primarily snow. A distinct summertime minimum was also evident, particularly in the $\geq$0.01in. day^{-1} curve. The minimum extended from July 4 to October 10 and averaged 13%.

The probability curves for $\geq$0.50 and $\geq$1.0 in. day^{-1} quantities were quite different from the $\geq$0.01 and $\geq$0.10 in. day^{-1} curves. The occurrences of the larger quantities of daily precipitation were quite rare in comparison. The $\geq$0.50 in. day^{-1} curve showed a single maximum around June 1 of only 1.6%. The $\geq$1.0 in. day^{-1} curve indicated two very small maxima of 0.2% centered on June 1 and October 1. Thus, the probability of daily precipitation totals of $\geq$0.50 and $\geq$1.0 in. day^{-1} are very small, but probably not insignificant over time, as will be discussed in the next paragraphs.

Precipitation Event Return Periods

Recurrence intervals for various precipitation amounts are a useful statistical tool for structure design and placement. They are often used in risk assessment for floods or other natural hazards. For a given event such as 1 inch of precipitation in 24 hours, the return period is the time interval in which one would expect to observe one such event on average. A precipitation event with a 100-year return period therefore is expected to occur on average once within a 100-year period. This means it has a 1/100 or 1% chance of occurring in any given year. Return periods for daily precipitation amounts can be estimated using historical data.

The return period is a statistical parameter and therefore does not mean the event will recur exactly at fixed intervals. Over a single 100-year interval, an event with a 100-year return period actually has a 37% chance of not occurring at all, 37% chance of occurring once, 18% chance of occurring twice, and 8% chance of occurring three times or more. The once per 100 years is just the average value of the possible outcomes.

Sagendorf (1996) analyzed 43 years of daily precipitation data at the INL and from several other longer term stations in the ESRP. The material presented below is derived from his analysis. Figure 66 shows the return period for different daily precipitation totals at the CFA station, also known as Idaho Falls 46W in the NCDC (2011) database. The solid line represents data from the entire year, while the dotted line represents data acquired only between November 15 and March 15. The latter time period only incorporates wintertime precipitation, which would usually be snow events. The curves are fairly straight for return periods up to several years. For longer periods, however, the curves deviate from one another. The events at the longer return periods are, of course, from extreme precipitation events that occurred only rarely and can have a large effect on this type of analysis. It may take a much longer period of record for these extreme events to order themselves as expected for a return year analysis. For example, a 100 year storm may have already occurred at this station within the 43-year measurement period. The analysis assumes that the record is a random sample of the unknown entire population. If the period of record were long enough, the curves would be expected to be similar for their entire length.

The dotted wintertime curve in Fig. 66 is quite straight. This indicates that a shorter period of record is required for making return year estimates for winter precipitation than for the entire year. This is likely because the extreme events in the entire year record are the result of convective season thunderstorms.

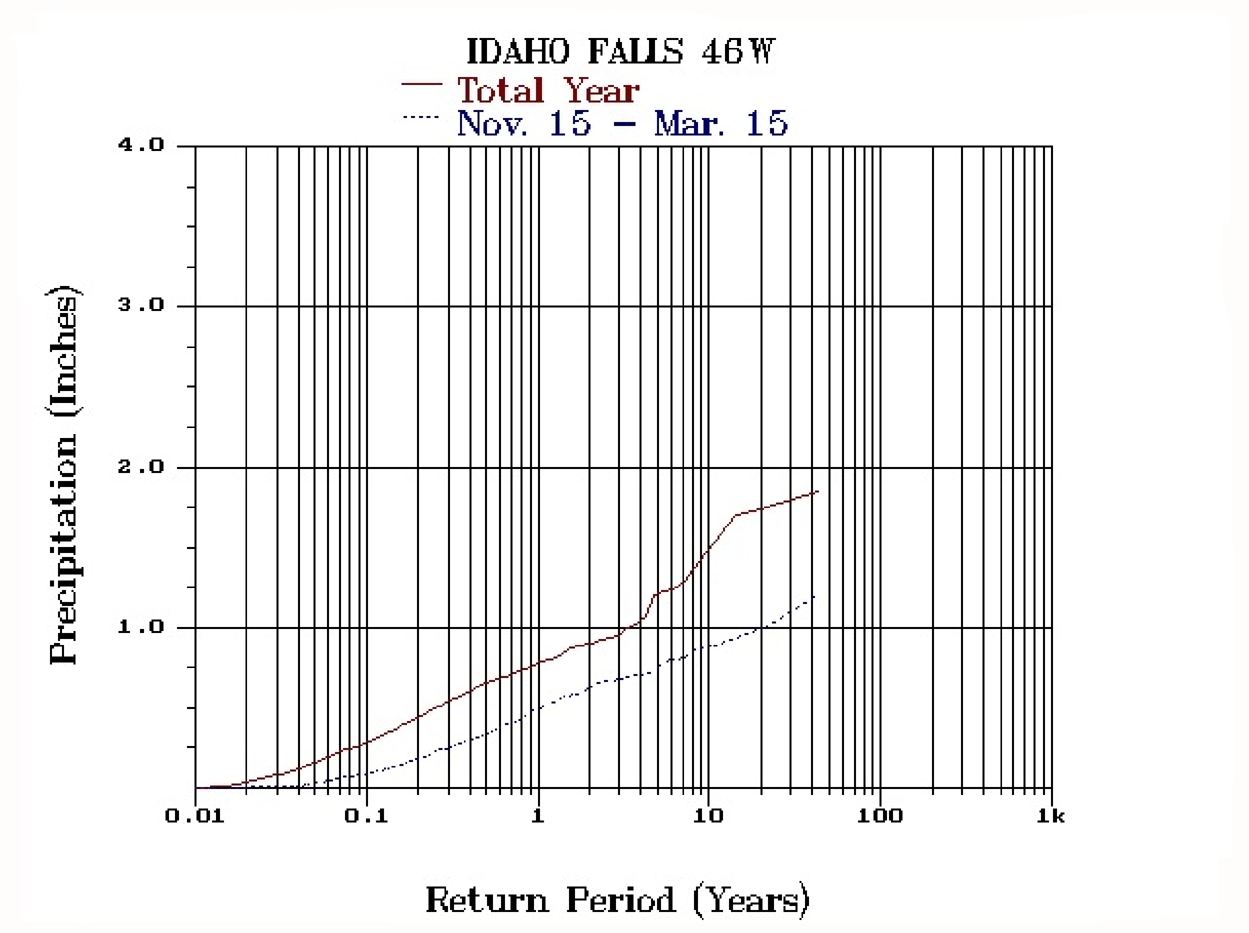

Figure 66. Idaho Falls 46W (CFA) precipitation amount versus return years.

Understanding wintertime precipitation is important because three flooding episodes have occurred since the early 1950s when meteorological data began to be recorded at the INL. Each of these episodes was associated with winter thaws, where rain combined with melting snow on a frozen surface resulted in unexpectedly large runoff amounts. Equation 1 describes a straight line through the wintertime curve. Winter season precipitation amounts can be calculated as follows:

$$\text{Precipitation (in.)} = 0.48 + 0.39\log_{10}(\text{Return Years}) \quad (1)$$

During the summer months, storms are typically convective in nature and affect a relatively small area. Therefore, storm return statistics that apply to one INL station may not apply to another. Return period precipitation estimates become more reliable when the entire ESRP is included in the analysis. This is a reasonable approach, since it is known that convective storms occur across the entire ESRP and are especially strong during the late spring and early summer months. Grouping precipitation data from the entire ESRP makes extreme precipitation events fall into their proper positions and form a well-behaved line.

To analyze return periods for summer months, Sagendorf (1996) combined data from 18 stations in the ESRP, some with a period of record that extended up to 81 years. Two of the 18 stations were from the INL. Data were added to the analysis only when daily precipitation amounts exceeded 0.5 in. during the period of April 15 through September 30. During this season, most of the precipitation that resulted in daily totals of more than 0.5 in. came as scattered showers or thundershowers. These storms generally cover a small area and do not last very long. The distance between stations was great enough that these precipitation events could be considered independent events so as not to violate the required assumption of statistical independence between stations. The combined record is equivalent to 765 years of data. The combined ESRP curve from the 18 stations for summertime convective storms is shown in Fig. 67. It shows a graph of the convective season precipitation amount versus return years. Equation 2 describes a straight line through the data points and can be used to estimate expected summertime precipitation amounts for the INL.

$$\text{Precipitation (in.)} = 0.70 + 0.74\log_{10}(\text{Return Years}) \qquad (2)$$

Sometimes engineers and hydrologists are required to estimate the potential precipitation that may occur in intervals shorter than one day. Hourly precipitation data permits calculation of precipitation return periods for storms less than 24 hours in length. Sagendorf (1996) selected 12 stations in the ESRP to analyze precipitation recorded on an hourly basis. Two of the 12 stations were on the INL. The combined statistics showed that 23% of the total daily

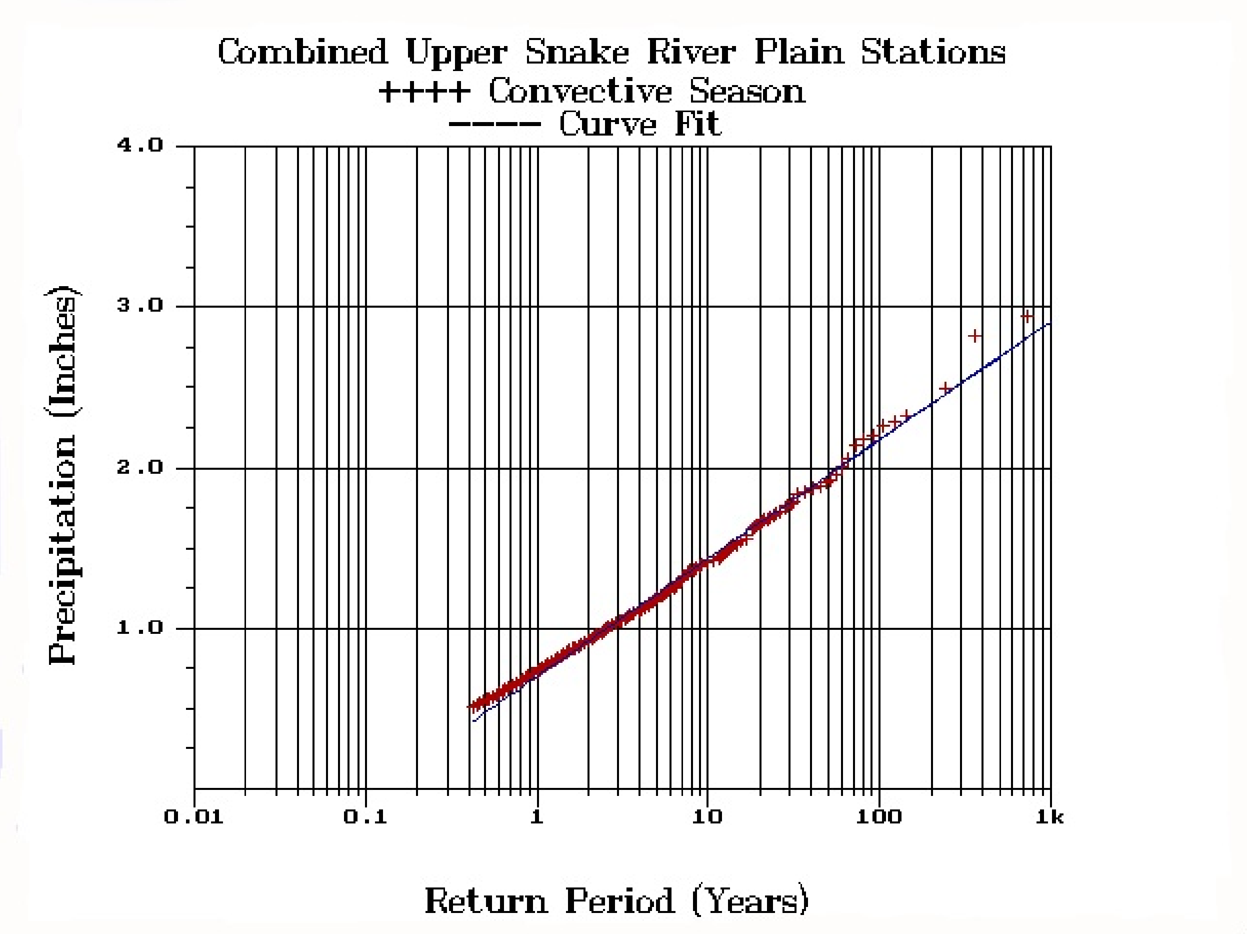

Figure 67. Combined Upper Snake River Plain Stations for daily (24 hour) precipitation.

precipitation is accumulated in a period of one hour. The values for 3, 6, and 12 hour periods are 41%, 56%, and 76% of the total daily precipitation, respectively. An equation that specifies this fraction of daily total precipitation was reported as follows:

$$F = 0.36 + 0.15D - 0.014D^2 + 6.86\times10^{-4}D^3 - 1.31\times10^{-5}D^4 \qquad (3)$$

where F is the fraction of the daily total precipitation and D is the storm duration in hours. This equation can be applied to INL daily precipitation totals to estimate precipitation for periods less than 24 hours.

Characterization of Precipitation Events

Modern recording devices now collect precipitation data over very short periods of time. This permits a more thorough analysis of both short-term and long-term precipitation events. There are a total of 8 NOAA/INL Mesonet stations located near every major INL facility that employ a tipping bucket rain gauge to measure five-minute precipitation totals. Using these data, a specific precipitation event can be characterized even if it spans several days. In the analysis described in the following paragraph, a precipitation event is defined as a period with one or more five-minute intervals for which precipitation was detected without a dry period of six hours or greater between these intervals. In other words, a precipitation event begins at the end of a dry period of six or more hours and ends at the beginning of the next dry period of six or more hours. Thus, a precipitation event as it is defined, may be more or less than the daily precipitation upon which all of the foregoing analyses were based. For the precipitation event analysis that follows, CFA was used as the representative station. The data period of record spans the 22-year period of January 1994 through December 2015.

The longest precipitation event observed in the 22-year period of record was over 56 hours in duration (Table 28). In all, 15 events lasted more than 24 hours, 27 events lasted more than 18 hours, and 43 events lasted more than 16 hours. Ten of the 15 events lasting longer than 24 hours occurred in just 4 years. Three $\geq$24-hour long precipitation events occurred in 1995 and 2005, while two precipitation events lasting more than 24 hours were observed in 2006 and 2009. Twelve years had no precipitation events that lasted longer than 24 hours. On average, however, an event lasting longer than 24 hours occurred approximately every 2 out of 3 years, but these events obviously occurred sporadically.

Table 29 shows the precipitation events with greatest totals. The highest total amount of precipitation recorded during an event was 1.83 in. This amount was recorded during the approximately 30-hour period beginning at 1305 MST on June 5, 1995. The next highest amount of precipitation of 1.41 in. was recorded during a 28 hour long event that began at 0510 MST on October 4, 2009. The longest event cited earlier (56-hours) provided the fourth highest precipitation event with 1.15 in. total precipitation.

Table 28. Precipitation events exceeding 16 hours duration at CFA.

Event Length (hours)	Begin Time HHMM (MST)	Begin Date	Ending Time HHMM (MST)	Ending Date	Event Total (in.)
56.3	1920	04 May 1995	0335	07 May 1995	1.15
36.9	1730	26 Sep 2014	0625	28 Sep 2014	0.76
35.8	0635	06 Oct 2011	1820	07 Oct 2011	1.22
35.6	1700	06 Jun 2009	0435	08 Jun 2009	0.85
34.9	2235	09 May 2005	0930	11 May 2005	0.75
33.3	0820	22 Mar 2005	1735	23 Mar 2005	0.51
31.7	0515	01 Jan 1997	1255	02 Jan 1997	0.77
30.8	1420	10 Mar 1995	2110	11 Mar 1995	0.68
29.3	1305	05 Jun 1995	1825	06 Jun 1995	1.83
27.8	0510	04 Oct 2009	0900	05 Oct 2009	1.41
27.7	0235	28 Apr 1999	0615	29 Apr 1999	0.57
27.2	0035	05 Apr 2006	0345	06 Apr 2006	0.50
26.3	0100	02 Jan 2006	0315	03 Jan 2006	1.06
25.7	0300	16 May 2005	0440	17 May 2005	0.76
25.6	2055	15 Sep 1996	2230	16 Sep 1996	0.50
23.7	0925	03 Dec 1994	0905	04 Dec 1994	0.16
23.7	2315	15 May 1996	2255	16 May 1996	0.77
22.5	0805	21 Nov 1998	0635	22 Nov 1998	0.27
22.4	0920	23 Oct 1997	0745	24 Oct 1997	0.43
22.1	2210	04 Oct 2011	2015	05 Oct 2011	0.43
21.9	0405	30 May 1999	0200	31 May 1999	0.47
21.9	0425	01 Dec 2005	0220	02 Dec 2005	0.57
21.6	1600	06 Feb 1999	1335	07 Feb 1999	0.49
19.9	0745	23 Apr 1997	0340	24 Apr 1997	0.58
19.1	1520	21 Dec 2008	1025	22 Dec 2008	0.36
18.8	2300	07 Nov 2010	1745	08 Nov 2010	0.57
18.1	1830	01 Jun 2009	1235	02 Jun 2009	0.63
17.8	2035	19 Apr 2005	1425	20 Apr 2005	0.12
17.7	0745	30 Dec 2005	0125	31 Dec 2005	0.27
17.6	0545	22 Apr 2010	2320	22 Apr 2010	0.97
17.4	1115	16 May 1994	0440	17 May 1994	0.34
17.2	1615	06 Feb 1998	0925	07 Feb 1998	0.36
17.1	2240	01 Oct 2015	1545	02 Oct 2015	0.47
16.7	0400	12 Dec 1995	2040	12 Dec 1995	0.65
16.6	0140	12 Sep 1998	1815	12 Sep 1998	0.70
16.4	0935	20 May 2015	0200	21 May 2015	0.26
16.3	2335	06 May 2006	1555	07 May 2000	0.65
16.3	0745	27 May 2010	0000	28 May 2010	0.50
16.2	0055	30 Sep 2009	1705	30 Sep 2009	0.42
16.2	2130	03 Dec 1998	1340	04 Dec 1998	0.54
16.2	1610	08 Feb 1999	0820	09 Feb 1999	0.16
16.1	1005	31 Mar 2006	0210	01 Apr 2006	0.43
16.0	0030	10 May 1998	1630	10 May 1998	0.62

a. Events are separated by six or more continuous hours without precipitation.

b. Data period of record spans from January 1994 through December 2015.

Table 29. CFA precipitation events with greatest totals.

Event Total (in.)	Begin Time HHMM	Begin Date	Ending Time HHMM	Ending Date
1.83	1305	05 Jun 1995	1825	06 Jun 1995
1.41	0510	04 Oct 2009	0900	05 Oct 2009
1.22	0635	06 Oct 2011	1820	07 Oct 2011
1.15	1920	04 May 1995	0335	07 May 1995
1.06	0100	02 Jan 2006	0315	03 Jan 2006
1.03	1130	30 Sep 1994	2305	30 Sep 1994
0.98	1945	04 Oct 2007	1040	05 Oct 2007
0.97	0545	22 Apr 2010	2320	22 Apr 2010
0.85	1700	06 Jun 2009	0435	08 Jun 2009
0.80	1505	18 Jun 1995	0530	19 Jun 1995
0.78	1840	19 Oct 2004	0535	20 Oct 2004
0.77	0515	01 Jan 1997	1255	02 Jan 1997
0.77	2315	15 May 1996	2255	16 May 1996
0.76	1730	26 Sep 2014	0625	28 Sep 2014
0.76	0300	16 May 2005	0440	17 May 2005
0.75	2235	09 May 2005	0930	11 May 2005
0.71	2220	15 May 2015	0755	16 May 2015
0.71	1045	16 Apr 2006	1835	16 Apr 2006
0.71	1830	13 Aug 2014	0220	14 Aug 2014
0.70	0645	04 Aug 2014	1245	04 Aug 2014
0.70	140	12 Sep 1998	1815	12 Sep 1998
0.70	1135	09 Jun 2006	1910	09 Jun 2006
0.69	1050	27 Jan 2008	0155	28 Jan 2008
0.68	1420	10 Mar 1995	2110	11 Mar 1995
0.68	0335	02 Apr 1996	1910	02 Apr 1996
0.65	2335	06 May 2000	1555	07 May 2000
0.65	0400	12 Dec 1995	2040	12 Dec 1995
0.63	1830	01 Jun 2009	1235	02 Jun 2009
0.63	0015	06 Jun 2007	1330	06 Jun 2007
0.62	2125	24 Dec 2008	1110	25 Dec 2008
0.62	920	22 Mar 2009	2310	22 Mar 2009
0.62	0030	10 May 1998	1630	10 May 1998
0.60	1600	29 Jul 1998	1850	29 Jul 1998
0.59	1510	22 Jul 2004	1535	22 Jul 2004
0.58	2055	01 Nov 2008	1145	02 Nov 2008
0.58	0745	23 Apr 1997	0340	24 Apr 1997
0.57	2300	07 Nov 2010	1745	08 Nov 2010
0.57	0425	01 Dec 2005	0220	02 Dec 2005
0.57	0235	28 Apr 1999	0615	29 Apr 1999
0.57	1715	06 Mar 2002	2300	06 Mar 2002
0.55	1350	14 Jul 2012	2225	14 Jul 2012
0.54	2130	03 Dec 1998	1340	04 Dec 1998
0.53	1145	28 Dec 2005	0215	29 Dec 2005
0.53	1650	13 Dec 2015	0550	14 Dec 2015
0.52	1915	05 May 2005	0605	06 May 2005
0.52	0935	02 Nov 2015	2010	02 Nov 2015
0.51	0820	22 Mar 2005	1735	23 Mar 2005
0.51	0155	28 Apr 2009	1100	28 Apr 2009
0.51	0450	10 Jun 1997	1455	10 Jun 1997
0.51	0800	12 Jul 1997	1515	12 Jul 1997

Note: Data record of period spans from January 1994 through December 2015.

The five-minute precipitation records also permit a rudimentary analysis of precipitation rates. This analysis is important in determining the potential for flash floods. Using data extracted from the precipitation event analysis, each event was subsequently analyzed for the highest precipitation rate during 5, 10, 15, 20, and 30 minute and 1, 2, 3, 4, 6, 8, 12, and 24 hour periods. The data were summarized for each month of the year and are presented in Table 30. The highest 5-minute precipitation amount recorded was 0.29 in. This occurred during a thunderstorm in the month of July. The highest 10, 15, and 20-minute precipitation amounts were also recorded in July with 0.40 in., 0.50 in., and 0.57 in. total, respectively. The highest 1, 3, 4, 6, 8, 12, and 24-hour precipitation amounts were recorded in June

Table 30. Monthly and annual greatest precipitation amounts (in.) during selected periods at CFA.

Month	5 min	10 min	15 min	20 min	30 min	1 hr	2 hr	3 hr	4 hr	6 hr	8 hr	12 hr	24 hr
January	0.05	0.08	0.10	0.11	0.12	0.14	0.24	0.35	0.46	0.57	0.66	0.76	1.02
February	0.03	0.05	0.06	0.08	0.10	0.17	0.26	0.34	0.43	0.49	0.49	0.49	0.49
March	0.04	0.07	0.10	0.13	0.19	0.32	0.47	0.53	0.54	0.57	0.57	0.57	0.64
April	0.08	0.13	0.16	0.17	0.18	0.24	0.34	0.42	0.45	0.58	0.71	0.71	0.97
May	0.12	0.15	0.17	0.19	0.20	0.27	0.35	0.45	0.48	0.59	0.65	0.71	0.77
June	0.25	0.34	0.41	0.45	0.48	0.71	0.92	0.94	1.03	1.36	1.45	1.48	1.79
July	0.29	0.40	0.50	0.57	0.59	0.59	0.59	0.60	0.60	0.60	0.60	0.60	0.60
August	0.15	0.22	0.23	0.24	0.26	0.29	0.41	0.51	0.58	0.70	0.71	0.71	0.94
September	0.17	0.19	0.23	0.25	0.28	0.37	0.44	0.51	0.61	0.77	0.92	1.03	1.11
October	0.25	0.33	0.37	0.37	0.38	0.38	0.38	0.48	0.56	0.71	0.80	1.02	1.30
November	0.06	0.10	0.13	0.15	0.17	0.28	0.34	0.40	0.44	0.45	0.45	0.53	0.58
December	0.04	0.05	0.07	0.08	0.11	0.19	0.28	0.31	0.38	0.47	0.50	0.61	0.65
ANNUAL	0.29	0.40	0.50	0.57	0.59	0.71	0.92	0.94	1.03	1.36	1.45	1.48	1.79

Note: Data period of record spans January 1994 through December 2015.

with 0.71 in., 0.92 in., 0.94 in., 1.03 in., 1.36 in., 1.45 in., 1.48 in., and 1.79 in. total, respectively. One inch or greater total precipitation amounts were first observed at the 4-hour period in June, at the 12-hour period in September and October, and at the 24-hour period in January. Recall that 24 hours in this analysis is not necessarily from midnight to midnight.

The average number of precipitation events in a month and annually are given in Table 31. For precipitation amounts of 0.01 in. or more, May shows the greatest number of occurrences of 8.4. The month with the lowest number of precipitation events of 0.01 in. or more was September with 3.8 events. Similarly, May shows the most precipitation events of 0.10 in. or more with 3.3 events. On an annual basis, there was on average 66 precipitation events of 0.01 in. or more. For precipitation amounts of 0.10 in., 0.50 in., and 1.00 in. or more the annual number of events was 21.2, 2.6, and 0.3, respectively.

Table 31. Average number of monthly precipitation events[a] at CFA.

	0.01 in. or More	0.10 in. or More	0.50 in. or More	1.00 in. or More
January	5.9	1.6	0.1	0.0
February	4.8	1.0	0.0	0.0
March	5.2	1.9	0.2	0.0
April	6.9	2.4	0.3	0.0
May	8.4	3.3	0.4	0.0
June	6.0	2.2	0.4	0.0
July	4.3	1.0	0.2	0.0
August	4.3	1.3	0.1	0.0
September	3.8	1.6	0.2	0.0
October	4.8	1.7	0.2	0.1
November	4.4	1.4	0.1	0.0
December	7.0	1.6	0.3	0.0
ANNUAL	65.7	21.2	2.6	0.3

a. Events are separated by six or more continuous hours without precipitation.
b. Data period of record spans from January 1994 through December 2015.

Snow

CFA is the official measurement location for snowfall and snow depth for the INL. It is the only location at the INL where these continuous measurements have been made. Snowfall is the amount of snow that falls within a given period, regardless of the amount that accumulates on the ground. Since snow may melt as it falls, the snowfall amount must occasionally be estimated from the water equivalent of snow. Snow depth is the amount of snow covering the ground as determined by a average of several depth measurements in the same vicinity. In the discussion that follows, snowfall will be discussed first, followed by snow depth. Within each category, daily characteristics will be presented first, followed by monthly and annual characteristics.

Snowfall

The database of average daily snowfall is quite noisy because of the discontinuous nature of the phenomenon. Therefore, daily characteristics of snowfall might best be described in terms of extreme events. The days with snowfall totals equal to or exceeding 5 in. at CFA are listed in Table 32. A total of 39 events occurred during the 66-year period of record. On average, a snowfall of ½ ft. or more occurred every four years at CFA. However, there is great variability in this average. Of the 18 recorded events, two occurred in 1970 and two occurred in 1973. Indeed, 6 of the $\geq$½ ft. daily snowfall events occurred in the decade of the 1970's, making this decade the most noted for heavy snowfall. Another record set in the 1970’s was the shortest number of days separating heavy snowfall events. Only 9 days separated daily snowfall events of 6.5 and 6.7 in. in April, 1970. Only one $\geq$½ ft. daily snowfall event occurred in each of the 1950’s and the 1990’s. Three events occurred in the decades of the 1960’s, 1980's, and the 2000's. The day with the highest snowfall total was January 2, 2006 with 9.0 inches. The day with the next highest snowfall total was March 22, 1973 with 8.6 in.

Daily Snowfall

The highest daily snowfall totals listed for each month of the year are given in Table 33. Daily snowfall totals $\geq$½ ft. have occurred in January, February, March, April, November, and December. Snowfall as late as May and as early as September has been observed at the INL. Snowfall in June, July, and August is insignificant.

The average percentage of days (from midnight to midnight) in a given month on which a specified amount of snowfall was recorded is listed in Table 34. Maximums and minimums daily snowfall totals are also listed for the quantities of $\geq$0.1, $\geq$1.0, and $\geq$3.0 in. day^{-1}.

Table 32. Greatest daily snowfall totals of 5.0 in. or more at CFA.

Amount (in.)	Date
9.0	02 Jan 2006
8.6	22 Mar 1973
8.5	20 Jan 1957
8.0	29 Dec 1992
7.5	08 Feb 1960
7.2	19 Feb 1971
7.0	04 Dec 1983
7.0	25 Dec 2008
7.0	19 Dec 2010
6.7	28 Apr 1970
6.5	19 Apr 1970
6.5	24 Nov 1981
6.5	01 Dec 1982
6.4	13 Feb 1973
6.0	20 Jan 1962
6.0	18 Dec 1967
6.0	22 Nov 1977
6.0	27 Jan 2008
5.6	11 Feb 1973
5.5	24 Dec 2014
5.1	24 Feb 1969
5.1	17 Nov 1964
5.0	02 Feb 1961
5.0	23 Nov 1963
5.0	23 Jan 1972
5.0	03 Dec 1972
5.0	19 Feb 1976
5.0	04 Jan 1977
5.0	10 Jan 1978
5.0	16 Jan 1978
5.0	10 Feb 1984
5.0	21 Jan 1985
5.0	27 Mar 1985
5.0	14 Feb 1998
5.0	23 Feb 2001
5.0	07 Jan 2005
5.0	03 Feb 2008
5.0	22 Jan 2010
5.0	13 Dec 2015

Note: Data period of record spans March 1950 through December 2015.

Table 33. Monthly and annual average, maximum, minimum and normal snowfall totals and daily extreme totals for CFA.

	Average (in.)	Maximum (in.)	Minimum (in.)	Largest Daily Maximum (in.)	Normal (in.)
January	6.1	18.1	0.0	9.0	6.1
February	4.6	16.1	0.0	7.5	4.4
March	2.8	10.2	0.0	8.6	2.2
April	1.8	16.5	0.0	6.7	1.2
May	0.4	8.3	0.0	4.4	0.0
June	0.0	0.0	0.0	0.0	0.0
July	0.0	0.0	0.0	0.0	0.0
August	0.0	0.0	0.0	0.0	0.0
September	0.0	1.0	0.0	1.0	0.0
October	0.5	7.2	0.0	4.5	0.4
November	3.0	12.3	0.0	6.5	3.6
December	6.5	22.3	0.0	8.0	7.1
ANNUAL	25.5	59.7	6.8	9.0	25.0

Note: Data period of record spans March 1950 through December 2015. Normal period spans 1981 through 2010.

Table 34. Monthly and annual average percentage of days and extreme percentage of days with snowfall amounts, of equal to or greater than 0.1, 1.0, and 3.0 in. day^{-1} for CFA.

	≥0.1 in. day^{-1}			≥1.0 in. day^{-1}			≥3.0 in. day-1		
	Ave (%)	Max (%)	Min (%)	Ave (%)	Max (%)	Min (%)	Ave (%)	Max (%)	Min (%)
January	18	55	0	8	23	0	2	10	0
February	14	39	0	6	25	0	2	7	0
March	9	29	0	4	13	0	1	6	0
April	5	33	0	2	13	0	1	7	0
May	1	10	0	1	10	0	0	6	0
June	0	0	0	0	0	0	0	0	0
July	0	0	0	0	0	0	0	0	0
August	0	0	0	0	0	0	0	0	0
September	0	3	0	0	3	0	0	0	0
October	2	13	0	1	6	0	0	3	0
November	9	23	0	4	17	0	1	10	0
December	18	45	0	8	29	0	2	6	0
ANNUAL	6	13	2	3	5	1	1	2	0

Note: Data period of record spans March 1950 through December 2015.

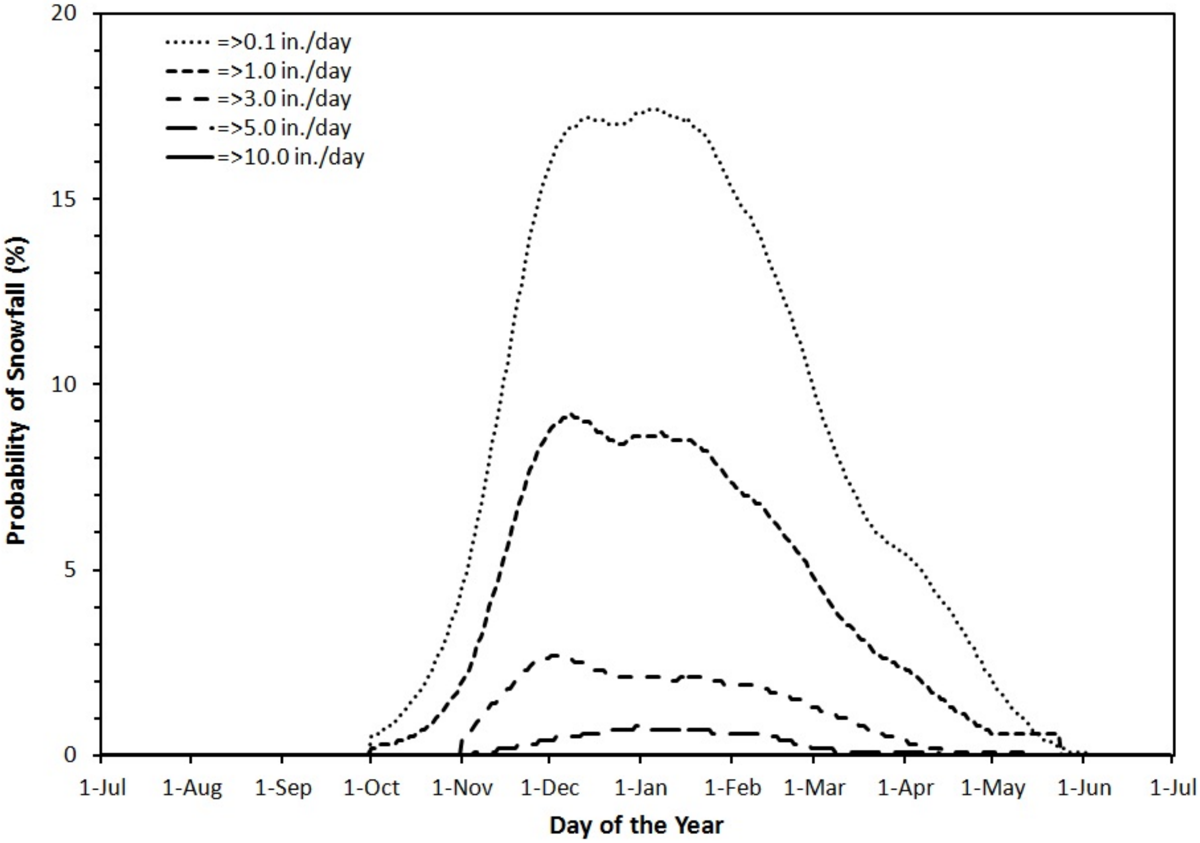

Figure 68. Probability of a daily snowfall total ≥0.1, 1, 3, 5, and 10 inches at CFA, normalized for the 30-year period of 1981-2010.

January and December, at 18% each, have the largest average number of days with snowfall ≥0.1 in. Snowfall has been observed on as many as 55% of the days in January and 45% of the days in December. Again, every month of the year has recorded no snowfall sometime during the period of record. Average daily occurrences of snowfalls ≥1.0 in. day^{-1} are about ½ as frequent as that for the ≥0.1 in. day^{-1} category. January and December, each at 8%, have the largest average number of days with snowfall ≥1.0 in. day^{-1}. The highest number of days of snowfall ≥1.0 in. day^{-1} was 29% in December. Average daily occurrences of snowfalls ≥3.0 in. day^{-1} were approximately 2% in frequency only in the months of December, January, and February. Daily occurrences as high as 10% were observed in January and November for the ≥3.0 in. day^{-1} category.

Another way to describe daily snowfall characteristics is with a probability graph. Figure 68 is a graph of the probability of a ≥0.1, ≥1.0, ≥3.0, ≥5.0, and ≥10.0 in. total daily snowfall from the normalized 30-year period of record (1981-2010) as provided by NCDC (2011). The curve for ≥0.1 in. day^{-1} snowfall rises from 0 over a 2-month period from October 1 to about a 17% probability at about December 10. Then a broad peak of about 17% probability was observed over a 35-day period until about January 15. The probability of a ≥0.1 in. day^{-1} snowfall then declined from that broad peak to 0% over a period of about 4 months, making the probability curve asymmetrical. The probability curves for the >1.0 and >3.0 in. day^{-1} snowfall curves were also asymmetrical with maximum probabilities of 9.2 and 2.7%, respectively, which occurred in early December. The maximum probability of a >5.0 in. day^{-1} snowfall was only 0.8% and occurred in early January. A probability of 0% was calculated for a snowfall of >10.0 in. day^{-1} for any day of the year.

Monthly Snowfall

Average monthly snowfall amounts for CFA are listed in Table 33. The highest monthly average snowfall occurred in December with a total of 6.5 in. January also received an amount comparable to December (6.1 in.). The month with the maximum snowfall total was December with a total of 22.3 in., which was observed in the year 1971. The month with the next highest monthly maximum snowfall was January with a total 18.1 in. This amount was observed in the year 1957. Three other months with maximum total snowfall over 1 ft. were February, April, and November. Considerable snowfall variation was also noted from year to year within a given month. December was the best example of this variability and exhibited a monthly total snowfall range of 22.3 in. from minimum (0.0 in.) to maximum (22.3 in.). As noted earlier, every month has recorded no snowfall at least once during the period of record.

Annual Snowfall

The annual average snowfall total was 25.5 in. as shown in Table 33. The minimum snowfall total for a year was 6.8 in., which occurred in 1986. The maximum annual snowfall total was 59.7 in., which occurred in 1971.

The average annual total snowfall from the CFA Thermoscreen data for the entire 66-year period of record from 1950-2015 is shown in Fig 69. A linear regression was conducted on the annual average dataset. Similarly to the annual precipitation, the data showed significant scatter and a downward trend. However, it is interesting that the slope of -0.0326" per year is a much steeper downward trend than precipitation of -0.0005" (Fig. 64). This may be in part due to slightly warmer temperatures (Fig. 56) since 1 or 2 degrees F could make a difference of whether the precipitation event was rain versus snow. The steeper downward trend could also be in part due to how measurements have been made since the office was moved from the INL into Idaho Falls in April 1984. Prior to April 1984, measurements were made every work day. However, since the move to Idaho Falls, the snow measurements are only made once a week (usually on Mondays) and daily snow fall for the previous week is estimated using the collocated Mesonet snow depth sensor, the amount of precipitation recorded, temperatures at the time of precipitation, and the NOAA/INL weather camera located at GRI and other nearby Idaho Transportation Department roadside cameras. It should also be noted that, given the significant scatter, any 1 or 2 years with well above average snowfall would change the slope.

The annual average percentage of days of snowfall totaling >0.1, >1.0, and >3.0 in. day^{-1} is given in Table 34. The average percentage of days in a year for these categories are in order: 6, 3, and 1%. The highest annual percentage of days with >0.1 in. day^{-1} total snowfall was 13% (about 45 days), and occurred in 1952. The lowest annual percentage of days with >0.1 in. was 2% (about 10 days) and occurred in 1974, 1986, and 1990. The highest annual percentage of days with >3.0 in. day^{-1} total snowfall was 2% (about 4 days), while the lowest was 0%.

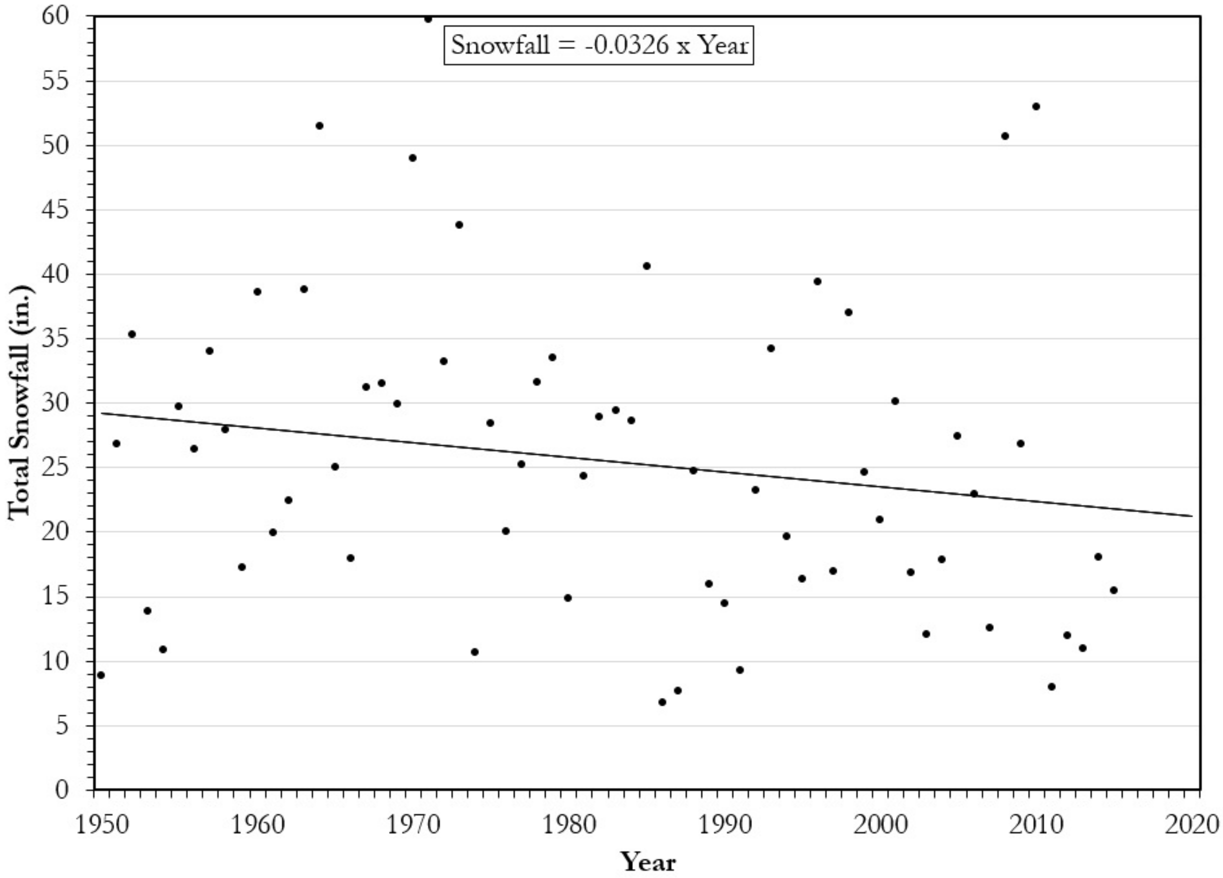

Figure 69. Total annual daily snowfall with linear regression lines and statistics from 1950-2015.

Snow Depth

Daily Snow Depth

Daily characteristics of snow depth are illustrated in Fig. 70. This graph is a plot of average snow depth for the 66-year period of record at CFA for each day of the year. On average, snow began to accumulate (continuous accumulation of ≥0.1 in.) on the ground around November 10. The average snow depth reached a peak of 5.6 in. on January 27. Snow depth began to gradually decline to 5.0 in. on February 18, and then decreased more rapidly to zero on April 5.

There was some noise that was observed in the average daily snow depth trace, particularly just after the peak snow depth and into the month of February. This illustrates the great variability of snow depth that occurred during that month. There was also considerable noise in the trace in late April. This was caused by the occurrence of late spring snow storms.

Table 35 summarizes the average date on which snow of various depths began to accumulate and the date on which the depth of the snow declined below those various depths. The number of days between those dates is also given. On average, there was 0.1 in. or more of snow on the ground from November 9 through April 4, a period of 147 days. Likewise, there was ≥ 1 in. of snow on the ground from November 28 through March 23, a period of 116 days. For snow depths ≥3 in., the dates

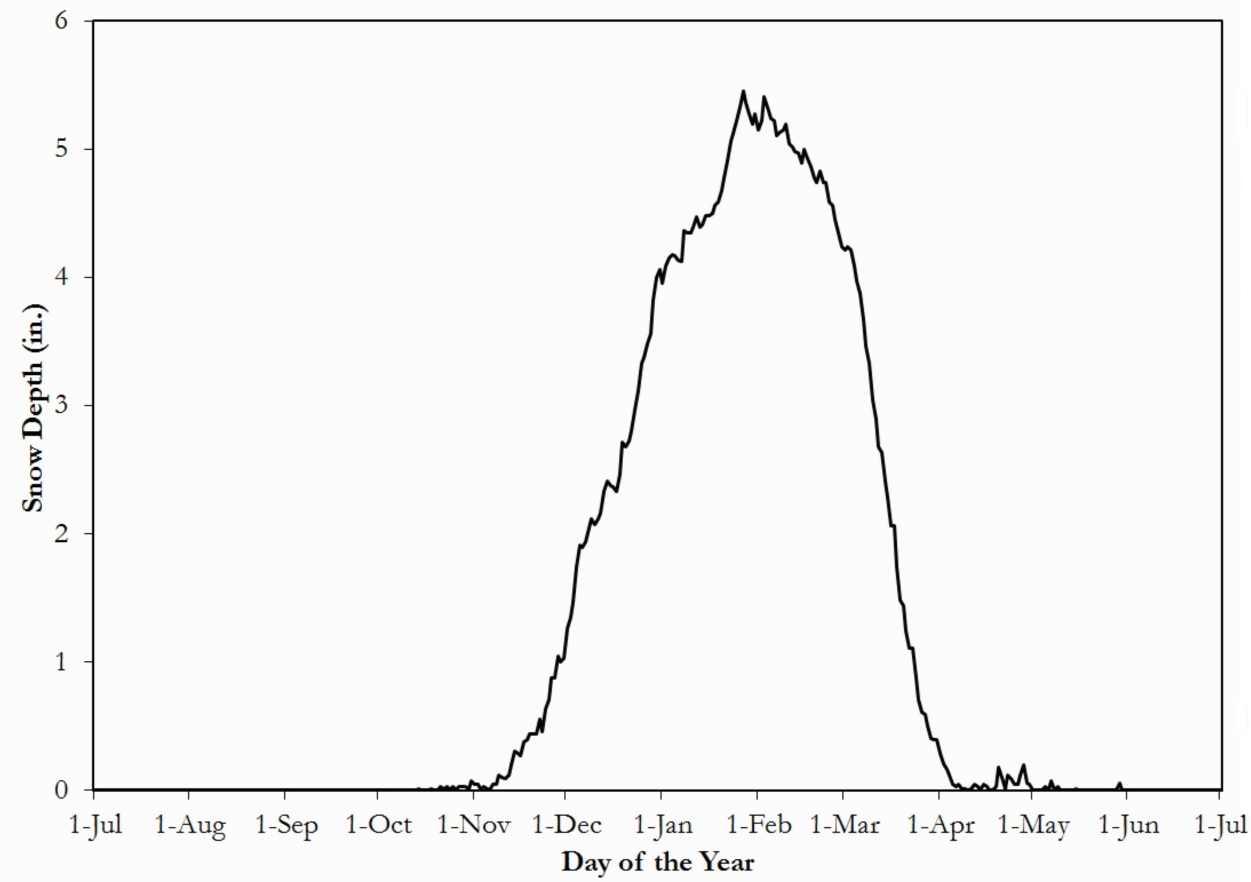

Figure 70. Average daily snow depth for CFA from 1950-2015 as a function of day of the year.

Table 35. Average date on which snow depth >0.1, >1.0, >2.0, >3.0, >4.0, and >5.0 in. began and ended, and the number of days between the beginning and ending date at CFA.

Depth (in.)	Beginning of Period	Ending of Period	Length of Period (days)
>0.1	09 Nov	04 Apr	147
>1.0	28 Nov	23 Mar	116
>2.0	08 Dec	17 Mar	100
>3.0	24 Dec	10 Mar	77
>4.0	30 Dec	04 Mar	65
>5.0	23 Jan	12 Feb	21

Note: Data period of record spans March 1950 through December 2015.

were December 24 through March 10, a period of 77 days. And for snow depths ≥5 in., the dates were January 23 through February 12, a period of 21 days.

Table 36 shows the longest periods at CFA with continuous snow cover of 1 in. or greater during the period of record. The longest period was 131 days, with five other periods of 120 days or more. These periods all began in mid to late November and extended into late March or early April. There were another 9 periods of 90 days to 120 days with continuous snow cover of ≥ 1 in. on the ground. In all, there were 14 years (approximately 25% of the years) when snow 1 in. or greater in depth covered the ground for three or more months during the 66-year period of record.

Table 36 also shows the greatest snow depths during the period of record. The 30 in. depth measured on February 23, 1993 was the highest snow depth ever recorded. The snow, in. fact, was 30 in. deep for a continuous period of 10 days, through March 5.

The probability of a snow depth of ≥1, ≥3, ≥5, and ≥10 in. as a function of day of the year is shown graphically in Fig. 71. The probability of a snow depth of ≥1 in. increases from 0 on October 1 to a maximum of 83.1% on January 18. The probability then declines to 0 on May 23. Probability curves for ≥3, ≥5, ≥10 in. depths are skewed, with the maximum probability occurring later in the year for increasing snow depth. This is logical because it takes time to accumulate more snow and then that accumulated snow rapidly melts when the spring thaw occurs. The peak probabilities for ≥3, ≥5, and ≥10 in. snow depths are 70.2, 59.8, and 30.3%, respectively. The dates on which the peak probabilities occur are in order: January 22, February 1, and February 10.

Table 36. Longest periods (≥90 days) at CFA with continuous snow cover of 1.0 in. or greater.

Beginning of Period	Ending of Period	Period Length (days)	Greatest Snow Depth During Period	
			Depth (in.)	Date
25 Nov 1984	04 Apr 1985	131	25	06 Mar 1985
24 Nov 1963	01 Apr 1964	130	12	02 Mar 1964
20 Nov 1983	27 Mar 1984	129	17	16 Feb 1984
22 Nov 1992	26 Mar 1993	125	30	23 Feb 1993
13 Nov 1988	15 Mar 1989	123	16	19 Feb 1989
24 Nov 2001	23 Mar 2002	120	13	03 Jan 2002
20 Nov 2010	11 Mar 2011	112	13	08 Jan 2011
10 Dec 2007	27 Mar 2008	109	20	03 Feb 2008
23 Dec 1951	05 Apr 1952	105	23	11 Mar 1952
11 Nov 1985	22 Feb 1986	104	14	05 Jan 1986
01 Dec 1970	12 Mar 1971	102	11	15 Jan 1971
22 Nov 1993	27 Feb 1994	98	6	21 Feb 1994
29 Nov 1982	04 Mar 1983	96	13	23 Dec 1982
13 Dec 2008	15 Mar 2009	93	17	25 Dec 2008
18 Dec 1977	17 Mar 1978	90	16	12 Feb 1978

Note: Data period of record spans March 1950 through December 2015.

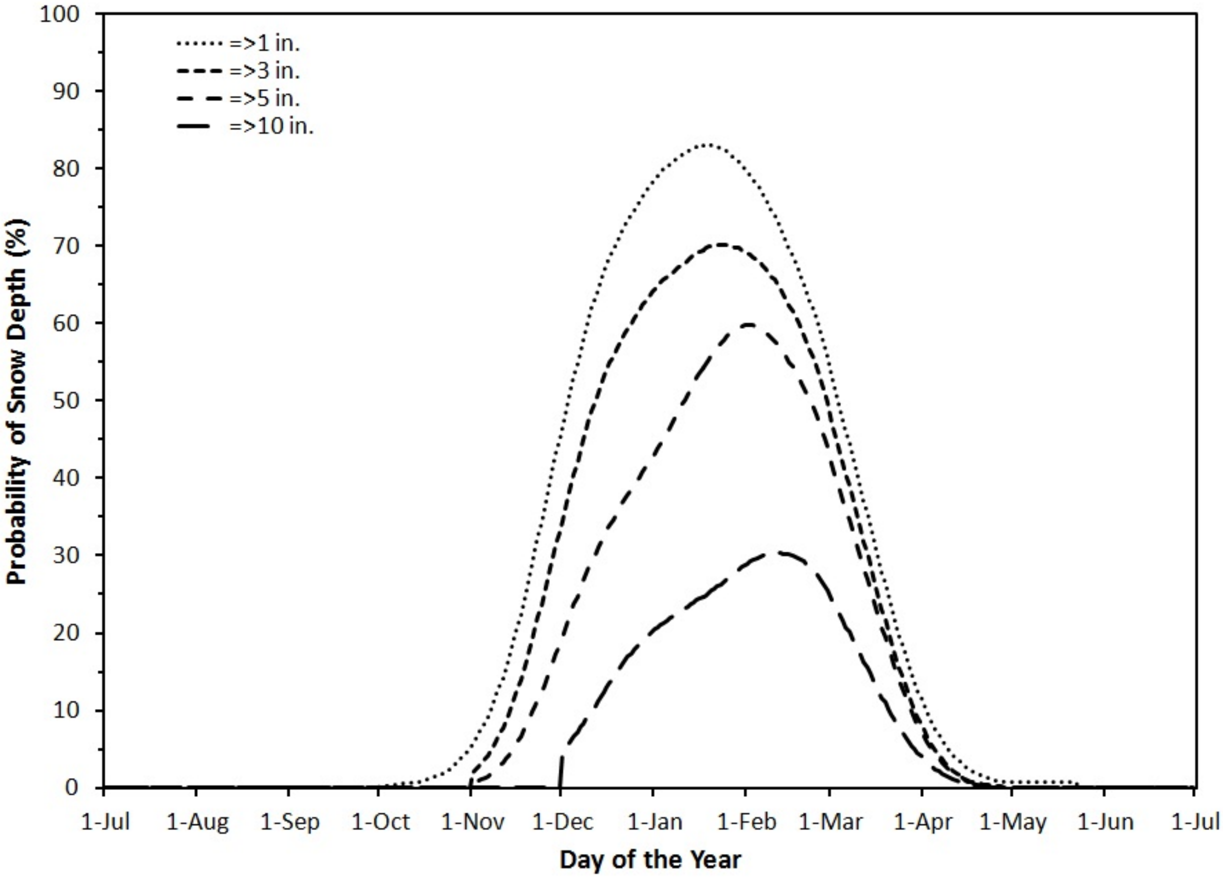

Figure 71. Probability of a snow depth of ≥1, ≥3, ≥ 5, and ≥10 in. at CFA, normalized for the 30 year period of 1981-2010.

Monthly Snow Depth

The monthly averages and extremes of snow depths are listed in Table 37. January and February were the months with the most snow on the ground, with an average depth of about 4.7 in and 5.0 in. The highest average monthly snow depth ever recorded was 25.1 in., and occurred during February 1993. Both January and March have also had snow depths greater than or equal to 20 in. Bare ground has been observed in every month of year at CFA.

Annual Snow Depth

The annual average, maximum, and minimum snow depths are also listed in Table 37. The annual average snow depth was 1.2 in. The maximum average annual snow depth was 5.6 in., which occurred in 1993. The minimum annual average snow depth was 0.1 in. The year in which the lowest average snow depth occurred was 1954.

Table 37. Monthly and annual average snow depths on the ground, and extreme snow depths for CFA.

	Average (in.)	Maximum (in.)	Minimum (in.)
January	4.7	20.4	0.0
February	5.0	25.1	0.0
March	2.2	20.0	0.0
April	0.1	0.9	0.0
May	0.0	0.2	0.0
June	0.0	0.0	0.0
July	0.0	0.0	0.0
August	0.0	0.0	0.0
September	0.0	0.0	0.0
October	0.0	0.3	0.0
November	0.4	3.6	0.0
December	2.5	12.0	0.0
ANNUAL	1.2	5.6	0.1

Note: Data period of record spans March 1950 through December 2015.

ATMOSPHERIC MOISTURE

Atmospheric moisture is a meteorological parameter that is important in facility design and operation. Atmospheric moisture has been continuously monitored at the INL since 1950. The primary observation location has been CFA. Originally, atmospheric moisture was recorded manually as hourly wet bulb temperatures. After discontinuing the hourly observations, atmospheric moisture was recorded as relative humidity on a chart using a hygrothermograph. Atmospheric humidity has also been recorded as dew point temperature with a chilled mirror. Since 1993, relative humidity has been recorded automatically at every NOAA/INL Mesonet tower as a five-minute average. Although the period of record for atmospheric moisture extends from 1950 to 2015, the discussion will be limited to the most recent period of record (1994-2015) because it is the most easily accessible for data analysis.

The following discussion of atmospheric moisture pertains to the atmospheric moisture content observed at CFA. Average atmospheric moisture varies only slightly over the relatively short distances within the INL. Hence, the moisture discussions derived from data collected at CFA are generally applicable to the entire INL.

Wet bulb temperature, relative humidity, dew point temperature, and other measures of atmospheric moisture are all related variables, i.e., each variable can be converted into the other using an appropriate formula along with other jointly measured variables such as atmospheric pressure and air temperature. Each atmospheric moisture variable has a particular application in building and equipment design and engineering. The following discussion of atmospheric moisture will begin with relative humidity.

Relative Humidity

The primary measurement of atmospheric moisture for the most recent period of record was relative humidity. It the most easily measured parameter of all the atmospheric

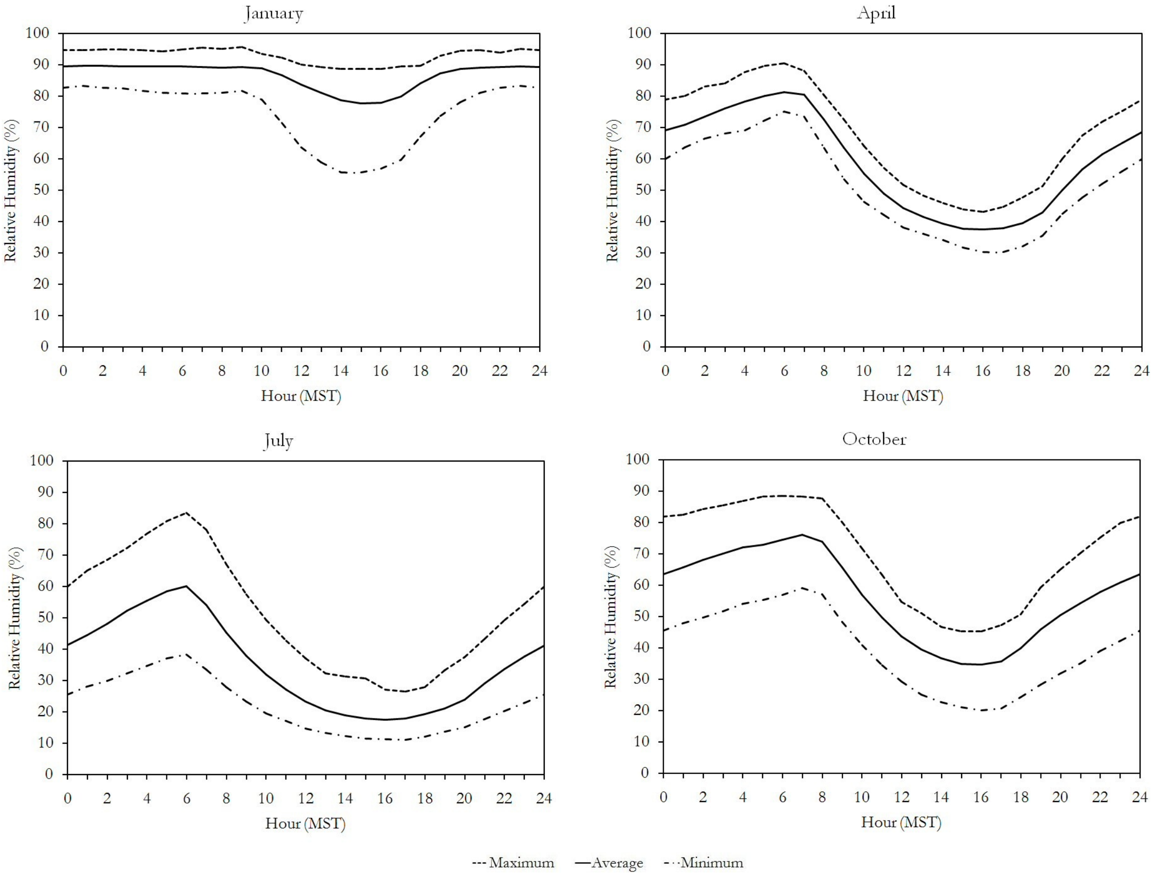

Figure 72. Diurnal depiction of hourly average, maximum, and minimum relative humidity values at CFA for winter, spring, summer, and fall represented by the months of January, April, July, and October, respectively.

moisture parameters in an automated mesonet like the NOAA/INL Mesonet. The period of this most recent record spans 22 years.

Relative humidity is defined as the ratio of the amount of water vapor contained in a given volume of air to the amount required for saturation at the same temperature and pressure. Relative humidity varies with changes in temperature and pressure. Pressure changes are small in comparison to temperature changes. Therefore, relative humidity is almost entirely a function of air temperature. It varies most dramatically on a diurnal basis, but also from day to day and seasonally.

Graphs of the diurnal response of relative humidity in each of the four seasons, represented by the months of January (winter), April (spring), July (summer), and October (autumn), are shown in Fig. 72. Also shown are the mean maximum and minimum hourly relative humidity values for the same months. The four graphs show many similar trends. The highest diurnal relative humidity values were generally observed near sunrise, while the lowest values were observed in the mid-afternoon. Relative humidity peaks and valleys always occurred in conjunction with the minimum and maximum diurnal air temperatures, respectively.

Looking at other features, relative humidity showed the smallest diurnal response and also the highest average values in the winter months. The hourly average relative humidity during this season was nearly flat at approximately 90% for more than 14 hours of the day, between 2000 and 1000 hours MST. It declined to approximately 78% in mid-afternoon. The range between the average hourly maximum and the average hourly minimum relative humidity was smallest in the winter months for most of the hours of the day. For more than 15 hours a day the range was less than 15%. The maximum range was about 33% in the mid-afternoon.

The largest diurnal response and also the lowest average values of relative humidity were observed in the summer months. Average hourly relative humidity reached a peak of 60% near sunrise and declined to a minimum of about 17% in the mid-afternoon. After about 1600 hours MST, relative humidity began to increase until the peak at sunrise. The widest range between average daily maximum and minimum relative humidity in the summer was observed near sunrise at a value of about 45%. Recall that the widest range in the winter was observed at midday.

Table 38 contains a list of five-minute average extreme maximum and minimum relative humidity values summarized by month and annually. Maximum five-minute relative humidity values of 100% were observed in every month of the year. These maximums of 100% humidity were not single events, but instead were compound five-minute periods thereby indicating proper equipment response and not a temporary instrument malfunction. The extreme lowest relative humidity observed was 3.8%, which was recorded on July 11, 2003 at 1640 MST. Such a low value is indicative of the very dry conditions that can be experienced in the summer and early autumn months at the INL in particular, and across the entire ESRP in general.

A summary of the average daily maximum and minimum relative humidity values for each month are given in Table 39. The monthly maximum and minimum values of the monthly averages of daily maximum and minimum relative humidity for the entire period of record are also presented in Table 39. Average daily maximum relative humidity in January and December is 94%, the highest of any of months. In August, the lowest average daily maximum humidity was observed at 65%. As mentioned earlier, the spread in between the daily average maximum and minimum relative humidity was largest in the late spring, summer, and early fall. The month with the largest average spread between maximum and minimum daily relative humidity was April.

Monthly and annual relative humidity averages, mean maximums, and mean minimums for CFA are listed in Table 38. Commensurate with the data shown in Fig. 72, the highest monthly relative humidity was observed in January, when the average was 86%. The range between the maximum and minimum was 24%. The months with the lowest average relative humidity were July and August with 35%. In July, the range between the maximum and minimum average relative humidity was 52%. The month with the largest range was April with a range of 57%.

The average annual relative humidity was 60%. The maximum annual average relative humidity was 83%, while the minimum annual average relative humidity was 37%.

Table 38. Monthly and annual averages and five-minute extremes of relative humidity for CFA.

	Monthly Values			Five-Minute Average Extreme Values	
	Average (%)	Highest Average (%)	Lowest Average (%)	Maximum (%)	Minimum (%)
January	86	94	70	100	19
February	81	93	62	100	9
March	69	91	43	100	9
April	56	86	29	100	8
May	51	82	26	100	7
June	45	76	21	100	5
July	35	66	14	100	4
August	35	65	14	100	5
September	42	72	20	100	5
October	57	83	30	100	8
November	75	92	48	100	10
December	84	94	67	100	14
ANNUAL	60	83	37	100	4

Note: Data period of record spans January 1994 through December 2015.

Table 39. Monthly and annual averages of daily maximum and minimum relative humidity for CFA.

	Average		Highest Average		Lowest Average	
	Maximum (%)	Minimum (%)	Maximum (%)	Minimum (%)	Maximum (%)	Minimum (%)
January	94	70	99	81	89	50
February	93	62	100	77	87	40
March	91	43	99	61	79	22
April	86	29	96	37	74	20
May	82	26	97	44	66	15
June	76	21	96	43	54	13
July	66	14	87	22	42	10
August	65	14	87	29	54	11
September	72	20	90	29	48	14
October	83	30	93	39	65	18
November	92	48	99	65	86	36
December	94	67	99	82	87	44
ANNUAL	83	37	92	44	77	32

Note: Data period of record spans January 1994 through December 2015.

Dew Point Temperature

The period and place of record for this discussion of dew point temperature are the same as for relative humidity, i.e., January 1994 through December 2015, and CFA, respectively. It is perhaps a more useful measure of atmospheric moisture than relative humidity. Dew point temperature is defined as the temperature to which air must be cooled at constant pressure for saturation to occur and is less responsive to the daily air temperature cycle than relative humidity.

The diurnal trend of dew point temperatures for winter, spring, summer, and autumn seasons is shown in Fig 73. This figure shows the average dew point temperature for each hour of the day for a given month for the entire period of record. It also shows the highest and lowest hourly average for each hour of the day for a given month. The largest diurnal change in dew point temperature was observed in the winter, where the range between the average daily maximum and the average daily minimum was about 10 °F. The trend in the winter was for dew point temperature to begin to rise at sunrise and to reach a maximum near sunset. It then declined through the long winter night to the minimum near sunrise. In the summer months, the range between the average daily maximum and the average daily minimum

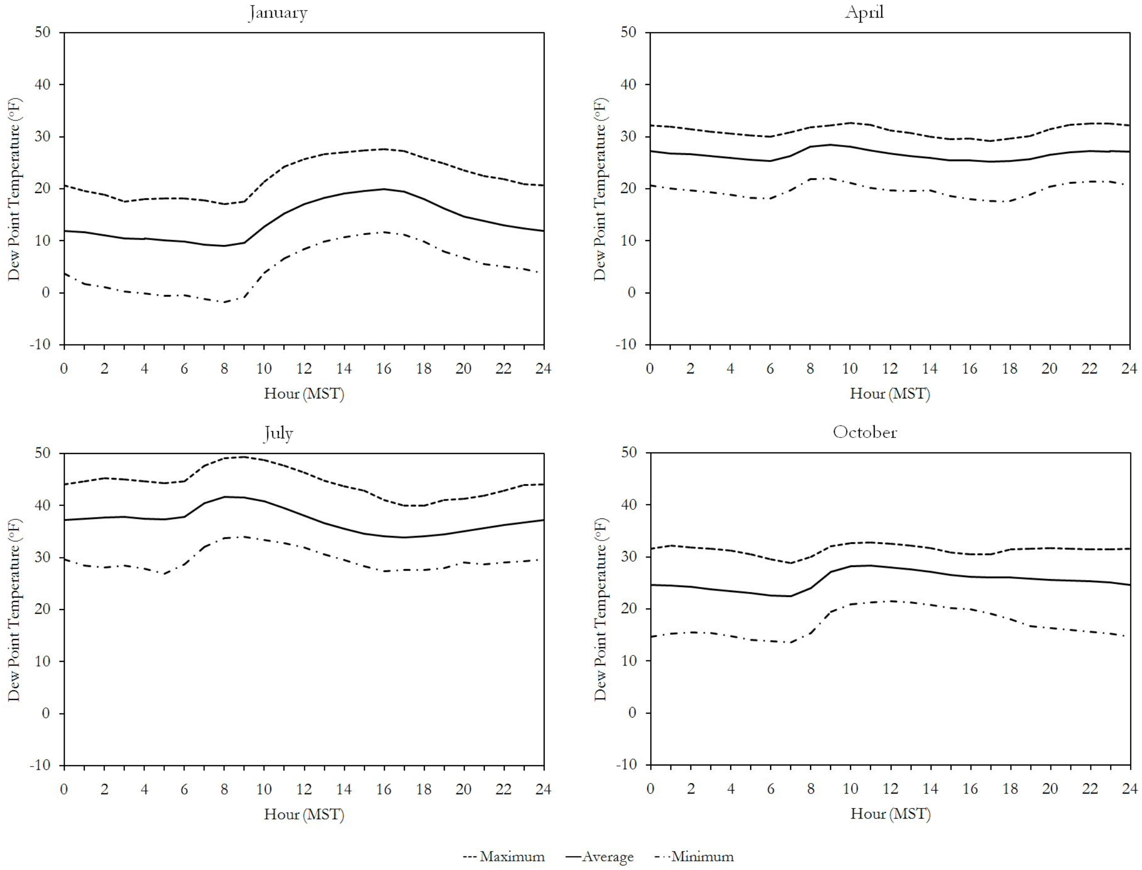

Figure 73. Diurnal depiction of hourly average, maximum, and minimum dew point temperatures at CFA for winter, spring, summer, and fall represented by the months of January, April, July, and October, respectively.

was approximately 8 °F. However, the time of the daily maximum and minimum were shifted in time compared with the winter months. In the summer, the maximum dew point temperature was reached about three hours after sunrise, while the minimum dew point temperature was reached in the late afternoon about 5 hours before sunset. The spring and autumn months exhibited characteristics of both winter and summer months but with the range between the daily minimum and the daily maximum being only 3 to 4 °F. The spring months also exhibited two minima during the day, although the evening minimum was quite subtle.

Table 40 contains a summary of the five-minute averaged extreme maximum and minimum dew point temperatures stratified by month. The lowest five-minute average dew point temperature was –39.0 °F, which was recorded on February 3, 1996 at 0545 hours MST. Later that same year, the highest five-minute average dew point temperature was recorded on July 29 at 1600 hours MST at 66.1 °F. Interestingly, dew point temperature has been as high as 45.1 °F in January (a winter month) and as low as 0.3 °F in August (a summer month). These values were recorded on January 2, 2007 at 0305 hours and on August 16, 2003 at 1945 hours, respectively. From this summary of extremes, it is reasonable to assume that dew point temperature at CFA would likely be bounded by -50 and 70 °F. Monthly and annual averages of dew point temperature observations are also given in Table 40. The average monthly dew point temperature ranged from a low of 13.6 °F in January to a high of 37.3 °F in July. The lowest single monthly average was recorded in January at 3.0 °F in 2002. The highest single monthly average was recorded in June at 44.8 °F in 1995. The annual average dew point temperature was 25.8 °F and ranged from a low of 22.1 °F in 2002 to a high of 30.7 °F in 1998.

Table 40. Monthly and annual averages and extremes of dew point temperatures for CFA.

	Monthly Values			Five-Minute Extreme Values	
	Average (°F)	Highest Average (°F)	Lowest Average (°F)	Maximum (°F)	Minimum (°F)
January	13.6	22.0	3.0	45.1	-37.3
February	16.1	25.7	3.9	42.7	-39.0
March	22.7	26.8	17.6	49.6	-21.9
April	25.4	30.9	19.7	49.1	-10.0
May	31.5	38.0	25.4	62.0	-6.3
June	35.4	44.8	26.9	61.8	-1.3
July	37.3	44.1	30.3	66.1	1.5
August	34.9	46.5	29.3	64.6	0.3
September	30.5	43.5	21.9	63.6	-3.7
October	26.3	34.4	17.9	56.0	-11.7
November	20.9	27.1	15.6	49.0	-29.8
December	14.6	20.9	7.8	44.1	-37.4
ANNUAL	25.8	30.7	22.1	66.1	-39.0

Note: Data period of record spans January 1994 through December 2015.

Wet Bulb Temperature

Wet bulb temperature is defined as the lowest temperature to which air can be cooled by evaporating water. For this reason, wet bulb temperatures are frequently used as a design criterion for evaporative cooling systems. Wet bulb temperature can be calculated from values of relative humidity, air temperature, and barometric pressure. The data for this discussion come from the database used for the relative humidity and dew point temperature discussions.

The diurnal trend of wet bulb temperatures for winter, spring, summer, and autumn seasons is shown in Fig 74. This figure shows the average wet bulb temperature for each hour of the day for a given month for the entire period of record. It also shows the highest and lowest hourly average for each hour of the day for a given month. In many respects, the traces look similar to inverted relative humidity traces discussed previously. The general trend in every season was for the wet bulb temperature to begin rising at about sunrise, with a maximum wet bulb temperature observed in the mid-afternoon. Wet bulb temperature then declined to a minimum near sunrise. The largest diurnal change in wet bulb temperature was observed in the fall, when the range between the average daily maximum

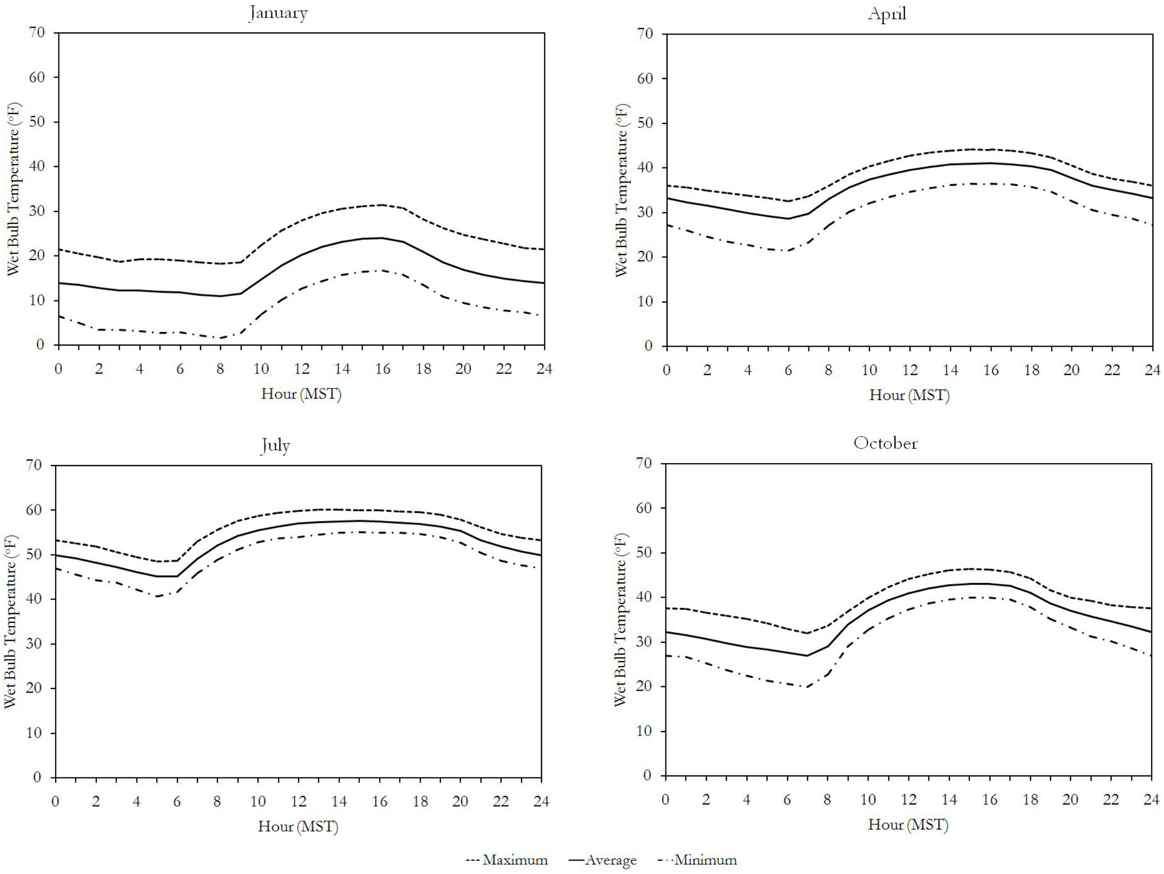

Figure 74. Seasonal hourly average, maximum, and minimum wet bulb temperatures for CFA, represented by the months of January, April, July, and October for winter, spring, summer, and autumn, respectively.

and the average daily minimum was about 16 °F. The range in the other months was about 13 °F.

Table 41 contains five-minute average maximum and minimum wet bulb temperatures stratified by month. The lowest five-minute average wet bulb temperature was -31.3 °F, and was recorded on February 3, 1996 at 0520 hours MST. The highest five-minute average wet bulb temperature was 67.4 °F which was recorded on July 29, 1996. It is interesting to note that both the minimum and maximum wet bulb temperatures occurred in the same year. Although 67.4 °F temperature was relatively high, the greatest cooling efficiency was normally observed during the summer months. During this time period, the potential for cooling was the greatest, i.e., the dry bulb/wet bulb temperature difference was the greatest.

Table 42 contains the monthly and annual averages of the daily maximum and minimum wet bulb temperatures. It also contains the monthly and annual extreme averages of the daily maximum and minimum wet bulb temperatures. The largest monthly average daily range was observed in January with a value of 20.4 °F. The smallest monthly average daily range was observed in June with a value of 15.6 °F. Thus, the summer months exhibited the smallest daily range on average, while the winter months exhibited the largest daily range. The winter months also exhibited the widest swings between the lowest average minimum and the highest average maximum, which is as large as 41.9 °F.

Monthly and annual averages of wet bulb temperature observations are also given in Table 41. The average monthly wet bulb temperature ranged from a low of 15.3 °F in January to a high of 52.9 °F in July. The lowest single monthly average was recorded in January 2013 at 6.5 °F. The highest single monthly average was recorded in July 2006 at 55.7 °F. The annual average wet bulb temperature was 35.1 °F and ranged from a low of 32.0 °F in 2002 to a high of 38.1 °F in 2001.

Table 41. Monthly and annual averages and extremes of hourly wet bulb temperatures for CFA.

	Monthly Values			Five-Minute Extreme Values	
	Average (°F)	Highest Average (°F)	Lowest Average (°F)	Maximum (°F)	Minimum (°F)
January	15.3	22.7	6.5	47.9	-30.3
February	18.9	28.1	7.0	48.2	-31.3
March	29.1	32.2	21.7	50.9	-17.7
April	35.4	38.2	30.0	56.0	4.8
May	42.4	46.4	38.1	66.0	8.8
June	48.1	51.5	45.5	66.2	19.8
July	52.9	55.7	49.8	67.4	24.2
August	50.8	54.1	48.0	65.6	21.3
September	44.4	50.9	40.3	65.6	11.3
October	35.8	42.4	30.8	57.2	-6.9
November	25.9	31.1	19.5	52.1	-23.5
December	17.3	23.4	8.9	46.8	-30.6
ANNUAL	35.1	38.1	32.0	67.4	-31.3

Note: Data period of record spans January 1994 through December 2015.

Table 42. Monthly and annual averages of daily maximum and minimum wet bulb temperatures for CFA.

	Average		Highest Average		Lowest Average	
	Maximum (°F)	Minimum (°F)	Maximum (°F)	Minimum (°F)	Maximum (°F)	Minimum (°F)
January	24.6	4.2	32.1	13.5	17.9	-5.7
February	27.8	8.1	36.2	19.3	19.2	-5.7
March	36.8	19.1	40.0	23.7	29.8	10.9
April	42.4	25.4	45.1	30.2	38.0	19.0
May	48.8	32.9	53.1	37.8	44.0	29.5
June	54.2	38.6	57.4	42.8	52.2	34.1
July	59.0	43.1	61.3	46.5	56.5	38.4
August	57.5	40.6	59.3	48.0	54.8	36.7
September	52.3	33.1	57.3	41.3	49.0	27.6
October	44.5	24.6	49.4	32.9	40.8	17.4
November	35.0	15.1	40.4	20.5	28.5	7.6
December	26.0	6.5	30.9	14.1	17.9	-2.7
ANNUAL	42.8	24.7	45.1	28.3	40.3	20.4

Note: Data period of record spans January 1994 through December 2015.

Mixing Ratio

Mixing ratio is a moisture parameter that is conserved within a fixed volume of air unless net condensation or evaporation is occurring within the volume. It is the mass of water vapor per unit mass of dry air, normally expressed in units of grams of water vapor per kilogram of dry air. The maximum value of the mixing ratio corresponding to 100% relative humidity is called the saturation mixing ratio. Because higher temperatures support much higher evaporation rates, the saturation mixing ratio increases rapidly with temperature. For comparison purposes, the saturation mixing ratio is 34.5 g kg^{-1} at 87.7 °F, which is the July average maximum air temperature at CFA, while at 5.0 °F, which is the average minimum air temperature in January at CFA, the saturation mixing ratio is 1.4 g kg^{-1}. At 42.4 °F, which is the annual average air temperature at CFA, the saturation mixing ratio is 6.8 g kg^{-1}. The mixing ratio discussion below covers the same time period as that of the preceding discussions of atmospheric moisture variables, from 1994 through 2015.

Graphs of the diurnal trend of mixing ratio, prepared in the same manner as for relative humidity, dew point temperature, and wet bulb temperature, are presented in Fig. 75. In general, the diurnal traces of mixing ratio were similar to that of dew point. In the autumn, winter, and spring months, the traces were nearly flat throughout the day. In July, there was a maximum mixing ratio observed at around 0800-0900 hours MST, and a minimum mixing ratio was observed around 1700 hours MST. The difference between the daily maximum and minimum in July was approximately 3.0 g kg^{-1}. The seasonal differences are described in greater detail below.

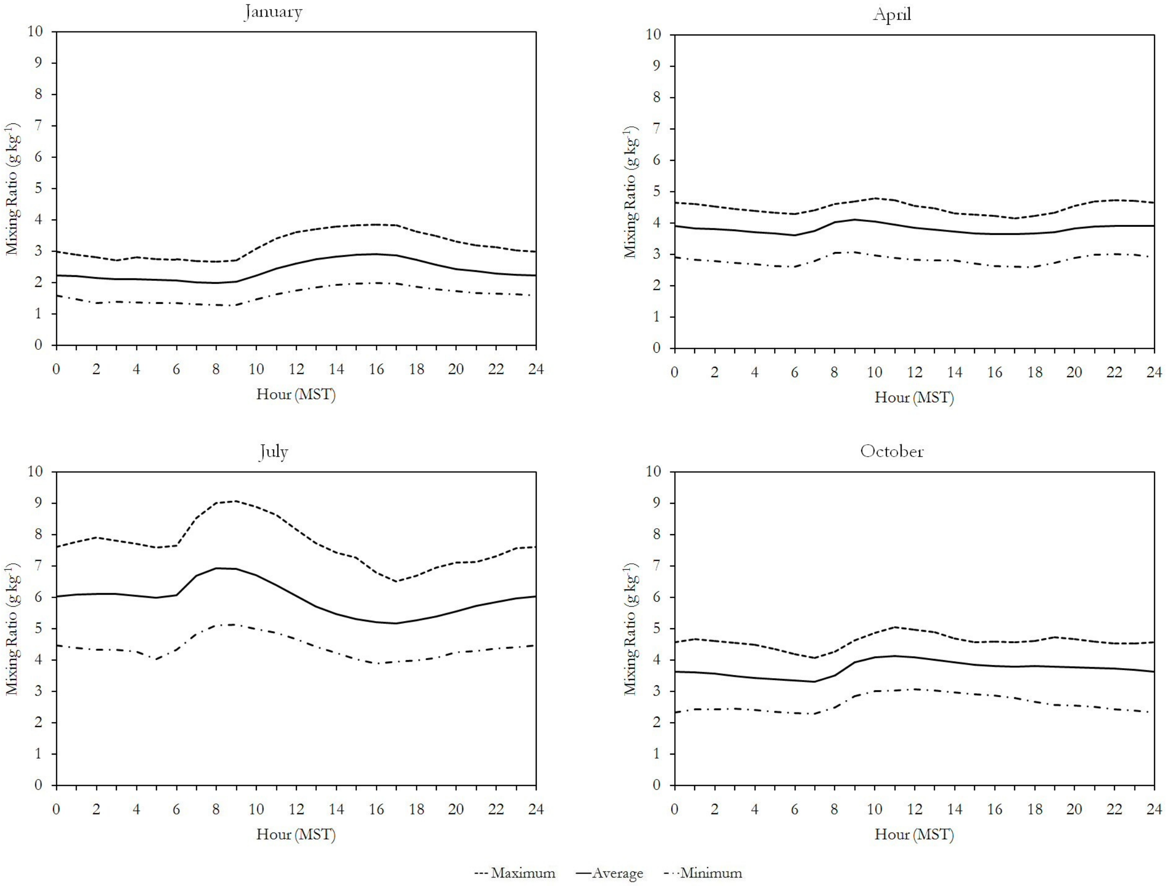

Figure 75. Seasonal hourly average, maximum, and minimum mixing ratios for CFA, represented by the months of January, April, July, and October for winter, spring, summer, and autumn, respectively.

Table 43 contains five-minute average maximum and minimum mixing ratios stratified by month. The lowest five-minute average mixing ratio was 0.15 g kg^{-1}. The highest five-minute average mixing ratio was 16.5 g kg^{-1}. The times of occurrence of these two extremes were the same as for dew point temperature, i.e., February 3, 1996 at 0545 hours MST and July 29, 1996 at 1600 hours MST, respectively.

Monthly and annual averages of mixing ratio observations are also given in Table 43. The average monthly mixing ratio ranged from a low of 2.4 g kg^{-1} in January to a high of 6.1 g kg^{-1} in July. The lowest single monthly average was recorded in January and February at 1.6 g kg^{-1}. The highest single monthly average was recorded in June and July at 7.8 g kg^{-1}. The times of occurrence of these two extremes were the same as the monthly dew point temperature extremes. The annual average mixing ratio was 4.0 g kg^{-1} and ranged from a low of 3.4 g kg^{-1} in 2002 to a high of 4.9 g kg^{-1} in 1995.

Table 43. Monthly and annual averages and extremes of hourly mixing ratios for CFA.

	Monthly Values			Five-Minute Extreme Values	
	Average ($g\ kg^{-1}$)	Highest Average ($g\ kg^{-1}$)	Lowest Average ($g\ kg^{-1}$)	Maximum ($g\ kg^{-1}$)	Minimum ($g\ kg^{-1}$)
January	2.4	3.2	1.6	7.7	0.16
February	2.6	3.7	1.6	6.9	0.15
March	3.3	3.9	2.7	9.1	0.37
April	3.7	4.5	2.8	9.0	0.70
May	4.8	6.0	3.7	14.6	0.82
June	5.6	7.8	3.9	14.3	1.08
July	6.1	7.8	4.7	16.5	1.21
August	5.6	8.3	4.4	15.8	1.18
September	4.7	7.6	3.4	15.1	0.94
October	3.9	4.5	2.7	11.6	0.63
November	3.1	3.8	2.5	8.8	0.25
December	2.5	3.1	1.8	7.4	0.16
ANNUAL	4.0	4.9	3.4	16.5	0.15

Note: Data period of record spans January 1994 through December 2015.

Vapor Pressure Deficit

The fifth and final atmospheric moisture variable to be presented here is a derived parameter. It is called the vapor pressure deficit (VPD) and is used to describe the evaporative demand potential. VPD is the major driving force for evaporating water from plants and bodies of water.

Each gas making up an air sample exerts its own partial pressure, and the partial pressure of water vapor is called the vapor pressure. As with mixing ratio, the vapor pressure at 100% relative humidity is called the saturation vapor pressure. VPD is simply the difference between the saturation vapor pressure and the actual vapor pressure at the current air temperature and pressure. It can be easily calculated from air temperature and relative humidity.

Graphs of the diurnal trend of VPD, prepared in the manner previously described for relative humidity, dew point temperature, wet bulb temperature, and mixing ratio are shown in Fig. 76. Like its cousin, wet bulb temperature, the diurnal curve followed the inverse curve of relative humidity. However, the winter curve was less amplified and the summer curve was greatly amplified. In the winter, VPD was nearly zero for much of the day and rose to a maximum of only about 1.2 mb for just a few hours of the day. In the summer, VPD exhibited a minimum of 5.7 mb at 0600 hours MST, and a maximum of 37.1 mb, which was a range of 31.4 mb. The minimum and maximum coincided approximately with the diurnal minimum and maximum air temperatures. It is obvious from these graphs that atmospheric evaporative demand is very low in the winter, but very high in the summer. Furthermore, the evaporative demand may be low during the summer nights, but it is far from zero. Therefore, evaporative loss from water bodies during the summer months would be expected even at night. The spring and autumn months were hybrids of the

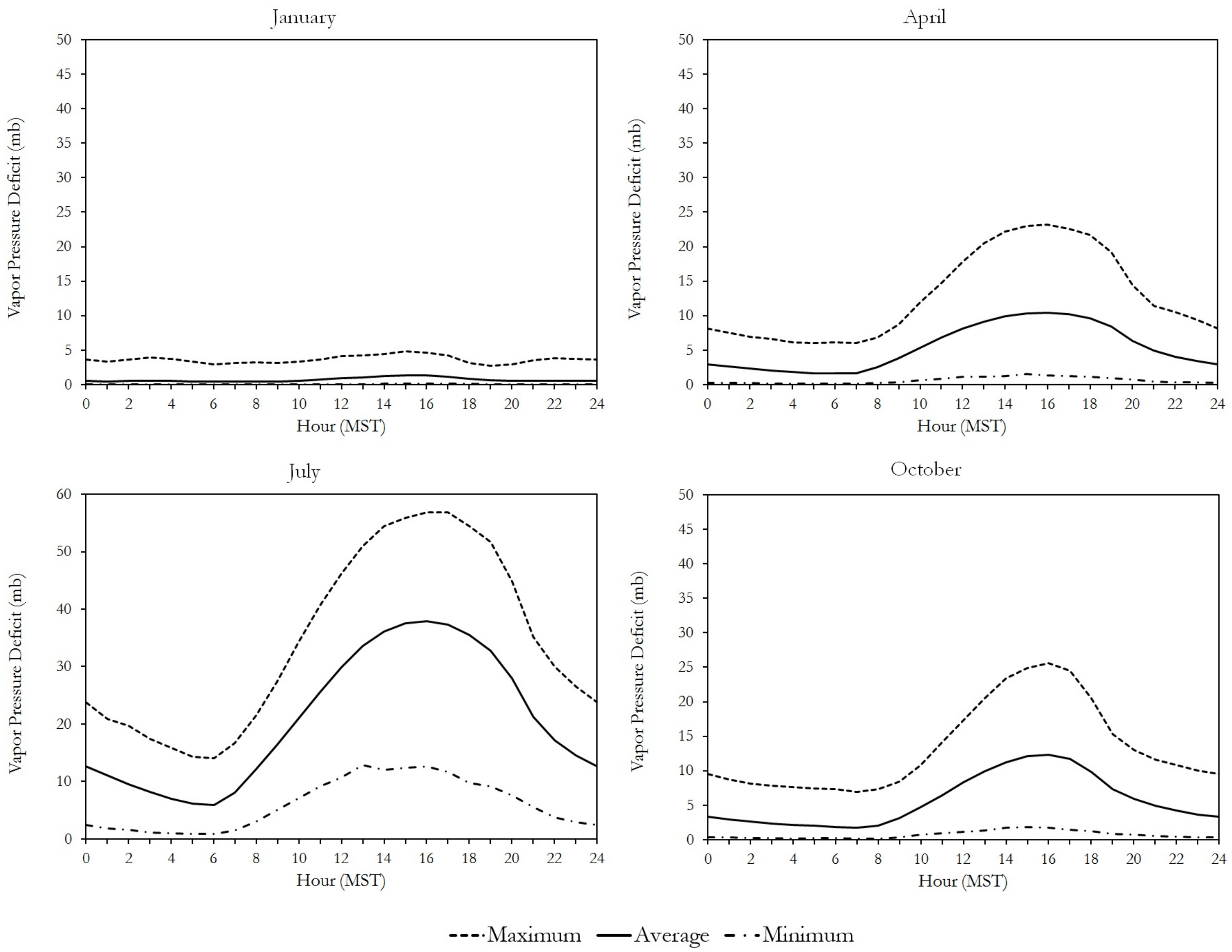

Figure 76. Seasonal hourly average, maximum, and minimum vapor pressure deficits for CFA, represented by the months of January, April, July, and October for winter, spring, summer, and autumn, respectively.

winter and summer characteristics. VPD was small during the night, but grew to about 12 mb during the day.

Another characteristic that was observed in the graphs of Fig. 76 concerns the range around the daily average diurnal curve. The spread was the smallest in the winter followed next by the spring months and then by the autumn months. The summer months exhibited the widest spread around the daily average. At around 1600 hours MST, near the time of the maximum daily air temperature in the summer, the spread was approximately 45 mb.

Table 44 contains five-minute average maximum and minimum vapor pressure deficits stratified by month. The lowest five-minute average vapor pressure deficit was 0 mb and was observed in every month. This observation was consistent with the values of relative humidity, which showed a maximum of 100% during a 5-minute period in every month of the year. The highest five-minute average vapor pressure deficit was 66.1 mb and occurred on July 13, 2002 at 1600 hours MST.

Monthly and annual averages of vapor pressure deficit observations are also given in

Table 44. Monthly and annual averages and extremes of hourly vapor pressure deficits for CFA.

	Monthly Values			Five-Minute Extreme Values	
	Average (mb)	Highest Average (mb)	Lowest Average (mb)	Maximum (mb)	Minimum (mb)
January	0.7	1.2	0.3	8.6	0.0
February	1.1	2.5	0.4	10.8	0.0
March	2.8	5.7	1.1	22.4	0.0
April	5.3	7.6	3.8	33.3	0.0
May	8.4	12.6	4.9	50.3	0.0
June	13.3	18.9	6.5	58.1	0.0
July	20.7	28.6	13.6	66.1	0.0
August	18.5	22.2	11.3	61.1	0.0
September	12.0	15.4	10.1	49.7	0.0
October	5.6	8.7	3.2	40.7	0.0
November	2.0	3.7	1.2	18.3	0.0
December	0.9	1.6	0.2	8.8	0.0
ANNUAL	7.8	9.4	6.2	66.1	0.0

Note: Data period of record spans January 1994 through December 2015.

Table 44. The average monthly vapor pressure deficit ranged from a low of 0.7 mb in January to a high of 20.7 mb in July. The lowest single monthly average was recorded in December 2002 at 0.2 mb. The highest single monthly average was recorded in July 2003 at 28.6 mb. The annual average vapor pressure deficit was 7.8 mb and ranged from a low of 6.2 mb in 1995 to a high of 9.4 mb in 2003.

ATMOSPHERIC PRESSURE

Station Pressure

Atmospheric pressure is an important consideration in many phases of design and operations at the INL. Pressure has been recorded nearly continuously at CFA since February, 1950, and is currently measured at 25 NOAA/INL Mesonet locations. The automated CFA record from January 1994 through December 2015 is the basis for the discussion that follows. It should be noted that the atmospheric pressure values in this discussion are the actual measured values at CFA ("station pressure") and are not adjusted to equivalent sea level pressure. The "standard atmosphere" correction for station pressure recorded at CFA's elevation is +5.03 inches of mercury (in. Hg) to yield an equivalent sea level pressure.

The average diurnal trend of barometric pressure is shown in Fig. 77 for winter, spring, summer, and fall seasons, as represented by the months of January, April, July, and October, respectively. The averages were obtained by calculating the mean pressure for all days in a given month for a given hour of the day and then calculating the average pressure over 22 years of record. Also included in the graph are the minimum and maximum hourly average pressure values for each hour of the day. The graphs show a distinct diurnal trend, with a daily high barometric pressure near mid-morning to midday. In the winter, the barometric pressure trace was fairly flat for most of the day except

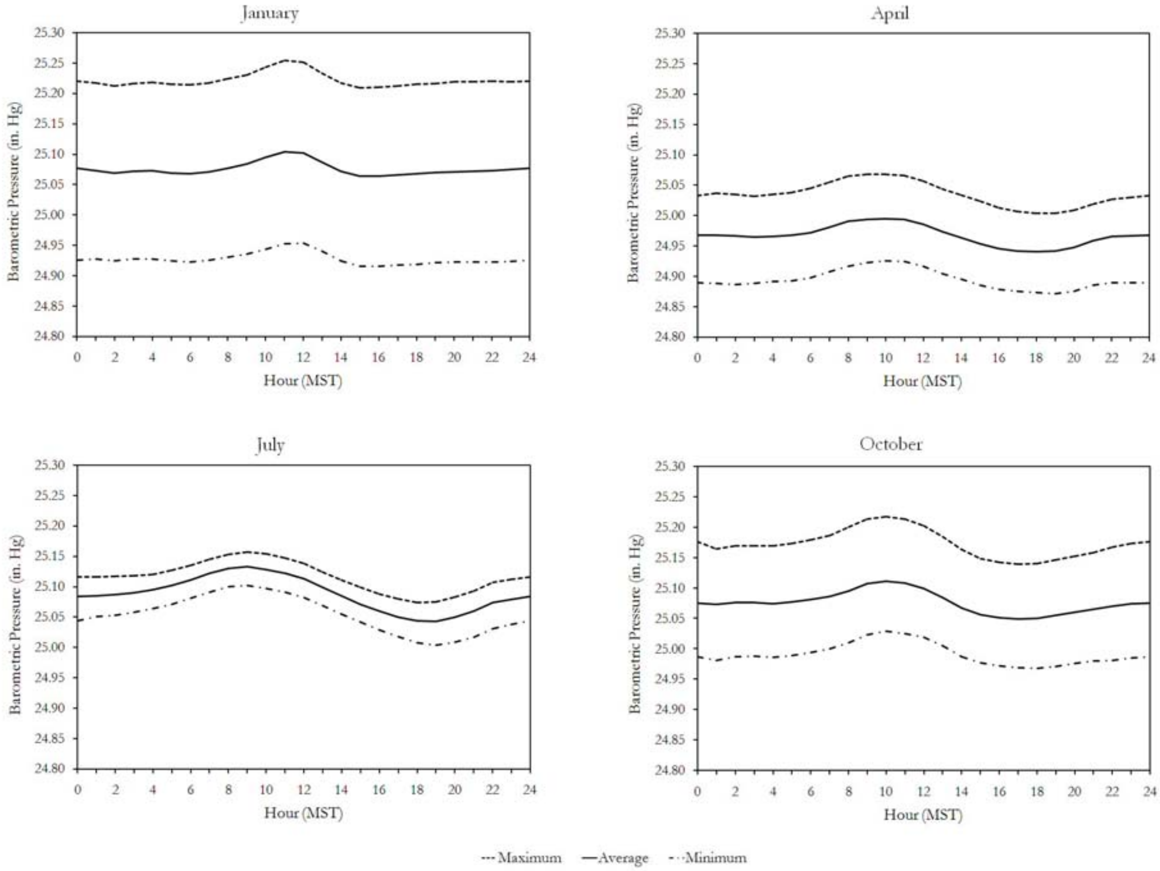

Figure 77. Seasonal hourly average, maximum, and minimum atmospheric pressure values for CFA, represented by the months of January, April, July, and October for winter, spring, summer, and autumn, respectively.

for the period between 900 and 1500 hours MST.

The average rise in barometric pressure was about 0.03 in. Hg. In the summer months, the diurnal barometric pressure trace was much more dynamic with a distinct daily high and low. The daily high occurred at 0900 hours and the daily low occurred at 1900 hours MST. The difference between the daily high and daily low was about 0.09 in. Hg. The spring and autumn months exhibited diurnal patterns that were a mixture of the winter and summer patterns. The difference between the average daily high and the average daily low barometric pressure was between 0.14-0.19 in. Hg. in the spring and autumn.

Another characteristic that was readily apparent in the diurnal barometric pressure graphs (Fig. 77) was the spread between the maximum and minimum hourly averages. These data are also summarized in Table 45 for each month of the year. In the winter, the range was about 0.18 in. Hg. In the summer, the range was much smaller at 0.12 in. Hg. In the spring and autumn months, the range was about 0.16 in. Hg. The seasonal dependence in the range of hourly barometric pressure values was largely a function of the passage of synoptic weather systems and the resultant barometric pressure changes. These passages occurred with greater frequency and with greater barometric pressure changes in the winter than in the summer. The

Table 45. Monthly and annual atmospheric station pressure[a] averages and daily extremes, and greatest 24-hr. and 1-hr. pressure changes for CFA[b].

Month	Monthly Average (in. Hg)	Average Daily Maximum (in. Hg)	Average Daily Minimum (in. Hg)	Extreme Daily Maximum (in. Hg)	Extreme Daily Minimum (in. Hg)	Greatest 24-Hour Change (in. Hg)	Greatest 1-Hour Change (in. Hg)
January	25.096	25.186	25.003	25.630	24.150	0.705	0.099
February	25.036	25.121	24.947	25.682	24.402	0.679	0.085
March	25.006	25.093	24.914	25.593	24.360	0.739	0.089
April	24.968	25.055	24.880	25.470	24.495	0.631	0.096
May	24.992	25.062	24.921	25.557	24.465	0.491	0.109
June	25.018	25.081	24.948	25.408	24.475	0.494	0.111
July	25.088	25.147	25.024	25.380	24.659	0.444	0.127
August	25.092	25.153	25.025	25.395	24.622	0.389	0.098
September	25.085	25.154	25.013	25.509	24.656	0.500	0.102
October	25.080	25.161	24.997	25.613	24.457	0.609	0.105
November	25.089	25.180	24.993	25.607	24.450	0.721	0.093
December	25.075	25.170	24.977	25.654	24.194	0.830	0.087
ANNUAL	25.052	25.130	24.970	25.682	24.150	0.830	0.127

a. Data are not adjusted to sea level.

b. Data period of record spans January 1994 through December 2015.

summer months were usually quiescent with few frontal passages accompanied by little synoptically induced pressure changes. The spring and autumn months had a greater frequency of frontal passages than the summer months, resulting in a wider range of barometric pressure readings than the summer months.

One additional feature that is illustrated in the graphs of Fig. 77 and Table 45 is the lower average barometric pressure of the spring months compared with the other seasons. April indicated an average barometric pressure about 0.24 in. Hg below the next lowest month. This phenomenon will be discussed in greater detail below.

Table 45 lists the extreme 5-minute average maximum and minimum barometric pressures for each month of the year. These are listed in the columns identified as Extreme Daily Maximum and Extreme Daily Minimum, respectively. The extreme minimum barometric pressure occurred on January 22, 2010 at 0545 hours MST with a value of 24.150 in. Hg. The extreme maximum barometric pressure occurred on February 10, 2007 at 1030 hours MST with a value of 25.682 in. Hg. This range indicates that the extreme limits of station pressure would probably be bounded by 24.00 and 26.80 in. Hg.

An additional analysis of the automatically recorded barometric pressure data of the last 22 years was undertaken to determine the largest 1-hour and 24-hour pressure changes. This analysis is summarized in Table 45. The largest 1-hour pressure change was 0.127 in. Hg. This was recorded on July 22, 2002 between the hours of 1625 and 1725 hours MST. It was the result of a sudden increase in barometric pressure from extremely dense air that came from the outflow of a local thunderstorm. One hour air temperature and relative humidity changes associated with the arrival of the dense air were -17.5 °F and +57%, respectively. A simultaneous wind shift from the north to the southwest accompanied by a wind gust of 55 mph were also observed. Solar radiation also decreased to near zero during the accompanying brief thunderstorm that dropped a total of only 0.10 inches of precipitation.

The largest 24-hour pressure change was 0.830 in. Hg, which was recorded between 0450 hours MST on December 12 and 0450 hours on December 13, 2008. It was the result of a decrease in barometric pressure caused by the approach and subsequent passage of a strong synoptic system. The barometric pressure decrease was associated with 0.05 in. of precipitation. Based on these recorded data, the expected largest 1-hour and 24-hour pressure changes will likely not exceed 0.15 and 1.0 in. Hg, respectively.

Table 45 contains monthly average barometric pressures for the 22-year data period of record between January 1994 and December 2015. The monthly average atmospheric pressure ranged from 24.968 in. Hg in April to 25.096 in. Hg in January. The spring months had the lowest barometric pressure due to the presence of the 500 mb jet stream that caused multiple low pressure systems to pass over the area, as discussed in earlier sections. The annual average station pressure was 25.052 in. Hg. The annual average daily minimum and maximum barometric pressures were 24.970 and 25.130 in. Hg, respectively.

Air Density

The average density of air at the INL is a value of some interest and is related to atmospheric pressure and temperature. It can be computed from the equation of state using average values of air temperature, atmospheric pressure, and atmospheric moisture. Using an average air temperature and atmospheric pressure of 42.4 °F from Table 12 and 25.052 in. Hg from Table 45, respectively, the equation of state yields an average air density value of 0.06604 lbs/ft^3 (1.06 kg/m^3) for CFA.

SOLAR RADIATION

The light from the sun, known as solar radiation, is the main source of the energy for movement of the atmosphere. The recent focus on generating electricity from renewable resources, and from solar energy in particular, makes this an important variable to quantify and describe. Solar radiation can be described in terms of its various components, e.g., global, direct, diffuse, and net. It can also be parameterized in terms of percent possible sunshine, percent sky cover, and day length, among others. Some of these measurements have been quantified at the INL and are described below. The most readily observed solar phenomena are the daily rising and setting of the sun. These phenomena will be presented first, followed by discussions of day length, twilight, and global solar radiation. Net solar radiation will be described in the next section on energy balance measurements.

Sunrise and Sunset

Sunrise and sunset times for CFA are listed in Table 46. These data were obtained from the U.S. Naval Observatory (USNO) web site http://www.usno.navy.mil/USNO/astronomical-applications. The USNO is the official source for astronomical phenomena as well as the official time keeper for the U.S. Government. All times listed in the table are in Mountain Standard Time (MST). Note that sunrise and sunset times on February 29 are considered to be equal to those on February 28. The resulting uncertainty is less than one minute. Local topographic effects and resultant shadows

Table 46. Sunrise and sunset times in Mountain Standard Time for CFA in 2015.

	January		February		March		April		May		June	
Day	Rise h m	Set h m	Rise h m	Set h m	Rise h m	Set h m	Rise h m	Set h m	Rise h m	Set h m	Rise h m	Set h m
1	0805	1706	0748	1743	0708	1820	0614	1858	0525	1934	0454	2006
2	0805	1707	0747	1744	0707	1822	0612	1859	0523	1935	0453	2007
3	0805	1708	0746	1746	0705	1823	0610	1901	0522	1936	0453	2007
4	0805	1709	0745	1747	0703	1824	0608	1902	0521	1937	0452	2008
5	0805	1710	0744	1749	0702	1826	0607	1903	0519	1938	0452	2009
6	0805	1711	0742	1750	0700	1827	0605	1904	0518	1940	0452	2010
7	0805	1712	0741	1751	0658	1828	0603	1905	0517	1941	0451	2010
8	0804	1713	0740	1753	0657	1829	0601	1907	0515	1942	0451	2011
9	0804	1714	0739	1754	0655	1831	0600	1908	0514	1943	0451	2012
10	0804	1715	0737	1755	0653	1832	0558	1909	0513	1944	0451	2012
11	0804	1716	0736	1757	0651	1833	0556	1910	0512	1945	0450	2013
12	0803	1717	0735	1758	0650	1834	0555	1911	0511	1946	0450	2013
13	0803	1718	0733	1759	0648	1835	0553	1913	0509	1947	0450	2014
14	0802	1720	0732	1801	0646	1837	0551	1914	0508	1949	0450	2014
15	0802	1721	0730	1802	0644	1838	0550	1915	0507	1950	0450	2015
16	0801	1722	0729	1803	0642	1839	0548	1916	0506	1951	0450	2015
17	0801	1723	0727	1805	0641	1840	0546	1917	0505	1952	0450	2015
18	0800	1725	0726	1806	0639	1842	0545	1918	0504	1953	0450	2016
19	0800	1726	0724	1807	0637	1843	0543	1920	0503	1954	0450	2016
20	0759	1727	0723	1809	0635	1844	0541	1921	0502	1955	0451	2016
21	0758	1728	0721	1810	0634	1845	0540	1922	0501	1956	0451	2016
22	0757	1730	0720	1811	0632	1846	0538	1923	0501	1957	0451	2017
23	0757	1731	0718	1813	0630	1848	0537	1924	0500	1958	0451	2017
24	0756	1732	0717	1814	0628	1849	0535	1926	0459	1959	0452	2017
25	0755	1734	0715	1815	0626	1850	0534	1927	0458	2000	0452	2017
26	0754	1735	0713	1817	0625	1851	0532	1928	0457	2001	0452	2017
27	0753	1736	0712	1818	0623	1852	0531	1929	0457	2002	0453	2017
28	0752	1738	0710	1819	0621	1854	0529	1930	0456	2003	0453	2017
29	0751	1739			0619	1855	0528	1931	0455	2003	0454	2017
30	0750	1740			0617	1856	0526	1933	0455	2004	0454	2017
31	0749	1742			0616	1857			0454	2005		

Table 46 (Continued).

	July		August		September		October		November		December	
Day	Rise h m	Set h m	Rise h m	Set h m	Rise h m	Set h m	Rise h m	Set h m	Rise h m	Set h m	Rise h m	Set h m
1	0455	2017	0521	1954	0555	1907	0629	1813	0707	1723	0745	1657
2	0455	2016	0522	1953	0557	1906	0630	1811	0708	1722	0746	1656
3	0456	2016	0523	1952	0558	1904	0631	1810	0710	1720	0747	1656
4	0456	2016	0524	1951	0559	1902	0633	1808	0711	1719	0748	1656
5	0457	2016	0525	1949	0600	1900	0634	1806	0712	1718	0749	1656
6	0458	2015	0526	1948	0601	1859	0635	1804	0714	1717	0750	1655
7	0458	2015	0528	1947	0602	1857	0636	1802	0715	1715	0751	1655
8	0459	2015	0529	1945	0603	1855	0637	1801	0716	1714	0752	1655
9	0500	2014	0530	1944	0604	1853	0638	1759	0718	1713	0753	1655
10	0500	2014	0531	1943	0605	1851	0640	1757	0719	1712	0754	1655
11	0501	2013	0532	1941	0607	1850	0641	1756	0720	1711	0755	1655
12	0502	2013	0533	1940	0608	1848	0642	1754	0721	1710	0755	1655
13	0503	2012	0534	1938	0609	1846	0643	1752	0723	1709	0756	1656
14	0504	2011	0535	1937	0610	1844	0645	1750	0724	1708	0757	1656
15	0504	2011	0536	1935	0611	1842	0646	1749	0725	1707	0758	1656
16	0505	2010	0538	1934	0612	1840	0647	1747	0727	1706	0759	1656
17	0506	2009	0539	1932	0613	1839	0648	1746	0728	1705	0759	1657
18	0507	2008	0540	1931	0614	1837	0649	1744	0729	1704	0800	1657
19	0508	2008	0541	1929	0615	1835	0651	1742	0730	1703	0800	1657
20	0509	2007	0542	1928	0617	1833	0652	1741	0732	1703	0801	1658
21	0510	2006	0543	1926	0618	1831	0653	1739	0733	1702	0802	1658
22	0511	2005	0544	1924	0619	1829	0654	1738	0734	1701	0802	1659
23	0512	2004	0545	1923	0620	1828	0656	1736	0735	1701	0803	1659
24	0513	2003	0547	1921	0621	1826	0657	1735	0737	1700	0803	1700
25	0514	2002	0548	1919	0622	1824	0658	1733	0738	1659	0803	1700
26	0515	2001	0549	1918	0623	1822	0659	1732	0739	1659	0804	1701
27	0516	2000	0550	1916	0625	1820	0701	1730	0740	1658	0804	1702
28	0517	1959	0551	1914	0626	1818	0702	1729	0741	1658	0804	1703
29	0518	1958	0552	1913	0627	1817	0703	1727	0743	1657	0804	1703
30	0519	1957	0553	1911	0628	1815	0705	1726	0744	1657	0805	1704
31	0520	1956	0554	1909			0706	1724			0805	1705

have a much larger influence on sunrise and sunset times than does leap year. Sunrise and sunset values will not change appreciably in the next 10 years.

Definitions of sunrise and sunset are very precise. Sunrise by definition occurs when the top of the sun's disc is just below the horizon. The definition of sunset is when the top of the sun's disc falls just below the horizon. Both of these events occur when the center of the sun is 0.883 degrees below the horizon. For this reason, day length on the spring and autumnal equinoxes is longer than 12 hours.

The data in Table 46 indicate that the sun rises as early as 4:50 and sets as late as 20:17 hours MST in June. It also rises as late as 8:05 and sets as early as 16:55 hours MST in December. On the spring and autumnal equinoxes, the sun rises at approximately 6:35 and sets at approximately 18:44 hours MST.

Sunrise and sunset times for other locations on the INL can be obtained from the USNO web site listed above. Comparison of the sunrise and sunset data from Table 46 with sunrise and sunset data for MFC and SMC indicated that sunrise and sunset differences were only up to three minutes maximum. Therefore, the table can be used for any INL location for all practical purposes.

Another solar phenomenon that is associated with sunrise and sunset is referred to in meteorology as local solar noon. This is also known as the time of the transit of the sun, which occurs when the sun is precisely south of the observer and when it is at its maximum elevation. Calculations of local solar noon were performed for CFA for the year 2015. CFA lies in the western portion of the time zone, so local solar noon occurred late in the noon hour. The time of local solar noon varied by approximately 15 minutes through the year. Local solar noon occurred 12:39, 12:33, 12:24, and 12:30 MST on the spring equinox, summer solstice, autumnal equinox, and winter solstice, respectively.

Day Length

Day length is a parameter of interest in determining the time available for reception of solar radiation. Longer days in the summer provide opportunity for more solar heating and more time for recreating and working outdoors without artificial lighting. Conversely, shorter days in the winter bring a cooling of the earth's surface and less time for outdoor activities without artificial lighting. Day length is defined as the time between sunrise and sunset.

A listing of day lengths for CFA for 2015 is provided in Table 47. It shows that on the spring and autumnal equinoxes (March 20 and September 22, respectively), the length of the day was approximately 12 hours and 9 minutes. Near the date of the equinoxes, day length changed from day to day at the rate of about 3 minutes per day. The longest day of the year, the summer solstice on June 21, was 15 hours, 26 minutes long. Six other days surrounding the summer solstice, when rounded to the nearest minute, were also the same length. The shortest day of the year, the winter solstice on December 21, was 8 hours, 56 minutes long. Three other days surrounding the winter solstice, when rounded to the nearest minute, were also the same length. Day lengths for MFC and SMC were obtained from the USNO web site listed above. Comparison of the day length data from Table 47 with day length data for MFC and SMC indicated that the differences in length were only up to three minutes maximum for the three sites.

Twilight

The strict definition of day length as defined by the UNSO does not adequately describe the time before sunrise or after sunset when outdoor activities might still be accomplished with sufficient solar illumination. The term twilight

Table 47. Day lengths for CFA in 2015.

Day	Jan (h:m)	Feb (h:m)	Mar (h:m)	Apr (h:m)	May (h:m)	Jun (h:m)	Jul (h:m)	Aug (h:m)	Sep (h:m)	Oct (h:m)	Nov (h:m)	Dec (h:m)
1	9:01	9:55	11:12	12:44	14:09	15:12	15:22	14:33	13:12	11:44	10:16	9:12
2	9:02	9:57	11:15	12:47	14:12	15:14	15:21	14:31	13:09	11:41	10:14	9:10
3	9:03	10:00	11:18	12:51	14:14	15:14	15:20	14:29	13:06	11:39	10:10	9:09
4	9:04	10:02	11:21	12:54	14:16	15:16	15:20	14:27	13:03	11:35	10:08	9:08
5	9:05	10:05	11:24	12:56	14:19	15:17	15:19	14:24	13:00	11:32	10:06	9:07
6	9:06	10:08	11:27	12:59	14:22	15:18	15:17	14:22	12:58	11:29	10:03	9:05
7	9:07	10:10	11:30	13:02	14:24	15:19	15:17	14:19	12:55	11:26	10:00	9:04
8	9:09	10:13	11:32	13:06	14:27	15:20	15:16	14:16	12:52	11:24	9:58	9:03
9	9:10	10:15	11:36	13:08	14:29	15:21	15:14	14:14	12:49	11:21	9:55	9:02
10	9:11	10:18	11:39	13:11	14:31	15:21	15:14	14:12	12:46	11:17	9:53	9:01
11	9:12	10:21	11:42	13:14	14:33	15:23	15:12	14:09	12:43	11:15	9:51	9:00
12	9:14	10:23	11:44	13:16	14:35	15:23	15:11	14:07	12:40	11:12	9:49	9:00
13	9:15	10:26	11:47	13:20	14:38	15:24	15:09	14:04	12:37	11:09	9:46	9:00
14	9:18	10:29	11:51	13:23	14:41	15:24	15:07	14:02	12:34	11:05	9:44	8:59
15	9:19	10:32	11:54	13:25	14:43	15:25	15:07	13:59	12:31	11:03	9:42	8:58
16	9:21	10:34	11:57	13:28	14:45	15:25	15:05	13:56	12:28	10:00	9:39	8:57
17	9:22	10:38	11:59	13:31	14:47	15:25	15:03	13:53	12:26	10:58	9:37	8:58
18	9:25	10:40	12:03	13:33	14:49	15:26	15:01	13:51	12:23	10:55	9:35	8:57
19	9:26	10:43	12:06	13:37	14:51	15:26	15:00	13:48	12:20	10:51	9:33	8:57
20	9:28	10:46	12:09	13:40	14:53	15:26	14:58	13:46	12:16	10:49	9:31	8:56
21	9:30	10:49	12:11	13:42	14:55	15:26	14:56	13:43	12:13	10:46	9:29	8:56
22	9:33	10:51	12:14	13:45	14:56	15:26	14:54	13:40	12:10	10:44	9:27	8:56
23	9:34	10:55	12:18	13:47	14:58	15:26	14:52	13:38	12:08	10:40	9:26	8:57
24	9:36	10:57	12:21	13:51	15:00	15:25	14:50	13:34	12:05	10:38	9:23	8:57
25	9:39	11:00	12:24	13:53	15:02	15:25	14:48	13:31	12:02	10:35	9:21	8:57
26	9:41	11:04	12:26	13:56	15:04	15:25	14:46	13:29	11:59	10:33	9:20	8:57
27	9:43	11:06	12:29	13:58	15:05	15:24	14:44	13:26	11:55	10:29	9:18	8:58
28	9:46	11:09	12:33	14:01	15:07	15:24	14:42	13:23	11:52	10:27	9:17	8:59
29	9:48		12:36	14:03	15:08	15:23	14:40	13:21	11:50	10:24	9:14	8:59
30	9:50		12:39	14:07	15:09	15:23	14:38	13:18	11:47	10:21	9:13	8:59
31	9:53		12:41		15:11		14:36	13:15		10:18		9:00

is used to describe this time period. There are actually three additional terms used to define the amount of light available before or after sunset: civil twilight, nautical twilight, and astronomical twilight. Civil twilight is defined as being the period before sunrise and after sunset when outdoor activities may be accomplished without the need for artificial illumination. Civil twilight begins before sunrise and ends after sunset when the center of the sun's disc is 6° below the horizon. In the period of nautical twilight, outlines of objects can be distinguished, but detailed outdoor activities are not possible. During this period, the horizon is visible on a moonless night and mariners can take reliable star-based navigation calculations. Nautical twilight begins and ends when the center of the sun's disc is between 6 and 12° below the horizon. Finally, astronomical twilight begins and ends when the center of the sun's disc is between 12 and 18° below the horizon. Sky illumination is practically imperceptible for a good portion of astronomical twilight. After astronomical twilight ends in the evening and before it begins in the morning, illumination from the sun is less than that of starlight and other natural illumination.

Since civil twilight provides additional time for work to be accomplished outdoors without the use of artificial illumination, the addition of this time to the length of the day when the sun is up provides a more accurate estimate of outdoor workable hours. Table 48 contains the total length of time from the beginning of civil twilight in the morning to the ending of civil twilight in the evening at CFA for 2015. In general, civil twilight added an additional hour to the length of the day. On the day of the summer solstice (June 21) the total length of civil twilight was 1 hour, 12 minutes. This time, added to day length (sun rise to sun set), yielded a total working daylight period of 16 hours, 37 minutes. On the shortest day of the year (winter solstice), total length of civil twilight was 1 hour 5 minutes. When added to the length of the day, the total working daylight hours was 10 hours, 2 minutes. On the spring and autumnal equinoxes, the total amount of civil twilight was 58 minutes. When added to day length, the total was 13 hours, 6 minutes.

Nautical and astronomical twilight times for CFA were also calculated for the year 2015. Generally, nautical twilight was, in total about 1 hour, 10 minutes long. On the day of the summer solstice, nautical twilight totaled 1 hour, 34 minutes. Likewise, astronomical twilight was generally about 1 hour, 10 minutes in total duration. However, on the summer solstice, astronomical twilight was nearly 2 hours in total duration. Thus, the sum of all twilight hours and the length of the day on the summer solstice was 20 hours, 10 minutes, leaving less than 4 hours of night.

Global Solar Radiation

Global solar radiation has been measured at 20 NOAA/INL Mesonet locations for over 22 years, and just under ten years at all stations in the Mesonet. Global solar radiation is the amount of energy received from the sun on a flat surface that is parallel to the surface of the earth. It is the sum of the direct solar beam (on the same surface) and diffuse sky radiation, also known as skylight. Global solar radiation measurements are useful for determining the energy generation capability of photovoltaic (PV) systems. Solar concentrators on the other hand, which are now the most widely used for electricity generation, rely on direct solar radiation. This later parameter has not been measured at the INL. The following discussion pertains almost entirely to CFA for the data period of January 1994 through December 2015.

Graphs of the diurnal response of solar radiation in each of the four seasons, represented by the months of January (winter), April (spring), July (summer), and October (autumn), are shown in Fig. 78. The months of the solstices and equinoxes were not chosen for this analysis because of the similarity of responses at the equinoxes and also to follow the established pattern of describing the four seasons. Fig. 78 also shows the mean maximum and minimum hourly solar radiation values for the same months.

The graphs in Fig. 78 clearly illustrate the effect of day length and solar elevation on the amount of solar energy that was received at CFA.

Table 48. Total working daylight hours from the beginning of morning twilight through the ending of evening twilight for CFA in 2015.

Day	Jan (h:m)	Feb (h:m)	Mar (h:m)	Apr (h:m)	May (h:m)	Jun (h:m)	Jul (h:m)	Aug (h:m)	Sep (h:m)	Oct (h:m)	Nov (h:m)	Dec (h:m)
1	10:06	10:56	12:10	13:43	15:11	16:21	16:32	15:38	14:11	12:41	11:15	10:16
2	10:07	10:58	12:12	13:45	15:14	16:23	16:32	15:36	14:07	12:38	11:13	10:15
3	10:08	11:01	12:15	13:48	15:17	16:25	16:31	15:32	14:04	12:35	11:11	10:14
4	10:09	11:03	12:18	13:51	15:19	16:26	16:31	15:30	14:02	12:33	11:09	10:13
5	10:10	11:05	12:21	13:55	15:23	16:27	16:29	15:28	13:59	12:29	11:06	10:12
6	10:11	11:07	12:24	13:58	15:25	16:28	16:28	15:25	13:56	12:26	11:03	10:10
7	10:12	11:10	12:27	14:00	15:28	16:29	16:26	15:23	13:53	12:23	11:01	10:09
8	10:14	11:13	12:30	14:03	15:30	16:31	16:26	15:19	13:49	12:21	10:59	10:08
9	10:15	11:15	12:33	14:07	15:33	16:31	16:24	15:17	13:46	12:18	10:57	10:07
10	10:16	11:18	12:36	14:10	15:36	16:32	16:23	15:14	13:44	12:15	10:54	10:07
11	10:17	11:20	12:39	14:13	15:38	16:32	16:21	15:12	13:41	12:12	10:52	10:07
12	10:19	11:23	12:41	14:15	15:40	16:34	16:19	15:09	13:38	12:09	10:50	10:06
13	10:20	11:25	12:44	14:19	15:44	16:35	16:18	15:06	13:35	12:06	10:48	10:05
14	10:21	11:28	12:48	14:22	15:46	16:35	16:16	15:03	13:31	12:04	10:45	10:04
15	10:23	11:31	12:51	14:25	15:48	16:36	16:14	15:00	13:28	12:01	10:43	10:04
16	10:24	11:33	12:54	14:27	15:50	16:36	16:13	14:58	13:25	11:59	10:42	10:04
17	10:27	11:36	12:56	14:31	15:52	16:36	16:11	14:55	13:23	11:55	10:40	10:03
18	10:28	11:39	12:59	14:34	15:54	16:37	16:09	14:52	13:20	11:52	10:38	10:03
19	10:30	11:41	13:03	14:37	15:57	16:37	16:07	14:49	13:17	11:50	10:35	10:03
20	10:31	11:44	13:06	14:39	16:00	16:37	16:05	14:46	13:14	11:47	10:34	10:03
21	10:33	11:47	13:09	14:43	16:02	16:37	16:03	14:44	13:10	11:45	10:32	10:02
22	10:35	11:50	13:11	14:46	16:04	16:37	16:01	14:40	13:07	11:41	10:30	10:02
23	10:37	11:52	13:15	14:48	16:05	16:37	15:59	14:37	13:05	11:39	10:29	10:03
24	10:39	11:55	13:18	14:52	16:07	16:37	15:57	14:34	13:02	11:36	10:27	10:03
25	10:41	11:58	13:21	14:55	16:09	16:36	15:55	14:32	12:59	11:34	10:26	10:03
26	10:42	12:01	13:24	14:57	16:11	16:36	15:53	14:29	12:56	11:31	10:23	10:04
27	10:45	12:04	13:26	15:00	16:13	16:35	15:50	14:25	12:53	11:28	10:22	10:04
28	10:47	12:06	13:30	15:03	16:15	16:35	15:47	14:22	12:49	11:26	10:20	10:04
29	10:49		13:33	15:06	16:16	16:34	15:46	14:18	12:45	11:23	10:19	10:05
30	10:52		13:36	15:08	16:18	16:34	15:44	14:15	12:43	11:21	10:18	10:05
31	10:54		13:39		16:20		15:41	14:13		11:19		10:06

The average midday solar radiation peak in January was 346 W m^{-2}. The average midday solar radiation peak in July was 882 W m^{-2}, which was more than double that received in January. The April average midday solar radiation peak was 667 W m^{-2}, while for October, it was 539 W m^{-2}.

The range between the average minimum and average maximum midday solar peak was different in each season. In January, the range observed in the midday solar radiation peak was 166 W m^{-2}, which was 48% of the average midday value. In July, the range observed in the midday solar radiation peak was 120 W m^{-2}, which was 14% of the average midday value. The ranges in April and October were 221 and 144 W m^{-2}, which were 32 and 27% of the average midday values, respectively. The ranking of the seasons in order from most to least range of midday solar radiation was: winter, spring, fall, and summer. It can be concluded that the summer months had fewer cloudy skies than the other seasons.

Theoretical clear-sky maximum solar radiation (R_{max}) curves together with curves for the theoretical clear-sky direct solar beam on a surface perpendicular to the sun were calculated for the four seasons. The curves were obtained from the model provided by Bird and Hulstrom, 1991. The model required estimates of several atmospheric and surface parameters that included: 1) atmospheric pressure, 2) total column ozone thickness, 3) total column water vapor, 4) aerosol optical depths at 380 and 500 nm, 5) a coefficient for forward scattered light, and 6) albedo. Values chosen for these parameters were based on recommendations from Bird and Hulstrom or were based on published values. The values of the coefficients, in order, were: 1) 848.3 mb, 2) 0.04 cm, 3) 1.5 cm, 4) 0.15 and 0.1 cm, 5) 0.85, and 6) 0.22. Bird and Hulstrom claim the formulas in the model agree to within ±10%

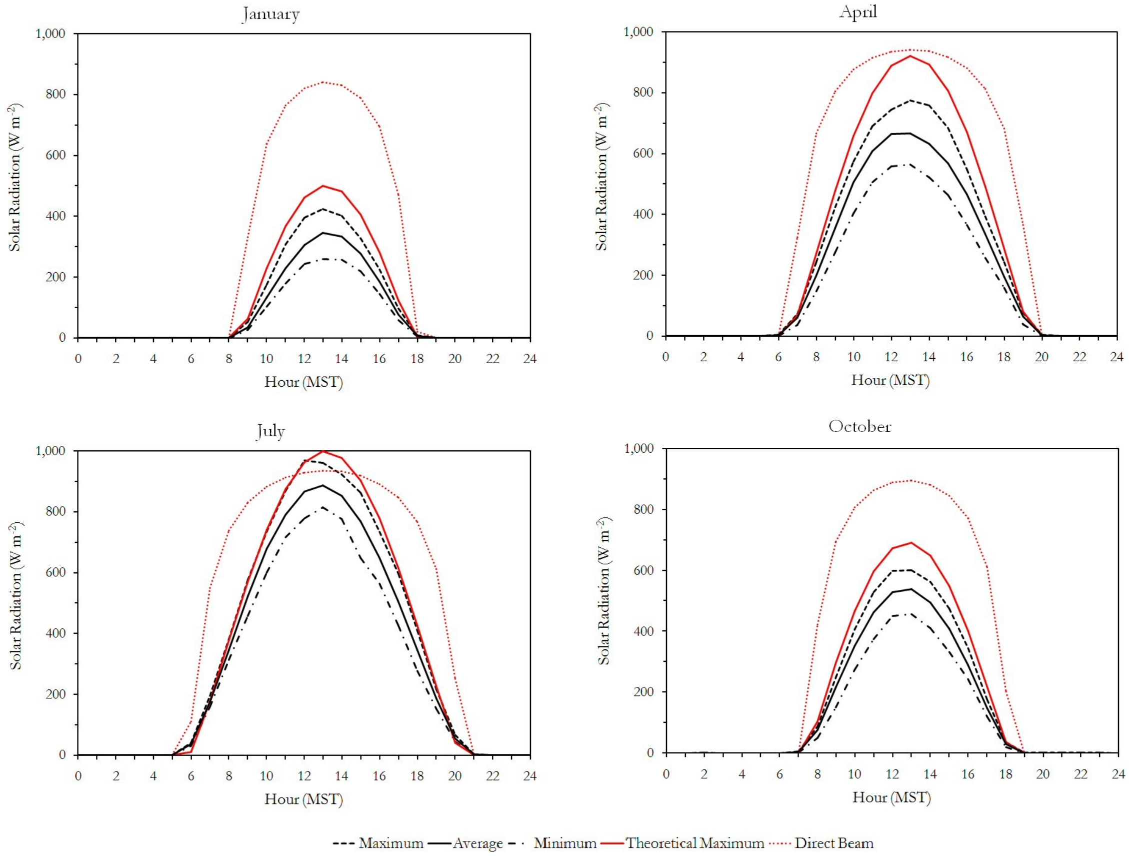

Figure 78. Diurnal depiction of hourly average, maximum, minimum, theoretical maximum (R_{max}), and theoretical direct beam solar radiation values at CFA for winter, spring, summer, and fall represented by the months of January, April, July, and October, respectively.

when compared with rigorous radiative transfer codes. The uncertainty of the required input values could produce even larger uncertainty in the calculated values. In practice, the values of the coefficients change based on regional influences such as synoptic flows, and on local influences such as wild fires. For the purposes of this analysis, the coefficients were held constant to permit comparison across the seasons.

R_{max} curves are shown in Fig. 78 for each of the four seasons together with the measured average, minimum, and maximum solar radiation curves previously discussed. The July R_{max} curve matched the measured maximum curve, which indicates that reasonable values for the model coefficients were selected, as least for the summer months. The lack of fit of the R_{max} curve to the measured maximum curve in the other seasons indicates that the model coefficients would need to be adjusted to provide a more accurate R_{max} estimate at other times of the year. Since R_{max} is for clear skies, the primary effect that would need to be accounted for is clouds. R_{max} peaks at midday for winter, spring, summer, and fall were 499, 921, 998, and 691 W m^{-2}, respectively.

A comparison of the average measured curves with R_{max} on an hour by hour basis indicated a hysteresis between the morning rise and the afternoon decline in solar radiation. This is most clearly observed in Fig. 79, which shows the measured percent of R_{max} for each of the four seasons for a 9-hour time period centered on local solar noon. If no hysteresis was present in Fig. 78, the curves in Fig. 79 would be flat; however, they are not. The biggest hysteresis between morning and evening was observed in the January (winter) curve. The measured solar radiation was only about 55% of R_{max} at 0900 hours MST, but increased to 69% at midday. The measured solar radiation then declined to 62% of R_{max} by 1700 hours MST. It is surmised that the observed morning to evening solar radiation hysteresis in the winter months was due to the presence of clouds and fog. It has been observed that clouds and fog tended to decrease or disappear by midday in the winter due to solar heating, but then reformed in the late afternoon as the sun descended from its maximum elevation and heating potential. In the summer months represented by July, the measured solar radiation was 91% of R_{max} at 0900 and 1000 hours MST , but then steadily declined to 82% by 1700 hours MST. In this case, it is surmised that afternoon cloud formation was the cause of the afternoon hysteresis.

The spring and autumn months showed R_{max} percentage responses that were similar to the winter season, but the time of the inflection point was different. In the spring months (April), the measured solar radiation reached a maximum of 77% of R_{max} at 1000 hours MST, but then declined steadily through the rest of the day to 68% at 1700 hours MST. In the autumn months, (October), the measured solar radiation reached a maximum of 78% of R_{max} at 1200 and 1300 hours MST, then declined to 68% at 1700 hours MST.

The daily direct beam as calculated using the model of Bird and Hulstrom, 1991, is shown in Fig. 78. The midday peak values for winter, spring, summer, and fall were 840, 941, 935, and 895 W m^{-2}, respectively.

Table 49 contains a list of five-minute averaged extreme maximum solar radiation values summarized by month and annually. Maximum measured values above Rmax were recorded in every month of the year. These maximums were not single events, but instead were multiple five-minute periods thereby indicating proper equipment response and not a temporary instrument malfunction. Measured solar radiation values above Rmax are possible when clouds cause additional solar radiation to be reflected into the sensor. The highest maximum five-

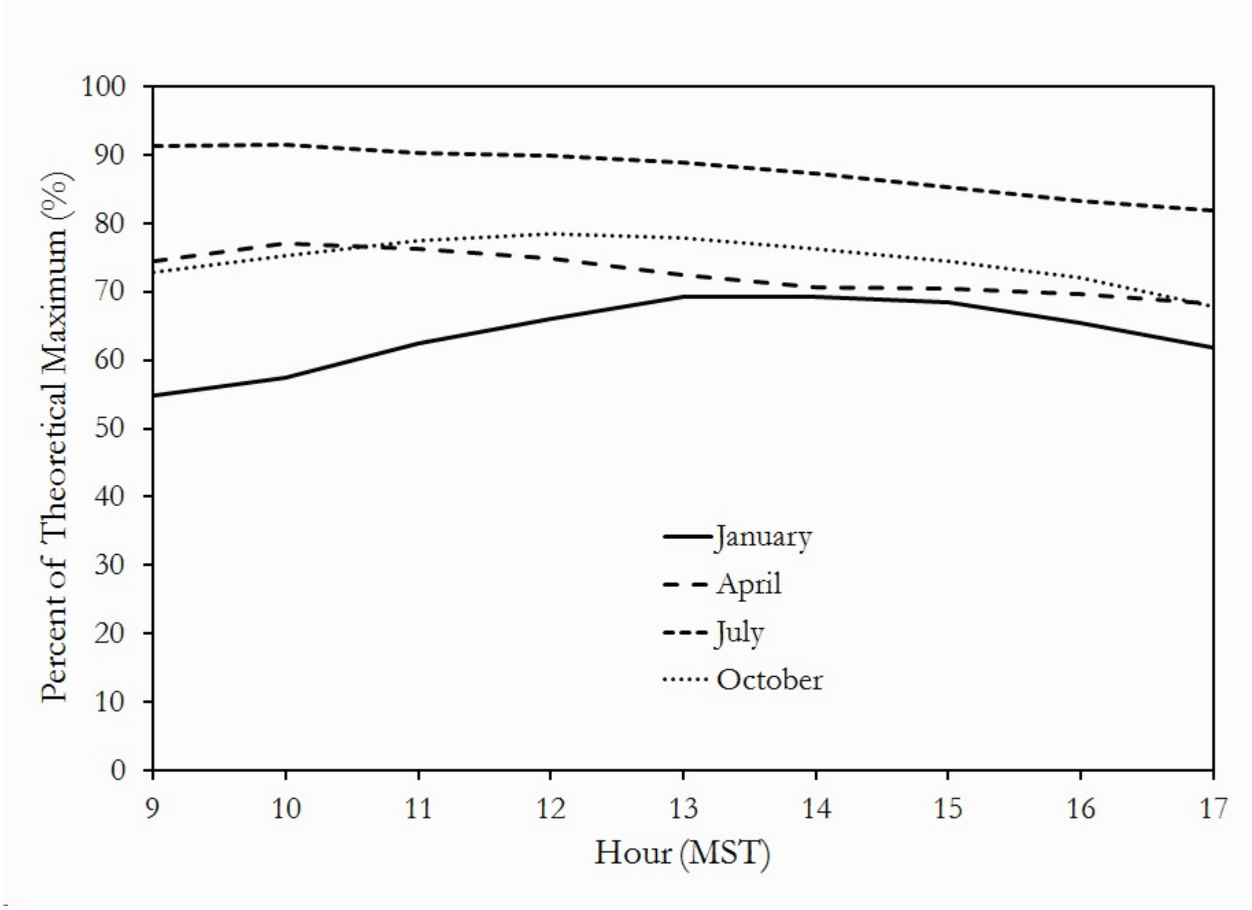

Figure 79. Measured solar radiation as a percent of the theoretical maximum (R_{max}) through the midday hours at CFA for winter, spring, summer, and fall, represented by the months of January, April, July, and October, respectively.

minute value recorded during the period of record was 1,380 W m^{-2}, which was recorded on May 26, 2006 at 1210 hours MST.

A summary of the average total daily solar radiation values for each month is given in Table 49. The maximum and minimum daily values for each month are also presented in Table 49. July was the month of the greatest daily solar radiation total with an average of 27.6 MJ m^{-2} day^{-1}. It was expected that June would have the highest daily total solar radiation since the summer solstice occurred during that month. A higher percentage of cloud cover in June, observed earlier in the month, likely caused the lower total daily solar radiation. The month with the lowest daily solar radiation total was December, as expected. The average daily solar radiation total in December was only 21% of the average recorded in July. The highest average daily solar radiation total was also recorded in June, in the year 2008, with a value of 31.4 MJ m^{-2} day^{-1}. The lowest average daily solar radiation total was likewise recorded in December 1994, with a value of 4.4 MJ m^{-2} day^{-1}.

The average daily solar radiation total on an annual basis was 16.8 MJ m^{-2} day^{-1}. The maximum annual average was 19.7 MJ m^{-2} day^{-1}, which was recorded in 2008, while the minimum annual average was 13.8 MJ m^{-2} day^{-1}, which was recorded in 1994.

Table 49. Monthly and annual averages and five-minute extremes of solar radiation for CFA.

	Monthly Values			Five-Minute Average Extreme Values	
	Average ($MJ\ m^{-2}\ day^{-1}$)	Highest Average ($MJ\ m^{-2}\ day^{-1}$)	Lowest Average ($MJ\ m^{-2}\ day^{-1}$)	Maximum ($W\ m^{-2}$)	Minimum (%)
January	7.0	8.7	5.4	880	21.0
February	11.2	13.7	9.0	1,008	16.6
March	16.1	18.7	13.9	1,120	8.8
April	19.6	23.3	15.5	1,276	9.8
May	23.3	28.4	19.1	1,380	7.2
June	26.6	31.4	21.7	1,365	4.8
July	27.6	30.8	24.3	1,337	3.8
August	24.1	28.1	19.5	1,278	4.8
September	19.1	22.1	16.4	1,228	5.1
October	13.0	14.8	10.4	1,018	8.0
November	8.0	9.3	5.5	834	9.5
December	5.8	7.2	4.4	691	13.6
ANNUAL	16.8	19.7	13.8	1380	3.8

Note: Data period of record spans January 1994 through December 2015.

SURFACE ENERGY BALANCE

An understanding of the surface energy balance helps to explain many of the microscale meteorological processes at the INL. The surface energy balance equation can be written as follows:

$$R_n = H + LE + G + M \quad (4)$$

where R_n is net radiation, H is sensible heat flux, LE is latent heat flux related to the evaporation or condensation of water, G is soil heat flux, and M is miscellaneous processes that include photosynthesis. Net radiation is in the visible and infrared bands and includes both incoming electromagnetic radiation reaching the surface and outgoing radiation emitted from the surface. Since M is small (usually less than 2%), the equation simply stated says the net radiative energy reaching the surface must result in either heating/cooling of the air, evaporation/condensation of water, or heating/cooling of the soil.

In humid regions, radiative cooling at night tends to be limited because water vapor is a greenhouse gas. Heating of the air during the day (H) is also reduced because a larger fraction of the available energy is used to evaporate water (LE). As a result, diurnal temperature swings in humid areas tend to be relatively small. Arid areas, in cortrast, have larger diurnal swings due to both strong nocturnal cooling and the limited availability of water for evaporation during the day.

To better understand the partitioning of energy and its effect of the climate at the INL, an eddy correlation flux station was installed at the Grid 3 facility in late 1999. Instrumentation includes both fast and slow response sensors as required by the eddy correlation flux calculation technique. These data are not a part of the NOAA/INL Mesonet data stream, but are acquired using separate data collection instrumentation. Fast response instrumentation, measured at 10 Hz, include two instruments: 1) a 3-d sonic anemometer (for measuring latent heat and momentum fluxes), and 2) a fast response infrared gas analyzer (for measuring latent heat and carbon dioxide fluxes). Use of the 3-d sonic anemometer provides an added benefit in that atmospheric stability in the form of the Monin-Obukhov stability parameter can be directly calculated from its output. Slow response instrumentation, measured at 1 Hz and recorded every 5 minutes, include a net radiometer, soil heat flux plates, soil moisture probes, and soil temperature probes. Prior to the middle of 2009 the data were collected in 30 minute averages so the following data discussed from the surface flux station is data collected between 2010 (the first full year of 5-min averages) and 2015. Discussions on surface soil temperature, surface soil heat flux, and net radiation follow. A more complete discussion of latent and sensible heat fluxes will follow in a future edition of the Climatology.

Near Surface Soil Temperatures

Soil temperatures fluctuate daily and seasonally depending on air temperature and solar radiation. Table 50 lists the monthly average soil temperatures from the eddy correlation surface flux station for the six-year period. Soil temperatures were the average of temperatures obtained from two probes at 0.79 in. and two probes at 2.4 in. depth. These averages can be considered to be indicative of conditions immediately below the soil surface. Similarly to air temperatures, soil temperatures have a natural seasonal dependancy where the highest soil temperatures are found in the summer and

Table 50. Monthly and annual near-surface soil temperature averages from the Grid 3 surface flux station.[a]

	Monthly Average Soil Temperature (°F)	Average Daily Maximum Soil Temperature (°F)	Average Daily Minimum Soil Temperature (°F)	Extreme Daily Maximum Soil Temperature (°F)	Extreme Daily Minimum Soil Temperature (°F)
January	25.5	27.3	25.5	35.5	8.3
February	29.3	31.5	29.4	45.2	8.9
March	37.4	42.5	37.9	70.0	23.8
April	48.2	56.0	48.2	73.9	31.3
May	57.5	65.9	57.5	81.4	37.3
June	69.4	79.3	69.5	97.7	46.1
July	77.5	88.3	77.5	97.7	52.8
August	73.5	83.4	73.5	93.8	49.8
September	64.4	73.6	64.4	85.8	44.1
October	48.8	56.1	48.8	75.7	32.2
November	33.2	36.9	33.3	52.3	13.2
December	26.5	28.7	26.7	41.0	9.41
ANNUAL	49.4	55.8	49.3	97.7	8.3

a. Data period of record spans January 2010 through 2015.

coldest are found in the winter. The monthly average maximum soil temperature is in July at 77.5 °F. Conversely, the coldest monthly average soil temperatures are recorded in January and December at 27.3 and 28.7 °F, respectively. The average soil temperature usually drops below freezing in late November and rises above freezing in late February to early March. The annual average soil temperature is 49.4 °F.

Net Radiation

Net radiation is defined as the balance between incoming and reflected solar radiation and incoming and emitted terrestrial radiation. The sign of the flux of net radiation is positive when directed toward the earth's surface (incoming energy) and negative when directed outward from the earth's surface to the atmosphere (outgoing energy).

Net radiation was measured with a net radiometer. The monthly data from the six year period are summarized in Fig. 80. The top two curves of the figure trace the net radiation during daylight hours only. The top curve represents the maximum monthly total net radiation observed on any given day during the six year measurement period. The other curve represents the monthly average of the total daily net radiation. The bottom curve of the figure traces the monthly average of the total daily net radiation during

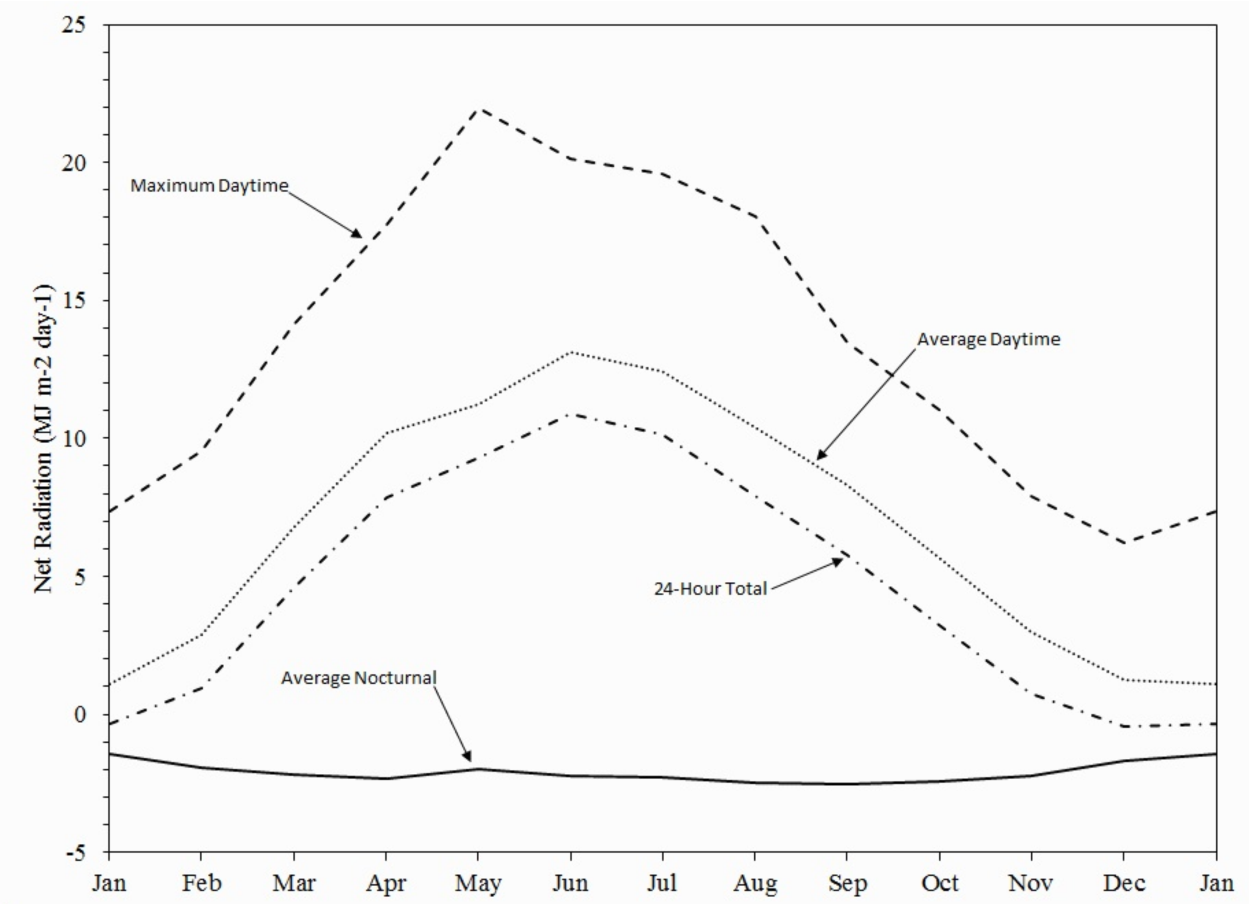

Figure 80. Monthly traces of maximum daytime, average daytime, 24-hour, and nocturnal total daily net radiation.

nocturnal hours. The last remaining curve is the difference between the monthly average daytime and monthly average nocturnal curves and represents the total amount of net radiation (incoming minus outgoing) measured during 24 hours.

The monthly maximum total daytime net radiation recorded for a particular day (top curve of Fig. 80) is the maximum amount that would be expected on a day with completely clear skies and with a minimum amount of atmospheric turbidity. The maximum amount of daytime net radiation during the last six years was found to be in May, although that high value may be due to a measuring artifact. Typically, during a clear day at the peak of the summer months, the INL can be expected to receive on average a total of about 20 MJ m^{-2} day^{-1} net incoming irradiation during the daylight hours. The total daily nocturnal net radiation (bottom curve) averaged about -2.0 and seldom exceeded -2.5 MJ m^{-2} day^{-1}.

The curves in Fig. 80 illustrate a seasonal dependency. In June, the average daytime net radiation was about 13.1 MJ m^{-2} day^{-1}. In January, the daytime net radiation decreases to about 1.0 MJ m^{-2} day^{-1}. The nocturnal and daylight net radiation values were nearly equal but opposite in sign during the height of the winter season. The low angle of the sun combined with high reflection from clouds and snow produces the near-zero values of total daily net radiation observed in the winter. Lower net radiation values during the winter result in diminished convective activity compared to the summer months. This decrease results in a deep vertical stable layering of the atmosphere. Thus, a reduced intensity and depth of vertical dispersion of effluents is to be expected during the winter.

Surface Soil Heat Flux

Surface soil heat flux is defined as the amount of heat that flows into or out of the soil and is an important part of the overall energy balance. Even though average values are almost zero, initial results show that surface soil heat flux can range up to nearly 40% of net radiation at midday during the summer when the soil is dry.

Soil heat flux at the Grid 3 flux site is measured by heat flux plates buried 3.1 in. beneath surface. The surface soil heat flux is then calculated using the flux measured by the heat flux plates, the amount of heat stored in the soil above the plates using temperatures measured by soil temperature probes, and the amount of water stored in the soil using the soil moisture probe. Surface soil heat flux is a difficult parameter to measure because it is greatly affected by vegetation covering the soil, which is very spotty in the sagebrush-steppe ecosystem on the INL. The sign convention used is the same as for net radiation, i.e., it is positive if the flux is to the surface and negative if it is away from the surface. Heat applied to the soil surface in the daytime by the sun causes energy to flow into the soil (negative flux). At night, the soil is warmer than the air, so heat flows from the soil to the surface (positive flux).

Table 51 displays the monthly average surface soil heat flux at the Grid 3 surface flux station for six-years. The highest monthly soil heat flux to the surface is found during November at 7.67 W m^{-2} day^{-1}. Net radiation is near its minimum with soil temperatures still

Table 51. Monthly and annual surface soil heat flux averages from the Grid 3 surface flux station[a].

Month	Monthly Average (W m^{-2})	Average Daily Maximum (W m^{-2})	Average Daily Minimum (W m^{-2})
January	3.73	37.3	-34.3
February	2.01	36.9	-37.0
March	-2.26	50.4	-76.7
April	-4.45	64.6	-111.7
May	-6.85	62.9	-117.1
June	-10.37	69.1	-127.0
July	-9.39	61.6	-118.7
August	-5.33	68.0	-117.0
September	-0.96	63.3	-98.6
October	5.33	63.3	-85.6
November	7.67	53.2	-50.9
December	6.04	43.0	-34.8
ANNUAL	-1.23	50.8	-92.3

a. Data period of record spans January 2010 through December 2015.

above freezing allowing for the soil heat flux to the surface. The highest monthly heat flux into the soil is found in the middle of the summer when soil temperatures are at the highest and there is maximum net radiation.

EVAPORATION AND EVAPOTRANSPIRATION

This section describes the atmospheric processes of evaporation (E) and evapotranspiration (ET) that remove liquid water from the surface of the earth or from plants, respectively, and return it in the form of water vapor to the air. The process of evaporation as used here refers to the loss of water from both open water and bare soil surfaces to the atmosphere. ET refers to the loss of water from both soil and plants where the processes of soil water evaporation and plant transpiration are combined.

No exhaustive studies of E or ET at the INL have been conducted by this office. However, an extensive study of E and ET for the entire state of Idaho was conducted by University of Idaho professors Richard Allen and Clarence Robison in 2006. The study was funded primarily by the Idaho Department of Water Resources to determine crop water consumptive use requirements throughout the entire state. The study also included ET estimates of naturally occurring vegetation such as sagebrush, and also E estimates of bare soil and open water surfaces. The study included the CFA data available from the National Climate Data Center (NCDC) known as Idaho Falls 46W.

Allen and Robinson reported their findings in 2007 and published their results on the website http://www.kimberly.uidaho.edu/ETIdaho/. Their estimates of E and ET used a mathematical formula known as the American Society of Civil Engineers (ASCE) standardized Penman-

Monteith method. It is based on a crop coefficient-reference ET approach, where a reference ET (ET_{ref}) is multiplied by a so-called crop coefficient (K_c) to obtain actual ET. ET_{ref} is a standardized value that approximates actual atmospheric demand for water vapor. K_c is defined as the ratio of ET of a specific land-cover or surface to ET_{ref}. The basic method has been calibrated over a period of more than 30 years with real E and ET from weighing lysimeters operated by the USDA Agricultural Research Service in Twin Falls, ID.

The form of the daily ET_{ref} equation requires total daily net radiation (R_n), total daily surface soil heat flux (G), average daily air temperature at 4.9 to 8.2 ft. AGL (T), average daily wind speed measured at 6 ft. AGL (u_2), and the air water vapor pressure deficit measured at the same height as air temperature (e_s-e_a), as follows:

$$ET_{ref}=\frac{0.408\Delta(R_n-G)+\gamma\frac{C_n}{T+273}u_2(e_s-e_a)}{\Delta+\gamma(1+C_d u_2)} \quad (5)$$

where ET_{ref} is expressed as mm day^{-1}, R_n and G are expressed in MJ m^{-2} day^{-1}, T is given in C, u is given in m s^{-1}, e_s is saturation vapor pressure is given in kPa and calculated as the average of saturation vapor pressure at maximum and minimum air temperature, e_a is mean actual vapor pressure also express in kPa, Δ is slope of the saturation vapor pressure-temperature curve (kPa C^{-1}), γ is the psychrometric constant in kPa C^{-1}, C_n is a constant that changes with reference type expressed in K mm s^3 Mg^{-1} day^{-1}, and C_d is a constant that changes with reference type and is expressed in s m^{-1}. Units for the 0.408 coefficient are m^2 mm MJ^{-1}.

Allen and Robison (2007) described a series of equations for calculating R_n and G based solely on daily maximum and minimum air temperature. They also described a procedure for estimating daily wind speed from nearby meteorological stations. These simplifications are likely sufficient for monthly and annual estimates of ET_{ref} even though this office could have calculated a more accurate ET_{ref} using many more of the primary variables from the CFA station. The reader is referred to Allen and Robison (2007) for complete details of their assumptions and calculation methods.

Monthly summaries of Allen and Robison's calculated E and ET values for three common land surfaces at the INL are included here for the convenience of the reader. ET and E values have also been converted to inches for the convenience of the reader. ET for sagebrush, and E for bare soil and for large ponds (< 12 ft. deep) based on 30-year normals from 1979 to 2008 are given in Table 52. Sagebrush ET exhibited a skewed curve from a low of 0.26 in. month^{-1} in January to a high of 3.67 and 3.57 in. month^{-1} in June and July back to a low of 0.24 in. month^{-1} in December. The skewness is indicative of plants that use most of the available soil water in the first part of the growing season. After that, ET is limited by low soil water and ET is then driven essentially by the amount of precipitation that occurs during the rest of the growing season. The annual average ET for Sagebrush was 18.82 inches. E for bare soil followed a similar pattern as Sagebrush, but the peak E was skewed to even earlier in the season. A peak of 1.89 in. month^{-1} was observed in May with a low of about 0.33 in. month^{-1} in December. Average yearly bare soil E was 12.79 inches. Pond evaporation exhibited a

Table 52. Thirty-year normal estimated monthly and annual evapotranspiration (ET) for Sagebrush and estimated monthly and annual evaporation (E) for bare soil and small ponds (< 13.1 ft. deep) at CFA. Also included is an estimate of precipitation deficit (P_{def}) for the three land surface types. Standard deviations are included with each estimate.

	Sagebrush		Bare Soil		Small Ponds	
	ET (in.)	P_{def} (in.)	E (in.)	P_{def} (in.)	E (in.)	P_{def} (in.)
January	0.26 ±0.08	-0.37±0.37	0.37±0.12	-0.03±0.22	0.47±0.09	-0.14±0.44
February	0.43±0.13	-0.18±0.45	0.61±0.20	0.16±0.18	0.74±0. 15	0.16±0.58
March	0.81±0.21	0.05±0.33	1.12±0.34	0.16±0.23	1.79±0.37	1.13±0.75
April	1.37±0.42	-0.01±0.29	1.51±0.39	0.00±0.20	3.16±0.40	2.30±0.78
May	3.04±0.60	0.16±0.39	1.89±0.65	0.01±0.13	4.22±0.46	2.96±1.21
June	3.67±0.38	0.30±0.43	1.75±0.61	0.02±0.14	4.94±0.49	3.92±1.41
July	3.57±0.40	0.29±0.31	1.48±0.50	-0.01±0.11	5.67±0.43	5.08±0.89
August	2.81±0.28	0.21±0.20	1.22±0.34	-0.01±0.07	4.89±0.29	4.49±0.59
September	1.60±0.50	-0.09±0.33	1.15±0.44	-0.04±0.17	3.44±0.34	2.76±0.81
October	0.73±0.27	-0.12±0.21	0.88±0.39	-0.02±0.19	2.42±0.31	1.86±0.64
November	0.30±0.11	-0.44±0.42	0.41±0. 18	-0.25±0.21	0.91±0. 20	0.22±0.63
December	0.24±0.09	-0.41±0.43	0.33±0.15	-0.04±0.22	0.50±0.10	-0.13±0.56
Annual	18.82±1.37	-0.59±0.82	12.79±1.70	-0.06±0.23	33.14±2.03	24.62±4.27

curve similar to an air temperature curve, with the maximum E of 5.67 in. month^{-1} being observed in July. A minimum pond evaporation of about 0.47 in. month^{-1} was observed in January. Eight months had E greater than 1.0 in. month^{-1}. Pond E averaged 33.14 in. year^{-1}.

Another parameter of interest is the precipitation deficit (P_{def}). It is defined as the difference between potential ET or potential E and the amount of precipitation for a given time period. If potential ET or potential E exceeds precipitation, the value of P_{def} is positive. When, precipitation exceeds potential ET or potential E, the value of P_{def} is negative. For bare soil, February and March had the highest monthly P_{def} as potential E exceeded precipitation by a 0.16 in. month^{-1}. November had the lowest monthly P_{def} average with precipitation exceeding potential E at 0.25 in. month^{-1}. Seven months out of the year, the monthly precipitation exceeded the monthly potential E. Total annual precipitation gained was 0.06 inches. For sagebrush, precipitation exceeded potential ET by as much as 0.44 in. month^{-1} during seven months of the year. However, potential ET exceeded precipitation by 0.30 in. month^{-1} in June. Sagebrush P_{def} was similar to bare soil in that annual precipitation totals exceeded potential ET by 0.59 in. month^{-1}, which was nearly ten times greater than bare soil. For small ponds, only two months, December and January, had a negative P_{def} where the precipitation exceeded the potential E. As a result, the water level in a small pond, in the absence of other types of inflow or outflow, would be expected to rise about 0.27 in. during these two months. In all other months, small pond potential E exceeded precipitation by as much as 5.08 in. month^{-1}. As a result, total annual evaporative water loss from a small pond is expected to be 24.62 in. This is the design basis number that can be used for small evaporative ponds at the INL.

SPECIAL PHENOMENA

Several other types of meteorological phenomena occur at the INL that have not been addressed in the preceding sections. Among these are thunderstorms, blowing snow, and tornadoes. Each of these subjects is discussed below in the order of its frequency of occurrence.

Dew

Dew forms on the surfaces of objects, e.g., vegetation or vehicles, whenever the temperature of the object reaches the dew point. Dew has been observed to form on nearly any clear or mostly clear summer night. It may form as early as sunset and may not dissipate until as late as three to four hours after sunrise. Its formation and dissipation can usually be expected to approximately coincide with the formation and dissipation of the nocturnal temperature inversion.

Frost

Frost, like dew, forms on the surfaces of objects whenever the temperature of the object reaches the dew point temperature and the dew point temperature is at or below freezing. It frequently occurs during all months of the year except for the summer season. Frost can be a safety concern, for example, when it forms on windshields. This is very common and requires removal before the vehicle can be operated. Frost can also cause problems to some of the Mesonet instrumentation. For example, frost buildup on the wind cup anemometer keeps it from turning and measuring the accurate wind speed. Data during this time that the cup anemometer is not turning is flagged as bad.

Thunderstorms

A thunderstorm-day is defined by the NWS as a day on which thunder is heard at a given observing station. According to the definition, lightning does not have to be seen, and rain fall and/or hail is not required. Following this strict definition, the INL may experience an average of two or three thunderstorm days during each of the summer months from June through August, with considerable year-to-year variation. Several individual thunderstorms may occur during each of those thunderstorm days. At the INL, thunderstorms have been observed during every month of the year. They are, however, seldom observed during the months of November through February. A noteable exception to this rule was the Valentine's Day Storm of 2000. During this storm, new record wind speed gusts were recorded at several Mesonet stations both on and off the INL, including, MIN at 96.3 mph and ROV at 87.7 mph. Wind damage was observed through the ESRP.

Thunderstorms over the INL are usually much less severe than what is normally experienced in the mountains surrounding the ESRP, or east of the Rocky Mountains. This is due, in part, to high cloud-base altitudes. Hence, the precipitation from many thunderstorms evaporates before reaching the ground (virga). The frequent result is little or no measurable precipitation. Occasionally, however, rain amounts exceeding the long-term average may result from a single thunderstorm.

Lightning

Thunderstorms may be accompanied by cloud-to-ground as well as cloud-to-cloud lightning. The INL is currently monitored by the United States Precision Lightning Detection Network (USPLN) and the Earth Networks Total Lightning Network (ENTLN). Data period of record for the USPLN began in 2007 while the ENTLN data period of record began in 2014. The following data discussed in this section are comprised of the USPLN dataset since there is a longer data period of record. Both lightning networks detect the location, polarity, and number of lightning strikes in real time for wild fire control and personnel safety.

The polarity of the lightning strike is important in that it determines if the strike is cloud-to-ground and if it is negative or positive. A negative lightning strike is produced by downward-propagating, negatively-charged leaders from the cloud that connects with an upward positive charge from the ground. On the other hand, positive lightning strikes originate in the part of the cloud that produces a downward-propagating, positively-charged leader to the ground (Jensenius, 2017). The majority of the strikes on the INL are negative with only 8.1% of the strikes being positive. Both types of strikes can be deadly but positive strikes are typically more dangerous since they are responsible for more forest (wildland) fires and power line damage. (JetStream, 2017).

Figure 81 presents the geographical distribution of lightning strike density in contour form in the INL vicinity for the period August 2007 through December 2015. The distribution shows some dominance on the southwest INL (likely from thunderstorms moving from the mountains onto the INL) and the higher terrain on the southern and eastern INL that roughly correlate with the edge of the Lost River Basin. Fairly equal distribution is noted elsewhere.

Figure 82 presents the geographical distribution of positive lightning strike density in contour form in the INL vicinity for the period August 2007 through December 2015. Fairly spotty distribution can be noted across most of the INL with a couple spots of higher density on the west INL and southeastern INL.

The year-to-year, and typical month-to-month variability in lightning activity at INL between 2007 and 2015 is shown in Table 53. The INL has averaged 1,374 lightning strikes per year. The maximum number of strikes per year was 2,540 and occurred in 2009. The minimum number of strikes per year was 806 and occurred in 2008. The maximum number of strikes in a month occurred in June of 2009 with close to 1,400 total strikes. Very few lightning strikes have occurred between November through February. It is important to note that the lack of natural targets and the poor conductivity of the dry desert soil and underlying lava rock cause man-made structures at the INL to be susceptible to lightning strikes.

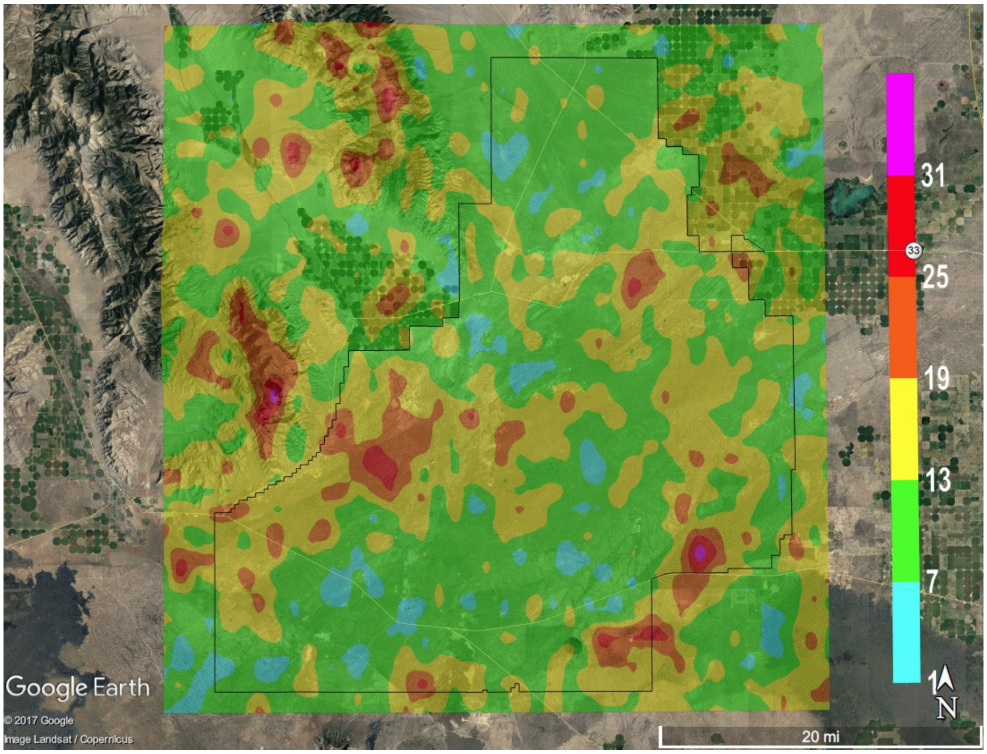

Figure 81. Total lightning strike density per square kilometer across the INL from 2007 to 2015.

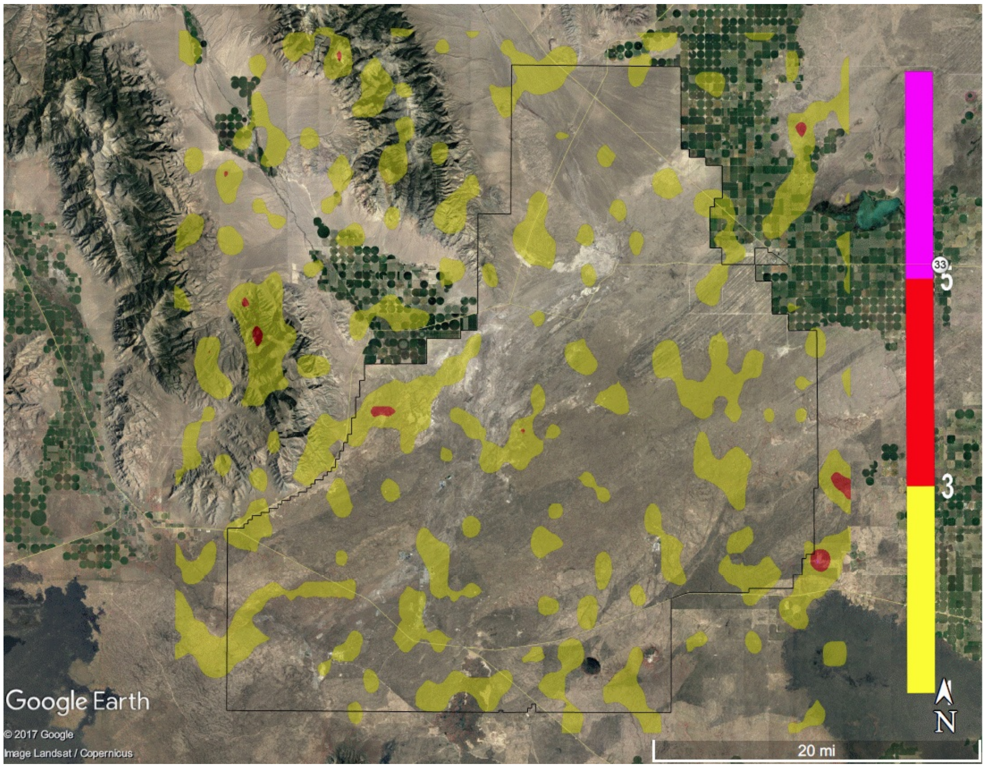

Figure 82. Positive lightning strike density per square kilometer across the INL from 2007 to 2015.

Table 53. Lightning strike variability for the INL from August 2007 through 2015[a].

	Year									Monthly		
	2007	2008	2009	2010	2011	2012	2013	2014	2015	Max	Min	Avg
January	-	0	0	0	0	0	0	0	0	0	0	0
February	-	0	0	0	0	0	0	0	0	0	0	0
March	-	0	6	0	0	0	42	1	0	42	0	6
April	-	8	28	235	187	33	10	0	6	235	0	63
May	-	242	147	40	43	71	283	30	203	283	30	132
June	-	84	1,388	213	84	18	130	15	274	1,388	15	276
July	-	46	398	741	358	419	551	23	406	741	23	368
August	629	369	555	104	716	172	106	1,093	90	1,093	90	426
September	23	57	17	73	30	267	121	252	0	267	0	93
October	0	0	0	72	2	6	19	4	92	92	0	22
November	0	0	0	0	0	0	0	1	0	1	0	0.1
December	0	0	1	1	0	2	0	0	3	3	0	0.8
ANNUAL	-	806	2,540	1,479	1,420	988	1,262	1,419	1,074	2,540	806	1,374

a. Source: United States Precision Lightning Detection Network. (USPLN).

Microbursts

Thunderstorms at the INL may also be accompanied by microbursts. A microburst is a localized column of rapidly sinking air that can produce damaging straight-line winds at the surface. There are two types of microbursts: wet microbursts and dry microbursts. Both occur at the INL and over the entire ESRP. Wet microbursts are accompanied by precipitation, while dry microbursts are associated with virga. Microbursts can appear suddenly and without warning and can cause severe damage, such as the Valentine's Day Storm cited earlier. Microbursts can sometimes be monitored with the NWS WSR-88D Doppler weather radar as the associated gust front kicks up dust and other radar reflecting material as it propagates away from the parent storm cell. An example of a WSR-88D radar-detected gust front is illustrated in Fig. 83. The gust front is shown in a V-shape, centered on the INL. An examination of the time-lapse sequence (not shown) indicates that the eastern flank of the gust front was moving southeast at about 30 mph. The storm cell that produced the microburst and the associated gust front is in the upper-right corner of the image. Microbursts can also be monitored using the Mesonet. Figure 84 illustrates a microburst recorded at the GRI station on July 31, 1994. The microburst arrived at 18:05 MST and created a gust of wind in excess of 80 mph. A concurrent drop in air temperature also occurred, which eventually approached 20 °F. Precipitation arrived 25 minutes after the gust front and delivered only 0.07 in. of rain.

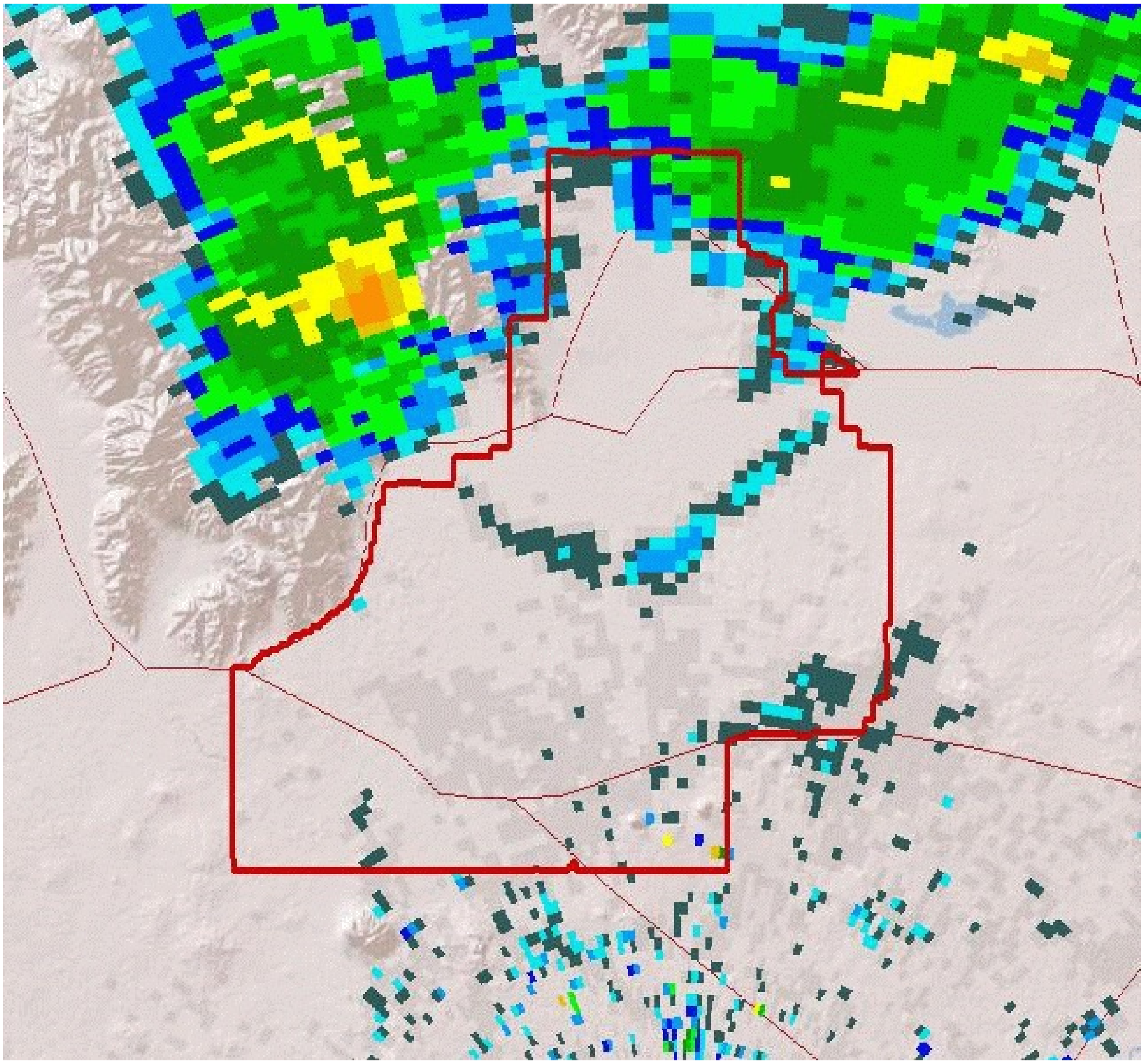

Figure 83. NWS WSR-88D Doppler weather radar illustration of a gust front from a microburst centered on the INL, at 17:48 MDT on June 25, 2004. The storm cell that produced the microburst is in the upper right hand corner of the image.

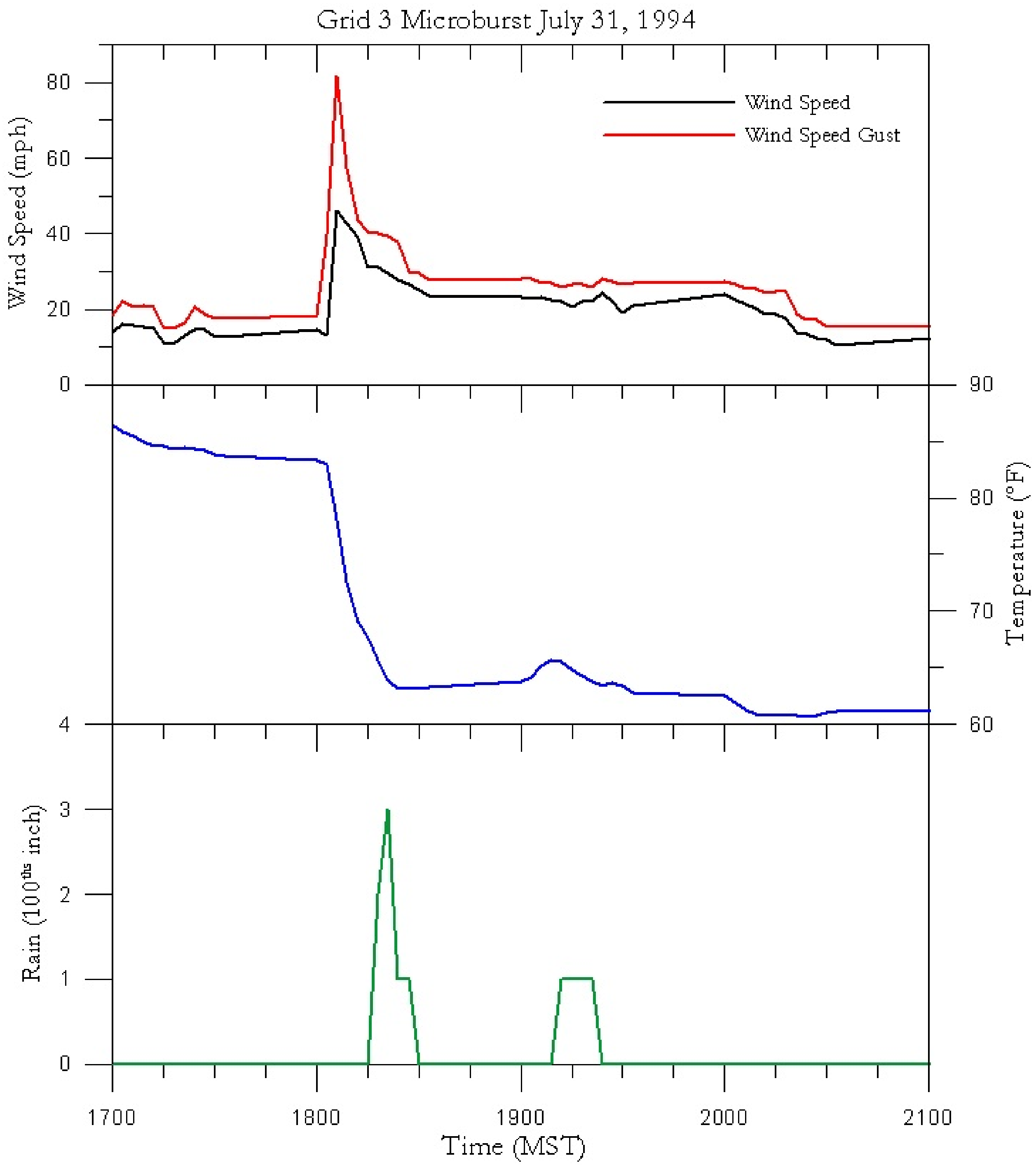

Figure 84. Example of a microburst as measured by the Grid 3 (GRI) Mesonet Station on July 31, 1994.

Hail

Small hail has been observed to occasionally occur in conjunction with thunderstorms. Hail size is usually smaller than 1/4 in. in diameter. Diameter may range up to 3/4 in., however, on very rare occasions. No hail damage has ever been reported at the INL. Nevertheless, crop damage from hail is not unusual on neighboring farms across the ESRP. Property damage in the city of Idaho Falls has been reported as well as in other local cities. Damage from hail still remains a distinct possibility at the INL.

Airborne Dust and Sand

A study of airborne dust at the INL was made in 1952 and 1953 (Humphrey et al., 1953) in disturbed areas and areas of natural vegetation. Dust concentrations ranged from a low of 14.1 $\mu g\ m^{-3}$ over a total snow cover to a high of 772 $\mu g\ m^{-3}$ during the summer. In an undisturbed area, even with dust devils present, a concentration of only 151 $\mu g\ m^{-3}$ was recorded. The annual average of 24-hour particulate samples was approximately 30 $\mu g\ m^{-3}$. Median sizes of dust particles in undisturbed areas ranged from 0.330 to 0.425 μm. Less than 1% of the particles were larger than 10 μm but these ranged in size up to several hundred μm. Petrographic examination of the dust resulted in a moderately abrasive classification of the particles.

During the daylight hours under conditions of strong winds, the concentration of dust sharply decreases with height up to approximately 70 ft. AGL. Vehicular traffic and construction equipment contribute more to high dust concentrations than do strong winds over undisturbed areas, however. It is therefore recommended that building fresh air inlets and motor vehicle air intakes should be located as high above the ground surface as possible.

Blowing dust and drifting sand can be a nuisance when the winds are strong in certain areas of the INL. These conditions may particularly affect the activities of construction personnel during the spring months after the winter thaw, when strong frontal systems pass through the ESRP, and during the summer months when thunderstorms are near.

Dust Devils

Dust devils are small atmospheric vortices that are generated over hot land surfaces. Dust devils form when hot air near the surface rises quickly enough through a small pocket of cooler, low pressure air above it. If conditions are just right, the air will begin to rotate. Dust devils are common in the summer at the INL when intense solar heating of the ground makes dust devil formation possible. They usually occur on calm, sunny days. Dust devils pick up dust and pebbles, and can overturn, blow down, or carry off unsecured objects. The dust cloud may be several hundred yards in diameter and extend several thousand feet into the air. Dust devils were particularly abundant in the late summer of 1996 in the area burned by a wildfire near MFC.

Blowing Snow

Blowing and/or drifting snow sometimes becomes a hazard as well as a nuisance during the winter months at the INL. Blowing snow greatly reduces visibility and slows down transportation. On rare occasions, the visibility has been reduced to zero in extreme blizzard conditions. Blowing snow usually accumulates in drifts on the leeward side of buildings, vehicles, fence posts, vegetation, etc. Drifts may occasionally render parking lots and highways on the INL and access highways to the INL impassable and cause traffic to be rerouted.

Fog

Fog is yet another meteorological phenomenon that occurs with some regularity in the cold winter months at the INL. By definition, fog is a cloud that is in contact with the ground. Fog forms when the difference between the air temperature and the dew point temperature is generally less than 4 °F. Fog begins to form when water vapor condenses into tiny liquid water droplets in the air. The type of fog that occurs at the INL in the winter is a valley fog, the result of a temperature inversion caused by heavier cold air settling onto the INL with warmer air aloft. This type of fog can last for days. Fog reduces visibility at the INL and can, at times, pose a safety risk to vehicular traffic.

Figure 85. Extreme rime icing on meteorological tower on the top of Big Southern Butte, in January 2002.

Icing

Rime ice occurs when fog droplets impinge upon objects at temperatures below freezing. The meteorological conditions for the formation of rime ice may persist for several days when the ground is covered with snow and an accompanying persistent high pressure system is present. This makes the formation of supercooled fog or low stratus clouds and subsequent rime ice formation a distinct possibility. An example of extreme icing is shown in Fig. 85 and 86. The figures show rime

Figure 86. Technician removing rime ice on meteorological tower on the top of Big Southern Butte, in January 2002.

ice that collected on the meteorological tower on the top of Big Southern Butte in January, 2002. Rime icing on the INL, however is not this severe. The accumulation of rime ice on power lines and air intakes has not been a constraint to operations at the INL.

Severe glaze icing, which accompanies freezing rain, rarely occurs at the INL. The meteorological condition which most frequently permits the formation of glaze ice is the transition period from rain to snow. Glaze ice results in slippery sidewalks and roads, and slows transportation. Glaze ice accumulation has been insufficient to damage power lines or communication cables at the INL.

Tornadoes

A tornado is potentially the most damaging weather disturbance on the earth. A tornado is defined as a rapidly rotating column of air (or vortex) descending from the base of a cloud that reaches the surface of the earth. The vortex is usually shaped in a funnel and is anywhere from a few tens of feet up to a mile wide. A tornado is accompanied with spiraling winds of high velocity that may exceed 300 mph and could demolish buildings and cause widespread damage.

Often times a vortex develops and dips below the bottom surface of the clouds and then disappears without reaching the ground. This kind of vortex is classified as a funnel cloud. Tornadoes and funnel clouds always occur in association with thunderstorms, especially those which produce hail.

Most of the tornado activity in the U.S. occurs east of the Rocky Mountains. Tornadoes in Idaho are rare, relatively speaking. The total number of tornadoes in Idaho for the years 1950 through 2015 was 204, according to NOAA's National Climatic Data Center (NCDC, 2016). They occur most frequently during the month of June (22% of occurrences), but were also common in April, May, July and August (12, 19, 13, and 12% of occurrences, respectively). Tornadoes occurred most frequently (73%) between the hours of 1400 to 2000 MST.

Idaho tornado statistics must be interpreted with some caution. For example only 5 tornadoes were reported to the Idaho State Weather Service Office during the period of 1916 through 1950 (Bob Glodo, personal communication). Many more have been reported since then. The rise in tornado sightings is probably due to an increase in population density and better communications rather than an increase in frequency. In the past, a lack of trained weather spotters and a poor local weather radar led to misidentification of tornadoes. In fact, some observers reported thunderstorm downpours as funnel clouds and tornadoes. Today, the NWS uses Doppler Radar which can help identify storms capable of producing tornadoes but still relies on trained weather spotters and the general public for tornado sightings. In addition, tornados are only confirmed once the NWS investigates and assesses the damage from the storm.

Each tornado is classified using the Fujita Scale (F-scale) system that rates the degree of damage to the strength of the winds. The F-scale was replaced by the Enhanced Fujita scale (EF-scale) in 2007. The EF-scale ranges from EF0 (little damage) to EF5 (most intense damage). Sixty-three percent of all Idaho tornadoes reported during this most recent 47-year period were EF0. An EF0 tornado is called a Gale Tornado, with wind speeds 65-85 mph. It causes some damage to chimneys, breaks branches off trees, pushes over shallow-rooted trees, and damages sign boards. Thirty-two percent of all Idaho tornadoes were classified as EF1 tornadoes with wind speeds of 86-110 mph. An EF1 tornado, known as a Moderate Tornado, peels the surface off roofs, mobile homes are pushed off foundations or overturned, moving autos are pushed off the roads, and attached garages may be destroyed. Only 5% of all Idaho tornadoes were classified as EF2, or significant tornadoes with winds speeds of 111- 135 mph. An EF2 tornado causes considerable damage: roofs are torn off frame houses, mobile homes are demolished, boxcars are pushed over, large trees are snapped or uprooted, and light object missiles are generated. To date, Idaho has not experienced an EF3 or stronger tornado. The potentiality for an EF2 tornado or larger is low, given Idaho's mountain setting and characteristically dry air masses when compared to U.S. Midwest air masses.

Locations of tornadoes which have been sighted in the ESRP and reported to the NCDC from1950 through 2015 are illustrated in Fig. 87. Most tornado sightings have been located near

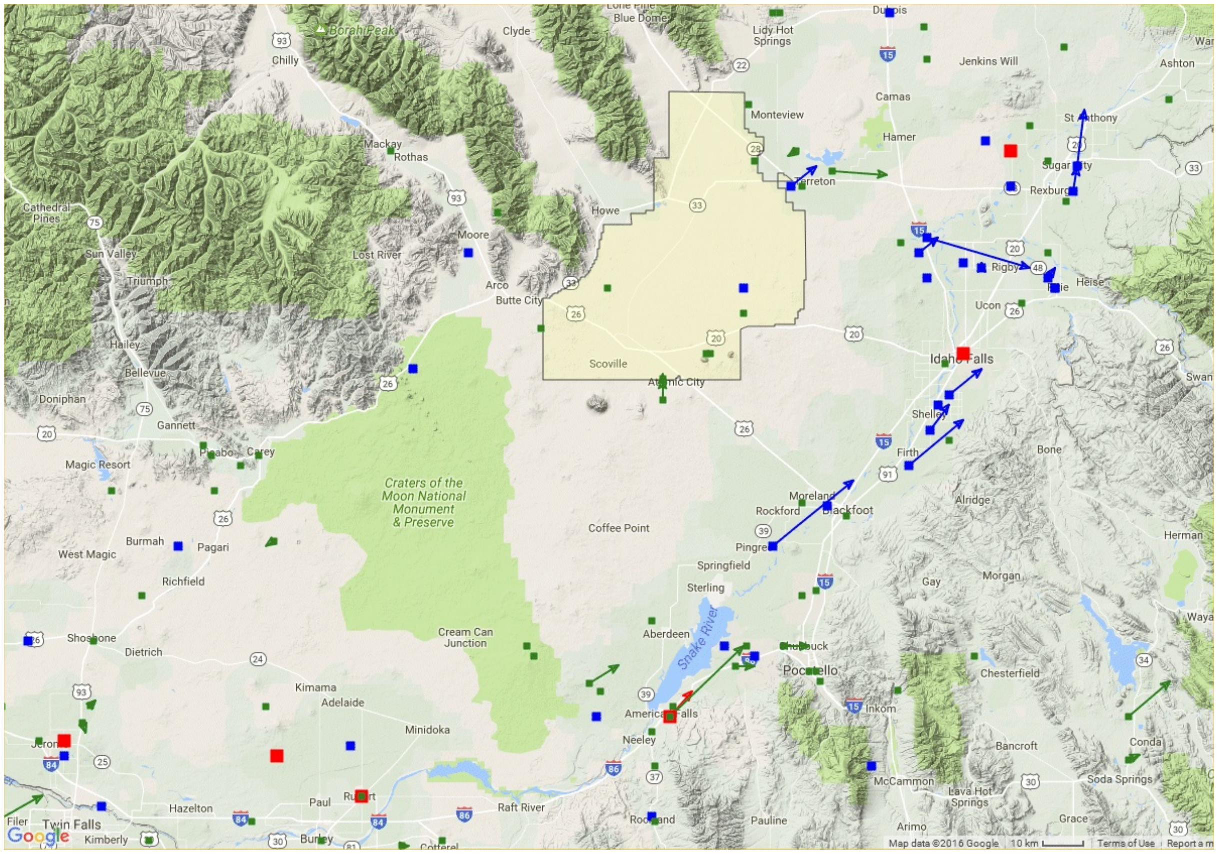

Figure 87. Tornado sightings in the ESRP according to National Climatic Data Center from 1950 through 2015. Each sighting is indicated by the strength (EF0-green square, EF1-blue square, and EF2-red square) and direction (arrow).

Table 54. Funnel cloud and tornado sightings observed on the INL[a].

Date	Time (MST)	Location	Type of Activity
28 April 1954	1220	6 mi. northeast of Atomic City	F0 Tornado[d]
9 June 1954	1210	5.5 mi. northeast of Atomic City	F0 Tornado[d]
6 June 1967	1200	1 mi. southeast of MFC	F0 Tornado[d]
27 July 1972	1330	3 mi. north northeast of MFC	F1 Tornado[d]
20 July 1974	1253	Within a triangle formed by Howe, TRA, and NRF	2 Funnel Clouds[c]
8 May 1975	M[b]	Near Middle Butte	2 Funnel Clouds[c]
23 July 1984	1225	10 mi. west south-west of TRA	1 Funnel Cloud[c]
16 June 1998	915	3 mi. east of DEA	F0 Tornado[d]
1 September 2000	1600	10 mi. east of Arco	1 Funnel Cloud[d]
4 April 2006	1905	5 mi. south west of Monteview	F0 Tornado[d]

a. Data period of record spans from January 1950 through December 2015.
b. Data is missing.
c. Data recorded by FRD.
d. Data recorded by the National Data Climatic Center.

higher populated areas. The large area within the ESRP where only a few tornadoes have been reported are less populated areas. It should not be assumed, however, that there is any less chance of a tornado occurring in those areas than in populated areas. Nonetheless, six tornados have been reported across the INL. A supplemental record of funnel clouds and tornado sightings has been maintained by NOAA personal for the INL. Table 54 combines both the supplemental record and the NCDC reports of the funnel clouds and tornado activity that have been observed on the INL since 1950.

A report was done to investigate tornado frequency at the INL (Clawson et al., 2014). The basis of the report was taken from a tornado climatology report done by Ramsdell and Rishel, 2007 (denoted R&R hereafter). R&R analyzed all of the lower 48 states tornado events in the NCDC database from 1950 through August 2003. R&R recommended tornado design basis wind speeds for the entire western U.S. These speeds are 100 (EF1), 130 (EF2), and 160 mph (EF3) for the 10^{-5}, 10^{-6}, and 10^{-7} yr^{-1} annual probability levels, respectively, and generally apply to the INL site.

Tornado design basis wind speed statistics, including the upper and lower 90th percentile confidence interval wind speeds applicable to the INL Site from R&R are presented in Table 55. For the standard 1 $x10^{-6}$ yr^{-1} probability, the expected wind speed is 129 mph, with a lower 90% confidence limit of 103 mph and an upper 90% confidence limit of 158 mph. The expected wind speed is nearly identical to the recommended wind speed of 130 mph for the entire western U.S.

Table 56 contains expected area and length values, including lower and upper 90th percent confidence intervals for a point and a finite structure with a characteristic length of 200 ft. at the INL Site. The expected area of a tornado's path is 0.331 sq. mi., and the length is expected to be 2.65 mi. Table 56 also contains the strike probabilities for a point and a finite structure

Table 55. Tornado design basis winds speeds for the INL Site (from Ramsdell and Rishell, 2007).

Design Criterion yr^{-1}	Expected Maximum Wind Speed (mph)	Lower 90th% Confidence Limit (mph)	Upper 90th% Confidence Limit (mph)
10^{-5}	82	60	115
10^{-6}	129	103	158
10^{-7}	169	144	196

Table 56. Expected area of a tornado with strike probabilities for a point location and a 200-ft. finite structure (from Ramsdell and Rishell, 2007).

Structure Type	Area (sq. mi.) --------- Length (mi.)	Lower 90th% Confidence Limit (sq. mi.) --------- (mi.)	Upper 90th% Confidence Limit (sq. mi.) --------- (mi.)	Strike Probability (yr^{-1})	Lower 90th % Confidence Limit (yr^{-1})	Upper 90th% Confidence Limit (yr^{-1})
Point	0.331	0.0742	1.47	1.39×10^{-5}	3.12×10^{-6}	6.20 x 10-5
200 ft.	2.65	1.31	5.33	4.21×10^{-6}	2.09×10^{-6}	8.49 x10-6

together with lower and upper 90th percent confidence limits. The strike probability for a point is 1.39 $\times 10^{-5}$ yr^{-1} and for a 200-ft finite structure it is 4.21 $\times 10^{-6}$ yr^{-1}. If a strike probability is desired for a structure with a characteristic length different from 200 ft., the values for the finite structure should be adjusted by the ratio of the characteristic dimension of the new structure to 200 ft. Thus, the strike probability for a 5-mile long power line is 5.56 $\times 10^{-4}$ yr^{-1}.

When considering the values to use for a beyond design basis scenario, it seems reasonable to use the extreme values from Tables 55 and 56. One could use the wind speed associated with the upper 90th percentile for the 10^{-7} yr^{-1} design criteria to bound the wind speed for the highest extreme event that may occur at the INL Site. This value is 196 mph (EF4). Following this same logic, the longest tornado path could be assumed to be 1.47 mi., with an area of 5.33 sq. mi. These values are from the upper 90th percent confidence intervals for a point and a 200-ft. finite structure.

Tornado forecasts and tornado warning lead times have improved greatly in the last 2 decades. Perhaps the most useful aid in advancing tornado warnings is the weather radar NEXRAD WSR-88D. It has built-in algorithms that continuously monitor every storm in the detection area for mesocyclone rotation and the likely presence of tornados. Once such recent occurrence is instructive.

On 04 October 2006, the local NEXRAD radar detected a possible tornado in a storm cell located approximately 10 mi. south of the INL boundary, approximately 15 mi. south-southwest of Atomic City. The predicted cell movement was toward the southeastern corner of the site.

The Pocatello NWS subsequently issued a tornado warning for the area that included MFC. The FRD duty forecaster followed-up with a revised forecast that was communicated to the INL Warning Communication Center that indicated that MFC was not in the direct path and that no tornado evasive action would be necessary. The supercell continued to increase in size and strength and also began to exhibit the tornado vortex signature. The radar reflectivity also began to show the classic bow echo of a tornadic supercell (Fig. 88). The supercell followed the forecast track as predicted from the NEXRAD algorithm and only skirted the southeast boundaries of the INL. MFC was not significantly affected by the storm. A tornado was spawned by this storm near Atomic City and verified by NWS personnel, as indicated in the NCDC tornado database. This account illustrates the improved ability of both the NWS and FRD to provide INL better warnings of severe storms and tornados.

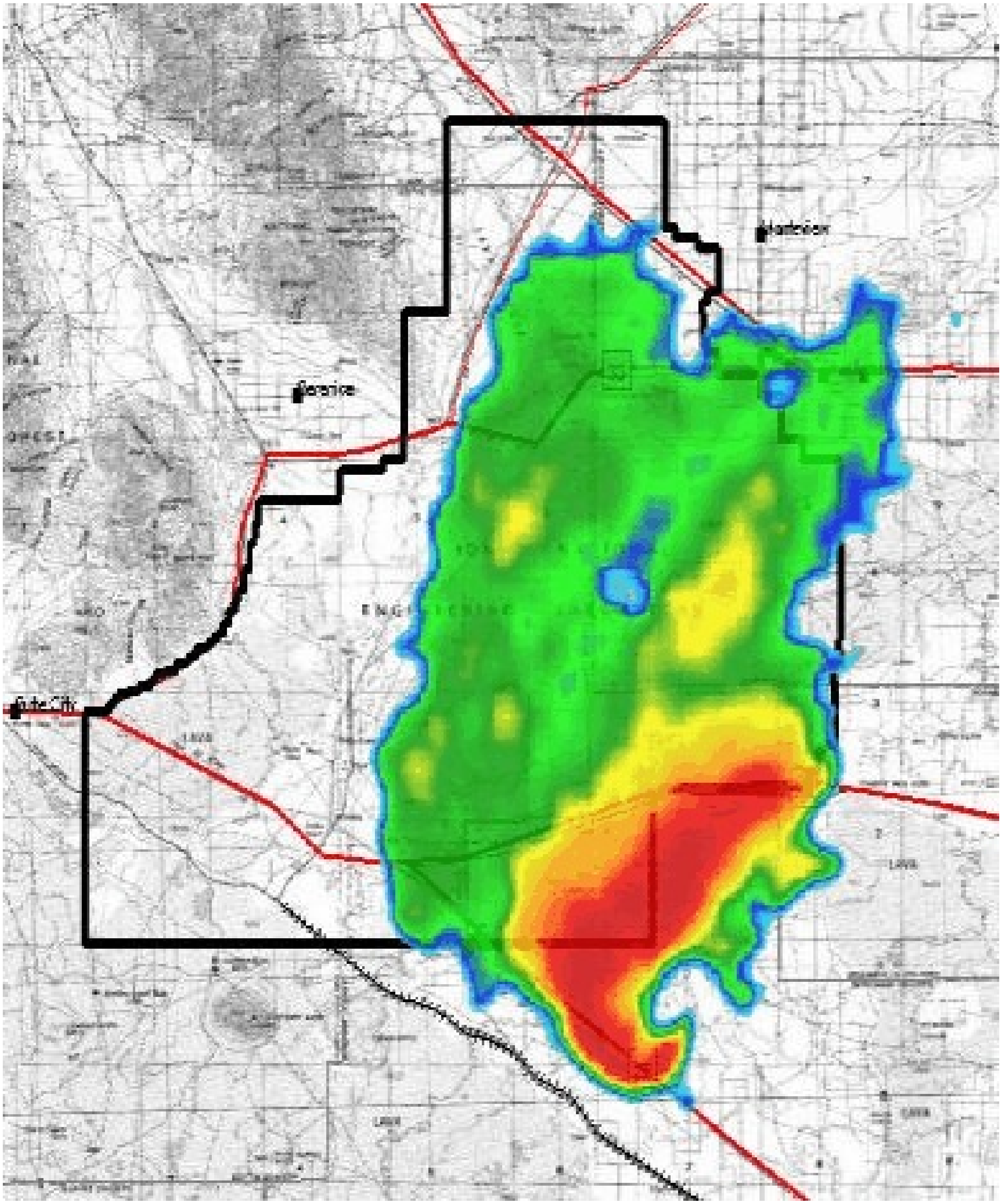

Figure 88. NWS WSR-88D Doppler weather radar illustration of a bow echo from a tornadic supercell thunderstorm centered on the INL, at 17:15 MDT on October 6, 2006.

RANGE FIRES

From 1994 to 2015 over 270,000 acres of the INL and several hundred thousand acres of Bureau of Land Management managed public lands burned on the Snake River Plain of southeast Idaho. Range fires have threatened INL facilities and have exposed soils to wind erosion, resulting in severe dust storms that have impacted operations and created traffic hazards that persisted for weeks. Figure 89 depicts the burned areas for fires that occurred in the period 1994 through 2015.

Major fires (more than 5,000 acres in size) occurred on the INL in 1994, 1995, 1996, 1999, 2000, 2007, and 2010. Some of these fires burned through areas in which NOAA/INL Mesonet stations were installed. In particular, the 1994 fire burned around the DEA and BAS stations and the 2000 fire burned around the ATR station. A graph of the five-minute average air temperature spike from the range fire on July 1, 1994 at DEA and BAS is shown in Fig. 90. The maximum air temperature spike during the time the fire burned through each station was 169 and 154 °F for BAS and DEA, respectively. Although range fires have burned around a few NOAA/INL Mesonet stations, the fires usually progress so rapidly that equipment does not get harmed. However, the Jefferson Fire in 2010 burned hot enough at the Rover Mesonet station to ruin most of the instrumentation near the ground (Fig. 91).

Statewide, approximately 65% of Idaho range fires are lightning-caused (DOE, 2003). At the INL, range fires typically occur in the late summer and fall, when annual grasses are dry, lightning activity is high, and dry atmospheric conditions evaporate much of the storm's rain (virga) before it reaches the ground. Lightning-caused fires spread rapidly when fanned by high winds that frequently accompany thunderstorms. The persistence of thunderstorm winds is limited, however, as exhibited in the surface diurnal wind patterns.

Human-caused wildfires have been most damaging when started during conditions of persistent strong southwesterly winds that are a common occurrence at the INL. This occurs when strong solar heating of the surface links the surface winds with strong southwesterly synoptic winds aloft.

Winds affect not only the spread of wildfires, but also the natural propagation of seeds of grasses and forbs, including sagebrush. Restoration of sagebrush is highly desirable in order to maintain a balance of desirable natural plant and animal species (DOE, 2003). Deposition of wind-blown materials shifts and impacts the balance of moisture-retaining soils at the INL, and thereby influences areas where natural fuels may preferentially grow and accumulate in the future.

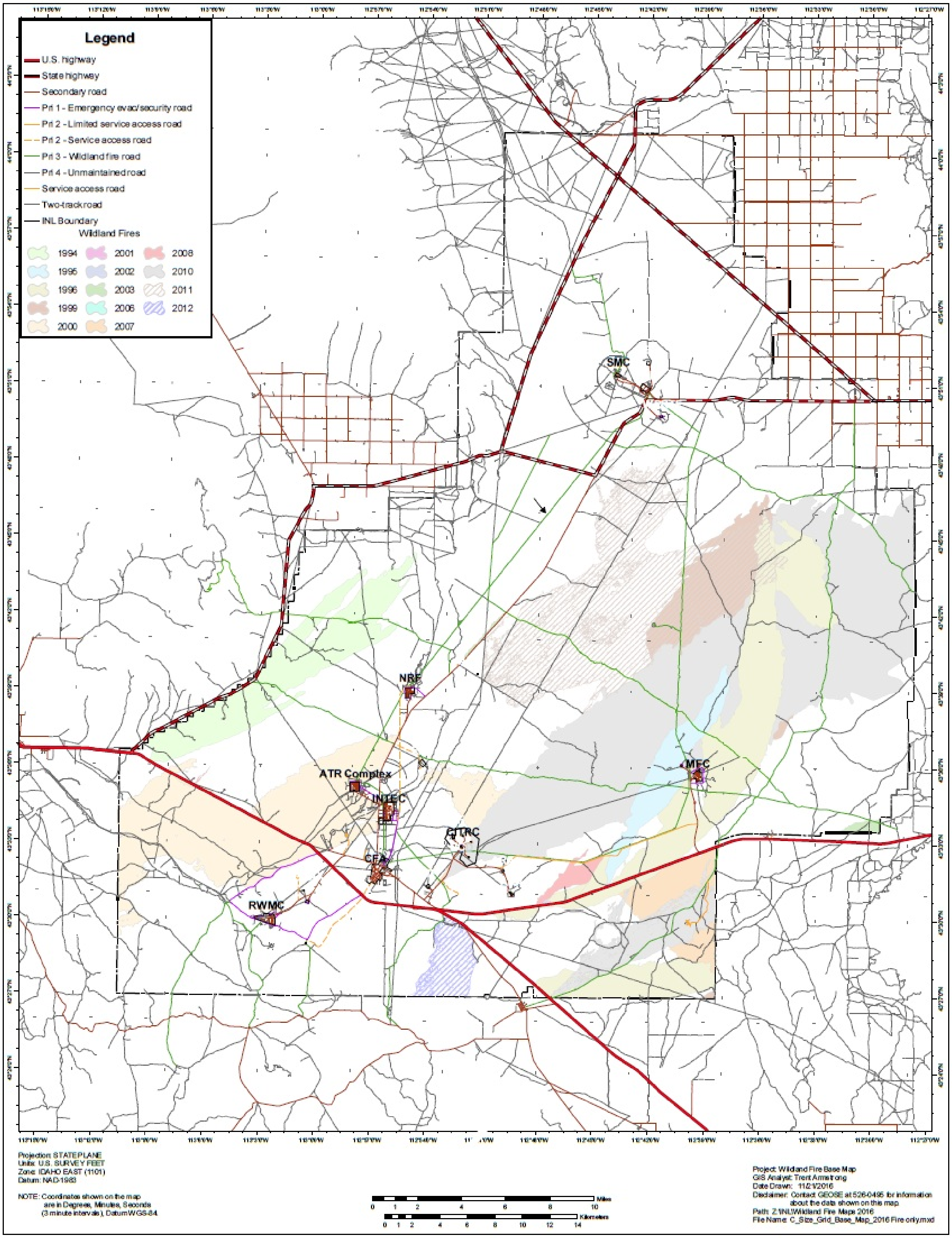

Figure 89. Wildland fire areas at INL from 1994 through 2015.

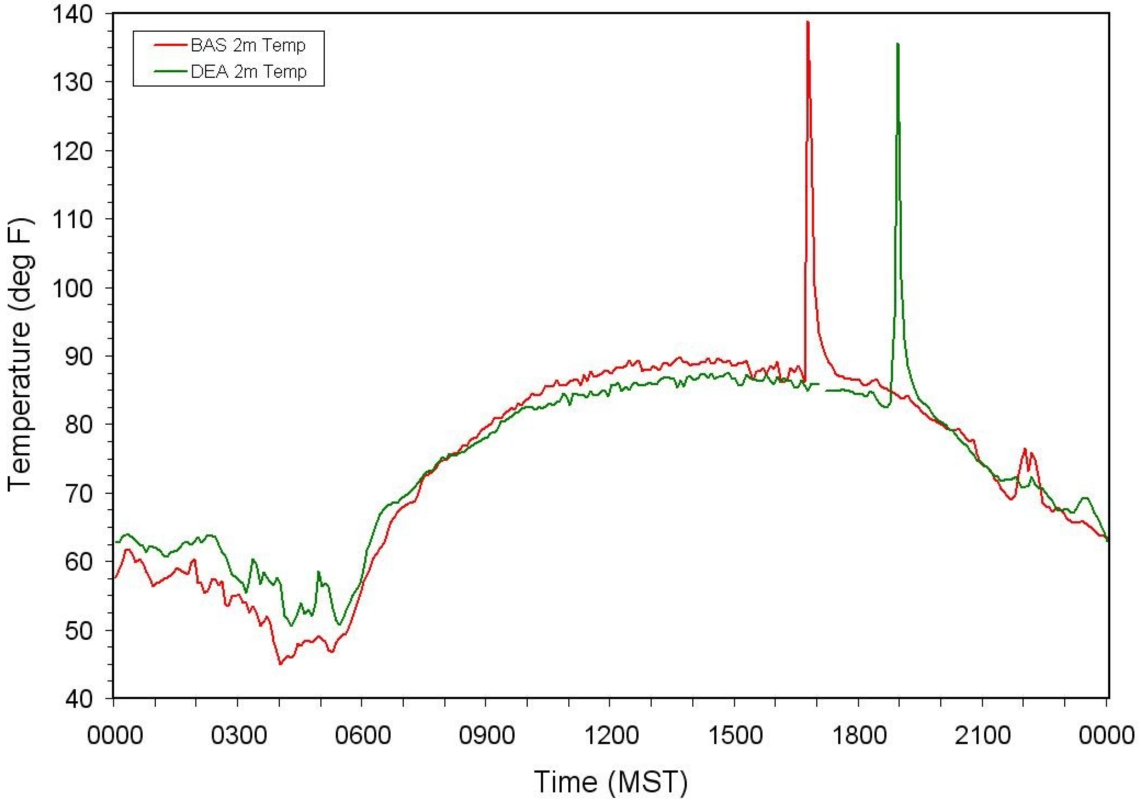

Figure 90. Five-minute air temperature spike from July 1, 1994 range fire at DEA and BAS.

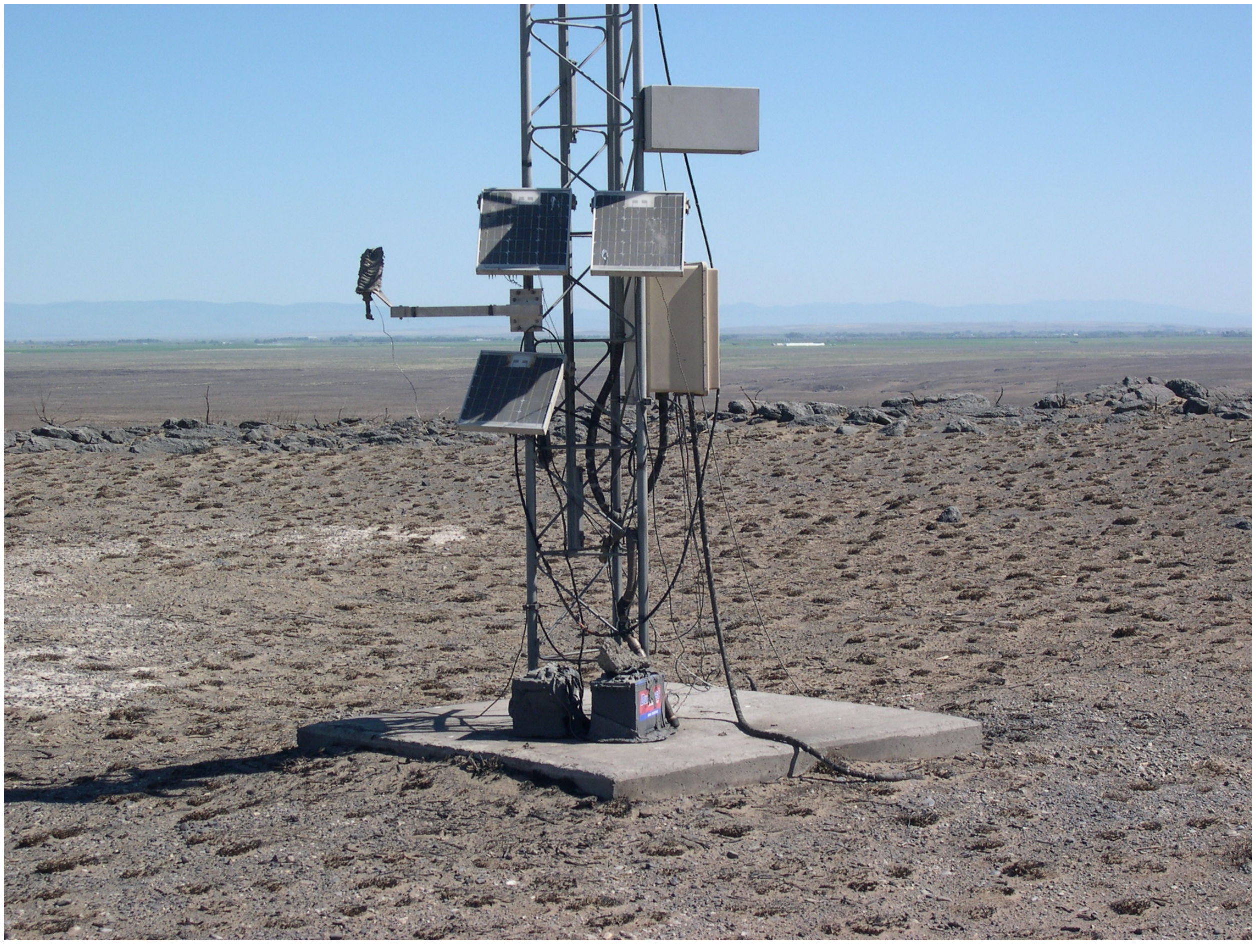

Figure 91. Picture of the ROV Mesonet site after the Jefferson fire in 2010.

ATMOSPHERIC TRANSPORT AND DIFFUSION

Operations at the INL frequently require a means of estimating the potential impacts of routine or accidental effluent releases into the atmosphere. The atmosphere has two primary effects on an effluent: transport and diffusion. Transport is the bulk motion of the effluent cloud caused by the wind. It is associated with atmospheric circulations having length scales significantly larger than the size of the cloud. Winds in the atmosphere are actually a composite of atmospheric circulations spanning a wide range of scales, from the 600 miles (1000 km) scale of synoptic weather systems down to local turbulent eddies having scales as small as 0.04" (1 mm). Only those circulations significantly larger than the size of an effluent cloud are effective in bulk transport. Smaller circulations tend to shred the effluent cloud apart and mix it with the surrounding clear air. This turbulent mixing process is called diffusion. The combination of transport and diffusion is often called atmospheric dispersion.

Any computer model that estimates the impact of an effluent release must deal with both the transport and diffusion of the cloud. To be successful, such models must contain a realistic description of atmospheric structure. Most dispersion models focus on effluent releases near the surface where people live, so they must accurately describe the structure of the lowest part of the atmosphere, known as the atmospheric boundary layer (ABL).

THE ATMOSPHERIC BOUNDARY LAYER

The ABL is the part of the atmosphere that responds directly to the presence of the earth's surface. Everyone is aware of the normal diurnal air temperature cycle with warming during the day and cooling at night. This cycle is caused by daytime solar heating of the surface and radiative cooling at night. The air just above the surface responds quickly to these changes in surface heating and cooling, but the atmosphere far above the surface shows no such response. Typically, only the atmosphere within the first few kilometers above the surface exhibits a direct response to diurnal changes at the earth's surface, and this lowest layer is the ABL. The atmosphere above the ABL is usually called the free atmosphere or free troposphere. The ABL responds to more than just surface heating and cooling. Aerodynamic drag at the surface also tends to reduce wind speeds. Winds within the ABL are directly affected by this surface drag and therefore typically have lower speeds than in the free atmosphere above.

Vertical mixing by turbulence is the primary mechanism that allows the ABL to respond to changes in surface conditions. Anything released near the surface, whether it is energy from the sun or an effluent, is mixed upward by turbulence through the ABL. Turbulence is generated in two primary ways (Garratt, 1992). Mechanical production of turbulence occurs when velocity shears develop within a mean wind flow. The drag exerted by the earth's surface is one common source of velocity shear, so mechanical turbulence is ubiquitous near the surface. Since mechanical turbulence derives its energy from an existing mean flow, larger atmospheric circulations such as synoptic weather systems must be present to sustain the mean flow. Energy is continually extracted from the larger circulations to maintain the mechanical turbulence. Generally, rough surfaces generate more mechanical turbulence than smooth surfaces, so the turbulence level over a forest is usually higher than over a smoother surface such as short grass.

The second primary turbulence generation mechanism is buoyant production. If the earth's surface is warmer than the overlying air, as is normally the case over land on sunny days, buoyant parcels of air will form and rise upward as convective thermals. These thermals are an additional source of turbulence within the ABL and can coexist with mechanical turbulence. Since buoyancy-generated turbulence derives its energy from temperature differences, it can exist even when no mean airflow is present.

Figure 92 is an idealized diagram of ABL structure during fair weather over land. The depth and structure of the ABL varies widely from day to night. Shortly after sunrise the heating at the earth's surface causes a rapid increase in the buoyant production of turbulence. The convective thermals tend to penetrate higher and higher as the morning wears on, so there is a rapid growth of the boundary layer until it reaches a quasi-steady depth of typically ½ - 2 miles (1-3 km) during the afternoon. Because the daytime boundary layer is dominated by convection, it is often called the convective boundary layer (CBL). The CBL is frequently capped by a temperature inversion which tends to block the continued upward motion of the thermals. However, some mixing of CBL and free-atmosphere air takes place at this level, so the capping layer is sometimes called the entrainment layer.

Near sunset the solar heating at the surface ceases, so there is a rapid decrease in buoyant turbulence production. This results in a collapse of the ABL depth as the convective thermals dissipate and only mechanical turbulence remains. After sunset, radiative cooling at the surface causes a surface-based inversion to develop and grow. The temperature profile within the inversion tends to suppress the production of mechanical turbulence, so the depth of the nocturnal boundary layer (NBL) is usually far less than that of the CBL.

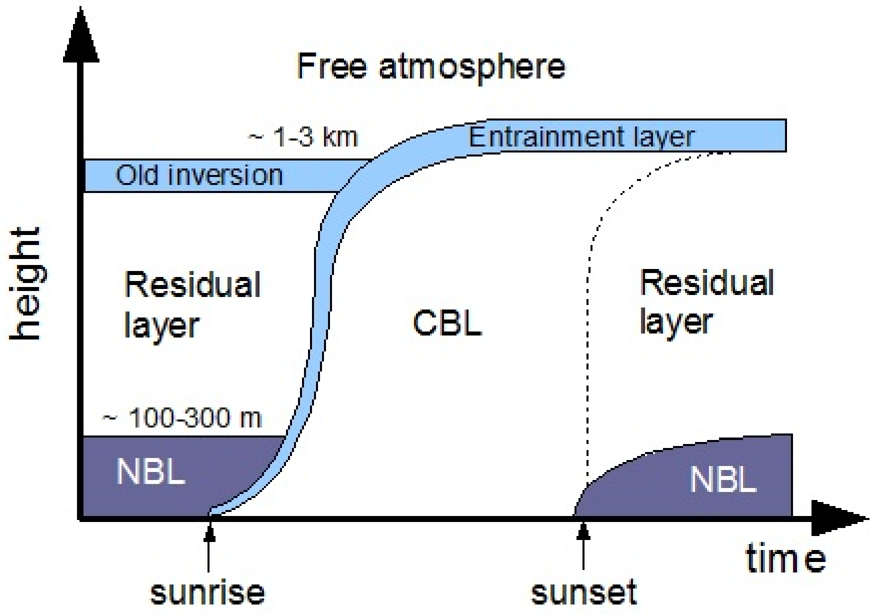

Figure 92. Schematic diagram of the atmospheric boundary layer (ABL) structure in fair weather. NBL is the nocturnal boundary layer, and CBL is the convective boundary layer

Above the NBL is the residual layer (RL), which is basically the remnants of the previous day's CBL. The temperature profile within the RL remains similar to what it was during the day, but there is no longer any steady turbulence production within this layer. Since the RL is cut off from the surface, it is not really part of the ABL. However, intermittent bursts of turbulence are possible within the RL due to a variety of mechanisms, including shears related to low-level jets and gravity waves.

Defining the depth of the NBL is not straightforward, because there is no capping inversion that clearly separates the NBL from the RL above. A variety of definitions have been proposed (Stull, 1988), including the total depth of the surface-based inversion and the height of the lowest-level wind jet. For dispersion applications, however, the depth that matters is the depth of the surface turbulence layer. Generally, the NBL turbulence layer is shallower than the inversion depth (Garratt, 1992) and is typically on the order of 300+ ft (100 m) when moderate winds are present but can be less than 165 ft (50 m) in light winds.

ATMOSPHERIC STABILITY

Transport and diffusion models usually require some kind of input related to atmospheric stability. The well-known Pasquill stability classes (Pasquill 1961) , with class A representing very unstable conditions and class F representing moderately stable conditions, are one type of stability input that has found common use in dispersion modeling. One can ask how this notion of stability is related to the ABL structure briefly described above. The problem here is that atmospheric stability has been defined in more than one way within the meteorology literature, and this often leads to confusion when applying this concept to dispersion.

Many meteorology textbooks discuss the idea of static stability (e.g., Wallace and Hobbs, 1977), which is associated with the behavior of an air parcel when it is vertically displaced. An atmospheric layer is said to be statically stable when an air parcel that is vertically displaced experiences a buoyancy force that causes it to settle back to its original level. Statically unstable conditions exist when a vertically displaced air parcel experiences a buoyancy force that causes it to continue moving away from its original level. Neutral stability exists when the displaced air parcel experiences no buoyancy force and therefore remains at its new level. Static stability is determined by the temperature profile within the atmospheric layer. Neutral conditions exist when the atmospheric temperature decreases at the dry adiabatic lapse rate of 5.38°F 1000 ft^{-1} (9.8°C km^{-1}). Any layers that have a lapse rate less than this are statically stable, whereas layers with larger lapse rates are unstable. The presence of water in the atmosphere adds additional complications to this simple concept of stability, but this is not discussed here.

Static stability is clearly a spatially local definition that can vary from point to point. The concept of stability that is more relevant for dispersion modeling is a bulk definition that applies to the whole ABL. From Fig. 92 it is clear that the daytime CBL corresponds overall to an “unstable” boundary layer, whereas the NBL fits the role of a “stable” boundary layer. The primary difference between the CBL and NBL is the direction of heat flow at the surface. This is quantified as the sensible heat flux H at the surface, which is the thermal energy passing through a unit area of the earth's surface per unit time (e.g., units of W m^{-2}). Positive values of H denote an upward heat flux from the surface to the atmosphere; negative values represent a downward flux that transfers energy from the atmosphere to the surface. From this, it is clear that the ABL is generally unstable when *H* is large and positive, and generally stable when *H* is negative.

Although the bulk ABL stability is related to the concept of static stability discussed above, they do not entirely overlap. Large portions of the CBL actually have a nearly neutral static stability. Buoyant thermals are generated near the surface in the CBL, and then rise up through the statically neutral middle portions. The turbulence observed in the middle CBL is therefore largely caused by nonlocal buoyant production originating at the earth's surface. Static stability is only useful as an indicator of local turbulence production within the layer where it is measured, so it has limited utility in situations, such as the CBL, where most of the turbulence is generated nonlocally.

From Fig. 92 it is not clear how one defines an ABL with neutral bulk stability. Neutral conditions should prevail when the surface heat flux *H* is close to zero, with neither buoyant production nor suppression of the turbulence. Under such conditions the ABL structure is determined mainly by mechanical turbulence acting in a layer with a nearly neutral static stability. In the fair weather depicted in Fig. 92, a neutral ABL is expected to exist only during short transitory periods near sunrise and sunset. One would expect a near-neutral ABL to be present for more extended periods in cloudy conditions when *H* is small or in windy conditions with only weak solar heating (e.g., in winter).

TRANSPORT AND DIFFUSION MODELING

Various approaches have been used to model the transport and diffusion of effluents. Over time, a better understanding of ABL structure and continually increasing computer speeds have allowed ever more complex dispersion models to be developed. However, the most complex models are not always the best models for a particular application. Complex models usually contain a large number of input variables that are not always easy to obtain from field measurements. If a lack of field measurements forces the user to guess at some important model inputs, a complex model may actually end up performing worse than a simpler model with fewer inputs. As a general rule, the most suitable model complexity will depend both on the specific model application and on what kind of field measurements are available.

Broadly, all dispersion models can be classified as using either an Eulerian or Lagrangian framework. In an Eulerian model, the properties of the effluent are tracked at a series of fixed points in space. Normally, this involves solving a conservation-of-mass equation for the effluent on a fixed grid of points. Eulerian models are most commonly used to estimate regional air pollution, because they are well suited to area emissions of pollutants and can include algorithms for chemical transformations. Such models are not well suited for individual plume or puff releases, because they would require an extremely dense grid of points to properly resolve the plume or puff.

Lagrangian models are commonly used to model effluent releases from a single source or from a small number of individual sources. These models track the motion of the air parcels containing the effluent as these parcels are dispersed by the atmosphere. Various simplifying assumptions are used to reduce the number of model parameters that are required to keep track of the effluent cloud. Depending on the level of simplification, the number of parameters required to track a single effluent cloud can be quite small, which is why Lagrangian models are highly favored for single plume or puff releases. Although Lagrangian models do not use fixed grids of points for computing the dispersion, they often include algorithms for interpolating the model outputs (e.g., concentrations) to a fixed grid. This is done for the convenience of the model end users, who usually want to know how the effluent cloud is expected to affect specific locations.

At the INL, almost all of the effluents of concern come from a relatively small number of point sources. Hence, all the dispersion modeling at INL has so far been performed with Lagrangian models. The following subsections describe in more detail some of the general categories of Lagrangian models in common use. No further discussion is devoted to Eulerian models, since they are currently not in use at INL.

Gaussian Plume Model

The Gaussian plume model is one of the simplest models for continuous emissions from a point source. It assumes that the concentration in both the horizontal and vertical directions follows a Gaussian (normal) distribution about the plume centerline. Moreover, the wind speed *U,* wind direction, and the turbulence levels are assumed to be constant in both space and time. For a point source with constant effluent release rate *q*, the ground-level concentration $\chi(x,y,0)$ according to this model is

$$\chi(x,y,0) = \frac{q}{\pi \sigma_y \sigma_z U} \exp\left[-\frac{y^2}{2\sigma_y^2} - \frac{h^2}{2\sigma_z^2} \right] \quad \textbf{(6)}$$

where *x* is downwind distance from the source, *y* is crosswind distance from the plume centerline, *h* is the height of the plume centerline, and σ_y and σ_z are respectively the horizontal and vertical standard deviations for the plume. This particular form of the model assumes that any portion of the plume extending underground is "reflected" at the surface.

The standard deviations σ_y and σ_z vary with downwind distance *x* and are interpreted as a measure of the horizontal and vertical sizes of the plume. Much of the effort associated with any Gaussian model is related to determining the rate of growth of these standard deviations. This is where the ABL structure described earlier comes into play. The growth rate of these parameters is directly linked to the level of turbulence present in the ABL.

While mathematically simple, the Gaussian plume model has significant limitations. It assumes the wind remains constant in speed and direction as the effluent is transported from the source to the receptor location at (x,y). Likewise, both the release rate *q* and the turbulence responsible for the growth of σ_y and σ_z are also assumed to remain constant. In practice, these assumptions are usually valid for only relatively short distances from the source. At the INL, for example, it is usually reasonable to assume a constant transport wind out to distances on the order of a half mile (kilometer) or so, but at longer ranges the wind often changes due to the influence of the topography or other factors. Even in flat terrain, the temporal changes in ABL structure shown in Fig. 92 can invalidate the underlying assumptions of the plume model for effluent travel times beyond an hour or so.

Gaussian Puff Model

Some of the limitations of a straight-line plume model are avoided by treating the effluent cloud as a series of instantaneous puffs.

Each puff is assumed to have a Gaussian distribution in all three directions. For a puff containing a mass *Q* of effluent, the concentration at a location (x_c, y_c, z_c) relative to the puff's center is

$$\chi(x_c, y_c, z_c) = \frac{Q}{(2\pi)^{3/2}\sigma_x\sigma_y\sigma_z} \cdot \exp\left[-\frac{x_c^2}{2\sigma_x^2} - \frac{y_c^2}{2\sigma_y^2} - \frac{z_c^2}{2\sigma_z^2}\right] \tag{7}$$

where the standard deviations σ_x, σ_y, and σ_z respectively apply to the alongwind, crosswind, and vertical directions. The wind speed *U* does not appear in this equation, because the coordinates (x_c, y_c, z_c) are defined relative to an origin at the puff's center. A separate computation is therefore required to estimate the transport of the puff's center by the wind. For simplicity, surface reflection of the puff is ignored in Eq. (7), although it can be added as in Eq. (6).

To model a continuous source, puff models simply release a sequence of puffs at fixed intervals. If the time interval is too long, the model plume will have unrealistic gaps between the individual puffs. If the interval is too short, the model becomes bogged down tracking a large number of puffs. Most models therefore seek an intermediate puff-release interval that provides a realistic representation of the plume but is still computationally efficient. The total plume concentration at a fixed receptor is obtained by adding the contributions from all the nearby puffs.

A primary advantage of puff models is that they can deal with both temporal and spatial changes in the meteorological conditions. After a puff is released, its transport is broken down into a sequence of time steps δt. Both the wind speed and direction at the puff's center can vary from one time step to another. This may be due either to temporal changes in the wind or to the puff moving into a region with different winds. A puff model can therefore deal with complex wind fields where a plume's centerline will no longer be straight. These models can even simulate recirculations, where a reversal in wind direction causes some of the puffs to move back over the original release location at a later time. The growth of the puff standard deviations is likewise computed in time steps, which allows changes in ABL turbulence to be factored into the model.

Puff models tend to be more realistic than straight-line models in complex flows, but this comes at a price. First, the user must have either measurements or forecast-model output that describes the complex, time-varying wind field. If such information is not available, a puff model may not perform any better than a simpler plume model. Second, puff models are computationally more expensive than plume models. This is less of an issue now than in the past, but some effort must still be made to keep the number of puffs being tracked to a reasonable level. An incorrectly configured puff model can still bog down to the point where the output is not available in a timely manner.

Puff models are a significant step up in realism from straight-line plume models, but they still have limitations. Many of these limitations are related to the steep gradients of meteorological variables that often exist in the vertical. Because of surface drag, vertical wind shear is almost always present in parts of the ABL. Generally, the vertical changes of winds and turbulence within the ABL are much larger than the horizontal changes. This can cause problems in Gaussian formulations such as Eq. (7), because there is an implicit assumption that the atmosphere is relatively uniform inside the volume occupied by the puff. This assumption can be quickly invalidated in the vertical even for values of σ_z as small as 33 ft (10 m).

Several alterations have been proposed to account for the large vertical shears in the ABL. One of the most common is to simply break a puff vertically into smaller puffs when σ_z becomes too large. Another is to increase the growth of σ_x and σ_y in response to the presence of vertical wind shear. A less common approach is to skew the vertical axis of each puff as a function of the observed wind shear.

All Gaussian models also come under some criticism for not taking into account the known structure of buoyancy-generated turbulence in the daytime CBL. As discussed earlier, much of the turbulence within the CBL is caused by thermals that are created near the surface and then rise up through the CBL. On average, these thermals occupy less than 50% of a given horizontal area; the remainder of the area contains a mean subsidence that offsets the mass transported upward by the thermals. The end result is that the vertical turbulence within the CBL has a skewed distribution, with larger but less frequent upward motions balanced by smaller but more frequent downward motions. This skewness directly affects the expected vertical distribution of an effluent cloud, so that the simple Gaussian distribution may not accurately reflect the true distribution in a CBL.

Lagrangian Particle Models

The increasing capabilities of computers have allowed an alternate type of dispersion model called a Lagrangian particle model to be employed (Luhar and Britter, 1989; Wilson and Sawford, 1996). These models use a large cloud of particles to represent the effluent. Unlike a puff, each particle is assumed to be small enough (e.g.,an air parcel) that its internal growth can be ignored. Hence, the particles are treated as points that move with the wind but have no internal structure. To represent an instantaneous release, a particle model must simultaneously release a large number of particles within a limited volume near the source. A continuous release is obtained by repeatedly releasing particles at some fixed interval.

Since the particles do not grow in size, both the transport and diffusion of the effluent must be accounted for in the particle motion. Each particle is assumed to have a mean velocity vector **U** that can vary with position and time. This mean velocity accounts for the bulk transport of the effluent, and performs a similar role to the mean motion of the puff centers in a puff model. To account for diffusion, an additional turbulent velocity increment is added to each particle's velocity components. This is done using a Markov equation for the velocity increment over a time interval from t to $t + \delta t$. Taking the particle velocity *v* along the *y* axis as an example, the Markov equation is

$$v(t+\delta t) = R(\delta t)v(t) + \sqrt{1 - R(\delta t)^2}\,\sigma_v \zeta \quad (8)$$

Here, $R(\delta t)$ is the velocity auto correlation for time lag δt , σ_v the standard deviation of the *v* velocity component, and ζ is a computer-generated random number from a unit normal distribution. The first term on the right side accounts for the observation that atmospheric turbulence has memory, whereas the second term is a random forcing that maintains the energy of the turbulence.

Equation (8) is applied independently to each particle, so over time the particles tend to spread apart at a rate proportional to the velocity standard deviation σ_v . In real particle models, this simple Markov equation is normally only used for the horizontal diffusion. The equation for the vertical diffusion is usually more complex to account for the rapid variation with height of the turbulence (e.g., Wilson et al., 1983). However, Eq. (8) still provides the gist of how Largangian particle models work. To obtain the concentration distribution from these models, the region of interest is divided into a series of rectangular volumes $\delta V = \delta x \delta y \delta z$, and the number of particles within each volume is counted.

The big advantage of particle models is that they can realistically simulate dispersion in the presence of complex velocity shears. As already noted, vertical wind shear is nearly always present near the earth's surface. Since each particle is driven by the wind and turbulence at its own location, particle models can directly simulate the stretching of an effluent cloud related to shear. These models are also capable of handling cases where plumes are split apart by topography. At the INL, for example, an effluent cloud can under the right conditions be split apart so that a portion of the cloud is drawn up one of the nearby tributary valleys (i.e., the Lost River or Birch Creek Valleys), whereas the remainder stays within the Snake River Plain. This type of plume splitting is much easier to simulate with a particle model than with the simpler Gaussian models.

The primary drawback of Lagrangian particle models is that a large number of particles must be released and tracked to produce a reasonably continuous concentration distribution. If too few particles are released, the resulting concentration distribution will be highly irregular because most of the grid volumes δV will contain only a small number of particles. The NOAA HYSPLIT model (Draxler and Hess, 1997) reduces the number of required particles by including a hybrid configuration that combines the puff and particle approaches. As noted earlier, vertical wind gradients are usually much larger than horizontal gradients. Hence, the particle approach provides the most benefit for vertical diffusion. HYSPLIT includes an option that uses the puff approach to model horizontal diffusion and the particle approach to model vertical diffusion. The resulting combination of particles and puffs resemble flat disks that grow horizontally but move randomly in the vertical based on a particle-type equation. This provides most of the benefits of the particle approach but requires far fewer particles and puffs than would be required in a full 3D particle simulation.

Turbulence Estimation

With all Lagrangian models, it is necessary to estimate the strength of the turbulence that is diffusing the effluent cloud. In Gaussian models the turbulence levels directly affect the growth of the plume standard deviations such as σ_y and σ_z. In particle models the turbulence shows up directly through the velocity standard deviations such as σ_v in Eq. (9). At short ranges from the source, there is actually a simple relation between the plume growth and the corresponding velocity standard deviation (Taylor, 1921). Taking the horizontal standard deviation σ_y as an example, the short-range Taylor formula is

$$\sigma_y^2 = \sigma_o^2 + \sigma_v^2 T^2 \tag{9}$$

where σ_o is the initial cloud standard deviation, and T is the travel time since release. When σ_o is negligible, this equation reduces to the even simpler form $\sigma_y = \sigma_v T$.

At longer ranges, Eq. (9) overestimates the cloud diffusion, but there is still a direct proportionality between cloud size (e.g., σ_y) and the velocity standard deviation (σ_v) when the turbulence is relatively constant. A generalized Taylor formula for σ_y at these longer ranges, ignoring σ_o, is (Arya, 1999)

$$\sigma_y = \sigma_v T f(T) \tag{10}$$

with $f(T)$ being some function that approaches unity at short ranges and varies with $T^{-1/2}$ at long ranges (to match the far-field limit of the Taylor theory). A similar formula can be used to relate σ_z to the standard deviation σ_w of the vertical velocity. Equations of this form are commonly used in Gaussian dispersion models to compute σ_y and σ_z from the turbulence parameters σ_v and σ_w.

Clearly, the ABL structure and its bulk stability directly affects the turbulence levels present at any given time. There are three general approaches that are used to relate bulk ABL stability to the dispersion parameters:

1. Empirical diffusion curves based on field data.
2. Formulas based on the theory of ABL structure.
3. Direct turbulence measurements.

The first approach was the earliest, partly because in pre-computer days it allowed dispersion estimates to be quickly derived from sets of graphs. Some of the best known examples of this approach are the Pasquill-Gifford curves (Gifford, 1961; Slade, 1968), which are based on the A through F Pasquill stability categories mentioned previously. These curves were obtained by fitting smoothed lines to sets of data collected in tracer field studies. Markee (1963) developed a modified set of curves based partly on data collected at the INL. Figure 93 shows one example of the Markee curves for the vertical-dispersion parameter σ_z. A modified version of the Markee curves is used in the MDIFF puff model (Sagendorf at al., 2001), which was one of the primary dispersion models used at INL prior to 2009.

A primary advantage of the empirical diffusion curves is that they do not require specialized turbulence measurements, such as an instrument that can directly measure σ_v and σ_w. In the original description of the stability categories (Pasquill 1961), the category could be determined from routine measurements of time-of-day, wind speed, cloud cover, and a qualitative estimate of daytime solar insolation (i.e., strong, moderate, or slight). A primary disadvantage of the approach is that the curves are really only valid for the specific conditions under which the underlying tracer data were taken. The Pasquill-Gifford curves, for example, were derived from a mix of data taken over flat and moderately rough terrain, and the data correspond to averaging times of 3-10 minutes. Differing topography, vegetation, and averaging times generally require a different set of empirically derived curves, although to some extent these variations can be accounted for by adjusting a base set of curves (Gifford, 1976).

A second way to estimate turbulence levels for dispersion applications is to make use of the models that have been developed to describe ABL structure. As noted in the section on atmospheric stability, the sensible heat flux *H* at the earth's surface is a primary parameter describing ABL structure. Another major parameter is the momentum flux at the earth's surface, since it represents the drag exerted by the surface and is therefore directly related to mechanical turbulence production. The momentum flux is normally represented by a variable called the friction velocity u_*, which is positive and increases as the momentum flux increases. A third parameter needed to describe the ABL is its depth *h*.

Based on a combination of field data and theory, researchers have developed expressions that relate turbulence levels in the ABL to *H*, u_*, and *h*. Many different formulas have been proposed (Stull, 1988) for convective, neutral, and stable boundary layers, and the details are beyond the scope of this report. As a simple example, both

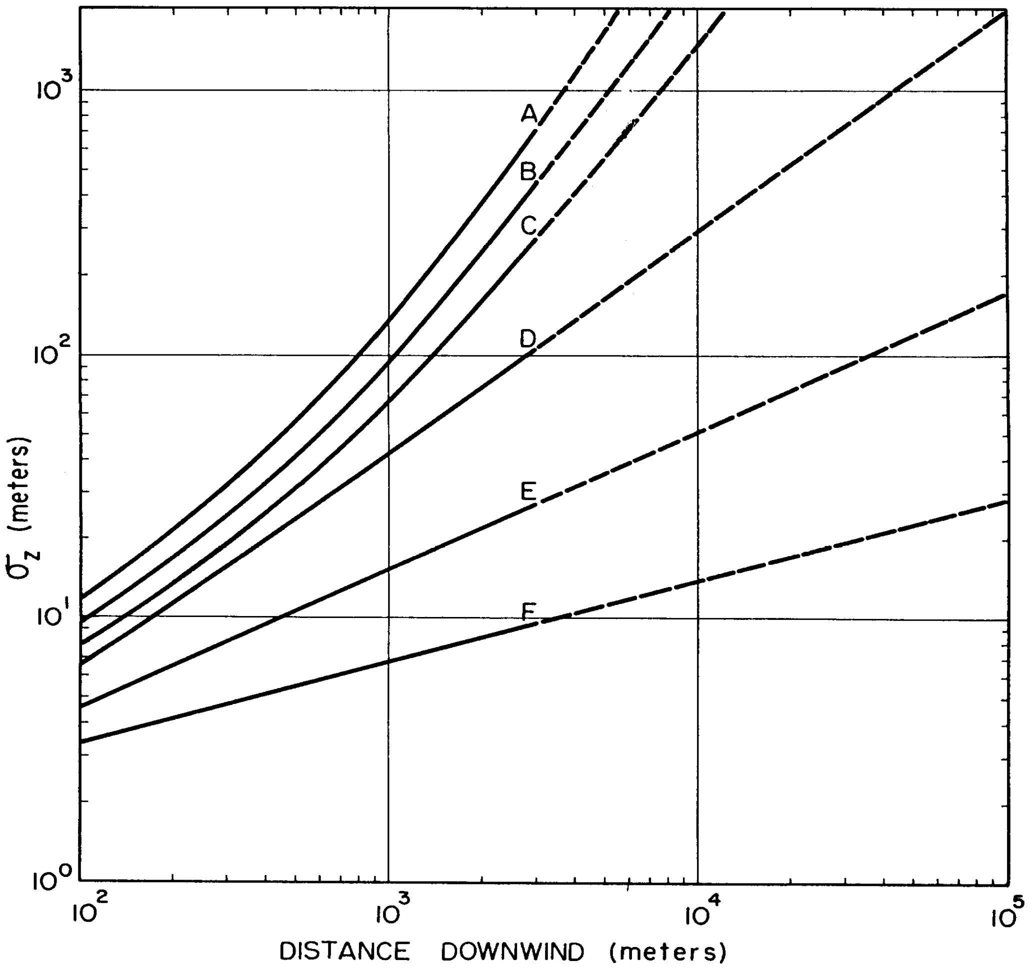

Figure 93. Plots of σ_z versus downwind distance as obtained by Markee (1963) for the five Pasquill stability classes.

σ_v and σ_w are directly proportional to u_* near the surface in neutral conditions. In stable conditions, Nieuwstadt (1984) suggested the formula

$$\sigma_w = 1.4\,u_* \left(1 - \frac{z}{h}\right)^{3/4} \tag{11}$$

to describe the variation of σ_w throughout the depth of the ABL. This equation produces a maximum value of σ_w at the surface, with a less-than-linear decline to zero at the top of the ABL.

These ABL models have the advantage that they are not as location-specific as the empirical diffusion curves. Differences in surface characteristics such as roughness will directly affect H, u_*, and h, so relations such as Eq. (11) are expected to be valid over a range of surface types. As one example, the semi-arid conditions at INL during the summer will normally lead to significantly larger daytime values of *H* compared to locations in wetter environments such as the Eastern U.S. Larger heat fluxes also tend to increase the ABL depth *h*, which is why the average summertime ABL depths are larger over the Western U.S. than in the eastern part of the country (Holzworth 1964). ABL models of turbulence are also useful in that numerical weather prediction models (Pielke, 2002), such as those used by the NWS for general weather forecasting, often include ABL variables such as H, u_*, and *h* in their standard output. This allows dispersion forecasts to be made based on the output of the weather prediction models.

A third general approach for estimating turbulence is to obtain direct turbulence measurements using specialized instruments. Until relatively recently, such instruments tended to be research-grade designs that were expensive and not well suited for extended deployments. This was particularly true of instruments capable of measuring the vertical turbulence fluctuations σ_w. More recently, three-axis sonic anemometers have fallen in price and become robust enough to be a viable option in many dispersion applications. These instruments can directly measure the velocity standard deviations in all three directions, so that the diffusion can be directly computed either from formulas like Eq, (10) in the case of Gaussian models or like Eq. (8) in the case of Lagrangian particle models.

Although the cost of turbulence instrumentation has dropped significantly, it still has not replaced more conventional tower instruments such as cup anemometers and wind vanes. At INL, NOAA operates over 30 conventional towers with cups and vanes, but currently has only a single 3D sonic anemometer near the center of the site. Lack of spatial coverage is the most serious problem with using a direct-measurement approach, particularly in complex terrain. If only a single turbulence measurement site is available, there is no easy method to extrapolate these observations to other locations in complex terrain. One way to mitigate this problem is by blending the direct-measurement and ABL-modeling approaches in a way that provides a reasonable estimate of the spatial variability of the turbulence.

Processes Affecting Transport and Diffusion

The Gaussian and Lagrangian-particle models represent general approaches for describing the dispersion of effluents. Depending on the situation, a variety of specific processes can have significant effects on the dispersion. Failure to account for these processes may compromise the overall skill of a model. The most important processes are briefly described here.

Effects of Source Configuration

Various aspects of the effluent source can have major effects on the resulting concentration distribution. Often the effluent has a significant vertical exit velocity at the source, and its initial temperature may be significantly higher than the ambient air temperature. Either of these events can cause the plume to rise well above its initial release height before it stabilizes. Many different formulas of different complexity have been derived to estimate plume rise (Briggs, 1984; Weil, 1988; Arya, 1999). As discussed by Arya (1999), the main variables related to plume rise are:

1. Initial vertical momentum of the effluent.
2. Initial buoyancy of the effluent cloud.
3. Ambient wind speed.
4. Time of travel when considering transitional effects.
5. Level of atmospheric turbulence.

Most of the plume-rise formulas are intended for routine stack emissions, but accidental releases can also involve considerable plume rise if an explosion or fire is involved.

Another potential source effect is building wakes. An isolated building can produce complex distortions of the oncoming flow, including a horseshoe vortex extending around the building and a wake cavity on the leeward side (Hosker, 1984). Overall, the wake tends to enhance the level of mechanical turbulence for some distance downwind of the building. In many Gaussian dispersion models, the dispersion coefficients σ_y and σ_z are enhanced at short ranges when the release is from a large building (Huber and Snyder, 1976; Scire and Schulman, 1980). The Schulman-Scire procedure also accounts for the observation that the enhanced mechanical turbulence from the building tends to reduce the total plume rise. Even when the effluent is released from a tall stack, the wake of the stack can draw the effluent down and reduce the effective release height (Briggs, 1984).

Removal Processes

An effluent can be removed from the atmosphere by several processes. One of these is the deposition of the material on the earth's surface. Material can be deposited by gravitational settling when it consists of particles that are heavy enough to have a terminal fall velocity. Smaller particles and gases can still be deposited through the interaction of the surface and the turbulent air just above it. Dry deposition is the general term used for this transfer of material. The mechanism of dry deposition is highly complex (Sehmel, 1980; Arya, 1999), involving many properties of the atmosphere, surface, and the effluent. Atmospheric turbulence has a strong influence on dry deposition, because it determines the rate at which the effluent is mixed downward to the vicinity of the surface. The friction velocity u_* therefore is one of the main atmospheric parameters that appears in deposition models.

Dry deposition is often parameterized by a deposition velocity v_d, which is related to the surface flux F (upward positive) and near-surface concentration χ of an effluent by

$$v_d = \frac{F}{\chi} \tag{12}$$

If χ has units of, say, g m^{-3}, then F has units of g m^{-2} s^{-1} and thus represents a mass per unit area per unit time. Although some aspects of v_d can be modeled through ABL theory, there is still much empiricism related to its estimation. For example, some gases are taken up by the stomata of plant leaves, so v_d is dependent on plant physiology in these cases.

Dispersion models can treat deposition in a couple of different ways (Arya, 1999). Source-depletion models account for deposition by reducing the effective amount of material released at the source. In the Gaussian plume of Eq. (6), this means reducing q to account for the material lost to deposition. This is clearly somewhat unrealistic, since it assumes that material is lost equally throughout the depth of the effluent cloud. Surface-depletion models are more realistic in that the deposited material is assumed to come largely from the lower part of the cloud near the surface. Lagrangian particle models can account for deposition either by reducing the mass of individual particles when they get near the surface or by assigning a probability that particles near the surface will be totally removed from the atmosphere.

Precipitation scavenging is another process that can remove effluent from the atmosphere (Slade, 1968; Chate et al., 2003). Usually, a distinction is made between in-cloud scavenging, called rainout, and below-cloud scavenging, called washout. In either case, the common approach to account for scavenging in dispersion models is to assume an exponential decay of the concentration χ over a time step δt :

$$\chi(t+\delta t) = \chi(t)\exp(-\Lambda\,\delta t) \qquad (13)$$

Λ is a scavenging coefficient that depends on precipitation rate and type and on the chemical composition of the effluent. Unlike dry deposition, it is realistic to remove material throughout the depth of the effluent cloud when considering precipitation scavenging.

Both dry deposition and precipitation scavenging remove material from the atmosphere, but this does not eliminate the deposited material from consideration. For toxic chemicals, the deposited material can contaminate water supplies or get into the food chain. Radionuclides will continue to emit radiation after being deposited, and this groundshine can be a significant component of the total dose to exposed individuals. In windy conditions, deposited material can be resuspended, which creates a potential area source of effluent that must be considered in modeling the atmospheric dispersion.

The total atmospheric mass of an effluent can also be changed by transformations. Chemical reactions can either increase or decrease the concentration of a particular species. Such reactions are important for may of the pollutants found in urban areas, including ozone, sulfur dioxide, and nitrogen oxides. Dispersion models that are designed for air quality applications must account for these reactions. With radionuclides, transformation by radioactive decay is an important issue. The radioactive decay removes some of the initial effluent, but it creates daughter products that may have to be tracked. It is treated in dispersion models using an exponential decay similar to Eq. (13), with the coefficient in this case being directly proportional to the half-life of the radionuclide.

Current INL Dispersion Models

HYRad is the primary radiological dispersion model in use at the INL for emergency management. HYRad is built upon the foundation provided by the NOAA HYSPLIT model. HYRad uses the HYSPLIT Lagrangian particle model to calculate individual nuclide air concentration, individual nuclide deposition, cumulative concentration or deposition, and radiological doses. One big advantage of HYRad compared to HYSPLIT is the ability to use current NOAA/INL Mesonet observations to drive the plume dispersion. The HYRad software is used for consequence assessment, hazard assessment, and safety analysis of facilities handling nuclear material. At present HYRad is only being used in the INL/EOC but there is interest and ongoing work to make it available to the wider Department of Energy (DOE) community.

ARLFRD also maintains a separate version of HYSPLIT for estimating annual emissions from INL Site facilities. This version is used to support the INL Annual Site Environmental Reports published each calendar year. Running a year-long simulation using HYSPLIT requires a different configuration than what is used in HYRad, since HYRad focuses on shorter-term events.

Aloha is the current dispersion model for a chemical release at the INL for emergency management. Aloha is a straight line Gaussian model developed jointly by NOAA and the Environmental Protection Agency (EPA). Based on information from the CAMEO chemical database, the program can track how the hazardous plume can travel downwind of the release and change over time. This in turn will make it easier to allow emergency management to assess the scope of any chemical incident. More information about Aloha can be found at Jones (2013).

Climatological Dispersion Patterns

Eckman (2003) conducted a study of dispersion climatology at INL using nine years of data from the NOAA/INL Mesonet. The study was based on the MDIFF puff model (Sagendorf et al., 2001), which at the time was ARLFRD's main model for supporting INL operations. Some of the results from that study are reproduced here, because they are instructive in understanding the general characteristics of dispersion at INL. Because much of the focus at INL is on accidental releases of radioactive materials, the study focused on the total integrated concentration (TIC), which is the time integral of the concentration χ at a fixed location:

$$\mathbf{TIC} = \int \chi \, dt \tag{10}$$

The integral extends over the duration of the model run. For radionuclides, the TIC is more useful than χ because it is more directly related to the radiological dose.

Figure 94 shows contours of TIC for surface releases at four of the INL facilities: INTEC, RWMC, SMC, and ATR. These plots were obtained by starting a new MDIFF run every hour during the period from April 1993 to December 2001, with a release duration of

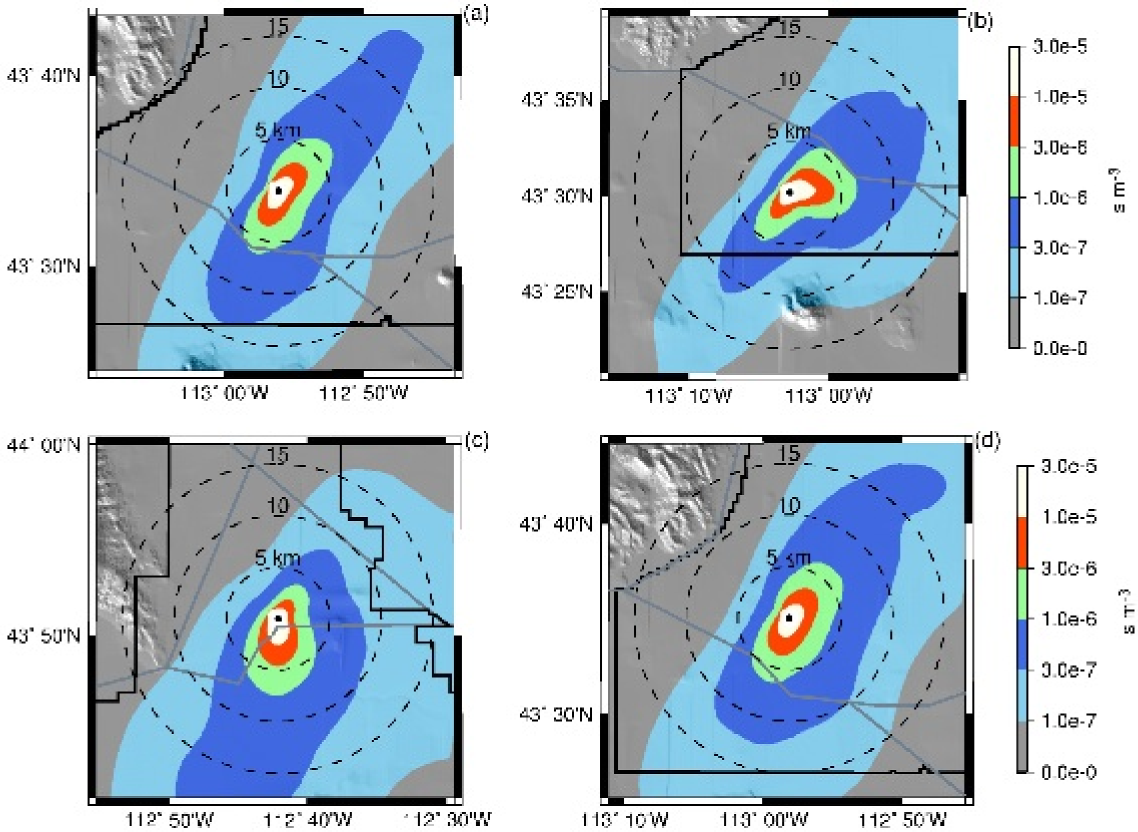

Figure 94. Contours of the 95th percentile TIC derived from hourly MDIFF model runs spanning the period from April 1993 to December 2001. The TIC values are normalized by the total mass *Q* of material released. The release points are (a) INTEC, (b) RWMC, (c) SMC, and (d) ATR.

2.5 hours for ATR and 1 hour for the other facilities. Over 76,000 individual MDIFF runs were therefore performed for each facility. The contours in Fig. 94 represent the 95th percentile values obtained from these sets of runs, which Eckman (2003) took as representative of worst-case dispersion conditions. Each TIC value was normalized by the total quantity *Q* of material released, so the contours have normalized units of s m^{-3}.

For both INTEC and ATR, the contours are generally elongated along a southwest to northeast axis, reflecting the channeling of the wind by the orientation of the Snake River Plain. The inner contours are to an approximation symmetric about the INTEC and ATR release points, indicating that the peak TIC values observed for up-valley (southwest) and down-valley (northeast) winds are similar in magnitude. Given the overall shape of the contours, it appears that straight-line pollutant transport may be a reasonable assumption out to 3-6 miles (5-10 km) from these two sources. A simple Gaussian plume model may therefore be appropriate out to such distances, at least when considering average dispersion over long time periods. Of course, the contours in the figure are based on statistics from a large number of runs. Additional complications arise when attempting to model a specific event (e.g., a real accident), such as wind reversals and recirculations. Such effects cannot be represented in a straight-line plume model.

RWMC is further south and west compared to the other facilities, and this has a significant effect on the 95th percentile TIC contours in Fig. 94. The contours to the south of the facility are similar in shape to those at INTEC and ATR, indicating that there is often a regional northeasterly wind that affects all three facilities in similar ways. However, RWMC also shows high TIC values extending to the east of the release point. The most likely explanation for this is associated with RWMC lying closer to the Big Lost River Valley that exits into the Snake River Plain at Arco. In fact, the bed of the Big Lost River passes near RWMC. It is reasonable to conclude that RWMC sometimes sees westerly drainage winds exiting out of the Big Lost River Valley.

SMC also has an unusual pattern in Fig. 94, with most of the high TIC values extending to the south of the facility. This site is affected both by regional downvalley winds within the Snake River Plain and more local drainage winds coming out of the Birch Creek Valley just to the northwest of SMC. These northerly flows appear to dominate the 95th percentile TIC values for SMC.

Figure 94 was based on higher resolution concentration grids that extended out to only 9-12 miles (15-20 km) from the release points. Eckman (2003) also performed MDIFF runs using a larger grid extending about 37 miles (60 km) from the release point. Figure 95 shows the 95th percentile TIC values for INTEC and ATR using this larger grid. The general southwest-to-northeast channeling of the dispersion is still evident at the larger scales. However, the contours have various bends in them that indicate the effects of the nearby topography on changing the direction of pollutant transport. Using a straight-line plume model based on a wind rose at the release point clearly can lead to transport errors at these larger scales. One caution with this figure is that the outermost contours may be affected by model algorithms. The version of MDIFF used for the study dropped puffs that were more than 12 miles (20 km) from any mesonet tower, so areas with poor tower coverage are artificially forced to have low TIC values.

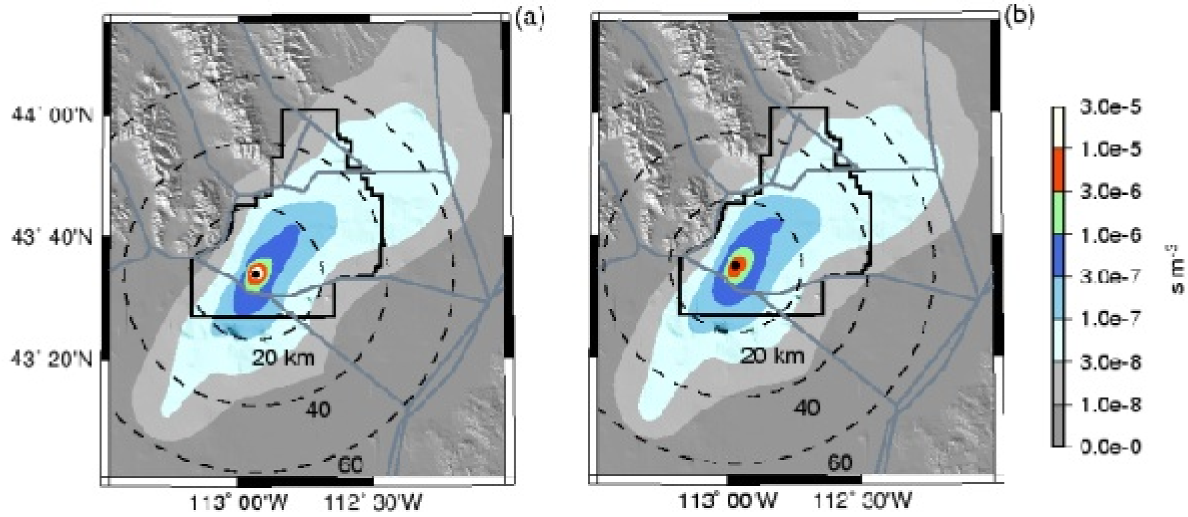

Figure 95. Contours of the 95th percentile TIC for (a) INTEC and (b) ATR using a larger model domain extending to about 37 miles (60 km) from the release points. As in Fig. 94, the TIC values are normalized by the total mass *Q* of material released.

ACKNOWLEDGMENTS

Funding for this project was provided by the U. S. Department of Energy, Idaho Operations Office and the National Oceanic and Atmospheric Administration.

In presenting this latest INL climatography, the current editors pay tribute to the talent and efforts of the authors and data analysts who developed the initial climatologies for INL, including G. A. DeMarrais, G. R. Yanskey, E. H. Markee, Jr., and A. P. Richter. The legacy work of these individuals continues to be seen in many of the data summary tables and in the "Markee" atmospheric dispersion curves, based on INL field experiments, that continue to be utilized.

The current editors also acknowledge the historical leadership of C. R. Dickson, G. E. Start, and F. E. White, who oversaw implementation of the telemetered "mesonet" data, installation of the radar wind profiler with RASS, the implementation of the current "modern" mesonet, and the development of the 2nd and 3rd edition of the INL Climatography (Clawson et al., 1989, 2007, respectively). J. F. Sagendorf and G. R. Ackermann played key roles in data analyses, dispersion modeling, and acquisition programming, respectively.

This latest edition of the INL Climatography is the culmination of the efforts of many employees and contractors, both past and present, employed by the Field Research Division of the Air Resources Laboratory. Their contributions are gratefully acknowledged. R. C. Johnson designed, implemented, and maintained the current mesonet hardware at the various monitoring sites, along with the able assistance of T. S. Strong and S. A. Beard. N. F. Hukari and J. D. Rich maintained the extremely high level of mesonet data quality and also provided some of the statistical programming systems and data processing for the meteorological data summaries found in this edition. R. M. Eckman provides mesoscale and dispersion modeling expertise and summarized the "state-of-the-science" of atmospheric transport and diffusion at the INL, which is contained in this volume. R. G. Carter and B. R. Reese currently maintain data collection and data display systems, including Viz+. We also thank Norm Ricks who under contract provided the initial ground work of this edition of the climatology.

This page intentionally left blank.

REFERENCES

Ackerman, G. R., and R. C. Johnson, 1989: Modernization of the INEL meteorological monitoring and emergency response capability, a general design. Final report (draft), 11 October 1989. U.S. Dept. of Commerce, NOAA, ERL, ARLFRD, Idaho Falls, ID, 84 pp.

Allen, R. G. and C. W. Robison, 2006 (Revised 2007): Evapotranspiration and Consumptive Irrigation Water Requirements for Idaho, Research Technical Completion Report, Kimberly Research and Extension Center, University of Idaho, Moscow, ID.

ANSI/ANS-3.2, 1994: Administrative Controls and Quality Assurance for the Operational Phase of Nuclear Power Plants. ANSI/ANS-3.2-1994.

ANSI/ANS-3.2, 2015: Administrative Controls and Quality Assurance for the Operational Phase of Nuclear Power Plants. ANSI/ANS-3.2-2015.

ANSI/ANS-3.11, 2015: Determining Meteorological Information At Nuclear Facilities. ANSI/ANS-3.11-2015. 29 pp.

Anderson, J.E., K.T. Ruppel, J.M. Glennon, K.E. Holte, and R.C. Rope, 1996: Plant Communities, Ethnoecology, and Flora of the Idaho National Engineering Laboratory. ESRF-005. *Environ. Sci. And Res. Foundation*, Idaho Falls, ID, 111 pp.

ARLFRD, 2010: Response to the 2004 INEEL meteorological program assessment and assist visit. NOAA ARLFRD, Idaho Falls, ID. February 19. 15 pp.

ARLFRD, 2012: Response to the DMCC 2010 INL meteorological programs follow-up assist visit. NOAA ARLFRD, Idaho Falls, ID. May 1. 17 pp.

Arya, S. P., 1999: *Air Pollution Meteorology and Dispersion.* Oxford University Press, 310 pp.

ASME NQA-1, 2004: Quality Assurance Requirements for Nuclear Facility Applications, ASME Standards. 228 pp.

ASME NQA-1, 2015: Quality Assurance Requirements for Nuclear Facility Applications, ASME Standards. 312 pp.

Bird , R.E. and R.L. Hulstrom, 1991: A Simplified Clear Sky model for Direct and Diffuse Insolation on Horizontal Surfaces, SERI Technical Report SERI/TR-642-761, Feb 1991. Solar Energy Research Institute, Golden, CO.

Briggs, G. A., 1984: Plume Rise and Buoyancy Effects. In *Atmospheric Science and Power Production*, D. Randerson, ed., U. S. Dept. of Energy, Oak Ridge, TN, 327-366.

Carter, R. G., N. Hukari, and J.D. Rich, 2007: Identifying Natural Clusters in Eastern Idaho Wind Fields. *unpublished manuscript.*, NOAA Air Resources Laboratory Field Research Division, Idaho Falls, ID.

Chate, D. M., P. S. P. Rao, M. S. Naik, G. A. Momin, P. D. Safai, and K. Ali, 2003: Scavenging of Aerosols and their Chemical Species by Rain. *Atmos. Environ.*, **37**, 2477-2484.

Clawson, K. L., G. E. Start, and N. R. Ricks, 1989: Climatography of the Idaho National Engineering Laboratory, 2nd Edition, Report DOE/ID-12118, U. S. Department of Energy, Idaho Operations Office, Idaho Falls, ID, 155pp.

Clawson, K. L., R.M. Eckman, N.F. Hukari, J.D. Rich, and N. R. Ricks, 2007: Climatography of the Idaho National Laboratory, 3rd Edition, NOAA Technical Memorandum OAR ARL-259. Air Resources Laboratory, Idaho Falls, ID, 240pp.

Clawson, K.L. R.M. Eckman, J.D. Rich, 2014: INL Site Tornado and High Wind Report. *unpublished manuscript.*, NOAA Air Resources Laboratory Field Research Division, Idaho Falls, ID.

Crescenti, G. H., K. L. Clawson, B. R. Reese, D. W. Walker, W. J. Behymer and A. Jensen, 2000: The Idaho Environmental Monitoring Network. Preprint, 9th Symposium on Education, January 9-14, 2000, Long Beach, California, American Meteorological Society, pp. 28-30.

DeMarrais, G. A. 1958a: The Climatography of the National Reactor Testing Station. U.S. AEC Rep. IDO-12003. U.S. Dept. of Comm., U.S. Weath. Bur., Idaho Falls, ID.

DeMarrais, G. A. 1958b: The Engineering Climatography of the National Reactor Testing Station. U.S. AEC Rep. IDO-12004. U.S. Dept. of Comm., U.S. Weath. Bur., Idaho Falls, ID.

DeMarrais, G. A., and N. F. Islitzer 1960. Diffusion Climatography of the National Reactor Testing Station. U.S. AEC Rep. IDO-12015. U.S. Dept. of Comm., U.S. Weath. Bur., Idaho Falls, ID.

Dickson, C. R., 1993: Quality Program Plan, National Oceanic and Atmospheric Administration, Air Resources Laboratory-Field Research Division. Idaho Falls, ID. November 15. 11 pp.

Dickson, C. R., and D. H. George, 1993: Air Resources Laboratory Field Research Division Quality Implementing Procedures. Idaho Falls, ID. November 15. 32 pp.

DMCC, 2004: Meteorological program assessment and assist visit, United States Department of Energy, Air Resources Laboratory Field Research Division, Idaho National Engineering and Environmental Laboratory. September 8-9, 2004, Idaho Falls, ID.. 80 pp.

DMCC, 2010: Meteorological program follow-up assist visit, United stated Department of Energy, Air Resources Laboratory Field Research Division, Idaho National Laboratory. April 20-21, 2010, Idaho Falls, ID. 191 pp.

DOE Guide 151.1-1, 2005: Emergency management guide, Vol 4. U.S. Dept. of Energy, Office of Emergency Management, Office of Nonproliferation and National Security, 52 pp.

Draxler, R. R. and G. D. Hess, 1997: Description of the HYSPLIT_4 modeling system. NOAA Technical Memorandum ERL ARL-224, NOAA Air Resources Laboratory, Silver Spring, Maryland, 25 pp.

Eckman, R. M., 1998: Observations and numerical simulations of winds within a broad forested valley. *J. Appl. Meteor.*, **37**, 206-219.

Eckman, R. M., 2003: A statistical investigation of atmospheric dispersion at the Idaho National Engineering and Environmental Laboratory (INEEL). NOAA Technical Memorandum OAR ARL-246, NOAA Air Resources Laboratory, Silver Spring, Maryland, 37 pp.

Egger, J., 1990: Thermally forced flows: Theory. In *Atmospheric Processes over Complex Terrain*, W. Blumen, ed., American Meteorological Society, Boston, MA, 43-58.

Finn D., J. D. Rich, B. Reese, K..L. Clawson, 2014: Diurnal Late Spring and Summertime Wind Patterns on the Snake River Plain and the Influence of Complex Terrain Factors. *unpublished manuscript.*, NOAA Air Resources Laboratory Field Research Division, Idaho Falls, ID.

Finn, D., B. Reese, B. Butler, N. Wagenbrenner, K. L. Clawson, J. D. Rich, E. Russell, Z. Gao, H. Liu, 2016: Evidence for gap flows in the Birch Creek Valley, Idaho, *Journal of the Atmospheric Sciences*, 73(12):4873-4894. doi.org/10.1175/JAS-D-16-0052.1

Garratt, J. R., 1992: *The Atmospheric Boundary Layer.* Cambridge University Press, 316 pp.

George, D. H. and N. F. Hukari., 1995: Real-time Meteorological Network Data Quality Assurance/Quality Control. *Proceedings, Fifth Topical Meeting on Emergency Preparedness and Response*, April 19-21, 1995, Savannah Georgia, American Nuclear Society, pp. 55-59.

George, D. H, 1996: The DOE/NOAA Meteorological Program at the Idaho National Engineering Laboratory. *Transactions of the 1996 Annual Meeting of the American Nuclear Society*, June 16-20, Reno, Nevada, Volume 74, pp. 47-48.

Gifford, F. A., 1961: Use of routine meteorological observations for estimating atmospheric dispersion. *Nucl. Saf.*, **2**, 47-51.

Gifford, F. A., 1976: Turbulent diffusion typing schemes: A review. *Nucl. Saf.*, **17**, 68-85.

Gross, G. and F. Wippermann, 1987: Channeling and countercurrents in the Upper Rhine Valley: Numerical simulations. *J. Climate Appl. Meteor.*, **26**, 1293-1304.

Hershfield, D. M., 1961: *Rainfall Frequency Atlas of the United States.* U.S. Weather Bureau Technical Paper 40, U.S. Department of Commerce, Washington, D. C.

Holzworth, G. C., 1964: Estimates of mean maximum mixing depths in the Contiguous United States. *Mon. Wea. Rev.*, **92**, 235-242.

Hosker, R. P., 1984: Flow and diffusion near obstacles. In *Atmospheric Science and Power Production*, D. Randerson, ed., U. S. Dept. of Energy, Oak Ridge, TN, 241-287.

Huber, A. H. and W. H. Snyder, 1976: Building wake effects on short stack effluent. Preprints, *Third Symposium on Atmospheric Diffusion and Air Quality*, Raleigh, NC, Amer. Meteor. Soc., 235-242.

Humphrey, P. A., E. M. Wilkins, and D. M. Morgan, 1953: *Atmospheric Dust at the National Reactor Testing Station, Final Report*, U. S. Department of Commerce Weather Bureau Office, Idaho Falls, ID.

IPCC, 2013: Climate Change 2013 The Physical Science Basis. , *IPCC Fifth Assessment Report* (WGI AR5), p5.

Jensensius, John S. Jr., National Weather Service (NWS), National Oceanic and Atmospheric Administration (NOAA), U.S. Department of Commerce (DOC). [accessed 2017 October 18]. Understanding Lightning. http://www.lightningsafety.noaa.gov/science/scienceintro.shtml

JetStream, 2017: JetStream - An Online School for Weather. National Weather Service (NWS), National Oceanic and Atmospheric Administration (NOAA), U.S. Department of Commerce (DOC). [accessed 2017 October 18]. Lightning. http://www.srh.noaa.gov/jetstream/lightning/lightning_intro.html

Johnson, O. J., and C. R. Dickson, 1962. An eight year summary of the temperature gradient below 250-feet at the National Reactor Testing Station. U. S. AEC Rep. IDO-12025. U. S. Dept. of Comm., U. S. Weath. Bur., Idaho Falls, ID.

Jones, R., W. Lehr, D. Simecek-Beatty, and R. M. Reynolds, 2013: ALOHA (Areal Locations of Hazardous Atmospheres) 5.4.4: Technical Documentation. NOAA Tech. Memo. NOS OR&R 43, 96 pp. [Available online at http://response.restoration.noaa.gov/sites/default/files/ALOHA_Tech_Doc.pdf.]

Kossmann, M., C. D. Whiteman, and X. Bian, 2002: Dynamic airflow channeling over the Snake River Plain, Idaho. In Preprints, 10th Conference on Mountain Meteorology , American Meteorological Society, 17-21 June 2002, Park City, Utah, Paper P3.14.

Luhar, A. K. and R. E. Britter, 1989: A random-walk model for dispersion in inhomogeneous turbulence in a convective boundary layer. *Atmos. Environ.*, **23**, 1911-1924.

Markee, E. H. Jr., 1963: Methods of estimating air pollutant dispersion over relatively smooth terrain from routine meteorological observations, Tech rep presentation, 219th Nat. Mtg. Of the American Meteorological Society, 20 Jun1963, Palo Alto, CA.

Nace, R. L., P. T. Voegeli, J. R. Jones, and M. Deutsch, 1975. Generalized geologic framework of the National Reactor Testing Station, Idaho. USGS Prof. Paper 725-B. U.S. Gov. Print. Off., Washington, DC.

National Climatic Data Center (NCDC), 2011: https://www.ncdc.noaa.gov.

National Climatic Data Center (NCDC), 2016: https://www.ncdc.noaa.gov/stormevents/choosedates.jsp?statefips=16%2CIDAHO. Accessed on November 18, 2016.

Nieuwstadt, F. T. M., 1984: The turbulent structure of the stable, nocturnal boundary layer. *J. Atmos. Sci.*, **41**, 2202-2216.

Olson, G.L, D.J. Jeppesen, R.D. Lee, 1995: The Status of Soil Mapping for the Idaho National Engineering Laboratory. U.S. Department of Energy INEL-95/0051. 48pp.

Osczevski, Randall and Maurice Bluestein, 2005: The New Wind Chill Equivalent Temperature Chart. *Bulletin of the American Meteorological Society*, Oct. 2005, p. 1453–1458

Pasquill, F., 1961: The estimation of the dispersion of windborne material. *Meteor. Mag.*, **90**, 33-49.

Pielke, R. A., Sr., 2002: *Mesoscale Meteorological Modeling.* Academic Press, San Diego, CA, second edition.

Ramsdell, J.V. and Rishel, J.P., 2007: Tornado Climatology of the Contiguous United States NUREG/CR-4461, Revision 2; PNNL-15112. 76 pp.

Sagendorf, J. F., 1996: *Precipitation Frequency and Intensity at the Idaho National Engineering Laboratory*, NOAA Technical Memorandum ERL ARL-238, Silver Spring, MD, 23 pp.

Sagendorf, J. F., R. G. Carter, and K. L. Clawson, 2001. *MDIFF Transport and Diffusion Models*, NOAA Technical Memorandum ERL ARL-215, Silver Spring, MD, 26 pp.

Scire, J. S. and L. L. Schulman, 1980: Modeling plume rise from low-level bouyant line and point sources. Proceedings, *Second Point Conference on Applications of Air Pollution Meteorology*, New Orleans, LA, Amer. Meteor. Soc., 133-139.

Sehmel, G. A., 1980: Particle and gas dry deposition: A review. *Atmos. Environ.*, **14**, 983-1011.

Soil Survey Staff, 1975: Soil Taxonomy: A Basic System of Soil Classification for Making and Interpreting Soil Surveys. Agric. Handbook p 436 USDA Soil Cons. Serv., Washington, D.C. 754 pp.

Slade, D. H., (Ed.) , 1968: Meteorology and Atomic Energy. U. S. Atomic Energy Commission, Office of Information Services, available as TID-24190 from National Technical Information Service, 445 pp.

Steadman, R. G. 1979a. The Assessment of Sultriness. Part I: A Temperature-Humidity Index Based on Human Physiology and Clothing Science. *J. Appl. Meteor. and Clim.*, 18:861-873.

Steadman, R. G. 1979b. The Assessment of Sultriness. Part II: A Temperature-Humidity Index Based on Human Physiology and Clothing Science. *J. Appl. Meteor. and Clim.*, 18:874-885.

Stewart, J. Q., C. D. Whiteman, W. J. Steenburgh, and X. Bian, 2002: A climatological study of thermally driven wind systems of the U. S. Intermountain West. *Bull. Amer. Meteor. Soc.*, **83**, 699-708.

R. G. Strauch, D. A. Merritt, K. P. Moran, K. B. Earnshaw, and D. Van De Kamp, 1984: The Colorado Wind-Profiling Network. *J. Atmos. Oceanic. Technol.* 1:37-49.

Stull, R. B., 1988: *An Introduction to Boundary Layer Meteorology*. Kluwer Academic Publishers, 666 pp.

Taylor, G. I., 1921: Diffusion by continuous movements. *Proc. London Math. Soc. (2)*, **20**, 196-212.

Trewartha, G. T., 1961: *The Earth's problem climates*. Univ. Of Wisconsin Press, Madison, WI. 334 pp.

U. S. Department of Agriculture (USDA), Forest Service, 1972: The Nation's Range Resources - - A Forest - Range Environmental Study. Forest Report No. 19. 147 pp.

U.S. Department of Energy (DOE), 2004: *Environmental Regulatory Guide for Radiological Effluent Monitoring and Environmental Surveillance,* DOE/EH-0173T

U. S. Department of Energy (DOE), 2003: Idaho National Engineering and Environmental Laboratory Final Wildland Fire Management, Environmental Assessment, DOE/EA-1372, April, 2003. U.S. Department of Energy, Idaho Falls, ID.

U. S. Geological Society (USGS), 2008: http://earthquake.usgs.gov/earthquakes/eventpage/USP0001zbv#executive. Accessed May 31, 2011.

Wallace, J. M. and P. V. Hobbs, 1977: *Atmospheric Science, An Introductory Survey.* Academic Press, 467 pp.

Weber, B. L., and D. B. Wuertz, 1991: Quality control algorithm for pro fIler measurements of winds and temperatures. NOAA Technical Memorandum ERL WPL-212, Boulder, CO, 32 pp.

Weber, B. L., D. B. Wuertz, D. C. Welsh, and R. McPeek, 1993: Quality controls for profiler measurements of winds and RASS temperatures. *J. Atmos. Oceanic Technol.,* 10,452-464.

Weil, J. C., 1988: Plume rise. In *Lectures on Air Pollution Modeling*, A. Venkatram and J. C. Wyngaard, eds., American Meteorological Society, Boston, MA, 119-166.

Whiteman, C. D., 1990: Observations of thermally developed wind systems in mountainous terrain. In *Atmospheric Processes over Complex Terrain*, W. Blumen, ed., American Meteorological Society, Boston, MA, 5-42.

Whiteman, C. D. and J. C. Doran, 1993: The relationship between overlying synoptic-scale flows and winds within a valley. *J. Appl. Meteor.*, **32**, 1669-1682.

Wilson, J. D. and B. L. Sawford, 1996: A review of Lagrangian stochastic models for trajectories in the turbulent atmosphere. *Bound.-Layer Meteor.*, **78**, 191-210.

Wilson, J. D., B. J. Legg, and D. J. Thompson, 1983: Calculation of particle trajectories in the presence of a gradient in turbulent velocity variance. *Bound.-Layer Meteor.*, **27**, 163-169.

Wippermann, F., 1984: Air flow over and in broad valleys: Channeling and countercurrent. *Beitr. Phys. Atmos.*, **57**, 92-105.

Yanskey, G. R., E. H. Markee, Jr., and L.P. Richter, 1966: Climatography of the National Reactor Testing Station. USAEC Rep. IDO-12048. U.S. Dept. Of Comm., Environ. Sci. Serv. Admin., Inst. for Atmos. Sci., Air Resour. Field Res. Off., Idaho Falls, ID.

This page intentionally left blank

APPENDIX A: NOAA/INL MESONET WIND ROSES

The following are the NOAA/INL Mesonet wind roses for each station. If a station has two levels of wind measurements, each level is shown separately. The top wind rose in each figure shows the daytime average (1200-1800 MST), the middle wind rose shows the nighttime average (0000-0600 MST), and the bottom wind rose shows the average for all hours combined.

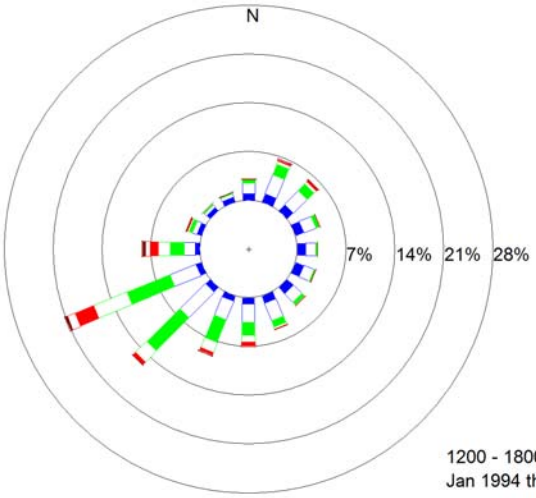

1200 - 1800 MST Wind Rose for ABE
Jan 1994 through Dec 2015   50 ft level

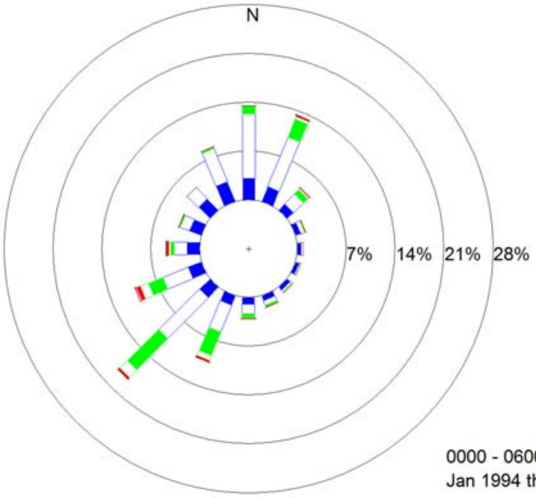

0000 - 0600 MST Wind Rose for ABE
Jan 1994 through Dec 2015   50 ft level

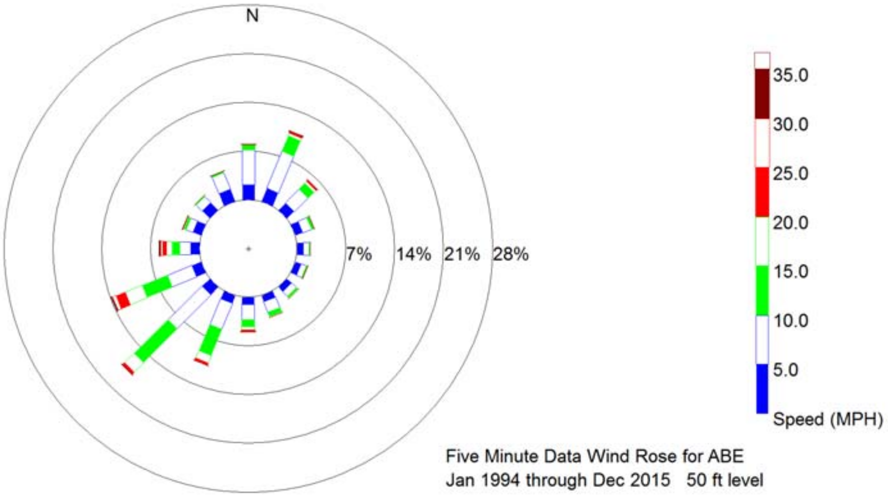

Five Minute Data Wind Rose for ABE
Jan 1994 through Dec 2015   50 ft level

Figure A-1. Daytime (top), nighttime (middle), and all hours (bottom) wind roses for the 50 ft. (15 m) level at Aberdeen (ABE).

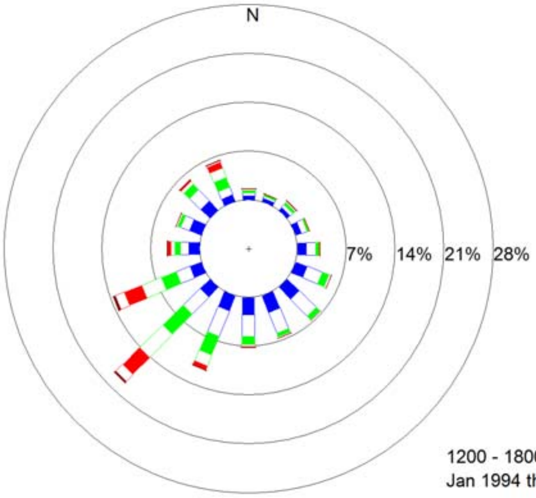

1200 - 1800 MST Wind Rose for ARC
Jan 1994 through Dec 2015 50 ft level

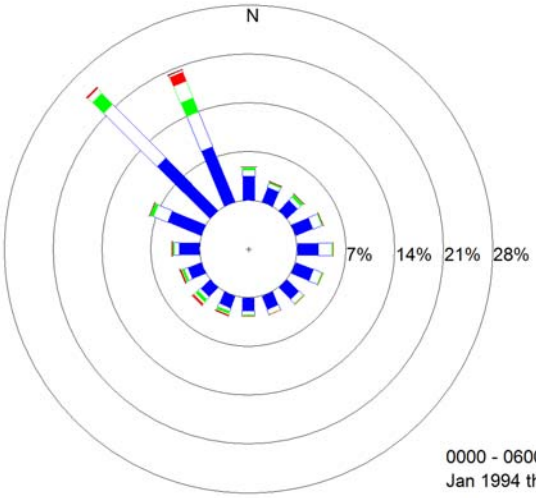

0000 - 0600 MST Wind Rose for ARC
Jan 1994 through Dec 2015 50 ft level

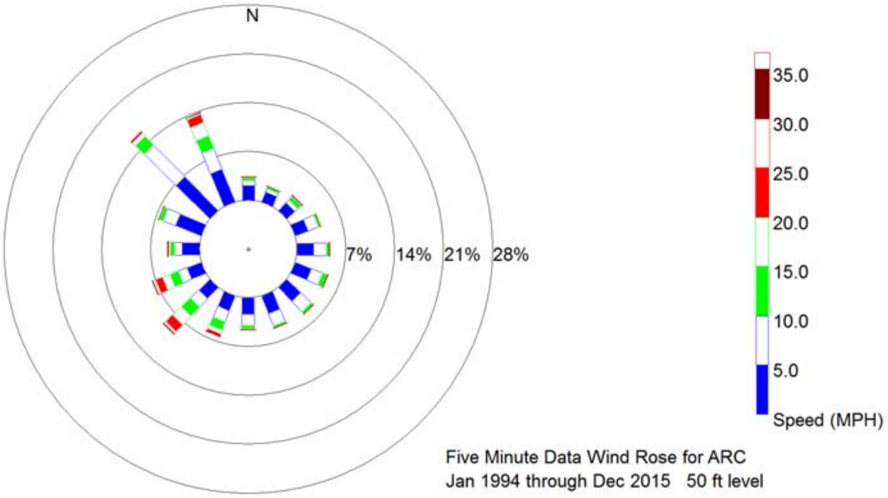

Five Minute Data Wind Rose for ARC
Jan 1994 through Dec 2015 50 ft level

Figure A-2. Daytime (top), nighttime (middle), and all hours (bottom) wind roses for the 50 ft. (15 m) level at Arco (ARC).

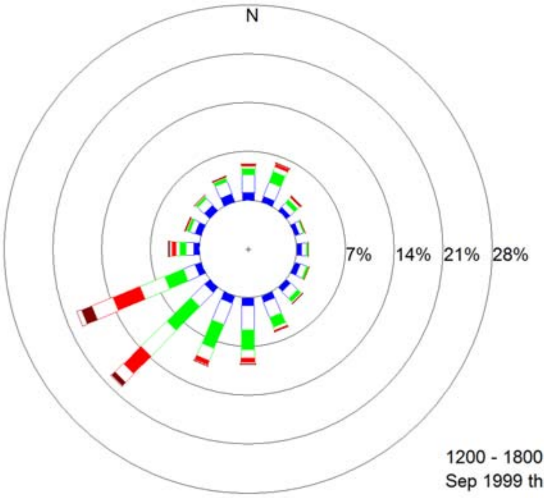

1200 - 1800 MST Wind Rose for ATO
Sep 1999 through Dec 2015 50 ft level

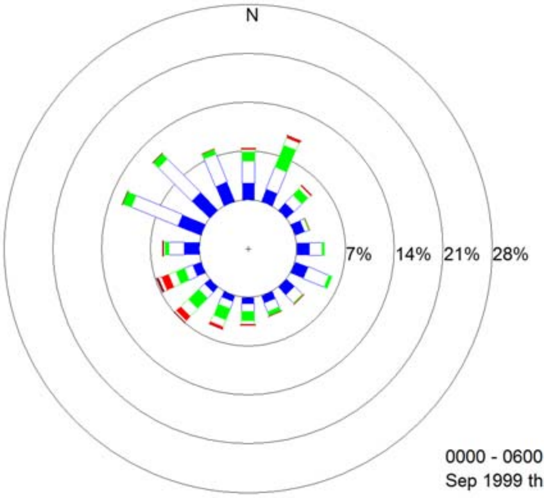

0000 - 0600 MST Wind Rose for ATO
Sep 1999 through Dec 2015 50 ft level

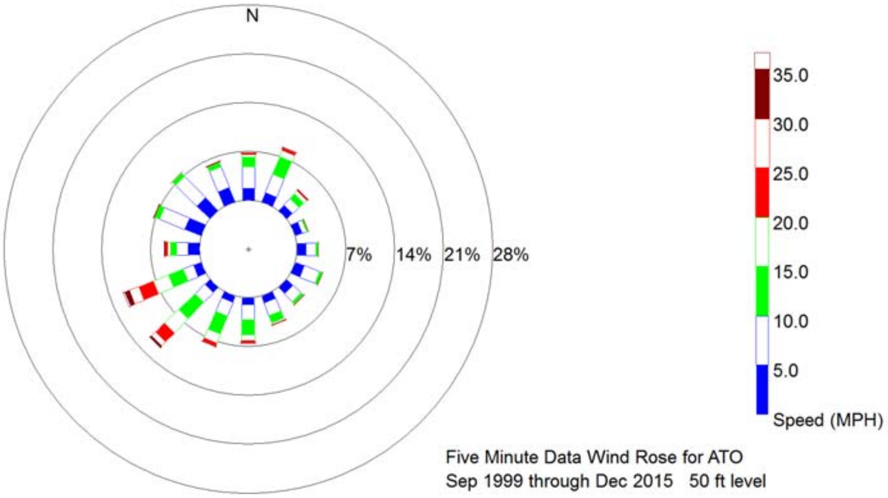

Five Minute Data Wind Rose for ATO
Sep 1999 through Dec 2015 50 ft level

Figure A-3. Daytime (top), nighttime (middle), and all hours (bottom) wind roses for the 50 ft. (15 m) level at Atomic City (ATO).

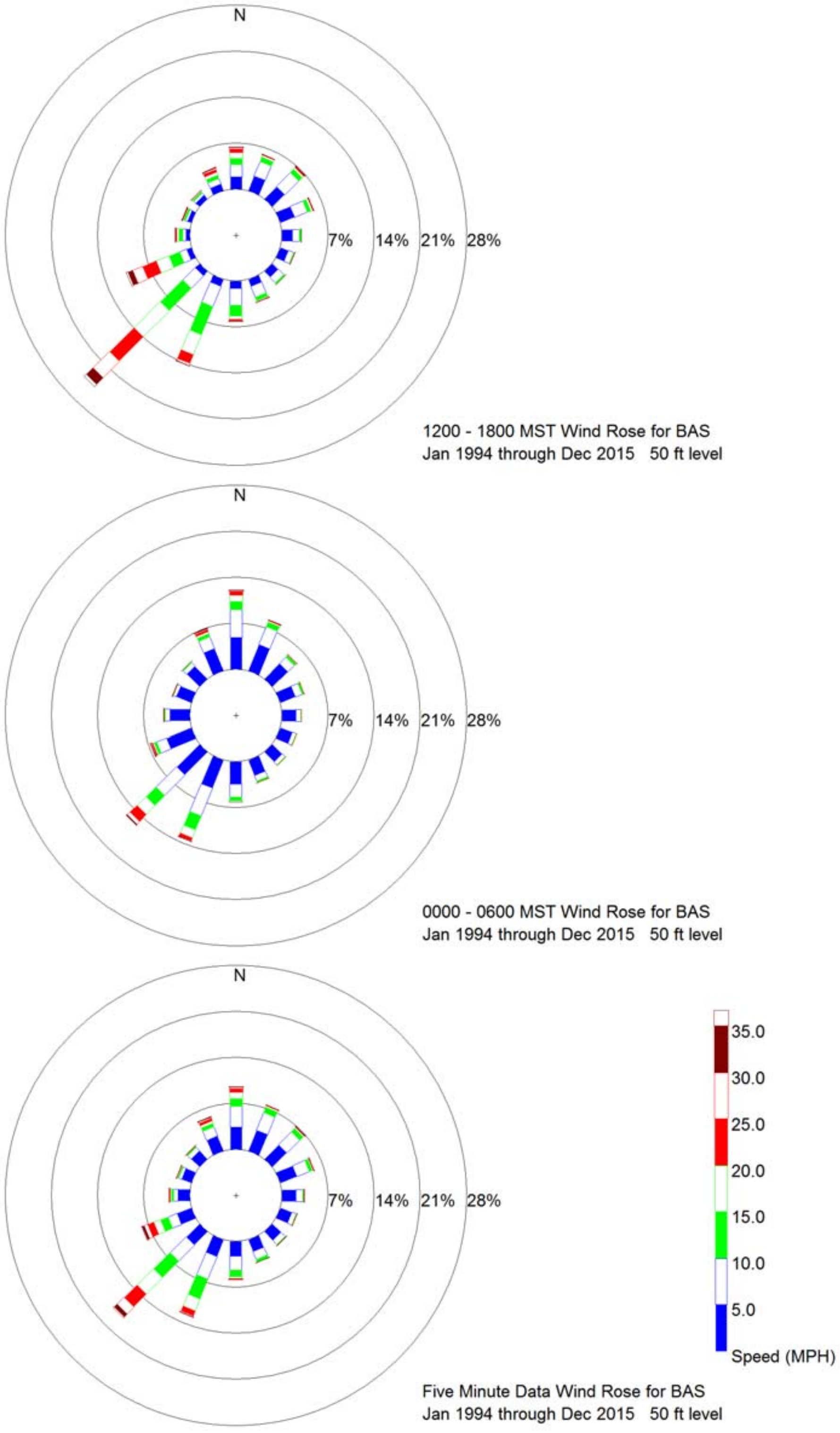

Figure A-4. Daytime (top), nighttime (middle), and all hours (bottom) wind roses for the 50 ft. (15 m) level at Base of Howe Peak (BAS).

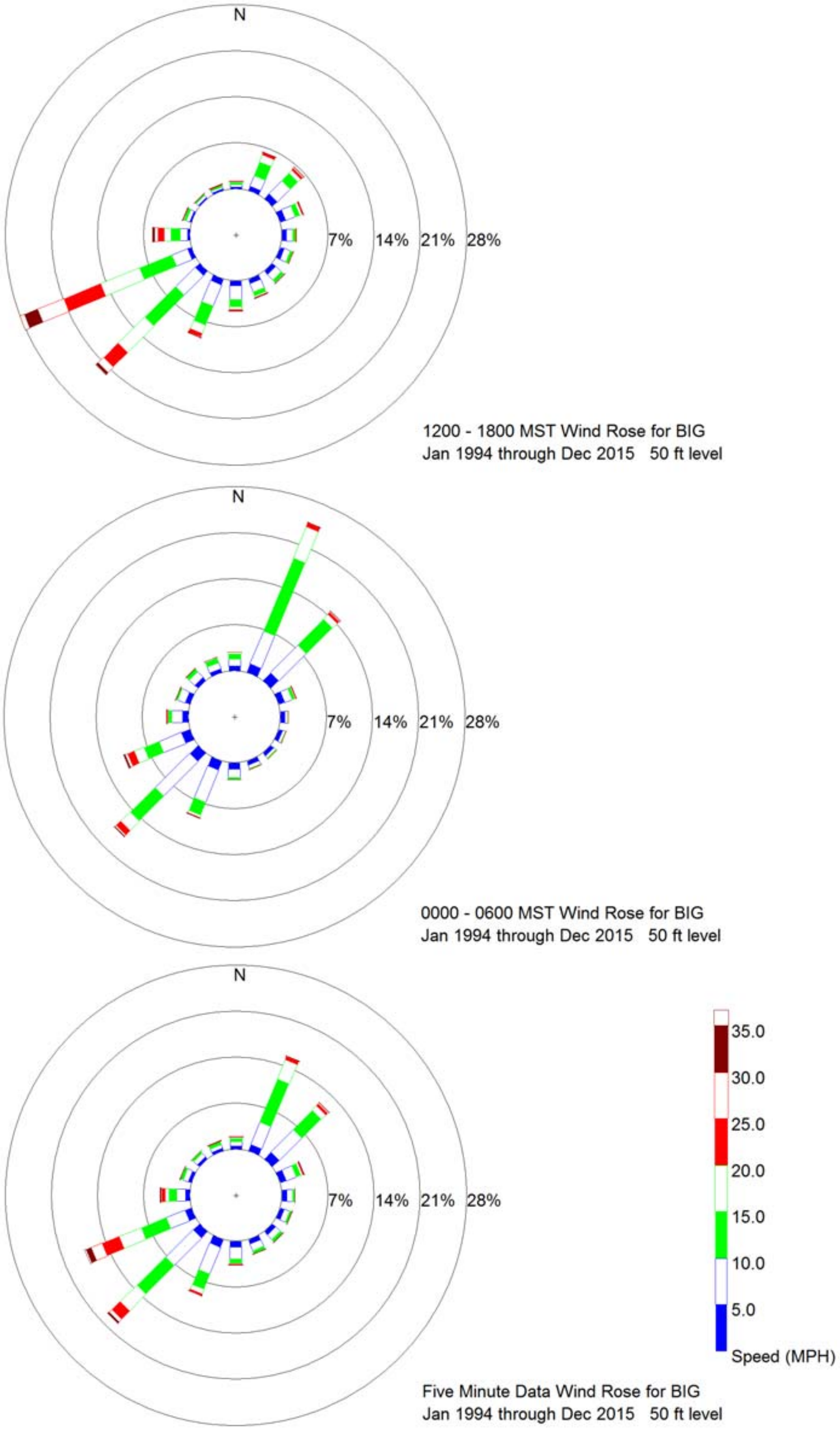

Figure A-5. Daytime (top), nighttime (middle), and all hours (bottom) wind roses for the 50 ft. (15 m) level at Cox's Well (BIG).

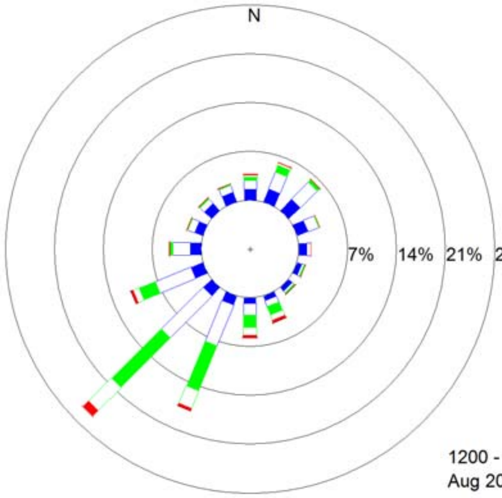

1200 - 1800 MST Wind Rose for BLK
Aug 2001 through Dec 2015   50 ft level

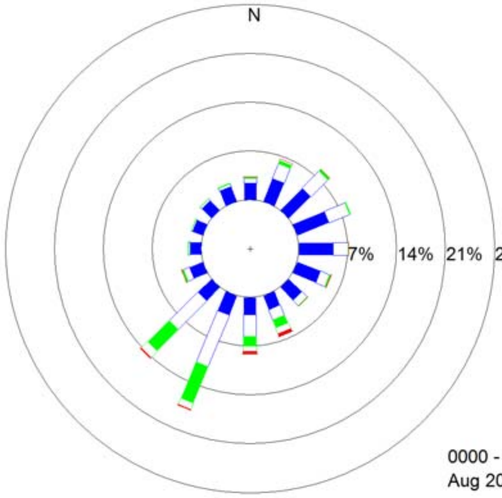

0000 - 0600 MST Wind Rose for BLK
Aug 2001 through Dec 2015   50 ft level

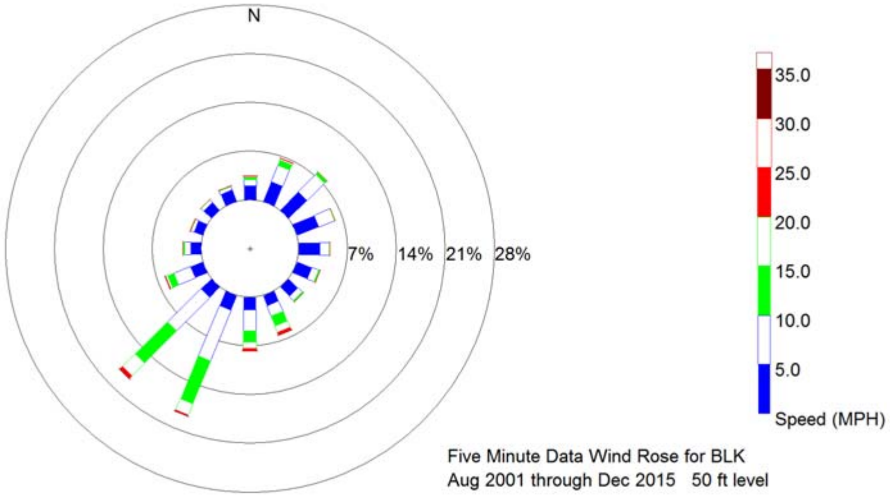

Five Minute Data Wind Rose for BLK
Aug 2001 through Dec 2015   50 ft level

Figure A-6. Daytime (top), nighttime (middle), and all hours (bottom) wind roses for the 50 ft. (15 m) level at Blackfoot (BLK).

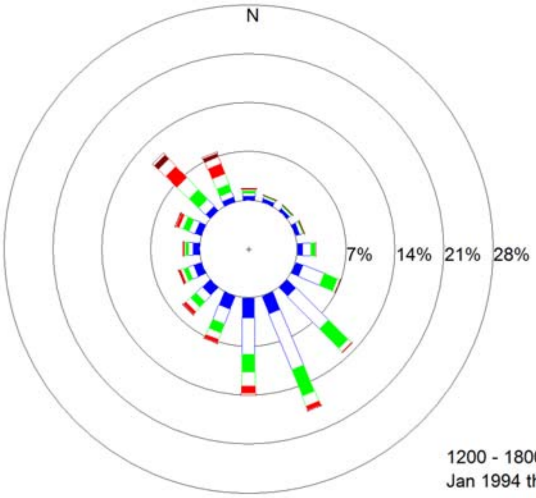

1200 - 1800 MST Wind Rose for BLU
Jan 1994 through Dec 2015   50 ft level

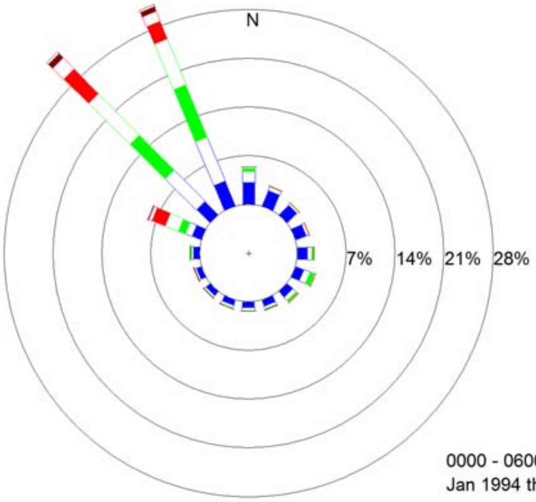

0000 - 0600 MST Wind Rose for BLU
Jan 1994 through Dec 2015   50 ft level

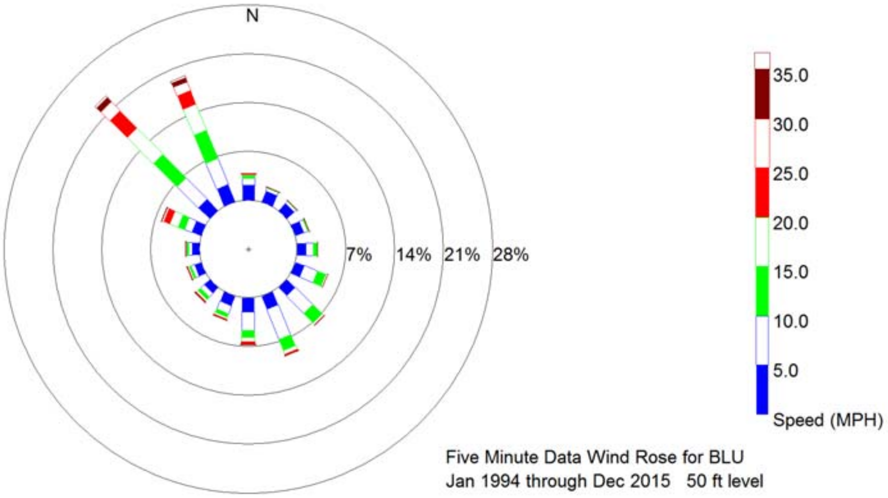

Five Minute Data Wind Rose for BLU
Jan 1994 through Dec 2015   50 ft level

Figure A-7. Daytime (top), nighttime (middle), and all hours (bottom) wind roses for the 50 ft. (15 m) level at Blue Dome (BLU).

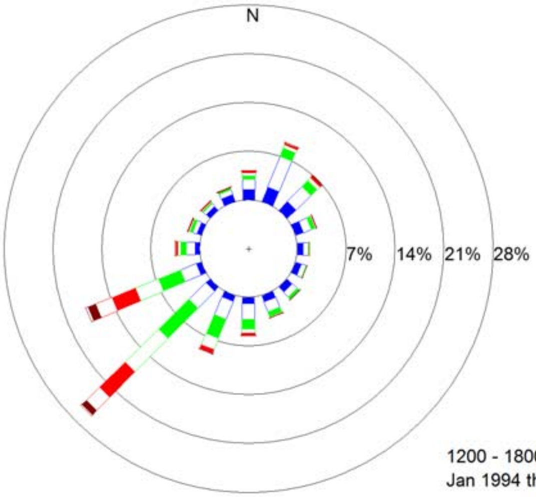

1200 - 1800 MST Wind Rose for CFA
Jan 1994 through Dec 2015 50 ft level

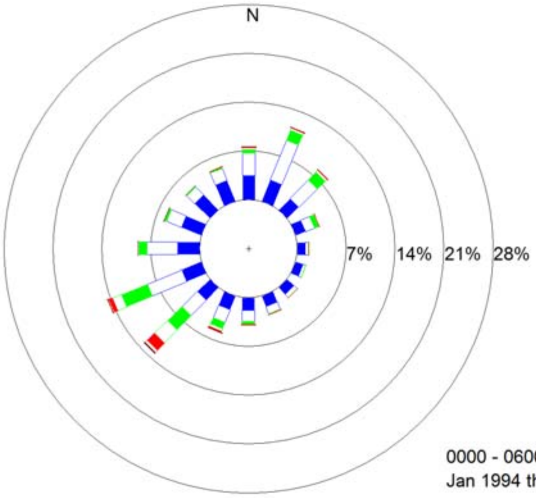

0000 - 0600 MST Wind Rose for CFA
Jan 1994 through Dec 2015 50 ft level

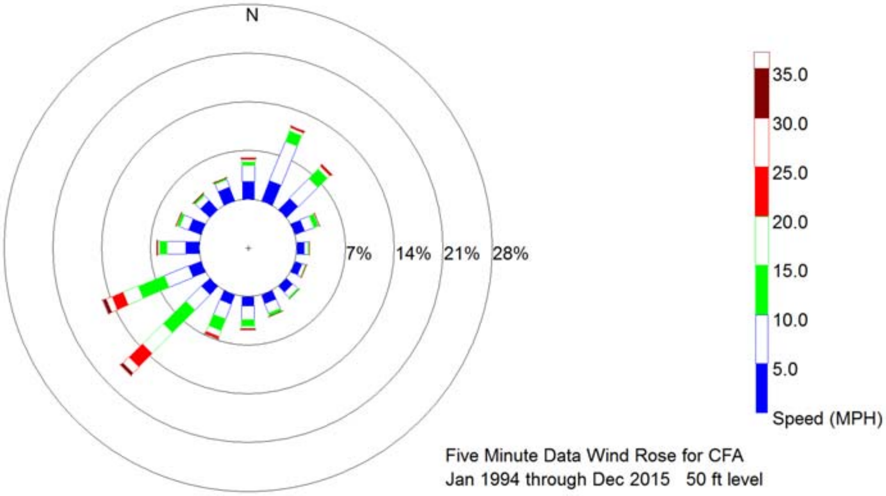

Five Minute Data Wind Rose for CFA
Jan 1994 through Dec 2015 50 ft level

Figure A-8. Daytime (top), nighttime (middle), and all hours (bottom) wind roses for the 50 ft. (15 m) level at Central Facilities Area Building 690 (CFA).

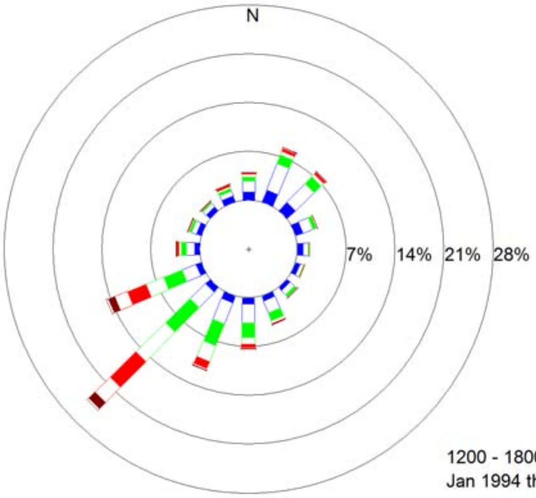

1200 - 1800 MST Wind Rose for CIT
Jan 1994 through Dec 2015 50 ft level

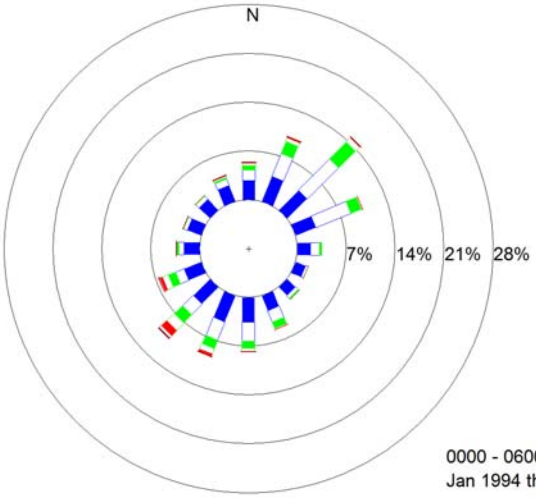

0000 - 0600 MST Wind Rose for CIT
Jan 1994 through Dec 2015 50 ft level

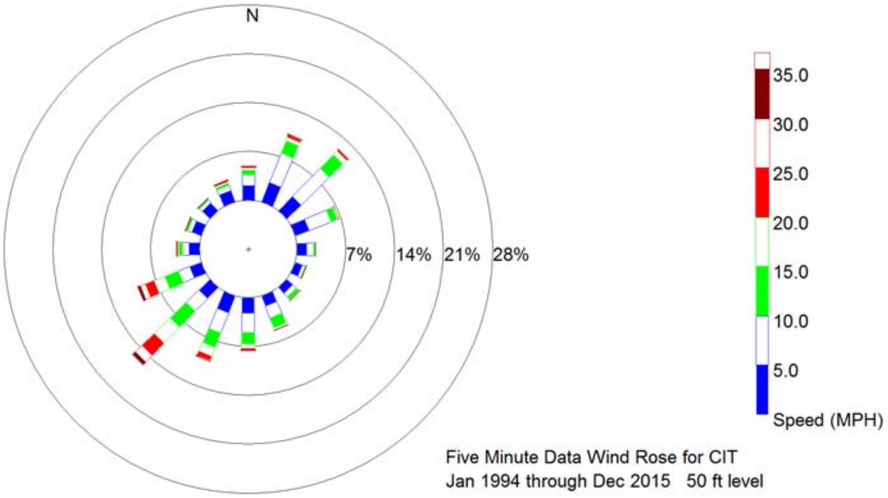

Five Minute Data Wind Rose for CIT
Jan 1994 through Dec 2015 50 ft level

Figure A-9. Daytime (top), nighttime (middle), and all hours (bottom) wind roses for the 50 ft. (15 m) level at Critical Infrastructure Test Range Complex (CIT).

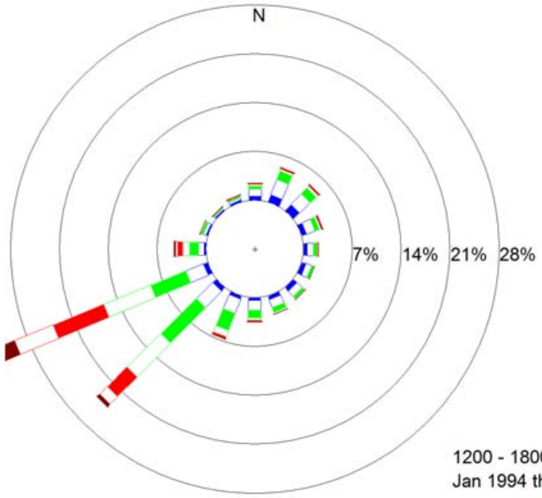

1200 - 1800 MST Wind Rose for CRA
Jan 1994 through Dec 2015 33 ft level

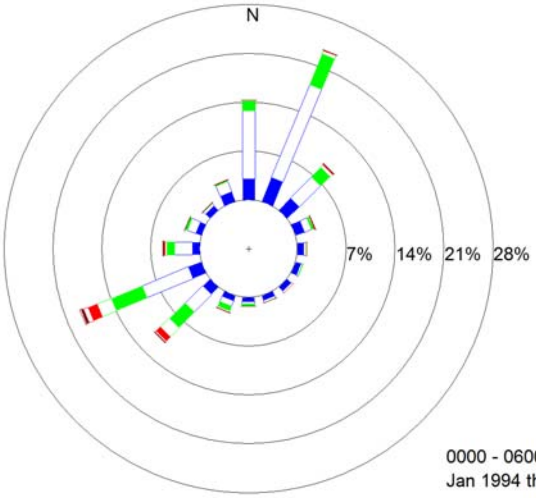

0000 - 0600 MST Wind Rose for CRA
Jan 1994 through Dec 2015 33 ft level

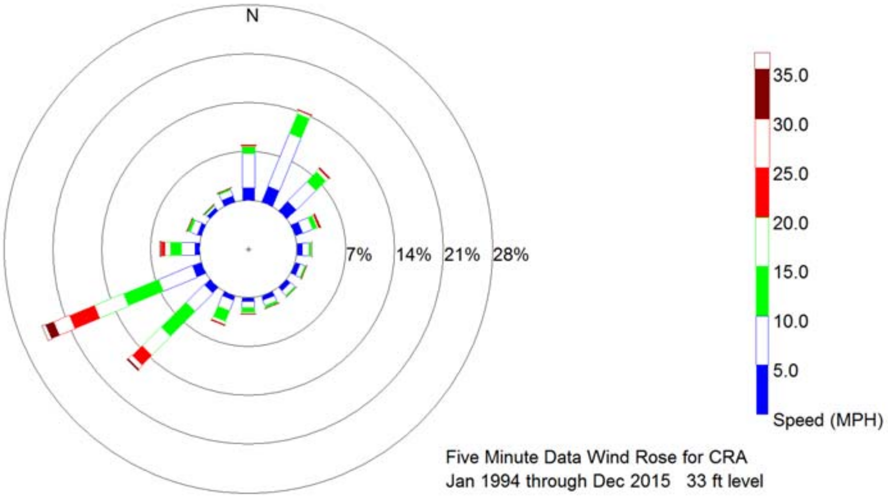

Five Minute Data Wind Rose for CRA
Jan 1994 through Dec 2015 33 ft level

Figure A-10. Daytime (top), nighttime (middle), and all hours (bottom) wind roses for the 30 ft. (9 m) level at Craters of the Moon (CRA).

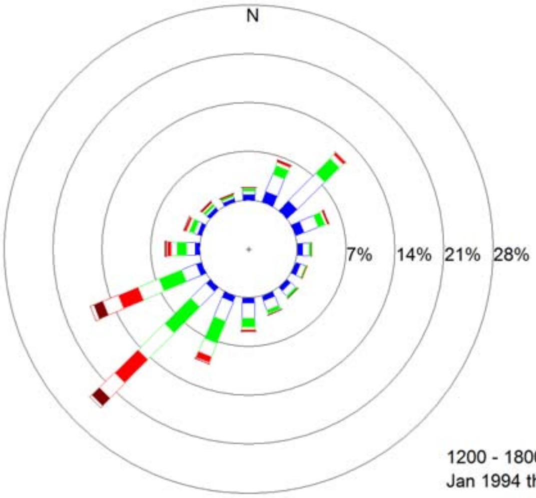

1200 - 1800 MST Wind Rose for DEA
Jan 1994 through Dec 2015 50 ft level

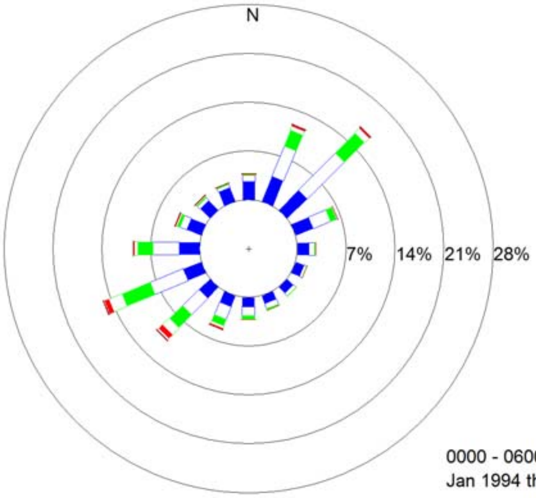

0000 - 0600 MST Wind Rose for DEA
Jan 1994 through Dec 2015 50 ft level

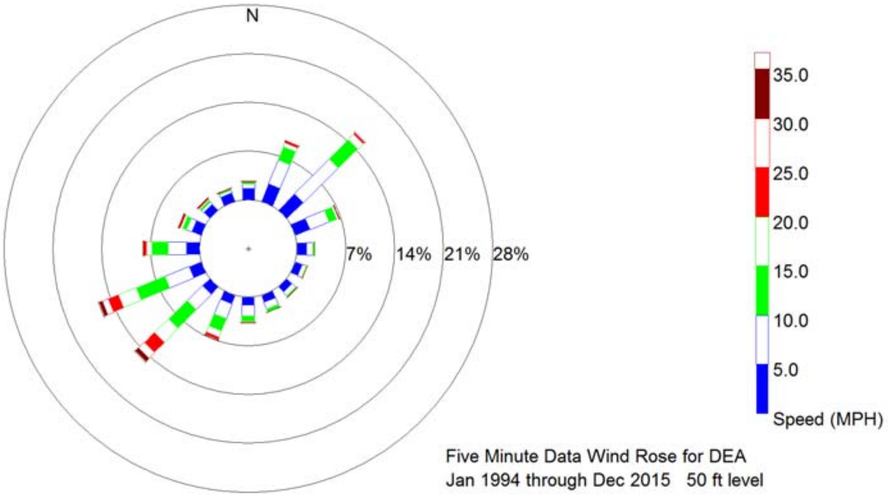

Five Minute Data Wind Rose for DEA
Jan 1994 through Dec 2015 50 ft level

Figure A-11. Daytime (top), nighttime (middle), and all hours (bottom) wind roses for the 50 ft. (15 m) level at Dead Man Canyon (DEA).

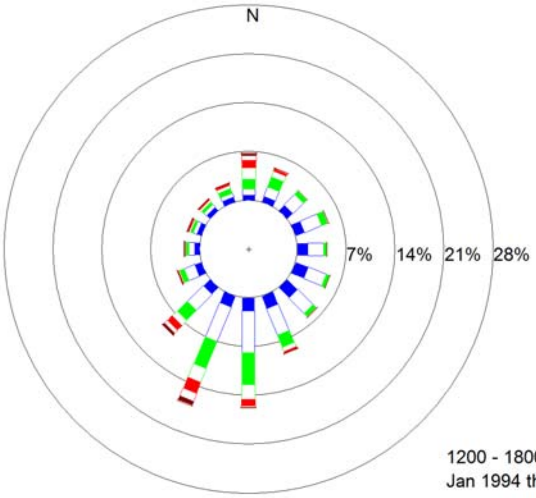

1200 - 1800 MST Wind Rose for DUB
Jan 1994 through Dec 2015   50 ft level

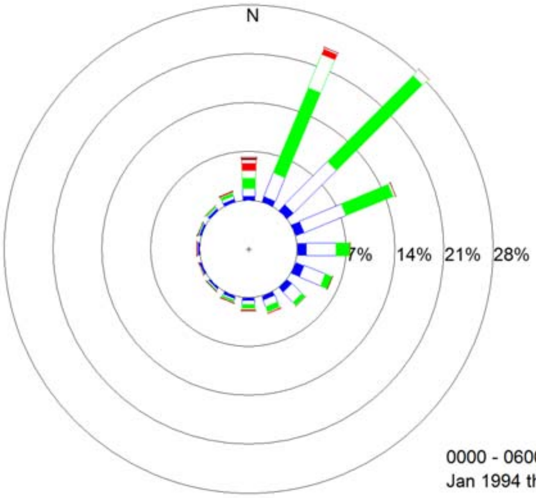

0000 - 0600 MST Wind Rose for DUB
Jan 1994 through Dec 2015   50 ft level

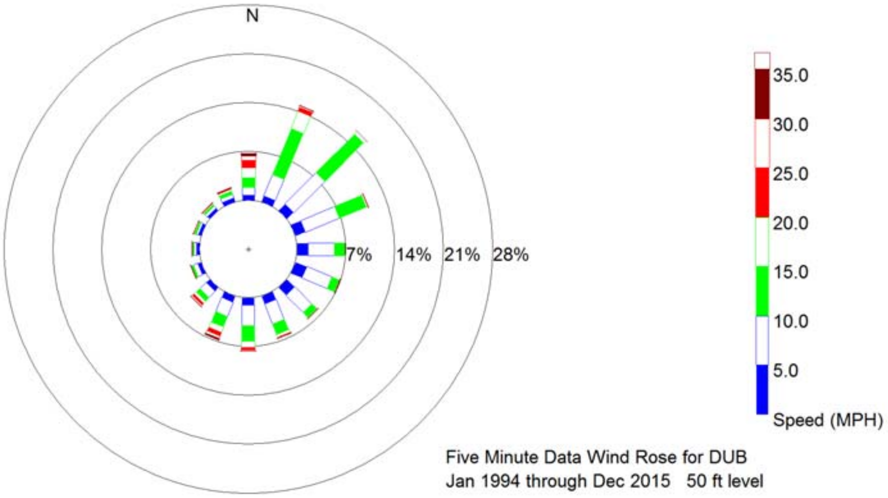

Five Minute Data Wind Rose for DUB
Jan 1994 through Dec 2015   50 ft level

Figure A-12. Daytime (top), nighttime (middle), and all hours (bottom) wind roses for the 50 ft. (15 m) level at Dubois (DUB).

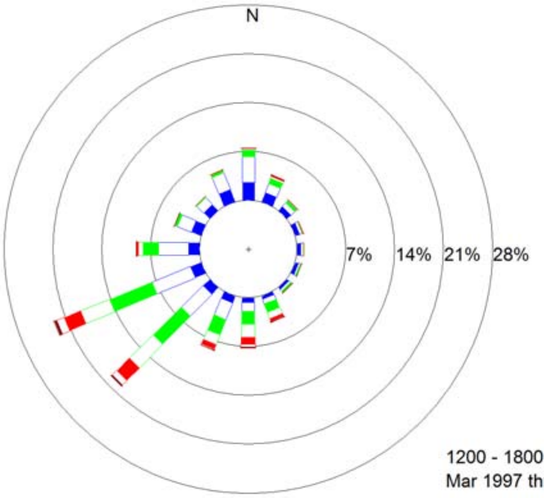

1200 - 1800 MST Wind Rose for FOR
Mar 1997 through Dec 2015 50 ft level

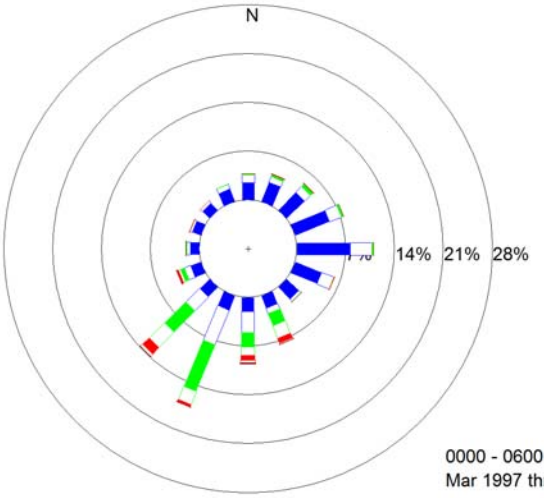

0000 - 0600 MST Wind Rose for FOR
Mar 1997 through Dec 2015 50 ft level

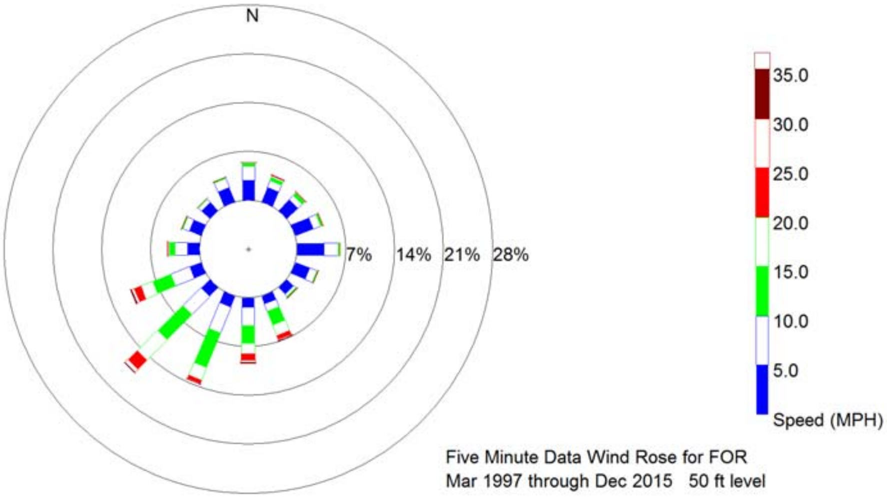

Five Minute Data Wind Rose for FOR
Mar 1997 through Dec 2015 50 ft level

Figure A-13. Daytime (top), nighttime (middle), and all hours (bottom) wind roses for the 50 ft. (15 m) level at Fort Hall (FOR).

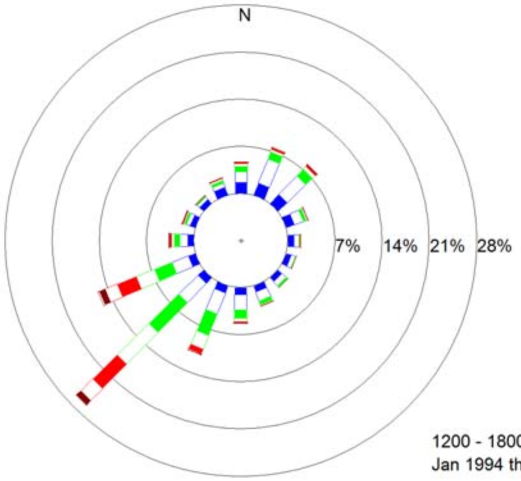

1200 - 1800 MST Wind Rose for GRI
Jan 1994 through Dec 2015 33 ft level

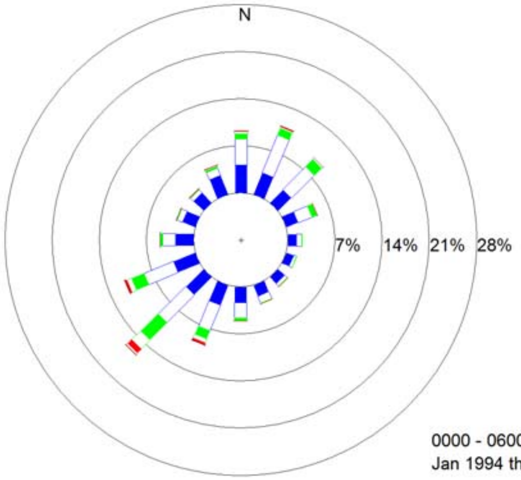

0000 - 0600 MST Wind Rose for GRI
Jan 1994 through Dec 2015 33 ft level

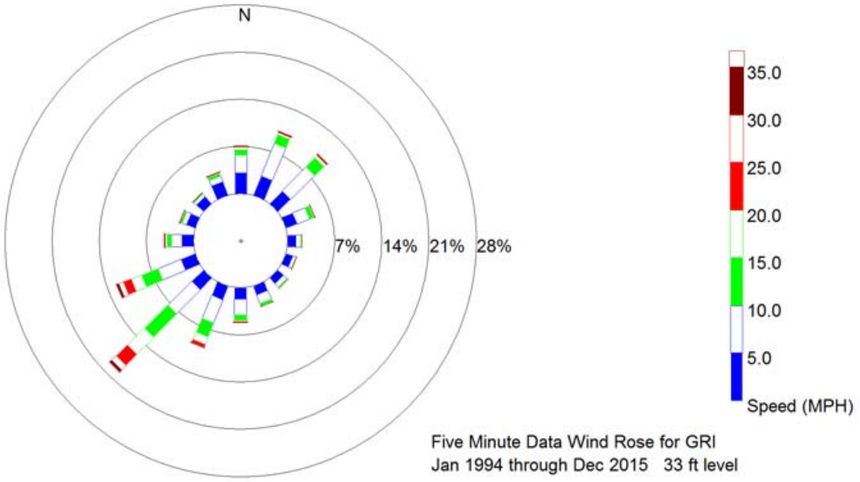

Five Minute Data Wind Rose for GRI
Jan 1994 through Dec 2015 33 ft level

Figure A-14. Daytime (top), nighttime (middle), and all hours (bottom) wind roses for the 33 ft. (10 m) level at Grid 3/INTEC (GRI).

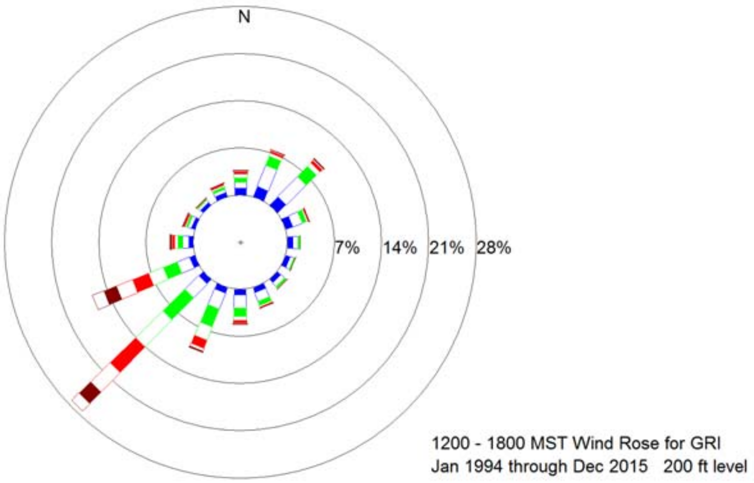

1200 - 1800 MST Wind Rose for GRI
Jan 1994 through Dec 2015 200 ft level

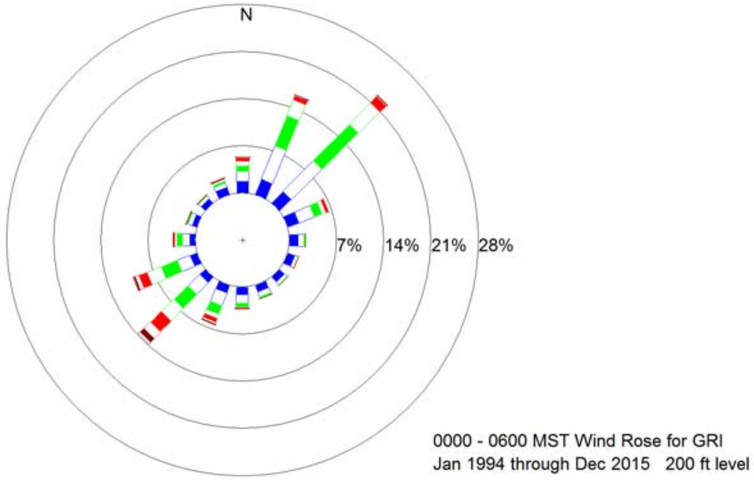

0000 - 0600 MST Wind Rose for GRI
Jan 1994 through Dec 2015 200 ft level

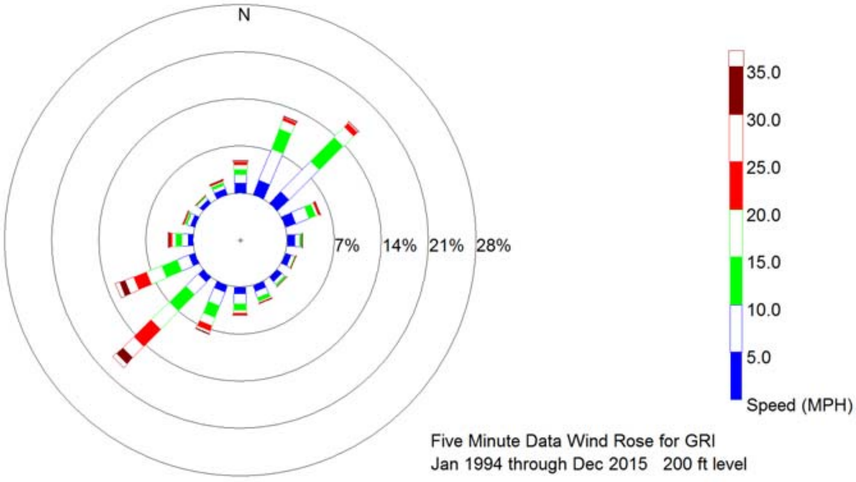

Five Minute Data Wind Rose for GRI
Jan 1994 through Dec 2015 200 ft level

Figure A-15. Daytime (top), nighttime (middle), and all hours (bottom) wind roses for the 200 ft. (61 m) level at Grid 3/INTEC (GRI).

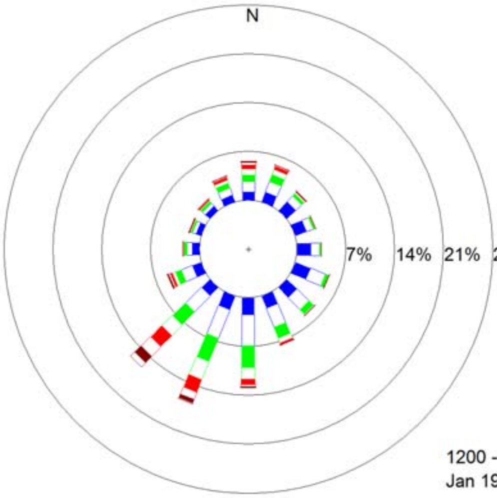

1200 - 1800 MST Wind Rose for HAM
Jan 1994 through Dec 2015   50 ft level

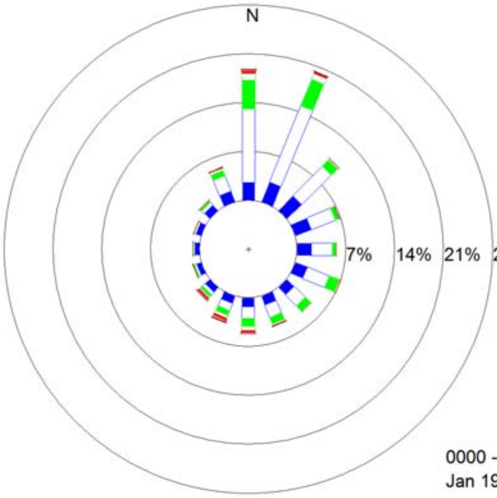

0000 - 0600 MST Wind Rose for HAM
Jan 1994 through Dec 2015   50 ft level

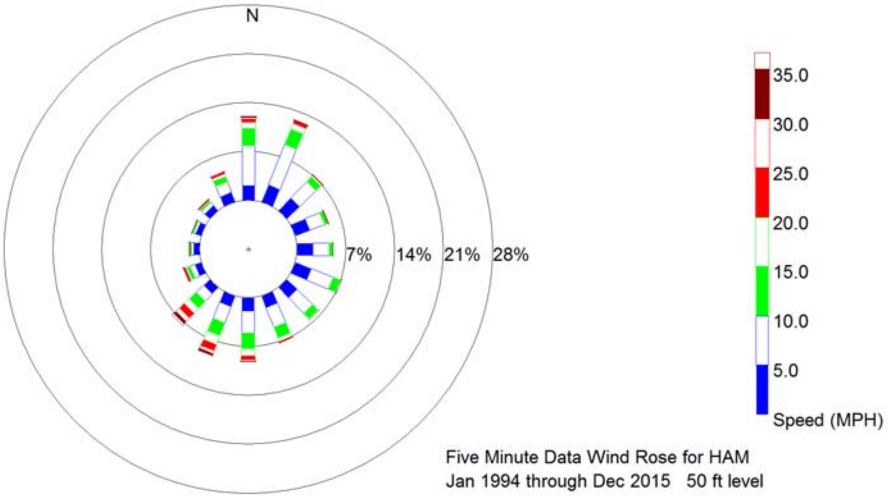

Five Minute Data Wind Rose for HAM
Jan 1994 through Dec 2015   50 ft level

Figure A-16. Daytime (top), nighttime (middle), and all hours (bottom) wind roses for the 50 ft. (15 m) level at Hamer (HAM).

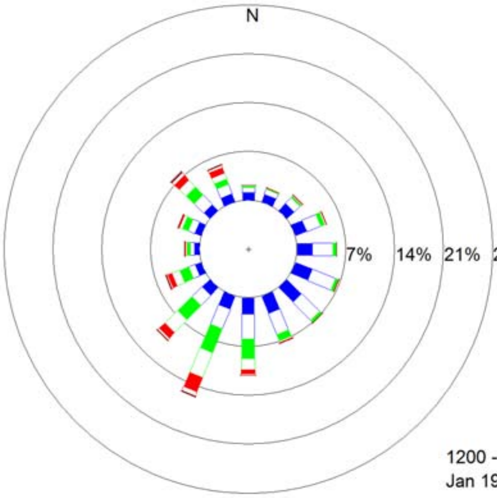

1200 - 1800 MST Wind Rose for HOW
Jan 1994 through Dec 2015   50 ft level

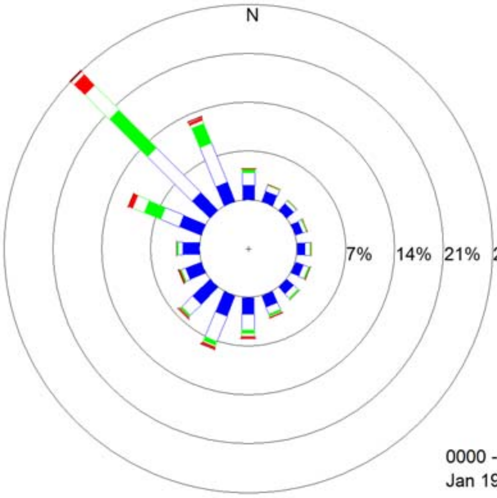

0000 - 0600 MST Wind Rose for HOW
Jan 1994 through Dec 2015   50 ft level

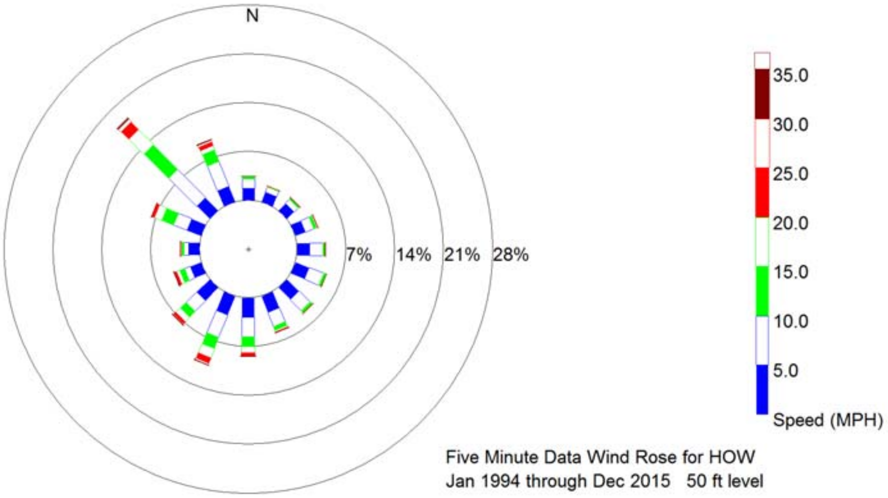

Five Minute Data Wind Rose for HOW
Jan 1994 through Dec 2015   50 ft level

Figure A-17. Daytime (top), nighttime (middle), and all hours (bottom) wind roses for the 50 ft. (15 m) level at Howe (HOW).

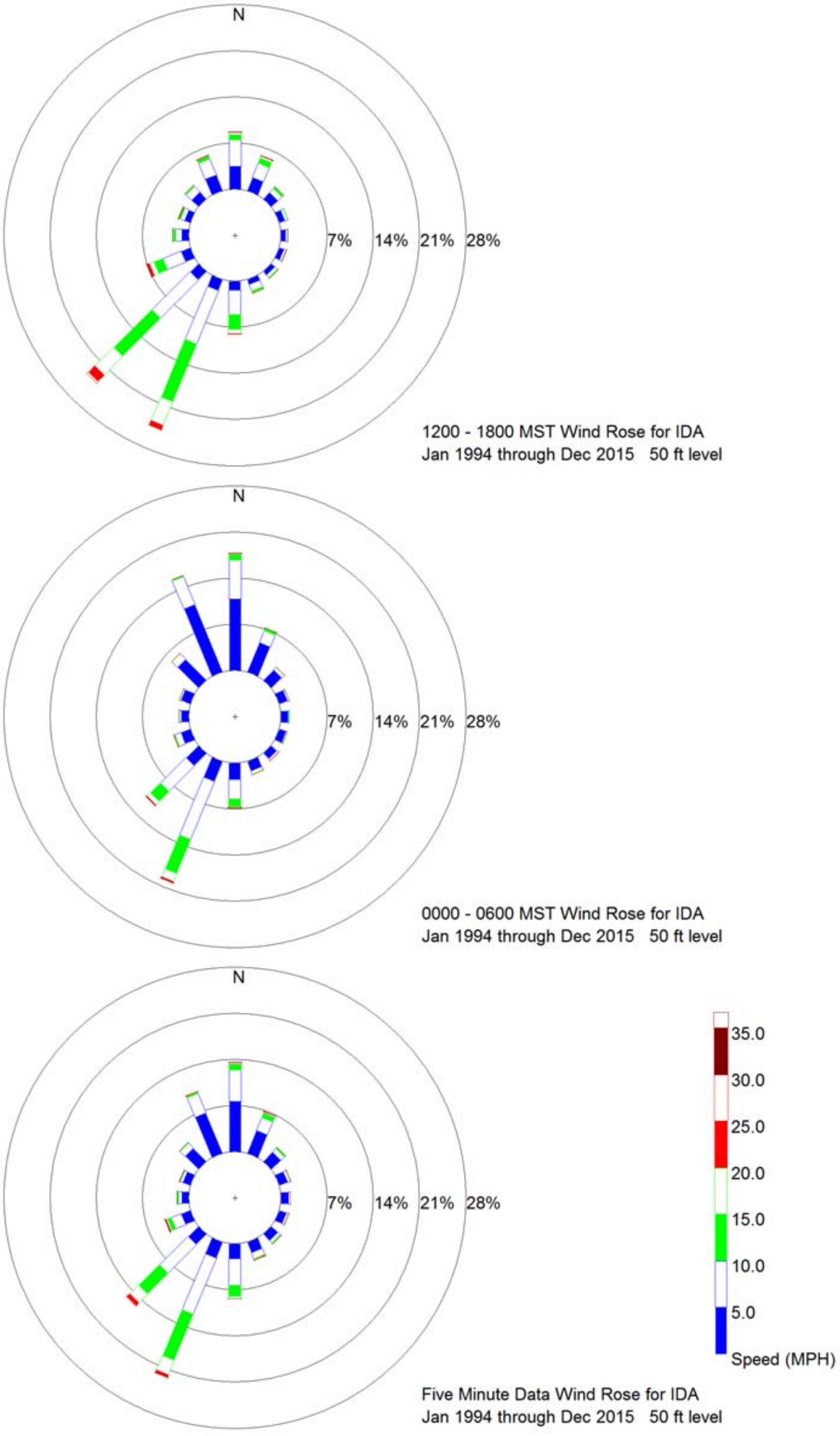

Figure A-18. Daytime (top), nighttime (middle), and all hours (bottom) wind roses for the 50 ft. (15 m) level at Idaho Falls (IDA).

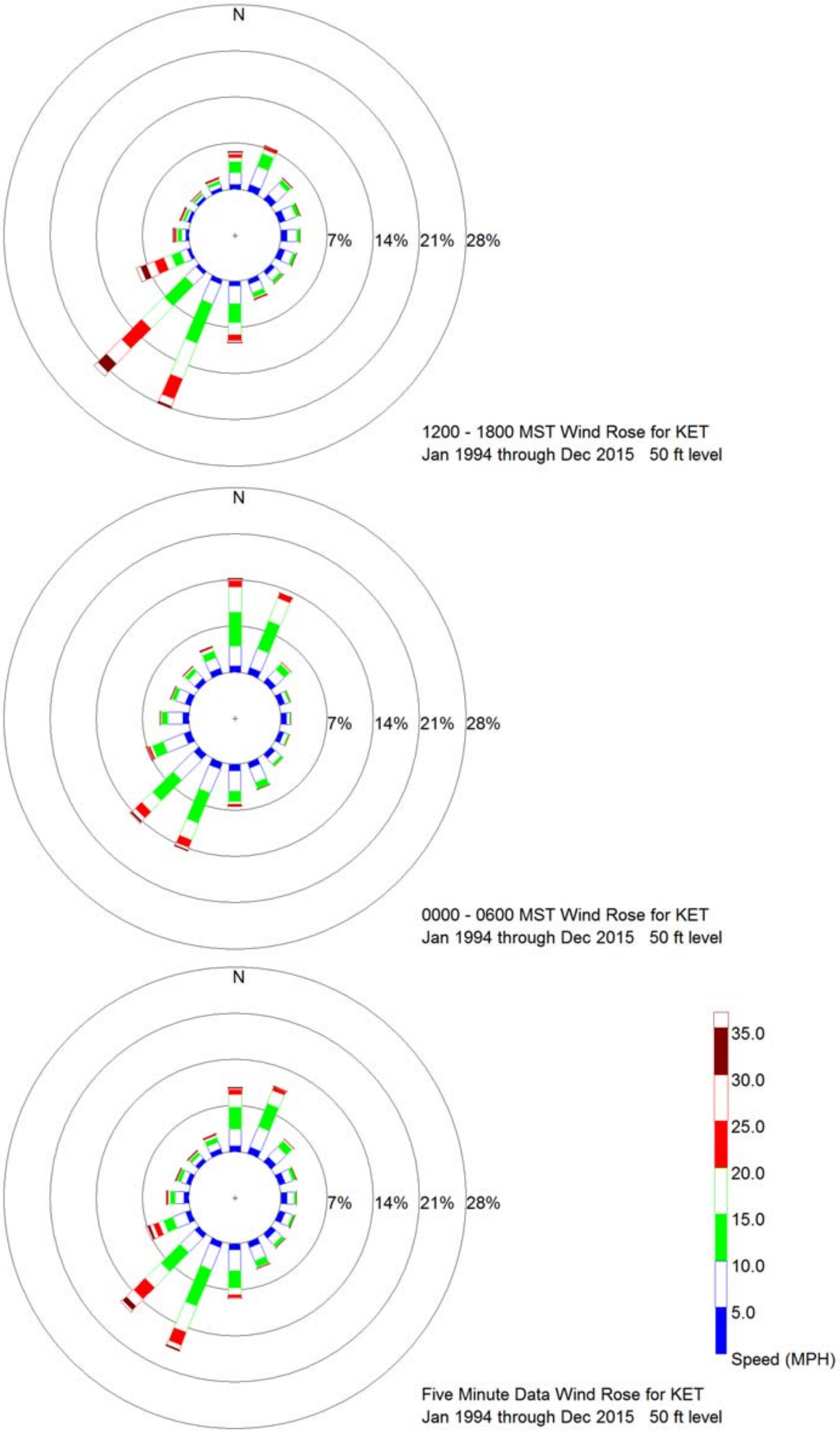

Figure A-19. Daytime (top), nighttime (middle), and all hours (bottom) wind roses for the 50 ft. (15 m) level at Kettle Butte (KET).

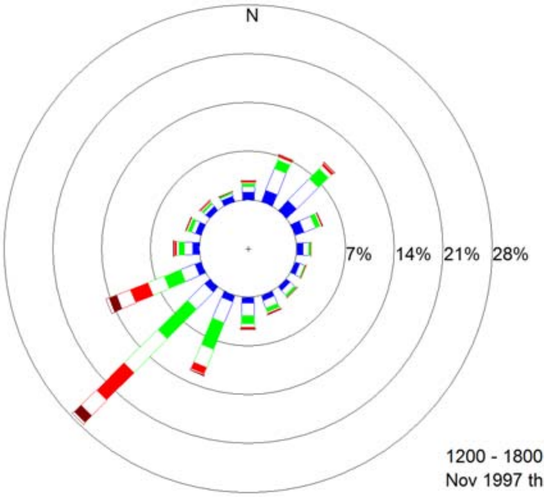

1200 - 1800 MST Wind Rose for LOS
Nov 1997 through Dec 2015 50 ft level

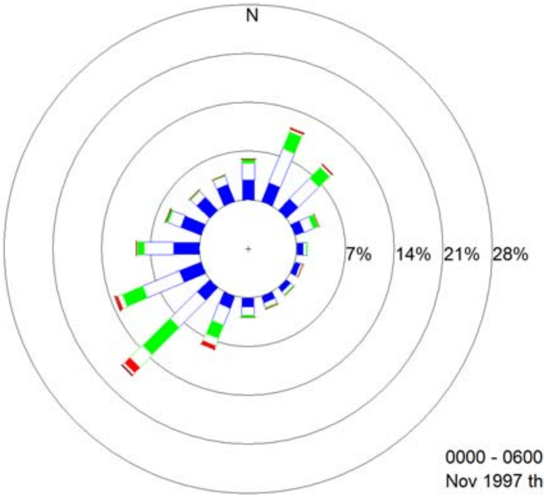

0000 - 0600 MST Wind Rose for LOS
Nov 1997 through Dec 2015 50 ft level

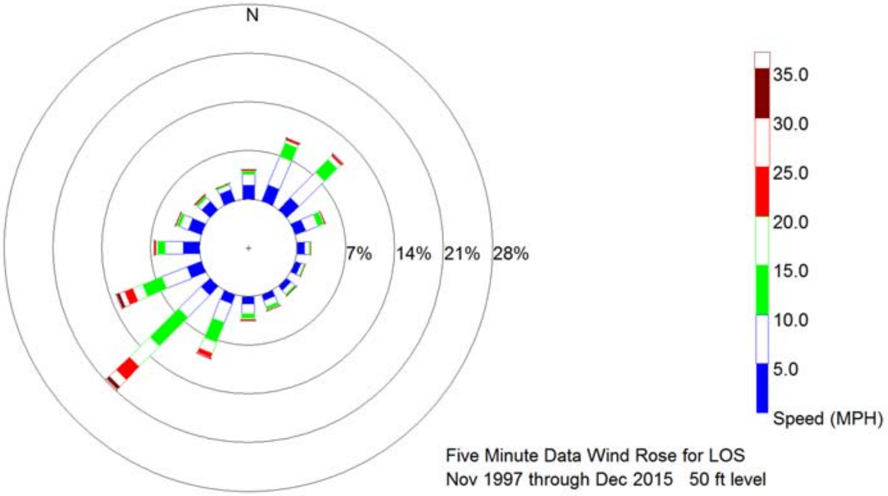

Five Minute Data Wind Rose for LOS
Nov 1997 through Dec 2015 50 ft level

Figure A-20. Daytime (top), nighttime (middle), and all hours (bottom) wind roses for the 50 ft. (15 m) level at Lost River Rest Area (LOS).

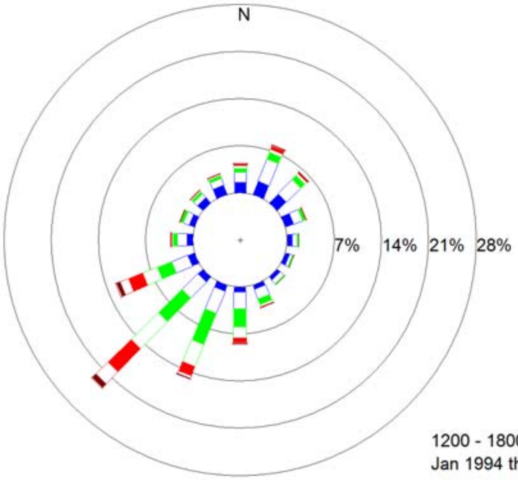

1200 - 1800 MST Wind Rose for MFC
Jan 1994 through Dec 2015 33 ft level

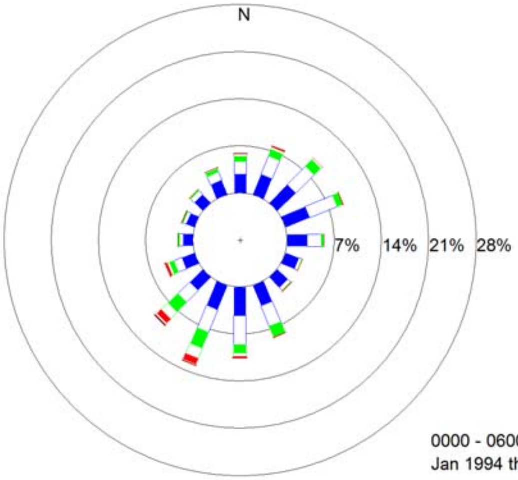

0000 - 0600 MST Wind Rose for MFC
Jan 1994 through Dec 2015 33 ft level

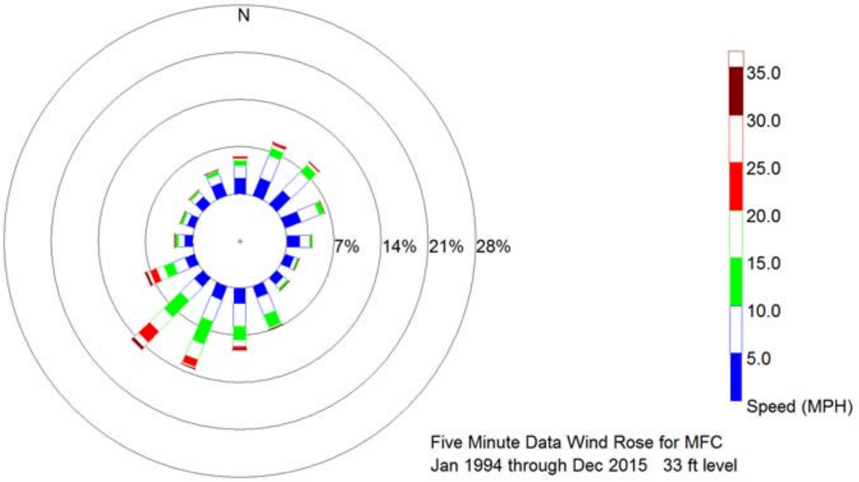

Five Minute Data Wind Rose for MFC
Jan 1994 through Dec 2015 33 ft level

Figure A-21. Daytime (top), nighttime (middle), and all hours (bottom) wind roses for the 33 ft. (10 m) level at the Materials and Fuels Complex (MFC).

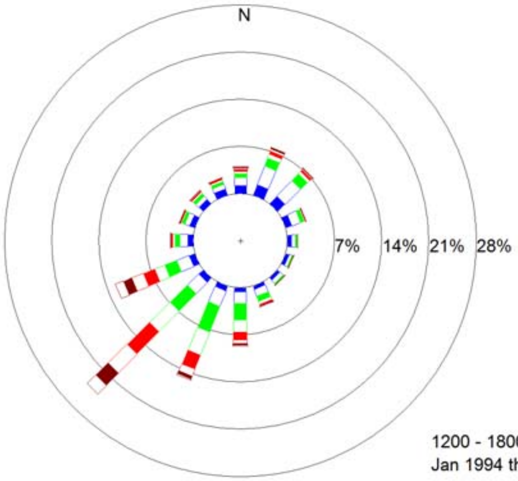

1200 - 1800 MST Wind Rose for MFC
Jan 1994 through Dec 2015 250 ft level

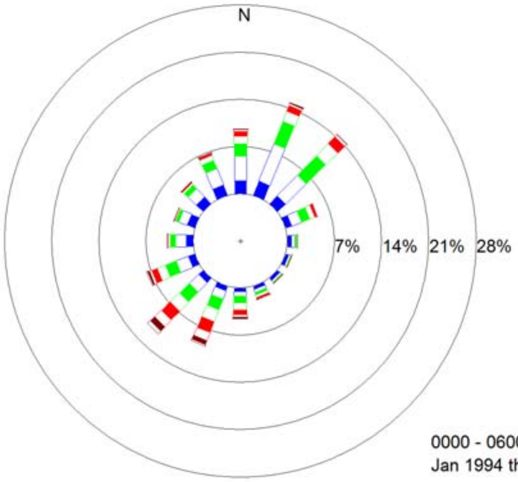

0000 - 0600 MST Wind Rose for MFC
Jan 1994 through Dec 2015 250 ft level

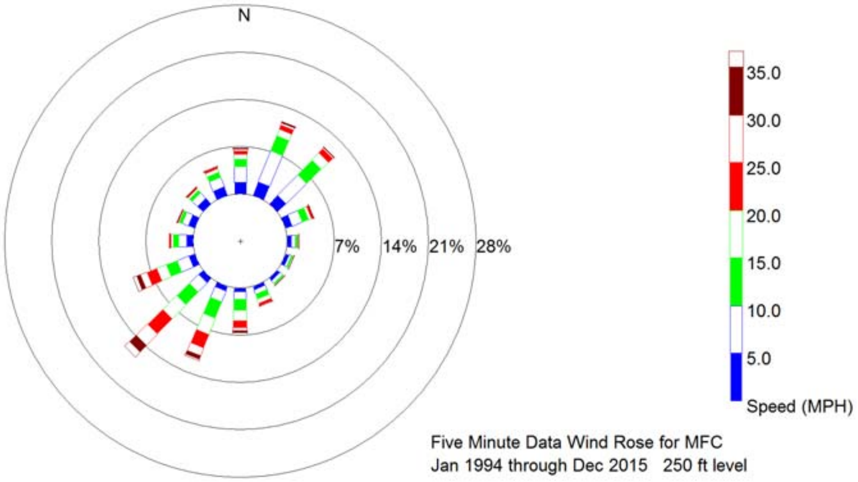

Five Minute Data Wind Rose for MFC
Jan 1994 through Dec 2015 250 ft level

Figure A-22. Daytime (top), nighttime (middle), and all hours (bottom) wind roses for the 250 ft. (76 m) level at the Materials and Fuels Complex (MFC).

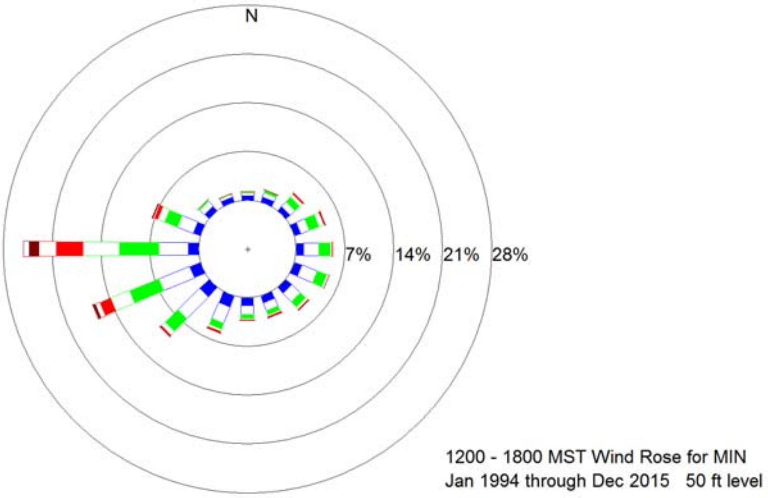

1200 - 1800 MST Wind Rose for MIN
Jan 1994 through Dec 2015 50 ft level

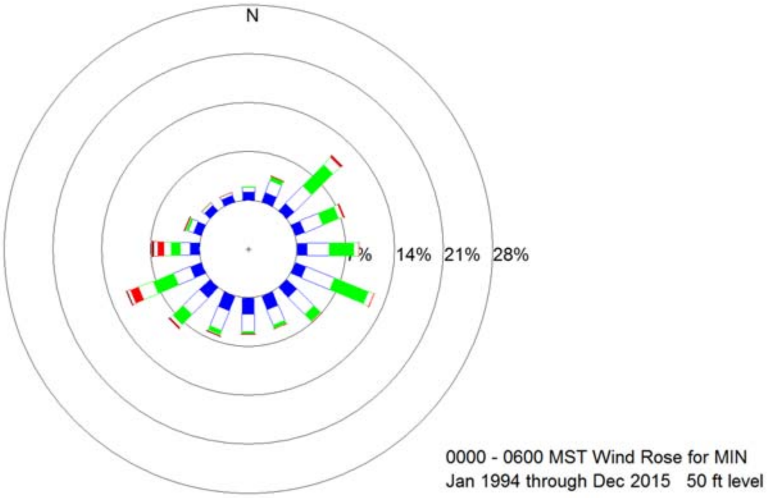

0000 - 0600 MST Wind Rose for MIN
Jan 1994 through Dec 2015 50 ft level

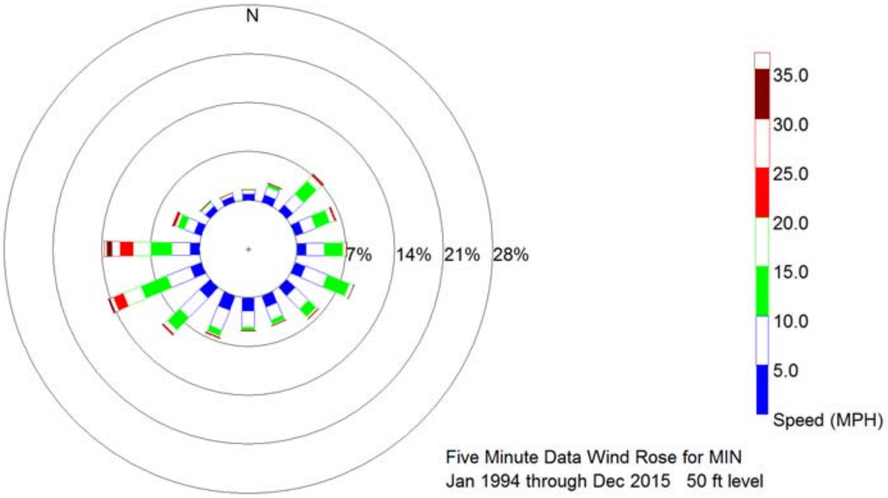

Five Minute Data Wind Rose for MIN
Jan 1994 through Dec 2015 50 ft level

Figure A-23. Daytime (top), nighttime (middle), and all hours (bottom) wind roses for the 50 ft. (15 m) level at Minnedoka (MIN).

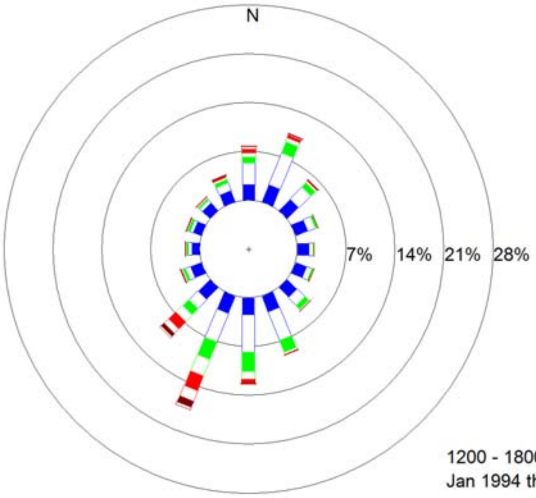

1200 - 1800 MST Wind Rose for MON
Jan 1994 through Dec 2015 50 ft level

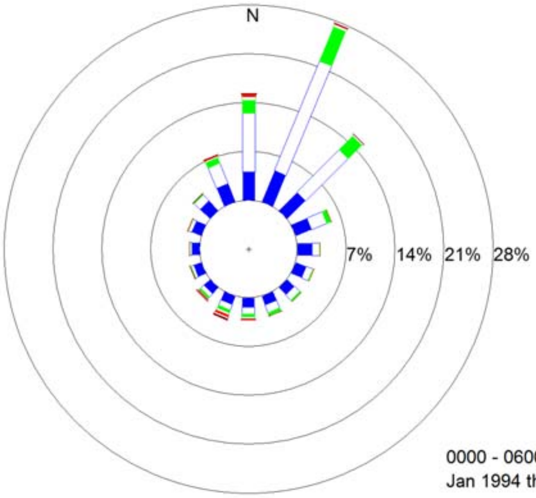

0000 - 0600 MST Wind Rose for MON
Jan 1994 through Dec 2015 50 ft level

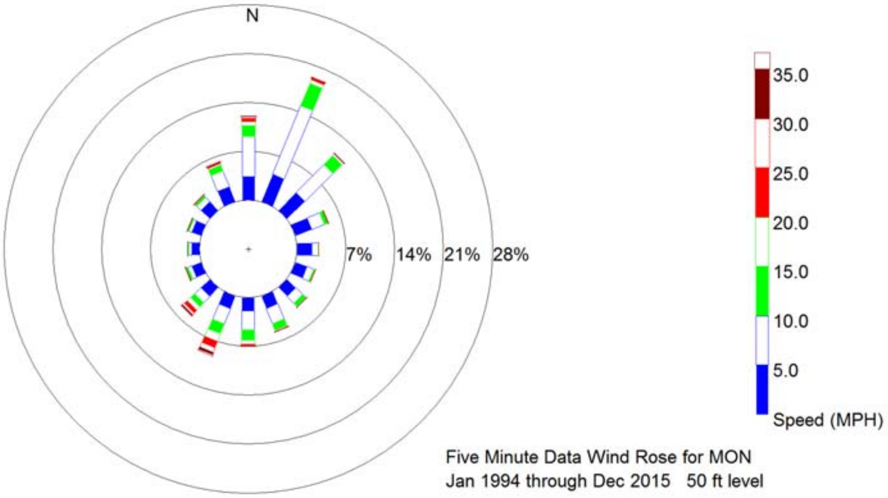

Five Minute Data Wind Rose for MON
Jan 1994 through Dec 2015 50 ft level

Figure A-24. Daytime (top), nighttime (middle), and all hours (bottom) wind roses for the 50 ft. (15 m) level at Monteview (MON).

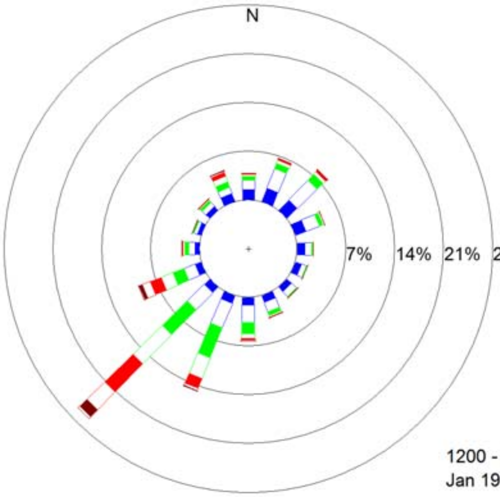

1200 - 1800 MST Wind Rose for NRF
Jan 1994 through Dec 2015 50 ft level

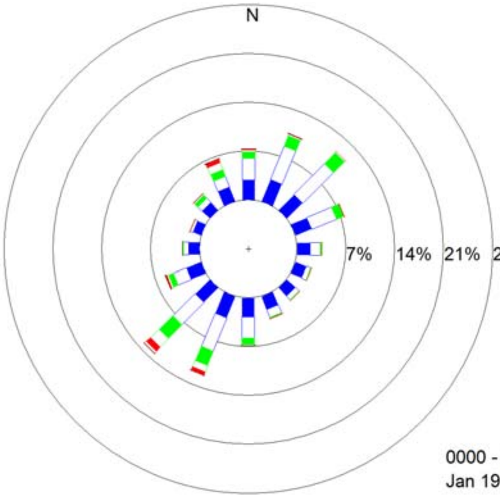

0000 - 0600 MST Wind Rose for NRF
Jan 1994 through Dec 2015 50 ft level

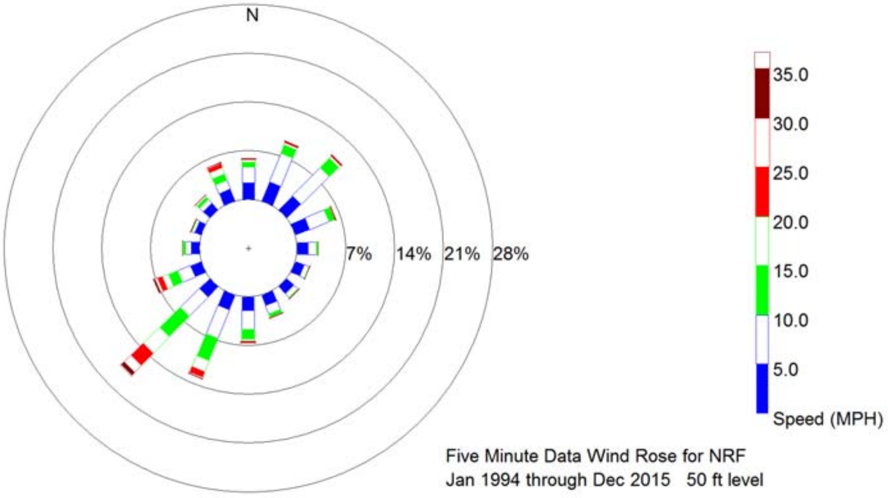

Five Minute Data Wind Rose for NRF
Jan 1994 through Dec 2015 50 ft level

Figure A-25. Daytime (top), nighttime (middle), and all hours (bottom) wind roses for the 50 ft. (15 m) level at National Reactor Facility (NRF).

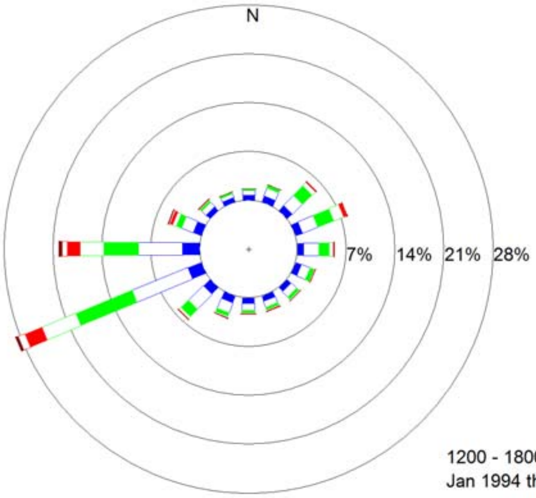

1200 - 1800 MST Wind Rose for RIC
Jan 1994 through Dec 2015 50 ft level

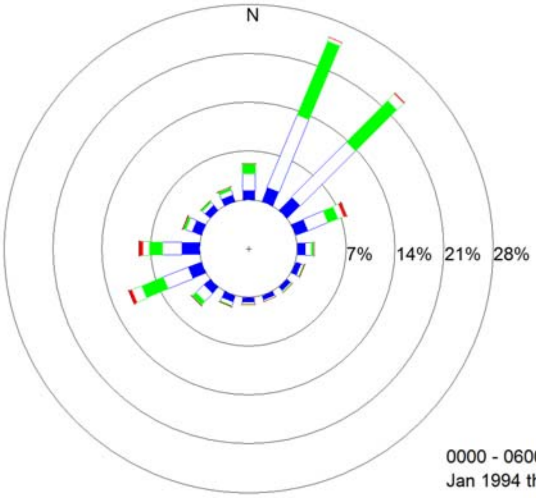

0000 - 0600 MST Wind Rose for RIC
Jan 1994 through Dec 2015 50 ft level

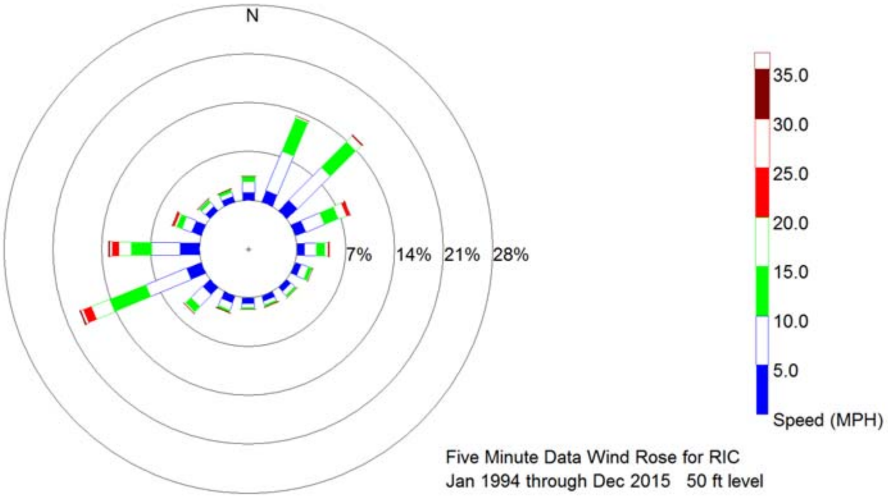

Five Minute Data Wind Rose for RIC
Jan 1994 through Dec 2015 50 ft level

Figure A-26. Daytime (top), nighttime (middle), and all hours (bottom) wind roses for the 50 ft. (15 m) level at Richfield (RIC).

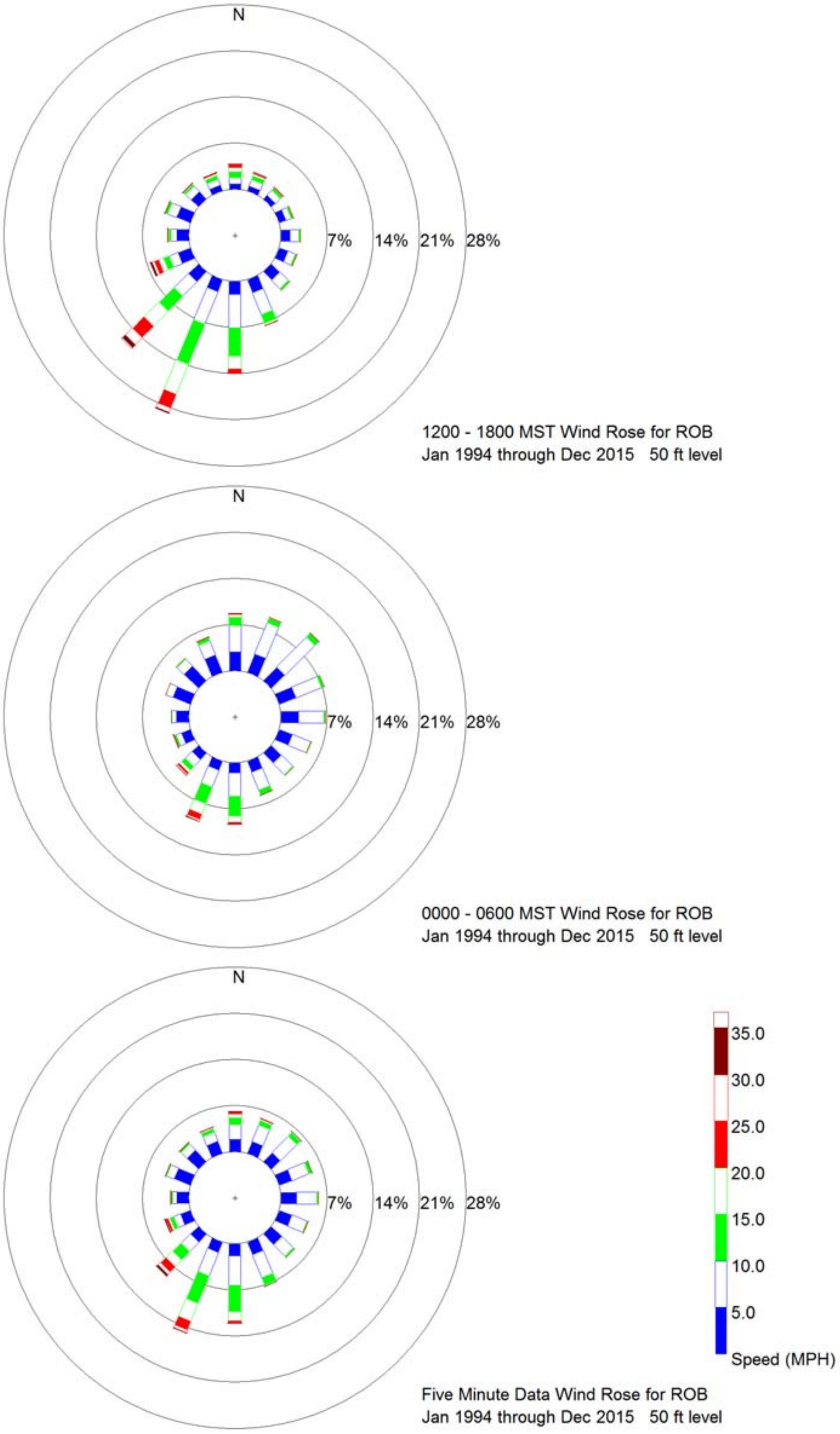

Figure A-27. Daytime (top), nighttime (middle), and all hours (bottom) wind roses for the 50 ft. (15 m) level at Roberts (ROB).

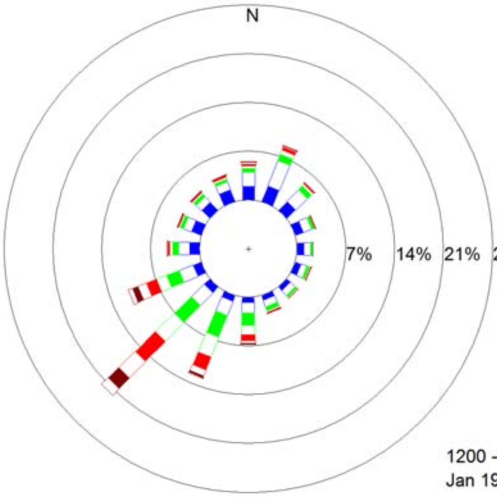

1200 - 1800 MST Wind Rose for ROV
Jan 1994 through Dec 2015 50 ft level

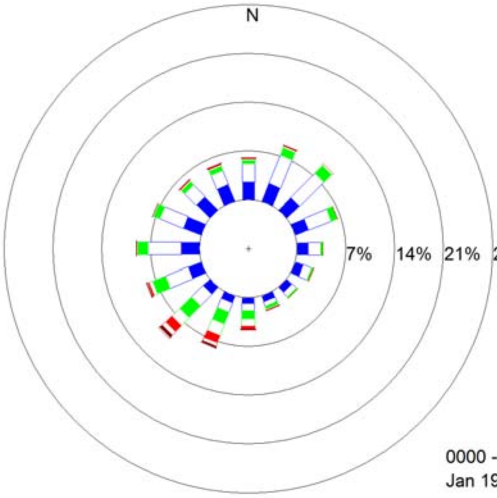

0000 - 0600 MST Wind Rose for ROV
Jan 1994 through Dec 2015 50 ft level

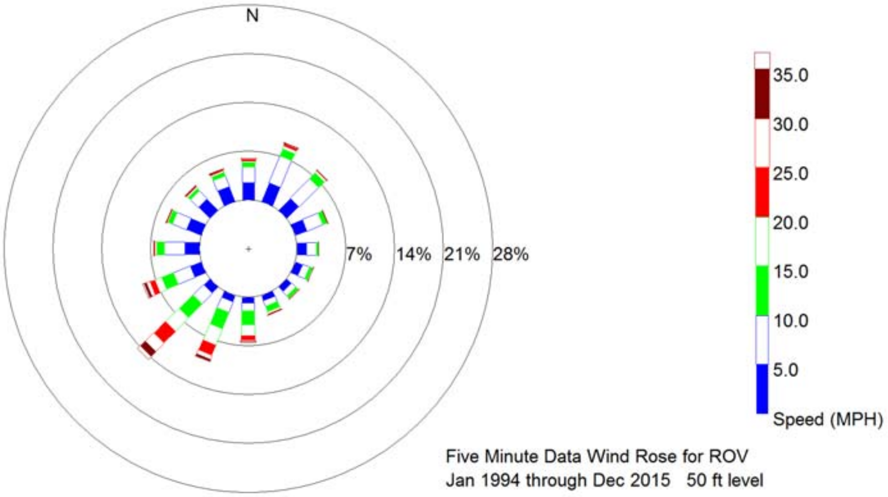

Five Minute Data Wind Rose for ROV
Jan 1994 through Dec 2015 50 ft level

Figure A-28. Daytime (top), nighttime (middle), and all hours (bottom) wind roses for the 50 ft. (15 m) level at Rover (ROV).

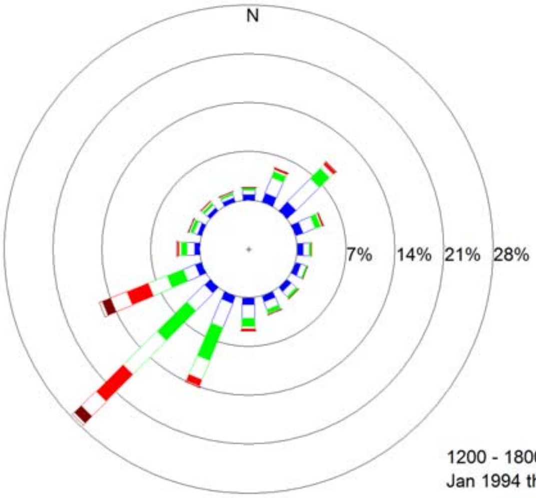

1200 - 1800 MST Wind Rose for RWM
Jan 1994 through Dec 2015 50 ft level

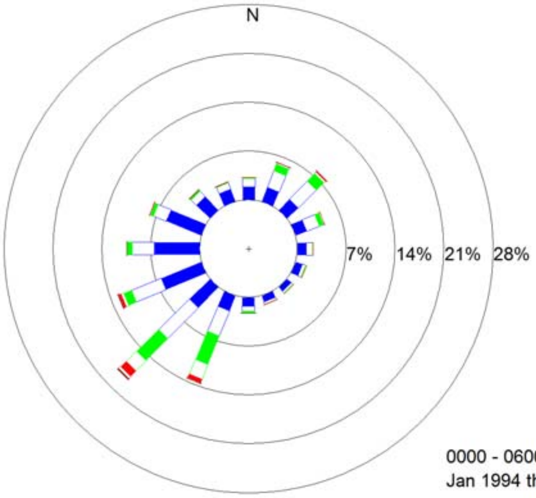

0000 - 0600 MST Wind Rose for RWM
Jan 1994 through Dec 2015 50 ft level

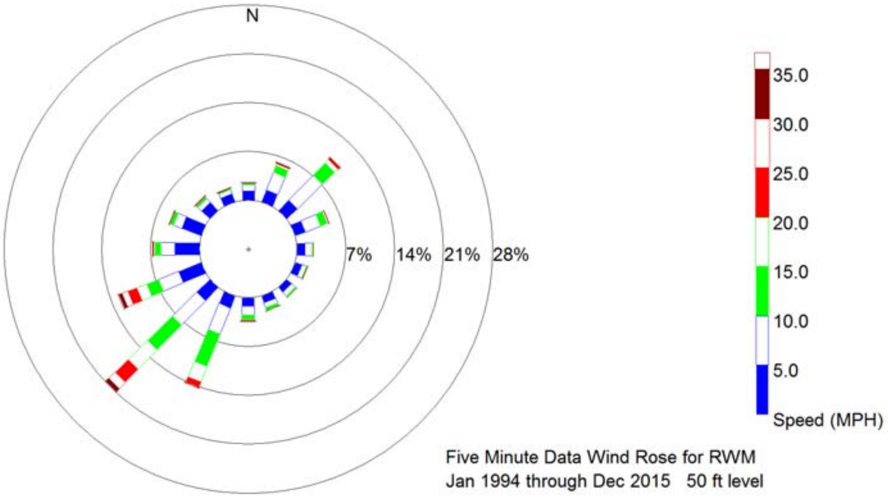

Five Minute Data Wind Rose for RWM
Jan 1994 through Dec 2015 50 ft level

Figure A-29. Daytime (top), nighttime (middle), and all hours (bottom) wind roses for the 50 ft. (15 m) level at the Radioactive Waste Management Complex (RWM).

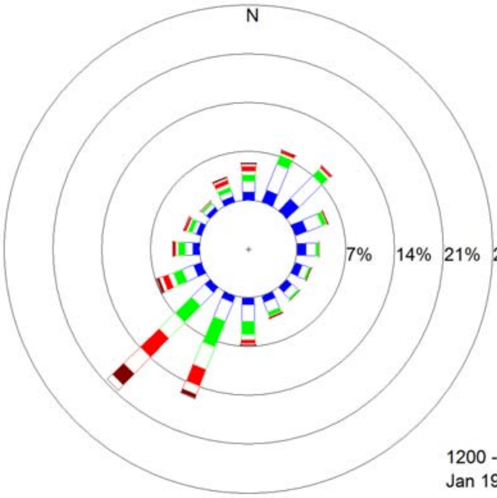

1200 - 1800 MST Wind Rose for SAN
Jan 1994 through Dec 2015   50 ft level

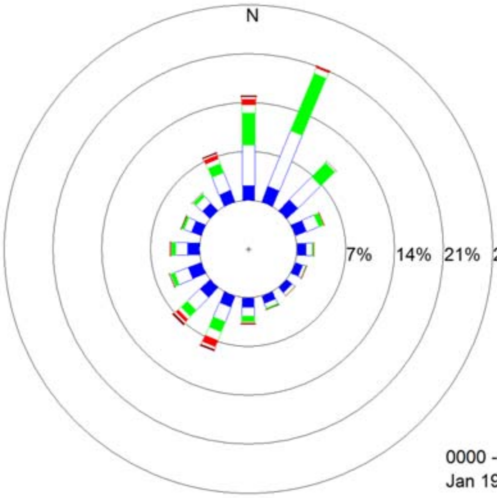

0000 - 0600 MST Wind Rose for SAN
Jan 1994 through Dec 2015   50 ft level

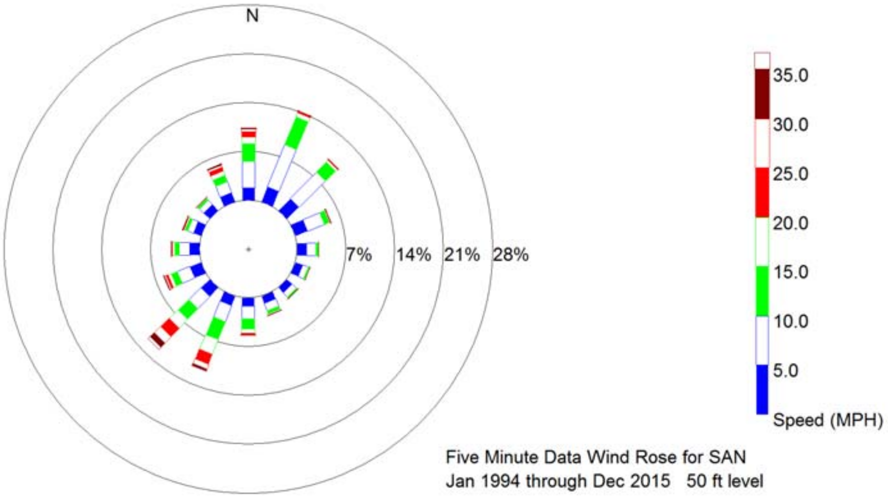

Five Minute Data Wind Rose for SAN
Jan 1994 through Dec 2015   50 ft level

Figure A-30. Daytime (top), nighttime (middle), and all hours (bottom) wind roses for the 50 ft. (15 m) level at San Dunes (SAN).

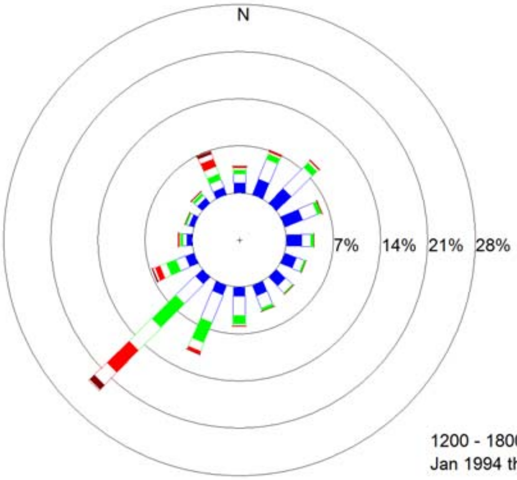

1200 - 1800 MST Wind Rose for SMC
Jan 1994 through Dec 2015 33 ft level

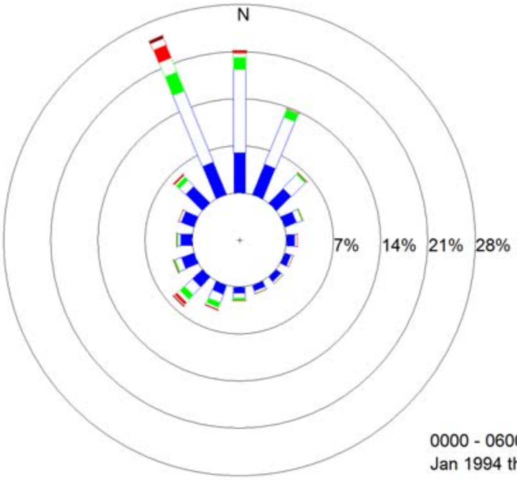

0000 - 0600 MST Wind Rose for SMC
Jan 1994 through Dec 2015 33 ft level

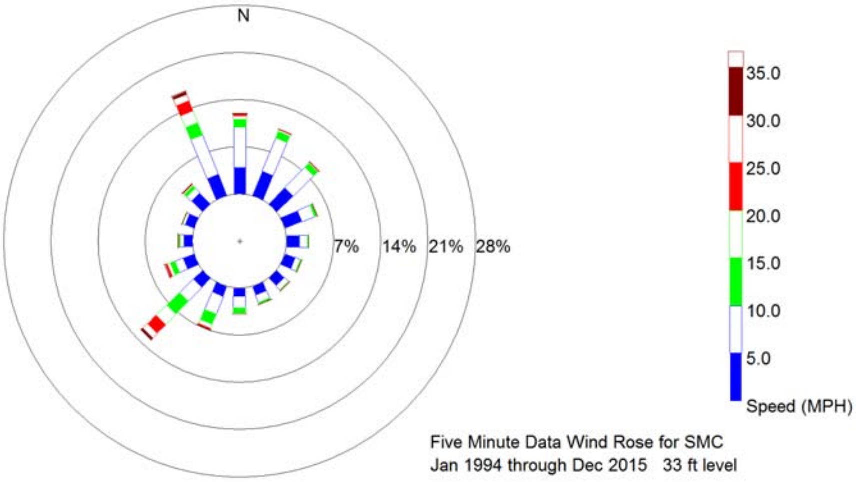

Five Minute Data Wind Rose for SMC
Jan 1994 through Dec 2015 33 ft level

Figure A-31. Daytime (top), nighttime (middle), and all hours (bottom) wind roses for the 33 ft. (10 m) level at Specific Manufacturing Capability (SMC).

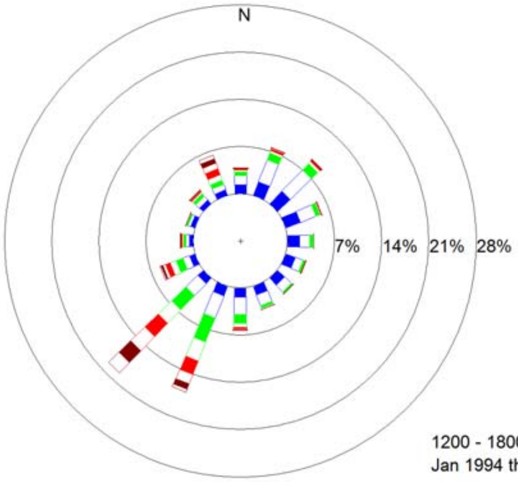

1200 - 1800 MST Wind Rose for SMC
Jan 1994 through Dec 2015 150 ft level

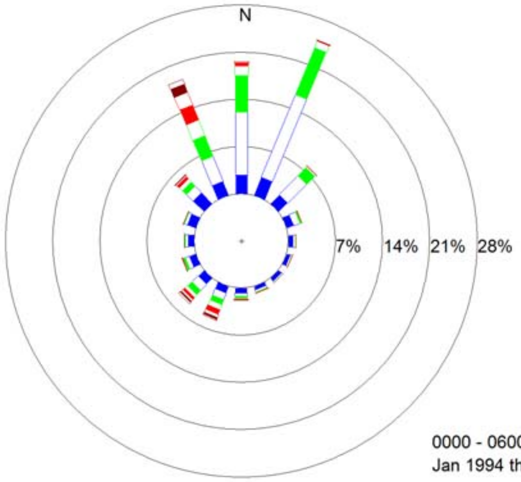

0000 - 0600 MST Wind Rose for SMC
Jan 1994 through Dec 2015 150 ft level

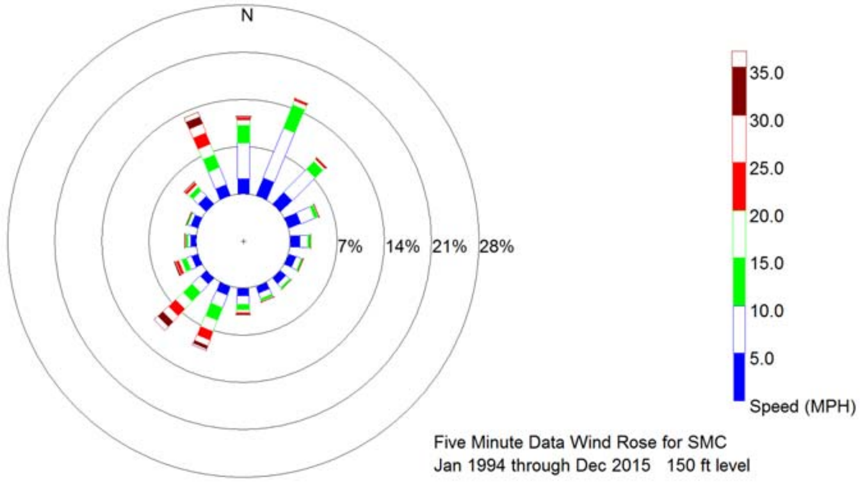

Five Minute Data Wind Rose for SMC
Jan 1994 through Dec 2015 150 ft level

Figure A-32. Day (top), night (middle), and all hours (bottom) wind roses for the 150 ft. (46 m) level at Specific Manufacturing Capability (SMC).

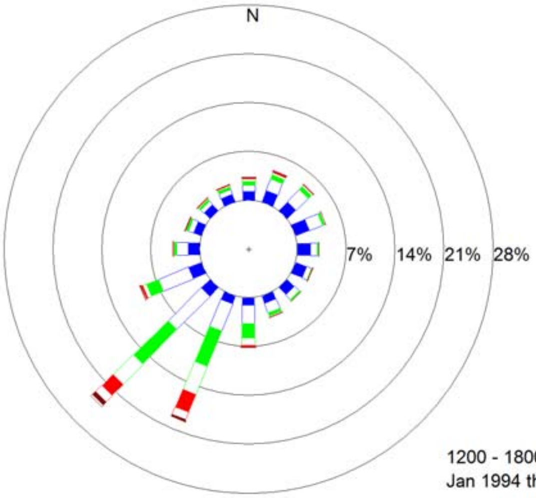

1200 - 1800 MST Wind Rose for SUG
Jan 1994 through Dec 2015 50 ft level

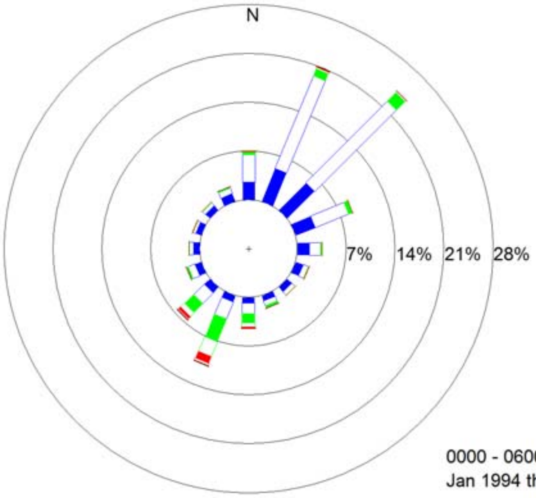

0000 - 0600 MST Wind Rose for SUG
Jan 1994 through Dec 2015 50 ft level

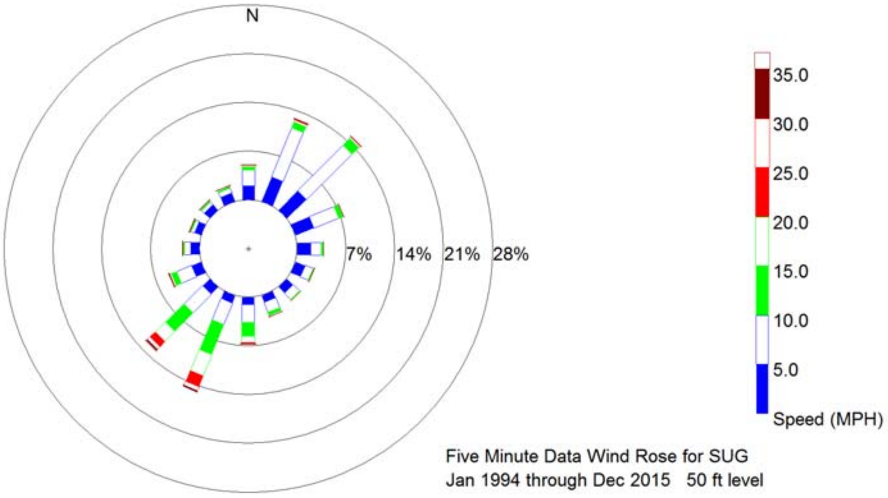

Five Minute Data Wind Rose for SUG
Jan 1994 through Dec 2015 50 ft level

Figure A-33. Day (top), night (middle), and all hours (bottom) wind roses for the 50 ft. (15 m) level at Sugar City (SUG).

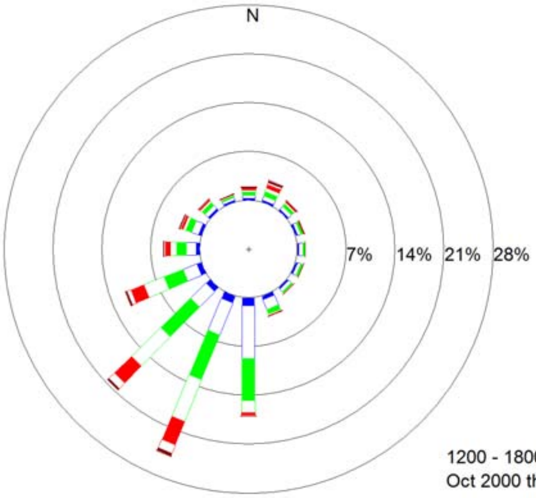

1200 - 1800 MST Wind Rose for SUM
Oct 2000 through Dec 2015 20 ft level

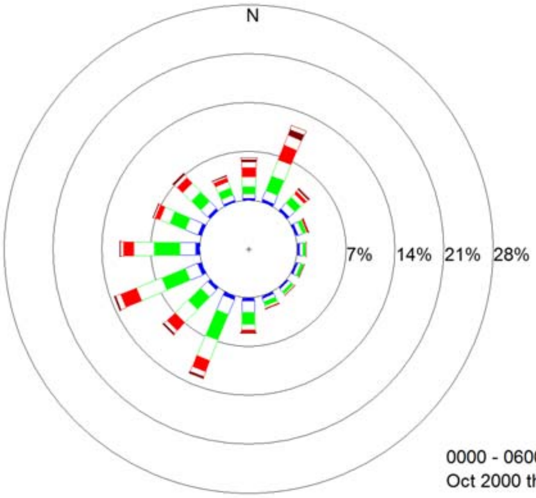

0000 - 0600 MST Wind Rose for SUM
Oct 2000 through Dec 2015 20 ft level

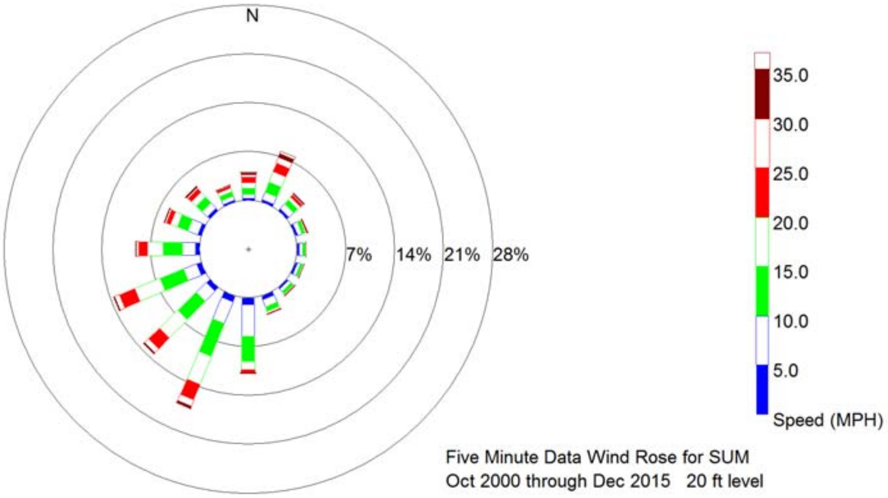

Five Minute Data Wind Rose for SUM
Oct 2000 through Dec 2015 20 ft level

Figure A-34. Day (top), night (middle), and all hours (bottom) wind roses for the 20 ft. (6 m) level at Big Southern Butte Summit (SUM).

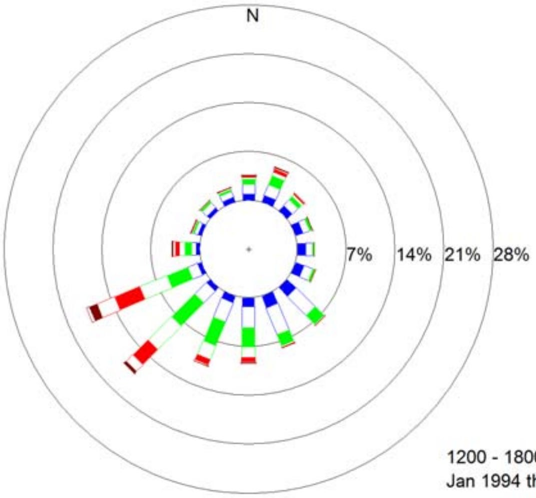

1200 - 1800 MST Wind Rose for TAB
Jan 1994 through Dec 2015   50 ft level

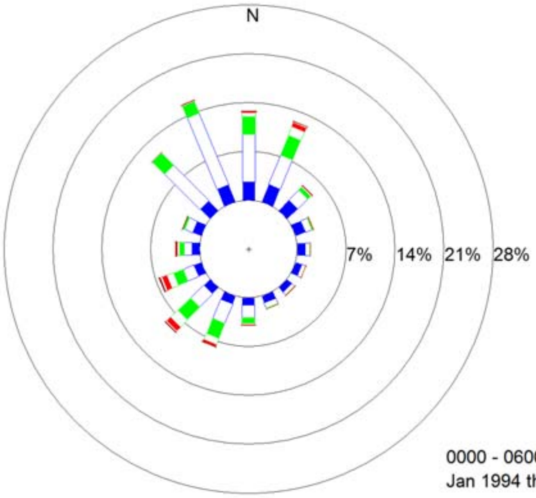

0000 - 0600 MST Wind Rose for TAB
Jan 1994 through Dec 2015   50 ft level

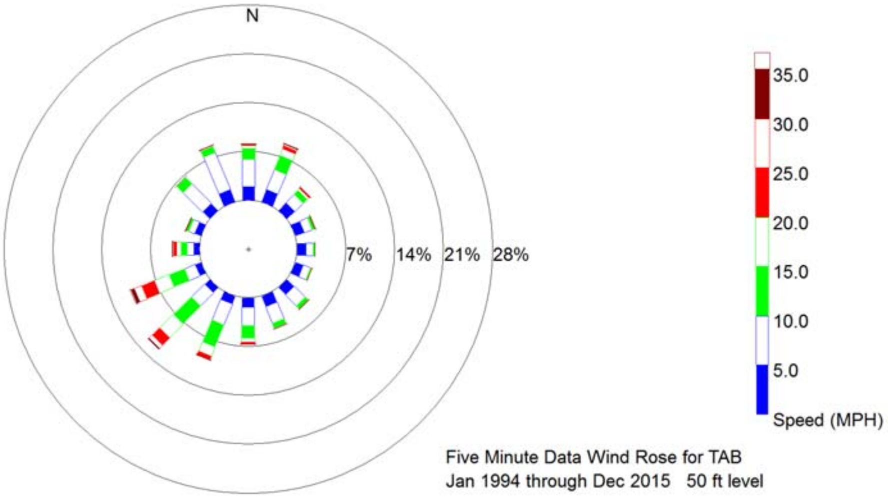

Five Minute Data Wind Rose for TAB
Jan 1994 through Dec 2015   50 ft level

Figure A-35. Day (top), night (middle), and all hours (bottom) wind roses for the 50 ft. (15 m) level at Taber (TAB).

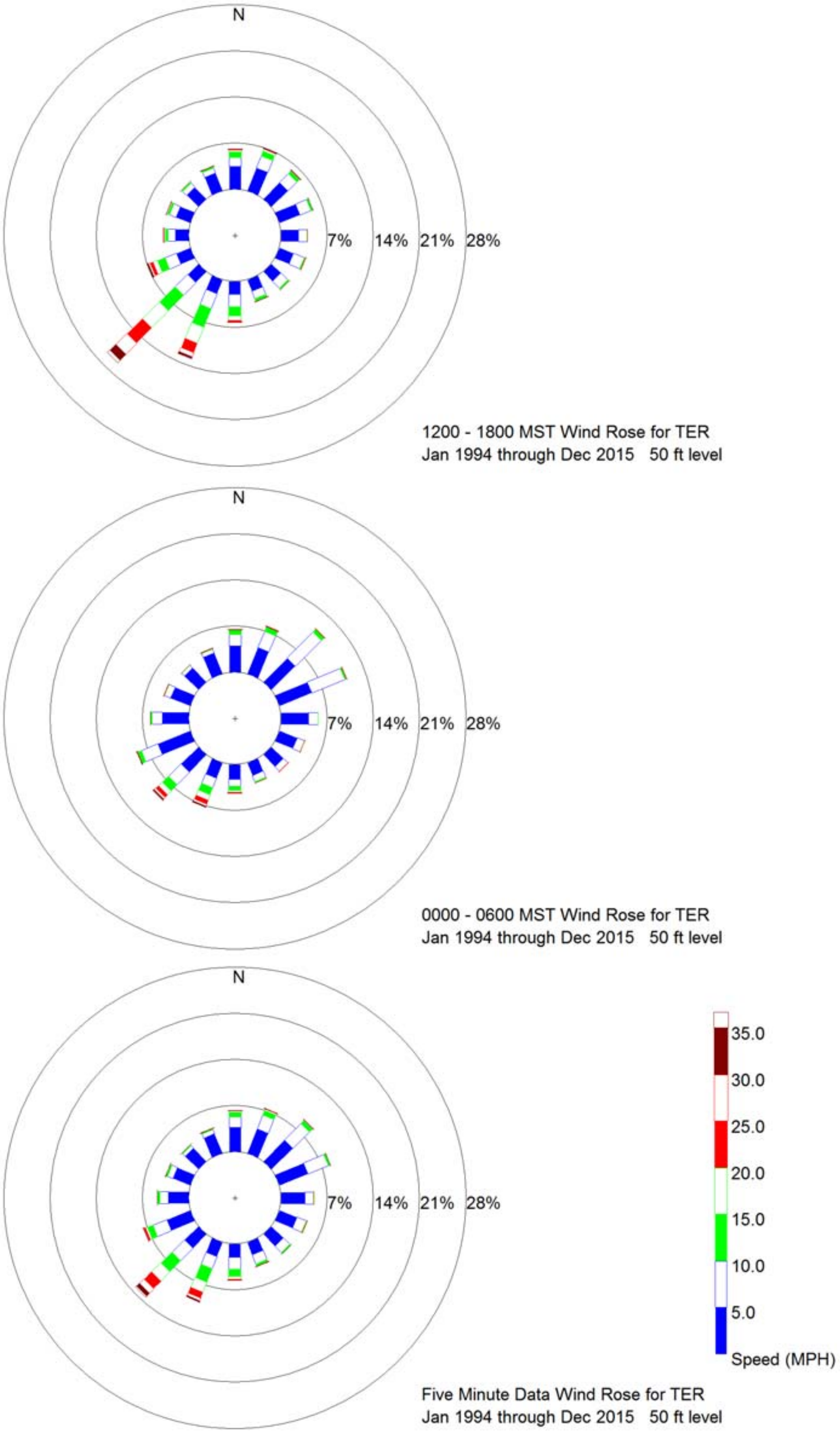

Figure A-36. Day (top), night (middle), and all hours (bottom) wind roses for the 50 ft. (15 m) level at Terreton (TER).

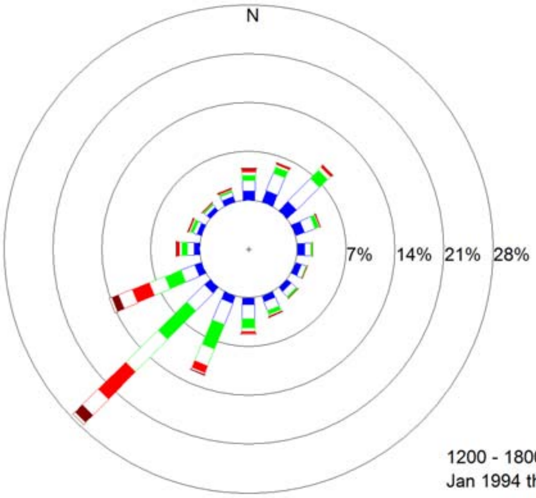

1200 - 1800 MST Wind Rose for ATR
Jan 1994 through Dec 2015   50 ft level

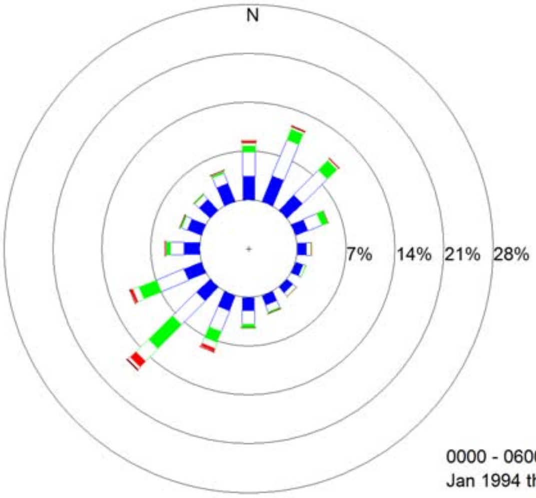

0000 - 0600 MST Wind Rose for ATR
Jan 1994 through Dec 2015   50 ft level

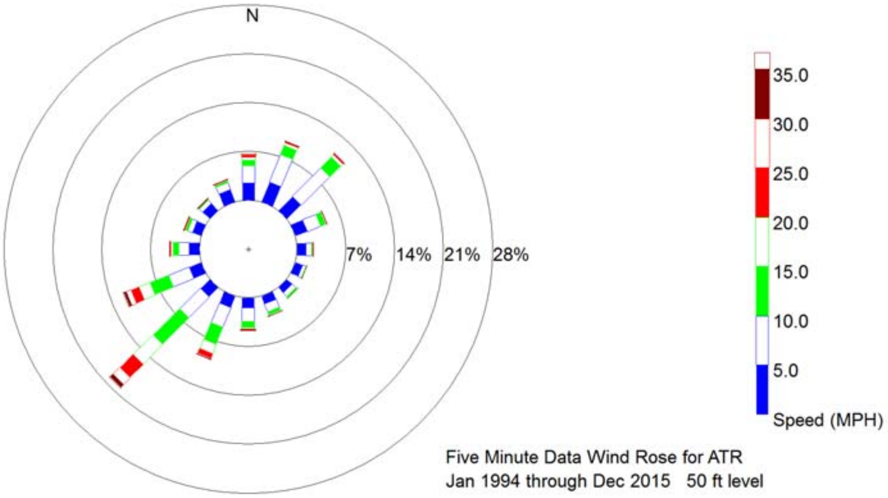

Five Minute Data Wind Rose for ATR
Jan 1994 through Dec 2015   50 ft level

Figure A-37. Day (top), night (middle), and all hours (bottom) wind roses for the 50 ft. (15 m) level at Advanced Test Reactor (ATR).

APPENDIX B: SURFACE AIR TEMPERATURE AVERAGES AND EXTREMES

The following data are the daily average and extreme surface air temperature records observed at CFA from January 1950 through December 2015. The data were obtained from maximum and minimum thermometers installed in a standard Cotton Region Shelter. These data compromise the National Climatic Data Center Coop station known as Idaho Falls 46W (IDF 46W). Table B-1 displays the daily average high and average low air temperatures. Tables B-2 through B-13 display the daily extreme surface air temperature records that include the highest and lowest maximum and the highest and lowest minimum air temperatures. As mentioned earlier in the report please be advised that the Thermoscreen temperature data prior to August 1966 could be susceptible.

Table B-1. CFA daily average high and low air temperatures.

	January		February		March		April	
	High	Low	High	Low	High	Low	High	Low
Day	°F	°F	°F	°F	°F	°F	°F	°F
1	25	0	29	6	38	15	50	25
2	25	0	28	4	37	14	51	25
3	26	1	29	4	37	14	51	23
4	25	1	30	5	38	13	54	25
5	26	3	31	6	39	15	55	26
6	25	3	32	4	40	17	54	27
7	26	2	33	8	40	17	53	26
8	27	4	34	7	42	18	54	25
9	28	6	33	8	43	19	54	27
10	29	7	32	9	43	19	55	26
11	28	6	34	8	42	19	56	26
12	28	6	34	11	43	17	57	26
13	28	7	34	11	43	18	58	27
14	29	9	33	11	43	18	57	27
15	29	9	33	12	44	19	57	28
16	29	8	34	12	45	21	59	27
17	29	7	35	13	44	22	59	29
18	28	7	34	12	45	21	57	29
19	29	5	36	13	46	21	57	29
20	30	6	36	12	46	20	57	28
21	30	5	35	12	47	22	59	29
22	27	4	36	12	48	23	60	30
23	28	4	36	13	48	23	59	31
24	28	4	37	13	48	22	58	30
25	29	7	37	13	48	22	58	30
26	29	7	36	12	48	23	58	30
27	29	6	36	12	47	24	59	29
28	28	5	37	12	48	23	60	31
29	27	4	37	13	49	23	59	31
30	28	4			50	23	60	30
31	29	5			52	24		

Table B-1. Continued.

	May		June		July		August	
Day	High °F	Low °F	High °F	Low °F	High °F	Low °F	High °F	Low °F
1	61	31	72	40	84	46	89	50
2	62	32	72	40	84	47	88	50
3	64	32	72	41	85	48	87	51
4	63	33	74	42	85	46	88	50
5	64	33	73	42	86	48	88	50
6	63	35	72	43	86	49	88	50
7	63	36	72	42	86	48	88	50
8	64	35	71	42	87	48	87	50
9	64	34	74	42	88	48	88	48
10	64	34	72	43	86	50	89	49
11	63	35	75	42	86	49	88	49
12	64	34	75	43	87	50	87	48
13	67	34	75	43	88	50	87	48
14	68	35	75	42	88	50	87	48
15	68	37	76	43	89	50	86	49
16	67	37	76	44	89	50	85	48
17	69	36	76	43	88	51	86	47
18	68	37	78	43	88	50	85	47
19	69	38	79	44	89	51	85	47
20	69	38	79	45	88	50	85	47
21	68	38	79	45	88	50	84	48
22	68	38	80	45	88	50	83	45
23	69	39	81	46	89	51	83	45
24	69	39	80	46	89	51	83	45
25	70	39	80	46	89	51	84	44
26	70	39	81	46	89	50	84	45
27	70	39	82	46	89	51	83	45
28	71	39	83	45	89	50	83	44
29	70	40	82	46	88	52	83	45
30	70	40	84	45	89	50	82	44
31	71	39			88	51	80	43

Table B-1. Continued.

	September		October		November		December	
Day	High °F	Low °F	High °F	Low °F	High °F	Low °F	High °F	Low °F
1	81	42	70	34	50	21	35	12
2	81	43	68	33	48	19	36	13
3	81	42	66	32	49	19	35	12
4	81	41	66	31	49	20	34	10
5	80	42	66	30	49	21	32	8
6	79	42	66	30	49	21	32	10
7	80	41	65	30	49	21	32	9
8	78	42	64	30	47	20	29	6
9	78	40	65	30	47	19	29	8
10	76	41	64	29	46	19	31	8
11	76	41	63	30	45	21	30	6
12	74	39	62	30	44	20	30	9
13	75	38	62	30	43	20	30	8
14	74	38	62	28	41	19	29	7
15	75	37	61	27	40	16	31	5
16	74	38	62	26	40	15	30	7
17	73	39	61	25	41	17	30	7
18	72	36	61	25	41	17	30	5
19	72	36	61	26	39	17	30	6
20	69	36	61	25	40	17	28	7
21	69	35	59	25	39	15	30	6
22	70	33	57	26	38	16	29	7
23	72	33	57	25	37	13	28	5
24	72	34	56	25	39	14	28	5
25	72	34	57	24	38	14	28	5
26	72	34	56	24	36	13	27	4
27	72	34	55	22	35	11	28	3
28	71	34	54	23	35	13	28	6
29	70	33	53	23	35	11	26	6
30	70	33	51	22	35	12	26	4
31			51	22			26	1

Table B-2. CFA daily surface air temperature extremes for January. Where an identical extreme value occurs two or more years, every year is listed.

Day	Highest Max (°F)	Year of Highest Max	Lowest Max (°F)	Year of Lowest Max	Lowest Min (°F)	Year of Lowest Min	Highest Min (°F)	Year of Highest Min
1	50	1981	0	1979	-28	1979	38	1997
2	48	1997	5	2011	-29	1974, 1978	36	1997
3	45	2012	6	1993, 2011	-23	1952	28	1998
4	46	1963	0	1972	-32	1973	28	1994
5	47	2012	0	1971	-28	1971	32	1956
6	44	1966	3	1971	-30	1979	33	1983
7	46	1956	5	1982	-33	1979	34	1983
8	46	1961	3	1989	-26	1979	32	1990
9	50	1990	6	1977	-28	1974	32	1953
10	50	1990	7	2011	-22	1977	35	1990
11	44	1981	-3	1963	-30	1977	30	1995, 2000
12	47	1953	-2	1963	-35	1963	32	1953
13	48	1981	-3	2013	-29	2013	34	1969, 1980
14	45	2012	-3	2013	-26	2013	33	1980
15	44	2000	7	2013	-23	1964	35	1974
16	51	1974	10	1960	-22	1957	36	1974
17	42	1961, 1974 1981, 1998	3	1984	-27	1960	35	1971
18	47	1981	-6	1984	-34	1984	33	1953
19	44	1997	2	1984	-32	1960	31	1953, 1972
20	48	1981	0	1984	-31	1984	34	1969
21	42	1953, 1981	6	1962	-40	1962	32	1969
22	49	1981	7	1962	-38	1962	31	1950, 1970
23	45	1970	2	1962	-37	1962	32	1970
24	48	1992	13	1957, 1962	-22	1964, 2008	31	1959
25	49	1953	9	1989	-20	1989	28	1953, 2000
26	46	1987	10	1980	-28	1957	31	1995
27	45	2003	2	2009	-28	1957	31	2003
28	44	1988	2	1951	-29	1957	32	2015
29	45	1953	5	2002	-26	1951, 1979	34	1954
30	50	2003	3	1979	-28	1957	32	2003
31	55	2003	-1	1985	-35	1985	31	1986, 2003

Table B-3. CFA daily surface air temperature extremes for February. Where an identical extreme value occurs two or more years, every year is listed.

Day	Highest Max (°F)	Year of Highest Max	Lowest Max (°F)	Year of Lowest Max	Lowest Min (°F)	Year of Lowest Min	Highest Min (°F)	Year of Highest Min
1	53	2003	-9	1985	-36	1985	33	2003
2	44	1987, 1995	3	1989	-29	1956	31	1987
3	53	1953	2	1989	-31	1996	37	1963
4	45	1954	3	1985	-34	1985	31	1963
5	57	1963	1	1982	-32	1982	30	1963
6	59	2015	5	1982	-29	1982	31	1978
7	54	1963, 2015	8	1989	-27	1989	37	2015
8	56	2015	11	1989	-24	1989	32	2015
9	51	2015	12	1982	-21	1989	35	1976
10	48	1970, 1987	8	1982	-25	1981	34	1961
11	53	1961	14	1984	-24	1982	32	1962, 2007
12	52	1987, 2015	12	2004	-17	2004	33	1954
13	53	2015	15	2004	-16	2004	34	1979
14	55	2015	13	1952	-16	1964	33	1979
15	49	1961, 2015	14	2002	-16	1989	33	1982
16	51	2007	4	1956	-24	1993	34	1991
17	48	1977, 2007, 2014	10	1993, 2006	-27	1993	33	1986
18	50	2015	15	1952	-22	1990	35	1980
19	56	1981	18	2006	-17	1955, 1990	34	1980
20	56	1991	11	1984	-21	1975	38	1992
21	53	1982	18	1952	-15	1952, 1971 1973	32	1992
22	58	1991	11	1952	-17	1952, 1975	30	1982, 1986 1992, 2000
23	49	1954, 1958 1991	18	1984	-14	2010	34	1986
24	57	1995	12	1960	-15	1952	32	1957, 1958
25	55	1995	13	1952	-20	1952	30	1957
26	56	1992	9	2002	-21	2002	33	1983
27	59	1992	11	1960, 1962 1993	-25	1960	35	1976
28	60	1992	20	1960	-22	1993	35	1972
29	57	1988	9	1960	-31	1960	27	1976, 1980

Table B-4. CFA daily surface air temperature extremes for March. Where an identical extreme value occurs two or more years, every year is listed.

Day	Highest Max (°F)	Year of Highest Max	Lowest Max (°F)	Year of Lowest Max	Lowest Min (°F)	Year of Lowest Min	Highest Min (°F)	Year of Highest Min
1	59	1986, 1992	14	1993	-28	1960	35	1974
2	61	1986	19	1993	-14	1960	37	1983
3	63	1986	11	2002	-18	2002	38	1992
4	58	1968	15	1985	-14	1985	35	1991
5	59	1986	16	1955	-15	1955	32	1990
6	58	1986	22	1952, 1955	-10	1955	39	1987
7	57	2015	21	1985	-6	1955	36	1987
8	57	2015	25	2002	-11	1964	34	1986, 1987
9	65	1972	22	1969, 2002	-13	1969	36	1954
10	62	1972, 2015	23	1969	-7	1969	41	1995
11	62	1992	24	1950	-14	1969	36	1982, 1995
12	65	1992	20	1993	-9	1962, 1969	34	2003
13	70	2003	25	1952	-10	1969	40	2007
14	68	1994	19	1952	-12	1952	35	2012
15	72	1994	26	2002	-5	1952, 1962 1985	41	2015
16	66	2007	29	2002	-3	1962	46	2015
17	70	2007	22	1965	-1	1971	42	2015
18	65	2007	21	1965	-7	1971	33	1990, 2003
19	67	1997	25	1952	-1	1971	36	2004
20	66	2015	24	1955	-13	1955	38	2007
21	67	2004	29	1985	2	1952, 1955	36	1997
22	69	1972	26	1952	-8	1952	35	1998
23	70	2004	29	1964	3	1964	38	1998
24	68	2012	23	1965	2	1964	38	1998
25	69	2012	29	1955	3	1965	38	1998
26	66	1966	28	1975	4	1955	34	1971, 1974 1989, 1998
27	71	2015	21	1975	8	1955	38	1990
28	73	1986	24	1975	2	1985	37	1968
29	70	1978, 1986	31	1977	-3	1985	38	1986
30	71	2004	32	1980	6	1985	38	2012
31	72	2012	31	1975	6	1954	40	2011

Table B-5. CFA daily surface air temperature extremes for April. Where an identical extreme value occurs two or more years, every year is listed.

Day	Highest Max (°F)	Year of Highest Max	Lowest Max (°F)	Year of Lowest Max	Lowest Min (°F)	Year of Lowest Min	Highest Min (°F)	Year of Highest Min
1	72	1966	34	1975	7	1952, 1997	38	1978, 2003, 2007
2	75	1990	36	1982	6	1953	41	2004
3	75	1992	33	1955	8	2015	37	1988, 1994
4	72	1960, 1987 1990, 2000	35	1958	13	1966	40	2006
5	75	1960	34	1997	9	1961	45	1991
6	73	1960	38	1957	9	1983	41	1995
7	75	1989	36	1953, 2011	6	2012	43	2004
8	78	1977	35	1975	7	1982	42	2004
9	79	1996	36	1999	8	1959	41	1992
10	75	2012	38	1999	9	1988	41	1992
11	73	2012	37	1970	10	1953	43	1978
12	77	1988	39	1974	6	1997	39	2000
13	74	1951, 1988	40	1970	13	1997	43	1954
14	78	1990	41	1970	13	2013, 2014	44	2002
15	79	1990	34	1967	15	1953, 1977 2005	45	1989
16	76	1987, 1994	41	1978, 2013	11	1982, 1995	45	1987
17	81	1994	40	2006	12	1963	44	1988
18	79	1994	38	1966	7	2013	43	1985
19	82	1962	35	1970	15	1982, 2011	46	1981
20	81	1994	35	1970	11	1982	44	1965
21	79	1994	34	1963	9	1982	45	2010
22	83	2012	39	1958	16	1968	48	1980
23	85	2012	37	1964	6	2013	47	2015
24	81	1977	39	1964	13	1992, 2002, 2011	45	1980
25	82	1977	35	1984	14	1950	49	1959
26	82	1987, 1992	34	1976	17	1972, 1988	45	1952
27	82	1987	41	1963	13	2008	44	1954
28	79	1987, 1992, 2007	39	1970	15	1966, 1984	45	2013
29	86	1992	36	1967	18	1994	46	1987
30	78	1977	33	1967	16	1950	49	1992

Table B-6. CFA daily surface air temperature extremes for May. Where an identical extreme value occurs two or more years, every year is listed.

Day	Highest Max (°F)	Year of Highest Max	Lowest Max (°F)	Year of Lowest Max	Lowest Min (°F)	Year of Lowest Min	Highest Min (°F)	Year of Highest Min
1	82	1985	43	1995	13	1972	45	1980
2	83	1985	42	1964	15	2011	45	1982
3	84	1966	42	1964	19	1965	48	1971
4	84	1966	36	1975	17	2001	48	1962
5	85	1992	45	1975	14	1982	49	1979
6	89	1992	35	1965	18	1968	48	2004
7	87	1992	45	1979, 2000	17	2010, 2012	52	1989
8	85	1987	42	1979	16	2002	47	1989
9	84	1954	42	1983	14	2002	49	1962
10	84	1960	45	1970, 1991	19	1953	49	1954
11	87	1960	42	1983	18	1999	49	1994
12	87	2001	45	1989	22	1992	51	1996
13	87	2013	47	1995	17	1985	54	1987
14	85	1987	48	1955	21	1970	52	1984
15	87	2013	39	1955	22	1986	49	2001
16	87	1988, 2012	43	1955	16	1974	51	1987
17	87	2006, 2007	49	1977	24	1984	49	1972
18	89	2009	48	1978	23	1971	50	2001
19	91	1954	47	1959	24	1950, 1960	60	2009
20	89	1958	46	1974	18	2003	57	1954
21	89	2012	43	1972	20	2001	54	1958
22	87	1967	48	2010	22	1953	51	2000
23	87	1988	49	1980	17	1966	50	1990
24	88	1992, 2001 2003	48	1980	25	1989	53	1979
25	89	2001	42	1980	23	1975	54	1958
26	88	1958	48	2012	20	1978	52	1992
27	88	1958	48	2006	21	1973	53	1974
28	95	2003	48	1982	23	1955, 1977	52	1990
29	96	2003	47	2011	28	1977	52	1961, 1983 2005
30	92	2003	44	1988	25	1974, 1977	59	2003
31	90	1986	52	1955, 1990	23	1978	52	2003

Table B-7. CFA daily surface air temperature extremes for June. Where an identical extreme value occurs two or more years, every year is listed.

Day	Highest Max (°F)	Year of Highest Max	Lowest Max (°F)	Year of Lowest Max	Lowest Min (°F)	Year of Lowest Min	Highest Min (°F)	Year of Highest Min
1	89	1977, 1986 2001	53	1971	27	1984	53	2002
2	89	1986	50	1950, 1953	26	1954	51	1960, 2001
3	89	1988	50	1989	27	1950	58	1986
4	92	1988	50	1980	30	1955	53	1997
5	93	1977	51	1954, 1991	26	1998	56	1957, 1985
6	93	1977	45	1995	28	1962	57	1977
7	92	1985	44	1950	22	2012	59	1977
8	92	1996	51	1995	23	1979	59	1996
9	92	2013	54	2002	24	1999	56	1977
10	92	2013	47	1984	30	1999, 2002 2005, 2011	59	2013
11	89	1979	55	2008	29	2002	56	2013
12	94	1959	51	1970	30	1984	54	1955, 1961
13	93	1974	50	1976	29	1966, 1993, 2008	60	1959
14	96	1974	56	1973	25	1976	58	1959
15	97	1974	56	1957	29	1981	59	1987
16	95	1974	55	1998	31	2011	58	1951, 1974
17	95	1974	53	1964, 1973	25	2011	56	2002
18	96	1974	51	1975	26	2010	53	1997, 2003
19	97	1988	58	1964	29	1954, 1973	60	1991
20	95	1961, 1994	60	2009	28	1978	66	1988
21	98	1988	54	1964	26	1989	62	1994
22	97	1961, 2001	62	1963, 1989	30	1956	62	1971
23	97	1988, 1992	61	1993	31	2009	69	1988
24	100	1988	51	1952	29	1997	65	2001
25	100	1988	55	1969	24	1966	63	1988
26	97	1990, 2002	59	1965	30	1999	60	1988
27	98	2015	58	1969	28	1976	63	1961
28	101	2015	62	1969	35	1975, 1976 1998	60	1988
29	101	2015	54	1959	32	1969 ,1971	63	2015
30	100	2013	65	1970	29	1955	59	2015

Table B-8. CFA daily surface air temperature extremes for July. Where an identical extreme value occurs two or more years, every year is listed.

Day	Highest Max (°F)	Year of Highest Max	Lowest Max (°F)	Year of Lowest Max	Lowest Min (°F)	Year of Lowest Min	Highest Min (°F)	Year of Highest Min
1	98	2013	63	1955	33	1984	63	2013
2	99	2013	69	1983	32	1973	59	1977, 2015
3	100	2001	67	1993	31	1997	62	2002, 2013
4	99	1985	57	1982	33	1994	59	2001, 2013
5	99	2007	65	1982	33	1999	61	1954, 2001
6	100	2007	68	1994	28	1986	65	2015
7	99	1989	68	1981	33	1988	71	1985
8	96	1975, 2005, 2014	73	2009	29	1981	60	1975, 1976 1985
9	99	1985	78	1982	33	1993	60	1960, 1989 1996
10	100	2002, 2013	61	1951	37	1999	62	2007
11	102	2002	64	1983	37	1983	65	1985
12	103	2002	60	1997	36	1951	62	2014
13	105	2002	63	1962	32	1993	63	1964, 2012
14	102	2002	73	1962	35	1993	64	2014
15	100	2005	74	1993	37	2010	66	1953
16	100	2006	65	1983	34	1983	65	1987
17	101	1998	66	1987	36	1993	71	1976
18	100	1998, 2003	63	1987	29	1993	62	1977
19	100	1960	73	1987	35	1987	66	1951
20	102	2003	57	1972	36	1952, 1996	62	2012
21	102	2003	64	1987	34	1983	65	2014
22	102	2003	64	1973, 1993	39	1952	70	2005
23	102	2003, 2007	56	1993	33	1954	66	1982
24	99	1978, 1988	67	1977	35	1970	68	2007
25	99	1978, 1988	73	1965	36	2014	66	2003
26	96	1959, 1960 1989, 1994, 2008, 2012	71	1993	40	1953, 1997 1999	61	1954
27	98	1975, 2013	70	2015	38	1993	65	1998
28	99	2006	73	2015	31	2015	67	1960
29	99	2000	71	1950	36	2015	65	1975
30	102	2007	61	1975	35	1950	65	1960
31	102	2000	71	1975	35	1995	67	2007

Table B-9. CFA daily surface air temperature extremes for August. Where an identical extreme value occurs two or more years, every year is listed.

Day	Highest Max (°F)	Year of Highest Max	Lowest Max (°F)	Year of Lowest Max	Lowest Min (°F)	Year of Lowest Min	Highest Min (°F)	Year of Highest Min
1	102	2000	74	1975	36	1995, 2001	62	1951
2	101	1992	67	1953	36	1963	65	1974
3	97	1961	66	1976	40	1970, 1981	63	2015
4	98	1961, 1979 1994	73	1951, 1996	36	1996	60	1951
5	97	1994, 2012	66	1950	35	1980	63	1964
6	99	2001	70	2014	38	1950, 1962	64	1961, 1971
7	100	1990	70	2009	35	1996	62	1979
8	101	1990	66	2009	39	1956, 1967	67	1983
9	98	1972	71	2010	35	1970, 1985 2002	60	1963, 1983 2000, 2001
10	99	1969	74	1997	38	2002	64	1954
11	99	1996	64	1985	38	1970, 1980	65	1969
12	99	1992	69	1988	37	2008	62	2015
13	99	1992	70	1978	39	1957, 1969 1982, 2000	63	2001
14	101	2003	62	1968	38	1959, 1978 1993	64	1991
15	98	2003	62	1968	32	1978	67	2003
16	96	1958, 2013	55	1978	36	1968, 1987	62	2004
17	95	1981, 1982, 2013	55	1968	32	1987	67	1958
18	98	1986	54	1968	28	1978	61	1977
19	96	1961, 1992, 2013	53	1968	31	1995	64	1999
20	95	1982, 2003	54	1968	33	1964	62	1961
21	98	2009	58	1968	33	1974	64	1951
22	96	1969	60	1968, 2014	33	1954, 1988 1996	58	2003
23	96	1991	59	1960, 2014	30	1978	64	1995
24	98	1988	58	1989	31	1992	59	1961
25	99	1988	65	1977, 2014	26	1992	61	1969, 2011
26	97	2010	64	2004	24	1992	60	2015
27	94	1981, 1986 2001, 2011	61	1956	28	1954	59	1991
28	94	1986	61	1964	31	1960	59	1958
29	95	1990	61	1964	28	1975	60	2015
30	96	1954, 2007	68	1951, 1965, 2010	30	1964, 1975	56	2000
31	95	1955	64	1999	25	2006	65	2007

Table B-10. CFA daily surface air temperature extremes for September. Where an identical extreme value occurs two or more years, every year is listed.

Day	Highest Max (°F)	Year of Highest Max	Lowest Max (°F)	Year of Lowest Max	Lowest Min (°F)	Year of Lowest Min	Highest Min (°F)	Year of Highest Min
1	96	1950	50	1973	29	1965	54	1991
2	95	1950, 2007	60	2000	29	1975	60	2013
3	96	1950	52	1971	27	1964, 1975	58	1978
4	96	1950	67	1971	27	1964	58	1982, 1990
5	94	1976	48	1970	30	1964, 2008	58	1978, 2013
6	96	1955	59	2001	24	1996	63	1976
7	93	1955, 1977 1979	62	2002	26	1996, 2000	60	1963
8	90	1979, 1990 1994, 2005	59	1962	26	2009	58	1950
9	90	1988, 1990	54	2010	22	1962	56	1998
10	90	1959	52	1972, 1978	24	1970	59	1950
11	94	1990	52	1978	29	1957, 1964, 2007, 2010	57	1976
12	92	1953	52	1978	25	2014	58	2013
13	90	1953	54	1970	24	2012	55	1953, 1959
14	93	1990	50	1982	21	1970	55	2013
15	93	2000	52	1982	21	1970	53	2013
16	89	1995, 2000	38	1965	20	1970	57	1953
17	90	1981	41	1965	24	1965	58	2000
18	89	1956, 1981	43	1978	14	1965	53	2014
19	89	1956	48	1986	16	1965	54	1973
20	84	1966, 1991	46	1983	14	1983	50	1963
21	87	1987	44	1968	16	1983	50	1952
22	90	1987	47	2000	17	1993, 1995	50	1976
23	92	1987	49	1961	21	1996	47	1966
24	91	1987	48	1984	15	2000	51	2012
25	90	2015	48	1955	12	1970	51	2012
26	88	2010	50	2013	18	1970	56	1997
27	88	2010	47	1959	19	1964	53	2014
28	89	2010	48	1965, 1985	18	1999	54	1991
29	86	1992	43	1971	15	1999	54	1994
30	88	1992	38	1971	15	1985	51	1994

Table B-11. CFA daily surface air temperature extremes for October. Where an identical extreme value occurs two or more years, every year is listed.

Day	Highest Max (°F)	Year of Highest Max	Lowest Max (°F)	Year of Lowest Max	Lowest Min (°F)	Year of Lowest Min	Highest Min (°F)	Year of Highest Min
1	89	2010	38	1971	15	1950	54	2015
2	89	2010	47	1989	19	1950	55	1976
3	85	2010	42	1994	16	1973	55	1974
4	82	1980, 1988 1993	46	1957, 2009	15	2012	49	2010
5	82	1988	39	2009	15	2012	47	1963, 2010
6	81	1979	40	2011	11	1955	50	1993
7	80	1979, 1980 1987	41	1961	14	2012	47	1960
8	81	1979, 1988	31	1985	15	2012	47	2015
9	81	1996	44	1985	12	1968	49	1983
10	84	1991	40	2008	13	2001	45	1962
11	83	1991	35	2008	12	1977	47	1989
12	81	1991	36	1969, 2008	11	2002	51	1962
13	79	1958	35	1969	10	2002	53	1962
14	81	1958	44	1981, 1983	7	1969	44	1957
15	79	1958, 1991	43	1994	7	1970	46	1979
16	77	1973	36	1969	9	1970, 1984	49	1988
17	77	1973	34	1984	4	1996	40	1950, 1988
18	78	2003	39	1984	12	1964	52	2015
19	75	1974, 2003	40	1984	8	1982	48	1955
20	79	2003	40	1984, 1996	7	1982	44	2012
21	78	2003	42	1951, 1953	6	1996	46	1975
22	80	2003	34	1975	9	1958, 2008	43	1991
23	72	1952, 1965	36	1975	9	1980, 1995	44	1983
24	75	1992	32	1975	8	1980	42	1989
25	73	1990, 1992, 2014	35	1975	10	1997, 2002 2003	41	1963
26	70	1999	37	2012	10	2002	41	1995
27	71	1990	38	1970	9	1954	47	1994
28	70	1952, 1987 1990, 2008	28	1971	5	1991	46	2001
29	70	1968	30	1991	8	1971	43	1950
30	71	1962	26	2002	1	1991	42	1950
31	68	1988	26	2002	-6	2002	41	1987

Table B-12. CFA daily surface air temperature extremes for November. Where an identical extreme value occurs two or more years, every year is listed.

Day	Highest Max (°F)	Year of Highest Max	Lowest Max (°F)	Year of Lowest Max	Lowest Min (°F)	Year of Lowest Min	Highest Min (°F)	Year of Highest Min
1	67	1965, 2014	27	1991	-5	2002	44	1987
2	66	1978	23	2002	-3	1955	45	1987
3	65	1962, 1965 1976, 1981	23	1991	-4	1973, 2002	41	1987
4	64	2010	28	1991	1	2002	41	1999
5	67	1980	33	2003	-10	2003	44	1983
6	66	1999, 2010	35	1971, 1992, 2011	-5	2003	42	2006
7	67	2006	31	1990	-6	2003	47	2006
8	65	1976	29	2000	6	1955, 1977 1993	36	1973
9	65	1958, 1973	25	1950	0	1977	36	1970, 1982 1991
10	63	1954	20	1950	-6	1950	34	2008
11	63	1953, 1999	23	2014	-3	2000	38	1983
12	66	1999	21	2014	0	2014	39	1954
13	63	1999	17	2014	-6	1955	38	1981, 2008
14	62	1963, 1999	24	1978	-2	1959	37	1981
15	60	1999	9	1955	-19	1955	39	1953
16	60	1953	7	1955	-24	1955	35	1975
17	57	1976	20	1958	-12	2014	38	1983
18	62	2008	19	2000	-10	2014	38	2007
19	57	2007	18	1985	-5	1953, 1977	42	1996
20	59	1966	18	1977	-6	2000	39	1955
21	58	1954	16	1985	-12	1977	33	1962, 2001
22	54	1976, 1995	17	1985	-20	1985	33	1974
23	60	1959	4	1985	-21	1985	35	1961
24	58	1995	7	2010	-19	1993	34	1960
25	56	1990	6	2010	-24	1993	41	1995
26	55	1998	14	1993	-23	1993	37	1999
27	57	2014	20	1952	-21	1993	31	1951
28	55	2014	15	1952	-13	1952	40	2014
29	51	1995	16	1975	-19	1979	37	1995
30	59	1999	16	1985	-23	1975	41	1995

Table B-13. CFA daily surface air temperature extremes for December. Where an identical extreme value occurs two or more years, every year is listed.

Day	Highest Max (°F)	Year of Highest Max	Lowest Max (°F)	Year of Lowest Max	Lowest Min (°F)	Year of Lowest Min	Highest Min (°F)	Year of Highest Min
1	57	1995	15	1985	-13	1967	37	1995
2	48	2013	19	1984	-11	1984	35	1987
3	55	1958	18	1984	-16	1984, 1992	35	1980
4	54	2007	6	1992	-28	1992	33	1980
5	51	1987	0	1972	-37	1972	32	2012
6	52	1987	8	2013	-21	2005	32	1975
7	47	1965, 1991	6	2005	-30	2005	35	1975
8	49	2015	1	1972	-29	2005	31	2015
9	53	2015	0	1972	-35	1972	30	1975
10	52	1990	-6	1972	-40	1972	33	1996
11	48	2014	3	1972	-34	1972	34	1995
12	46	1995	5	1972	-19	1963, 1985	35	1995
13	45	1956	6	1972	-26	1972	32	2006
14	47	2002	8	2008	-21	1972	36	1977
15	45	1977, 2006	9	1972	-29	1972	38	1977
16	48	1962	12	1967, 1992	-20	1964	32	1957
17	47	1962	0	1964	-33	1964	32	1957
18	43	1962, 1979	12	1964, 1983 1992	-26	1964	29	1950
19	43	1979	6	1998	-21	1984	30	1952
20	44	1958	-2	1990	-27	1998	30	1952, 1957 1964, 1969
21	45	1974	-4	1990	-38	1983	33	1955, 1964
22	51	1964	-9	1990	-38	1990	37	1964
23	50	1955	-8	1983	-47	1983	34	1964
24	45	1964	-1	1990	-38	1983	33	1964
25	43	1980	1	1990	-24	1990	30	1980
26	49	1976	-1	2015	-23	2015	31	1980
27	53	1980	2	2015	-28	1988	32	1996
28	42	2004	7	1983	-20	1983	33	2005
29	42	1965, 2008	5	1988, 1990	-27	1990	33	1996
30	49	2011	-4	1990	-29	1978	31	1996
31	48	2011	3	1978	-37	1978	35	1996

APPENDIX C: PRECIPITATION AVERAGES AND EXTREMES

The following are daily precipitation statistics observed next to the CFA thermoscreen station. These data compromise the National Climatic Data Center Coop station known as Idaho Falls 46W (IDF 46W). The averages (C-1) have been smoothed over the 66-year period from 1950 through 2015. Table C-2 to C-13 show the daily extreme precipitation records observed at CFA from 1950 through 2015 by month. The extreme records tables include the greatest daily accumulation of precipitation, greatest daily snowfall, and greatest daily snow depth with their corresponding year(s).

Table C-1. CFA daily precipitation averages.

Day	January (in.)	February (in.)	March (in.)	April (in.)	May (in.)	June (in.)
1	0.02	0.02	0.02	0.02	0.03	0.04
2	0.02	0.02	0.02	0.02	0.03	0.04
3	0.02	0.02	0.02	0.02	0.03	0.04
4	0.02	0.02	0.02	0.02	0.03	0.04
5	0.02	0.02	0.02	0.02	0.03	0.04
6	0.02	0.02	0.02	0.02	0.03	0.04
7	0.02	0.02	0.02	0.02	0.03	0.04
8	0.02	0.02	0.02	0.02	0.03	0.04
9	0.02	0.02	0.02	0.02	0.03	0.04
10	0.02	0.02	0.02	0.02	0.04	0.04
11	0.02	0.02	0.02	0.02	0.04	0.04
12	0.02	0.02	0.02	0.02	0.04	0.04
13	0.02	0.02	0.02	0.02	0.04	0.04
14	0.02	0.02	0.02	0.02	0.04	0.04
15	0.02	0.02	0.02	0.02	0.04	0.04
16	0.02	0.02	0.02	0.02	0.04	0.04
17	0.02	0.02	0.02	0.02	0.04	0.04
18	0.02	0.02	0.02	0.03	0.04	0.04
19	0.02	0.02	0.02	0.03	0.04	0.04
20	0.02	0.02	0.02	0.03	0.04	0.04
21	0.02	0.02	0.02	0.03	0.04	0.04
22	0.02	0.02	0.02	0.03	0.04	0.04
23	0.02	0.02	0.02	0.03	0.04	0.04
24	0.02	0.02	0.02	0.03	0.04	0.03
25	0.02	0.02	0.02	0.03	0.04	0.03
26	0.02	0.02	0.02	0.03	0.04	0.03
27	0.02	0.02	0.02	0.03	0.04	0.03
28	0.02	0.02	0.02	0.03	0.04	0.03
29	0.02	0.02	0.02	0.03	0.04	0.03
30	0.02		0.02	0.03	0.04	0.03
31	0.02		0.02		0.04	

Table C-1. Continued.

Day	July (in.)	August (in.)	September (in.)	October (in.)	November (in.)	December (in.)
1	0.03	0.01	0.02	0.02	0.02	0.02
2	0.03	0.01	0.02	0.02	0.02	0.02
3	0.03	0.01	0.02	0.02	0.02	0.02
4	0.02	0.01	0.02	0.02	0.02	0.02
5	0.02	0.01	0.02	0.02	0.02	0.02
6	0.02	0.01	0.02	0.02	0.02	0.02
7	0.02	0.01	0.02	0.02	0.02	0.02
8	0.02	0.01	0.02	0.02	0.02	0.02
9	0.02	0.01	0.02	0.02	0.02	0.02
10	0.02	0.02	0.02	0.02	0.02	0.02
11	0.02	0.02	0.02	0.02	0.02	0.02
12	0.02	0.02	0.02	0.02	0.02	0.02
13	0.02	0.02	0.02	0.02	0.02	0.02
14	0.02	0.02	0.02	0.02	0.02	0.02
15	0.02	0.02	0.02	0.02	0.02	0.02
16	0.01	0.02	0.02	0.02	0.02	0.02
17	0.01	0.02	0.02	0.02	0.02	0.02
18	0.01	0.02	0.02	0.02	0.02	0.02
19	0.01	0.02	0.02	0.02	0.02	0.02
20	0.01	0.02	0.02	0.02	0.02	0.02
21	0.01	0.02	0.02	0.02	0.02	0.02
22	0.01	0.02	0.02	0.02	0.02	0.02
23	0.01	0.02	0.02	0.02	0.02	0.02
24	0.01	0.02	0.02	0.02	0.02	0.02
25	0.01	0.02	0.02	0.02	0.02	0.02
26	0.01	0.02	0.02	0.02	0.02	0.02
27	0.01	0.02	0.02	0.02	0.02	0.02
28	0.01	0.02	0.02	0.02	0.02	0.02
29	0.01	0.02	0.02	0.02	0.02	0.02
30	0.01	0.02	0.02	0.02	0.02	0.02
31	0.01	0.02		0.02		0.02

Table C-2. CFA daily precipitation extremes for January.

Day	Greatest Daily Precipitation (in.)	Year of Greatest Daily Precipitation	Greatest Daily Snowfall (in.)	Year of Greatest Daily Snowfall	Greatest Daily Snow Depth (in.)	Year of Greatest Daily Snow Depth
1	0.43	1997	3.5	1955	18	1993
2	0.96	2006	9.0	2006	18	1993
3	0.23	2002	3.0	2002	18	1993
4	0.27	1977	5.0	1977	18	1993
5	0.25	1976	3.0	1976	17	1993
6	0.44	1965	1.5	1959	17	1993
7	0.47	1965	5.0	2005	17	1993
8	0.52	1975	3.0	1975	18	1993
9	0.12	1970, 1985	1.4	1970	18	1993
10	0.24	2013	5.0	1978	18	1993
11	0.25	1979	4.0	1971	20	1993
12	0.22	1960	3.3	1960	20	1993
13	0.45	1980	3.1	1957	20	1993
14	0.58	1990	4.0	1990	21	1993
15	0.35	1990	2.0	1952, 1988, 1990	20	1993
16	0.51	1978	5.0	1978	20	1993
17	0.24	1998	4.0	1998	20	1993
18	0.37	1974	3.0	2000	20	1993
19	0.79	1969	4.4	1969	20	1993
20	0.61	1957	8.5	1957	22	1993
21	0.65	1985	5.0	1985	23	1993
22	0.36	2010	5.0	2010	25	1993
23	0.40	1954	5.0	1972	24	1993
24	0.25	1965	2.6	1967	24	1993
25	0.15	2009	4.0	2009	23	1993
26	0.32	1969	3.5	1956	23	1993
27	0.68	2008	6.0	2008	23	1993
28	0.52	1987	2.0	1981	22	1993
29	0.21	1981	2.5	1981	22	1993
30	0.25	1981	3.0	1981	22	1993
31	0.72	1963	2.6	1967	22	1993

Table C-3. CFA daily precipitation extremes for February.

Day	Greatest Daily Precipitation (in.)	Year of Greatest Daily Precipitation	Greatest Daily Snowfall (in.)	Year of Greatest Daily Snowfall	Greatest Daily Snow Depth (in.)	Year of Greatest Daily Snow Depth
1	0.43	1963	2.5	1952	21	1993
2	0.44	1961	5.0	1961	20	1993
3	0.26	2008	5.0	2008	20	1993, 2008
4	0.17	1974	1.0	1976	19	2008
5	0.13	1978	3.5	1975	19	2008
6	0.28	1998	3.0	1966, 1998	19	2008
7	0.29	1999	2.0	2004	18	1993
8	0.77	1960	7.5	1960	19	1993
9	0.58	1962	4.0	1978, 1993	23	1993
10	0.58	1962	5.0	1984	25	1993
11	0.54	1962	5.6	1973	25	1993
12	0.20	1978	2.1	1969	25	1993
13	0.54	1954	6.4	1973	25	1993
14	0.46	1998	5.0	1998	25	1993
15	0.61	1986	3.2	1962	27	1993
16	0.39	1986	4.0	1952	27	1993
17	0.25	1994	2.1	1955	27	1993
18	0.79	1986	2.0	1961, 1989, 1999	27	1993
19	0.64	1993	7.2	1971	28	1993
20	0.36	1981	3.2	1956	28	1993
21	0.30	1999	4.0	1999	28	1993
22	0.16	1977	1.0	1974, 1977, 1980, 1984	28	1993
23	0.55	2001	5.0	2001	30	1993
24	0.47	1969	5.1	1969	30	1993
25	0.30	1958	3.0	1966	30	1993
26	0.21	1957	0.7	1964	30	1993
27	0.15	1965, 2007	2.0	1979	30	1993
28	0.23	2006	2.5	1983	30	1993
29	0.40	1976	3.0	2012	19	1952

Table C-4. CFA daily precipitation extremes for March.

Day	Greatest Daily Precipitation (in.)	Year of Greatest Daily Precipitation	Greatest Daily Snowfall (in.)	Year of Greatest Daily Snowfall	Greatest Daily Snow Depth (in.)	Year of Greatest Daily Snow Depth
1	0.42	1964	4.9	1964	30	1993
2	0.27	1974	3.0	1979	30	1993
3	0.26	1985	3.0	1985	30	1993
4	0.89	1991	2.0	1956	30	1993
5	0.29	1996	2.3	1960	30	1993
6	0.59	2002	3.0	2002	29	1993
7	0.25	1960	1.8	1960	29	1993
8	0.17	1989	0.5	1951	28	1993
9	0.35	1986	2.0	2000	27	1993
10	0.19	1995	2.0	1952	26	1993
11	0.55	1995	2.7	1954	26	1993
12	0.33	1967	3.3	1967	26	1993
13	0.39	2002	4.0	2002	25	1993
14	0.43	1983	3.0	2006	25	1993
15	0.18	1958, 2011	3.6	1958	23	1993
16	0.22	2012	1.9	1971	22	1952, 1985, 1993
17	0.25	1950	3.0	1982	21	1952, 1985
18	0.25	2006	1.0	1977, 1982	21	1952
19	0.19	2000	1.5	1989	21	1952
20	0.26	1995	0.9	1964	21	1952
21	0.39	1958	1.0	1980, 1981	20	1952
22	0.62	2009	8.6	1973	20	1952
23	0.44	2005	3.0	2005	19	1952
24	0.16	1995	0.7	1954	18	1952
25	0.30	1993	3.0	1975	16	1952
26	0.45	1975	0.7	2008	14	1952
27	0.35	1981, 1985	5.0	1985	17	1985
28	0.47	1996	2.0	1996	17	1985
29	0.45	1982	2.0	1970	16	1985
30	0.39	1914	1.2	1959	15	1985
31	0.40	2006	2.0	1997	14	1985

Table C-5. CFA daily precipitation extremes for April.

Day	Greatest Daily Precipitation (in.)	Year of Greatest Daily Precipitation	Greatest Daily Snowfall (in.)	Year of Greatest Daily Snowfall	Greatest Daily Snow Depth (in.)	Year of Greatest Daily Snow Depth
1	0.18	1978	0.7	1967	12	1985
2	0.75	1996	3.0	1955	8	1985
3	0.43	1958	1.5	2009	5	1985
4	0.23	1993	1.0	1980	3	1952
5	0.53	2006	1.0	2010	1	1952, 1958 2010
6	0.48	1957	3.4	1957	2	1957
7	0.39	1965	2.4	1965	1	1957, 1965, 2011
8	0.54	1990	2.0	1999	1	1999
9	0.31	1984	1.0	1984	1	1984
10	0.24	1966	0.4	1955	0	ALL
11	0.17	2001	1.0	1975	1	1975
12	0.20	1993	2.0	1993	2	1975
13	0.24	1973	0.5	1975	2	1975
14	0.14	2003	0.2	1955, 1970 1973, 1995	0	ALL
15	0.36	2002	2.0	2002, 2008	2	2008
16	0.81	2006	0.3	1959, 1975	1	1970, 1971
17	0.16	2006	0.4	1968	0	ALL
18	0.48	2000	1.0	1996	0	ALL
19	0.54	1970	6.5	1970	1	1957, 1963
20	1.51	1981	1.0	1963	6	1970, 1971
21	0.44	2010	3.0	1958	3	1970, 1971
22	1.10	2010	3.4	1958	1	1958
23	0.54	1997	3.9	1964	5	1964
24	0.52	1994	2.2	1961	2	1960, 1961
25	0.67	1975	3.0	1984	3	1984
26	0.57	1963	1.5	1976	2	1976
27	0.88	1963	4.7	1963	6	1976
28	0.53	2009	6.7	1970	6	1970, 1971
29	0.24	1983	2.0	1967	2	1970, 1971
30	0.21	1999	2.0	ALL	2	2008

Table C-6. CFA daily precipitation extremes for May.

Day	Greatest Daily Precipitation (in.)	Year of Greatest Daily Precipitation	Greatest Daily Snowfall (in.)	Year of Greatest Daily Snowfall	Greatest Daily Snow Depth (in.)	Year of Greatest Daily Snow Depth
1	0.82	1959	0.0	ALL	0	ALL
2	0.30	1960	0.0	ALL	0	ALL
3	0.49	1993	0.0	ALL	0	ALL
4	0.37	1993	0.0	ALL	0	ALL
5	0.57	1995	2.0	1978	2	1978
6	0.40	1965, 1995	3.9	1965	0	ALL
7	0.68	2000	4.4	1965	5	1965
8	0.47	1991	1.0	1979	0	ALL
9	0.61	1979	2.0	1979	2	1979
10	0.70	1998	0.0	ALL	0	ALL
11	0.60	1966	1.7	1966	0	ALL
12	0.76	1957	0.7	1970	0	ALL
13	0.70	1957	0.2	1951, 1970	0	ALL
14	0.40	1962	0.2	1955	0	ALL
15	0.58	1961	1.8	1955	1	1955
16	0.95	1987	2.7	1955	0	ALL
17	0.46	1987	0.0	ALL	0	ALL
18	0.59	1957	1.1	1960	0	ALL
19	0.33	1957	1.2	1959	0	ALL
20	0.30	1970	0.0	ALL	0	ALL
21	0.48	1972	0.0	ALL	0	ALL
22	0.21	1991	0.0	ALL	0	ALL
23	0.56	1959	0.0	ALL	0	ALL
24	0.70	1953	0.0	ALL	0	ALL
25	0.30	1956	0.0	ALL	0	ALL
26	0.42	2012	0.0	ALL	0	ALL
27	0.53	2010	0.0	ALL	0	ALL
28	0.65	1964	0.0	ALL	0	ALL
29	0.85	1971	4.0	1979	4	1979
30	0.47	1999	0.0	ALL	0	ALL
31	0.21	1990	0.0	ALL	0	ALL

Table C-7. CFA daily precipitation extremes for June.

Day	Greatest Daily Precipitation (in.)	Year of Greatest Daily Precipitation	Greatest Daily Snowfall (in.)	Year of Greatest Daily Snowfall	Greatest Daily Snow Depth (in.)	Year of Greatest Daily Snow Depth
1	0.51	2005	0	ALL	0	ALL
2	0.56	1964	0	ALL	0	ALL
3	0.33	1993	0	ALL	0	ALL
4	0.61	1991	0	ALL	0	ALL
5	1.55	1995	0	ALL	0	ALL
6	0.78	1993, 2007	0	ALL	0	ALL
7	0.66	1968	0	ALL	0	ALL
8	0.55	1984	0	ALL	0	ALL
9	0.84	2006	0	ALL	0	ALL
10	1.64	1969	0	ALL	0	ALL
11	0.16	1968	0	ALL	0	ALL
12	0.21	1955	0	ALL	0	ALL
13	0.84	1967	0	ALL	0	ALL
14	0.43	1992	0	ALL	0	ALL
15	0.50	1962	0	ALL	0	ALL
16	0.39	1976	0	ALL	0	ALL
17	0.49	1997	0	ALL	0	ALL
18	0.56	1995	0	ALL	0	ALL
19	0.34	1995	0	ALL	0	ALL
20	0.31	1977	0	ALL	0	ALL
21	0.28	1995	0	ALL	0	ALL
22	0.38	2002	0	ALL	0	ALL
23	0.47	1972	0	ALL	0	ALL
24	0.49	1989	0	ALL	0	ALL
25	0.79	1965	0	ALL	0	ALL
26	0.65	1965	0	ALL	0	ALL
27	0.55	1959	0	ALL	0	ALL
28	0.42	2006	0	ALL	0	ALL
29	0.47	1962	0	ALL	0	ALL
30	0.11	2008	0	ALL	0	ALL

Table C-8. CFA daily precipitation extremes for July.

Day	Greatest Daily Precipitation (in.)	Year of Greatest Daily Precipitation	Greatest Daily Snowfall (in.)	Year of Greatest Daily Snowfall	Greatest Daily Snow Depth (in.)	Year of Greatest Daily Snow Depth
1	0.79	1987	0	ALL	0	ALL
2	0.10	2004	0	ALL	0	ALL
3	0.46	1980	0	ALL	0	ALL
4	0.12	1961	0	ALL	0	ALL
5	0.10	1950, 2001	0	ALL	0	ALL
6	0.21	2015	0	ALL	0	ALL
7	0.44	2012	0	ALL	0	ALL
8	0.05	1975	0	ALL	0	ALL
9	0.51	1990	0	ALL	0	ALL
10	0.71	1983	0	ALL	0	ALL
11	0.40	1970	0	ALL	0	ALL
12	0.53	1997	0	ALL	0	ALL
13	0.53	1962	0	ALL	0	ALL
14	0.55	2012	0	ALL	0	ALL
15	0.38	1985	0	ALL	0	ALL
16	0.29	1996	0	ALL	0	ALL
17	0.40	1987	0	ALL	0	ALL
18	0.21	2004	0	ALL	0	ALL
19	0.42	1973	0	ALL	0	ALL
20	0.35	1973	0	ALL	0	ALL
21	0.83	1987	0	ALL	0	ALL
22	0.73	1973	0	ALL	0	ALL
23	1.25	1979	0	ALL	0	ALL
24	0.35	1977	0	ALL	0	ALL
25	0.40	1991	0	ALL	0	ALL
26	0.18	1951	0	ALL	0	ALL
27	0.78	1984	0	ALL	0	ALL
28	0.23	1997	0	ALL	0	ALL
29	0.70	1984	0	ALL	0	ALL
30	0.43	2010	0	ALL	0	ALL
31	0.56	1985	0	ALL	0	ALL

Table C-9. CFA daily precipitation extremes for August.

Day	Greatest Daily Precipitation (in.)	Year of Greatest Daily Precipitation	Greatest Daily Snowfall (in.)	Year of Greatest Daily Snowfall	Greatest Daily Snow Depth (in.)	Year of Greatest Daily Snow Depth
1	0.45	1952	0	ALL	0	ALL
2	0.23	2004	0	ALL	0	ALL
3	0.43	1951	0	ALL	0	ALL
4	0.70	2014	0	ALL	0	ALL
5	0.38	2014	0	ALL	0	ALL
6	0.54	1951	0	ALL	0	ALL
7	0.45	2014	0	ALL	0	ALL
8	0.41	1961	0	ALL	0	ALL
9	0.56	1982	0	ALL	0	ALL
10	0.31	1997	0	ALL	0	ALL
11	0.72	1950	0	ALL	0	ALL
12	0.23	1989	0	ALL	0	ALL
13	0.59	1968	0	ALL	0	ALL
14	0.42	2014	0	ALL	0	ALL
15	0.13	1979	0	ALL	0	ALL
16	0.31	1960	0	ALL	0	ALL
17	0.31	2004	0	ALL	0	ALL
18	0.55	1990	0	ALL	0	ALL
19	0.70	1959	0	ALL	0	ALL
20	0.74	1959	0	ALL	0	ALL
21	0.50	2014	0	ALL	0	ALL
22	0.80	1960	0	ALL	0	ALL
23	0.65	1976	0	ALL	0	ALL
24	0.18	1987	0	ALL	0	ALL
25	0.07	1977	0	ALL	0	ALL
26	0.23	2012	0	ALL	0	ALL
27	0.58	1991	0	ALL	0	ALL
28	0.08	1964	0	ALL	0	ALL
29	0.37	1971	0	ALL	0	ALL
30	0.23	1986	0	ALL	0	ALL
31	0.40	1963	0	ALL	0	ALL

Table C-10. CFA daily precipitation extremes for September.

Day	Greatest Daily Precipitation (in.)	Year of Greatest Daily Precipitation	Greatest Daily Snowfall (in.)	Year of Greatest Daily Snowfall	Greatest Daily Snow Depth (in.)	Year of Greatest Daily Snow Depth
1	0.36	1973	0.0	ALL	0	ALL
2	0.14	1985	0.0	ALL	0	ALL
3	0.56	1971	0.0	ALL	0	ALL
4	0.14	2007	0.0	ALL	0	ALL
5	0.12	1970	0.0	ALL	0	ALL
6	0.45	1978	0.0	ALL	0	ALL
7	0.73	1971	0.0	ALL	0	ALL
8	0.66	1980	0.0	ALL	0	ALL
9	1.09	1961	0.0	ALL	0	ALL
10	0.27	1985	0.0	ALL	0	ALL
11	0.20	1997	0.0	ALL	0	ALL
12	0.82	1976	0.0	ALL	0	ALL
13	0.44	1982	0.9	1970	0	ALL
14	0.34	1986	0.0	ALL	0	ALL
15	0.31	1959	0.0	ALL	0	ALL
16	0.39	1996	0.0	ALL	0	ALL
17	0.45	1961	0.5	1965	0	ALL
18	1.55	1961	0.0	ALL	0	ALL
19	0.27	1963	0.0	ALL	0	ALL
20	0.70	1962	0.0	ALL	0	ALL
21	0.62	2006	1.0	1961	0	ALL
22	0.08	1968	0.0	ALL	0	ALL
23	0.29	1973	0.0	ALL	0	ALL
24	0.15	2012	0.0	ALL	0	ALL
25	0.31	2012	0.0	ALL	0	ALL
26	0.20	1982	0.0	ALL	0	ALL
27	0.93	1989	0.0	ALL	0	ALL
28	0.60	2014	0.0	ALL	0	ALL
29	0.34	2007	0.0	ALL	0	ALL
30	1.10	1994	0.2	1959, 1971	0	ALL

Table C-11. CFA daily precipitation extremes for October.

Day	Greatest Daily Precipitation (in.)	Year of Greatest Daily Precipitation	Greatest Daily Snowfall (in.)	Year of Greatest Daily Snowfall	Greatest Daily Snow Depth (in.)	Year of Greatest Daily Snow Depth
1	0.60	1971	4.5	1971	0	ALL
2	0.51	1976	1.5	1969	0	ALL
3	0.32	1957	0.2	1969	0	ALL
4	1.04	2009	0.0	ALL	0	ALL
5	0.65	2007	2.5	2009	0	ALL
6	1.15	2011	0.0	ALL	0	ALL
7	0.41	2006	3.0	1961	0	ALL
8	0.58	1973	0.0	ALL	0	ALL
9	0.39	1983	0.0	ALL	0	ALL
10	0.30	1972	0.2	1985	0	ALL
11	0.20	2000	0.4	2008	0	ALL
12	0.38	1981	0.0	ALL	0	ALL
13	0.14	2009	0.0	ALL	0	ALL
14	0.36	1993	0.8	1981	1	1981
15	0.35	1953	0.0	ALL	0	ALL
16	0.42	1980, 2012	0.2	1969	0	ALL
17	0.17	1984	0.0	ALL	0	ALL
18	0.17	1986	1.0	1984	1	1984
19	0.77	2004	0.0	ALL	0	ALL
20	0.15	2004	0.0	ALL	0	ALL
21	0.52	1975	1.5	1975	2	1975
22	0.37	2012	0.0	ALL	1	1975
23	0.35	1997	2.8	1970	1	1975, 1997
24	0.31	2010	0.5	1997	0	ALL
25	0.37	1996	2.0	1996	2	1996
26	0.22	1991	0.1	1970	0	ALL
27	0.74	1956	2.0	1991	2	1991
28	0.20	2013	0.4	1991	2	1991
29	0.09	1992, 2015	0.5	2013	2	1991
30	0.65	1964	2.0	1971	1	1991
31	0.11	1982	0.6	1956	2	1971

Table C-12. CFA daily precipitation extremes for November.

Day	Greatest Daily Precipitation (in.)	Year of Greatest Daily Precipitation	Greatest Daily Snowfall (in.)	Year of Greatest Daily Snowfall	Greatest Daily Snow Depth (in.)	Year of Greatest Daily Snow Depth
1	0.23	1987	0.2	1991	1	1956, 1971, 1991
2	0.59	2015	0.2	1994	1	1956, 1971, 1991
3	0.60	1968	0.7	1961	1	1991
4	0.27	2008	1.8	1956	1	1956, 1991
5	0.19	1973	1.0	1998	1	1956
6	0.43	1969	0.0	ALL	0	ALL
7	0.57	1969	3.0	1998	3	1998
8	0.53	2010	1.5	1986	2	1998
9	0.31	1994	3.0	1994	3	1994
10	0.20	1958	2.0	1975	2	1975, 1998
11	0.38	1985	3.0	1985	3	1985
12	0.48	1973	3.1	1964	3	1985
13	0.34	1988	3.5	1988	3	1978, 1985
14	0.34	1971	1.5	1957, 1971	5	1988
15	0.48	1954	1.1	1971	4	1988
16	0.31	1972	2.0	1972	4	1988
17	0.51	1964	5.1	1964	6	1964
18	0.44	1996	2.0	1996	7	1988
19	0.29	1982	2.5	1979	7	1988
20	0.21	1950, 2010	2.6	2010	6	1964, 1985, 1988
21	0.22	1998	2.5	2010	6	1964, 1985, 1988
22	0.70	1977	6.0	1977	6	1964, 1977, 1985
23	0.36	1988	5.0	1963	6	1985
24	0.58	1981	6.5	1981	6	1981, 1985
25	0.50	1984	4.0	1983	8	1985
26	0.33	1964	3.0	1964, 1989, 1997	8	1985
27	0.12	1991	1.0	1951	8	1985
28	0.28	1984	4.0	1975, 1984	8	1985
29	0.71	1970	2.0	1970	8	1985
30	0.27	1970	2.5	1970	9	1985

Table C-13. CFA daily precipitation extremes for December.

Day	Greatest Daily Precipitation (in.)	Year of Greatest Daily Precipitation	Greatest Daily Snowfall (in.)	Year of Greatest Daily Snowfall	Greatest Daily Snow Depth (in.)	Year of Greatest Daily Snow Depth
1	0.52	2005	6.5	1982	9	1985
2	0.38	2012	4.0	2001	10	1985
3	0.41	1980	5.0	1972	13	1985
4	0.44	1974	7.0	1983	12	1983
5	0.34	1966	3.4	1966	14	1983
6	0.32	2010	4.0	2010	14	1983
7	0.30	1950	3.6	1950	14	1983
8	0.27	1985	3.0	1963, 1997	13	1985
9	0.33	1970	3.0	1970	12	1985
10	0.26	1964	2.6	1964	12	1985
11	0.16	1996	2.0	1996	12	1985
12	0.60	1995	3.0	1971, 1983	13	1983
13	0.50	2015	5.0	2015	13	1983
14	0.30	1977	2.0	2001	13	1983
15	0.14	1977	2.0	2008	13	1983
16	0.16	1984	2.0	1984	13	1983
17	0.23	1973	2.1	1973	13	1983
18	0.39	1967	6.0	1967	13	1983
19	0.67	2010	7.0	2010	13	1983
20	0.17	1981	1.2	1963	13	1983
21	0.62	1964	3.0	1973	13	1983
22	1.07	1964	4.5	1971	13	1983
23	0.59	1982	2.0	1979, 2012	13	1982, 1983
24	0.52	1959	5.5	2014	13	1983
25	0.72	2008	7.0	2008	17	2008
26	0.24	1955	2.6	1968	16	2008
27	0.27	1964	2.7	1964	16	2008
28	0.48	2005	4.1	1972	16	2008
29	0.51	1992	8.0	1992	18	1992
30	0.29	1977	4.0	1977, 1981	18	1992
31	0.37	2004	4.0	2004	18	1992

This page left intentionally blank.

APPENDIX D: NOAA INL WEATHER CENTER

The Field Research Division developed a NOAA INL Weather Center (NIWC) web page (Fig. D-1). The web page URL is http://niwc.noaa.inel.gov/. This one-stop weather web page has been designed to simultaneously provide "INL site specific" meteorological information to both emergency and daily operations managers.

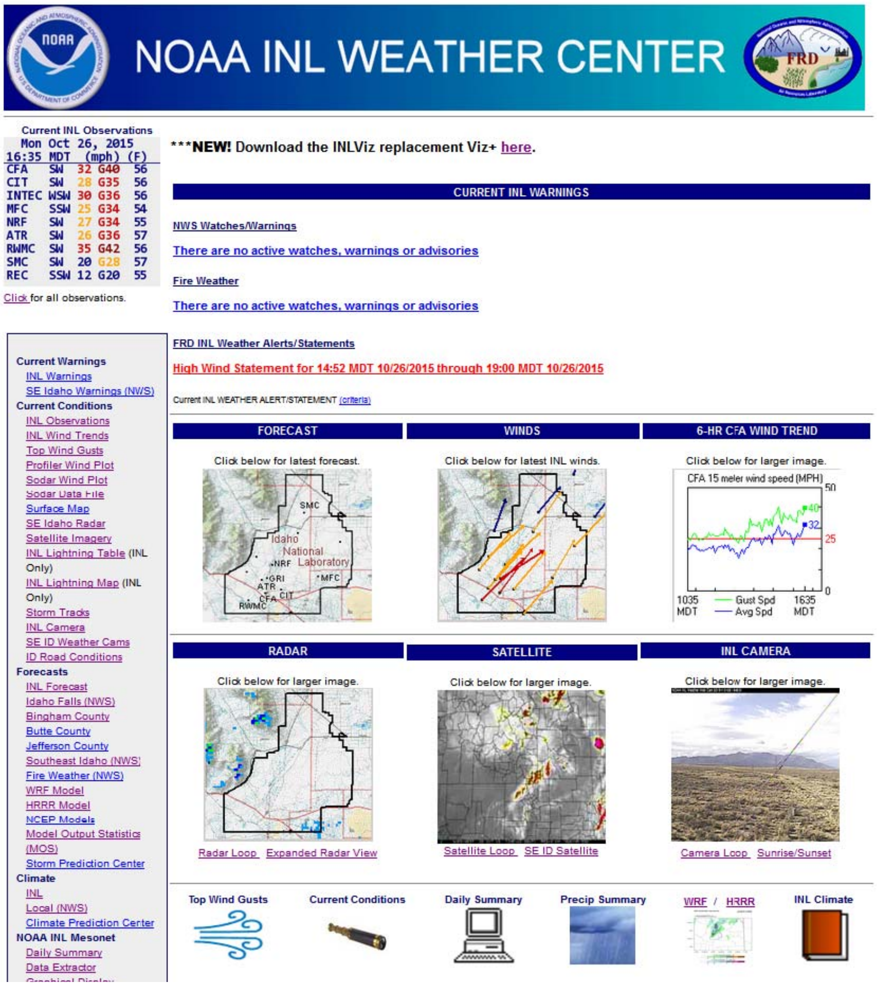

NOAA INL WEATHER CENTER

Current INL Observations

```
  Mon Oct 26, 2015
16:35 MDT  (mph) (F)
CFA   SW  32 G40  56
CIT   SW  28 G35  56
INTEC WSW 30 G36  56
MFC   SSW 25 G34  54
NRF   SW  27 G34  55
ATR   SW  26 G36  57
RWMC  SW  35 G42  56
SMC   SW  20 G28  57
REC   SSW 12 G20  55
```

Click for all observations.

***NEW! Download the INLViz replacement Viz+ here.

CURRENT INL WARNINGS

NWS Watches/Warnings

There are no active watches, warnings or advisories

Fire Weather

There are no active watches, warnings or advisories

FRD INL Weather Alerts/Statements

High Wind Statement for 14:52 MDT 10/26/2015 through 19:00 MDT 10/26/2015

Current INL WEATHER ALERT/STATEMENT (criteria)

Figure D-1. Snapshot of the NOAA INL Weather Center web page.

The highlight of the weather page is the presentation of severe weather hazard information. Weather watches, warnings, and advisories issued by the National Weather Service (NWS) in Pocatello are displayed at the top of the page under the "Current INL Warnings" section. However, since the INL forecast zone covers all of the Upper Snake River Plain, some warnings may not always apply to or be relevant to the INL. Therefore, FRD issues other weather alerts and statements to give additional weather information specific to INL needs or when no watch, warning, or advisory is issued by the Pocatello NWS. These INL weather alerts and statements are also displayed under the "Current INL Warnings" section. The NWS issues watches and warnings 24 hours a day, 7 days a week while FRD-issues weather statements or alerts only during normal FRD working hours. A list of current weather alerts and criteria can be found on the website.

Six large thumbnail images located beneath the "Current INL Warnings" section display popular INL related weather products. These thumbnails include a link to the INL weather forecast, a plot of the NOAA/INL Mesonet wind vectors, a plot of the wind speed trends for the last 6-hours, an INL site-specific weather radar image, the SE Idaho satellite image, and the current image of the INL weather camera. These thumbnail images give emergency and daily operations managers a glance of the overall weather across the site. Each of the images can be enlarged for more detail and easier viewing.

The web page automatically refreshes every 5-minutes to keep weather watches, warnings, statements, alerts, and images current.

Other INL related and general weather information is available in the menu on the left-hand side of the NIWC page and is available at the click of a mouse button. Some of these products are current observations that include a lightning map and table (only available to INL Internet users), links to NWS zone and weather forecast models, INL climate information, NOAA/INL Mesonet data, and weather safety information.

Many positive comments have been received from the INL emergency managers. The new page will continue to undergo improvements, updates, and additions over the coming months.

APPENDIX E: NOAA INL MESONET INSTRUMENTATION

Figure 1. Example NOAA INL Mesonet station layout, with the addition of the community monitoring station kiosk (foreground) on the Idaho Falls Greenbelt at the John's Hole Bridge and Forebay.

1. Wind Speed - Wind speed is measured using a 3-cup anemometer. Most cup anemometers consist of three (or more) hemispherical cups mounted on a vertical shaft. The difference in wind pressure from one side of a cup to the other causes the cups to spin about the shaft. The rate at which they rotate is directly proportional to the speed of the wind measured in miles per hour.

Wind speed gust - The wind gust is the highest 3-second wind speed average measured at the tower during the last five minutes.

Wind Chill - Is a measurement of how much heat is lost by your body based on the current temperature and wind speed.

2. Wind Direction - Wind direction is measured with an instrument called a wind vane. The vane always points into the wind and always gives the wind direction in compass degrees ***from*** which the wind is blowing.

3. Top Temperature - The temperature is measured using a thermocouple placed inside a metal housing (aspirator). This housing provides aspiration and shielding to eliminate the effects of radiative heating and cooling. The temperature is measured at two heights on the tower to provide information necessary to calculate the stability of the atmosphere.

4. Pyranometer - The pyranometer measures the electromagnetic radiation emitted by the sun or solar radiation. It is measured using solar cells that collect sunlight and converts it into electrical energy measured in watts per meter squared.

5. 6 - Foot (2 m) Temperature - The temperature is measured using a precision platinum resistance sensor placed inside a metal housing (aspirator). This housing provides aspiration and shielding to eliminate the effects of radiative heating and cooling. The temperature at 6 feet (2 m) is a true air temperature without the effects of radiative and convective heating and cooling. The temperature is measured at two heights on the tower to provide information necessary to calculate the stability of the atmosphere.

Relative Humidity - Sensors also located inside the metal housing (aspirator) measure the amount of moisture in the air. The amount of moisture in the air versus how much the air could hold at the current temperature is called relative humidity.

Dew Point Temperature - The humidity sensor's output is used to calculate the temperature at which the current moisture in the air would condense to form dew.

6. Heated Tipping Bucket Rain Gauge - Rain and snow is collected using a heated tipping bucket rain gauge. When the amount of water equivalent to 0.01 inch of precipitation has been collected in the bucket, it tips over emptying the bucket. The accumulated precipitation in a given time period is calculated from the number of tips.

7. Weighing Rain Gauge - Rain gauge used to measure the amount of precipitation based on its weight. This rain gauge is setup temporarily only at the Idaho Falls station.

8. Pressurized Ionized Chamber (PIC) - Nuclear radiation in the form of gamma rays is measured using a high-pressurized ion chamber. The PIC is capable of measuring background levels of radiation in the environment as well as additional contributions from manmade activities. The units for the measurement of gamma radiation are micro-Roentgens (μR) per hour on the number of ionizations in the air that occur during an hour-long period. The PIC is owned and maintained by the State of Idaho.

9. Electronics Box - The electronics box, located on the tower behind the HiVol, contain the datalogger and barometric pressure sensor. The datalogger collects data from the meteorological

instrumentation and transmits it via radio back to the ARLFRD office storage computers.

Barometric Pressure - The barometric pressure is measured in inches of mercury. The values are reported in actual pressure. Local weather reports will often convert the actual pressure to adjusted sea-level measured values.

10. High Volume Air Sampler (HiVol) - An auxiliary air sampler that is capable of drawing large quantities of air through a particulate filter is placed on selected monitoring towers. The high volume air sampler can be activated remotely in the unlikely event that an accidental release occurs at the INL facility. By sampling large quantities of air over a short period of time, the ability to detect low-level radioactivity in the atmosphere is increased. In essence, the larger quantity of air drawn, the lower the measurement sensitivity becomes.

11. Community Monitoring Station (CMS) kiosk- Several stations, called Community Monitoring Stations (CMS), are sited at schools and other places frequented by the public to enhance relations with the local communities. The CMS stations include a walk-up kiosk that displays current meteorological parameters and describes each of the measured variables. These stations are located in Terreton, Big Lost River Rest Area, Fort Hall, and Idaho Falls.

Instruments not shown

Air Sampler - Particulate matter in the atmosphere is collected by an air sampler that is operated continuously around the clock. Each week the filter used to collect and retain the particulate matter is removed from the sampler and exchanged with a new filter. The used filter is sent to a laboratory where it can be analyzed for the gross or total amount of radioactivity collected from the atmosphere at this location. Air samplers are operated at several locations throughout southeast Idaho to evaluate the air quality both from the natural contributions of background sources and any manmade sources. These air samplers are not owned, maintained or operated by NOAA.

INSTRUMENT SPECIFICATIONS

Met One Instruments, Inc. Model 010C - Wind Speed Summary

Maximum Operating Range:	0 to 125 mph (0 to 56 m s^{-1})
Starting Speed:	0.6 mph (0.27 m s^{-1})
Calibrated Range:	0 to 100 mph (0 to 50 m s^{-1})
Accuracy:	±1% or 1 mph (0.45 m s^{-1})
Temperature Range:	-58°F to +185°F (-50° C to +85° C)
Response:	Distance Constant less than 5 feet (1.5 meters)* of the flow

* The distance traveled by the air after a sharp-edged gust has occurred for the anemometer rate to reach 63% of the new speed.

Met One Instruments, Inc. Model 020C - Wind Direction (Azimuth) Summary

Azimuth:	0 to 360°
Threshold:	0.6 mph (0.27 m s^{-1})
Linearity:	±0.5% of full scale
Accuracy:	±3°
Damping Ratio:	0.4 to 0.6
Delay Distance:	less than 3 ft. (0.91 m)
Temperature Range:	-58°F to +185°F (-50° C to +85° C)

Campbell Scientific Inc. Model HMP45C - Temperature and Relative Humidity Probe Summary

Temperature Sensor Specifications

Temperature and Measurement Range:	-40°F to +140°F (-40° C to +60° C)
Temperature Accuracy:	±0.9°F (0. 5° C)

Relative Humidity Sensor Specifications

Relative Humidity Measurement Range:	0 to 100% non-condensing
Accuracy at 68° F (20° C):	±2% RH (0 to 90% Relative Humidity) ±3% RH (90 to 100% Relative Humidity)
Temperature Dependence of Relative Humidity Measurement:	±0.05% RH/° C
Typical Long Term Stability:	Better than 1% RH per year

Rotronic Model HC2S3 - Temperature and Relative Humidity Probe Summary

Temperature Sensor Specifications

Temperature and Measurement Range:	-58°F to +212°F (-50° C to +100° C)
Temperature Accuracy:	±0.63°F (0. 35° C)

Relative Humidity Sensor Specifications

Relative Humidity Measurement Range:	0 to 100% non-condensing
Accuracy at 73.4° F (23° C) :	±0.8%
Typical Long Term Stability:	<1% RH per year

Campbell Scientific Inc. Model 076B - Fan Aspirated Radiation Shield Summary

Errors Reduced:	< 0.05° F (0.028° C)

LICOR Model LI200X - PYRANOMETER Summary

Range	0 to 3000 m W $^{-2}$
Stability:	<± 2% change over a 1 year period
Response Time:	10 µs
Cosine Correction:	Cosine corrected up to 80° angle of incidence
Operating Temperature	-40° + 149°F (-40 to +65° C)
Temperature Dependence:	0.15% per °C
Relative Humidity:	0 to 100%
Accuracy:	Absolute error in natural daylight ±5% max; ±3% typical
Sensitivity:	0.2 kW $^{-2}$ mV^{-1}
Linearity:	Maximum deviation of 1% up to 3000 W $^{-2}$

Setra Systems Model 270 - Barometric Pressure Summary

Range:	800 to 1100 hPa/mb
Accuracy:	±0.05% FS or 0.55 mb

Vaisala Model PTB101B - Barometric Pressure Summary

Range:	600 to 1060 hPa/mb
Accuracy:	±0.5% FS ±6mb @ -40 to 140° F (-40 to 60° C)

Friez Engineering Company Model 7405H - Tipping Bucket Rain Gauge Summary

Accuracy: ±2% to 2" (5.08 cm) per hour
±4% to 10" (25.4 cm) per hour
Sensitivity: 0.01 inch (0.25 mm) per tip

Met One Model 385 Tipping Bucket Rain Gauge Summary

Accuracy: ±0.5% < 0.5" (1.3 cm) per hour
±2.0% < 3.0" (7.6 cm) per hour
Sensitivity: 0.01 inch (0.25 mm) per tip

Campbell Scientific Model TE525WS Tipping Bucket Rain Gauge Summary

Accuracy: ±1.0% up to 2" (5.08 cm) per hour

Campbell Scientific Model SR50 Snow Depth Summary

Accuracy: 0 to 2.34 ft. (0 to 0.72 m)

Accuracy: ±0.39" (1 cm)